

Nonlocal Torque Coupling in Disk Galaxies: A Continuum Framework for Interpreting Rotation Curves

Ridwan Sakidja*, Armita Dutta

Dept. of Physics, Astronomy and Materials Science, Missouri State University, USA

Justus Lau

Dept. of Physics and Astronomy, Heidelberg University, Germany

* Corresponding author (ridwansakidja@missouristate.edu)

Abstract

Observed galactic rotation curves rise, bend, and remain flat at radii where a purely baryonic Newtonian potential predicts declining velocities. The conventional interpretation introduces non-luminous dark matter to supply the missing rotational support. Here we propose an alternative dynamical architecture based on rotational coherence transmission. In this framework the stellar disk is treated not as a set of mechanically isolated Keplerian annuli but as a continuum of energy-coupled shells capable of inheriting, transmitting, and eventually saturating rotational coherence from inner regions.

From this premise we derive three scale-free, falsifiable observables, namely the **Curl Index**, the **Fractional Uplift**, and the **Surplus Index**, quantify torque inheritance, rotational energy surplus, and radial coherence export. These indices can be computed directly from observed rotation curves without invoking additional mass. Applying the framework to the full SPARC database, we find that galaxies cluster into three dynamical regimes predicted by the model. The structured scaling of outer rotation curves is not explained by strictly local baryonic dynamics but follows naturally from nonlocal torque transport.

This particular work concerns only the dynamical inference drawn from galactic rotation curves. It does not address cosmological evidence for dark matter from lensing, CMB anisotropies, or large scale structure. The framework is therefore offered as a galactic-scale dynamical alternative to the enclosed-mass interpretation.

1. Introduction

The standard explanation for flat galactic rotation curves is the presence of extended dark matter halos. This framework successfully reproduces observed velocities but does so by introducing a non-luminous mass component whose microscopic identity remains unknown after more than five decades of experimental and observational searches. In practice, constraining dark matter halo profiles at the galactic scale is challenging, as discrepancies between prediction and measurement can often be accommodated by adjusting halo parameters within their plausible ranges. This work explores whether such adjustments might be obviated by a more complete treatment of baryonic disk dynamics.

The empirical foundation of the rotation-curve problem itself is not in dispute. Seminal observations by Rubin, Ford, and Thonnard[1] established that disk galaxies exhibit rotation curves that remain flat or

continue rising well beyond their optical extents. The subsequent interpretation of these measurements as evidence for large reservoirs of unseen mass, however, relies on an additional dynamical assumption: that the observed mean azimuthal velocity at each radius may be identified with a local circular velocity determined solely by the enclosed mass. This identification implicitly treats each radius as mechanically isolated, with no transfer of angular momentum or rotational energy between neighboring annuli except through the local gravitational field. While historically natural, this assumption is rarely examined and may be overly restrictive.

The question addressed in this work is therefore narrow and specific: whether the apparent need for dark matter on galactic scales arises, at least in part, from a mechanical blind spot in the classical interpretation of disk dynamics. Importantly, this issue does not concern the observations themselves, but the dynamical closure imposed when interpreting them.

Observations and theory alike indicate that real disks are not mechanically isolated systems. Spiral patterns maintain phase coherence across tens of kiloparsecs. Bars redistribute angular momentum throughout the disk. Density waves, wakes, and resonant structures propagate torque and information non-locally. These phenomena demonstrate that disk galaxies behave as gravitationally coupled continua rather than as collections of independent circular orbits. Motivated by these facts, this paper develops a constrained and falsifiable framework based on the idea that rotational coherence can be transmitted non-locally within the disk, supplying additional rotational support in outer regions without modifying gravity or introducing new mass components.

The approach is grounded in three principles:

1. **Coherence transmission rather than modification of gravity.**
The mechanism operates entirely within Newtonian dynamics and established disk physics.
2. **Scalar diagnostics rather than adjustable parameters.**
The model introduces falsifiable indices that quantify rotational uplift and radial structure.
3. **Direct comparison with observational data.**
Predictions are tested against the full SPARC database[2] rather than hypothetical idealized curves.

2. Context and Positioning Within Established Galaxy Dynamics

The standard interpretation of disk–galaxy rotation curves assumes a strictly local relation between the circular velocity and the enclosed baryonic mass. In this picture, the disk is treated as a sequence of dynamically isolated test masses, where the equilibrium speed at radius R is given by

$$v_{\text{circ}}^2(R) = R \frac{\partial \Phi(R)}{\partial R}, \quad (1)$$

where $\Phi(R)$ is determined solely by the baryonic mass interior to R . Under this assumption, any excess of the observed velocity $v_{\text{obs}}(R)$ over $v_{\text{circ}}(R)$ is attributed to additional unseen mass. This methodology originates from classical disk models [3], is formalized in standard texts such as *Galactic Dynamics* [4], and underlies the historical inference of dark matter [5], [6].

However, this assumption of local isolation is neither required by Newtonian gravity nor consistent with the kinetic description of stellar disks. A collisionless galaxy is governed not by a set of independent

orbits but by the Vlasov–Poisson system [7], which describes the full phase-space evolution of stars under their collective gravitational field:

$$\frac{\partial f}{\partial t} + \mathbf{v} \cdot \nabla_x f - \nabla_x \Phi \cdot \nabla_v f = 0, \quad (2)$$

$$\nabla^2 \Phi = 4\pi G \int f d^3 v. \quad (3)$$

The Vlasov equation specifies how the phase-space density $f(\mathbf{x}, \mathbf{v}, t)$ is transported along stellar trajectories, while the Poisson equation enforces a global coupling between all radii through the gravitational potential. Because $\Phi(\mathbf{x})$ depends on the full mass distribution, the gravitational field cannot be assigned to any locally isolated annulus. This nonlocal coupling is absent in ring-isolation treatments and is precisely what enables collective dynamical responses.

Such collective behavior is well established observationally and theoretically, appearing through spiral density waves transmitting angular momentum [8], [9], swing amplification coupling adjacent annuli [10], bar-driven resonances redistributing angular momentum over kiloparsec scales [11] [12], gravitational wakes and dynamical friction [13], and radial migration without heating [14]. These processes are direct consequences of the Vlasov–Poisson dynamics and cannot occur in models that treat annuli as dynamically independent.

Within this kinetic framework, the angular-momentum surface density inside cylindrical radius R is obtained directly from the Vlasov distribution (see Supplementary A). With specific angular momentum $\ell = Rv_\phi$,

$$L(R, t) = \int R v_\phi f d^3 v dz. \quad (4)$$

Since R is independent of all velocity coordinates and of z , this may be written as

$$L(R, t) = R \int v_\phi f d^3 v dz. \quad (5)$$

Defining the surface density

$$\Sigma(R, t) = \int f d^3 v dz, \quad (6)$$

and the mean azimuthal velocity

$$\langle v_\phi \rangle(R, t) = \frac{1}{\Sigma(R, t)} \int v_\phi f d^3 v dz, \quad (7)$$

the angular-momentum surface density becomes

$$L(R, t) = \Sigma(R, t) R \langle v_\phi \rangle. \quad (8)$$

In the axisymmetric limit of nearly circular motion, $\langle v_\phi \rangle = R\Omega(R, t)$, yielding

$$L(R, t) = \Sigma(R, t) R^2 \Omega(R, t), \quad (9)$$

which is the familiar axisymmetric expression recovered as a special case of the full Vlasov moment.

Multiplying the Vlasov equation (2) by Rv_ϕ and integrating over velocity space gives an *exact evolution equation* for the angular-momentum surface density (see Supplementary A for the full derivation),

$$\frac{\partial L}{\partial t} = -\frac{1}{R} \frac{\partial}{\partial R} [R F_L(R, t)], \quad (10)$$

where the radial flux of angular momentum is

$$F_L(R, t) = \int R v_\phi v_R f(R, v_R, v_\phi, v_z, t) d^3 v dz. \quad (11)$$

Equation (10) is already the complete torque law for a collisionless disk. No source term appears. All changes in $L(R, t)$ arise solely from the *radial divergence of the Vlasov flux* F_L .

Integrating Eq. (10) over the full disk,

$$\frac{d}{dt} \int_0^\infty L(R, t) dR = - \int_0^\infty \frac{1}{R} \frac{\partial}{\partial R} [R F_L] dR, \quad (12)$$

and assuming vanishing boundary flux,

$$\lim_{R \rightarrow 0} RF_L = \lim_{R \rightarrow \infty} RF_L = 0, \quad (13)$$

yields

$$\frac{dJ_{\text{tot}}}{dt} = 0, \quad J_{\text{tot}} \equiv \int_0^\infty L(R, t) dR. \quad (14)$$

Thus, *total angular momentum is strictly conserved*, as required for a Hamiltonian Vlasov–Poisson system. The flux divergence redistributes angular momentum in radius but does not create or destroy it.

Although the radial integral of Eq. (10) vanishes, the local divergence

$$-\frac{1}{R} \frac{\partial}{\partial R} [R F_L(R, t)] \quad (15)$$

need not vanish pointwise. Regions with $\partial_R(RF_L) < 0$ *lose angular momentum*, while regions with $\partial_R(RF_L) > 0$ *gain angular momentum*. Because the specific angular momentum scales as $\ell = Rv_\phi$, a small transfer from the inner disk can generate a large rotational response at large radius, where the energetic cost is low. The rotational kinetic-energy surface density,

$$E_{\text{rot}}(R, t) = \frac{1}{2} \Sigma(R, t) R^2 \Omega^2(R, t), \quad (16)$$

therefore evolves through *spatial redistribution* rather than creation of energy. Quantities such as the rotational surplus measure where conserved rotational energy resides within the disk, not whether additional energy has been introduced. Equation (10) thus reframes the classical torque picture [15], [16], [17] as a transport law: angular momentum growth and redistribution arise from the divergence of a measurable Vlasov flux rather than from localized source terms. Any approximation enforcing $F_L = 0$ deletes this transport channel and collapses the dynamics back to the isolated-ring limit. Once non

axisymmetric structure is admitted, correlated radial and azimuthal motions activate this channel, enabling outward coherence transmission without invoking additional mass components.

Physically, this expresses the fact that the specific angular momentum $R\nu_\phi$ is transported across radius by stars with nonzero radial velocity ν_R . Because eq. (10) is obtained as a direct moment of the Vlasov equation, it is exact and applies to any self-gravitating collisionless system—stellar disks, collisionless plasmas, or more general Vlasov–Poisson media. This torque-divergence structure is also an instance of a broader class of transport-driven phenomena discussed in the Curvature–Transport Correspondence (CTC), which interprets such flux divergences as the local drivers of dynamical curvature (see [18]). As a consequence, any approximation that enforces $F_L = 0$ therefore deletes this transport channel and collapses the dynamics back to the isolated-ring limit (see **Supplementary A**).

To further support this interpretation, we examine the SPARC dataset [2] for signatures that would not be expected in the isolated annulus limit, where $F_L = 0$. In that limit, the torque density vanishes identically, and no radial coupling exists between annuli. Consequently, both of our diagnostics—Surplus Index and Curl Index—would be (close to) zero for every galaxy. Instead, SPARC galaxies populate structured, low-dimensional manifolds in uplift space (Surplus Index vs. Curl Index), demonstrating systematic, radius-spanning coherence that cannot arise in any model with $F_L = 0$. These nonzero values are fully consistent with Vlasov–Poisson dynamics, which naturally predicts radial transport and collective modes, but they are absent from enclosed-mass formulations.

The present work translates these classical Vlasov principles into a direct explanation of observed rotation-curve behavior. Mathematically, it differs from prior treatments in three essential ways:

1. Nonlocal coupling is retained.
No closure is imposed that would force $F_L = 0$; radial transport remains operative at all radii.
2. A transmission factor encodes F_L -driven coherence between annuli.
This restores the continuum character of the Vlasov torque law and allows uplift to propagate outward with decreasing amplitude.
3. Two empirical diagnostics—Surplus Index and Curl Index—quantify uplift and radial structure.
Both must vanish in a fully local disk, yet SPARC galaxies do not. Their nonzero structure is a direct observational signature of nonlocal angular-momentum flow.

Together, these elements generate the observed three-regime response of disk galaxies: a linear inheritance region, a nonlinear bending region, and a saturated outer plateau. These regimes emerge naturally from the structure of F_L -mediated torque transport and require no modification of gravity or mass.

For completeness, we emphasize that the standard dark matter halo framework [19] and MOND [20] has been the foundational benchmarks for explaining rotation curves. Both numerically succeed by altering the mass distribution or the force law. In this study, our model remains strictly Newtonian and attributes the observed phenomenology to coherence transmission and angular-momentum transport inherent in the dynamical architecture of rotating disks.

2.1 Transport versus Mass Augmentation

At this point it is important to clarify how the present framework differs procedurally from dark matter- and MOND-based approaches. Many dark matter models implicitly rely on **energy and angular-momentum redistribution** as a central dynamical ingredient. In numerical simulations, dark matter halos are not passive mass reservoirs; they exchange angular momentum with the disk, absorb torques from non axisymmetric structure, and provide long-range dynamical coupling that stabilizes rotation over secular timescales.

The framework developed here assigns this transport role to the visible collisionless disk itself, through the angular-momentum flux that arises naturally in 7. SPARC Diagnostics, Correlations, and the Failure of Radius as an Organizer

We test the transmission framework using all 175 late-type galaxies in the SPARC Rotmod_LTG sample [2] (see **Supplementary E, F and G**). For each galaxy we reconstruct the baryonic circular velocity and compute three diagnostics derived directly from the model: the Curl Index, measuring torque contrast; the mean uplift, measuring fractional velocity enhancement; and the Surplus Index, measuring fractional excess rotational energy in the outer disk. We also extract characteristic radii, including the outermost measured radius R_{\max} , to test whether uplift is controlled by physical extent.

Here, the SPARC velocities are reconstructed using a tilted-ring, axisymmetric model. Mild non-circular motions—such as warps, oval flows, asymmetric drift, or small inclination uncertainties—can alter the local slope of the baryonic curve. These effects tend to reduce the apparent torque contrast and therefore bias the Curl Index downward rather than produce spurious high-curl structure. The fact that the empirical Curl–Surplus distribution displays a strong, coherent sequence despite these conservative biases indicates that the transport signal should be interpreted as a lower bound.

(a) Radius plots.

When Surplus Index and mean uplift are plotted against R_{\max} (Figures 1a and 2a), the SPARC galaxies show little systematic organization. Galaxies spanning more than an order of magnitude in size occupy overlapping ranges of surplus and uplift, and systems with nearly identical radii can differ strongly in both diagnostics. No monotonic relation between galaxy size and rotational enhancement is observed. This indicates that radius alone is not the controlling variable of outer-disk rotational support.

(b) Curl plots.

In contrast, when the same diagnostics are plotted against Curl Index (Figures 1b and 2b), the SPARC sample forms a highly structured sequence. At low curl ($\lesssim 1$), both surplus and uplift rise approximately linearly, corresponding to the linear inheritance regime. At intermediate curl ($\sim 2\text{--}5$), the trends bend: surplus continues to increase while uplift begins to flatten. At high curl ($\gtrsim 6\text{--}8$), Surplus Index settles into a stable band ($\sim 0.3\text{--}0.6$) while Curl Index spreads horizontally, indicating saturation of transmission.

The central empirical result is that **Curl Index, not radius, organizes rotational uplift in disk galaxies**. The SPARC sample is highly structured in curl space but essentially unorganized in radius space, exactly as expected if outer rotational support arises from torque-mediated coherence export rather than from purely radial mass augmentation.

The SPARC scaling relations identified by Ghari et al. (2019) [21] provide important statistical context. Within the present framework, these relations can be interpreted as observational signatures of torque-mediated coherence transmission: Curl Index parallels the baryon-induced acceleration correlation, while Surplus Index mirrors the core-density relation. The three-stage progression of inheritance, bending, and saturation reflects the same structured behavior observed in the SPARC sample.

Inner–Outer Energy Balance and the Absence of a Required Inner Deficit

In reference to Section 5.1, it is important to emphasize that the transmission framework does not require a clearly resolved inner deficit in the observed rotation curve. In practice, baryonic rotation curves are constructed relative to an inferred inner baseline that rarely corresponds to a true dynamical zero point. The innermost regions of disk galaxies are typically influenced by bulges, bars, beam smearing, finite spatial resolution, and uncertainties in mass to light ratios. Any early withdrawal of rotational coherence occurring at radii smaller than the observational core is therefore naturally absorbed into the reconstructed baryonic profile and does not appear as an explicit inner dip.

From an energetic standpoint, this behavior is expected. The rotational energy surface density is given by

$$E_{\text{rot}}(R) = \frac{1}{2} \Sigma(R) R^2 \Omega^2(R), \quad (17)$$

and for late type disks with approximately flat rotation curves, $\Omega(R) \approx v_0/R$. In this regime, the dominant radial dependence enters through the surface density $\Sigma(R)$. Because $\Sigma(R)$ declines exponentially, the cumulative rotational energy stored in the inner disk exceeds that of the outer disk by several orders of magnitude. As a result, only a percent level redistribution of inner rotational coherence is sufficient to generate the observed velocity excess at large radii.

In systems with extended radial coverage and high spatial resolution, a shallow inner deficit or transition region is sometimes observed. Its absence in most galaxies does not contradict the transmission picture. Rather, it reflects the fact that the energetic withdrawal required to support the outer disk is dynamically small and often occurs at radii below the observational core, where it is difficult to resolve observationally.

For a small subset of SPARC galaxies, the reported rotation velocities are systematically low at all measured radii. Such behavior is inconsistent with any physical disk equilibrium and is most naturally attributed to geometric or observational systematics, including inclination uncertainties, distance errors, asymmetric drift, or non circular motions associated with bars and spiral structure. Because these effects uniformly suppress the inferred rotation curve, these galaxies do not provide reliable constraints on dynamical models and are excluded from further analysis.

More generally, once non axisymmetric structure is admitted, angular momentum and energy transport arise naturally within the collisionless disk. The distinction between competing dynamical interpretations is therefore not whether transport is required, but where that transport is permitted to reside. In dark matter based models, the halo functions as the carrier of angular momentum and energy flow. In the present work, the same dynamical role is supplied by the stellar disk itself through nonzero phase space flux, without introducing additional mass or modifying gravity.

Accordingly, the present framework should be understood not as an alternative force law, but as a logically prior step. It asks whether the fully closed collisionless Vlasov Poisson dynamics of visible matter are sufficient to account for the observed rotation curves before assigning the required transport to an unseen component.

2.2. Distinction Between Circular Velocity and Mean Azimuthal Velocity

A crucial point often left implicit in rotation-curve modeling is that the baryonic circular velocity,

$$v_{\text{bar}}^2(R) = R \partial_R \Phi_{\text{bar}}, \quad (18)$$

is a *local equilibrium diagnostic* valid only in the limit where each annulus behaves as a dynamically isolated test ring. By contrast, the observed rotation curve measures the mean azimuthal velocity,

$$\langle v_\phi(R) \rangle = \Sigma^{-1}(R) \int v_\phi f(R, \mathbf{v}, t) d^3v, \quad (19)$$

which is a phase-space moment of the full distribution function. These two quantities are equal only when radial angular-momentum flux vanishes.

Taking the angular-momentum moment of the Vlasov equation yields

$$\frac{\partial L}{\partial t} = -\frac{1}{R} \frac{\partial}{\partial R} (RF_L), \quad (20)$$

where $F_L = \int R v_R v_\phi f d^3v$ is the radial flux of angular momentum. Dividing by ΣR and integrating in time gives

$$\langle v_\phi(R) \rangle = v_{\text{bar}}(R) + \frac{1}{\Sigma(R)R} \int^t \left[-\frac{1}{R} \frac{\partial}{\partial R} (RF_L) \right] dt', \quad (21)$$

showing explicitly that deviations between the observed velocity and the baryonic circular speed arise from the divergence of the angular-momentum flux. The resulting velocity uplift therefore reflects redistribution of conserved angular momentum rather than the presence of additional mass or modified gravity. This distinction explains how outer disks can exhibit velocities exceeding the baryonic circular expectation while remaining fully consistent with Newtonian dynamics and global energy conservation.

2.3. Why This Connection Has Not Been Emphasized in Rotation-Curve Modeling

Although the ingredients of nonlocal disk dynamics have long been established within galactic dynamics and kinetic theory, they have not traditionally been incorporated into the interpretation of galactic rotation curves. This reflects a historical separation between complementary research traditions rather than any deficiency in the underlying theory.

Rotation-curve analyses developed primarily within observational astronomy, where enclosed-mass constructions and halo fitting provided a practical phenomenology. Within this framework, discrepancies between baryonic predictions and observed velocities were naturally interpreted as evidence for additional mass, and disk galaxies were treated, to leading order, as collections of dynamically decoupled annuli.

In parallel, studies of bars, spiral structure, resonances, and secular evolution focused on collective behavior in collisionless disks, emphasizing wave–particle coupling, gravitational torques, and angular-momentum redistribution. In these analyses, rotation curves typically entered as background constraints rather than as primary dynamical diagnostics. As a result, the continuum transport structure implied by the Vlasov–Poisson system was not routinely applied to the interpretation of the observed circular velocity profile $v(R)$.

Formally, the enclosed-mass relation commonly used in rotation-curve modeling corresponds to a restricted subset of Vlasov–Poisson solutions in which the radial angular-momentum flux F_L vanishes. This limit describes an idealized, perfectly axisymmetric disk lacking nonaxisymmetric structure. While useful, it does not represent the generic behavior of real galactic disks.

The present work relaxes this restriction by retaining the angular-momentum flux term in the exact moment equation derived from the Vlasov equation. Writing the equation in cylindrical coordinates and multiplying by the specific angular momentum $l = Rv_\phi$ yields a conservation law in which F_L governs nonlocal angular-momentum transport. In disks hosting persistent or slowly evolving asymmetries, this flux is generically nonzero.

A related objection is that visible-matter–only models have already been tested and found insufficient, necessitating the introduction of dark matter. This conclusion follows only if the visible disk is evaluated under the restrictive assumption of vanishing angular-momentum flux, imposed implicitly through axisymmetry and isolated-annulus closures. When the resulting system fails to sustain the observed rotation, dark matter is introduced to supply the missing gravitational support and angular-momentum exchange. This procedure effectively introduces an external reservoir to supply transport that is suppressed by the imposed closure and therefore does not test whether the fully closed collisionless Vlasov–Poisson system of visible matter can self-consistently generate the required torque.

This distinction concerns the closure of the Vlasov–Poisson system rather than its use: standard treatments employ the same equations but close them by assigning the required transport to a dark matter component, whereas the present work tests whether that transport can arise self-consistently from the visible disk alone.

The broader context includes the extensive literature on secular evolution, reviewed comprehensively by Sellwood [12], in which bars, spiral density waves, and associated resonances redistribute angular momentum over long timescales. Secular evolution refers to the slow internal reconfiguration of a galaxy that is driven by nonaxisymmetric gravitational torques and is most efficient at the resonances first formalized by Lynden-Bell and Kalnajs [8]. These phenomena represent structured solutions of the Vlasov–Poisson system in which coherent asymmetries generate sustained gravitational torques. Classical work correctly demonstrated that resonances can transfer angular momentum and energy, but this was usually presented as a resonance-localized mechanism rather than as one instance of a more general continuum transport process. The transmission framework developed here is fully consistent with this classical picture and extends it by showing that any persistent or slowly varying asymmetry produces a nonlocal flux, even far from formal resonances. Secular evolution is therefore a well-established and important subset of the more general continuum coupling described in this work. The present model connects that transport directly to observable rotation-curve structure through the Surplus and Curl Indices, which serve as measurable projections of the underlying angular momentum flux F_L .

Taken together, this historical and geometric context shows that the dark matter paradigm emerged within a modeling framework that imposed restrictive geometric and kinetic closures on galactic disks, rather than from the demonstrated failure of the fully closed collisionless Vlasov–Poisson dynamics of visible matter.

3. Rotational Coherence Transmission

Classical rotation-curve analyses implicitly treat each radius as an isolated test particle responding only to the gravitational potential interior to it. While mathematically convenient, this picture neglects the fact that real galactic disks are mechanically connected systems. In a rotating disk, angular momentum, energy, and phase coherence can be redistributed across radius through internal torques, even in the absence of dissipation or external forcing.

To account for this, we introduce a rotational coherence transmission framework. In this picture, rotational support generated in the inner disk can be partially inherited by outer regions through non-local torque continuity. This transmission does not introduce a new force and does not modify Newtonian gravity. It represents the cumulative effect of established dynamical mechanisms—such as gravitational torques, shear responses, density-wave coupling, resonant interactions, and collisionless phase-space mixing—that redistribute angular momentum within disks but are typically omitted from rotation-curve modeling.

The model is implemented using a schematic radial construction that represents **accumulation**, not composition. The alternating radial response layers employed here do not correspond to physical gas, stars, or additional matter components. Instead, they encode different effective radial coherence response lengths within a collisionless system and serve as a bookkeeping device for how rotational coherence accumulates and propagates outward.

Within this framework, three generic dynamical behaviors emerge:

1. **Inner coherence sourcing.**

The central disk region, which is typically more rigidly rotating and dynamically dense, acts as a source of rotational coherence that can be exported outward.

2. **Gradual radial attenuation.**

The ability of outer regions to inherit coherence weakens with radius as mechanical coupling becomes less efficient. This decline is continuous rather than abrupt, reflecting structural connectivity rather than isolation.

3. **Saturation at large radius.**

Beyond a characteristic scale, outer regions cannot absorb additional inherited coherence linearly. The transmitted rotational support bends and approaches a plateau, preventing divergence of outer velocities and naturally producing flattened rotation curves.

This formulation preserves Newtonian gravity while incorporating a mechanically necessary ingredient: **non-local torque continuity in a rotating disk**. By allowing rotational coherence to accumulate and propagate across radius, the galaxy is treated not as a collection of independent annuli, but as a dynamically structured system capable of exporting rotational support outward without invoking additional mass components or modified gravity.

4. Justification for a Collisionless Gravitational Continuum Treatment

A common objection to coherence-based interpretations of disk kinematics is that a stellar disk is a collection of discrete stars and cloud complexes following individual orbits. This perspective motivates the standard ring-based rotation-curve method, in which each radius is treated as dynamically independent and responds only to the mass interior to it. Within that construction, any mismatch between baryonic prediction and observed velocity must be attributed to additional unseen mass. The assumption of locality is therefore imposed by the modeling choice rather than emerging from the disk's true dynamics.

At the dynamical scales relevant for galactic structure, this picture is *incomplete*. Although a disk is composed of discrete bodies, their orbits are not independent. Real disks host spiral arms, bars, molecular complexes, tidal wakes, and other non axisymmetric features that act as long-range gravitational couplers. These structures generate torques and transmit phase information across large radial intervals. The result is that a collisionless stellar disk behaves as a weakly coupled gravitational continuum, not as a set of isolated Keplerian rings. Coherent modes, such as spiral density waves, bar-driven resonances, and transient over-densities, enable coordinated angular-momentum exchange over global scales.

Such coupling gives rise naturally to the type of transmission behavior that produces the observed rotation-curve morphology. Inner material rotates more rapidly than outer material. In a model of isolated rings this shear has no dynamical consequence. In a disk supporting global modes, it becomes a driver of outward angular-momentum flow. Faster inner orbits exert torques on slower outer orbits, permitting coherence to propagate in the same way stresses propagate in elastic media. The canonical rotation-curve shape—linear rise, bending transition, extended flat regime—emerges from this nonlocal redistribution of angular momentum rather than from the gravitational influence of a hypothesized dark matter halo.

The continuum treatment used here is therefore not an analogy to fluid dynamics nor a phenomenological convenience. It reflects the fact that macroscopic disk kinematics cannot be deduced by summing the trajectories of individual stars. Once global asymmetry, self-gravity, and collective modes are acknowledged, the apparent conflict between discreteness and continuum behavior disappears. The continuum approach restores the dynamical processes that the traditional ring-segmented methodology eliminates by construction. A formal derivation of the angular-momentum transport hierarchy is provided in **Supplementary A**.

5. Rotational Energy Budget of Disk Galaxies

A central but often overlooked point in rotation-curve studies is that the inner disk contains an enormous surplus of rotational energy compared to what the outer disk requires to sustain its observed velocities. The relevant quantity is the rotational-energy surface density (from eq. 17)

$$E_{\text{rot}}(R) = \frac{1}{2} \Sigma(R) R^2 \Omega^2(R),$$

which depends not only on radius but on the joint behavior of the surface density and the angular frequency.

In real disk galaxies both the surface density and the angular frequency are strongly weighted toward the inner regions, and together they produce a very steep radial decline in rotational energy. The surface density follows an exponential profile, $\Sigma \sim e^{-R/R_d}$, which means that most of the mass is concentrated within the inner two or three scale lengths, while the outer disk contains only a few percent of the central surface density. At the same time, the angular frequency typically scales as $\Omega \sim 1/R$ once the rotation curve reaches its flat portion, so the inner disk also rotates much faster in terms of angular rate. Because the rotational energy surface density depends on the product $\Sigma R^2 \Omega^2$, these two trends combine to amplify the contrast: the surface density collapses exponentially, and the angular frequency decreases as $1/R$. The result is that the inner few scale lengths contain two to three orders of magnitude more rotational energy per unit area than the diffuse outer disk. Even though the outer disk can have nearly the same circular speed as the inner disk, *its much lower mass density and angular frequency make its rotational energy content extremely small by comparison.*

5.1. Numerical Illustration

The contrast between the inner and outer disk may be understood directly from the structure of the rotational-energy surface density from the equation (12). For a late-type disk with an approximately flat rotation curve, the angular frequency satisfies $\Omega(R) = v_0/R$. Substituting this form into the definition above *eliminates* the explicit dependence on R and yields $E_{\text{rot}}(R) = \frac{1}{2} \Sigma(R) v_0^2$, so that the rotational energy per unit area is proportional to the local surface density. With an exponential disk, $\Sigma(R) = \Sigma_0 \exp(-R/R_d)$, the surface density at 1 kpc remains high, $\Sigma(1) \approx 0.67 \Sigma_0$, whereas by 10 kpc it has fallen to $\Sigma(10) \approx 0.02 \Sigma_0$. The corresponding ratio $\Sigma(1)/\Sigma(10) \approx 37$ therefore gives the leading contribution to the energy contrast between these radii.

A second factor arises from the angular frequency prior to substitution. The exact expression for E_{rot} contains the combination $R^2 \Omega^2(R)$, which scales as $R^2(v_0^2/R^2) = v_0^2$. Although this cancellation is exact, it conceals the fact that the outer disk occupies a region where both R and Ω vary over large dynamic range. Evaluating the ratio of angular frequencies before simplification gives $\Omega(1)/\Omega(10) = 10$, so that the square of this ratio contributes a factor of 100. In the full expression,

$$\frac{E_{\text{rot}}(1)}{E_{\text{rot}}(10)} = \frac{\Sigma(1)}{\Sigma(10)} \frac{1^2}{10^2} \frac{\Omega^2(1)}{\Omega^2(10)}, \quad (22)$$

the factor $1^2/10^2$ cancels the factor 10^2 from the angular-frequency ratio, leaving

$$\frac{E_{\text{rot}}(1)}{E_{\text{rot}}(10)} \approx \frac{0.67}{0.02} \approx 37. \quad (23)$$

This ratio pertains to the comparison at single radii. When one integrates the rotational-energy surface density over the entire inner disk, where both $\Sigma(R)$ and $\Omega(R)$ remain large across several kiloparsecs, the cumulative energy exceeds that in the outer disk by *three to four orders* of magnitude.

The energetic requirement to raise the outer-disk velocity from the Newtonian expectation 120 km s^{-1} to the observed 200 km s^{-1} is correspondingly small. The fractional increase in the rotational energy at $R = 10 \text{ kpc}$ is

$$\frac{\Delta E}{E_{\text{rot}}} = \frac{200^2 - 120^2}{200^2} \approx 0.65, \quad (24)$$

yet the absolute value of this increment is *suppressed* by the very low surface density at large radii, giving

$$\Delta E_{\text{outer}} \sim 10^{-3} \Delta E_{\text{inner}}. \quad (25)$$

This expresses the essential result: *even a percent-level redistribution of the inner-disk rotational energy is more than sufficient to supply the entire outer disk*. This statement concerns the energy budget alone. Whether such support manifests as a dynamically admissible and stable rotation profile depends on how the transmitted torque reshapes the angular-momentum distribution and force balance in the disk, which is addressed by the transmission framework developed below.

5.2. Why Only the Inner Radii Require Strong Transmission?

This steep energy gradient has a crucial consequence: the amount of torque that must be transported outward decreases rapidly with radius. Since almost all rotational energy resides near the center, the transmission mechanism needs to operate efficiently only at small radii, where the reservoir is concentrated and non axisymmetric structures are strongest.

Beyond the inner disk, the energetic demand falls so sharply that even a weak, gradually diminishing flux of angular momentum is more than sufficient. The “mass” of rotational support that needs to be carried outward becomes progressively smaller, so *the channel can weaken by orders of magnitude and still maintain the observed outer-disk rotation*.

5.3. Implication: The Limitation Is Transmission, Not Energy

The constraint on outer-disk rotation therefore cannot be attributed to a lack of energy. The true bottleneck is how angular momentum and rotational coherence propagate from the inner disk to large radii. In the full Vlasov–Poisson system, *any non axisymmetric feature—spirals, bars, swing-amplified patches, bending modes, or gravitational wakes—naturally generates a nonzero angular-momentum flux $F_L \neq 0$* (See Supplementary B). As long as this flux is not destroyed by strong shocks or rapid phase mixing, it transports torque outward and supports the outer disk. In this interpretation, the transmission mechanism introduced in this work is not an additional energy source but it is originated from the vast inner-disk rotational reservoir to be redistributed rather. This phenomena won’t be numerically observed if it is artificially trapped behind the closure $F_L = 0$ through simplified and isolated-ring treatments.

Thus, a flat outer rotation curve is a *transmission outcome, not an energetic anomaly*. Treating the disk as a gravitationally connected continuum, rather than a set of isolated rings, leads naturally to the conclusion that outer-disk flatness emerges from the internal structure and continuity of the Vlasov–Poisson system.

5.4. Relation to Radially Declining M/L Models

Sipols and Pavlovich (2020) [22] recently suggested that the rotation-curve discrepancy could be removed if the stellar mass-to-light ratio decreases with radius. Their proposal is that the outer disk contains faint stellar populations that standard photometry does not fully capture. This correctly emphasizes an important observational fact: the surface density of real disks drops steeply with radius, so the outer regions are diffuse and energetically weak.

The present framework accepts this observational reality but interprets it differently. The decisive factor is the *rotational-energy budget*. The inner two or three scale lengths contain orders of magnitude more rotational energy than the outer disk ever needs. A very small outward transfer is already sufficient to maintain a flat rotation curve, regardless of whether additional faint stars exist in the outskirts. In other words, the fundamental issue is not how the mass is assigned, but how a small fraction of the inner rotational reservoir is transmitted outward.

Such transmission requires a physical mechanism, which mass reassignment alone does not provide. Real galaxies supply that mechanism through nonaxisymmetric structure such as spiral arms, bars, warps, wakes, and lopsided modes. These features naturally generate a nonzero angular-momentum flux and allow rotational coherence to propagate across radii. In this view, the radial decline in surface density sets the demand for support, while the flux of angular momentum provides the supply. Outer rotation curves are therefore not anomalies in mass accounting but dynamical consequences of coherence transferred from the inner disk.

6. Transmission Model with Alternating Coupling Layers

We introduce a phenomenological transmission model designed to represent how **rotational coherence and energy** propagate through a heterogeneous galactic disk. Rather than treating the disk as uniform, we represent its radial structure using alternating shells that act as **distinct coupling phases** in an energy-transfer chain.

These shells are **not physical components** and do not correspond to specific material species. Instead, they provide a coarse-grained representation of the fact that different radial zones inherit and transmit rotational coherence with different efficiencies. Each layer functions either as an efficient conduit or as a partial barrier for torque-driven energy transfer, depending on its position in the radial chain.

The alternation is therefore **purely functional**. It encodes heterogeneous coupling strengths within a stratified disk, not the presence or dominance of any particular baryonic component. This distinction is essential: the observed redistribution of rotational energy cannot be explained by the mass budget of any single component, but instead reflects how non axisymmetric torques export a small fraction of the large inner energy reservoir outward.

As developed in the main text and in the supplementary Vlasov–Poisson derivation, the true driver of transmission is the **non axisymmetric torque field** (see Supplementary B). The alternating-layer representation is a geometric abstraction of this mechanism: it discretizes the radial disk into zones of alternating coupling efficiency through which rotational coherence is inherited, attenuated, or deposited.

A pedagogical implementation of this alternating-coupling scheme, intended for teaching and reproducibility, is provided in the accompanying GitHub repository.

6.1 Alternating geometric coupling $k(r)$

Each radial shell is assigned a geometric transmission coefficient with **two distinct decay scales**, representing alternating high- and low-coupling phases:

$$k(r_i) = \begin{cases} \exp(-r_i/R_{k,\text{high}}), & i \text{ even (high-coupling)} \\ \exp(-r_i/R_{k,\text{low}}), & i \text{ odd (low-coupling)} \end{cases} \quad (26)$$

High-coupling layers decay slowly (large $R_{k,\text{high}}$), while low-coupling layers decay rapidly (small $R_{k,\text{low}}$). The resulting alternating pattern approximates the heterogeneous susceptibility of real disks to torque inheritance without attributing that behavior to any specific material carrier.

To avoid numerical artifacts and to reflect the smoothness of real disks, we apply a mild three-point smoothing:

$$k_i \rightarrow \frac{1}{4}k_{i-1} + \frac{1}{2}k_i + \frac{1}{4}k_{i+1}. \quad (27)$$

The innermost region is treated as a rigidly locked core,

$$k(r < r_{\text{core}}) = 1, \quad (28)$$

consistent with the near-perfect coupling expected in the bulge-dominated inner disk, where rotational coherence is generated and initially stored.

6.2 Curl-stress and the three-stage transmission map

Transmission efficiency is not controlled by geometry alone. The disk's ability to **inherit additional rotational energy** depends on a local curl-stress amplitude,

$$S_{\text{raw}}(r) = \left| \frac{1}{r} \frac{d}{dr} [r v_N(r)] \right|, \quad (29)$$

which corresponds to the z-component of the curl of the velocity field for an axisymmetric flow. This quantity contains the same combination of velocity gradients that appear in the Oort constants and in the epicyclic frequency.

Physically, S_{raw} measures the local differential-rotation stress: it is weak where the flow bends gently and strong where the disk twists sharply. We normalize this field to obtain a dimensionless stress measure,

$$S(r) = \frac{S_{\text{raw}}(r)}{\max_r S_{\text{raw}}(r)} \in [0,1]. \quad (30)$$

The response of the disk to incoming rotational coherence is modeled by a three-stage transmission map,

$$T(S) = T_{\text{max}} \tanh \left(\frac{S}{S_0} \right). \quad (31)$$

At low curl, $T(S) \approx S$, and coherence is inherited linearly.

At intermediate curl, the response bends as the disk approaches its local absorption limit.

At high curl, $T \rightarrow T_{\text{max}}$, reflecting saturation: the disk cannot absorb additional transmitted coherence.

The transmission law $T(S)$ should be understood as an effective, coarse-grained response rather than a new dynamical interaction. It *does not modify the Poisson equation or introduce any additional gravitational source*; instead, it constrains the efficiency with which existing non axisymmetric torque flux is transmitted once finite absorptive capacity is reached. From a kinetic-theory perspective, the saturating hyperbolic-tangent form represents the minimal response consistent with collisionless dynamics under energetic constraints, and emerges naturally from a Lagrangian extension of the Vlasov–Poisson system (**Supplementary C and D**).

6.3 Effective transmission coefficient

The effective local transmission rate is the product of geometric coupling and curl-limited response:

$$k_{\text{eff}}(r) = k(r) T(S(r)). \quad (32)$$

A radial zone therefore transmits rotational energy efficiently only if:

1. it lies in a high-coupling phase of the radial chain, and
2. its local curl-stress remains below the saturation threshold.

Low-coupling phases, large radii, and high-curl zones naturally suppress transmission. This alternating, radius-decaying, stress-regulated structure constitutes the core transmission rule of the model.

6.4 A simplified energy-lock surrogate

To evaluate how this transmission modifies the rotation curve, we introduce an **energy-lock surrogate**. Instead of solving full hydrodynamics, we augment the Newtonian rotation curve by adding the fraction of inner rotational energy deposited at radius r :

$$v_{\text{obs}}^2(r) = v_N^2(r) + k_{\text{eff}}(r) (\Omega_{\text{inner}} r)^2. \quad (33)$$

This surrogate is intended as an illustrative mapping of how nonzero angular-momentum flux reshapes the rotation profile. It does not, by itself, enforce full Jeans equilibrium. A steady-state closure would follow from solving the angular-momentum flux equation together with the axisymmetric Jeans equation under a prescribed $F_L(R)$. In this paper, we focus on the surrogate to isolate the observable imprint of torque transmission, while the formal flux derivation is provided in Supplementary A. This surrogate captures:

- how much energy a shell inherits from the inner engine,
- how rapidly that energy attenuates with radius,
- how local stress limits further inheritance, and
- how a small leakage from the inner reservoir produces a large outer response.

The alternating-layer structure should not be interpreted as literal rigid shells. It approximates the heterogeneous coupling landscape of real disks, where different radial zones respond differently to the same torque field.

6.5 Why this formulation matters

This construction delivers three essential outputs directly from the model:

- a Newtonian baseline $v_N(r)$,
- a transmission-enhanced surrogate curve $v_{\text{obs}}(r)$, and
- a complete set of SPARC-consistent diagnostics, including the Surplus Index, mean uplift $\langle U \rangle$, and Curl Index.

Because transmission is **local and radial**, while diagnostics integrate **deposited energy globally**, the two need not organize in the same variable. Section 6 defines the transmission rules—radius-dependent, coupling-limited, and stress-saturated—while Section 7 shows how the resulting energy redistribution organizes the observed phenomenology.

A full synthetic parameter sweep illustrating the linear, bending, and saturated regimes is provided in **Supplementary E**.

6.6 Falsifiable Diagnostics

The transmission model leads to three observational diagnostics that follow directly from the torque formulation and require no adjustable parameters. The first is the **Curl Index**, defined by

$$\text{Curl Index} = \frac{\int \left| \frac{d\tau_{\text{obs}}}{dR} - \frac{d\tau_{\text{bar}}}{dR} \right| dR}{\int \left| \frac{d\tau_{\text{bar}}}{dR} \right| dR} \quad (34)$$

This index measures the extent to which the observed torque gradient differs from that implied purely by the baryonic mass distribution. In any model that enforces $F_L = 0$, the torque is generated locally and the two profiles coincide, forcing the Curl Index to vanish. A nonzero value therefore represents a direct observational signal of torque inheritance across radii: it records the imprint of nonlocal angular-momentum transport predicted by the Vlasov formulation but eliminated in enclosed-mass models. We should note that because the Curl Index is constructed to probe large scale radial structure, smoothing suppresses small-scale noise; the diagnostic is intended to capture global transport signatures rather than fine-grained fluctuations.

A second quantity, the **Fractional Uplift**,

$$U(R) = \frac{v_{\text{obs}}^2 - v_{\text{bar}}^2}{v_{\text{bar}}^2} \quad (35)$$

captures the local enhancement of the rotational velocity relative to the baryonic expectation. Because uplift responds point-by-point to the arrival of transmitted coherence, its radial structure traces the same progression that appears in the transmission map: a region of linear inheritance at small radii, a bending zone where the disk begins to saturate, and an outer plateau where additional inheritance becomes dynamically ineffective. In a system without nonlocal coupling, uplift cannot show such structured behavior and reduces to noise around zero.

The third diagnostic, the **Surplus Index**,

$$\text{Surplus Index} = \frac{\int_{0.5R_{\max}}^{R_{\max}} [v_{\text{obs}}^2 - v_{\text{bar}}^2] dR}{\int_0^{R_{\max}} v_{\text{obs}}^2 dR} \quad (36)$$

provides a global measure of the excess rotational energy stored in the outer disk. The choice of integration limits is deliberate. The numerator integrates only over the outer half of the galaxy, from $0.5R_{\max}$ to the edge of the measured rotation curve at R_{\max} . This isolates the radial domain in which the disk cannot generate rotational support through its own local baryonic mass and must therefore rely on energy inherited from interior radii. A nonzero surplus indicates rotational support beyond what the local baryonic mass alone provides. Within the present framework, this is naturally interpreted as exported angular momentum from interior radii, although alternative explanations such as additional mass distributions cannot be ruled out purely from this diagnostic. The denominator integrates the total observed rotational energy over the entire disk; normalizing by this quantity expresses the outer surplus as a fraction of the galaxy's overall rotational budget.

Note that all three diagnostics rely only on quantities directly provided by the SPARC database[2]. For each galaxy, SPARC tabulates both the observed circular speed $V_{\text{obs}}(R)$ and the full baryonic contribution $V_{\text{bar}}(R)$ on a common radial grid. From these profiles the Newtonian torque follows simply as $\tau(R) = RV^2(R)$, and its radial derivative is obtained using standard spline smoothing without introducing additional dynamical assumptions. Likewise, the integrals defining the uplift and surplus follow directly from the tabulated velocities. Thus, each diagnostic is an observational construct, obtained entirely from SPARC without modeling freedom or hidden parameters.

In the transmission model, this quantity is expected to be positive because torque is transported outward whenever $F_L \neq 0$, leading to a measurable accumulation of rotational support in the outer annuli. By contrast, in any model where the outer disk is dynamically decoupled, whether through the enclosed-mass framework or by implicitly enforcing $F_L = 0$, the outer region cannot acquire additional rotational energy from the interior, and the Surplus Index necessarily collapses to negligible values.

It is worth noting that other recent approaches, such as the dual-density formulation of Suleiman (2023) [23], also seek to extract structural information from the rotation curve. These valuable approaches often operate as algebraic mappings from the velocity field to a density field. Our framework is complementary but distinct: it introduces an explicit, physically motivated mechanism for angular momentum transmission, which in turn generates the new diagnostics (Curl Index, Surplus Index) that quantify this process. Our diagnostics are therefore tied to a specific dynamical transport mechanism, rather than to a reinterpretation of the density profile itself.

7. SPARC Diagnostics, Correlations, and the Failure of Radius as an Organizer

We test the transmission framework using all 175 late-type galaxies in the SPARC Rotmod_LTG sample [2] (see Supplementary E–G). For each galaxy, we reconstruct the baryonic circular velocity and compute three diagnostics derived directly from the model: the Curl Index, measuring torque contrast; the mean uplift, measuring fractional velocity enhancement; and the Surplus Index, measuring fractional excess rotational energy in the outer disk. We also extract characteristic radii, including the outermost measured radius R_{\max} , to test whether rotational uplift is controlled by physical extent.

Interpretation of near-zero Surplus values.

Because the Surplus Index is defined as an integrated, signed measure of excess rotational energy in the

outer disk, values near zero do not necessarily indicate the absence of angular-momentum transport. Such values may arise either from genuinely weak transport or from partial cancellation between positive and negative radial contributions. For this reason, galaxies with Surplus Index ≈ 0 are retained in the sample rather than reclassified. Their radial uplift profiles, shown in Supplementary G, frequently exhibit coherent uplift of a single sign over most of the disk, interrupted by localized counter-contributions, indicating balanced but physically active transport rather than dynamical quiescence. The diagnostic therefore encodes net transport balance, not a binary on/off criterion.

The SPARC velocities are reconstructed using a tilted-ring, axisymmetric model. Mild non-circular motions—such as warps, oval flows, asymmetric drift, or small inclination uncertainties—can alter the local slope of the inferred baryonic curve. These effects tend to reduce the apparent torque contrast and therefore bias the Curl Index downward rather than generate spurious high-curl structure. The presence of a strong, coherent Curl–Surplus sequence despite these conservative biases indicates that the inferred transport signal should be interpreted as a lower bound.

(a) Radius as an organizer

When the Surplus Index and mean uplift are plotted against R_{\max} (Figures 1a and 2a), the SPARC galaxies show little systematic organization. Galaxies spanning more than an order of magnitude in size occupy overlapping ranges of surplus and uplift, and systems with nearly identical radii can differ substantially in both diagnostics. No monotonic relation between galaxy size and rotational enhancement is observed, indicating that radius alone does not control outer-disk rotational support.

(b) Curl as an organizer

In contrast, when the same diagnostics are plotted against Curl Index (Figures 1b and 2b), the SPARC sample forms a highly structured sequence. At low curl ($\lesssim 1$), both surplus and uplift increase approximately linearly, corresponding to the linear inheritance regime. At intermediate curl ($\sim 2\text{--}5$), the trends bend: surplus continues to rise while uplift begins to flatten. At high curl ($\gtrsim 6\text{--}8$), the Surplus Index settles into a stable band ($\sim 0.3\text{--}0.6$) while Curl Index spreads horizontally, indicating saturation of transmission.

The central empirical result is that Curl Index, not radius, organizes rotational uplift in disk galaxies. The SPARC sample is highly structured in curl space but essentially unorganized in radius space, exactly as expected if outer rotational support arises from torque-mediated coherence export rather than from purely radial mass augmentation.

The SPARC scaling relations identified by Ghari et al. (2019) [21] provide useful statistical context. Within the present framework, these relations can be interpreted as observational signatures of torque-mediated coherence transmission: Curl Index parallels the baryon-induced acceleration correlation, while Surplus Index mirrors the core-density relation. The three-stage progression of inheritance, bending, and saturation reflects the same structured behavior observed across the SPARC sample.

Inner–Outer Energy Balance and the Absence of a Required Inner Deficit

As discussed in Section 5.1, the transmission framework does not require a clearly resolved inner deficit in the observed rotation curve. In practice, baryonic rotation curves are constructed relative to an

inferred inner baseline that rarely corresponds to a true dynamical zero point. The innermost regions of disk galaxies are typically influenced by bulges, bars, beam smearing, finite spatial resolution, and uncertainties in mass-to-light ratios. Any early withdrawal of rotational coherence occurring at radii smaller than the observational core is therefore naturally absorbed into the reconstructed baryonic profile.

From an energetic standpoint, this behavior is expected. The rotational-energy surface density is

$$E_{\text{rot}}(R) = \frac{1}{2} \Sigma(R) R^2 \Omega^2(R), \text{ (eq. 17)}$$

and for late-type disks with approximately flat rotation curves, $\Omega(R) \approx v_0/R$. Because $\Sigma(R)$ declines exponentially, the cumulative rotational energy of the inner disk exceeds that of the outer disk by several orders of magnitude. Consequently, only a percent-level redistribution of inner rotational coherence is sufficient to generate the observed outer-disk velocity excess.

In systems with extended radial coverage and high spatial resolution, a shallow inner deficit or transition region is sometimes observed. Its absence in most galaxies does not contradict the transmission picture but reflects the fact that the required energetic withdrawal is dynamically small and often occurs below the observational core.

For a small subset of SPARC galaxies, the reported rotation velocities are systematically low at all measured radii. Such behavior is inconsistent with any physical disk equilibrium and is most naturally attributed to geometric or observational systematics, including inclination uncertainties, distance errors, asymmetric drift, or non-circular motions associated with bars and spiral structure. Because these effects uniformly suppress the inferred rotation curve, these galaxies do not provide reliable constraints on dynamical models and are excluded from further analysis.

8. Surplus–Curl Structure and the tanh Transmission Law

The Surplus Index and Curl Index probe complementary aspects of inherited rotational support. Defining

$$\Delta V^2(R) = V_{\text{obs}}^2(R) - V_{\text{bar}}^2(R), \quad (37)$$

the Surplus Index (Eq. 23) measures the **amplitude** of inherited rotational energy in the outer disk, while the Curl Index measures the **radial variation** of this support through the torque gradient.

Using

$$\tau(R) = RV^2(R), \quad (38)$$

one finds

$$\frac{d\tau_{\text{obs}}}{dR} - \frac{d\tau_{\text{bar}}}{dR} = \Delta V^2(R) + R \frac{d\Delta V^2}{dR}. \quad (39)$$

Thus, Surplus Index responds mainly to ΔV^2 , whereas Curl Index responds to both ΔV^2 and its radial gradient. When inherited support is rising, both indices increase together; when ΔV^2 flattens, surplus saturates while curl spreads. This directly reproduces the SPARC pattern.

The tanh transmission law,

$$T(S) = T_{\max} \tanh(S/S_0), \quad (40)$$

implements the minimal physically required behavior: linear inheritance at low stress, bending at intermediate stress, and saturation at high stress (Eqs. 28–33). Its success in reproducing the three-regime SPARC structure supports the interpretation that rotational-coherence transmission, not local mass augmentation, governs disk rotation curves.

9. Relation to the Standard Vlasov–Poisson Dynamics

Within the Vlasov–Poisson framework [7], angular momentum evolution follows directly from the collisionless Boltzmann equation. Taking the angular-momentum moment yields

$$\frac{\partial L}{\partial t} = -\frac{1}{R} \frac{\partial}{\partial R} (RF_L), \quad (41)$$

with

$$F_L(R, t) = \langle Rv_R v_\phi \rangle. \quad (42)$$

Crucially, Eq. (10) contains no source term. Angular momentum is conserved locally and globally; all redistribution arises solely from the divergence of the flux F_L . Nonzero F_L therefore does not indicate angular-momentum or energy creation, but the presence of correlated radial and azimuthal motions. Whether these correlations remain localized or organize coherently over extended radii is controlled by disk geometry and symmetry, not by conservation laws.

Classical results on spiral density waves, swing amplification, and bar-driven resonances [9], [10], [11], [12] establish that collisionless disks behave as gravitationally coupled continua. The transmission model developed here does not modify this theory; it restores the nonlocal coupling implicitly omitted when disks are treated as isolated annuli. Setting $F_L = 0$ recovers the isolated-ring limit and suppresses precisely the transport processes responsible for secular evolution in real disks.

10. Extreme Transport Regimes and Control Cases

To delineate the dynamical regimes relevant to the transmission framework, we examine two complementary sets of extreme systems. The first consists of galaxies drawn from the SPARC sample that exhibit unusually large rotational surplus, with Surplus Index values approaching $\simeq 0.6$. These objects are selected to highlight disks in which strong non-axisymmetric structure—such as prominent spiral arms, bars, warps, or large-scale curvature asymmetries—enforces sustained angular-momentum and energy transport. In these systems, rotational uplift emerges at large radii in direct association with persistent torque generation.

In parallel, we consider a second, independent set of five galaxies widely cited in the literature as dark-matter-suppressed systems. These objects are not selected from SPARC by surplus, but are included as a contrasting extreme. Their morphologies and kinematics place them near the zero-transport or transport-irrelevant limit: they are either pressure-supported or dynamically regular and nearly axisymmetric, and they lack the structural features required to generate significant nonlocal torque flux. Consequently, they exhibit negligible rotational surplus and rotation curves that remain consistent with the local baryonic potential within the regions probed.

The purpose of this comparison is not to equate the two populations, but to bracket the boundaries of the transmission framework. High-surplus SPARC disks occupy a transport-dominated regime in which rotational energy is redistributed outward through non-axisymmetric structure, while dark-matter-suppressed galaxies define the limiting case in which transport is ineffective or dynamically unnecessary. Together, these extremes demonstrate that rotational surplus emerges only when angular-momentum transport is structurally enabled, and collapses when such channels are absent. The two regimes and their representative systems are summarized in Table 1 and detailed in Supplementary H.

Table 1. Extreme-Case Galaxies Used to Anchor the Transmission Framework

Galaxy	Regime	Morphology / Kinematics	Diagnostic Signature	Transport Interpretation
NGC 3109	High-surplus (Transmission-dominant)	Elongated stellar disk; strongly warped H I; tidal interaction with Antlia; filamentary group with coherent velocity gradient	High Surplus Index; large Curl Index; positive mean uplift	Sustained non-axisymmetry enforces strong torque flux ($FL \neq 0$), driving coherent redistribution of rotational energy
NGC 3741	High-surplus (Inheritance regime)	Extremely extended H I disk (~ 42 scale lengths); persistent warp; non-circular motions across most radii	High Curl Index with linearly rising surplus	Radial flows and warps enforce long-range angular-momentum transport; surplus tracks torque divergence
DDO 154	Inheritance / falsifiability anchor	Gas-dominated dwarf; extended warped H I disk; asymmetric outer velocity field; quiescent inner reservoir	Moderate surplus and curl; surplus collapses where asymmetry vanishes	Demonstrates falsifiability: surplus appears only where flux divergence exists and collapses in transport-free zones
UGC 01281	Bending / saturation regime	Low-surface-brightness disk; asymmetric baryonic distribution; slowly rising rotation curve	Intermediate surplus and curl	Moderate torque gradients sustain partial transmission; surplus saturates as coherence export weakens
ESO 444 G084	Inheritance (compact end)	Lopsided dwarf irregular; outer H I distortions; kinematic warp beyond inner disk	High surplus relative to size	Structural asymmetry alone enforces transmission, independent of scale or stellar mass
NGC 1052-DF2	Transport-suppressed	Ultra-diffuse; pressure-supported; no disk rotation or asymmetry	Near-zero surplus and curl	Absence of torque pathways places system near the isolated-annulus ($FL \approx 0$) limit
NGC 1052-DF4	Transport-suppressed	Ultra-diffuse twin of DF2; dispersion-dominated	Near-zero surplus and curl	Dark-matter deficiency coincides with intrinsically inactive transport geometry
FCC 224	Transport-suppressed	Quenched ultra-diffuse dwarf; no disk rotation; old stellar populations	Near-zero surplus and curl	Random stellar motions dominate; nonlocal transport dynamically irrelevant
AGC 114905	Transport-suppressed (rotating)	Gas-rich UDG; thin, regular H I disk; weak shear; no bars or spirals	Low surplus despite rotation	Rotation without torque: coherent circular motion but negligible angular-momentum flux
NGC 1277	Control ($FL \approx 0$)	Compact, massive ETG; axisymmetric; equilibrium stellar kinematics	No surplus; equilibrium Jeans/orbit models	Absence of inferred dark matter reflects lack of transport demand, not suppressed transport

11. Geometry-Dependent Angular-Momentum Transport: Spherical versus Spiral Disks

To verify that the transmission mechanism arises directly from collisionless dynamics, we perform a minimal N-body realization of the Vlasov–Poisson system using the REBOUND integrator. In this

representation, the phase-space distribution is sampled by discrete particles, and the angular-momentum flux

$$F_L(r, t) = \sum_i m_i r_i v_{r,i} v_{\phi,i} \quad (43)$$

provides a direct discrete estimator of the continuum torque flux appearing in the Vlasov–Poisson moment equation. When the disk is constrained to remain axisymmetric, this quantity fluctuates around zero and produces no secular transport. When weak non-axisymmetry is permitted, coherent correlations between radial and azimuthal motions emerge, generating sustained outward angular-momentum flux without mass accumulation at large radii (Figures 3–6). Full numerical details are provided in **Supplementary I**.

To isolate the role of geometry in enabling angular-momentum and energy transport, we compare two controlled N-body simulations evolved under identical gravitational and numerical conditions but differing only in their initial symmetry:

- **Case A (spherical control):** an axisymmetric disk initialized with perturbation amplitude $\epsilon = 0$, preserving spherical symmetry.
- **Case B (spiral disk):** the same disk seeded with a weak non axisymmetric perturbation ($\epsilon = 0.05$), generating a long-lived spiral pattern.

Both systems are evolved to $t = 60$ using the same particle number, softening length, and timestep. All diagnostics are constructed from azimuthally averaged quantities in radial bins (see Supplementary I).

Particle Trajectories and Disk Morphology

The geometric origin of the contrasting behavior is illustrated in Figures 3 and 4, which show representative particle snapshots for the two cases.

In **Case A** (Figure 3), particle trajectories remain quasi-circular and radially confined. Orbits exhibit only weak diffusion associated with discreteness noise, and no coherent collective motion develops. The disk retains its near-spherical symmetry throughout the evolution.

In **Case B** (Figure 4), particles organize into spiral-like trajectories that mediate correlated radial and azimuthal motion. Individual particles intermittently gain or lose angular momentum as they interact with the spiral pattern, producing sustained radial transport. The spiral acts as a long-lived conduit for angular-momentum exchange rather than as a transient disturbance.

Surface-Density Evolution

Figure 5 shows the time–radius evolution of the surface density $\Sigma(R, t)$ for both cases.

In **Case A**, the surface density remains smooth and monotonic throughout the integration. Apart from stochastic fluctuations associated with finite particle number, no systematic radial redistribution of mass is observed. The outer disk remains persistently low-density, and the overall profile retains its initial exponential-like form.

In **Case B**, the spiral perturbation generates coherent overdense and underdense features that propagate radially over time. Although the absolute surface density at large radii remains small, these features persist over multiple dynamical times. The spiral therefore introduces organized structure into the disk without requiring a net outward migration of mass.

This comparison demonstrates that the key distinction between the two cases is not the magnitude of the surface density in the outskirts, but the presence or absence of spatially coherent non axisymmetric structure.

Angular-Momentum Flux

The dynamical consequences of these geometric differences are quantified by the angular-momentum flux

$$F_L(R, t) = \langle R v_R v_\phi \rangle. \quad (44)$$

In **Case A**, $F_L(R, t)$ fluctuates around zero with no persistent radial structure. While instantaneous nonzero values arise from discreteness noise, the flux divergence averages out over time, and no systematic redistribution of angular momentum occurs.

In **Case B**, a coherent, outward-propagating structure appears in $F_L(R, t)$. This feature persists over many dynamical times and produces a nonzero flux divergence. Although the surface density at large radii remains low, angular momentum is efficiently transported outward because the transported quantity scales with the specific angular momentum $R v_\phi$, rather than with mass alone.

As a result, the spiral case develops a substantial outer-disk rotational surplus, whereas the axisymmetric case does not. This demonstrates that **geometry—not mass content, force law, or numerical resolution—controls the existence of a transport channel**.

Conservation and Symmetry

It is essential to emphasize that the angular-momentum flux equation contains **no source term**. In the collisionless Vlasov–Poisson system, angular momentum is conserved both locally and globally; any redistribution must therefore arise exclusively from the divergence of the flux itself. Nonzero values of F_L do not indicate angular-momentum creation, but the presence of correlated radial and azimuthal motions.

The physical distinction between the two cases is whether these correlations remain spatially localized or instead organize coherently over extended radial ranges. In perfectly symmetric systems, angular momentum is locally exchanged but globally trapped. Once non axisymmetric structure is admitted—even at low amplitude—angular momentum and rotational energy propagate outward naturally through an expanding radial domain.

Implication

These results show that the absence of angular-momentum transport in spherical systems is not a failure of dynamics, but a consequence of symmetry. When realistic disk geometry is admitted, outward transport arises naturally and robustly, providing a purely dynamical pathway for sustaining extended rotation curves without invoking additional mass components.

12. Limitations and Scope of the Present Analysis

The present work is intentionally structural and dynamical in nature, focusing on the consequences of the Vlasov Poisson system viewed from an energy and transport based perspective, rather than as a fully closed phenomenological model of galaxy formation. While we demonstrate that only a small redistribution of inner disk rotational energy is sufficient to generate the observed outer velocity excess, several limitations and qualifications must be stated clearly.

First, although the Vlasov Poisson framework rigorously governs collisionless gravitational dynamics, it places stringent requirements on how energy transfer and angular momentum flux are analyzed. Our results highlight that even a percent level leakage of inner rotational coherence can produce a substantial velocity increase at large radii. This sensitivity underscores the need for careful treatment of energy bookkeeping within the Vlasov Poisson system, especially when interpreting small residuals in rotation curves. The present analysis demonstrates this principle but does not yet constitute an exhaustive dynamical accounting of all transport channels.

Second, the SPARC database, while the most comprehensive and internally consistent rotation curve compilation currently available, is not free of observational limitations. These include incomplete radial coverage for some galaxies, uncertainties in inclination and distance estimates, nonuniform data quality, and residual systematics associated with mass to light ratio assumptions. Such factors can introduce scatter and local discrepancies that are not fully captured by any single diagnostic. Consequently, our results should be interpreted statistically and structurally, rather than as precise reconstructions for every individual system.

Third, the governing Vlasov Poisson equations are fundamentally conservative, whereas real galaxies are subject to complex and time dependent processes such as disk heating, secular evolution, bar formation, spiral winding, and environmental interactions. The present work does not attempt to model these processes explicitly. Instead, it isolates the minimal dynamical requirement for rotational inheritance and torque transmission within a collisionless framework. In this sense, our analysis should be viewed as a baseline dynamical constraint, rather than a complete evolutionary model.

Fourth, the transmission law employed in this work remains empirical in form, even though its structure is motivated by saturation arguments and supported by numerical experiments. While the observed correlations strongly suggest that galaxies exhibiting large surplus values are characterized by efficient geometrically mediated transfer mechanisms such as spirals, bars, or other non axisymmetric structures, this study does not yet provide a first principles derivation linking specific morphological features to quantitative transmission efficiencies. That connection remains an important target for future work.

Finally, while we include an analysis of dark matter deficient galaxies and show that their behavior is consistent with the same transport based interpretation, the present sample remains limited. A more systematic expansion of such cases, including a broader characterization of their morphology,

kinematics, and environment, will be necessary to fully assess the universality of the proposed framework.

In summary, this work should be understood as a starting point rather than a final statement. It establishes that the standard collisionless Vlasov Poisson system, when analyzed with proper attention to energy transport and angular momentum flux, naturally permits the observed outer disk velocity behavior without invoking modifications to gravity or additional matter components. Further observational refinement, dynamical modeling, and targeted numerical experiments will be essential to extend and test these conclusions.

13. Conclusion

This work re examines the rotation curve problem by questioning a foundational assumption of standard modeling, namely that each galactic radius behaves as a mechanically independent annulus. When a disk is treated instead as a gravitationally coupled continuum, as required by the Vlasov Poisson equations, non axisymmetric structures such as bars, spiral arms, rings, and tidal wakes naturally couple different radii through torques, coherence exchange, and phase correlations. This nonlocal coupling enables angular momentum and rotational coherence generated in the inner disk to propagate outward, thereby modifying the velocity profile that would be expected from the enclosed baryonic mass alone.

The three stage transmission law developed here provides a compact and predictive description of this behavior. It identifies an inner inheritance region, a nonlinear mid disk bending region, and an outer saturation regime. When applied to the full SPARC sample, this framework reproduces the dominant structural features of observed rotation curves, including systematic trends in both the Curl Index and the Surplus Index, using only the measured baryonic distributions.

Taken together, these results indicate that the flatness and coherence of outer rotation curves can arise from intrinsic disk dynamics, without requiring additional unseen mass at galactic scales within the rotation-curve inference itself. The proposed diagnostics also provide explicit falsification criteria. A galaxy exhibiting a sustained outer region in which both indices remain consistent with zero within observational uncertainty would pose a direct challenge to the transmission interpretation.

More broadly, this study emphasizes the role of torque transport, continuum coupling, and collective disk behavior in shaping spiral galaxy kinematics. For clarity, the present analysis is restricted to dynamical inferences drawn from rotation curve data. It does not address cosmological probes of dark matter, including gravitational lensing, cosmic microwave background anisotropies, or large scale structure. The conclusions presented here are therefore dynamical in scope rather than cosmological.

14. Acknowledgement

The authors gratefully acknowledge computational support from Missouri State University, which facilitated the execution of the three-stage CRT simulations and the extraction and evaluation of the SPARC database. While large-language-model tools provided assistance in conceptual refinement and code development, the authors assume full responsibility for all scientific observations, modeling procedures, theoretical formulations, and analytical results reported in this manuscript.

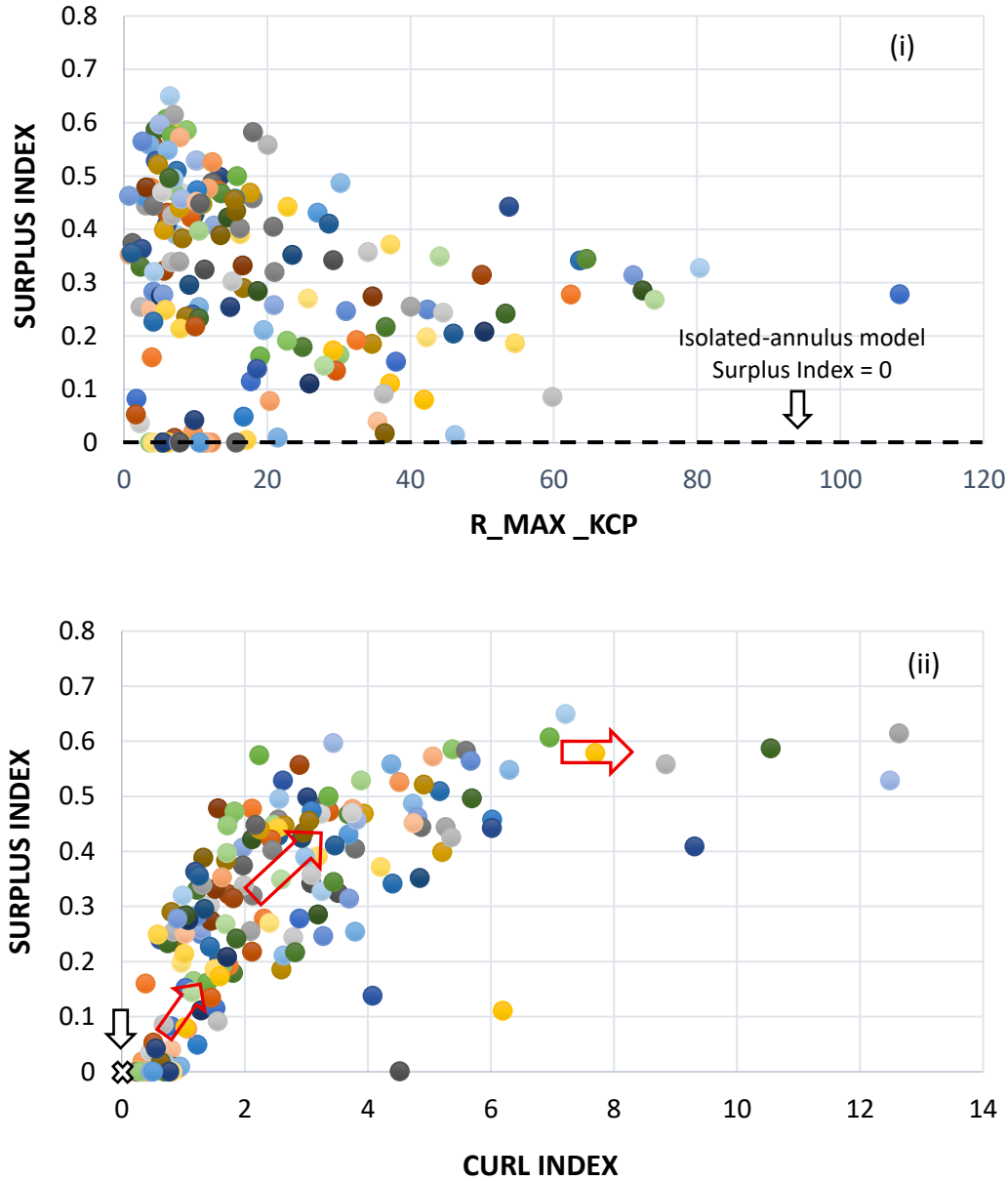


Figure 1 Surplus behavior in the SPARC sample (i) Surplus Index versus R_{max} . The surplus shows no dependence on galaxy size, indicating that it is a dynamical effect rather than a geometric one. The horizontal dashed line at Surplus Index = 0 represents the isolated-annulus baseline: if torque flux $F_L = 0$, no rotational surplus is inherited. The persistent nonzero values across the sample demonstrate active coherence transmission. (ii) Surplus Index versus Curl Index. The distribution exhibits the expected three-stage structure: an initial rising branch, a bending transition, and a saturated surplus band where curl spreads horizontally. The white "X" at (0, 0) marks the local-only baseline. This three-stage pattern reflects the shift from coherence inheritance to nonlinear bending and eventual saturation in the transmission model, indicating that torque flux is nonzero and dynamically significant.

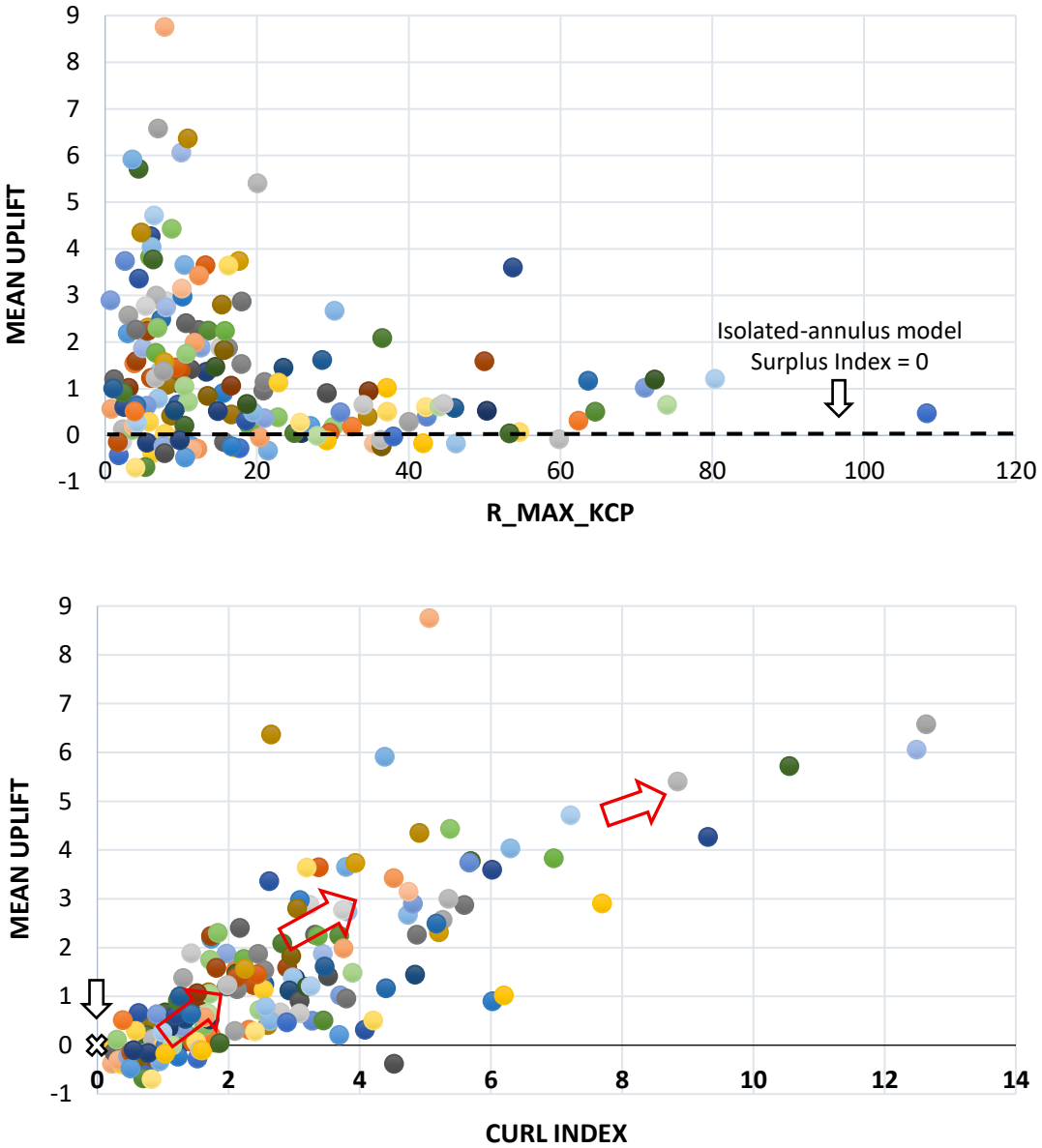


Figure 2. Mean Uplift behavior across the SPARC sample. (i) Mean Uplift versus R_{max} . The uplift shows no systematic dependence on galaxy size, indicating that it is set by disk dynamics rather than by the extent of the observational baseline. The horizontal dashed line at Uplift = 0 represents the isolated-annulus baseline: under the standard model with torque flux $F_L = 0$, no rotational enhancement is expected. The persistent positive uplift across the sample confirms active coherence transmission. (ii) Mean Uplift versus Curl Index. The points trace a clear rising trend with a broadening at higher curl, consistent with the transition from linear inheritance to nonlinear bending and eventual saturation in the transmission model. The white “X” at (0, 0) marks the local-only baseline. The structured departure from this point provides direct evidence of torque-driven uplift and falsifies the assumption of annulus isolation.

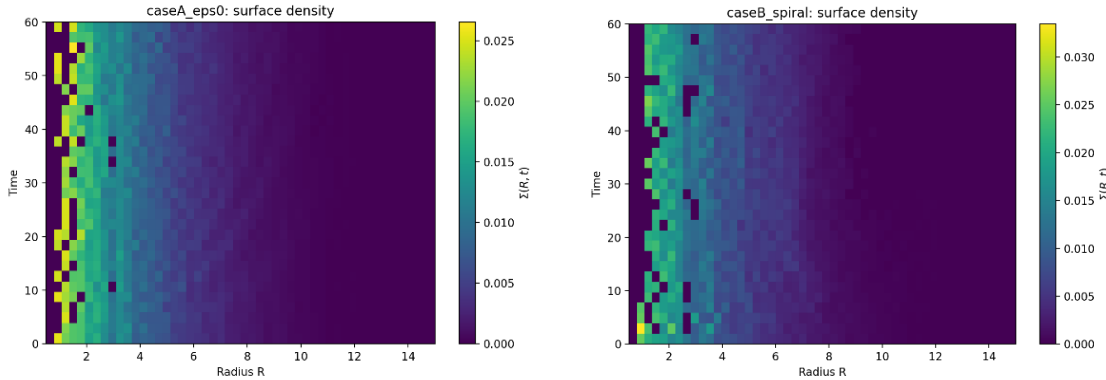


Figure 3 Time–radius evolution of the azimuthally averaged surface density, $\Sigma(R, t)$, for the two N -body simulations ($M_C=5$). **Left:** Case A (axisymmetric control, $\epsilon = 0$). **Right:** Case B (spiral disk, $\epsilon = 0.05$). Colors indicate $\Sigma(R, t)$ in radial bins as a function of time. In the spherical case, the surface density remains smooth and monotonic, with no systematic radial redistribution beyond finite- N fluctuations. In the spiral case, transient overdense and underdense features appear and propagate radially while the outer disk remains low-density. The comparison demonstrates that the presence of non axisymmetric structure modifies the spatiotemporal organization of the disk without requiring significant mass accumulation at large radii.

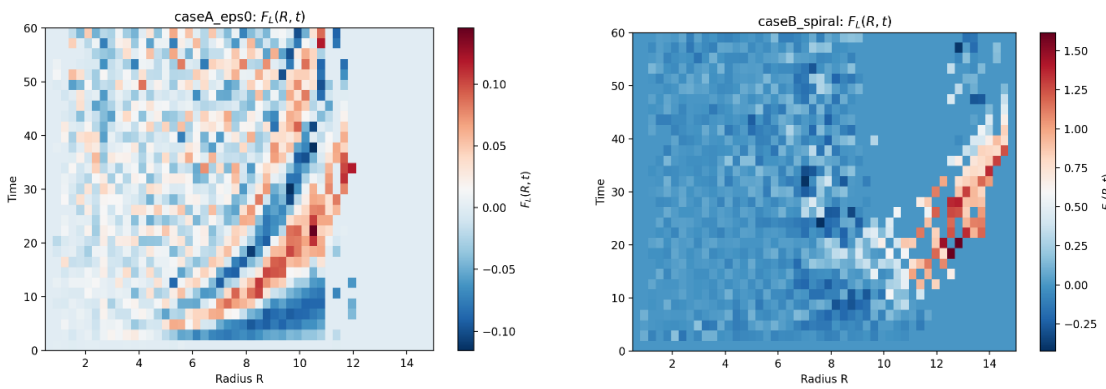


Figure 4 Time–radius heat maps of the angular-momentum flux $F_L(R, t) = \langle R v_R v_\phi \rangle$ for the two simulations ($M_C=5$). **Left:** Case A (axisymmetric control, $\epsilon = 0$). **Right:** Case B (spiral disk, $\epsilon = 0.05$). In the axisymmetric case, the flux fluctuates around zero with no persistent radial coherence, consistent with finite- N noise and the absence of a transport channel. In contrast, the spiral case exhibits a coherent, outward-propagating structure in $F_L(R, t)$ that persists over many dynamical times. Despite the low surface density at large radii, the spiral geometry sustains significant angular-momentum transport, demonstrating that non axisymmetric structure enables efficient redistribution of angular momentum independent of mass accumulation.

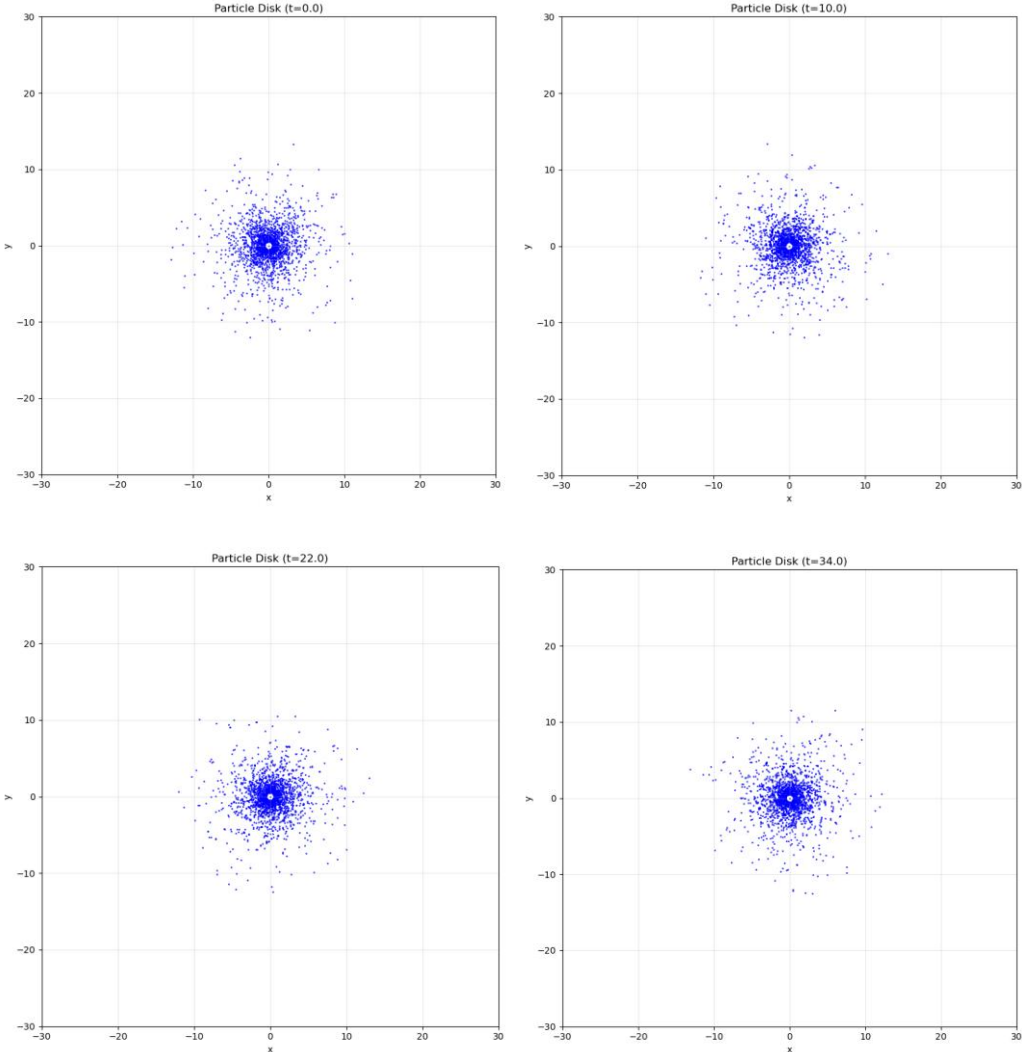


Figure 5 Particle configuration snapshots for the axisymmetric control simulation (Case A, $\epsilon = 0$, $M_c=5$) shown at four representative times during the evolution. The particle distribution remains approximately isotropic at all times, with no persistent non axisymmetric structure developing. Although individual particle orbits evolve and scatter due to discreteness effects, the global morphology preserves spherical symmetry and exhibits no coherent spiral features or organized radial streaming. This geometric constraint is consistent with the absence of sustained angular-momentum transport observed in the corresponding flux diagnostics.

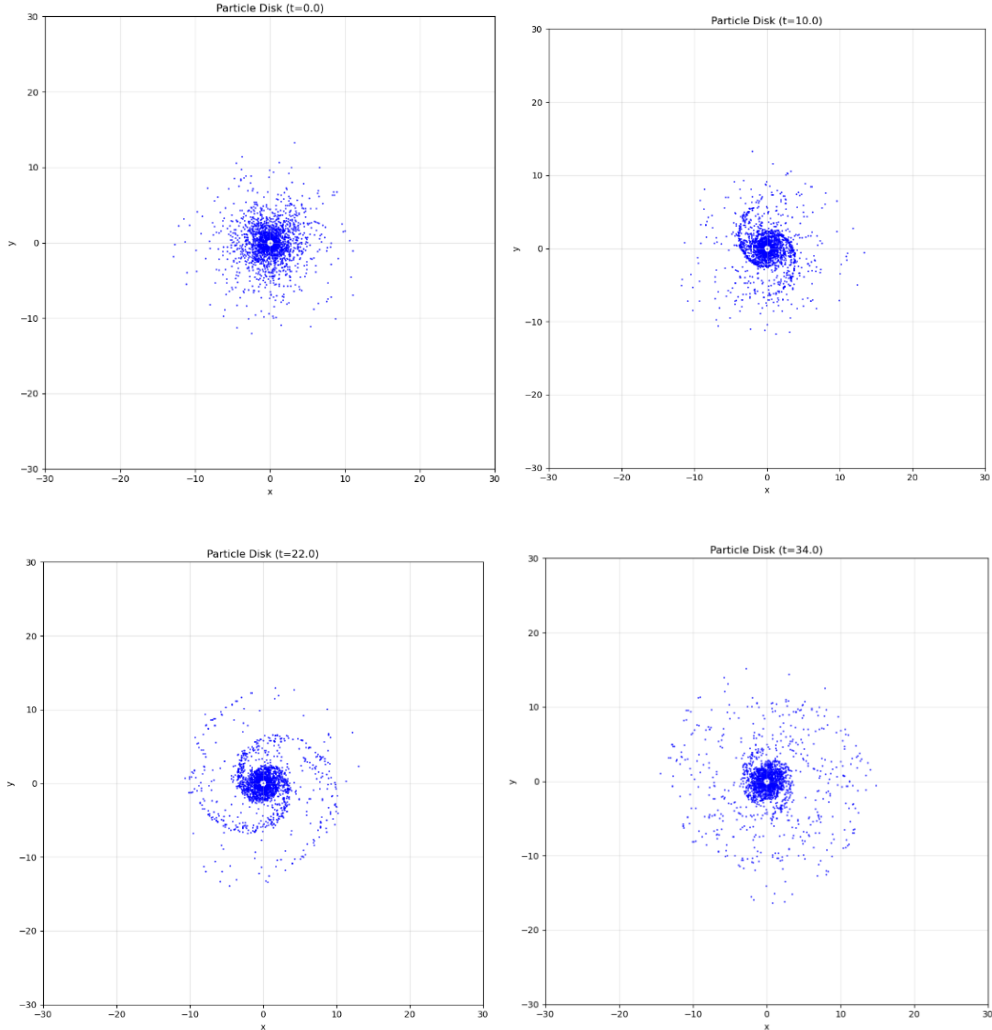


Figure 6 Particle configuration snapshots for the non axisymmetric simulation (Case B, $\epsilon = 0.05$, $M_c=5$) shown at the same four representative times as Fig. 11. A coherent spiral pattern emerges early in the evolution and persists over multiple dynamical times. The spiral induces correlated radial and azimuthal motions, producing organized streaming and clear departures from spherical symmetry. At later times, the spiral structure weakens as particles phase-mix, but its earlier presence leaves a lasting imprint in the angular-momentum flux diagnostics. This transient but coherent geometric structure provides an efficient channel for outward angular-momentum transport absent in the axisymmetric control case.

REFERENCES

- [1] V. C. Rubin, W. K. Ford Jr., and N. Thonnard, "Extended rotation curves of high-luminosity spiral galaxies. IV. Systematic dynamical properties, Sa -> Sc.," *The Astrophysical Journal*, vol. 225, pp. L107–L111, Nov. 1978, doi: 10.1086/182804.
- [2] F. Lelli, S. S. McGaugh, and J. M. Schombert, "SPARC: Mass Models for 175 Disk Galaxies with Spitzer Photometry and Accurate Rotation Curves," *The Astronomical Journal*, vol. 152, p. 157, Dec. 2016, doi: 10.3847/0004-6256/152/6/157.
- [3] K. C. Freeman, "On the Disks of Spiral and S0 Galaxies," *The Astrophysical Journal*, vol. 160, p. 811, June 1970, doi: 10.1086/150474.
- [4] J. Binney and S. Tremaine, *Galactic Dynamics: Second Edition*. in Princeton Series in Astrophysics. Princeton University Press, 2008. [Online]. Available: <https://books.google.com/books?id=qxWt20TH--cC>
- [5] A. Bosma, "21-cm line studies of spiral galaxies. II. The distribution and kinematics of neutral hydrogen in spiral galaxies of various morphological types.," *The Astronomical Journal*, vol. 86, pp. 1825–1846, Dec. 1981, doi: 10.1086/113063.
- [6] V. C. Rubin, W. K. Ford Jr., and N. Thonnard, "Extended rotation curves of high-luminosity spiral galaxies. IV. Systematic dynamical properties, Sa -> Sc.," *The Astrophysical Journal*, vol. 225, pp. L107–L111, Nov. 1978, doi: 10.1086/182804.
- [7] W. Braun and K. Hepp, "The Vlasov dynamics and its fluctuations in the 1/N limit of interacting classical particles," *Communications in Mathematical Physics*, vol. 56, no. 2, pp. 101–113, June 1977, doi: 10.1007/BF01611497.
- [8] D. Lynden-Bell and A. J. Kalnajs, "On the generating mechanism of spiral structure," *Monthly Notices of the Royal Astronomical Society*, vol. 157, p. 1, Jan. 1972, doi: 10.1093/mnras/157.1.1.
- [9] C. C. Lin and F. H. Shu, "On the Spiral Structure of Disk Galaxies.," *The Astrophysical Journal*, vol. 140, p. 646, Aug. 1964, doi: 10.1086/147955.
- [10] A. Toomre, "What amplifies the spirals," presented at the Structure and Evolution of Normal Galaxies, Jan. 1981, pp. 111–136. [Online]. Available: <https://ui.adsabs.harvard.edu/abs/1981seng.proc..111T>
- [11] E. Athanassoula, "What determines the strength and the slowdown rate of bars?," *Monthly Notices of the Royal Astronomical Society*, vol. 341, no. 4, pp. 1179–1198, June 2003, doi: 10.1046/j.1365-8711.2003.06473.x.
- [12] J. A. Sellwood, "Secular evolution in disk galaxies," *Rev. Mod. Phys.*, vol. 86, no. 1, pp. 1–46, Jan. 2014, doi: 10.1103/RevModPhys.86.1.
- [13] R. W. Nelson and S. Tremaine, "The damping and excitation of galactic warps by dynamical friction," *Monthly Notices of the Royal Astronomical Society*, vol. 275, pp. 897–920, Aug. 1995, doi: 10.1093/mnras/275.4.897.
- [14] J. A. Sellwood and J. J. Binney, "Radial mixing in galactic discs," *Monthly Notices of the Royal Astronomical Society*, vol. 336, pp. 785–796, Nov. 2002, doi: 10.1046/j.1365-8711.2002.05806.x.
- [15] S. D. M. White, "Angular momentum growth in protogalaxies," *The Astrophysical Journal*, vol. 286, pp. 38–41, Nov. 1984, doi: 10.1086/162573.

- [16] P. J. E. Peebles, "Origin of the Angular Momentum of Galaxies," *The Astrophysical Journal*, vol. 155, p. 393, Feb. 1969, doi: 10.1086/149876.
- [17] A. G. Doroshkevich, "Spatial structure of perturbations and origin of galactic rotation in fluctuation theory," *Astrophysics*, vol. 6, pp. 320–330, Oct. 1970, doi: 10.1007/BF01001625.
- [18] R. Sakidja, "The Curvature–Transport Correspondence (CTC) and Its Implications for Cosmic Structure Formation." Zenodo, Dec. 2025. doi: 10.5281/zenodo.17844548.
- [19] J. F. Navarro, C. S. Frenk, and S. D. M. White, "A Universal Density Profile from Hierarchical Clustering," *The Astrophysical Journal*, vol. 490, pp. 493–508, Dec. 1997, doi: 10.1086/304888.
- [20] M. Milgrom, "A modification of the Newtonian dynamics as a possible alternative to the hidden mass hypothesis.,," *The Astrophysical Journal*, vol. 270, pp. 365–370, July 1983, doi: 10.1086/161130.
- [21] A. Ghari, B. Famaey, C. Laporte, and H. Haghi, "Dark matter–baryon scaling relations from Einasto halo fits to SPARC galaxy rotation curves*", *A&A*, vol. 623, 2019, doi: 10.1051/0004-6361/201834661.
- [22] A. Sipols and A. Pavlovich, "Dark Matter Dogma: A Study of 214 Galaxies," *Galaxies*, vol. 8, no. 2, 2020, doi: 10.3390/galaxies8020036.
- [23] R. Suleiman, *Prediction of the dark matter distribution and fraction in individual galaxies based solely on their rotation curves*. 2023.
- [24] J. Binney and S. Tremaine, *Galactic Dynamics: Second Edition*. 2008. [Online]. Available: <https://ui.adsabs.harvard.edu/abs/2008gady.book.....B>
- [25] S. Chandrasekhar, "Dynamical Friction. I. General Considerations: the Coefficient of Dynamical Friction.,," *JApJ*, vol. 97, p. 255, Mar. 1943, doi: 10.1086/144517.
- [26] F. Lelli, S. McGaugh, and J. Schombert, "SPARC Galaxy Rotation Curve," Nov. 2016.
- [27] M. Jobin and C. Carignan, "The dark side of NGC 3109," *Astronomical Journal; (USA)*, vol. 100, 1 AD, doi: 10.1086/115548.
- [28] M. Bellazzini, T. Oosterloo, F. Frernali, and G. Beccari, "Dwarfs walking in a row," *A&A*, vol. 559, Nov. 2013, doi: 10.1051/0004-6361/201322744.
- [29] D. G. Barnes and W. J. G. de Blok, "On the Neutral Gas Content and Environment of NGC 3109 and the Antlia Dwarf Galaxy," *The Astronomical Journal*, vol. 122, no. 2, p. 825, Aug. 2001, doi: 10.1086/321170.
- [30] J. W. Menzies, P. A. Whitelock, M. W. Feast, and N. Matsunaga, "Luminous AGB variables in the dwarf irregular galaxy, NGC 3109," *Monthly Notices of the Royal Astronomical Society*, vol. 483, no. 4, pp. 5150–5165, Mar. 2019, doi: 10.1093/mnras/sty3438.
- [31] G. Gentile, P. Salucci, U. Klein, and G. L. Granato, "NGC 3741: the dark halo profile from the most extended rotation curve," *Monthly Notices of the Royal Astronomical Society*, vol. 375, pp. 199–212, Feb. 2007, doi: 10.1111/j.1365-2966.2006.11283.x.
- [32] A. Banerjee, N. N. Patra, J. N. Chengalur, and A. Begum, "A slow bar in the dwarf irregular galaxy NGC 3741," *Monthly Notices of the Royal Astronomical Society*, vol. 434, no. 2, pp. 1257–1263, Sept. 2013, doi: 10.1093/mnras/stt1083.
- [33] C. Carignan and C. Purton, "The ‘Total’ Mass of DDO 154," *The Astrophysical Journal*, vol. 506, no. 1, p. 125, Oct. 1998, doi: 10.1086/306227.

- [34] A. B. Watts, G. R. Meurer, C. D. P. Lagos, S. M. Bruzzese, P. Kroupa, and T. Jerabkova, “Star formation in the outskirts of DDO 154: a top-light IMF in a nearly dormant disc,” *Monthly Notices of the Royal Astronomical Society*, vol. 477, no. 4, pp. 5554–5567, July 2018, doi: 10.1093/mnras/sty1006.
- [35] P. Li, F. Lelli, S. McGaugh, and J. Schombert, “Fitting the radial acceleration relation to individual SPARC galaxies,” *A&A*, vol. 615, 2018, doi: 10.1051/0004-6361/201732547.
- [36] N. Bar, K. Blum, J. Eby, and R. Sato, “Ultralight dark matter in disk galaxies,” *Phys. Rev. D*, vol. 99, no. 10, p. 103020, May 2019, doi: 10.1103/PhysRevD.99.103020.
- [37] R. A. Swaters, R. Sancisi, T. S. van Albada, and J. M. van der Hulst, “The rotation curves shapes of late-type dwarf galaxies,” *A&A*, vol. 493, no. 3, pp. 871–892, 2009, doi: 10.1051/0004-6361:200810516.
- [38] B. Namumba *et al.*, “Investigating the H I distribution and kinematics of ESO444-G084 and [KKS2000]23: New insights from the MHONGOOSE survey,” *A&A*, vol. 699, 2025, doi: 10.1051/0004-6361/202554391.
- [39] P. van Dokkum, S. Danieli, R. Abraham, C. Conroy, and A. J. Romanowsky, “A Second Galaxy Missing Dark Matter in the NGC 1052 Group,” *Japjl*, vol. 874, no. 1, p. L5, Mar. 2019, doi: 10.3847/2041-8213/ab0d92.
- [40] A. W. S. Man *et al.*, “An Exquisitely Deep View of Quenching Galaxies through the Gravitational Lens: Stellar Population, Morphology, and Ionized Gas,” *The Astrophysical Journal*, vol. 919, no. 1, p. 20, Sept. 2021, doi: 10.3847/1538-4357/ac0ae3.
- [41] M. L. Buzzo *et al.*, “A new class of dark matter-free dwarf galaxies?,” *A&A*, vol. 695, 2025, doi: 10.1051/0004-6361/202453522.
- [42] P. E. Mancera Piña *et al.*, “Off the Baryonic Tully–Fisher Relation: A Population of Baryon-dominated Ultra-diffuse Galaxies,” *The Astrophysical Journal Letters*, vol. 883, no. 2, p. L33, Sept. 2019, doi: 10.3847/2041-8213/ab40c7.
- [43] P. E. Mancera Piña *et al.*, “Robust H I kinematics of gas-rich ultra-diffuse galaxies: hints of a weak-feedback formation scenario,” *Monthly Notices of the Royal Astronomical Society*, vol. 495, pp. 3636–3655, July 2020, doi: 10.1093/mnras/staa1256.
- [44] A. Yıldırım *et al.*, “MRK 1216 and NGC 1277 – an orbit-based dynamical analysis of compact, high-velocity dispersion galaxies,” *Monthly Notices of the Royal Astronomical Society*, vol. 452, no. 2, pp. 1792–1816, Sept. 2015, doi: 10.1093/mnras/stv1381.
- [45] S. Comerón *et al.*, “The massive relic galaxy NGC 1277 is dark matter deficient,” *A&A*, vol. 675, 2023, doi: 10.1051/0004-6361/202346291.

SUPPLEMENTARY A: Formal Vlasov–Poisson Moment Equations

A.1 Purpose and scope

This supplement summarizes the standard moment equations of the collisionless Vlasov–Poisson system and highlights the appearance of the angular-momentum flux term that underlies rotational coherence transmission. No new physics is introduced here. The goal is solely to establish notation and to show that a nonzero angular-momentum flux arises generically in non axisymmetric disks. A complete derivation based on Liouville’s theorem and Hamiltonian phase-space flow is standard in galactic dynamics and may be found in textbooks such as *Galactic Dynamics*[24]. For completeness, we summarize only the essential ingredients relevant to the present discussion.

All saturation and energetic considerations are treated separately in Supplementary H.

A.2 Vlasov equation and lowest moments

The evolution of a collisionless, self-gravitating system is governed by the Vlasov equation,

$$\frac{\partial f}{\partial t} + \mathbf{v} \cdot \nabla_{\mathbf{x}} f - \nabla_{\mathbf{x}} \Phi \cdot \nabla_{\mathbf{v}} f = 0, \quad (\text{A-1})$$

where $f(\mathbf{x}, \mathbf{v}, t)$ is the phase-space distribution function and Φ is the gravitational potential.

The surface density and mean velocity are defined as

$$\Sigma(\mathbf{x}, t) = \int f d^3 v, \Sigma \mathbf{u} = \int \mathbf{v} f d^3 v. \quad (\text{A-2})$$

Taking the zeroth velocity moment yields the continuity equation,

$$\frac{\partial \Sigma}{\partial t} + \nabla \cdot (\Sigma \mathbf{u}) = 0. \quad (\text{A-3})$$

A.3 Angular-momentum moment and flux

The specific angular momentum about the symmetry axis is

$$L_z = r v_{\phi}. \quad (\text{A-4})$$

Multiplying the Vlasov equation by L_z and integrating over velocity space yields the angular-momentum balance equation,

$$\frac{\partial}{\partial t} (\Sigma L_z) + \frac{1}{r} \frac{\partial}{\partial r} (r F_L) = \tau_{\text{grav}}, \quad (\text{A-5})$$

where

$$F_L = \Sigma \langle v_r v_\phi \rangle \quad (\text{A-6})$$

is the radial flux of angular momentum and τ_{grav} is the gravitational torque density arising from non axisymmetric structure.

Equation (A-4) is exact and follows directly from collisionless dynamics.

A.4 Generic nonzero flux in real disks

In a perfectly axisymmetric, time-independent disk, the velocity correlations vanish and $F_L = 0$. However, any non axisymmetric structure—spiral arms, bars, lopsidedness, or transient density waves—induces correlated radial and azimuthal motions, producing a nonzero angular-momentum flux.

Thus, $F_L \neq 0$ is a generic property of realistic galactic disks and does not rely on dissipation, hydrodynamics, or modified gravity.

A.5 Connection to the transmission framework

The Rotational Coherence Transmission (RCT) framework introduced in the main text does not modify Eq. (A-4). Instead, it provides an effective description of how the **net, time-averaged angular-momentum flux** is inherited, attenuated, and redistributed with radius.

The saturation of this transmission—arising from finite absorptive capacity and energetic constraints—is not addressed here. Its field-theoretic and energetic origin is derived separately in Supplementary H.

SUPPLEMENTARY B: Physical Interpretation of the Angular-Momentum Flux F_L

B.1 Purpose

This supplement provides a physical interpretation of the angular-momentum flux $F_L(R, t)$ that appears in the exact Vlasov–Poisson angular-momentum moment equation,

$$\frac{\partial}{\partial t}(\Sigma L_z) = -\frac{1}{R} \frac{\partial}{\partial R}[R F_L(R, t)] + \tau_{\text{grav}}(R, t), \quad (\text{B-1})$$

with emphasis on how familiar non axisymmetric disk structures generate nonzero flux. No new formalism is introduced. The goal is to show, mechanism by mechanism, why realistic disks generically violate the isolated-annulus assumption $F_L = 0$.

B.2 Stress decomposition

In collisionless galactic dynamics, the radial angular-momentum flux naturally decomposes into **kinematic** and **gravitational** stress contributions[8], [24] :

$$F_L = F_L^{\text{kin}} + F_L^{\text{grav}}, \quad (\text{B-2})$$

where

$$F_L^{\text{kin}} \sim R \Sigma \langle v_R v_\phi \rangle \quad (\text{B-3})$$

arises from correlated radial and azimuthal motions, and

$$F_L^{\text{grav}} \sim \frac{1}{4\pi G} \int_0^{2\pi} (\partial_R \Phi_1)(\partial_\phi \Phi_1) d\phi \quad (\text{B-4})$$

arises from non axisymmetric potential gradients. Either contribution being nonzero is sufficient to produce angular-momentum transport.

B.3 Spiral structure

Spiral density waves are intrinsically non axisymmetric and therefore generate angular-momentum flux through gravitational stress. In the Lynden-Bell–Kalmajs formalism, spiral patterns transport angular momentum via phase-shifted coupling between the perturbed potential and the stellar response[8]. As a result, any spiral pattern of finite amplitude generically produces

$$F_L^{\text{grav}} \neq 0, \quad (\text{B-5})$$

driving secular redistribution of angular momentum across the disk[8], [24].

B.4 Swing-amplified transients

Swing amplification produces short-lived, sheared non axisymmetric patterns[10] [8]. Such transients typically generate:

- correlated streaming motions, yielding $\langle v_R v_\phi \rangle \neq 0$ (kinematic stress), and
- time-dependent non axisymmetric potentials (gravitational stress).

Although intermittent in time, swing-amplified structures therefore realize $F_L \neq 0$ through mixed stress channels[4], [10].

B.5 Bars

Bars are global, large-amplitude non axisymmetric perturbations extending over several kiloparsecs. Their potentials necessarily possess both radial and azimuthal gradients, producing sustained gravitational torque and therefore

$$F_L^{\text{grav}} \neq 0 \quad (\text{B-6})$$

throughout the bar region[11]. While resonances (ILR/CR/OLR) amplify the stellar response locally, the existence of angular-momentum transport does not rely on isolating specific resonant radii; the non axisymmetric bar potential alone guarantees radial coupling [4], [11].

B.6 Gravitational wakes and dynamical friction

A massive perturber (e.g., a giant molecular cloud, a satellite sub-halo, a globular cluster) moving through a stellar disk produces a **gravitational wake** in the surrounding collisionless medium. This wake modifies both the velocity distribution and the gravitational potential, producing *simultaneous* contributions to the kinematic and gravitational parts of the angular-momentum flux F_L .

Formally, the total flux is

$$F_L(R, t) = \int R v_R v_\phi f d^3v dz + \frac{1}{4\pi G} \int_0^{2\pi} \underbrace{\left(\frac{\partial \Phi}{\partial R} \right)}_{\text{kinematic stress}} \underbrace{\left(\frac{\partial \Phi}{\partial \phi} \right)}_{\text{gravitational stress}} d\phi. \quad (\text{B-7})$$

A gravitational wake excites **both** terms.

Massive perturbers embedded in disks (e.g. giant molecular clouds, satellites, substructure) generate gravitational wakes. These wakes:

- induce correlated velocity distortions (kinematic stress), and
- produce asymmetric potential perturbations (gravitational stress).

Consequently, wakes provide a clear example where both stress channels contribute simultaneously to F_L , consistent with classical dynamical-friction analyses in collisionless systems[13], [25].

B.7 Radial migration

Radial migration corresponds to systematic changes in guiding-center radii driven by weak, transient non axisymmetric patterns. Although heating is minimal, migration involves a nonzero velocity covariance $\langle v_R v_\phi \rangle$, implying

$$F_L^{\text{kin}} \neq 0 \quad (\text{B-8})$$

even when gravitational stress is small. Migration thus demonstrates that significant angular-momentum transport can occur purely through kinematic stress, without strong potential distortions [14][12].

B.8 Failure of the isolated-ring rotation-curve assumption

The textbook rotation-curve relation

$$v_{\text{circ}}^2(R) = R \partial_R \Phi(R) \quad (\text{B-9})$$

corresponds to the special limit in which the disk is stationary, axisymmetric, and torque-free so that $F_L = 0$. However, real disks commonly host spirals, bars, transients, wakes, and migration, each of which implies $F_L \neq 0$ through one or both stress channels.

The breakdown of the isolated-ring approximation therefore reflects suppressed angular-momentum coupling, not a failure of Newtonian gravity.

B.9 Connection to the transmission framework

The Rotational Coherence Transmission (RCT) framework introduced in the main text does not modify the Vlasov–Poisson equations. Instead, it provides an effective closure describing how the **net, time-averaged angular-momentum flux** implied by $F_L \neq 0$ is inherited, attenuated, and redistributed with radius. The saturating response used in the model reflects energetic constraints and is derived from a minimal Lagrangian extension in Supplementary H.

SUPPLEMENTARY C: Numerical Implementation of the Three-Stage Transmission Model

This section documents the Jupyter Notebook/Python implementation (included in GitHub: https://github.com/sakidja/CTC_related_papers) used to generate all synthetic transmission cases summarized in Supplementary E. The code translates the analytic structure of the three-stage transmission framework into a fully reproducible numerical pipeline that produces rotation curves, curl-stress fields, and SPARC-style diagnostics (CurlIndex, SurplusIndex, and $\langle U \rangle$).

Several expressions appearing below—such as the definitions of the Newtonian rotation curve, the curl-stress field, torque gradients, and SPARC-style indices—are also presented in the main text. They are restated here intentionally. The goal of this supplement is not to introduce additional derivations, but to make the numerical pipeline **explicit, self-contained, and directly executable**. Repetition ensures that readers can follow each computational step without navigating between sections.

All definitions are therefore fully consistent with, and subordinate to, the formulations provided in the main paper.

The implementation proceeds in five steps.

C.1 Newtonian baseline and curl-stress field

The disk is initialized using an exponential surface-density profile,

$$\Sigma(r) = \Sigma_0 e^{-r/R_d}, \quad (\text{C-1})$$

from which the enclosed mass $M(< r)$, the Newtonian circular velocity

$$v_N(r) = \sqrt{\frac{GM(< r)}{r}}, \quad (\text{C-2})$$

and the baseline angular frequency $\Omega_N(r) = v_N/r$ are computed.

The Newtonian curl-stress field is evaluated as

$$S_{\text{raw}}(r) = \left| \frac{1}{r} \frac{d}{dr} [r v_N(r)] \right|, \quad (\text{C-3})$$

which supplies the dimensionless shear amplitude entering the transmission map.

C.2 Alternating transmission geometry

To represent heterogeneous coupling across the disk, the code imposes **alternating high- and low-coupling radial shells**. These shells do **not** correspond to material components; they are a numerical discretization of spatially varying transmission efficiency.

The geometric coupling functions are defined as

- **high-coupling shells**

$$k_{\text{high}}(r) = \exp \left(r/R_{k,\text{high}} \right), \quad (\text{C-4})$$

- **low-coupling shells**

$$k_{\text{low}}(r) = \exp \left(r/R_{k,\text{low}} \right), \quad (\text{C-5})$$

assigned to even and odd radial indices respectively. The innermost ten grid points are treated as a rigidly locked core with $k = 1$, reflecting near-perfect coupling in the central region.

An optional three-point smoothing pass removes sharp discontinuities and enforces monotonic decay. This alternating geometry provides a coarse-grained representation of the heterogeneous transmission landscape through which rotational energy propagates.

C.3 Three-stage transmission map

The curl-stress field enters the three-stage response law defined in the main text. First, the raw shear is normalized:

$$S(r) = \frac{S_{\text{raw}}(r)}{\max S_{\text{raw}}}, \quad (\text{C-6})$$

and then passed through the saturation map

$$T(r) = T_{\text{max}} \tanh \left(\frac{S(r)}{S_0} \right). \quad (\text{C-7})$$

For $S \ll S_0$, the response is linear (Stage I).

For intermediate shear, the response bends (Stage II).

For $S \gg S_0$, the transmission approaches the asymptotic value T_{max} (Stage III).

The effective transmission efficiency is then

$$k_{\text{eff}}(r) = k(r) T(r), \quad (\text{C-8})$$

which determines how much inner-engine rotational coherence can be inherited at each radius.

C.4 Energy-lock surrogate for the observed rotation curve

The synthetic “observed” rotation curve is constructed using the energy-lock surrogate,

$$v_{\text{obs}}^2(r) = v_N^2(r) + k_{\text{eff}}(r) [\Omega_{\text{inner}} r]^2. \quad (\text{C-9})$$

This expression implements the idea that the injected pattern speed Ω_{inner} acts as a coherent energy reservoir whose contribution to v_ϕ^2 is modulated by the local openness of the transmission chain. Curl fields and angular velocities for the synthetic curve are computed identically to the Newtonian case.

Shell-wise increments in rotational energy and angular momentum are evaluated as

$$\begin{aligned} \Delta E(r) &= \frac{1}{2} m(r) [v_{\text{obs}}^2(r) - v_N^2(r)], \\ \Delta L(r) &= m(r) r [v_{\text{obs}}(r) - v_N(r)], \end{aligned} \quad (\text{C-10}), (\text{C-11})$$

and are used to compute total and outer-constrained surplus quantities.

C.5 SPARC-style diagnostics

To enable direct comparison with the SPARC sample, the synthetic curves are reduced using the same quantitative indicators applied to the observational data.

Fractional uplift

$$U(r) = \frac{v_{\text{obs}}^2 - v_N^2}{v_N^2}. \quad (\text{C-12})$$

SurplusIndex

$$\text{SurplusIndex}_{\text{SP}} = \frac{\int_{r \geq 0.5 R_{\text{max}}} (v_{\text{obs}}^2 - v_N^2) dr}{\int_0^{R_{\text{max}}} v_{\text{obs}}^2 dr}. \quad (\text{C-13})$$

CurlIndex

$$\text{CurlIndex}_{\text{SP}} = \frac{\int |(d\tau_{\text{obs}}/dr) - (d\tau_N/dr)| dr}{\int |d\tau_N/dr| dr}, \quad (\text{C-14})$$

with $\tau = r v^2$.

Mean uplift

$$\langle U \rangle = \text{mean}[U(r)]. \quad (\text{C-15})$$

These definitions are matched exactly to the SPARC analysis pipeline (Supplementary D), enabling one-to-one comparison between synthetic and empirical trends.

C.6 Output and diagnostics

For each run, the script reports:

- total and outer rotational-energy surplus,
- total and outer angular-momentum surplus,
- model-level (energy-lock) curl and surplus indices,
- SPARC-style $\text{CurlIndex}_{\text{SP}}$, $\text{SurplusIndex}_{\text{SP}}$, and $\langle U \rangle$.

The code also generates:

- an eight-panel diagnostic figure (rotation curve, angular velocity, curl-stress field, coupling functions, ΔE , ΔL , cumulative surplus, and outer-zone uplift), and
- a SPARC-style three-panel figure matching the format used for empirical rotation curves.

Together, these outputs provide a complete and transparent numerical realization of the transmission model used to generate all synthetic cases presented in Supplementary E.

SUPPLEMENTARY D: Lagrangian Formulation of Rotational Coherence Transmission

D.1. Overview

This supplement provides a first-principles foundation for the rotational coherence transmission (RCT) framework. We begin by deriving the standard Vlasov–Poisson equations from an action principle. We then show how the observed saturation of torque transmission in disk galaxies follows naturally when the action is extended to include a term representing the finite absorptive capacity of the outer disk.

The key result is that the empirical **tanh transmission law** used in the main text is **not an arbitrary choice**, but the simplest mathematical expression of a physically required saturation mechanism.

D.2. Lagrangian Formulation of the Vlasov–Poisson System

A collisionless, self-gravitating system is described by:

- a phase-space distribution function $f(\mathbf{x}, \mathbf{v}, t)$,
- a gravitational potential $\Phi(\mathbf{x}, t)$,
- and a Lagrange multiplier $\lambda(\mathbf{x}, \mathbf{v}, t)$ enforcing phase-space conservation.

The total action is written as

$$S_{\text{VP}} = S_{\text{constraint}} + S_{\text{field}} \quad (\text{D-1})$$

D.2.1. Constraint Term (Vlasov Equation)

The Vlasov equation is enforced as a constraint:

$$S_{\text{constraint}} = \int dt d^3x d^3v \lambda \left(\frac{\partial f}{\partial t} + \mathbf{v} \cdot \nabla_x f - \nabla_x \Phi \cdot \nabla_v f \right) \quad (\text{D-2})$$

Variation with respect to λ gives

$$\frac{\partial f}{\partial t} + \mathbf{v} \cdot \nabla_x f - \nabla_x \Phi \cdot \nabla_v f = 0 \quad (\text{D-3})$$

which is the Vlasov equation.

D.2.2. Field Term (Poisson Equation)

The gravitational field energy is

$$S_{\text{field}} = - \int dt d^3x \frac{1}{8\pi G} (\nabla_x \Phi)^2 \quad (\text{D-4})$$

Variation with respect to Φ yields

$$\nabla^2 \Phi = 4\pi G \int f d^3v \quad (\text{D-5})$$

Together, Eqs. (H-3) and (H-5) fully describe collisionless dynamics. However, this formulation corresponds to the **special case** where radial angular-momentum transport vanishes ($F_L = 0$), i.e. the isolated-annulus limit.

D.3. Why Torque Transmission Must Saturate

D.3.1. Physical Origin of Saturation

The saturation of rotational coherence transmission follows directly from the galaxy's energy budget and does not require new physics. The logic is simple:

(1) Large inner energy reservoir

As shown in Section 5 of the main text, the inner disk contains orders of magnitude more rotational energy than the outer disk requires. The inner region therefore acts as a powerful source of rotational coherence.

(2) Only a small net flux is required

Because the outer disk is energetically weak, only a small and persistent outward transfer of angular momentum is needed to sustain a flat rotation curve. The transport mechanism need not be strong—only nonzero on average.

(3) Finite capacity of the outer disk

The outer disk cannot absorb unlimited coherence. Two effects limit absorption:

- **Finite phase-space volume:** low surface density restricts the number of accessible high-angular-momentum orbits.
- **Shear-induced damping:** increased shear suppresses the non axisymmetric modes that drive transport.

As a result, transmission must transition from an initially linear regime to a saturated one.

D.3.2. Saturation Potential and Transmission Law

We represent this behavior using a scalar field $C(x, t)$ that measures local curl-stress. The transmitted torque is assumed to decrease in efficiency as this stress increases.

The simplest potential that produces a **linear response at low stress** and **saturation at high stress** is

$$V_{\text{sat}}[C] = \frac{F_{\max} S_0}{\alpha} \ln [\cosh (\alpha C)] \quad (\text{D-6})$$

Limits

- **Low stress ($\alpha C \ll 1$)**

$$\ln(\cosh y) \approx \frac{1}{2}y^2 \Rightarrow V_{\text{sat}} \propto C^2 \quad (\text{D-7})$$

Linear inheritance regime.

- **High stress ($\alpha C \gg 1$)**

$$\ln(\cosh y) \approx |y| \Rightarrow V_{\text{sat}} \propto |C| \quad (\text{D-8})$$

Saturated transmission regime.

Thus, the tanh form follows directly from modeling a system with a large energy source feeding a receiver with finite capacity.

D.3.3. Transmission-Enhanced Action

The full action becomes

$$S_{\text{TVP}} = S_{\text{VP}} + S_{\text{sat}} \quad (\text{D-9})$$

with

$$S_{\text{sat}} = - \int dt d^3x V_{\text{sat}}[C] \quad (\text{D-10})$$

D.3.4. Deriving the Tanh Law

Stationary action with respect to C gives

$$\frac{\delta S_{\text{TVP}}}{\delta C} = 0 \quad (\text{D-11})$$

Since only S_{sat} depends on C ,

$$\tau_{\text{trans}} = \frac{\partial V_{\text{sat}}}{\partial C} \quad (\text{D-12})$$

Evaluating the derivative,

$$\tau_{\text{trans}}(\mathbf{x}, t) = F_{\max} S_0 \tanh(\alpha C) \quad (\text{D-13})$$

This is the transmission law used in the main text.

D.3.5. Connection to the Empirical Model

Identifications:

- $T_0(r) \equiv F_{\max}S_0$ (maximum transmissible torque)
- $C(r) \propto S(r)$ (normalized curl-stress)

Absorbing constants into α , we recover

$$\tau_{\text{trans}}(r) = T_0(r) \tanh [\alpha S(r)] \quad (\text{D-14})$$

D.4. Conclusion

This supplement provides a Lagrangian basis for the rotational coherence transmission framework. The standard Vlasov–Poisson system describes ideal collisionless dynamics but implicitly enforces vanishing angular-momentum flux. Accounting for the finite absorptive capacity of the outer disk requires extending the action by a saturation potential. The resulting Euler–Lagrange equation yields a tanh transmission law as the minimal functional form consistent with linear response at low stress and saturation at high stress.

The empirical transmission model is therefore not a fitting ansatz, but the natural consequence of incorporating energetic and phase-space constraints into a first-principles Lagrangian description of disk dynamics

SUPPLEMENTARY E: Classification of Synthetic Transmission Cases

E.1. Overview

To compare the synthetic transmission experiments with the empirical SPARC sample, each model realization is assigned to one of three dynamical groups using three SPARC-style diagnostics, all summarized in Table E1:

- SurplusIndex_SP – the primary discriminator; measures whether outward transmission has activated and how efficiently rotational energy accumulates in the outer disk.
- CurlIndex_SP – amplitude of non-axisymmetric shear in the disk.
- $\langle U \rangle$ (mean uplift) – the net enhancement of rotational support relative to the Newtonian baseline.

The grouping is entirely empirical and mirrors the same structure seen in the SPARC data: a subcritical low-surplus cloud, an intermediate bending regime, and a high-surplus saturated sequence. The individual synthetic realizations, their indices, and their assigned dynamical group are listed in Table E1, while the global trends of these indices are shown in Figure E1(a,b). For the Jupyter Notebook, please see the GitHub repository: https://github.com/sakidja/CTC_related_papers.

E2. Summary of Diagnostic Trends

The behavior of the synthetic sample is most clearly seen by plotting the diagnostics against CurlIndex_SP. Figure E1(a) shows the mean uplift $\langle U \rangle$ as a function of CurlIndex_SP, and Figure E1(b) shows SurplusIndex_SP versus CurlIndex_SP. Together with Table E1, they organize the synthetic cases into the three dynamical regimes.

(i) Mean uplift vs. CurlIndex_SP

In Figure E1(a), the synthetic cases trace out a tight, monotonic trend that is identical in form to the SPARC pattern:

- $\langle U \rangle \approx 0$ when $\text{CurlIndex_SP} \lesssim 1$
- $\langle U \rangle$ grows quasi-linearly for $1 \lesssim \text{CurlIndex_SP} \lesssim 10$
- High-curl systems ($\text{CurlIndex_SP} \gtrsim 10$) reach $\langle U \rangle \approx 6\text{--}8$

This confirms that uplift behaves as a kinematic response to the shear amplitude: once curl crosses a threshold, uplift rises systematically with CurlIndex_SP rather than with radius or mass alone.

(ii) SurplusIndex_SP vs. CurlIndex_SP

In Figure E1(b), the SurplusIndex_SP values from Table E1 reproduce the same three-part structure as the SPARC galaxies:

- A low-curl, low-surplus floor (subcritical regime), where SurplusIndex_SP ≈ 0 even though $\text{CurlIndex_SP} > 0$.
- A rising bending sequence, where SurplusIndex_SP increases with CurlIndex_SP as transmission activates but remains limited in radial reach.
- A saturated plateau, where SurplusIndex_SP approaches $\sim 0.30\text{--}0.45$ at large curl, indicating nearly maximal inheritance of inner rotational support.

The synthetic population therefore not only spans the same numerical range in $(\text{CurlIndex_SP}, \text{SurplusIndex_SP}, \langle U \rangle)$ as the SPARC sample but also arranges itself into the same three dynamical regimes. The detailed case-by-case assignments in Table E1 simply make this organization explicit.

Each model realization is assigned to a dynamical group (Group 1: subcritical, Group 2: bending, Group 3: saturated) based on its SurplusIndex_SP, CurlIndex_SP, and mean uplift ($\langle U \rangle$). SurplusIndex_SP serves as the primary discriminator (defining whether transmission has activated), while CurlIndex_SP and $\langle U \rangle$ provide secondary dynamical context. The table lists each synthetic case together with its three diagnostics and its resulting group assignment. The full distribution of these points is shown in Figures E1 and E2.

Table E1. Classification of all synthetic transmission cases by SPARC-style diagnostics

Case	CurlIndex_SP	SurplusIndex_SP	$\langle U \rangle$ (Mean uplift)	Group
I.1	0.0217	0.0011	0.0098	Group 1
I.2	0.0739	0.0054	0.0337	Group 1
I.3	0.2927	0.0315	0.1478	Group 1
I.4	0.5906	0.0342	0.2696	Group 1
I.5	2.1693	0.0513	0.9761	Group 1
I.6	0.5734	0.0559	0.2736	Group 1
I.7	0.3960	0.0772	0.2481	Group 1
II.1	2.6532	0.1284	1.4039	Group 2
II.2	1.7926	0.1768	1.0257	Group 2
II.3	5.7500	0.2200	3.1623	Group 2
III.1	11.4933	0.3112	6.8143	Group 3
III.2	3.7303	0.3130	1.5390	Group 3
III.3	6.7665	0.3202	4.2280	Group 3
III.4	8.5692	0.3281	5.4642	Group 3
III.5	5.3338	0.3293	3.1979	Group 3
III.6	10.4446	0.3372	6.3638	Group 3
III.7	11.1909	0.4320	4.5910	Group 3
III.8	14.6228	0.4520	5.9989	Group 3

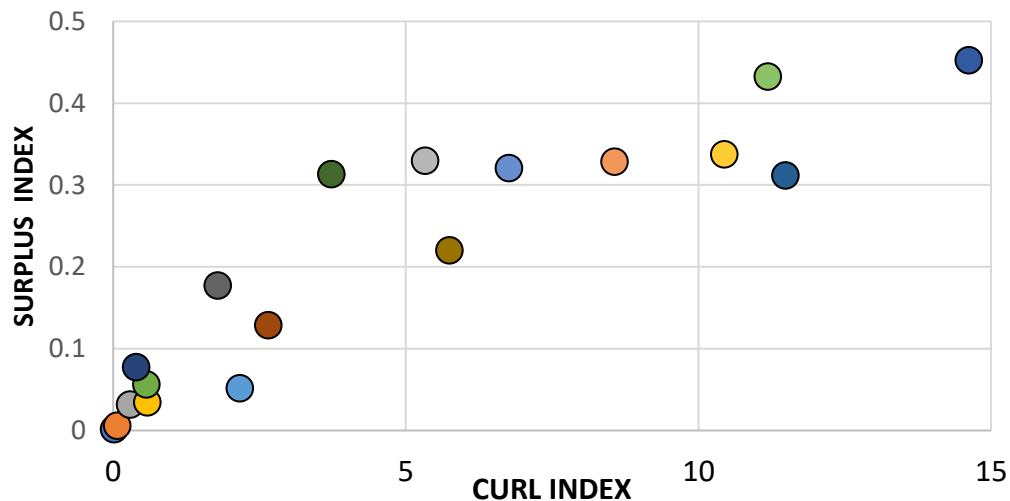


Figure E1. SurplusIndex_SP versus CurlIndex_SP for the synthetic sample.

The synthetic realizations reproduce the same three-regime structure found in the SPARC dataset. Low-curl models cluster on a subcritical floor with $\text{SurplusIndex}_{\text{SP}} \approx 0$. Intermediate models occupy a rising “bending” branch where surplus increases with curl as transmission activates. High-curl systems saturate at $\text{SurplusIndex}_{\text{SP}} \approx 0.30\text{--}0.45$, reflecting global, radius-limited coherence transfer. Together with Figure E1, this plot shows that the synthetic transmission model naturally generates the three dynamical regimes observed in real disks.

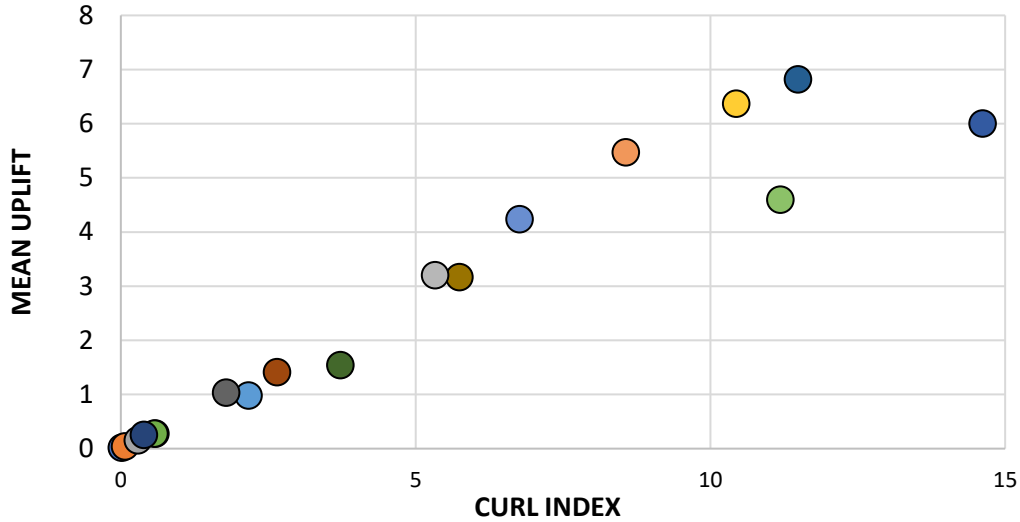


Figure E2. Mean uplift versus $\text{CurlIndex}_{\text{SP}}$ for all synthetic transmission cases.

This plot shows how the mean uplift ($\langle U \rangle$) responds to increasing non axisymmetric shear. The synthetic models follow the same monotonic sequence observed in the SPARC galaxies: (1) a near-zero uplift floor for $\text{CurlIndex}_{\text{SP}} \lesssim 1$, (2) a quasi-linear rise for $1 \lesssim \text{CurlIndex}_{\text{SP}} \lesssim 10$, and (3) a high-curl plateau with $\langle U \rangle \approx 6\text{--}8$. The trend demonstrates that uplift is a direct kinematic response to shear amplitude, not to radius or mass alone.

Group 1 — Subcritical / Low-Surplus Regime

Definition : A model belongs to Group 1 if:
 $\text{SurplusIndex}_{\text{SP}} < 0.10$,

Physical Interpretation

Transmission does not meaningfully activate.

The inner engine injects insufficient coherent torque for the signal to propagate beyond the inner few rings. Mild shear produces nonzero curl (i.e., $K_L \neq 0$), but the surplus energy never departs from the Newtonian baseline. These runs reproduce the subcritical regime seen in galaxies such as UGC 02455 and Holmberg II, where the disk is mildly distorted but torque inheritance is effectively absent.

CASE I.1

```

N = 5000
r = np.linspace(0.1, 30.0, N) # kpc
dr = r[1] - r[0]
idx = np.arange(N)

# Disk / gravity
Sigma0, R_d = 1e9, 3.5      # Msun/kpc^2, kpc
G = 4.302e-6                # kpc·(km/s)^2 / Msun

# Inner “engine”
Omega_inner = 50.0          # km/s/kpc
i_solid = 10                 # rigid-core edge index

# Alternating-layer geometric coupling
Rk_alt = 5.0                 # kpc
Rk_star = 1.0                 # kpc

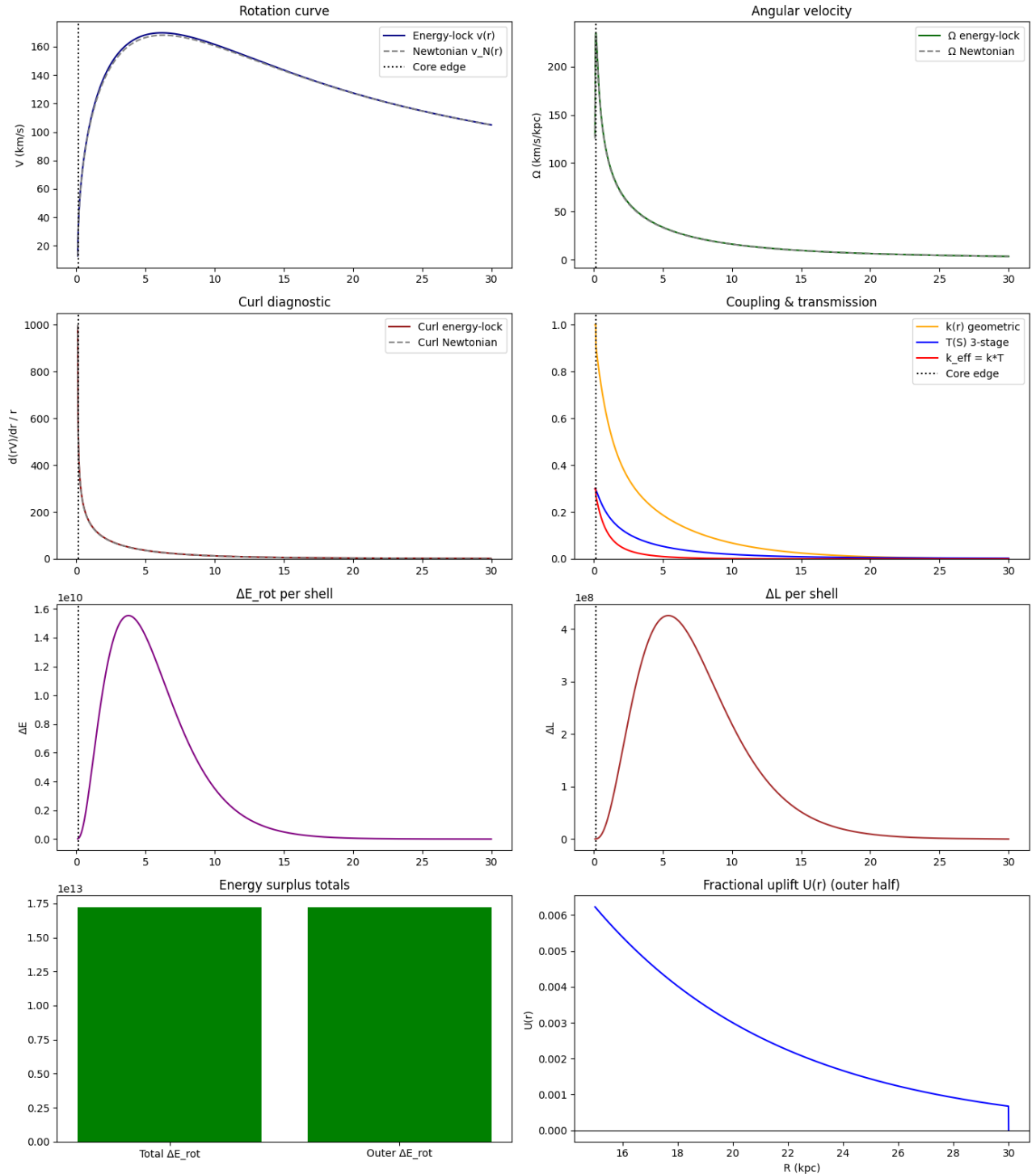
# Three-stage transmission parameters (tune these)
T_MAX = 0.3                  # max transmitted fraction
S0 = 0.2                      # curl-stress scale for bending/saturation

===== Energy / L diagnostics (model) =====
Total ΔE_rot: 1.720877e+13
Outer ΔE_rot: 1.720843e+13
Fractional uplift (outer ΔE/Newtonian): 0.019
Total ΔL: 5.945477e+11
Outer ΔL: 5.945461e+11

===== Model indices (energy-lock vs Newtonian) =====
Curl_Index_model = 0.0098
Surplus_Index_model= 1.0000

===== SPARC-style indices (using vN vs v_partial) =====
CurlIndex_SP = 0.0217
SurplusIndex_SP = 0.0011
Mean uplift <U> = 0.0098
R_max = 30.00 kpc

```



CASE I.2

```

N = 5000
r = np.linspace(0.1, 30.0, N)      # kpc
dr = r[1] - r[0]
idx = np.arange(N)

# Disk / gravity
Sigma0, R_d = 1e9, 3.5             # Msun/kpc^2, kpc
G = 4.302e-6                      # kpc · (km/s)^2 / Msun

# Inner "engine"
Omega_inner = 100.0                # km/s/kpc
i_solid = 10                        # rigid-core edge index

# Alternating-layer geometric coupling
Rk_alt = 6                         # kpc
Rk_star = 0.2                       # kpc

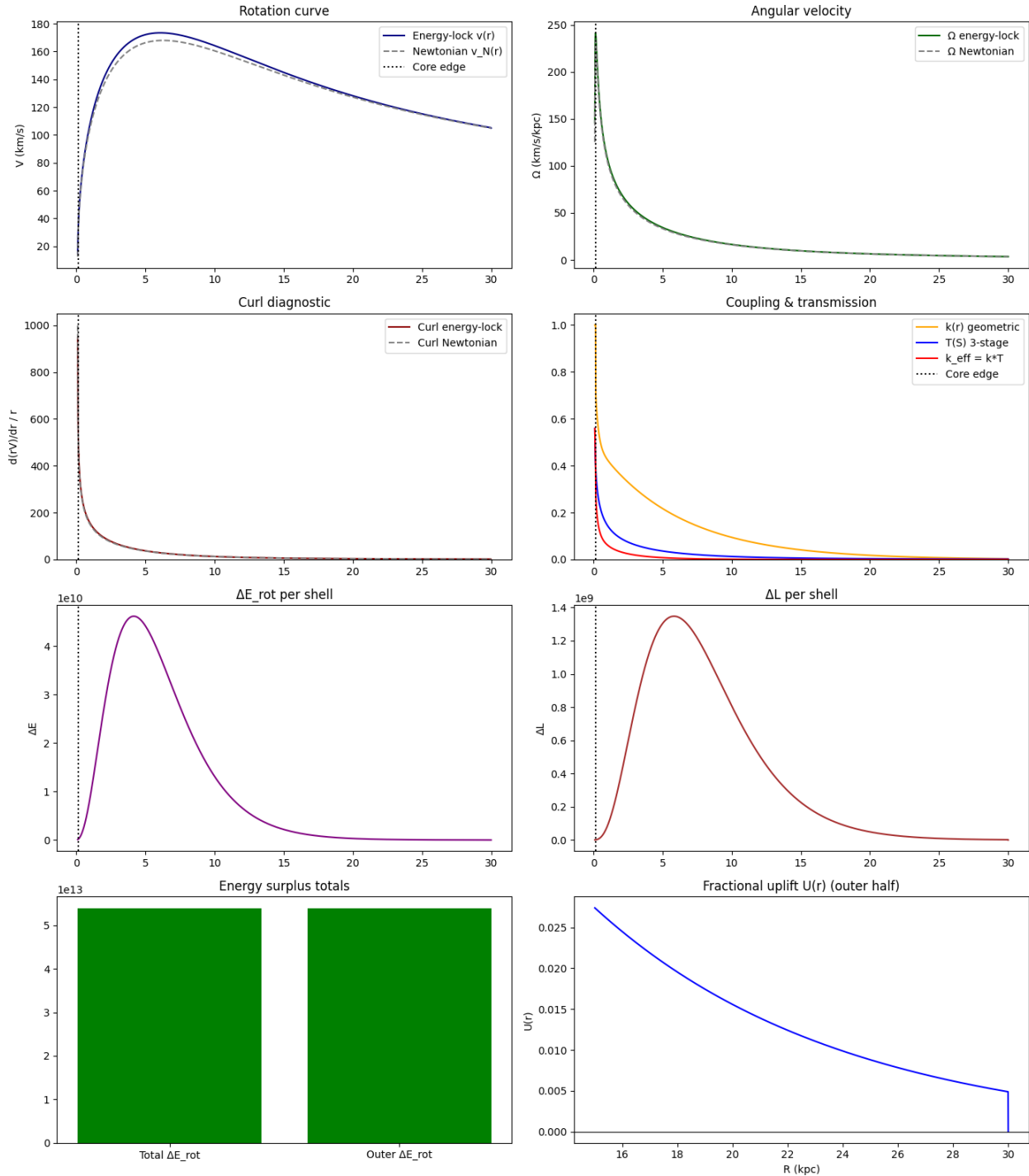
# Three-stage transmission parameters (tune these)
T_MAX = 0.6                         # max transmitted fraction
S0     = 0.6                         # curl-stress scale for bending/saturation

===== Energy / L diagnostics (model) =====
Total ΔE_rot:          5.387538e+13
Outer ΔE_rot:          5.387339e+13
Fractional uplift (outer ΔE/Newtonian): 0.059
Total ΔL:              1.996647e+12
Outer ΔL:              1.996638e+12

===== Model indices (energy-lock vs Newtonian) =====
Curl_Index_model = 0.0279
Surplus_Index_model= 1.0000

===== SPARC-style indices (using vN vs v_partial) =====
CurlIndex_SP       = 0.0739
SurplusIndex_SP    = 0.0054
Mean uplift <U>   = 0.0337
R_max              = 30.00 kpc

```



CASE I.3

```

N = 5000
r = np.linspace(0.1, 30.0, N)      # kpc
dr = r[1] - r[0]
idx = np.arange(N)

# Disk / gravity
Sigma0, R_d = 1e9, 3.5             # Msun/kpc^2, kpc
G = 4.302e-6                      # kpc · (km/s)^2 / Msun

# Inner "engine"
Omega_inner = 50.0                 # km/s/kpc
i_solid = 10                        # rigid-core edge index

# Alternating-layer geometric coupling
Rk_alt = 9                          # kpc
Rk_star = 4                         # kpc

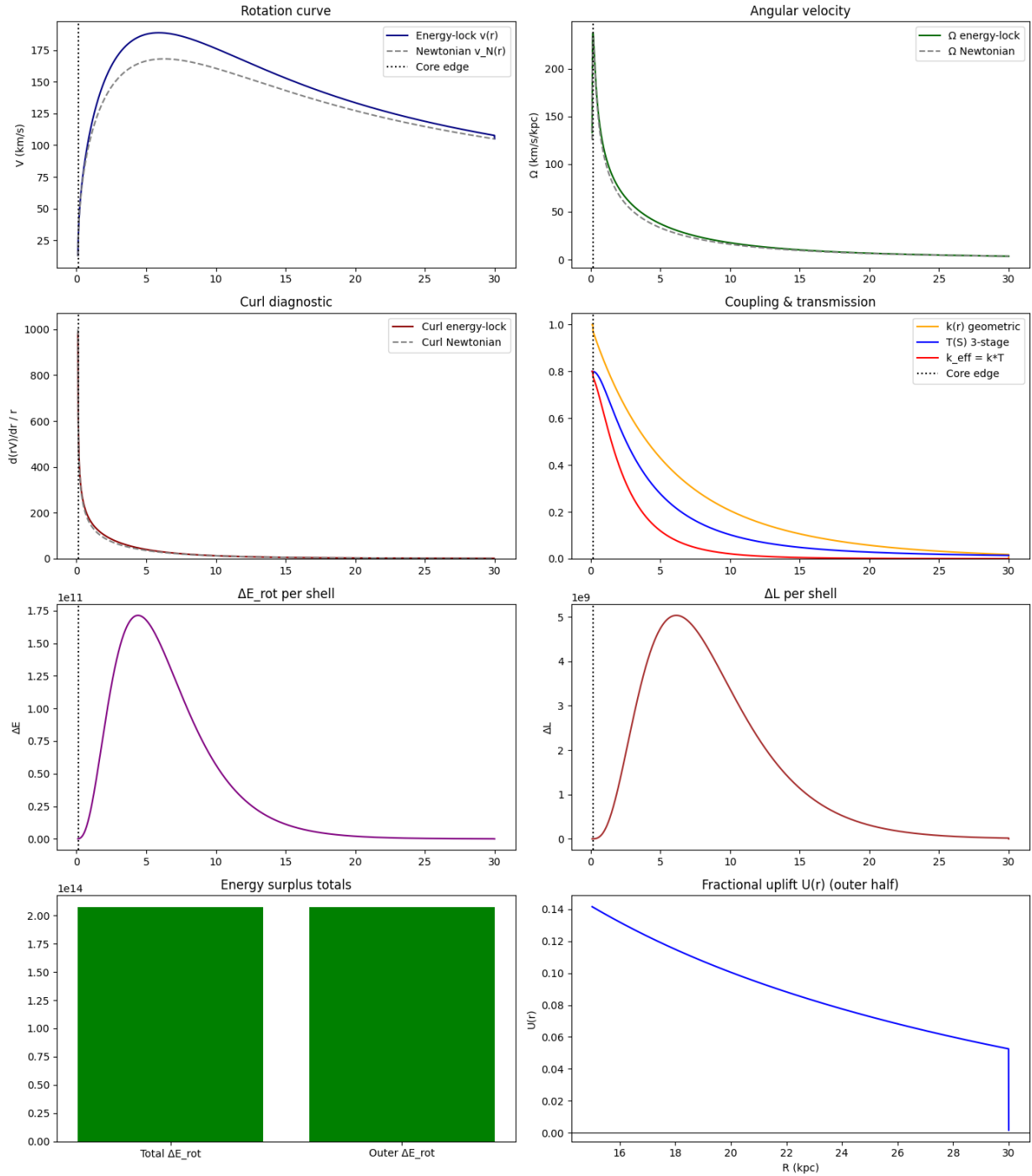
# Three-stage transmission parameters (tune these)
T_MAX = 0.8                         # max transmitted fraction
S0     = 0.1                         # curl-stress scale for bending/saturation

===== Energy / L diagnostics (model) =====
Total ΔE_rot:          2.073152e+14
Outer ΔE_rot:          2.073143e+14
Fractional uplift (outer ΔE/Newtonian): 0.228
Total ΔL:               7.974187e+12
Outer ΔL:               7.974183e+12

===== Model indices (energy-lock vs Newtonian) =====
Curl_Index_model = 0.0953
Surplus_Index_model= 1.0000

===== SPARC-style indices (using vN vs v_partial) =====
CurlIndex_SP       = 0.2927
SurplusIndex_SP    = 0.0315
Mean uplift <U>   = 0.1478
R_max              = 30.00 kpc

```



CASE I.4

```

N = 5000
r = np.linspace(0.1, 30.0, N)      # kpc
dr = r[1] - r[0]
idx = np.arange(N)

# Disk / gravity
Sigma0, R_d = 1e9, 3.5             # Msun/kpc^2, kpc
G = 4.302e-6                      # kpc · (km/s)^2 / Msun

# Inner "engine"
Omega_inner = 200.0                # km/s/kpc
i_solid = 10                        # rigid-core edge index

# Alternating-layer geometric coupling
Rk_alt = 6                         # kpc
Rk_star = 0.5                       # kpc

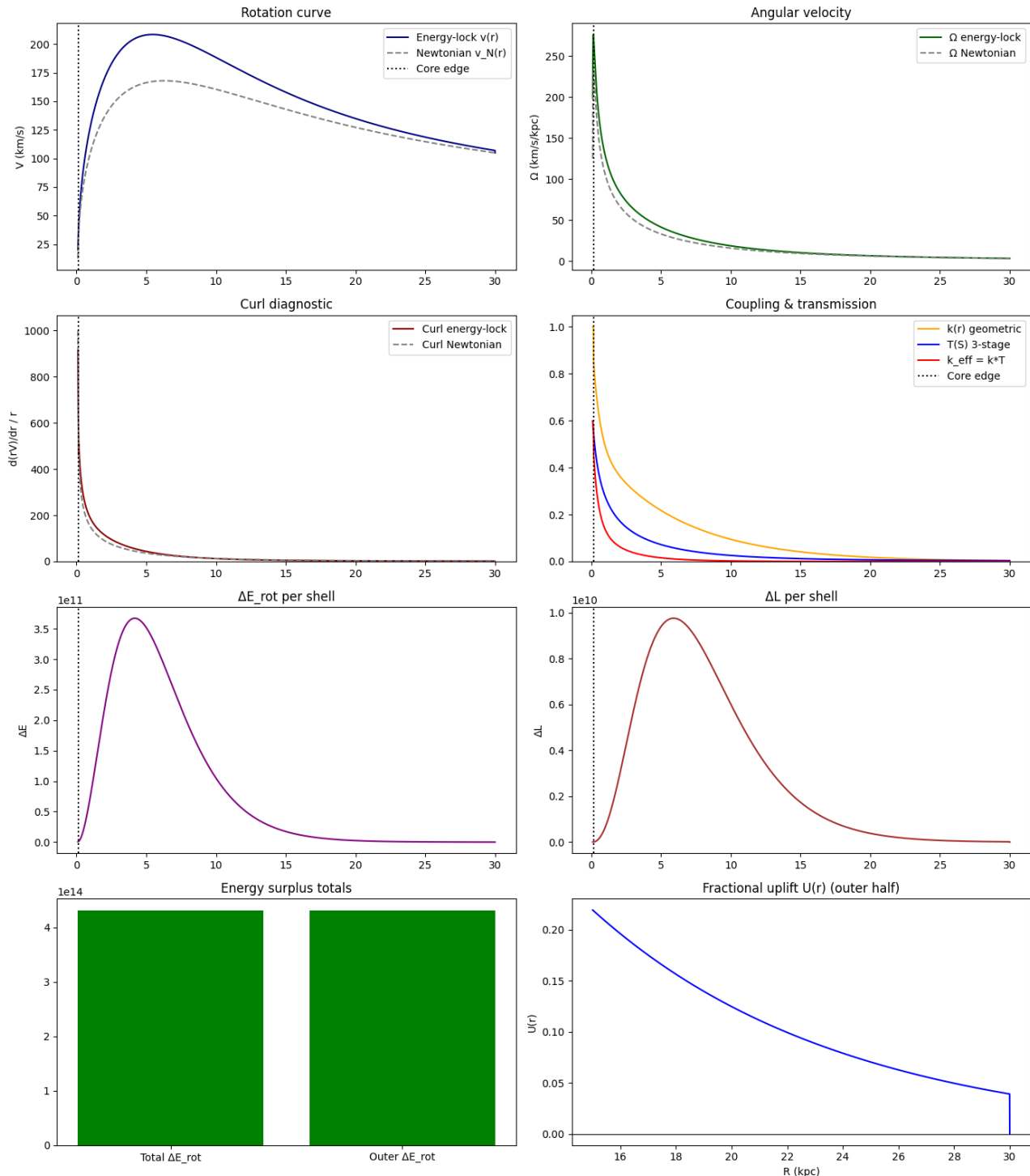
# Three-stage transmission parameters (tune these)
T_MAX = 0.6                         # max transmitted fraction
S0     = 0.3                         # curl-stress scale for bending/saturation

===== Energy / L diagnostics (model) =====
Total ΔE_rot:          4.309016e+14
Outer ΔE_rot:          4.308912e+14
Fractional uplift (outer ΔE/Newtonian): 0.474
Total ΔL:              1.468654e+13
Outer ΔL:              1.468650e+13

===== Model indices (energy-lock vs Newtonian) =====
Curl_Index_model = 0.2080
Surplus_Index_model= 1.0000

===== SPARC-style indices (using vN vs v_partial) =====
CurlIndex_SP        = 0.5906
SurplusIndex_SP      = 0.0342
Mean uplift <U>      = 0.2696
R_max                 = 30.00 kpc

```



CASE I.5

```

N = 5000
r = np.linspace(0.1, 30.0, N)      # kpc
dr = r[1] - r[0]
idx = np.arange(N)

# Disk / gravity
Sigma0, R_d = 1e9, 3.5             # Msun/kpc^2, kpc
G = 4.302e-6                      # kpc · (km/s)^2 / Msun

# Inner "engine"
Omega_inner = 500.0                # km/s/kpc
i_solid = 10                        # rigid-core edge index

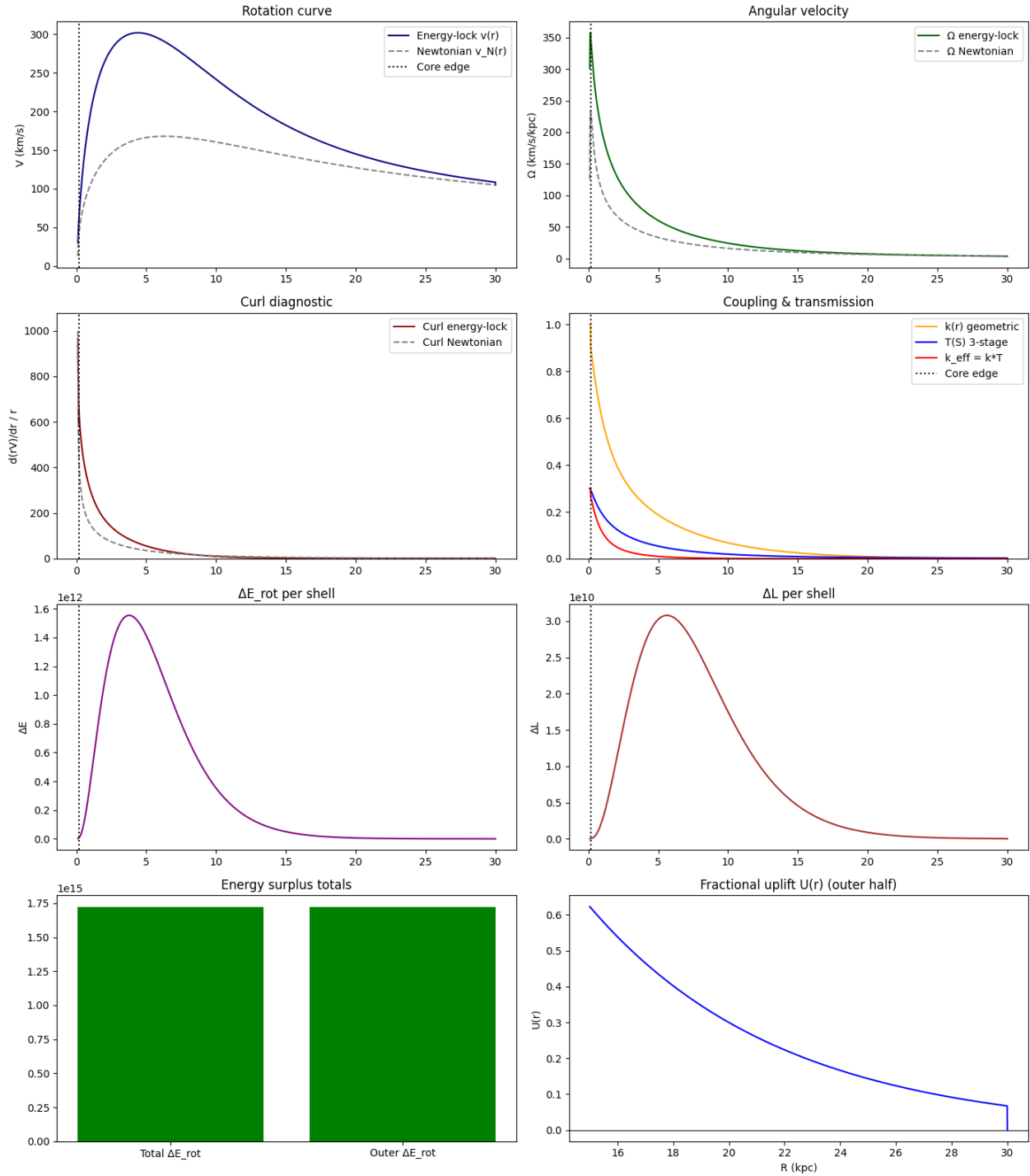
# Alternating-layer geometric coupling
Rk_alt = 5.0                       # kpc
Rk_star = 1.0                       # kpc

# Three-stage transmission parameters (tune these)
T_MAX = 0.3                         # max transmitted fraction
S0 = 0.2                             # curl-stress scale for bending/saturation
===== Energy / L diagnostics (model) =====
Total ΔE_rot:           1.720877e+15
Outer ΔE_rot:            1.720843e+15
Fractional uplift (outer ΔE/Newtonian): 1.893
Total ΔL:                  4.500366e+13
Outer ΔL:                  4.500354e+13

===== Model indices (energy-lock vs Newtonian) =====
Curl_Index_model = 0.7072
Surplus_Index_model= 1.0000

===== SPARC-style indices (using vN vs v_partial) =====
CurlIndex_SP       = 2.1693
SurplusIndex_SP    = 0.0513
Mean uplift <U>   = 0.9761
R_max              = 30.00 kpc

```



CASE I.6

```

N = 5000
r = np.linspace(0.1, 30.0, N)      # kpc
dr = r[1] - r[0]
idx = np.arange(N)

# Disk / gravity
Sigma0, R_d = 1e9, 3.5             # Msun/kpc^2, kpc
G = 4.302e-6                      # kpc · (km/s)^2 / Msun

# Inner "engine"
Omega_inner = 50.0                 # km/s/kpc
i_solid = 10                        # rigid-core edge index

# Alternating-layer geometric coupling
Rk_alt = 9                         # kpc
Rk_star = 4                         # kpc

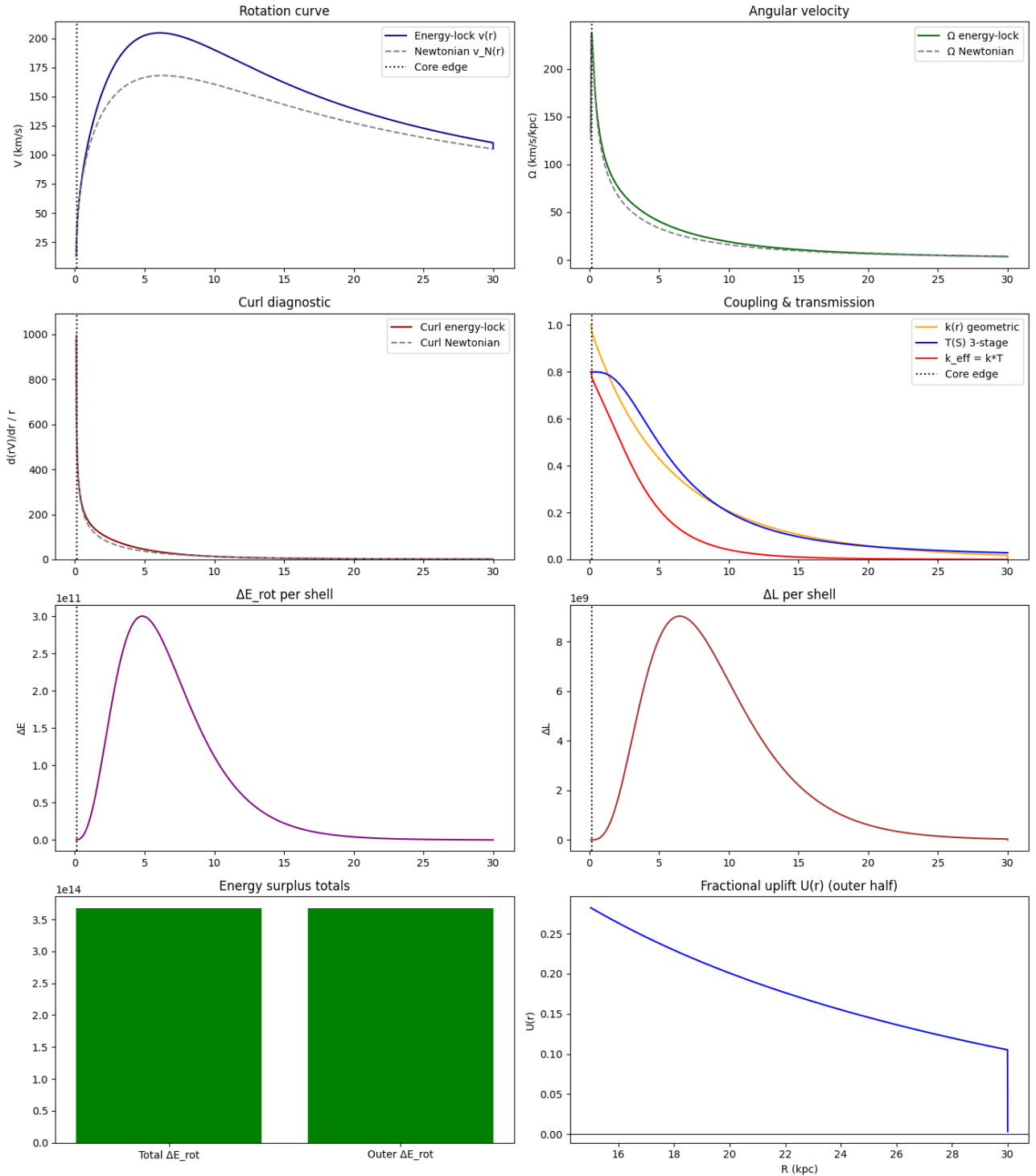
# Three-stage transmission parameters (tune these)
T_MAX = 0.8                         # max transmitted fraction
S0     = 0.05                         # curl-stress scale for
bending/saturation

===== Energy / L diagnostics (model) =====
Total ΔE_rot:          3.674096e+14
Outer ΔE_rot:          3.674087e+14
Fractional uplift (outer ΔE/Newtonian): 0.404
Total ΔL:               1.431512e+13
Outer ΔL:               1.431512e+13

===== Model indices (energy-lock vs Newtonian) =====
Curl_Index_model = 0.1572
Surplus_Index_model= 1.0000

===== SPARC-style indices (using vN vs v_partial) =====
CurlIndex_SP        = 0.5734
SurplusIndex_SP     = 0.0559
Mean uplift <U>     = 0.2736
R_max                = 30.00 kpc

```



CASE I.7

```

N = 5000
r = np.linspace(0.1, 30.0, N)      # kpc
dr = r[1] - r[0]
idx = np.arange(N)

# Disk / gravity
Sigma0, R_d = 1e9, 3.5             # Msun/kpc^2, kpc
G = 4.302e-6                      # kpc · (km/s)^2 / Msun

# Inner "engine"
Omega_inner = 100.0                # km/s/kpc
i_solid = 10                        # rigid-core edge index

# Alternating-layer geometric coupling
Rk_alt = 15                         # kpc
Rk_star = .6                         # kpc

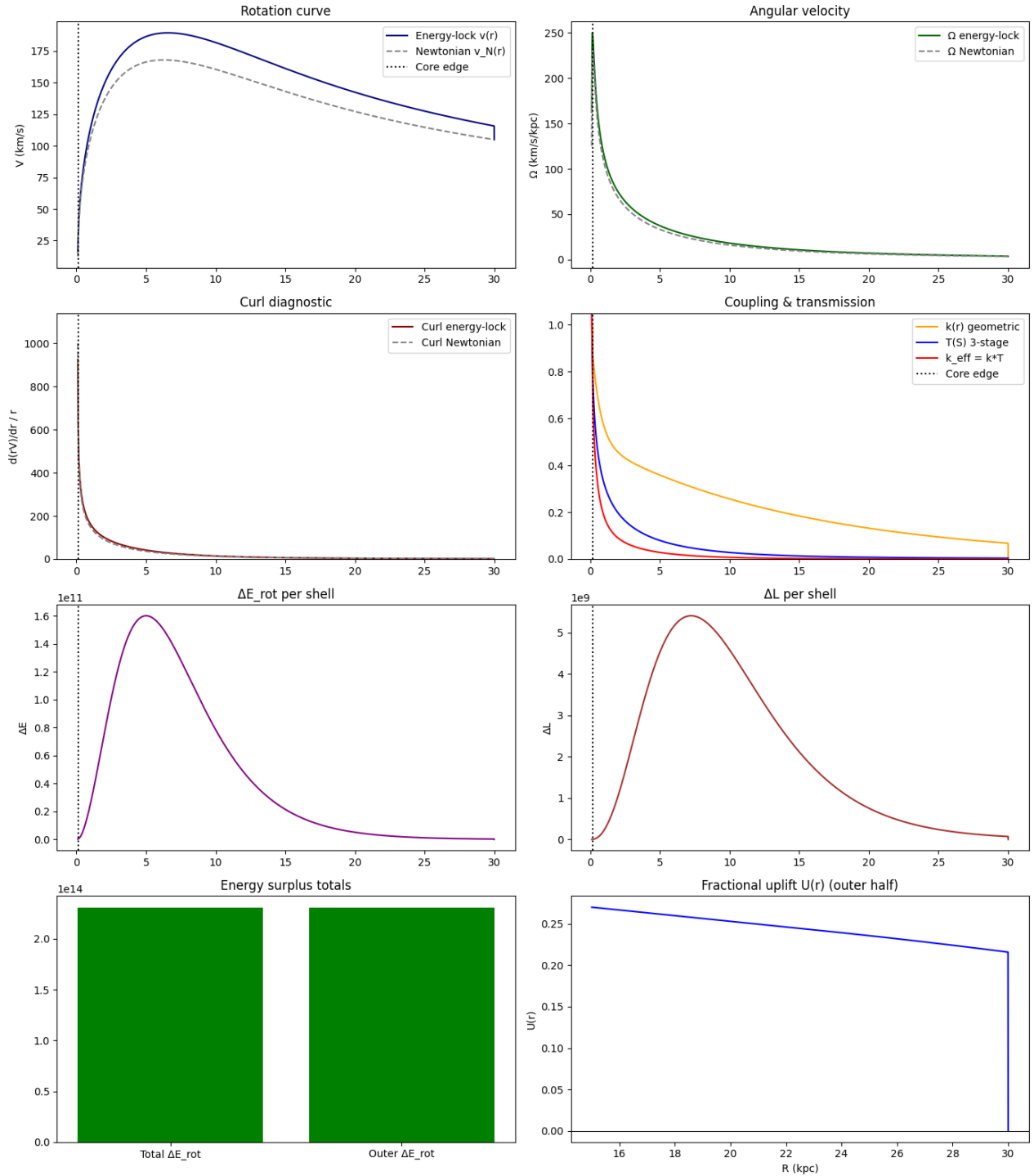
# Three-stage transmission parameters (tune these)
T_MAX = 1.1                          # max transmitted fraction
S0 = 0.5                             # curl-stress scale for bending/saturation

===== Energy / L diagnostics (model) =====
Total ΔE_rot:           2.306767e+14
Outer ΔE_rot:           2.306727e+14
Fractional uplift (outer ΔE/Newtonian): 0.254
Total ΔL:                 1.020012e+13
Outer ΔL:                 1.020010e+13

===== Model indices (energy-lock vs Newtonian) =====
Curl_Index_model = 0.1292
Surplus_Index_model= 1.0000

===== SPARC-style indices (using vN vs v_partial) =====
CurlIndex_SP       = 0.3960
SurplusIndex_SP    = 0.0772
Mean uplift <U>   = 0.2481
R_max              = 30.00 kpc

```



Group 2— Intermediate / Bending Regime

Definition: A model belongs to Group 2 if:
 $0.10 \leq \text{SurplusIndex}_{\text{SP}} < 0.30$,

Physical Interpretation

Transmission is active but throttled.

Increasing either the inner-engine strength Ω_{inner} or the gas-coupling length $R_{k,\text{gas}}$ produces visible uplift and curvature in the rotation curve, but the propagation chain stalls part-way out. This occurs because either (i) the geometric decay across “star-like” rings remains too steep, or (ii) curl-stress saturation halts growth before the torque can be exported globally. These models correspond to the **bending regime** of SPARC dwarfs where strong non-axisymmetry is present but full surplus saturation is not achieved.

CASE II.1

```

N = 5000
r = np.linspace(0.1, 30.0, N)      # kpc
dr = r[1] - r[0]
idx = np.arange(N)

# Disk / gravity
Sigma0, R_d = 1e9, 3.5             # Msun/kpc^2, kpc
G = 4.302e-6                      # kpc · (km/s)^2 / Msun

# Inner "engine"
Omega_inner = 300.0                # km/s/kpc
i_solid = 10                        # rigid-core edge index

# Alternating-layer geometric coupling
Rk_alt = 9                         # kpc
Rk_star = 4                         # kpc

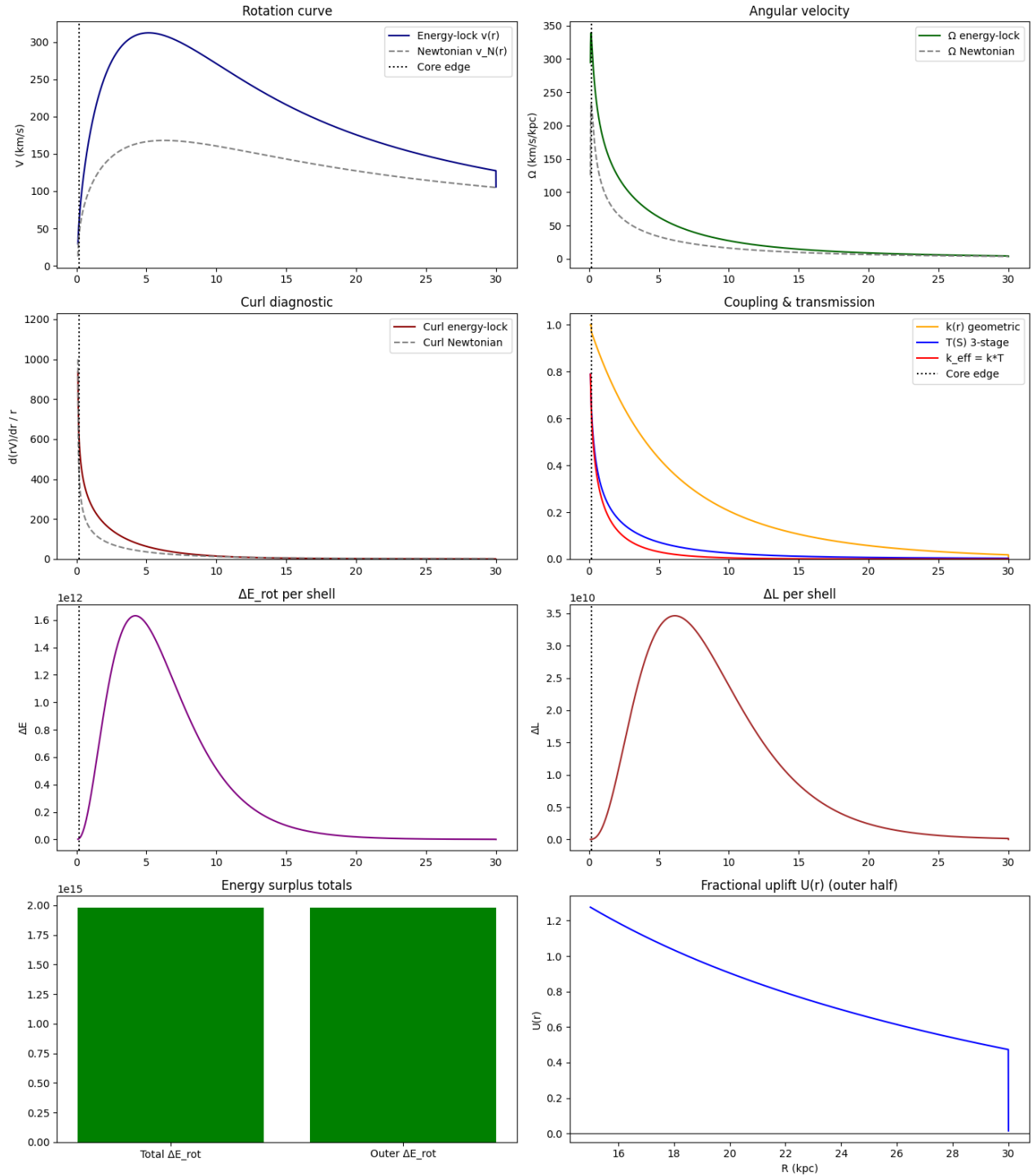
# Three-stage transmission parameters (tune these)
T_MAX = 0.8                         # max transmitted fraction
S0     = 0.4                         # curl-stress scale for bending/saturation

===== Energy / L diagnostics (model) =====
Total ΔE_rot:          1.979969e+15
Outer ΔE_rot:          1.979940e+15
Fractional uplift (outer ΔE/Newtonian): 2.178
Total ΔL:               5.694597e+13
Outer ΔL:               5.694586e+13

===== Model indices (energy-lock vs Newtonian) =====
Curl_Index_model = 0.7378
Surplus_Index_model= 1.0000

===== SPARC-style indices (using vN vs v_partial) =====
CurlIndex_SP       = 2.6532
SurplusIndex_SP    = 0.1284
Mean uplift <U>   = 1.4039
R_max              = 30.00 kpc

```



CASE II.2

```

N = 5000
r = np.linspace(0.1, 30.0, N)      # kpc
dr = r[1] - r[0]
idx = np.arange(N)

# Disk / gravity
Sigma0, R_d = 1e9, 3.5             # Msun/kpc^2, kpc
G = 4.302e-6                      # kpc · (km/s)^2 / Msun

# Inner "engine"
Omega_inner = 100.0                # km/s/kpc
i_solid = 10                        # rigid-core edge index

# Alternating-layer geometric coupling
Rk_alt = 12                         # kpc
Rk_star = .6                         # kpc

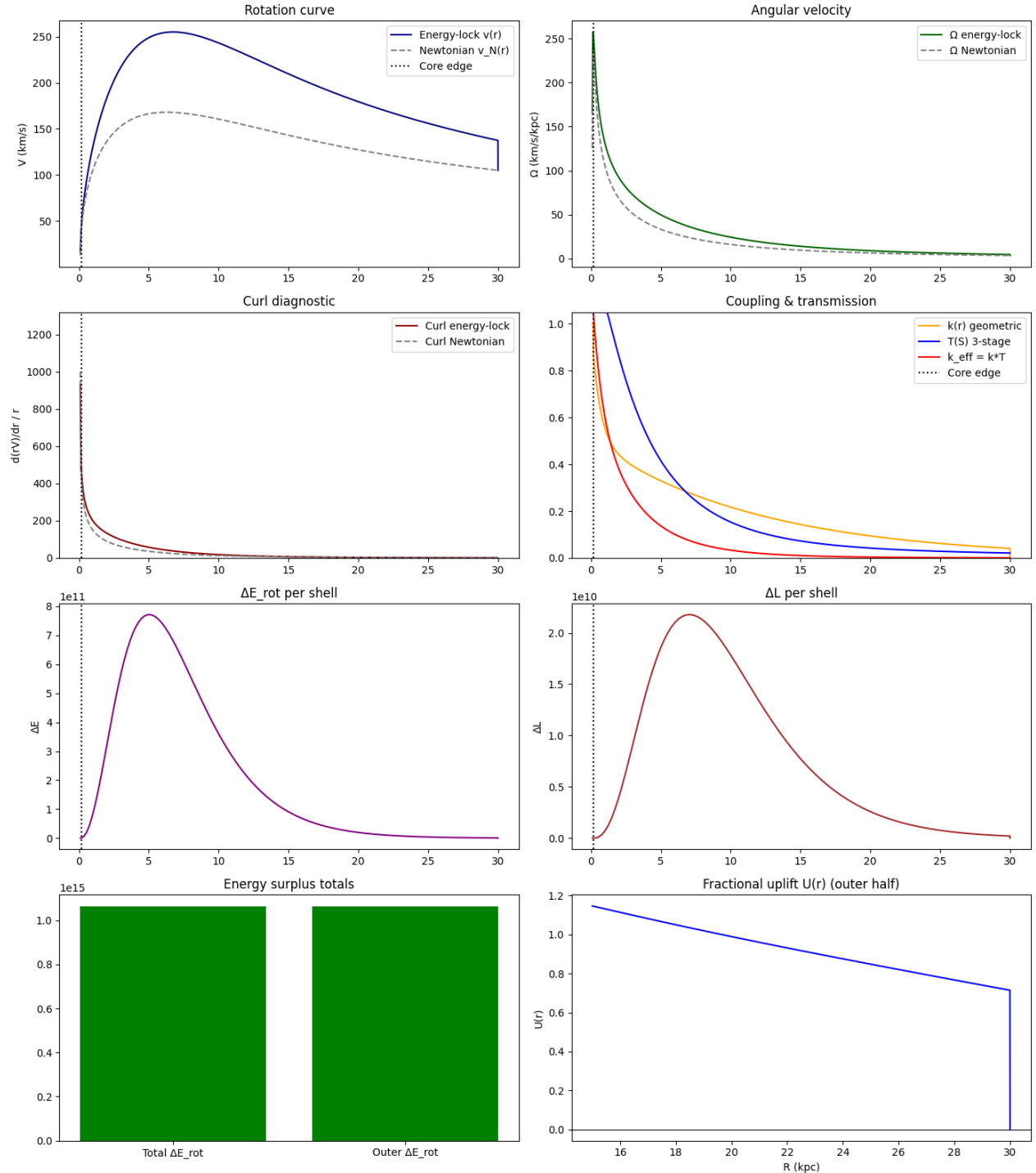
# Three-stage transmission parameters (tune these)
T_MAX = 1.2                          # max transmitted fraction
S0     = 0.1                          # curl-stress scale for bending/saturation

===== Energy / L diagnostics (model) =====
Total ΔE_rot:           1.062327e+15
Outer ΔE_rot:           1.062322e+15
Fractional uplift (outer ΔE/Newtonian): 1.169
Total ΔL:                3.944952e+13
Outer ΔL:                3.944950e+13

===== Model indices (energy-lock vs Newtonian) =====
Curl_Index_model = 0.4581
Surplus_Index_model= 1.0000

===== SPARC-style indices (using vN vs v_partial) =====
CurlIndex_SP        = 1.7926
SurplusIndex_SP     = 0.1768
Mean uplift <U>    = 1.0257
R_max               = 30.00 kpc

```



CASE II.3

```

N = 5000
r = np.linspace(0.1, 30.0, N)      # kpc
dr = r[1] - r[0]
idx = np.arange(N)

# Disk / gravity
Sigma0, R_d = 1e9, 3.5             # Msun/kpc^2, kpc
G = 4.302e-6                      # kpc · (km/s)^2 / Msun

# Inner "engine"
Omega_inner = 200.0                # km/s/kpc
i_solid = 10                        # rigid-core edge index

# Alternating-layer geometric coupling
Rk_alt = 10                         # kpc
Rk_star = 1.0                        # kpc

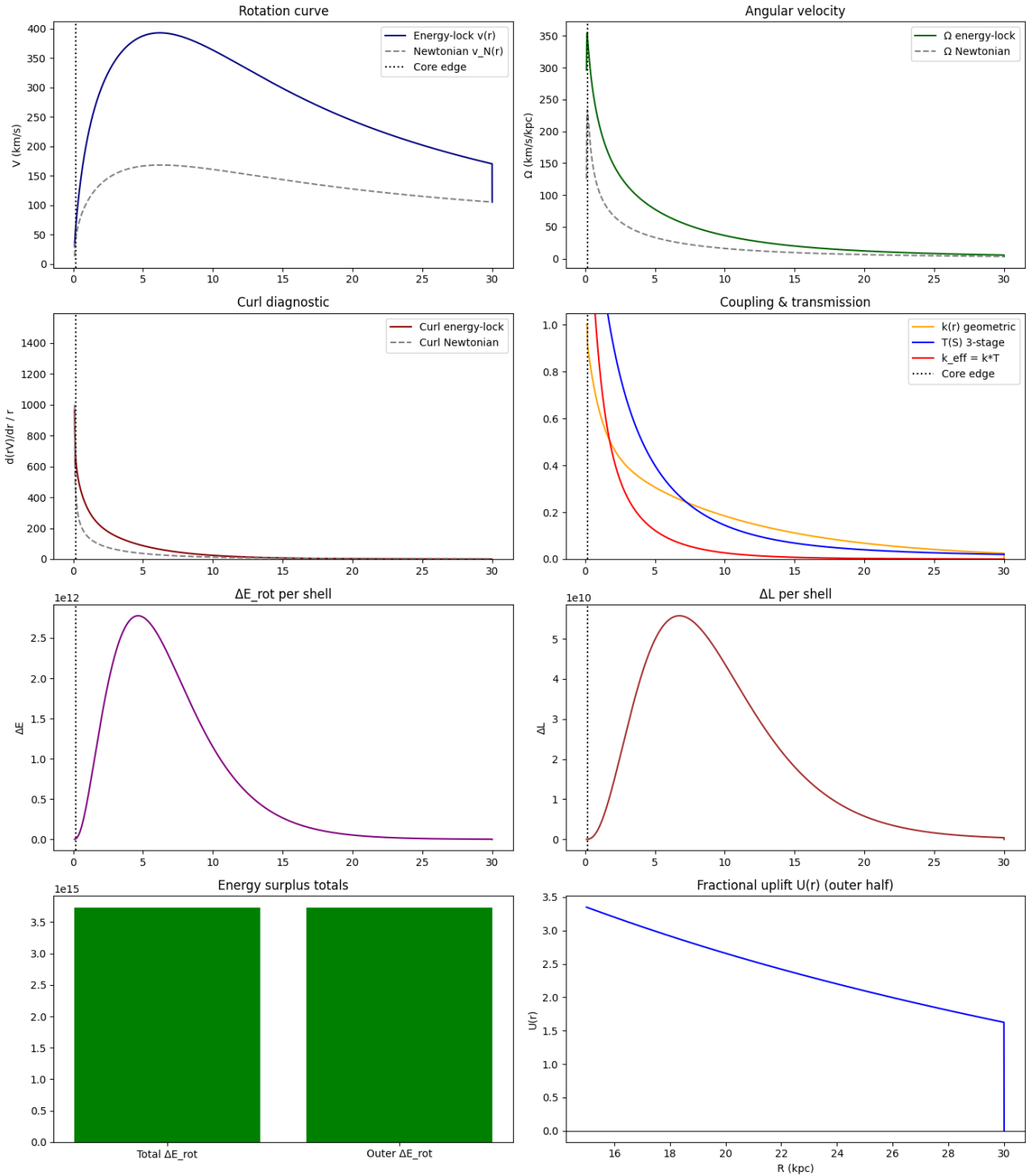
# Three-stage transmission parameters (tune these)
T_MAX = 1.8                          # max transmitted fraction
S0     = 0.16                          # curl-stress scale for
bending/saturation

===== Energy / L diagnostics (model) =====
Total ΔE_rot:          3.729374e+15
Outer ΔE_rot:          3.729341e+15
Fractional uplift (outer ΔE/Newtonian): 4.103
Total ΔL:              9.958281e+13
Outer ΔL:              9.958270e+13

===== Model indices (energy-lock vs Newtonian) =====
Curl_Index_model = 1.2361
Surplus_Index_model= 1.0000

===== SPARC-style indices (using vN vs v_partial) =====
CurlIndex_SP        = 5.7500
SurplusIndex_SP     = 0.2200
Mean uplift <U>    = 3.1623
R_max                 = 30.00 kpc

```



Group 3 — High-Surplus / Saturated Transmission Regime

Definition: A model belongs to Group 3 if:
 $\text{SurplusIndex}_{\text{SP}} \geq 0.30$,

Physical Interpretation

Transmission is global and highly efficient.

The inner engine produces sufficient coherent torque, and the geometric chain remains open enough for the signal to propagate across the entire disk. Curl grows strongly with radius, surplus builds rapidly, and the outer rotational energy approaches the injected inner-engine budget. This regime matches the **upper-locus systems** in the SPARC dataset, analogous to disks with strong, large scale non axisymmetric modes. In these models, surplus growth becomes radius-limited rather than stress-limited, matching the observed outer flattening of surplus in large high-curl galaxies

CASE III.1

```

N = 5000
r = np.linspace(0.1, 30.0, N)      # kpc
dr = r[1] - r[0]
idx = np.arange(N)

# Disk / gravity
Sigma0, R_d = 1e9, 3.5             # Msun/kpc^2, kpc
G = 4.302e-6                      # kpc · (km/s)^2 / Msun

# Inner "engine"
Omega_inner = 300.0                # km/s/kpc
i_solid = 10                        # rigid-core edge index

# Alternating-layer geometric coupling
Rk_alt = 13                         # kpc
Rk_star = 1                          # kpc

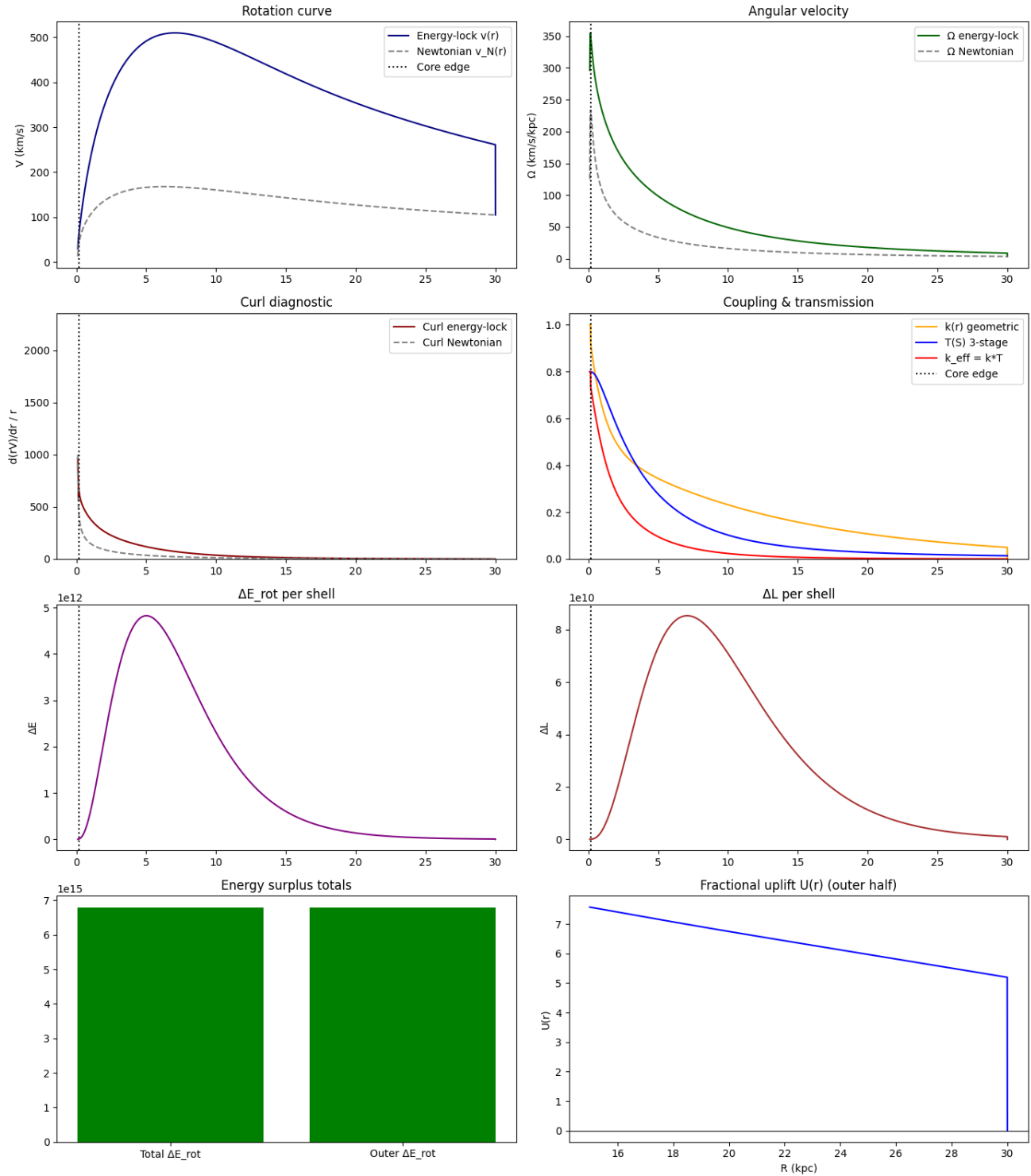
# Three-stage transmission parameters (tune these)
T_MAX = 0.8                          # max transmitted fraction
S0     = 0.1                          # curl-stress scale for bending/saturation

===== Energy / L diagnostics (model) =====
Total ΔE_rot:          6.788082e+15
Outer ΔE_rot:          6.788049e+15
Fractional uplift (outer ΔE/Newtonian): 7.468
Total ΔL:              1.594571e+14
Outer ΔL:              1.594569e+14

===== Model indices (energy-lock vs Newtonian) =====
Curl_Index_model = 1.9803
Surplus_Index_model= 1.0000

===== SPARC-style indices (using vN vs v_partial) =====
CurlIndex_SP        = 11.4933
SurplusIndex_SP     = 0.3112
Mean uplift <U>     = 6.8143
R_max               = 30.00 kpc

```



CASE III.2

```

N = 5000
r = np.linspace(0.1, 30.0, N)      # kpc
dr = r[1] - r[0]
idx = np.arange(N)

# Disk / gravity
Sigma0, R_d = 1e9, 3.5             # Msun/kpc^2, kpc
G = 4.302e-6                      # kpc · (km/s)^2 / Msun

# Inner "engine"
Omega_inner = 250.0                # km/s/kpc
i_solid = 10                        # rigid-core edge index

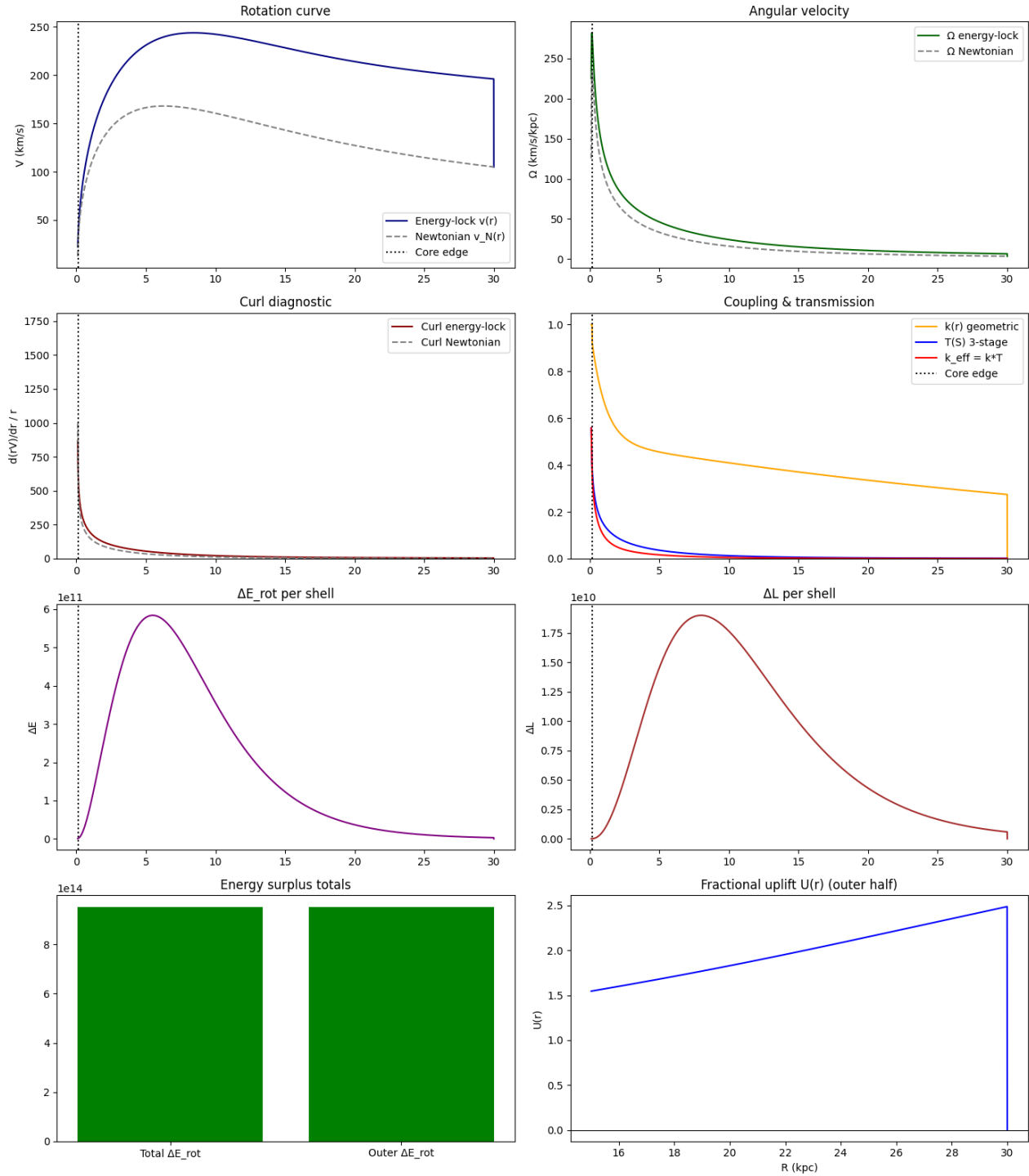
# Alternating-layer geometric coupling
Rk_alt = 50.0                      # kpc
Rk_star = 1.0                       # kpc

# Three-stage transmission parameters (tune these)
T_MAX = 0.6                         # max transmitted fraction
S0 = 0.6                             # curl-stress scale for bending/saturation
===== Energy / L diagnostics (model) =====
Total ΔE_rot:          9.519933e+14
Outer ΔE_rot:          9.519806e+14
Fractional uplift (outer ΔE/Newtonian): 1.047
Total ΔL:                4.036263e+13
Outer ΔL:                4.036258e+13

===== Model indices (energy-lock vs Newtonian) =====
Curl_Index_model = 0.6776
Surplus_Index_model= 1.0000

===== SPARC-style indices (using vN vs v_partial) =====
CurlIndex_SP       = 3.7303
SurplusIndex_SP    = 0.3130
Mean uplift <U>   = 1.5390
R_max              = 30.00 kpc

```



CASE III.3

```

N = 5000
r = np.linspace(0.1, 30.0, N)      # kpc
dr = r[1] - r[0]
idx = np.arange(N)

# Disk / gravity
Sigma0, R_d = 1e9, 3.5             # Msun/kpc^2, kpc
G = 4.302e-6                      # kpc · (km/s)^2 / Msun

# Inner "engine"
Omega_inner = 200.0                # km/s/kpc
i_solid = 10                        # rigid-core edge index

# Alternating-layer geometric coupling
Rk_alt = 16                         # kpc
Rk_star = 1.6                        # kpc

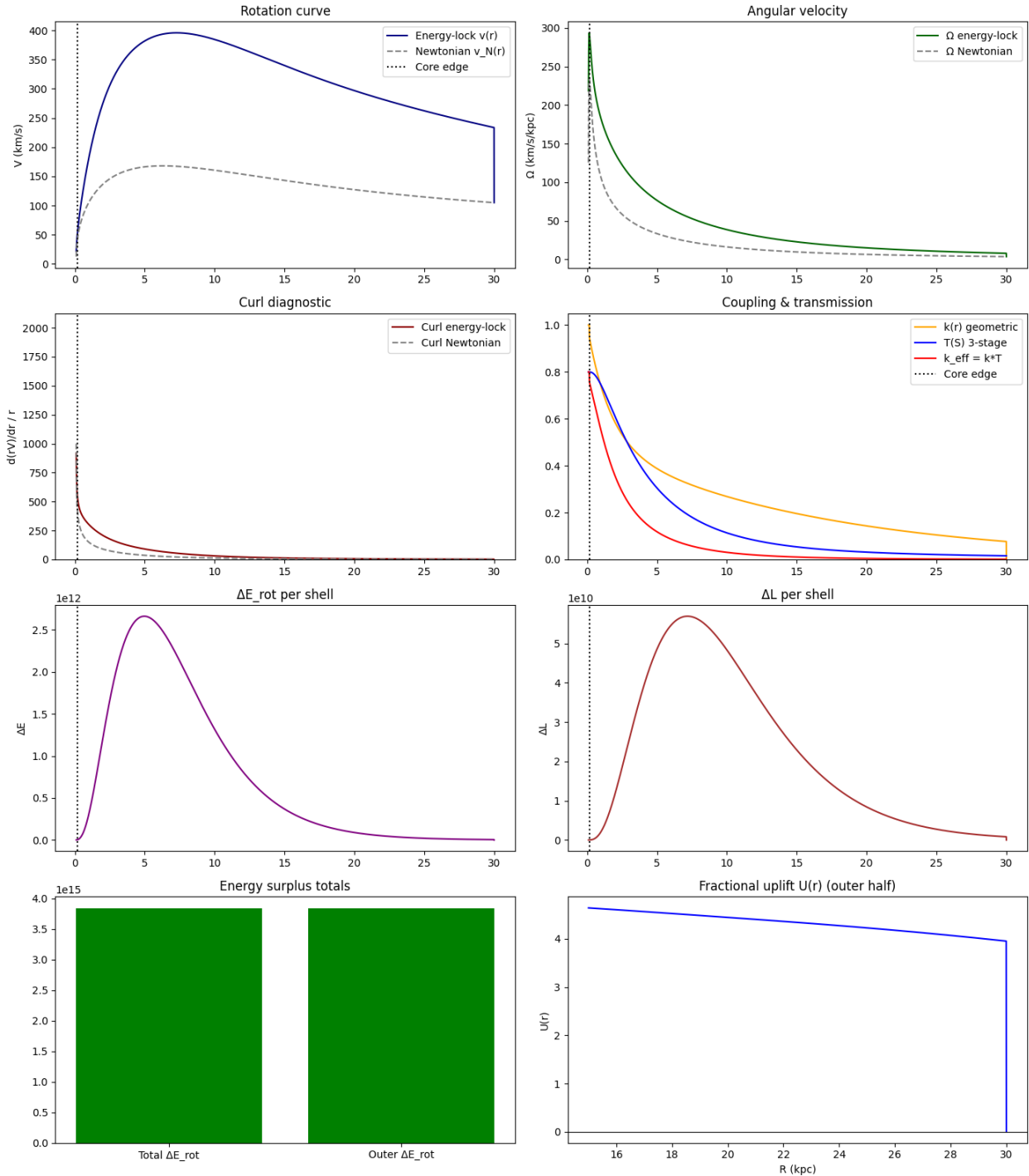
# Three-stage transmission parameters (tune these)
T_MAX = 0.8                          # max transmitted fraction
S0     = 0.09                          # curl-stress scale for
bending/saturation

===== Energy / L diagnostics (model) =====
Total ΔE_rot:          3.836091e+15
Outer ΔE_rot:          3.836076e+15
Fractional uplift (outer ΔE/Newtonian): 4.220
Total ΔL:              1.093284e+14
Outer ΔL:              1.093284e+14

===== Model indices (energy-lock vs Newtonian) =====
Curl_Index_model = 1.4155
Surplus_Index_model= 1.0000

===== SPARC-style indices (using vN vs v_partial) =====
CurlIndex_SP        = 6.7665
SurplusIndex_SP     = 0.3202
Mean uplift <U>     = 4.2280
R_max                 = 30.00 kpc

```



CASE III.4

```

N = 5000
r = np.linspace(0.1, 30.0, N)      # kpc
dr = r[1] - r[0]
idx = np.arange(N)

# Disk / gravity
Sigma0, R_d = 1e9, 3.5             # Msun/kpc^2, kpc
G = 4.302e-6                      # kpc · (km/s)^2 / Msun

# Inner "engine"
Omega_inner = 200.0                # km/s/kpc
i_solid = 10                        # rigid-core edge index

# Alternating-layer geometric coupling
Rk_alt = 16                         # kpc
Rk_star = 1.6                        # kpc

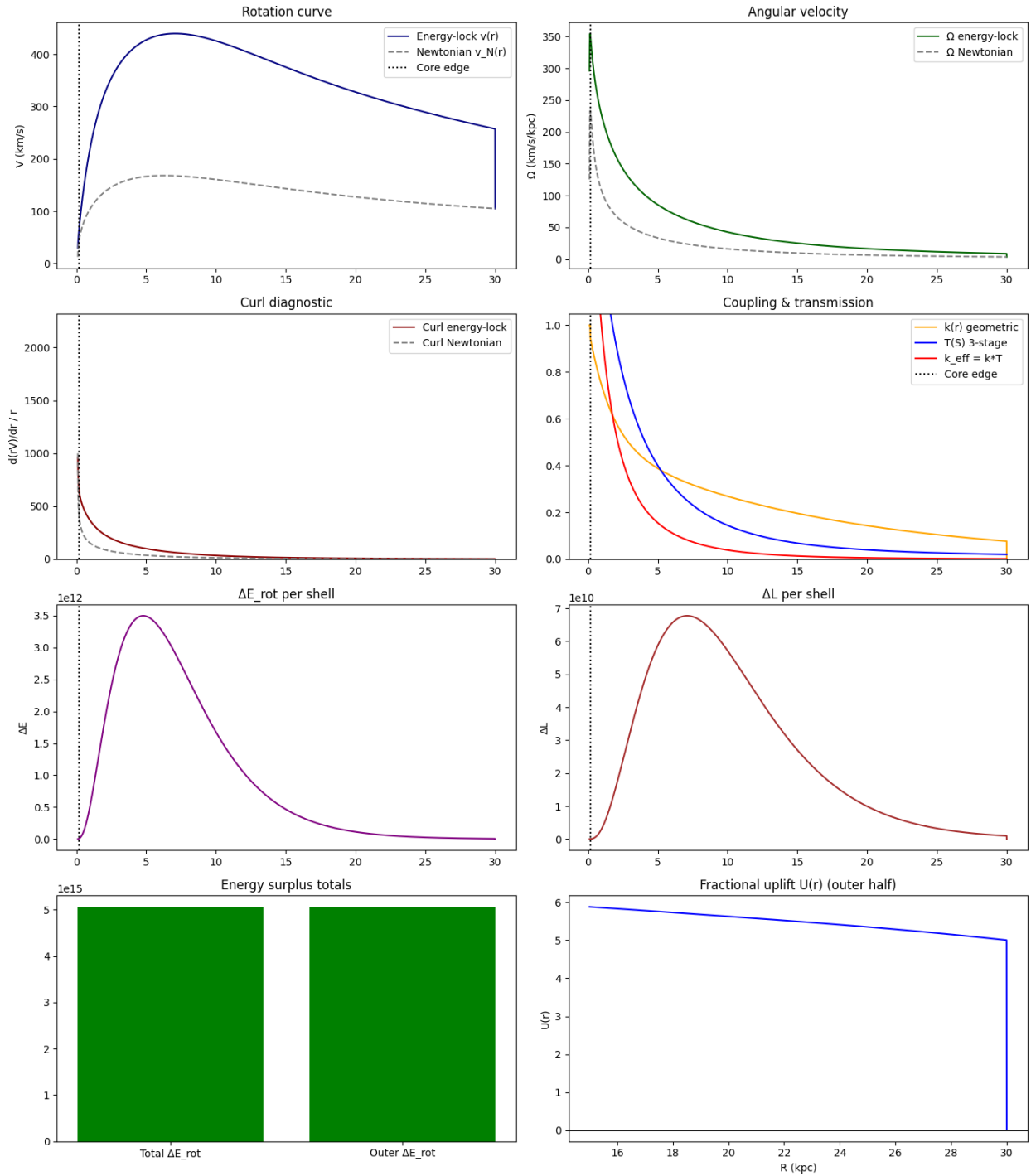
# Three-stage transmission parameters (tune these)
T_MAX = 1.8                          # max transmitted fraction
S0     = 0.16                          # curl-stress scale for
bending/saturation

===== Energy / L diagnostics (model) =====
Total ΔE_rot:           5.053581e+15
Outer ΔE_rot:           5.053548e+15
Fractional uplift (outer ΔE/Newtonian): 5.560
Total ΔL:                1.308683e+14
Outer ΔL:                1.308682e+14

===== Model indices (energy-lock vs Newtonian) =====
Curl_Index_model = 1.7590
Surplus_Index_model= 1.0000

===== SPARC-style indices (using vN vs v_partial) =====
CurlIndex_SP        = 8.5692
SurplusIndex_SP     = 0.3281
Mean uplift <U>     = 5.4642
R_max                 = 30.00 kpc

```



CASE III.5

```

N = 5000
r = np.linspace(0.1, 30.0, N) # kpc
dr = r[1] - r[0]
idx = np.arange(N)
# Disk / gravity
Sigma0, R_d = 1e9, 3.5      # Msun/kpc^2, kpc
G = 4.302e-6                # kpc·(km/s)^2 / Msun
# Inner "engine"
Omega_inner = 250.0          # km/s/kpc
i_solid = 10                 # rigid-core edge index
# Alternating-layer geometric coupling
Rk_gas = 20.0                # kpc
Rk_star = 1.0                 # kpc
# Three-stage transmission parameters (tune these)
T_MAX = 0.7                  # max transmitted fraction
S0 = 0.2                      # curl-stress scale for bending/saturation

```

===== Energy / L diagnostics (model) =====

```

Total ΔE_rot:    2.606247e+15
Outer ΔE_rot:   2.606227e+15
Fractional uplift (outer ΔE/Newtonian): 2.867
Total ΔL:        8.420015e+13
Outer ΔL:        8.420007e+13

```

===== Model indices (energy-lock vs Newtonian) =====

```

Curl_Index_model = 1.1767
Surplus_Index_model= 1.0000

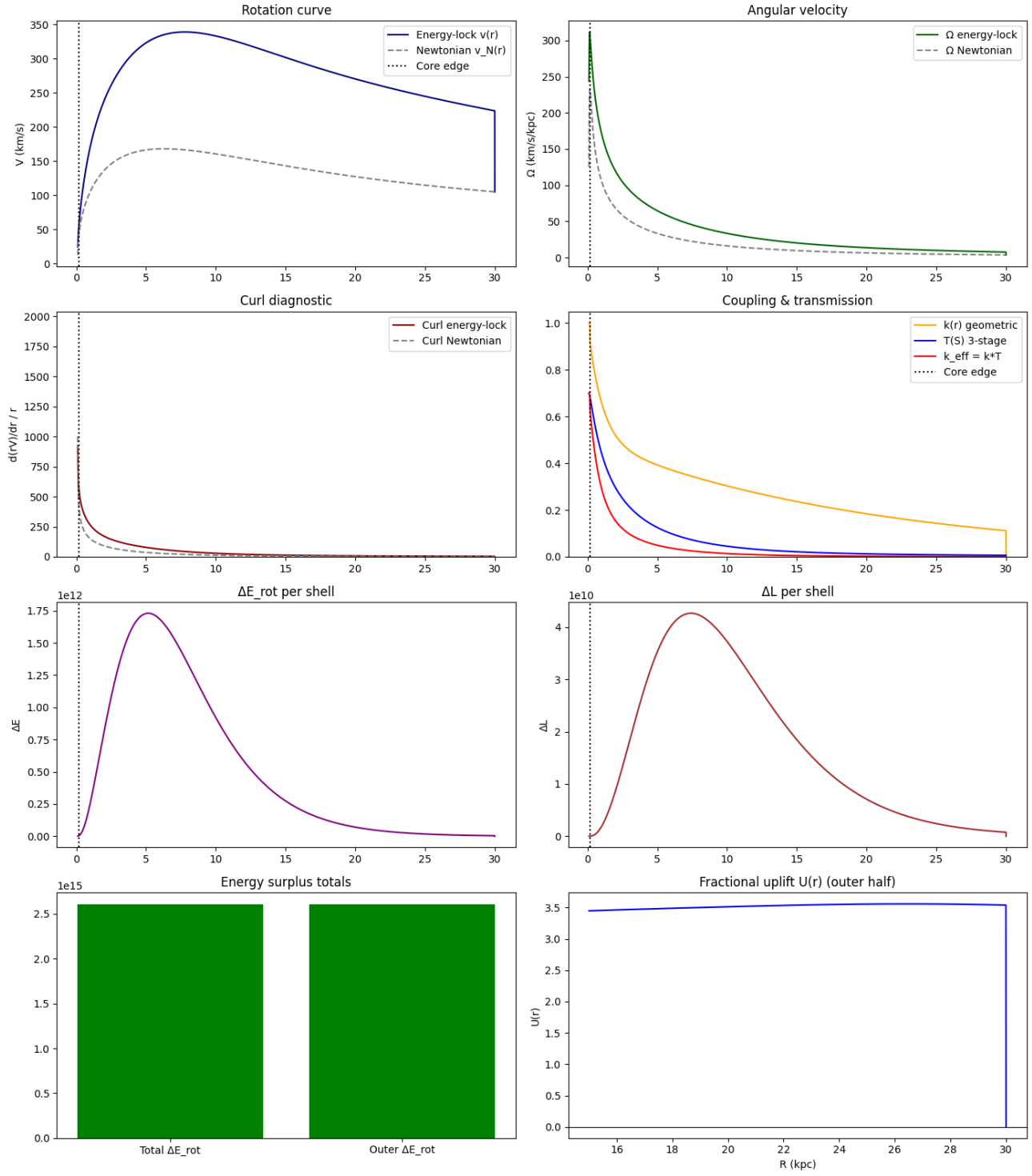
```

===== SPARC-style indices (using vN vs v_partial) =====

```

CurlIndex_SP     = 5.3338
SurplusIndex_SP  = 0.3293
Mean uplift <U>  = 3.1979
R_max           = 30.00 kpc

```



CASE III.6

```

N = 5000
r = np.linspace(0.1, 30.0, N)      # kpc
dr = r[1] - r[0]
idx = np.arange(N)

# Disk / gravity
Sigma0, R_d = 1e9, 3.5             # Msun/kpc^2, kpc
G = 4.302e-6                      # kpc · (km/s)^2 / Msun

# Inner "engine"
Omega_inner = 220.0                # km/s/kpc
i_solid = 10                        # rigid-core edge index

# Alternating-layer geometric coupling
Rk_alt = 15                         # kpc
Rk_star = .6                         # kpc

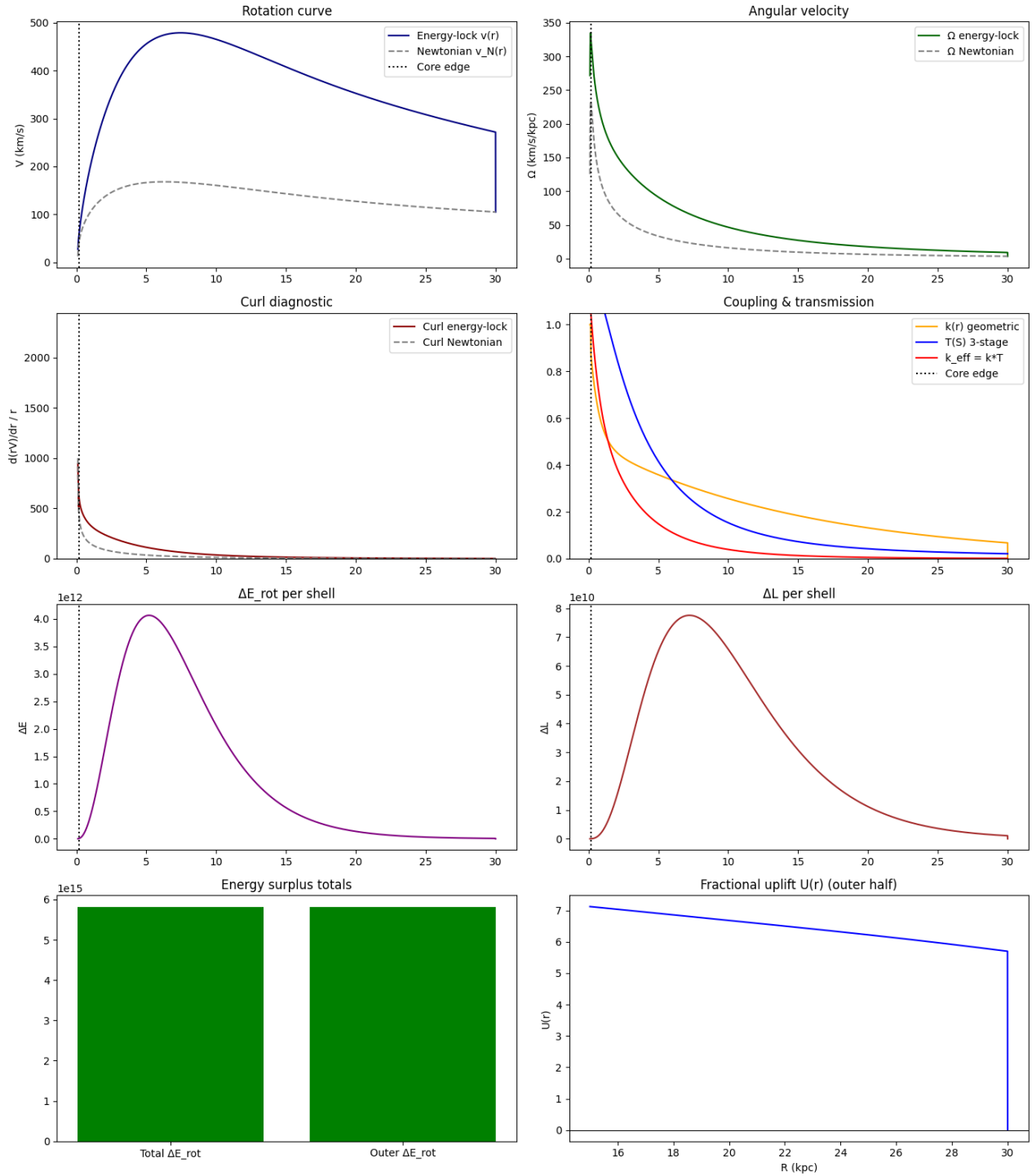
# Three-stage transmission parameters (tune these)
T_MAX = 1.2                          # max transmitted fraction
S0     = 0.1                          # curl-stress scale for bending/saturation

===== Energy / L diagnostics (model) =====
Total ΔE_rot:           5.811107e+15
Outer ΔE_rot:           5.811081e+15
Fractional uplift (outer ΔE/Newtonian): 6.393
Total ΔL:                1.470448e+14
Outer ΔL:                1.470447e+14

===== Model indices (energy-lock vs Newtonian) =====
Curl_Index_model = 1.8549
Surplus_Index_model= 1.0000

===== SPARC-style indices (using vN vs v_partial) =====
CurlIndex_SP        = 10.4446
SurplusIndex_SP     = 0.3372
Mean uplift <U>    = 6.3638
R_max               = 30.00 kpc

```



CASE III.7

```

N = 5000
r = np.linspace(0.1, 30.0, N)      # kpc
dr = r[1] - r[0]
idx = np.arange(N)

# Disk / gravity
Sigma0, R_d = 1e9, 3.5             # Msun/kpc^2, kpc
G = 4.302e-6                      # kpc · (km/s)^2 / Msun

# Inner "engine"
Omega_inner = 250.0                # km/s/kpc
i_solid = 10                        # rigid-core edge index

# Alternating-layer geometric coupling
Rk_alt = 50.0                      # kpc
Rk_star = 1.0                       # kpc

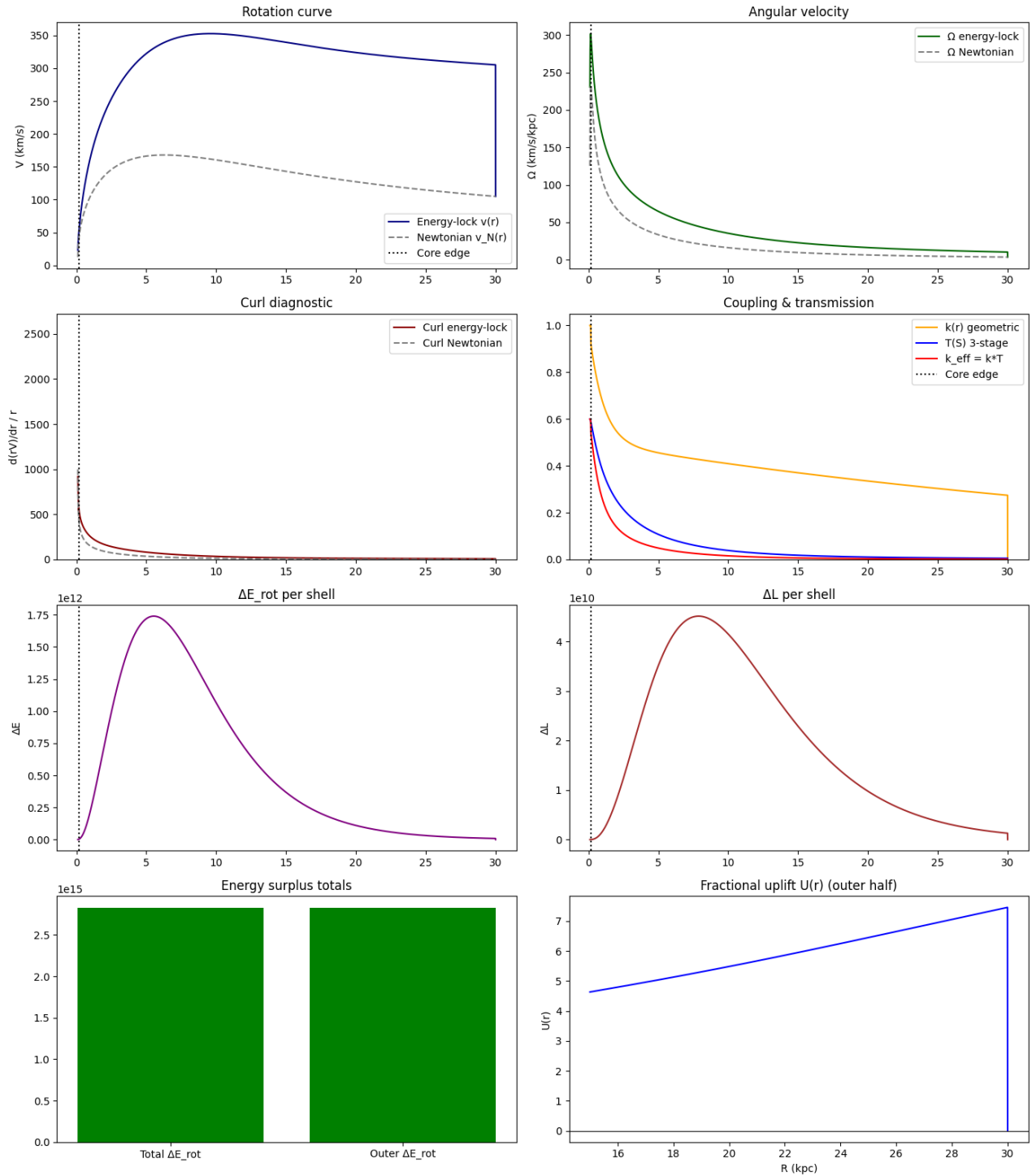
# Three-stage transmission parameters (tune these)
T_MAX = 0.6                         # max transmitted fraction
S0     = 0.2                          # curl-stress scale for bending/saturation

===== Energy / L diagnostics (model) =====
Total ΔE_rot:          2.825390e+15
Outer ΔE_rot:          2.825373e+15
Fractional uplift (outer ΔE/Newtonian): 3.108
Total ΔL:               9.474579e+13
Outer ΔL:               9.474572e+13

===== Model indices (energy-lock vs Newtonian) =====
Curl_Index_model = 1.5373
Surplus_Index_model= 1.0000

===== SPARC-style indices (using vN vs v_partial) =====
CurlIndex_SP        = 11.1909
SurplusIndex_SP     = 0.4320
Mean uplift <U>    = 4.5910
R_max                 = 30.00 kpc

```



CASE III.8

```

N = 5000
r = np.linspace(0.1, 30.0, N)      # kpc
dr = r[1] - r[0]
idx = np.arange(N)

# Disk / gravity
Sigma0, R_d = 1e9, 3.5             # Msun/kpc^2, kpc
G = 4.302e-6                      # kpc · (km/s)^2 / Msun

# Inner "engine"
Omega_inner = 350.0                # km/s/kpc
i_solid = 10                        # rigid-core edge index

# Alternating-layer geometric coupling
Rk_alt = 50.0                      # kpc
Rk_star = 1.0                       # kpc

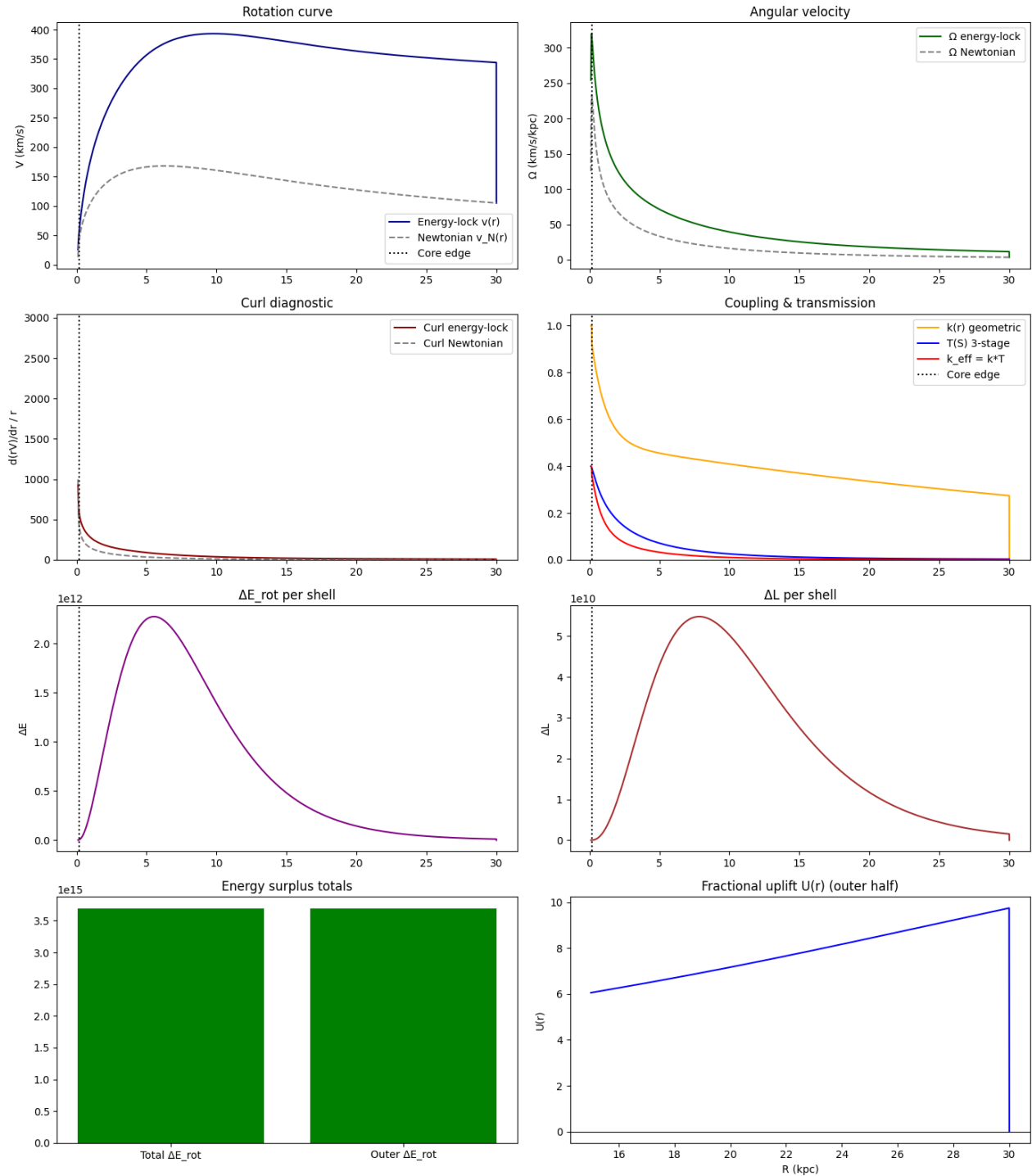
# Three-stage transmission parameters (tune these)
T_MAX = 0.4                         # max transmitted fraction
S0     = 0.2                         # curl-stress scale for bending/saturation

===== Energy / L diagnostics (model) =====
Total ΔE_rot:          3.691843e+15
Outer ΔE_rot:          3.691821e+15
Fractional uplift (outer ΔE/Newtonian): 4.062
Total ΔL:              1.148007e+14
Outer ΔL:              1.148006e+14

===== Model indices (energy-lock vs Newtonian) =====
Curl_Index_model = 1.8542
Surplus_Index_model= 1.0000

===== SPARC-style indices (using vN vs v_partial) =====
CurlIndex_SP        = 14.6228
SurplusIndex_SP     = 0.4520
Mean uplift <U>    = 5.9989
R_max               = 30.00 kpc

```



SUPPLEMENTARY F: SPARC Diagnostic Extraction Script

The SPARC-processing script (Github: https://github.com/sakidja/CTC_related_papers) provides a fully automated pipeline for converting every rotation-curve file in the Rotmod_LTG archive[26] into the three dynamical diagnostics used throughout the paper. For each galaxy, the script loads the SPARC table, extracts the observed velocity $V_{\text{obs}}(R)$, constructs the baryonic velocity

$$V_{\text{bar}}(R) = \sqrt{V_{\text{gas}}^2 + V_{\text{disk}}^2 + V_{\text{bulge}}^2}, \quad (\text{G-1})$$

and evaluates the fractional uplift

$$U(R) = \frac{V_{\text{obs}}^2(R) - V_{\text{bar}}^2(R)}{V_{\text{bar}}^2(R)}. \quad (\text{G-2})$$

The torque fields are computed as

$$\tau_{\text{obs}}(R) = R V_{\text{obs}}^2(R), \quad \tau_{\text{bar}}(R) = R V_{\text{bar}}^2(R), \quad (\text{G-3}), (\text{G-4})$$

and their radial derivatives are converted into the **CurlIndex**,

$$\text{CurlIndex} = \frac{\int \left| \frac{d\tau_{\text{obs}}}{dR} - \frac{d\tau_{\text{bar}}}{dR} \right| dR}{\int \left| \frac{d\tau_{\text{bar}}}{dR} \right| dR}, \quad (\text{G-5})$$

a dimensionless measure of the mismatch between the observed torque gradient and the purely baryonic prediction.

The **SurplusIndex** is computed over the outer half of the galaxy (from $0.5 R_{\text{max}}$ to R_{max}):

$$\text{SurplusIndex} = \frac{\int_{0.5R_{\text{max}}}^{R_{\text{max}}} \max [V_{\text{obs}}^2(R) - V_{\text{bar}}^2(R), 0] dR}{\int_0^{R_{\text{max}}} V_{\text{obs}}^2(R) dR}. \quad (\text{G-6})$$

Although it was not used in this paper, the script also identifies two structural radii used in the main text:

1. R_{turnover} , the radius of maximum V_{obs} , and
2. R_{core} , where the inner slope dV_{obs}/dR first declines below a fixed fraction (30%) of its initial rising value.

For each galaxy, the routine saves a three-panel figure (rotation curve, uplift profile, and extra rotational energy) in a designated directory, and appends a single-line summary to a table containing:

(galaxy, CurlIndex, SurplusIndex, $\langle U \rangle$, R_{max} , $0.5R_{\text{max}}$, R_{core} , R_{turnover}).

In this way, the script provides a reproducible, equation-level implementation of the SPARC diagnostics used in the paper, ensuring that all indices reported in the main text and supplement follow directly and transparently from the publicly available SPARC rotation curves.

SUPPLEMENTARY G: GALAXY-BY-GALAXY DIAGNOSTIC PROFILES FROM SPARC

Table F-1: Rotational Coherence Diagnostics (RCT): Curl Index, Surplus Index, Mean Uplift, and Maximum Radius R_{\max} for the Full SPARC Database[2]

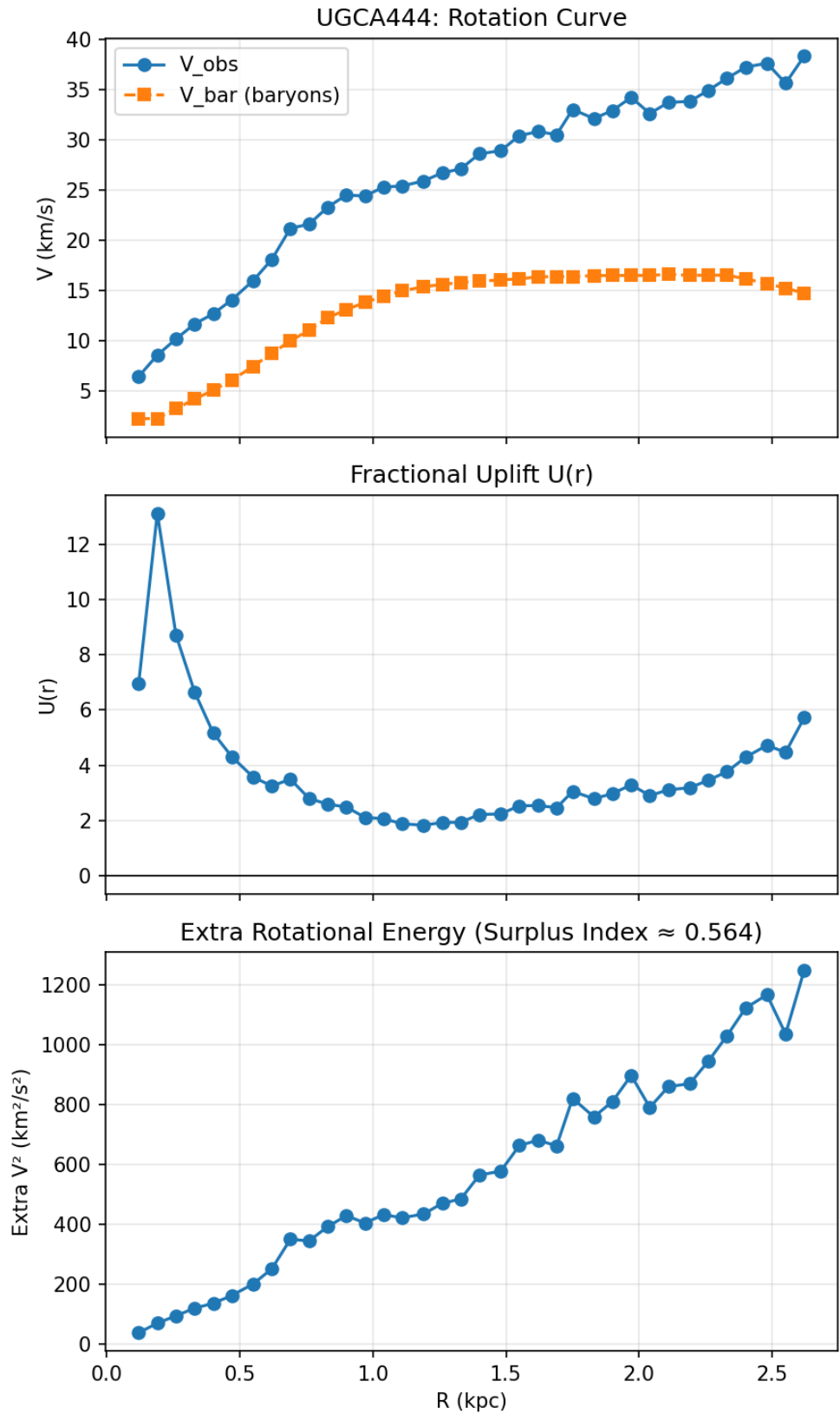
Galaxy	CurlIndex	SurplusIndex	MeanUplift	R_max_kpc
CamB	0.803245	0.0820345	-0.430958	1.79
D512-2	2.11866	0.477715	1.5382	3.83
D564-8	5.26707	0.44423	2.5658	3.07
D631-7	7.69557	0.578692	2.90393	7.19
DDO064	1.73893	0.459758	2.18185	2.98
DDO154	6.95679	0.606728	3.82527	5.92
DDO161	3.02079	0.498017	1.3643	13.37
DDO168	2.89394	0.557171	1.59192	4.12
DDO170	3.32093	0.487077	2.25829	12.33
ESO079-G014	0.809862	0.289856	0.442381	16.67
ESO116-G012	2.54572	0.428208	1.24612	9.86
ESO444-G084	10.5497	0.586825	5.71633	4.44
ESO563-G021	1.28593	0.249665	0.396143	42.41
F561-1	0.341117	0.0188553	-0.0795925	9.66
F563-1	8.84603	0.558233	5.40359	20.1
F563-V1	0.259061	0.00213804	0.011021	7.87
F563-V2	3.79467	0.254188	3.65096	10.47
F565-V2	5.37657	0.585359	4.42917	8.8
F567-2	0.630184	0.239918	0.658858	9.59
F568-1	3.37484	0.472488	3.64352	13.23
F568-3	2.54492	0.45767	1.52975	17.98
F568-V1	3.93557	0.468567	3.73531	17.63
F571-8	6.02334	0.457611	0.900205	15.55
F571-V1	3.69023	0.467204	2.24345	13.59
F574-1	1.96925	0.406873	1.87626	12.6
F574-2	0.22252	0	-0.380848	10.83
F579-V1	1.43465	0.302024	1.88051	15.16
F583-1	3.19234	0.390787	3.63662	16.26
F583-4	2.98122	0.389559	1.38404	7.29
IC2574	3.89112	0.528592	1.4829	10.23
IC4202	1.29199	0.110903	0.0489658	25.9
KK98-251	1.56475	0.478108	1.0185	3.13
NGC0024	3.51945	0.324355	1.41206	11.27
NGC0055	1.32637	0.388623	0.842208	13.5
NGC0100	2.92813	0.424025	1.12112	9.62
NGC0247	2.12165	0.422005	1.468	14.54
NGC0289	3.70069	0.313891	1.01497	71.12
NGC0300	3.754	0.476746	1.98246	11.8

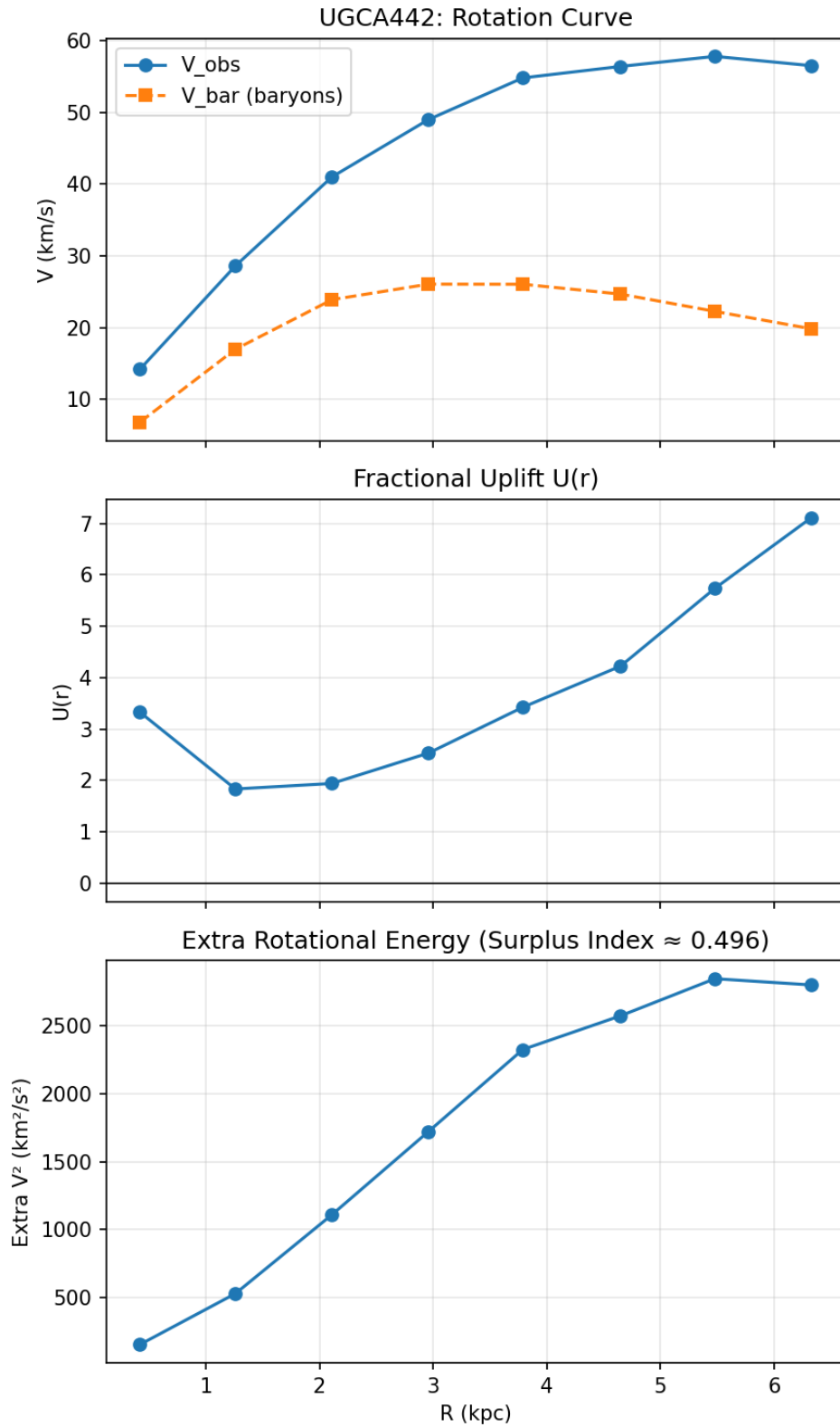
NGC0801	0.683467	0.0855029	-0.0861924	59.82
NGC0891	0.915209	0.0050065	-0.27111	17.11
NGC1003	4.73615	0.486625	2.66936	30.24
NGC1090	1.17281	0.164468	0.179542	30.09
NGC1705	9.3106	0.408673	4.2681	6
NGC2366	2.38779	0.431179	1.22911	6.06
NGC2403	3.7953	0.404719	0.957635	20.87
NGC2683	2.59888	0.185324	0.408959	34.62
NGC2841	4.40313	0.341261	1.16553	63.64
NGC2903	1.8107	0.179027	0.0446104	24.96
NGC2915	12.4891	0.528574	6.05588	10.04
NGC2955	0.804226	0.0394492	-0.175523	35.43
NGC2976	0.463011	0.0355276	-0.129321	2.27
NGC2998	0.972827	0.197318	0.605801	42.28
NGC3109	7.21588	0.64949	4.70948	6.45
NGC3198	2.59051	0.348927	0.618407	44.08
NGC3521	1.52713	0.114835	-0.27769	17.74
NGC3726	1.741	0.192085	0.186044	32.52
NGC3741	12.6343	0.61399	6.57231	7
NGC3769	6.19779	0.110626	1.01615	37.16
NGC3877	0.432923	0	-0.229419	11.35
NGC3893	1.39315	0.161832	0.185105	19.05
NGC3917	1.01652	0.25415	0.51859	14.86
NGC3949	0.843017	0.00860284	-0.252187	7.07
NGC3953	0.255857	0	-0.143714	15.68
NGC3972	0.879845	0.236002	0.417473	8.72
NGC3992	1.5854	0.204639	0.583767	46.02
NGC4010	0.747319	0.233342	0.206145	10.47
NGC4013	3.27623	0.246283	0.495281	31.01
NGC4051	0.401566	0	-0.289619	12.19
NGC4068	0.846307	0.25396	0.126347	2.33
NGC4085	0.367737	0	-0.387946	6.2
NGC4088	0.950403	0.00916781	-0.331056	21.48
NGC4100	1.62662	0.190741	0.387661	22.76
NGC4138	4.0802	0.13797	0.314535	18.58
NGC4157	1.45479	0.134533	0.0566355	29.61
NGC4183	2.12954	0.31962	1.14367	21.02
NGC4214	5.21035	0.398515	2.30908	5.63
NGC4217	1.23163	0.0486957	-0.235844	16.72
NGC4389	0.699376	0	-0.683663	5.32
NGC4559	1.29371	0.257606	0.367589	20.97
NGC5005	0.325966	0	-0.310703	11.47
NGC5033	2.79246	0.243886	0.67087	44.59

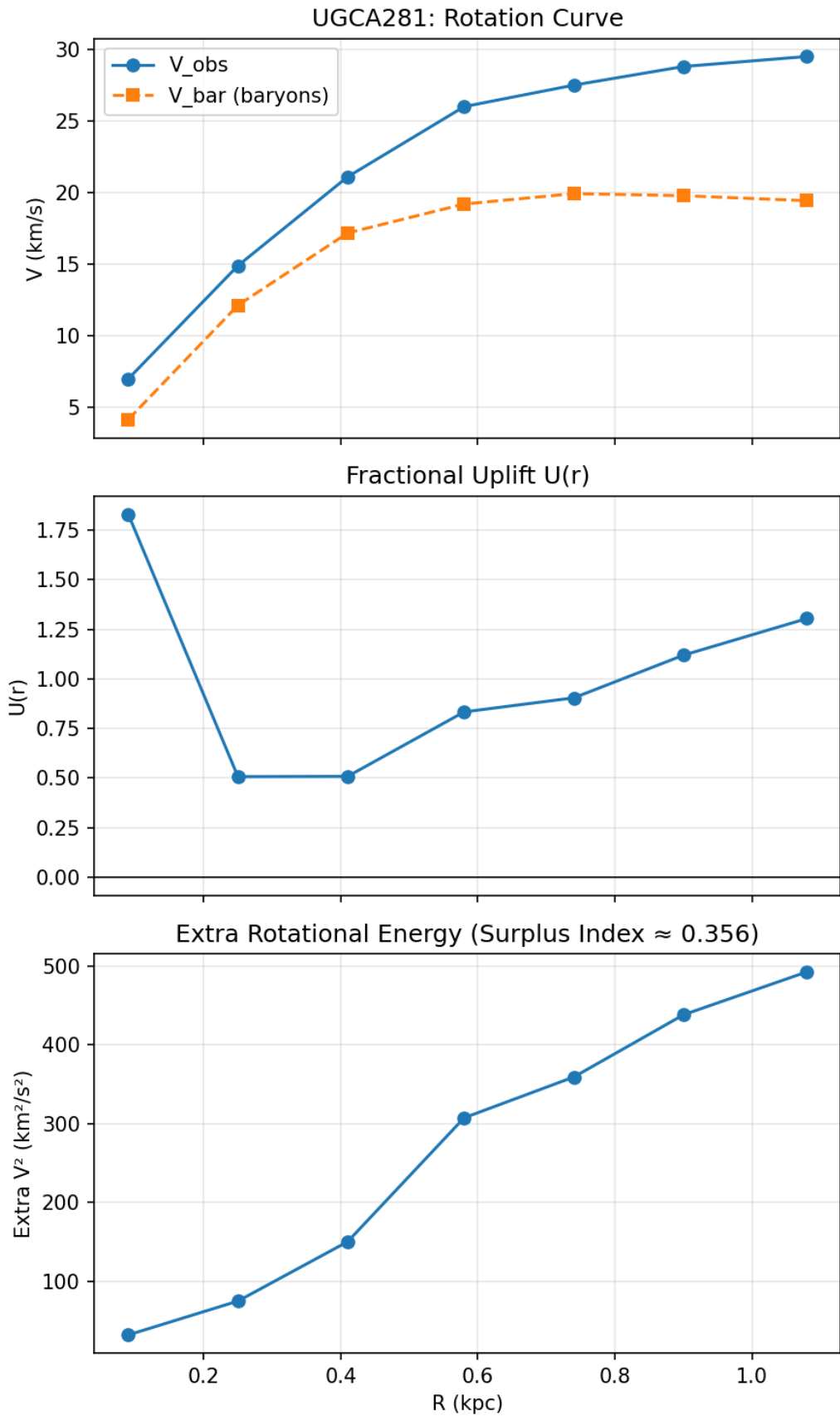
NGC5055	1.5097	0.186184	0.0642308	54.59
NGC5371	0.711913	0.0142672	-0.181181	46.24
NGC5585	2.46919	0.447807	0.716871	10.96
NGC5907	1.7128	0.20798	0.523537	50.33
NGC5985	1.45751	0.273791	0.944117	34.72
NGC6015	3.08356	0.342105	0.906287	29.23
NGC6195	0.640351	0.0173551	-0.238028	36.43
NGC6503	4.84449	0.35177	1.44451	23.5
NGC6674	3.19264	0.285191	1.19388	72.41
NGC6789	4.81163	0.462453	2.89413	0.71
NGC6946	1.0677	0.0778051	-0.0480223	20.4
NGC7331	1.56425	0.0912967	-0.099318	36.31
NGC7793	1.01826	0.213841	0.0262518	7.87
NGC7814	2.63207	0.210953	0.491503	19.53
PGC51017	0.300405	0	0.114235	3.63
UGC00128	6.01807	0.442325	3.59474	53.75
UGC00191	2.12114	0.217858	1.38844	9.98
UGC00634	5.59712	0.582201	2.86778	18.01
UGC00731	2.64809	0.446989	6.36517	10.91
UGC00891	5.17268	0.509225	2.49028	7.39
UGC01230	2.81889	0.21648	2.08275	36.54
UGC01281	3.43726	0.596382	1.86611	4.99
UGC02023	1.02934	0.249971	0.194225	3.78
UGC02259	3.23718	0.467736	2.87514	8.14
UGC02455	0.827226	0	-0.69786	4.03
UGC02487	3.25286	0.327581	1.20738	80.38
UGC02885	1.68862	0.267469	0.648881	74.07
UGC02916	1.038	0.151707	-0.0263464	38
UGC02953	2.31486	0.277679	0.311427	62.39
UGC03205	2.09653	0.25498	0.287398	40.04
UGC03546	1.59825	0.172803	-0.112621	29.23
UGC03580	3.69057	0.430694	0.203137	27.06
UGC04278	2.23645	0.574756	1.76504	6.69
UGC04305	0.774692	0	-0.161436	5.52
UGC04325	1.73658	0.321904	2.23578	5.59
UGC04483	1.97368	0.374367	1.20027	1.21
UGC04499	1.69736	0.383202	1.08373	8.18
UGC05005	3.46497	0.410762	1.611	28.61
UGC05253	1.86839	0.241753	0.0422898	53.29
UGC05414	1.22575	0.282844	0.651696	4.11
UGC05716	4.5169	0.525816	3.42309	12.37
UGC05721	5.35637	0.425569	2.99467	6.74
UGC05750	2.53868	0.442215	1.1312	22.85

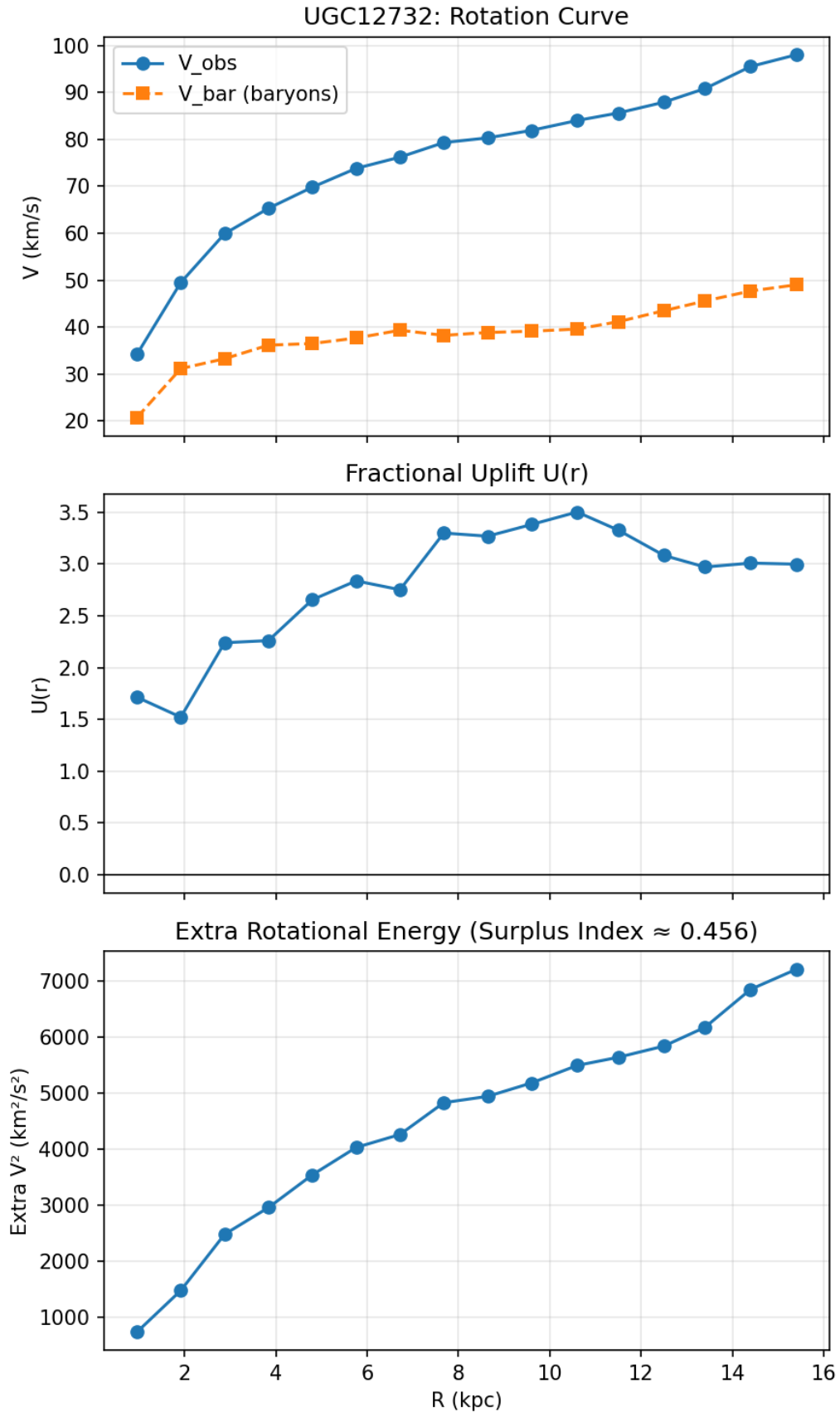
UGC05764	4.38228	0.558292	5.90988	3.62
UGC05829	1.83635	0.472242	2.30168	6.91
UGC05918	2.62412	0.528329	3.35863	4.46
UGC05986	2.43133	0.421439	1.45203	9.41
UGC05999	2.45216	0.401968	1.87098	16.22
UGC06399	2.24704	0.44013	1.56589	7.85
UGC06446	3.09	0.472995	2.9717	10.22
UGC06614	3.44583	0.344497	0.505978	64.59
UGC06628	0.470161	0	-0.22894	7.69
UGC06667	5.0597	0.572066	8.74843	7.85
UGC06786	3.08607	0.357352	0.648904	34.05
UGC06787	4.20946	0.371208	0.502613	37.19
UGC06818	2.56335	0.494982	0.782154	6.98
UGC06917	1.71339	0.396739	1.04951	10.47
UGC06923	1.08681	0.275114	0.352929	5.16
UGC06930	1.52065	0.331892	1.06557	16.61
UGC06973	4.52283	0.000594019	-0.380781	7.85
UGC06983	2.95898	0.43409	1.82613	15.68
UGC07089	1.34222	0.295589	0.534758	9.16
UGC07125	1.03829	0.284237	0.671829	18.68
UGC07151	0.907189	0.277737	0.630231	5.5
UGC07232	1.63348	0.352573	0.567124	0.82
UGC07261	1.98678	0.338195	1.22943	6.67
UGC07323	0.587692	0.24881	0.28775	5.82
UGC07399	6.3005	0.547836	4.0322	6.13
UGC07524	1.71838	0.446687	1.74758	10.69
UGC07559	1.19628	0.362996	0.604604	2.53
UGC07577	0.518332	0.0528237	-0.147127	1.69
UGC07603	4.87158	0.444001	2.26045	4.11
UGC07608	4.90944	0.521293	4.34682	4.78
UGC07690	1.43368	0.226641	0.63442	4.13
UGC07866	1.22764	0.329794	0.917867	2.32
UGC08286	3.81831	0.456921	2.73903	8.04
UGC08490	4.74434	0.451611	3.14539	10.15
UGC08550	3.74336	0.469401	2.77073	5.36
UGC08699	2.40679	0.269762	0.273	25.7
UGC08837	0.992812	0.319695	0.264924	4.2
UGC09037	1.1449	0.143815	-0.0098658	27.96
UGC09133	2.88991	0.277961	0.468956	108.31
UGC09992	0.391315	0.159688	0.511431	3.89
UGC10310	1.3124	0.339004	1.37453	7.74
UGC11455	1.03512	0.0804479	-0.17185	41.93
UGC11557	0.509944	0	-0.476009	10.56

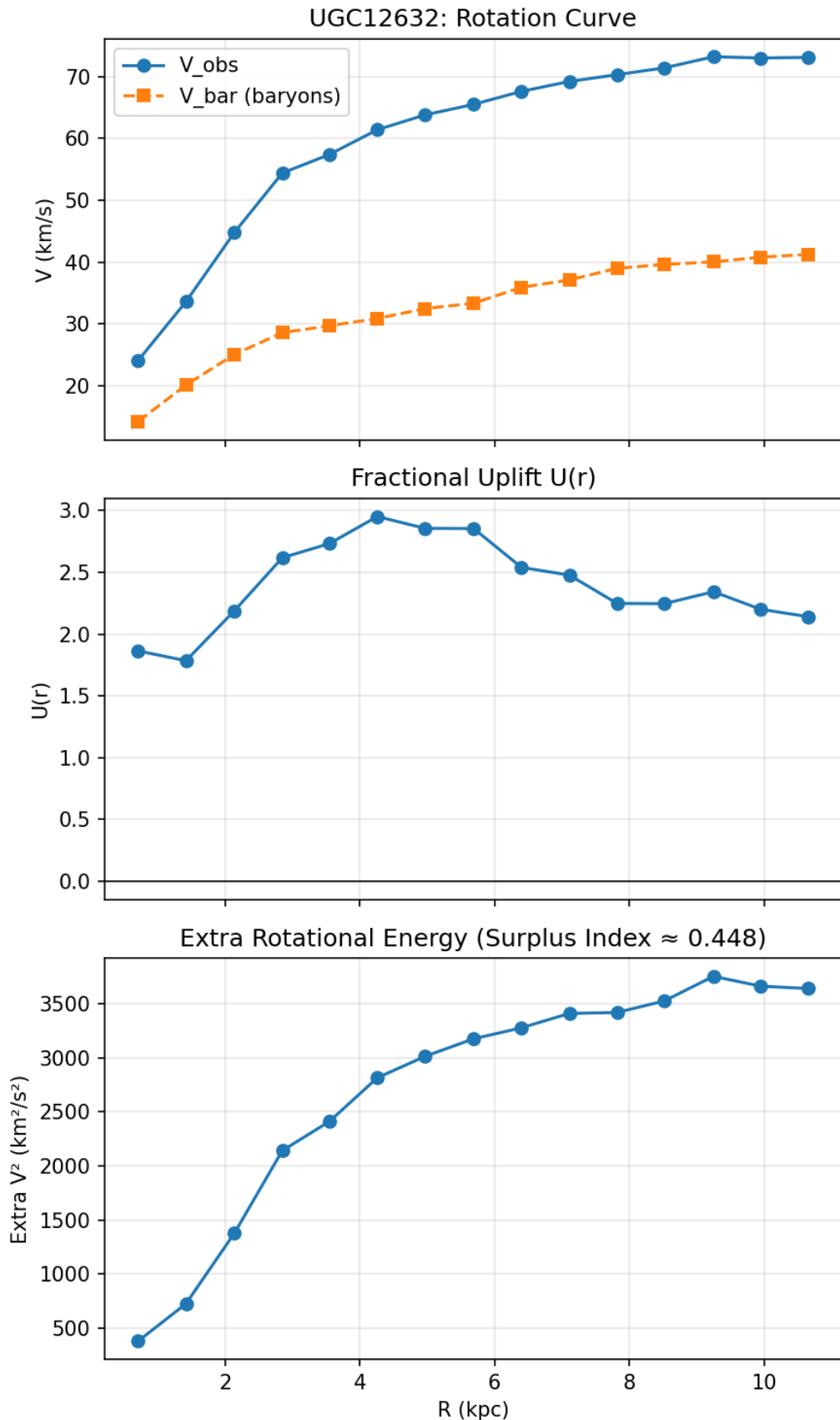
UGC11820	3.36437	0.499607	2.23787	15.82
UGC11914	0.556775	0.0420436	-0.105106	9.83
UGC12506	1.81575	0.314518	1.58411	49.99
UGC12632	2.17572	0.448138	2.40378	10.66
UGC12732	3.04778	0.455556	2.8009	15.4
UGCA281	1.25732	0.355593	1.00077	1.08
UGCA442	5.69324	0.49614	3.76878	6.33
UGCA444	5.6723	0.564483	3.73617	2.62

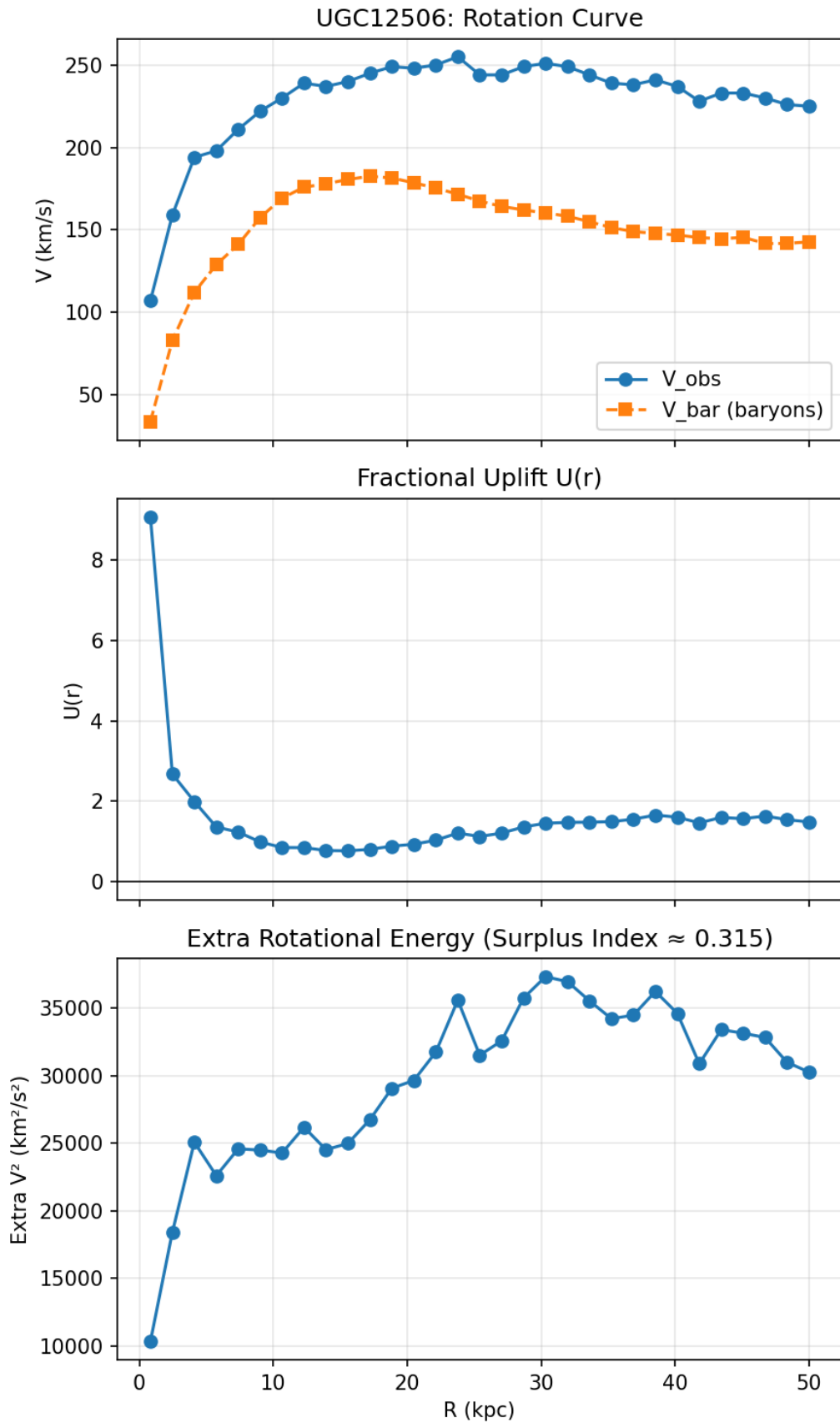


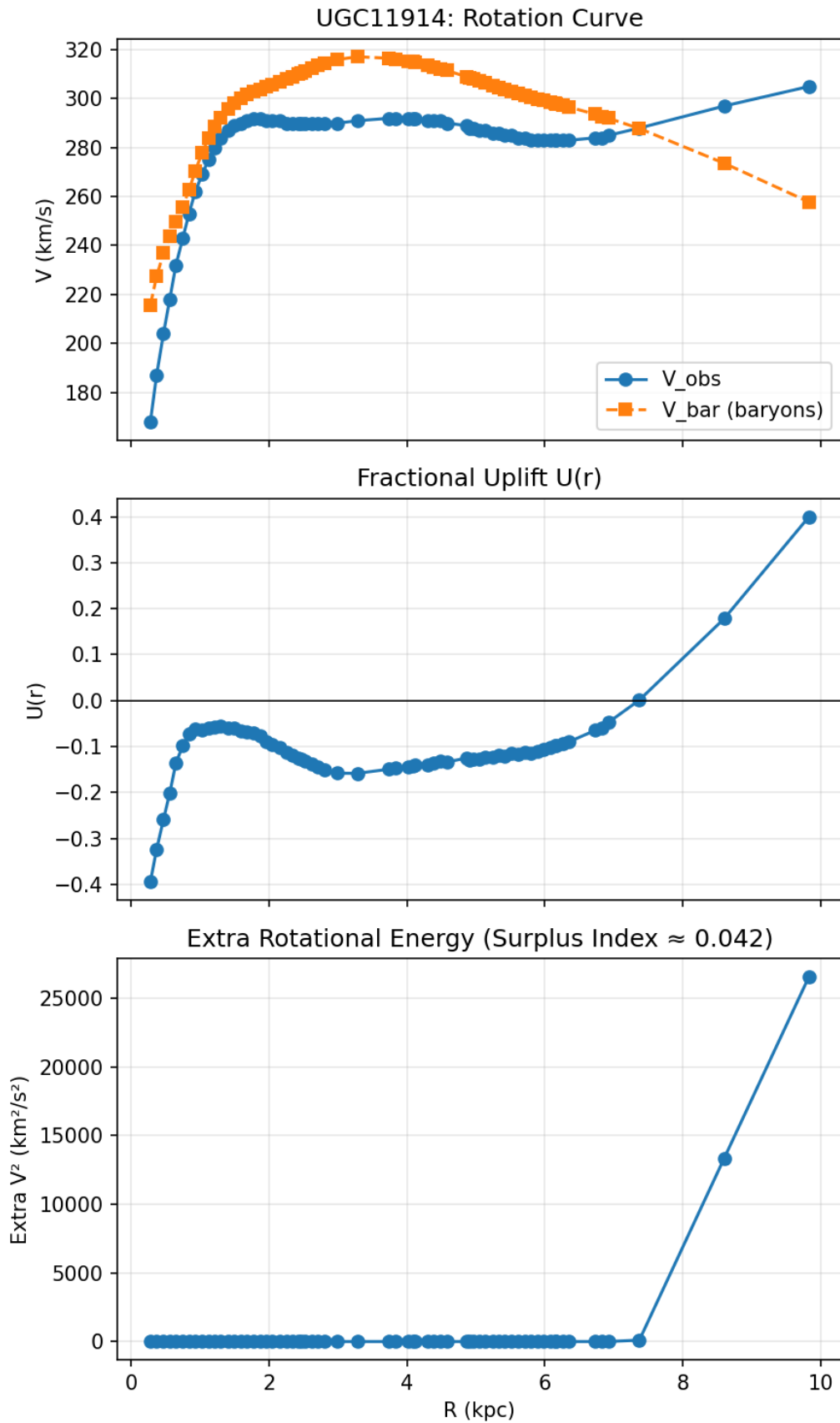


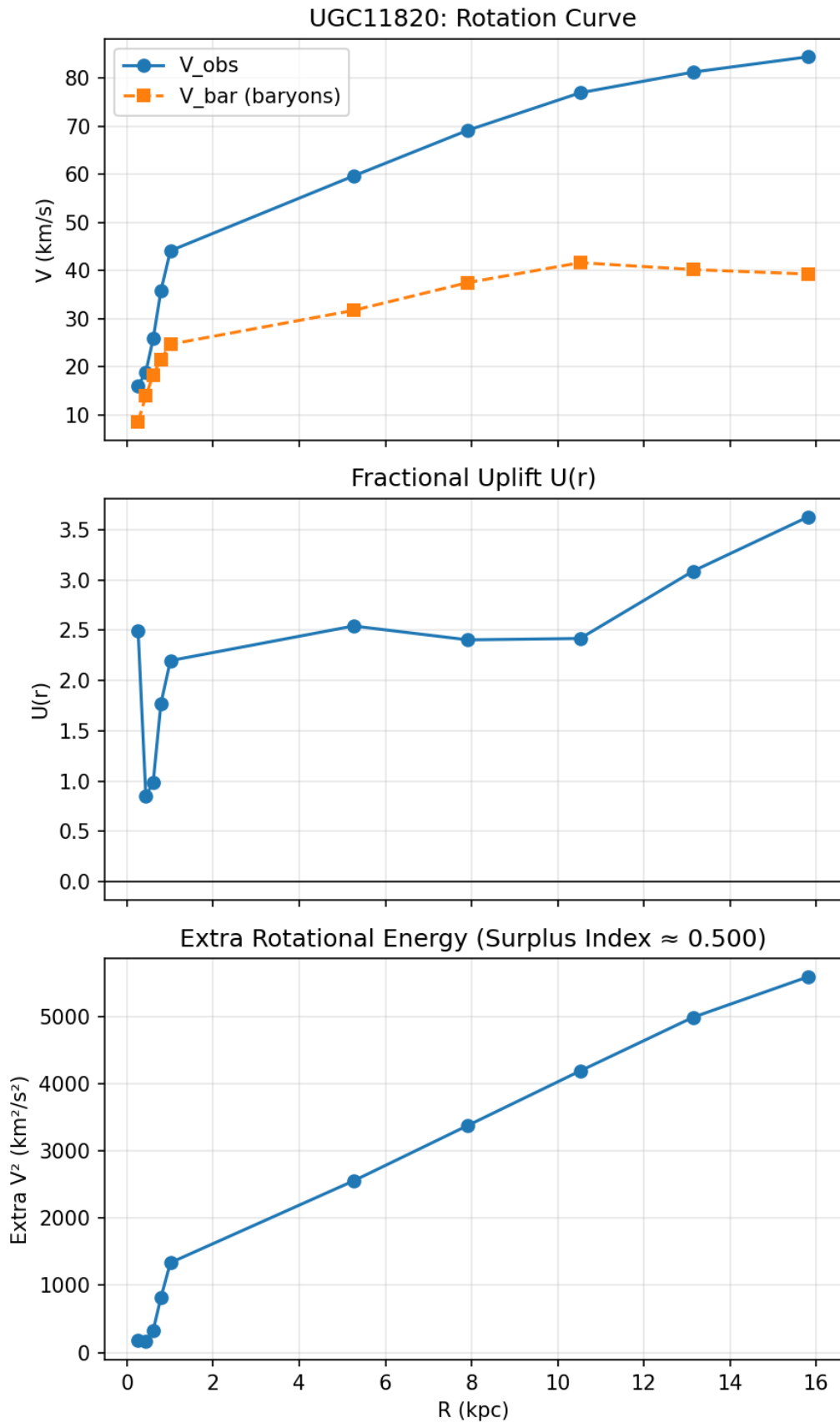


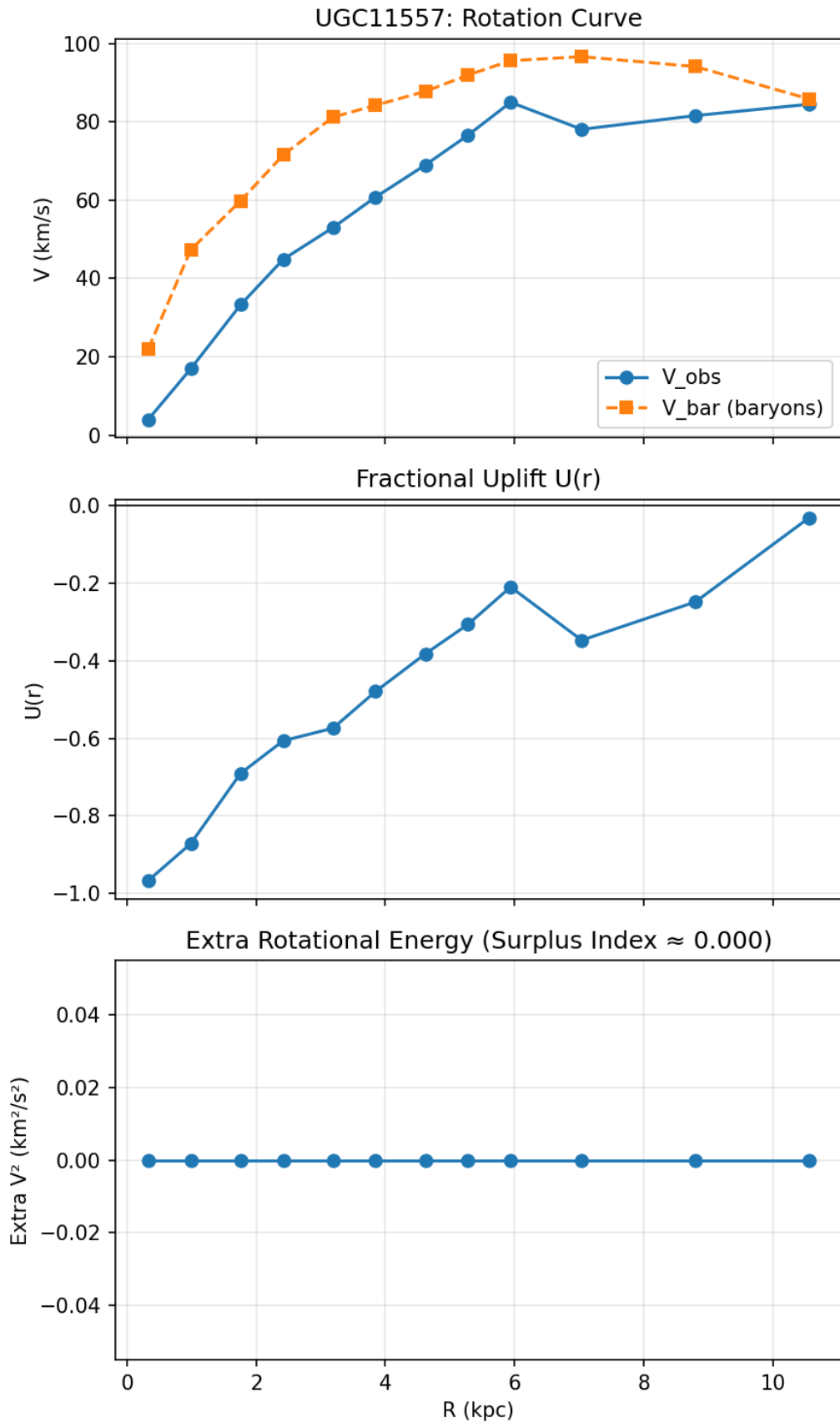


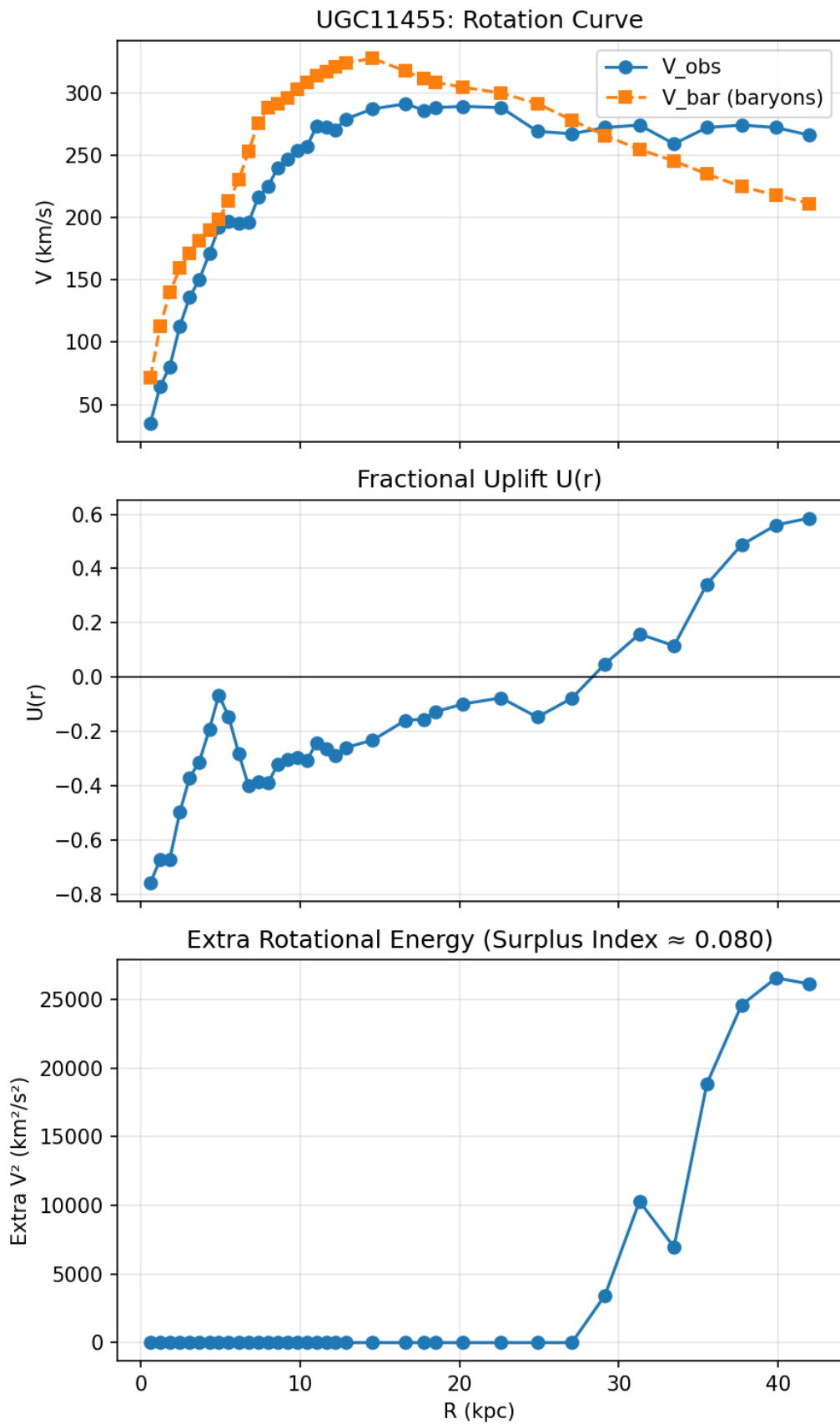


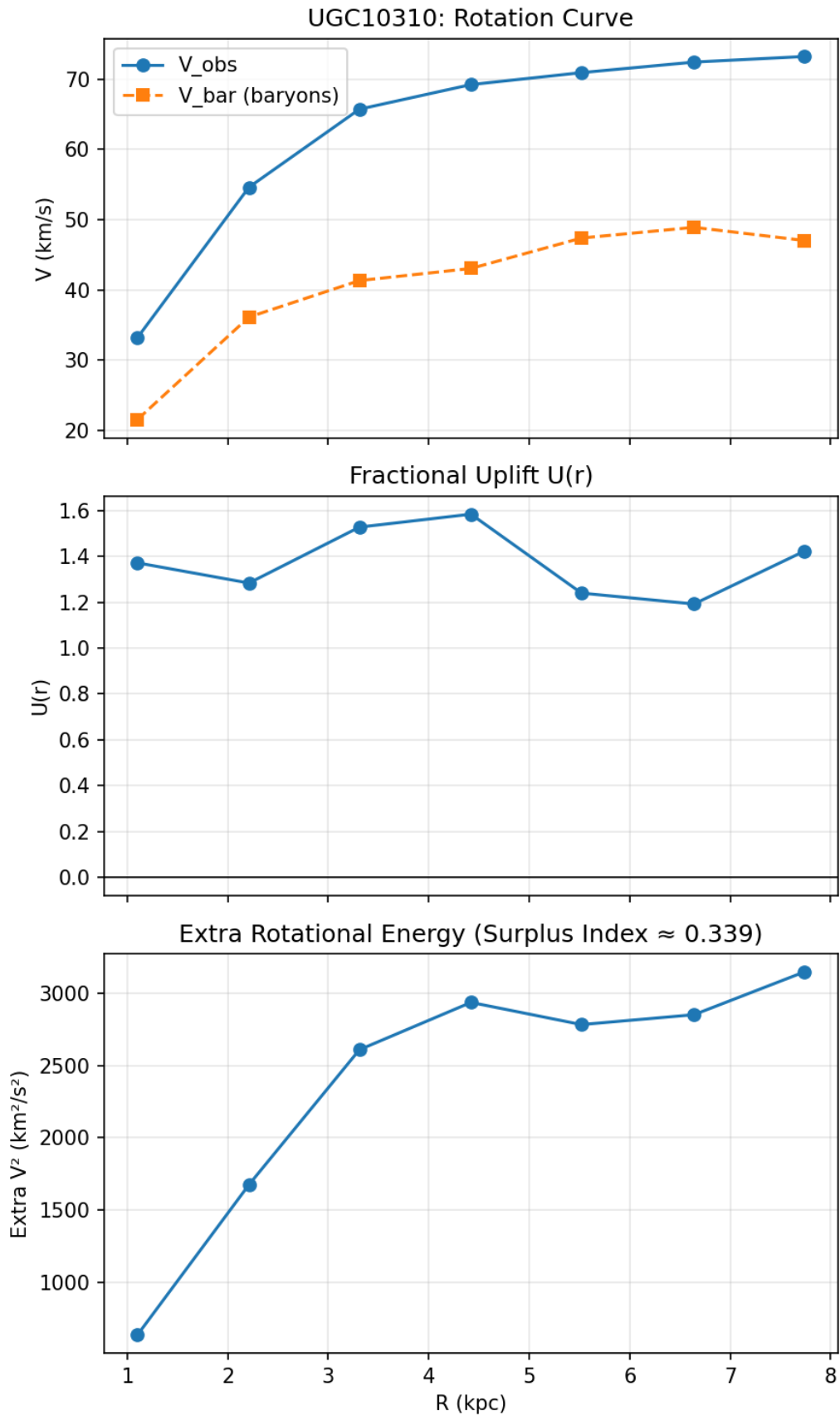


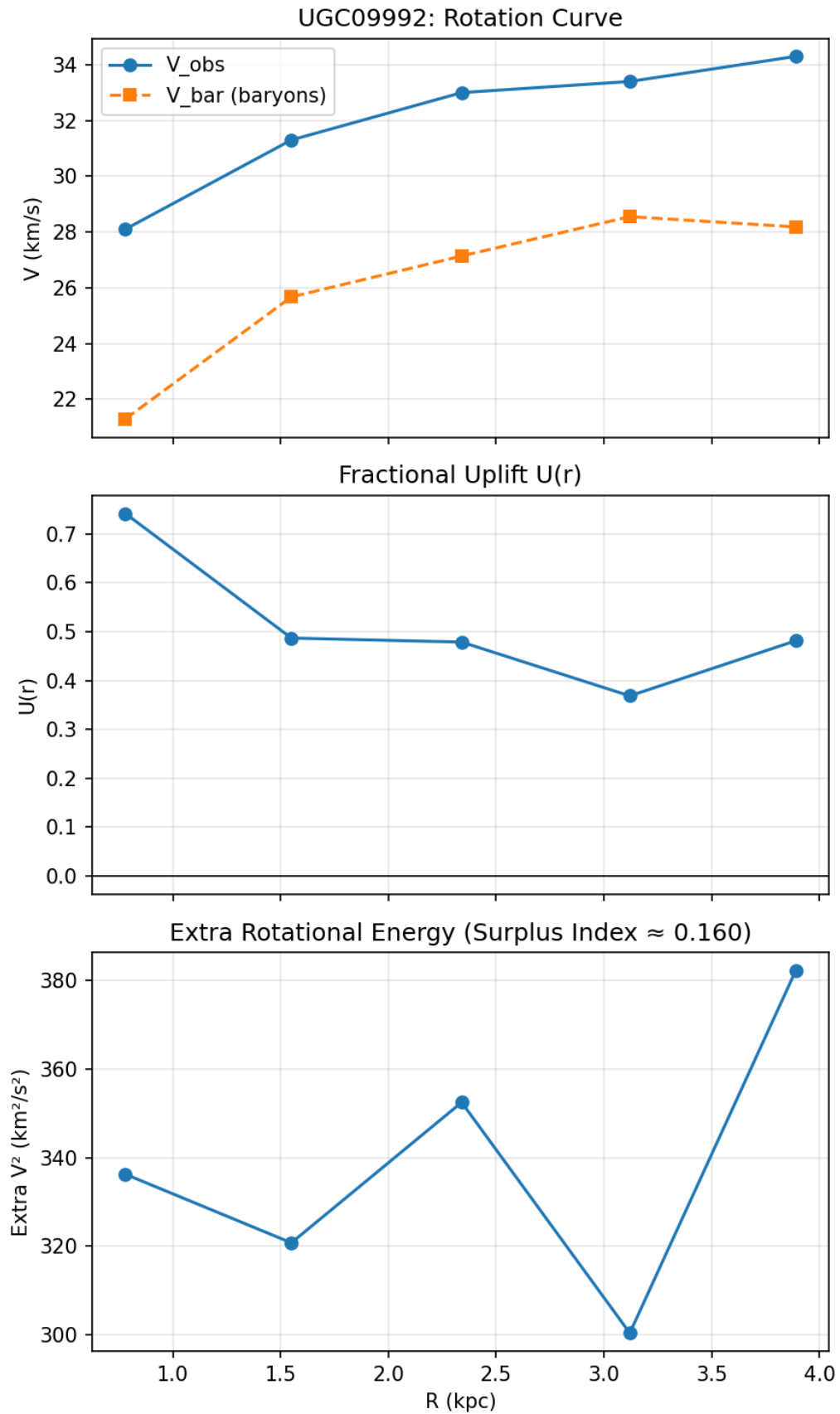


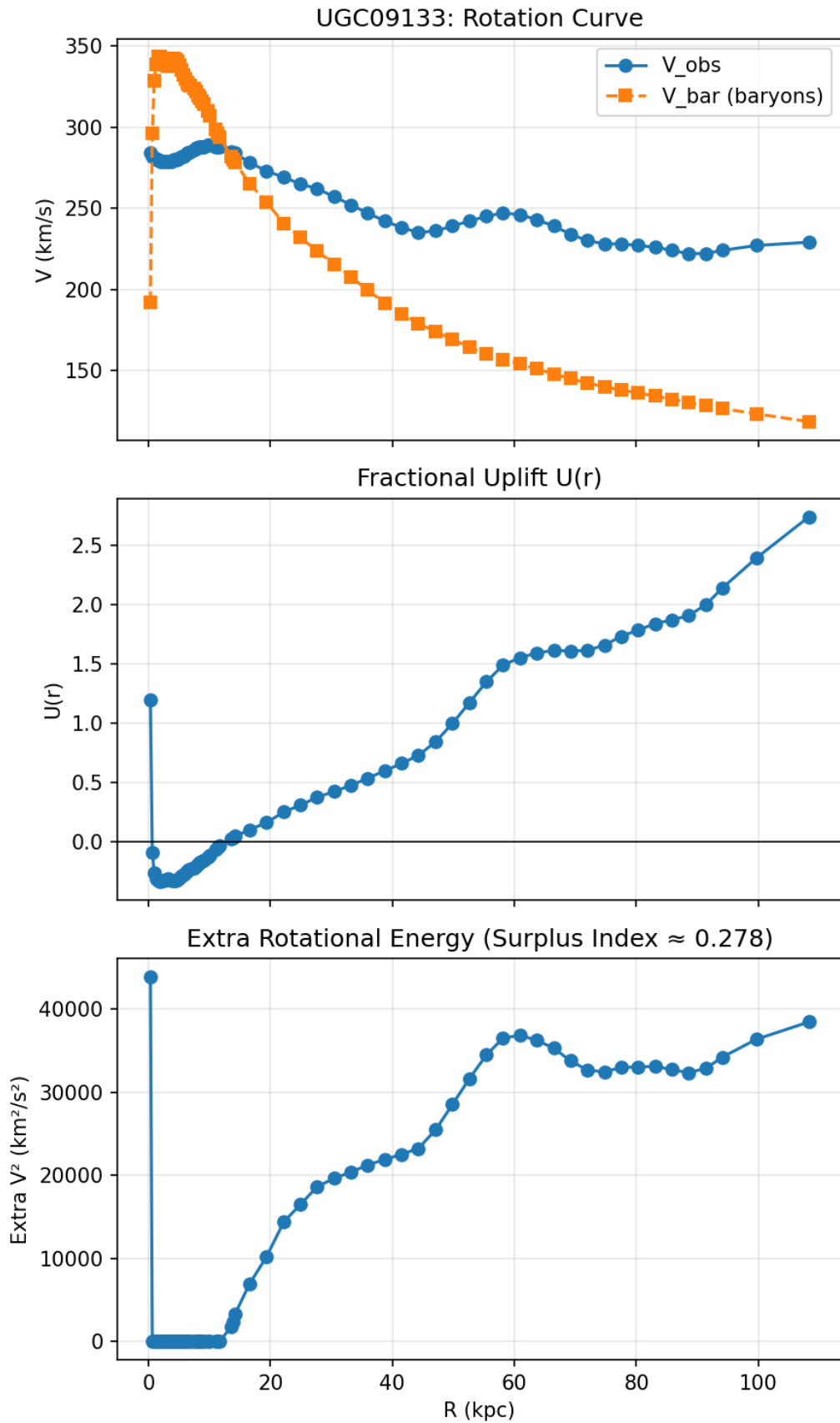


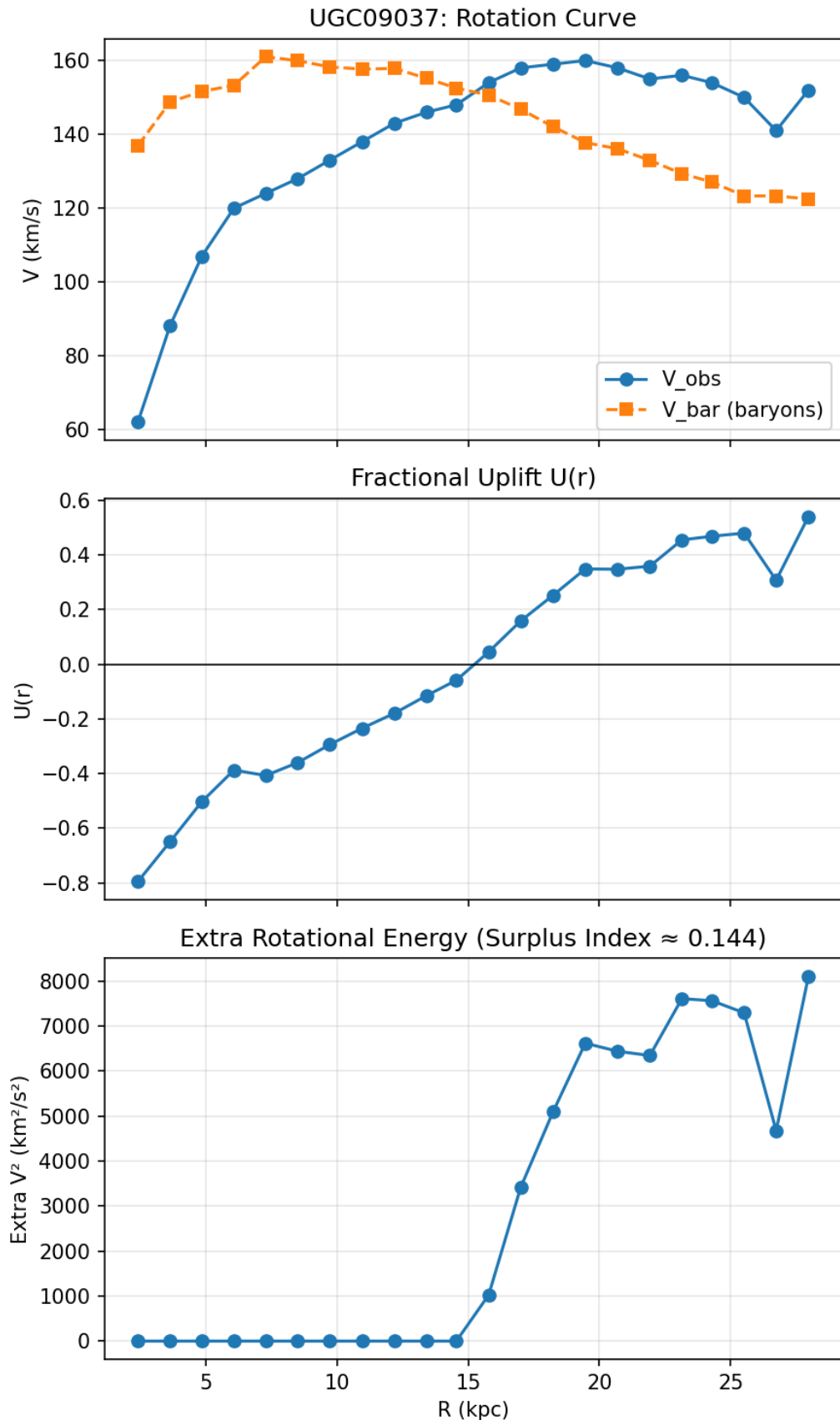


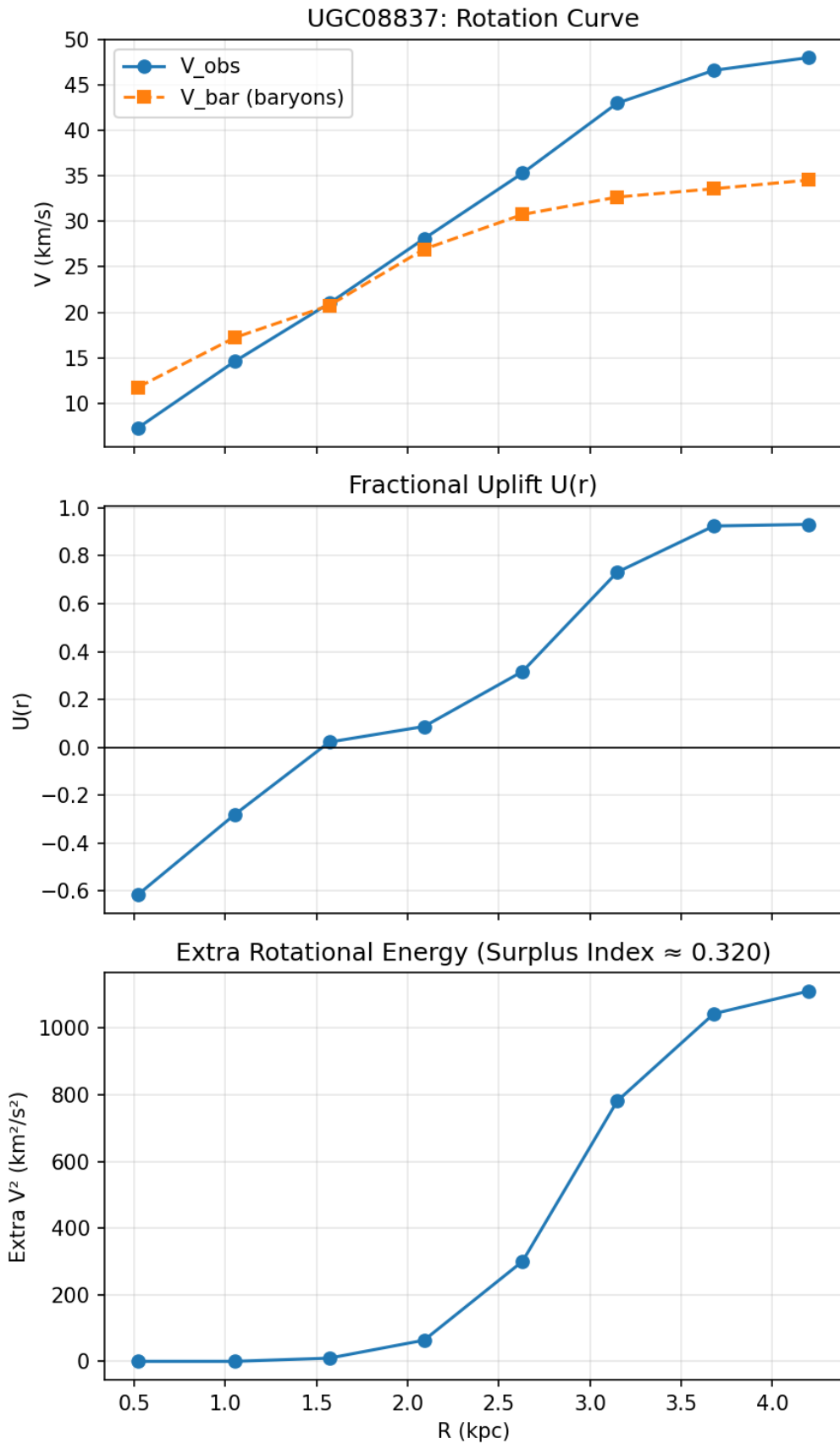


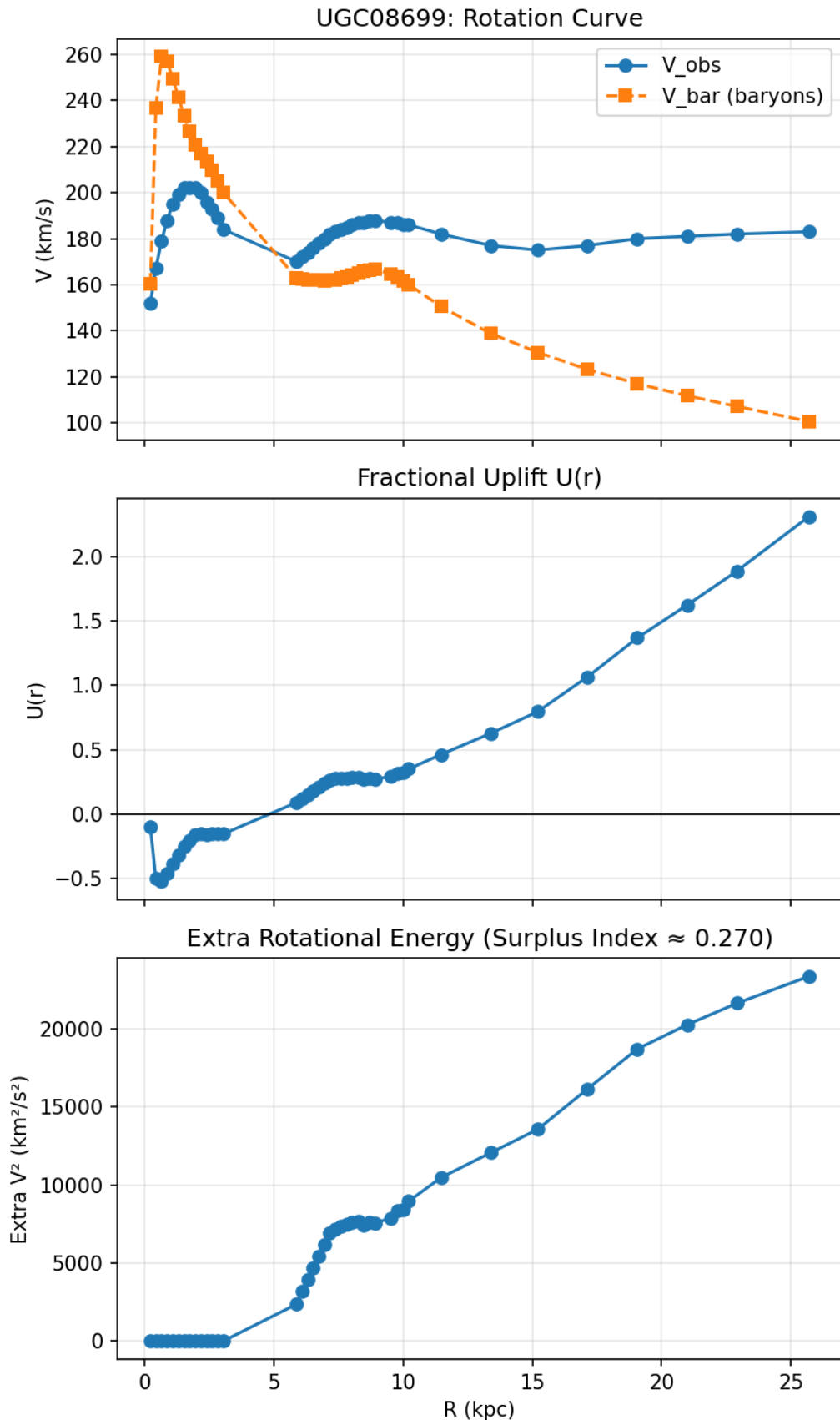


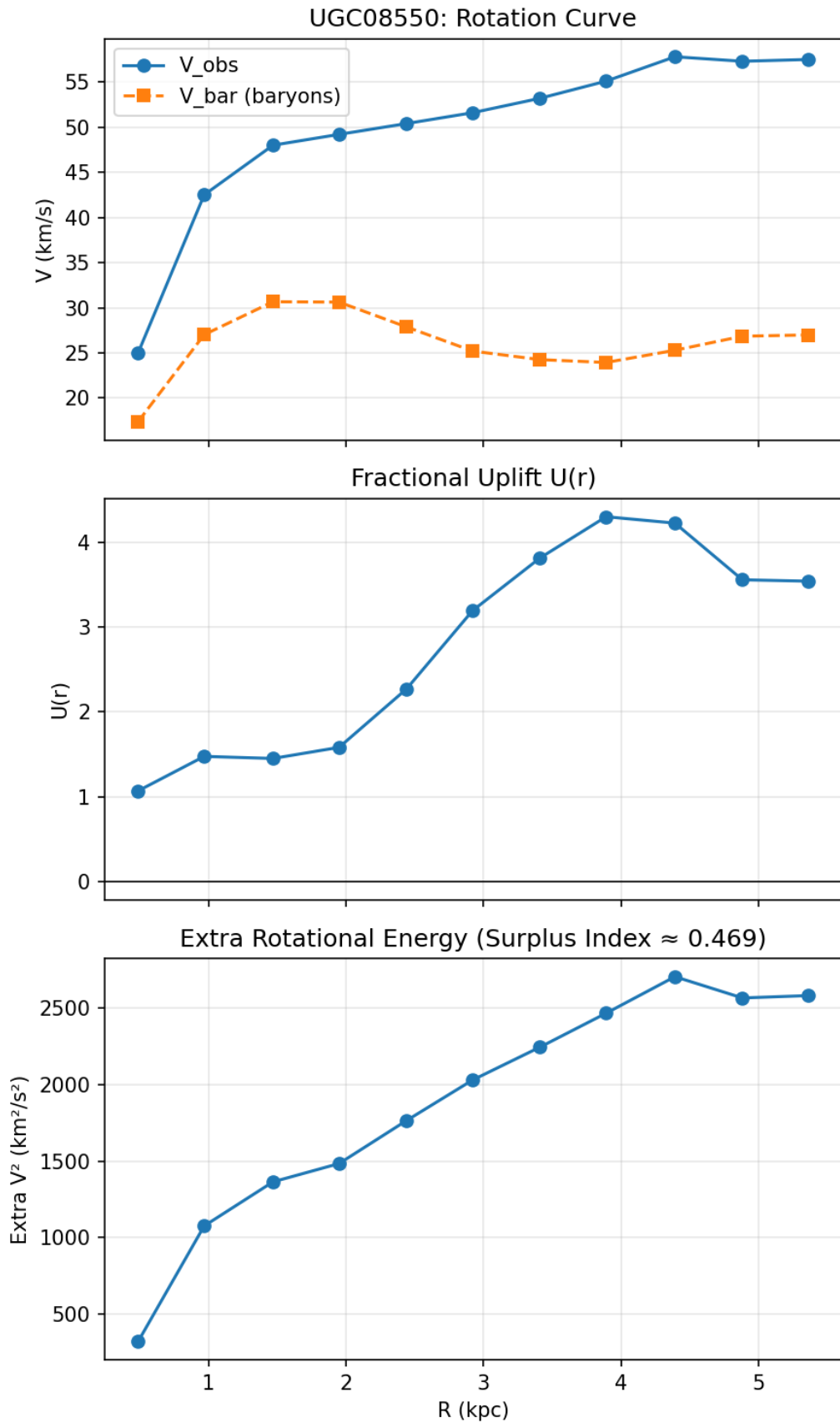


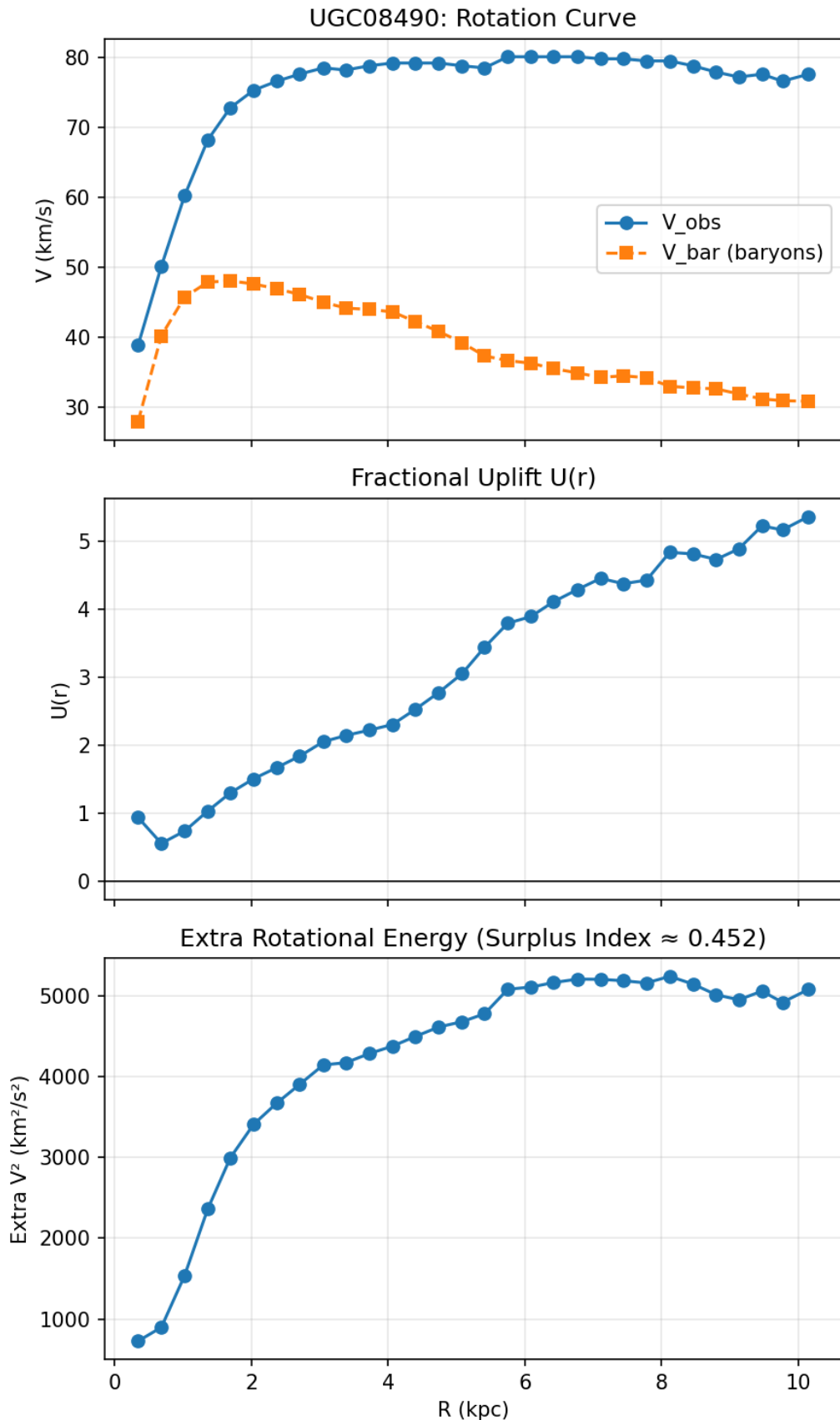


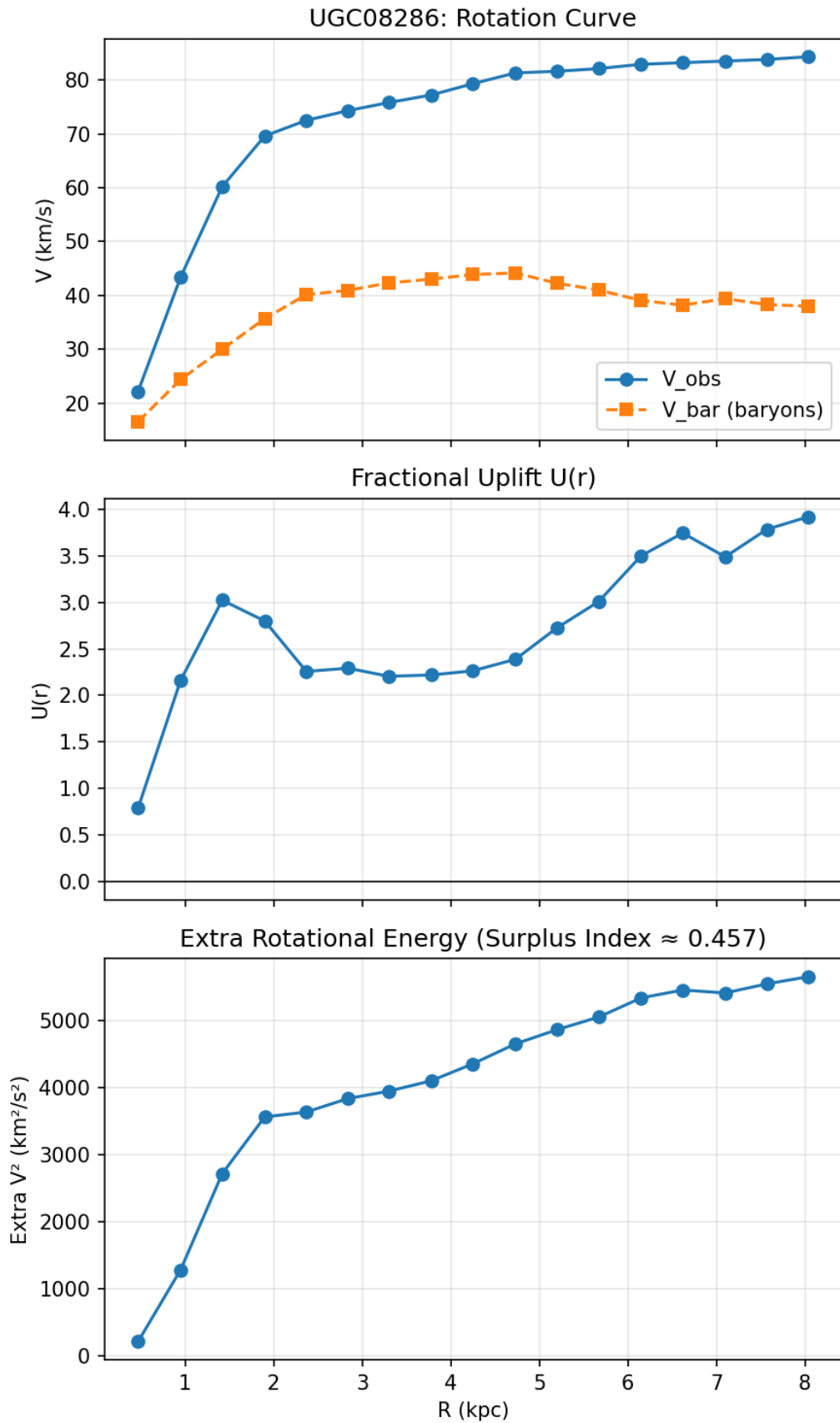


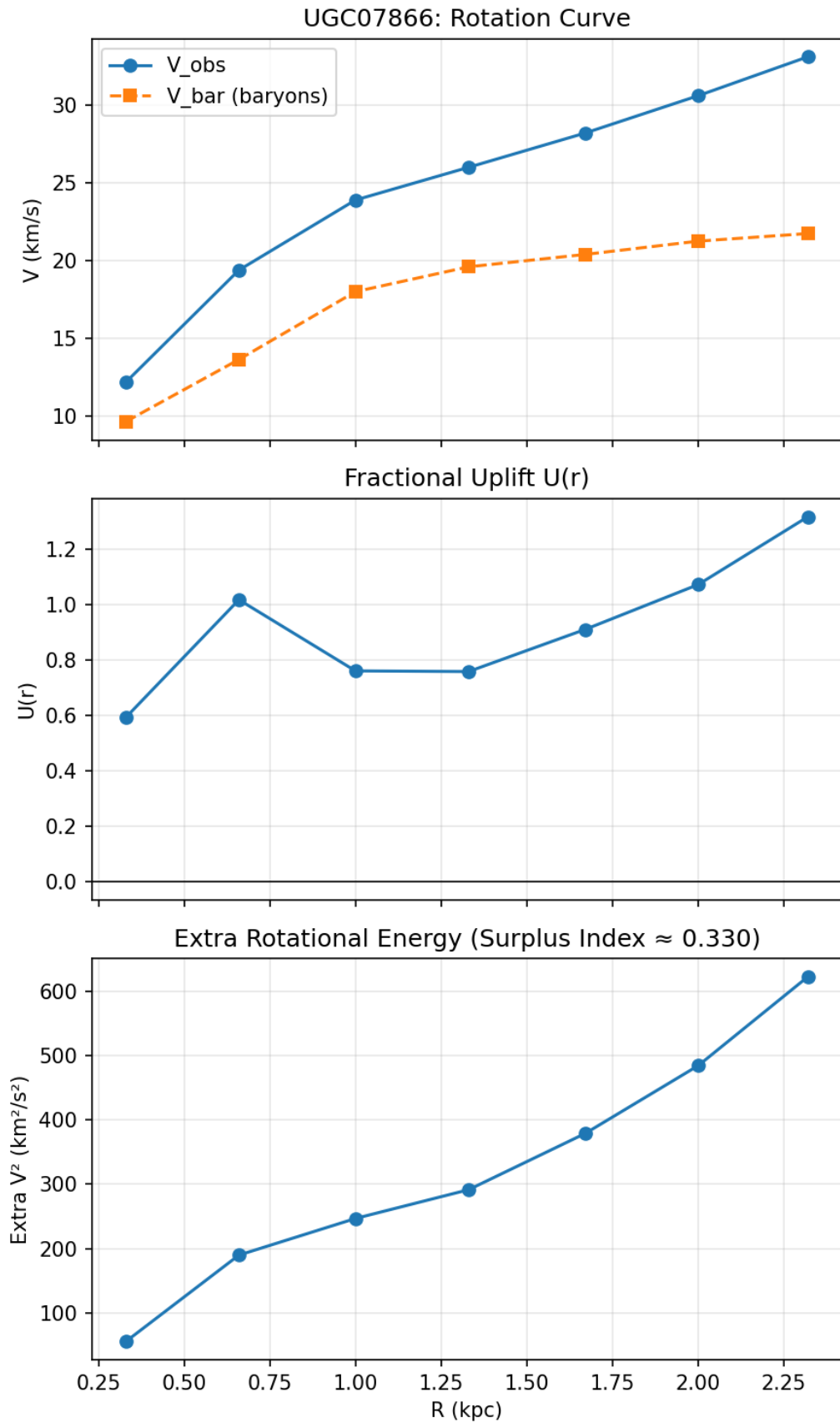


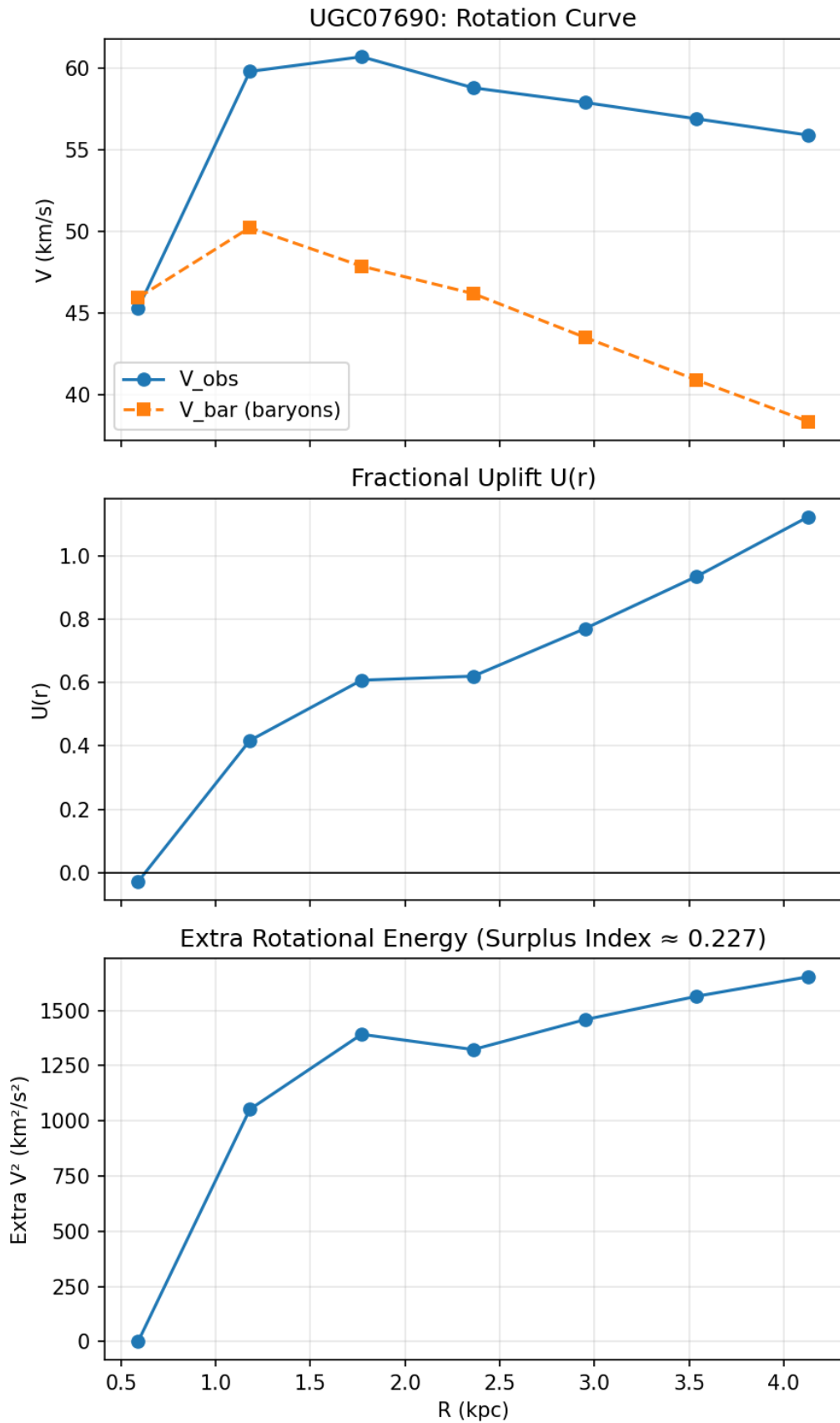


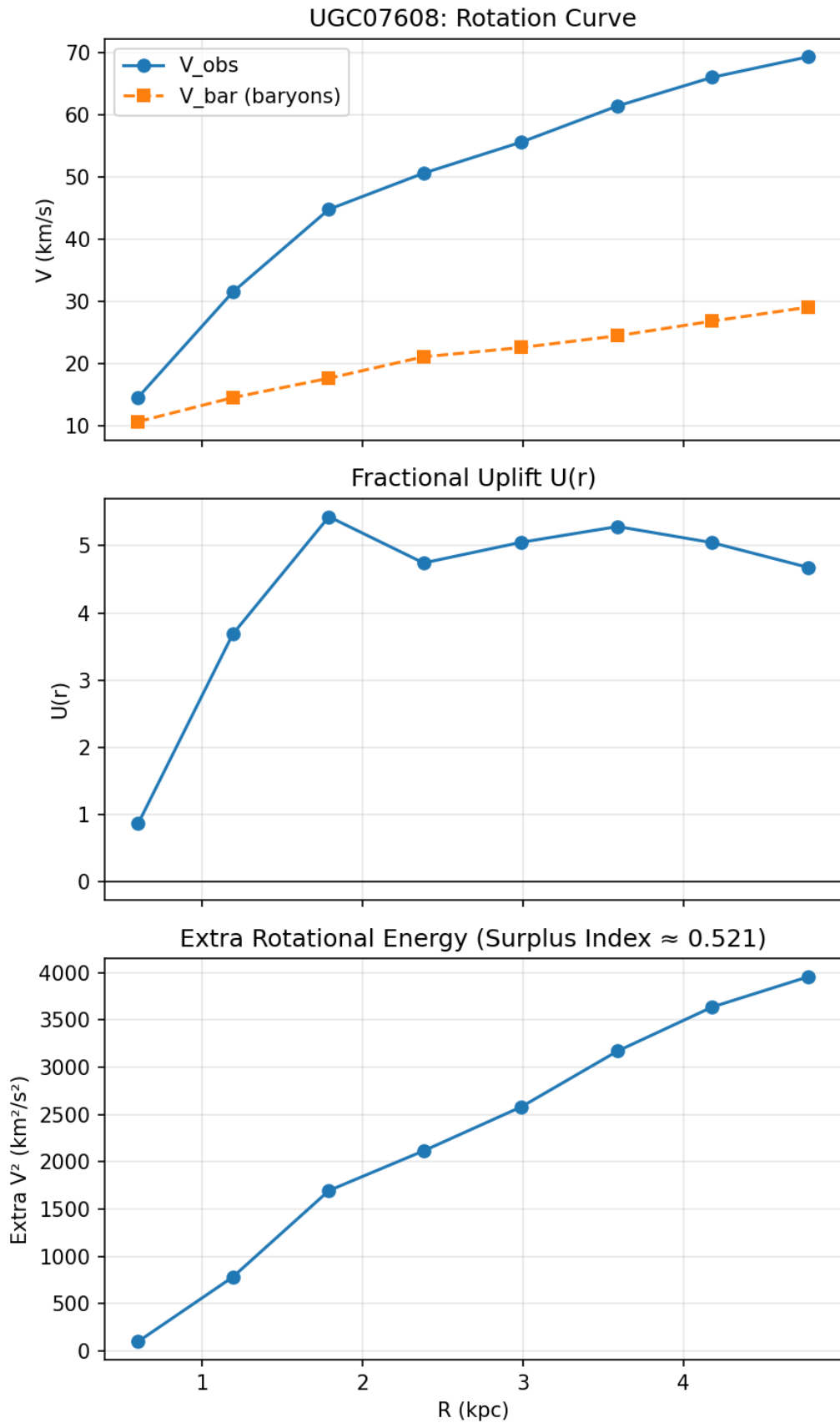


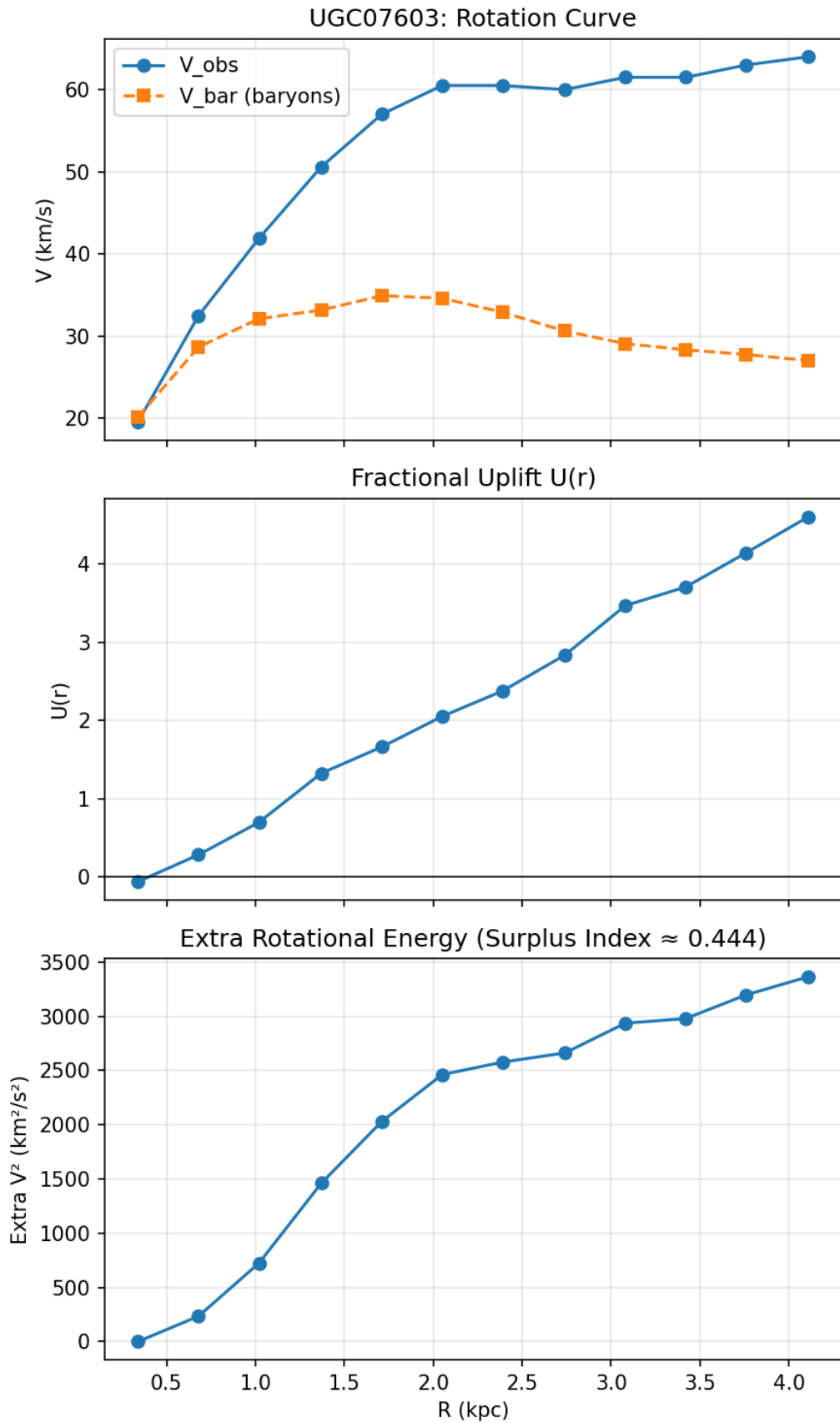


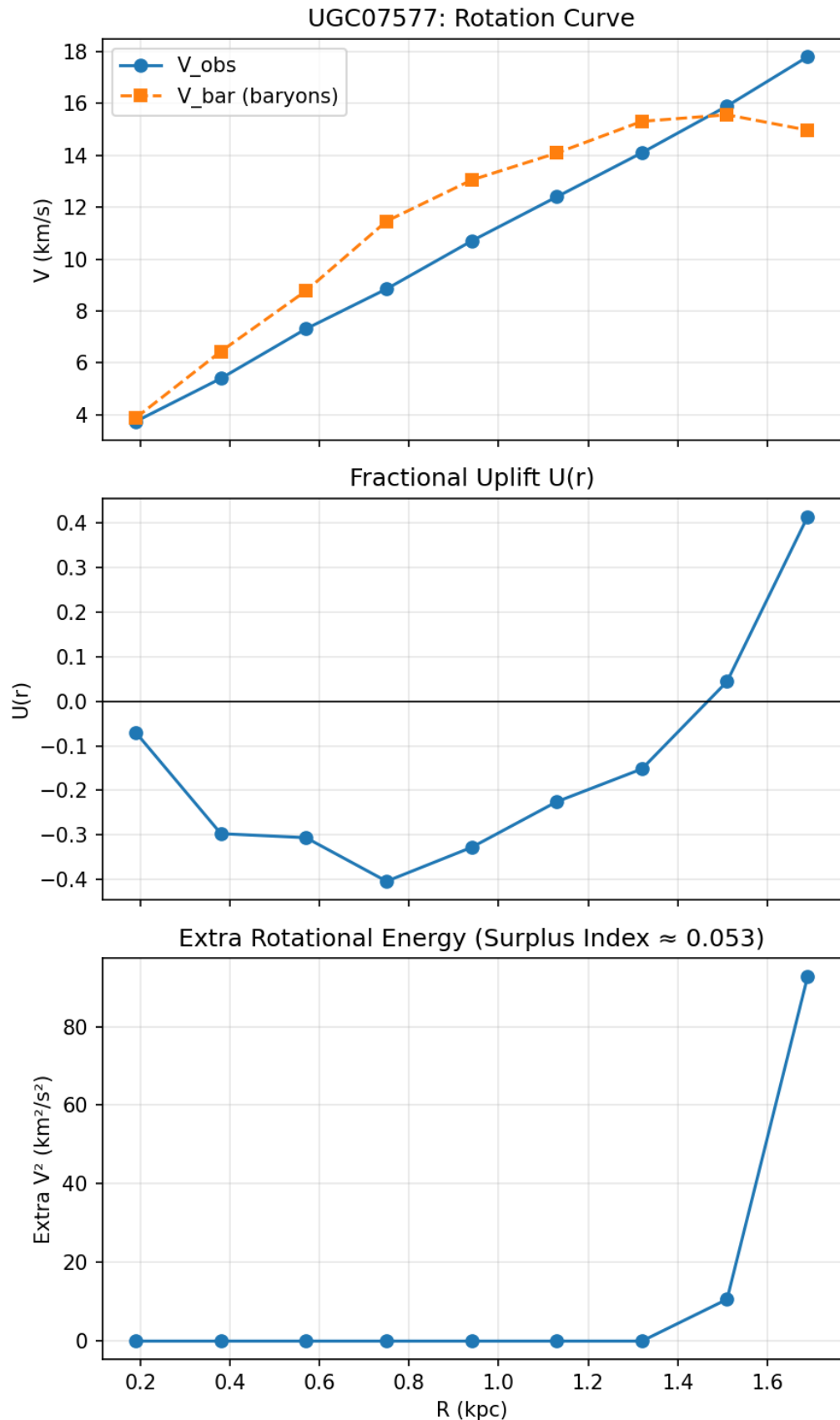


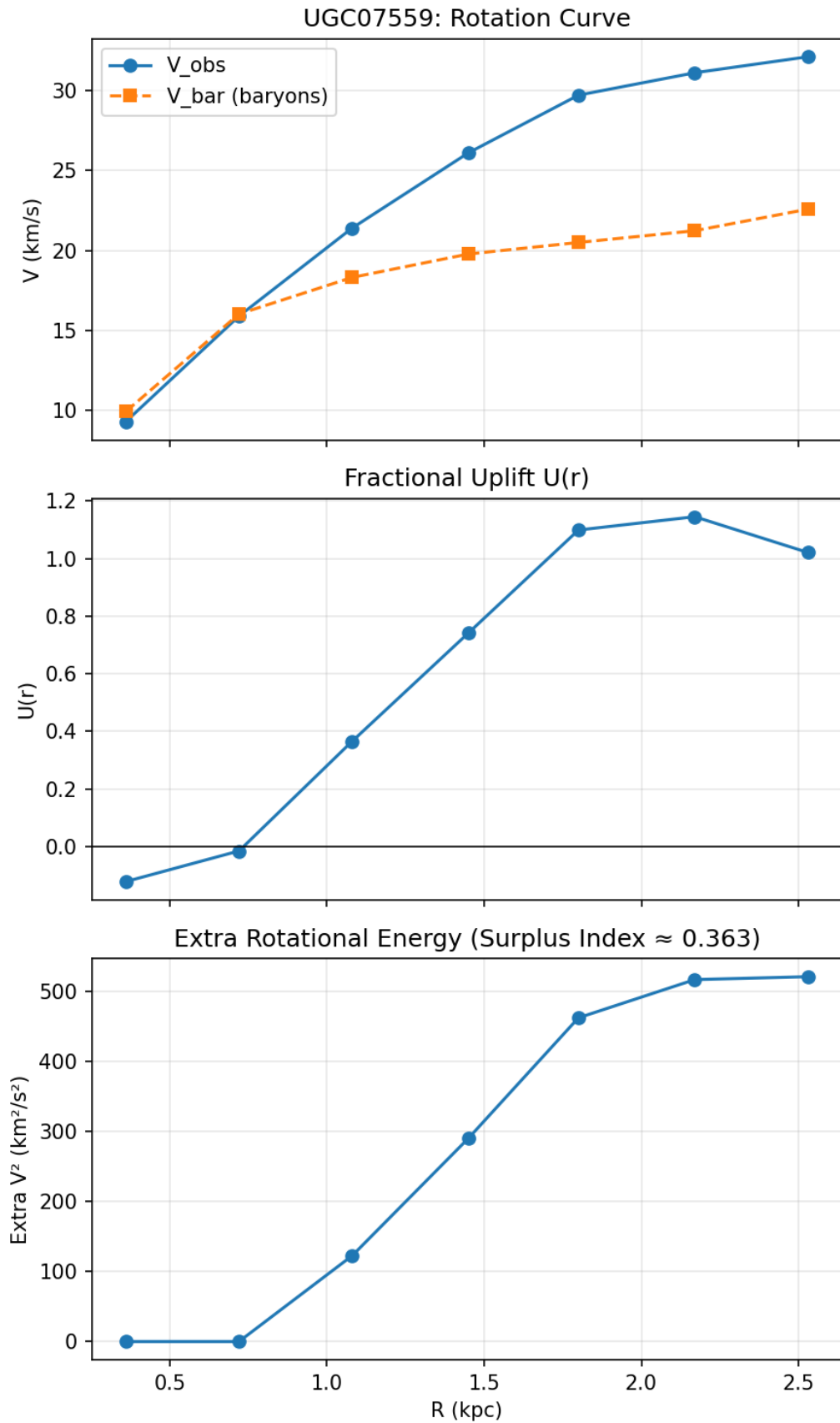


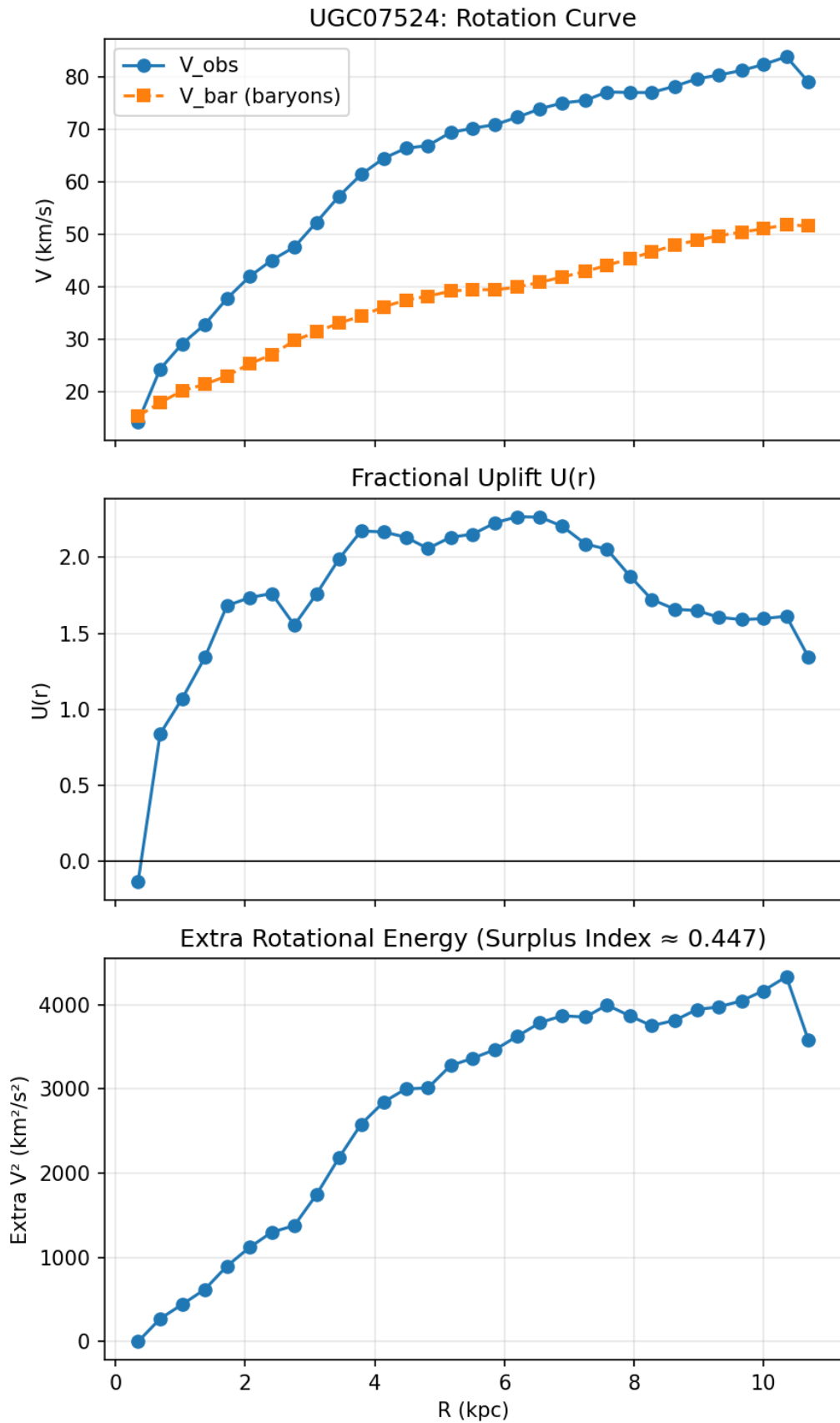


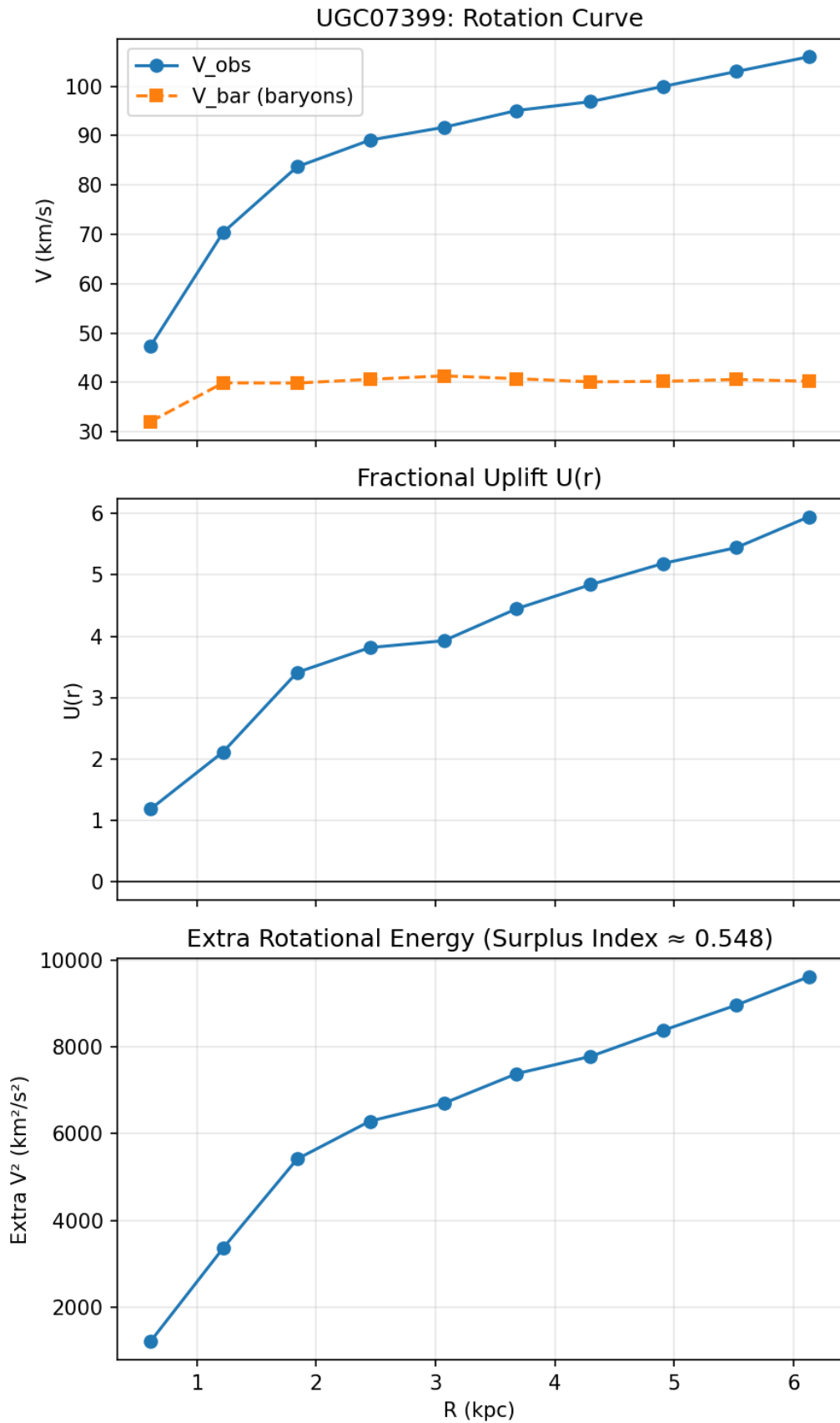


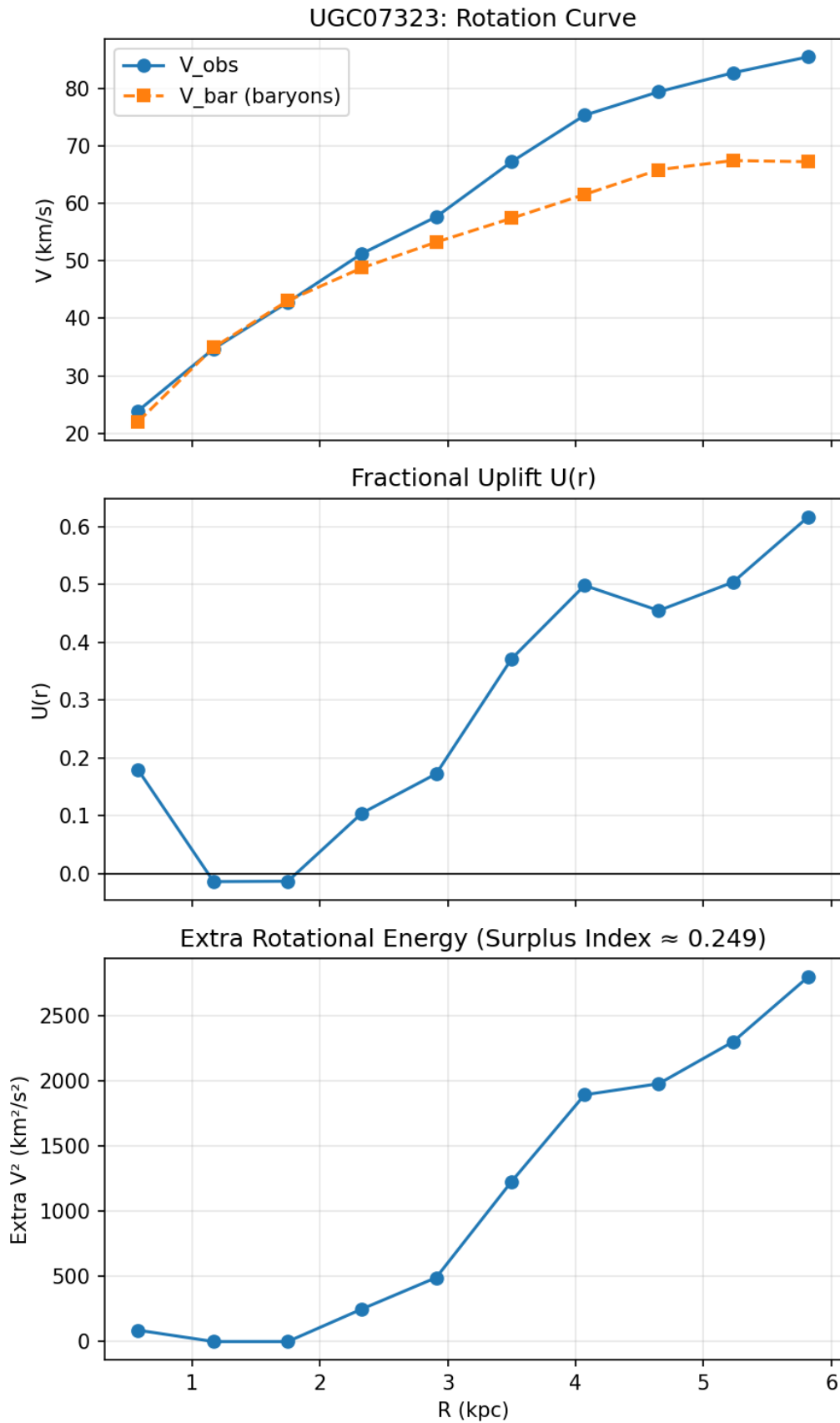


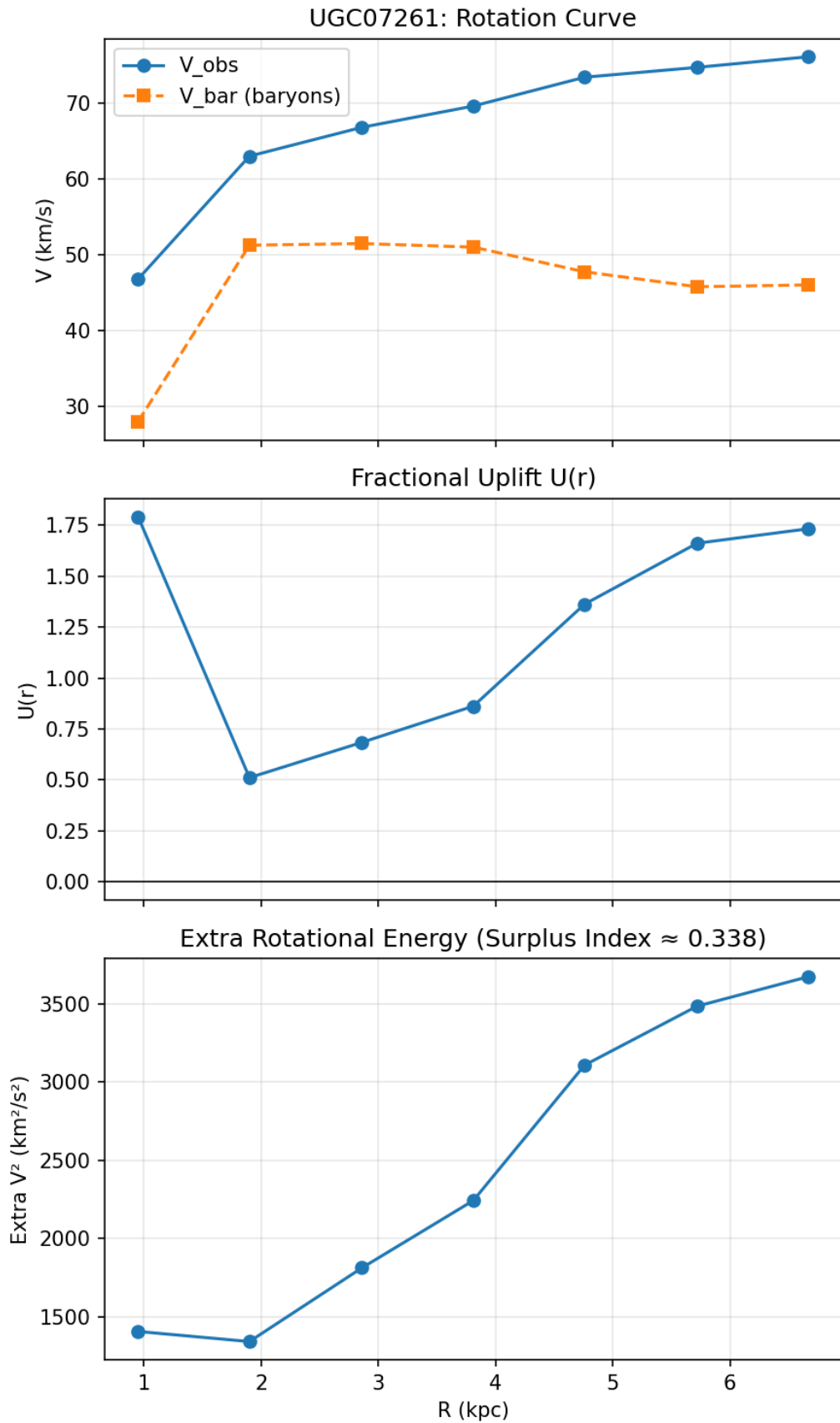


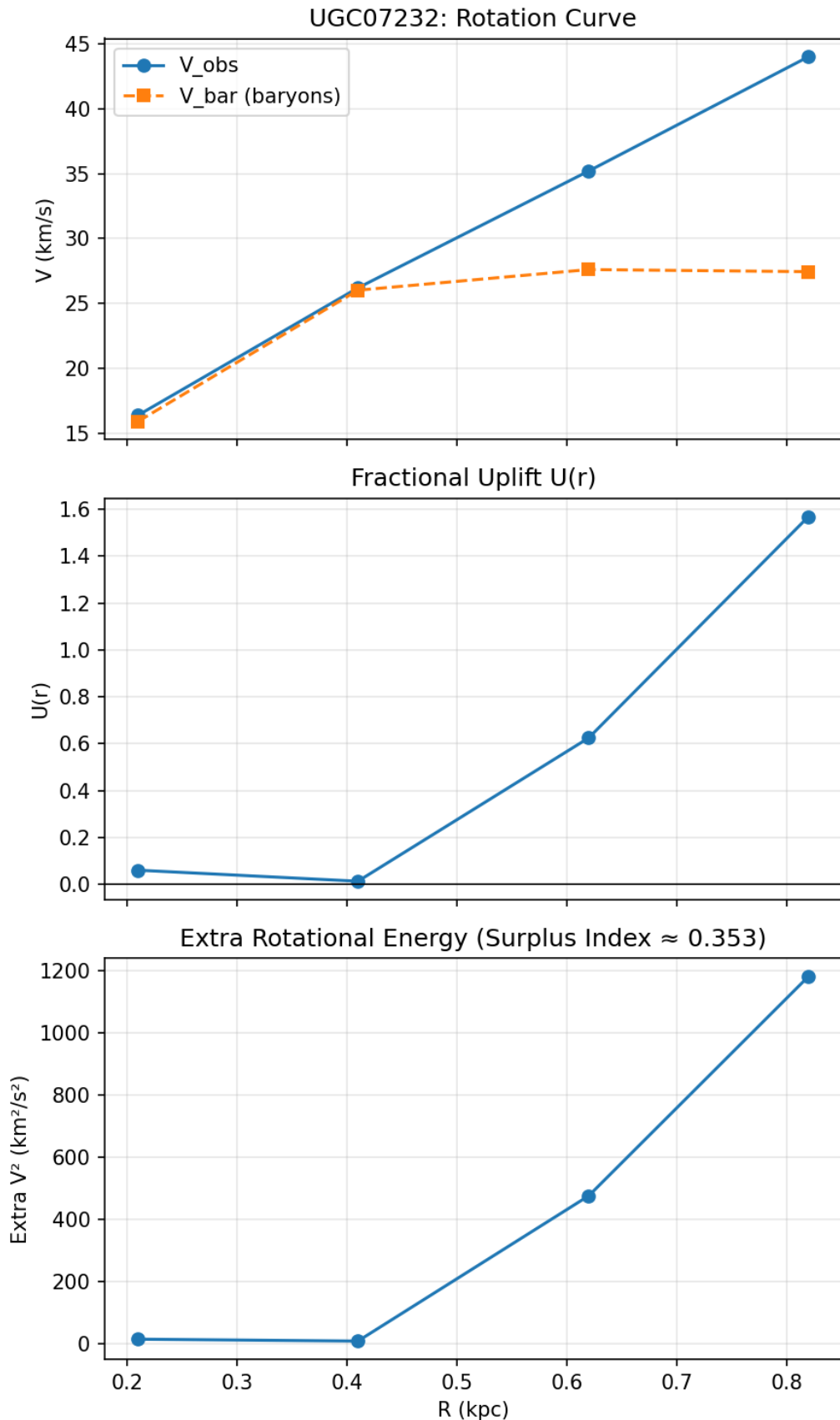


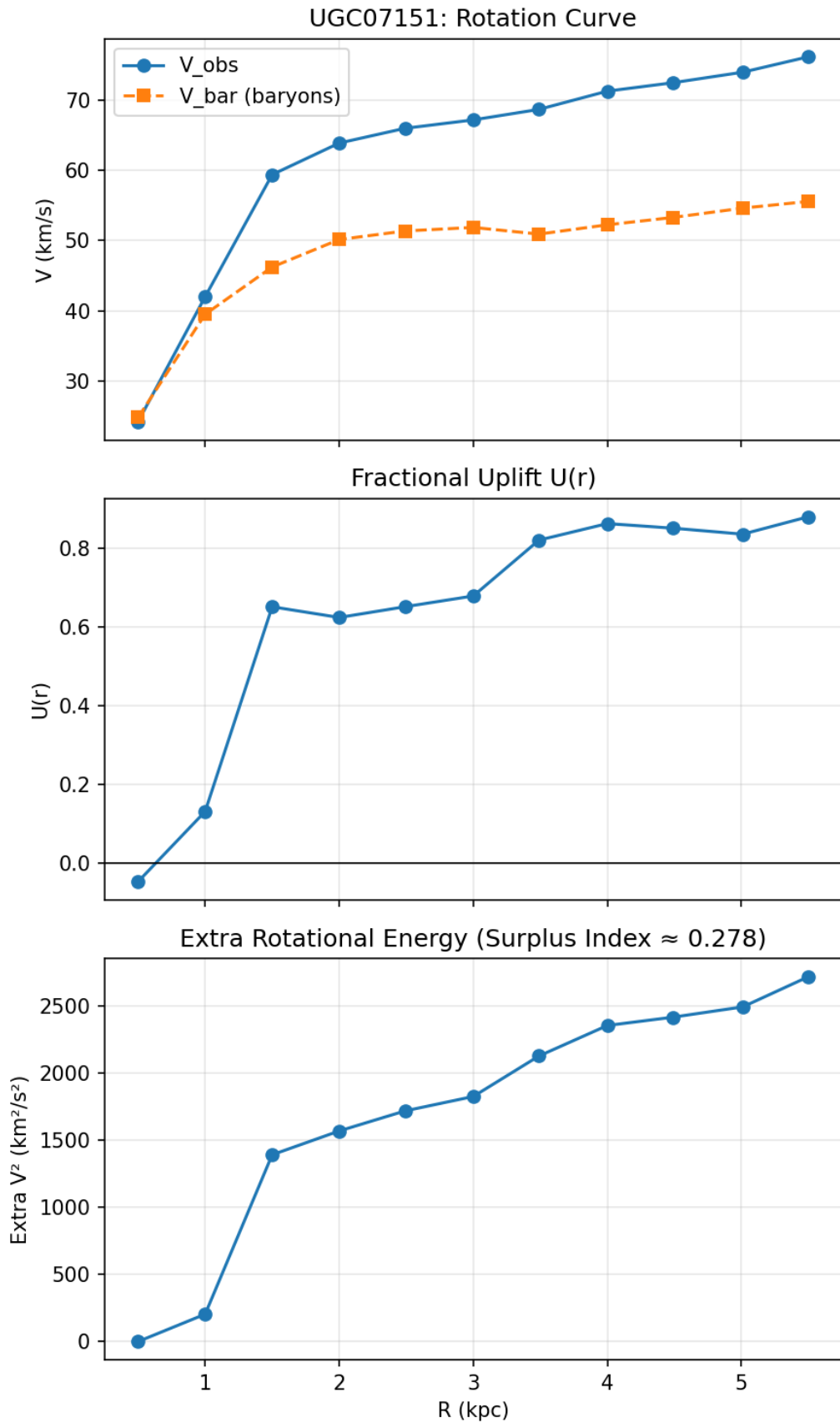


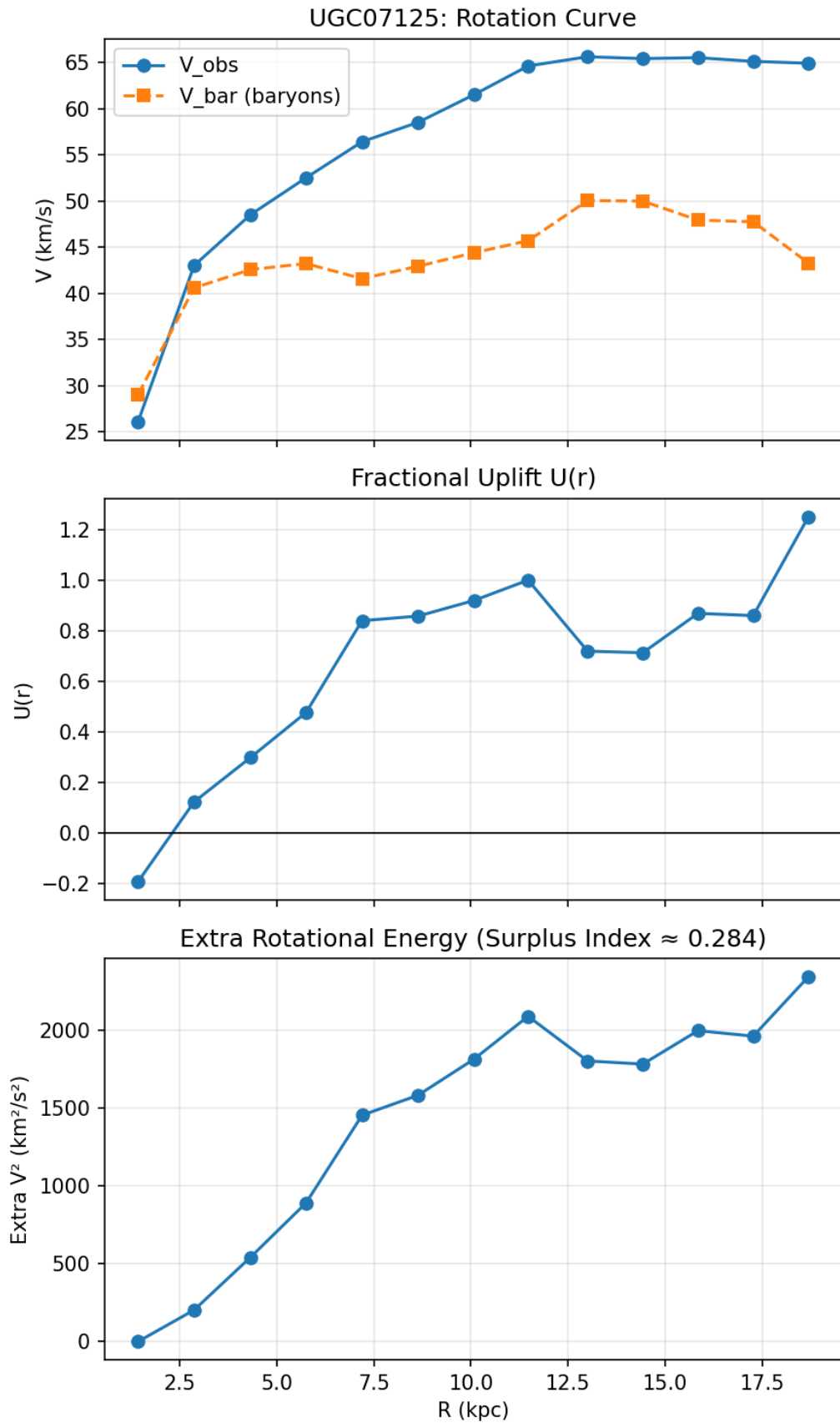


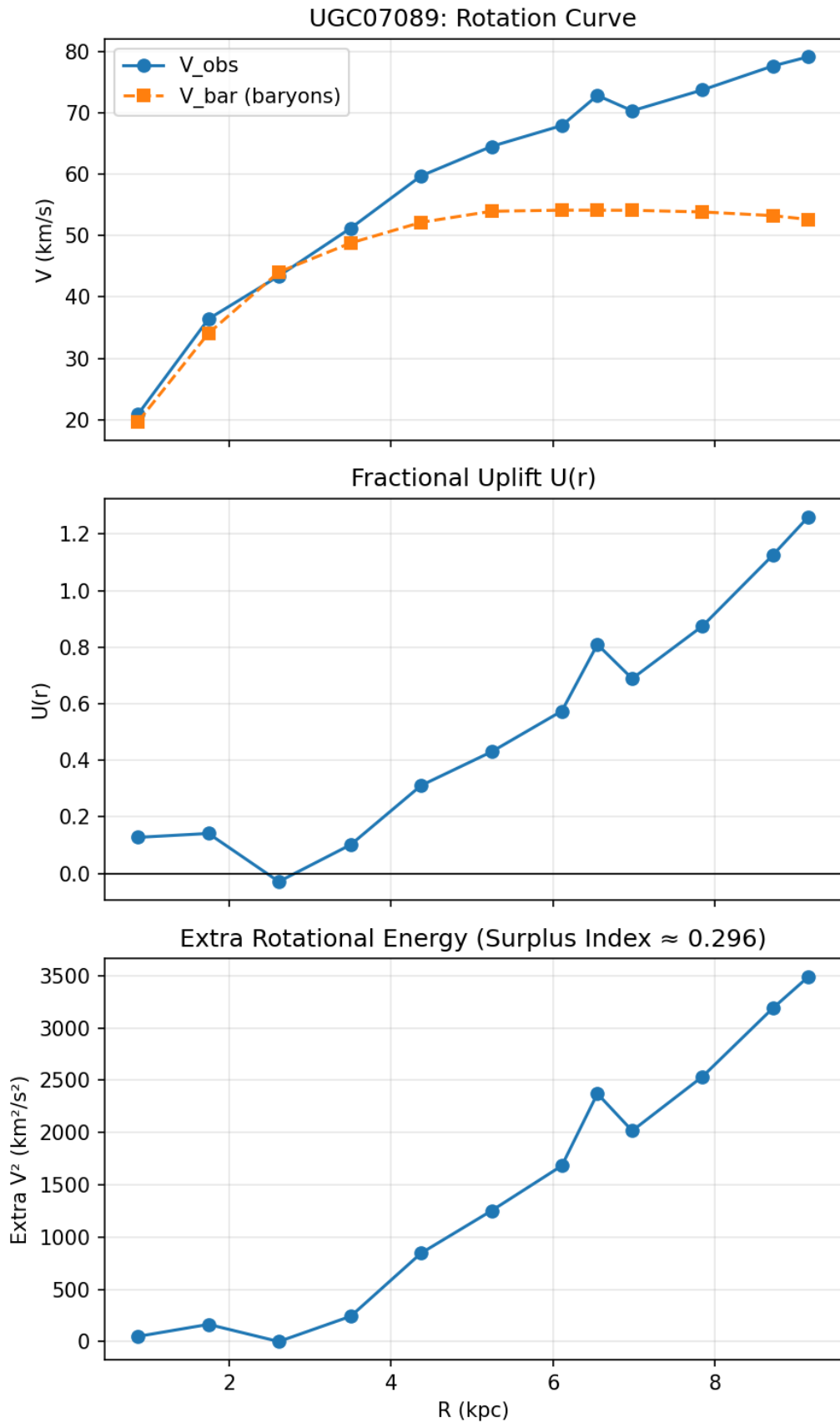


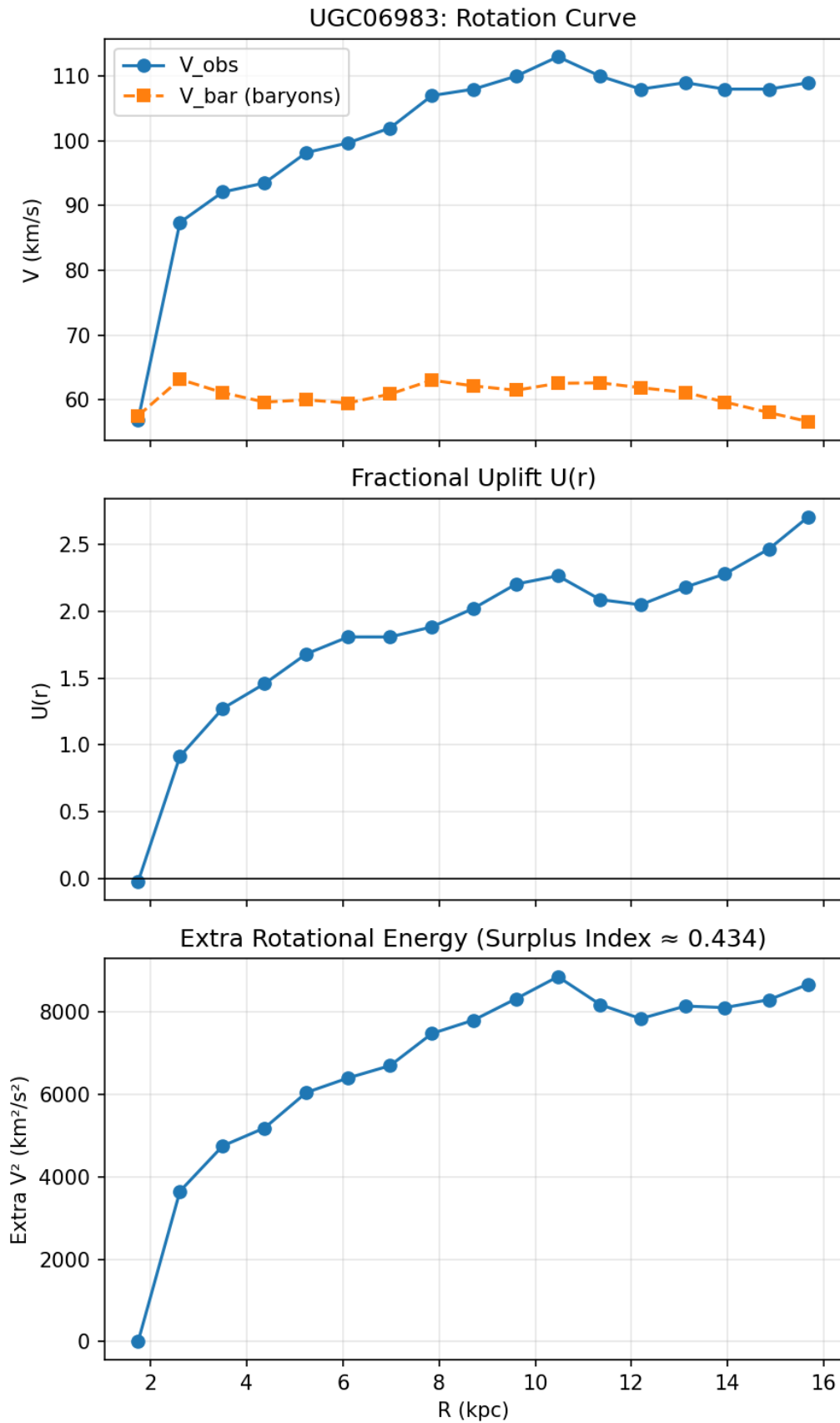


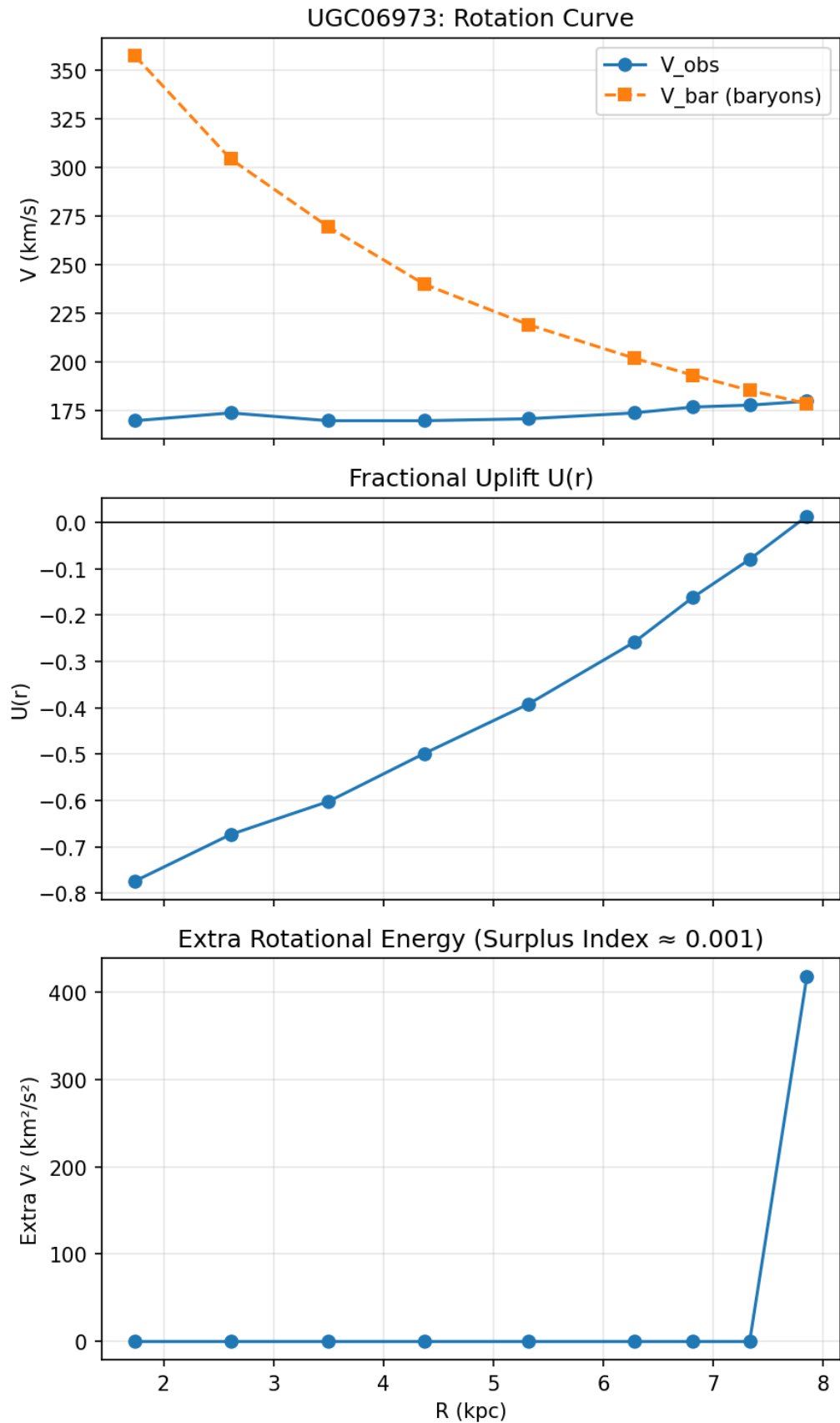


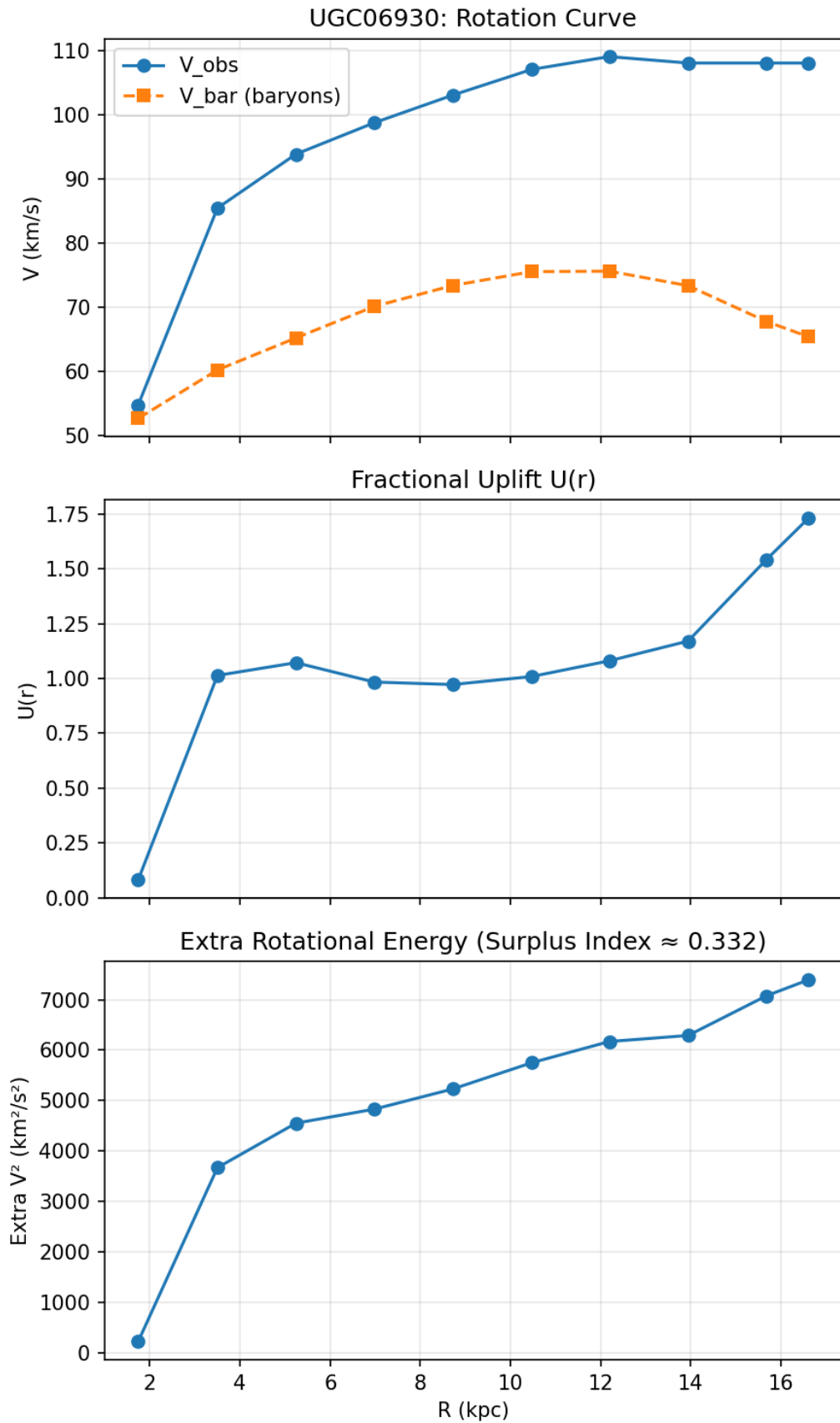


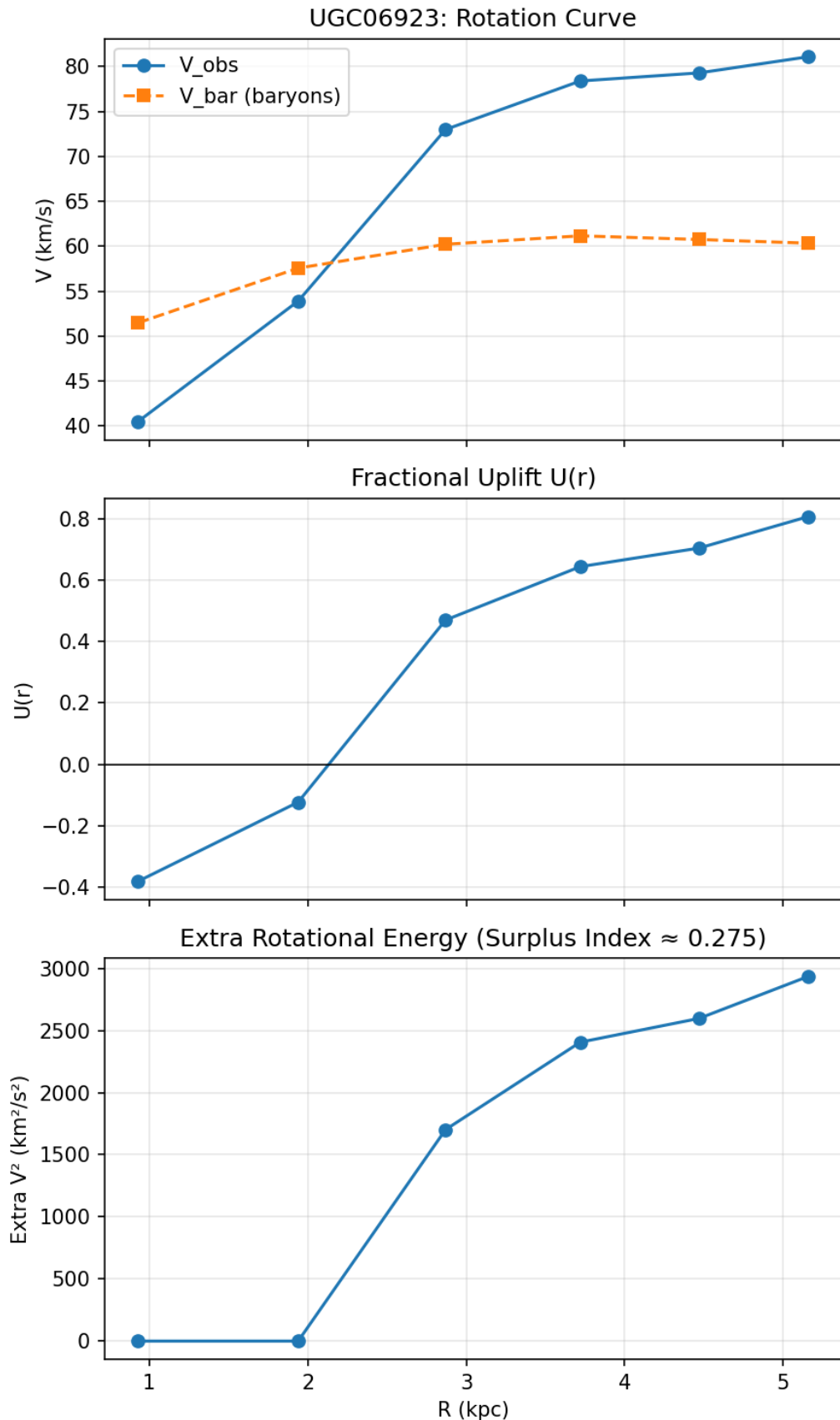


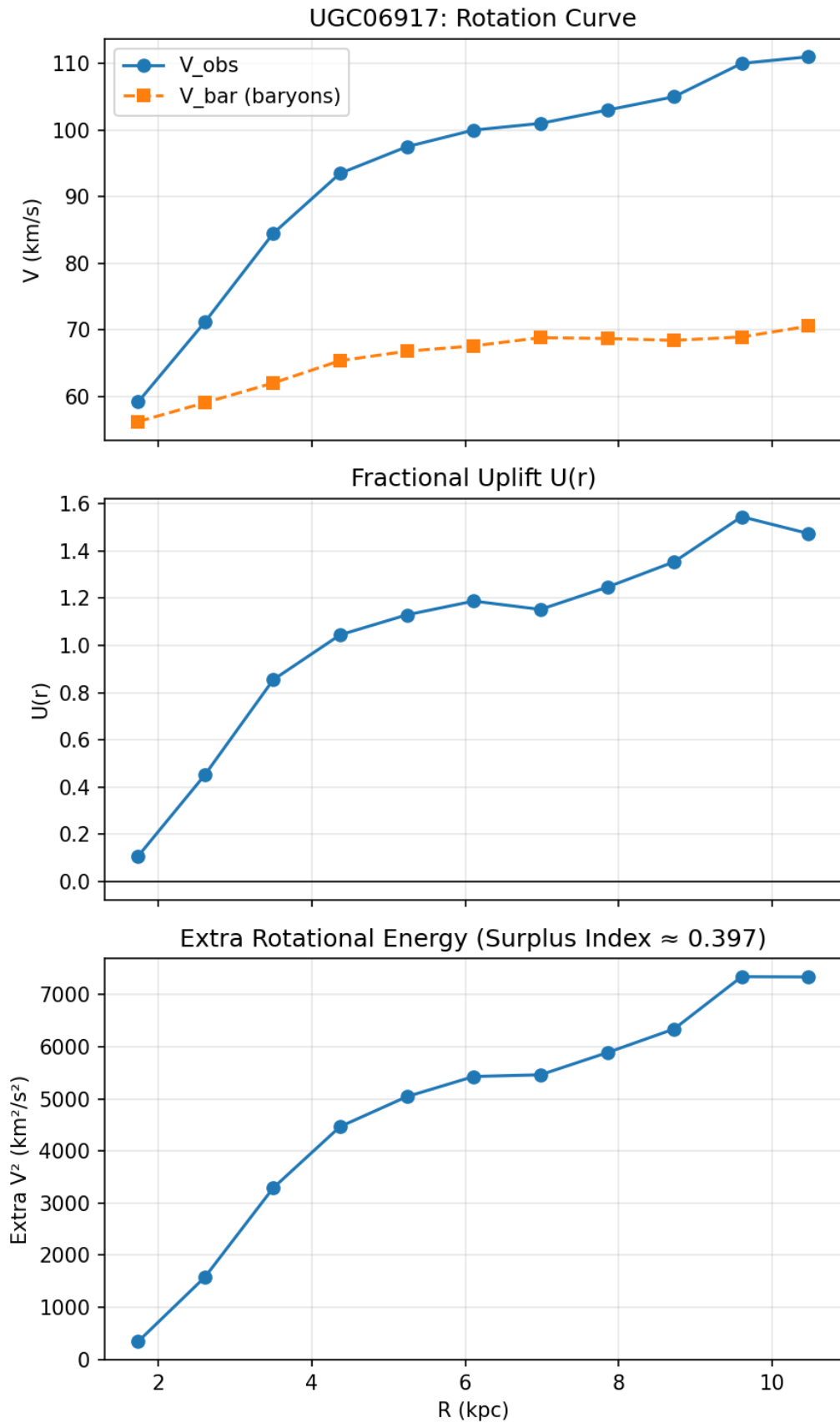


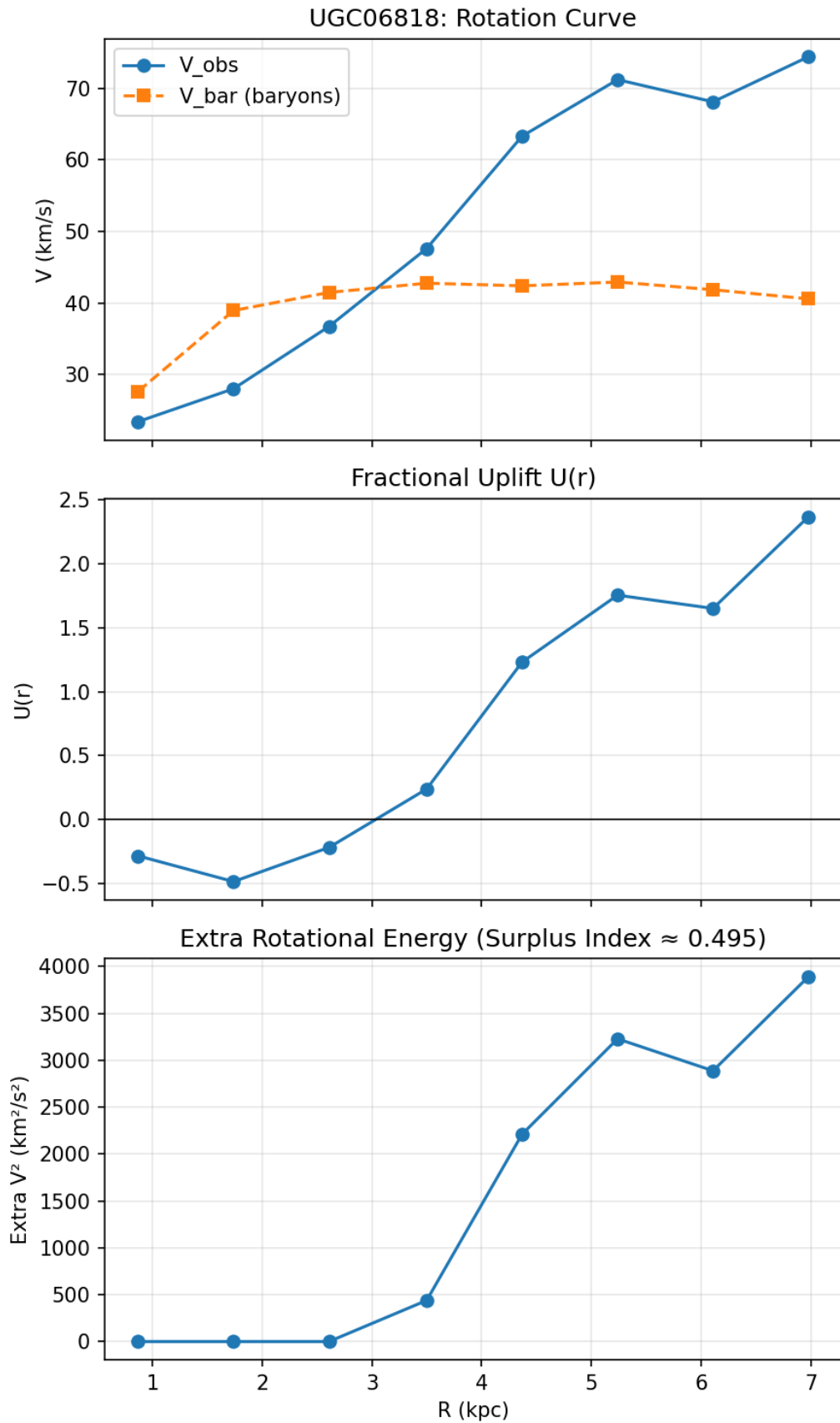


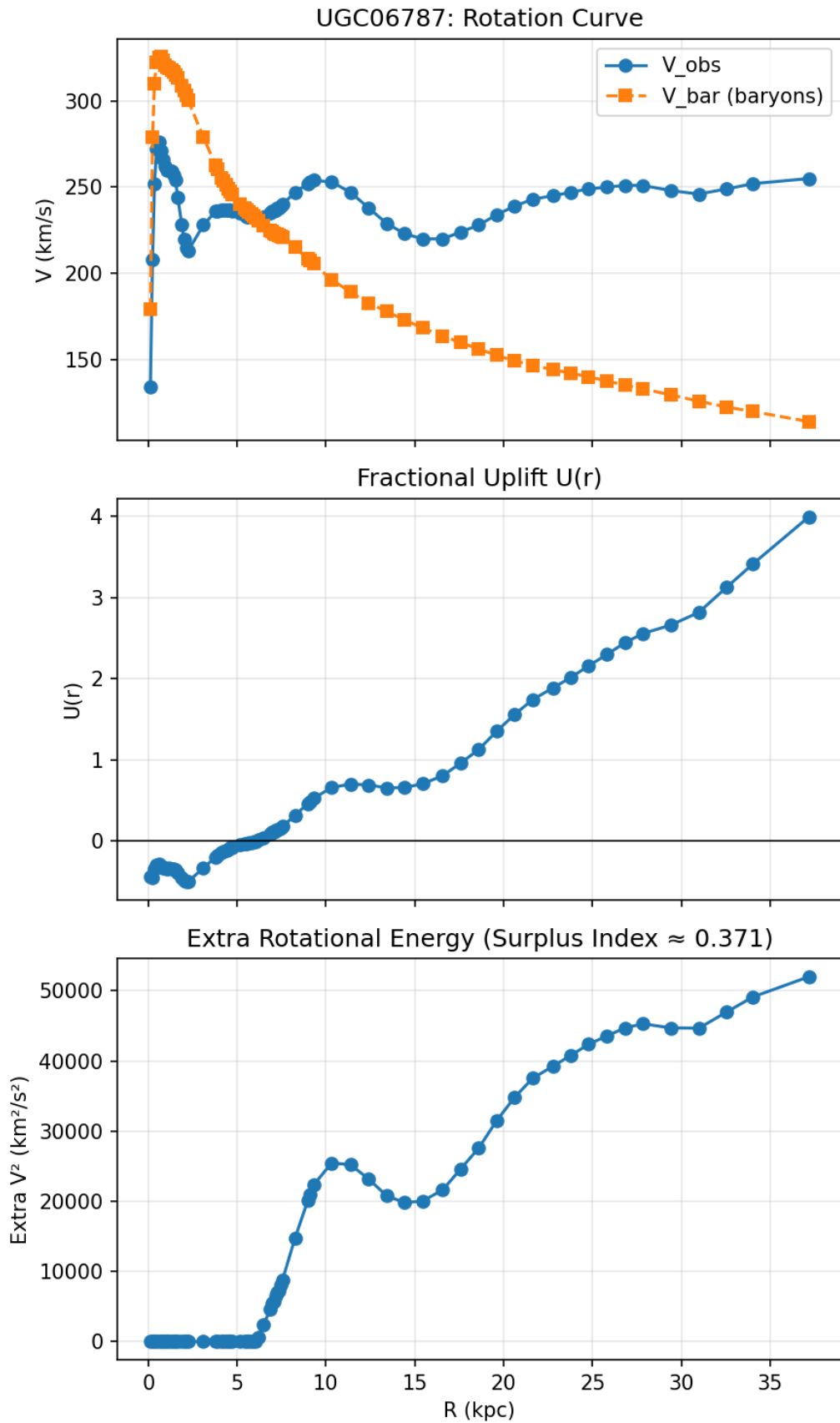


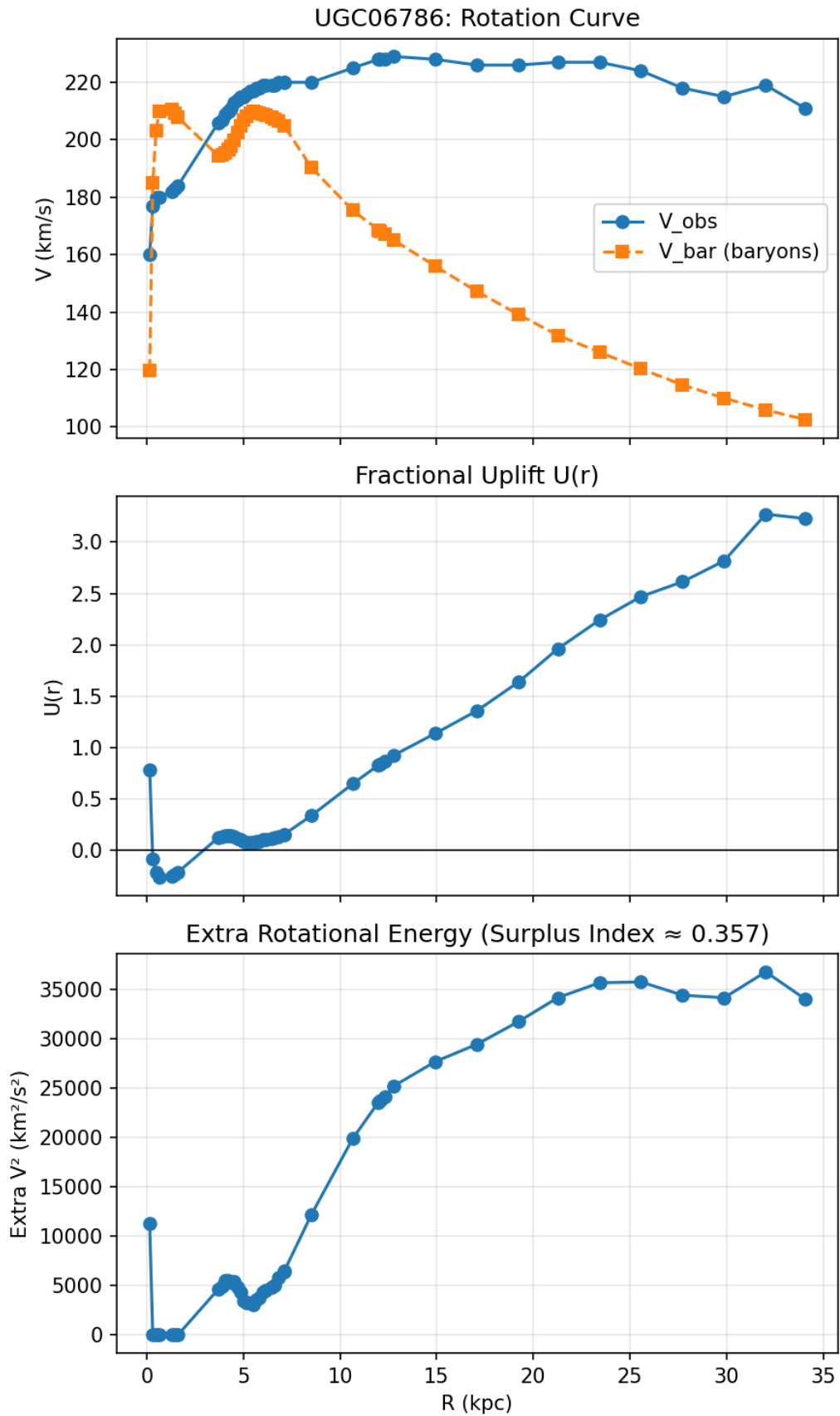


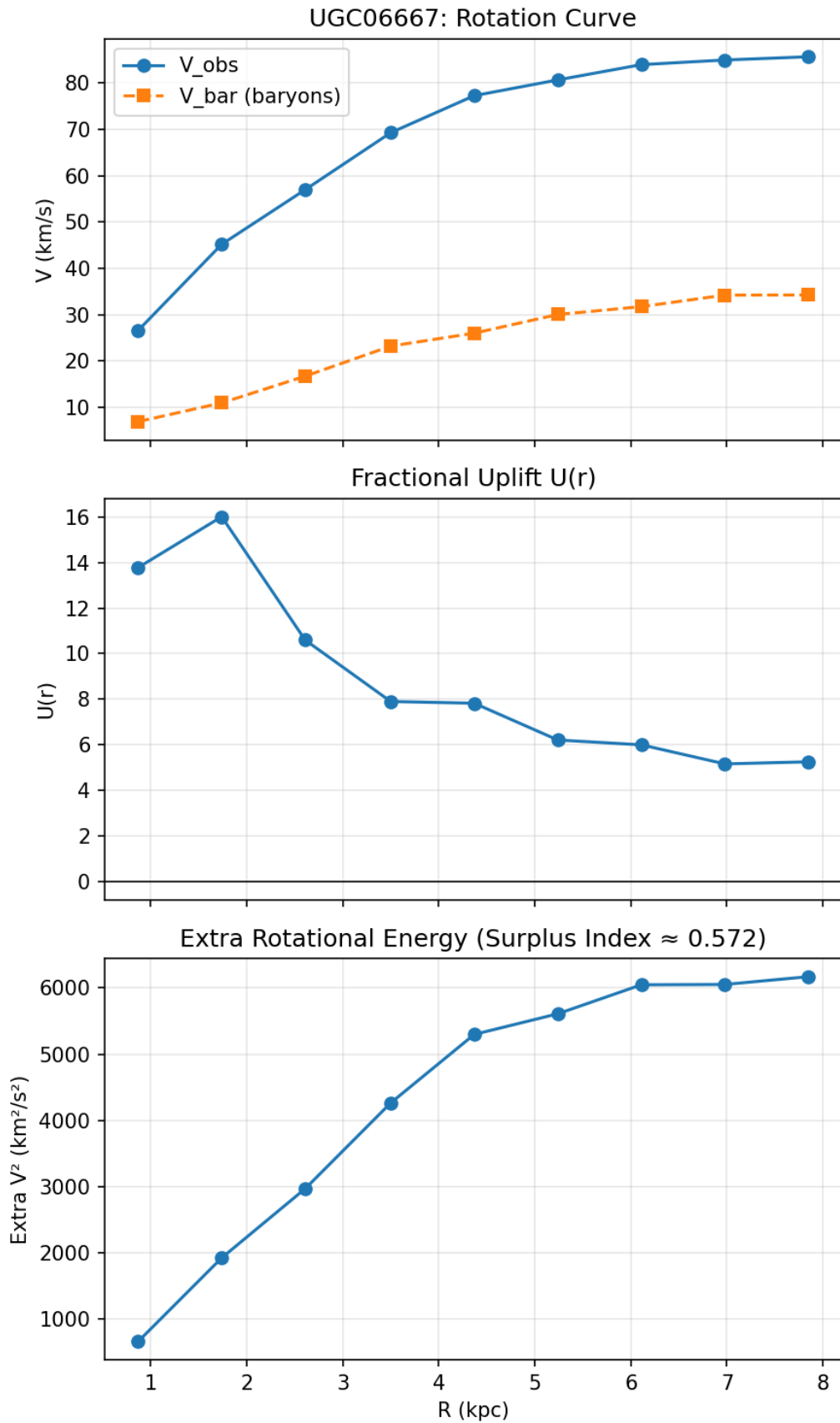


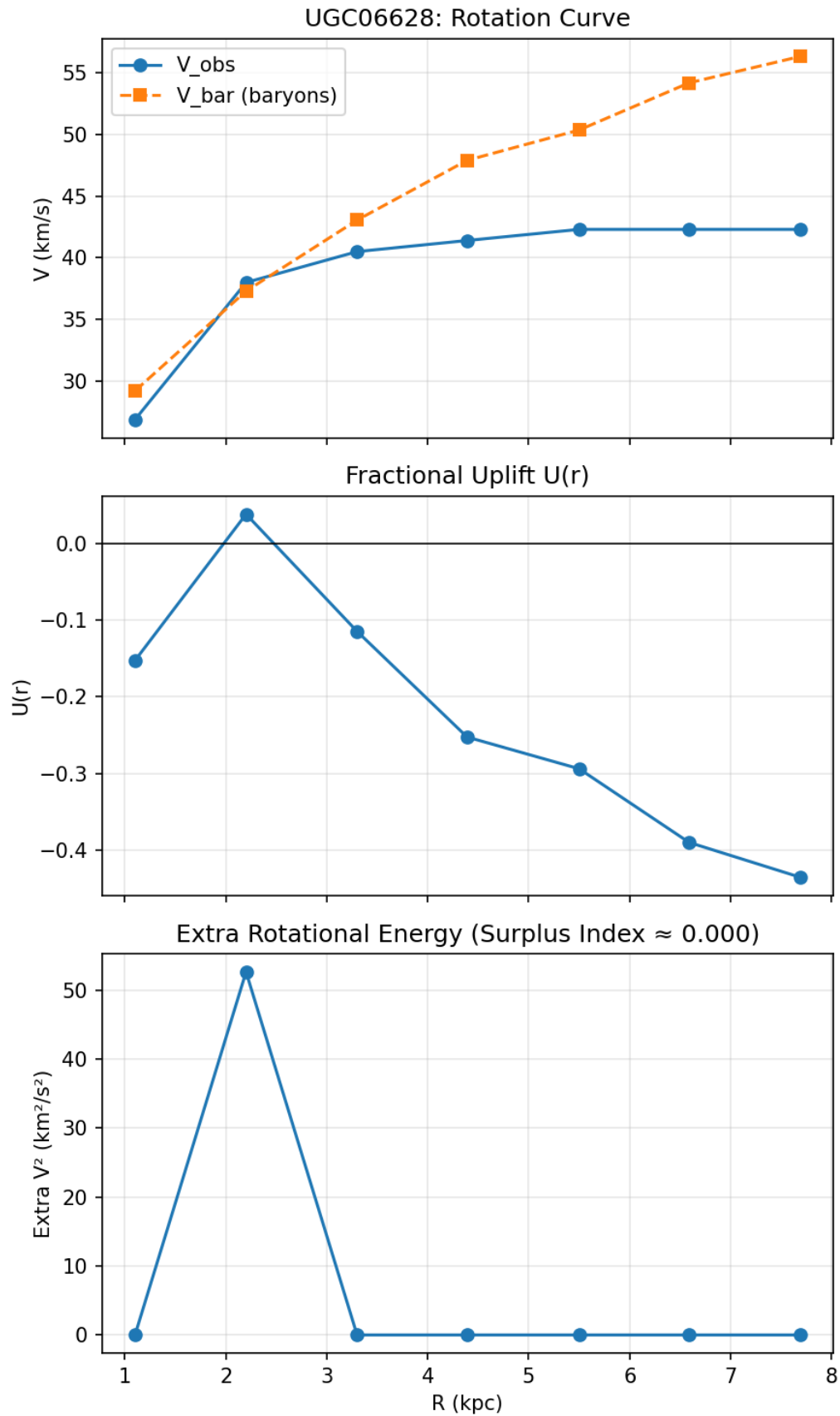


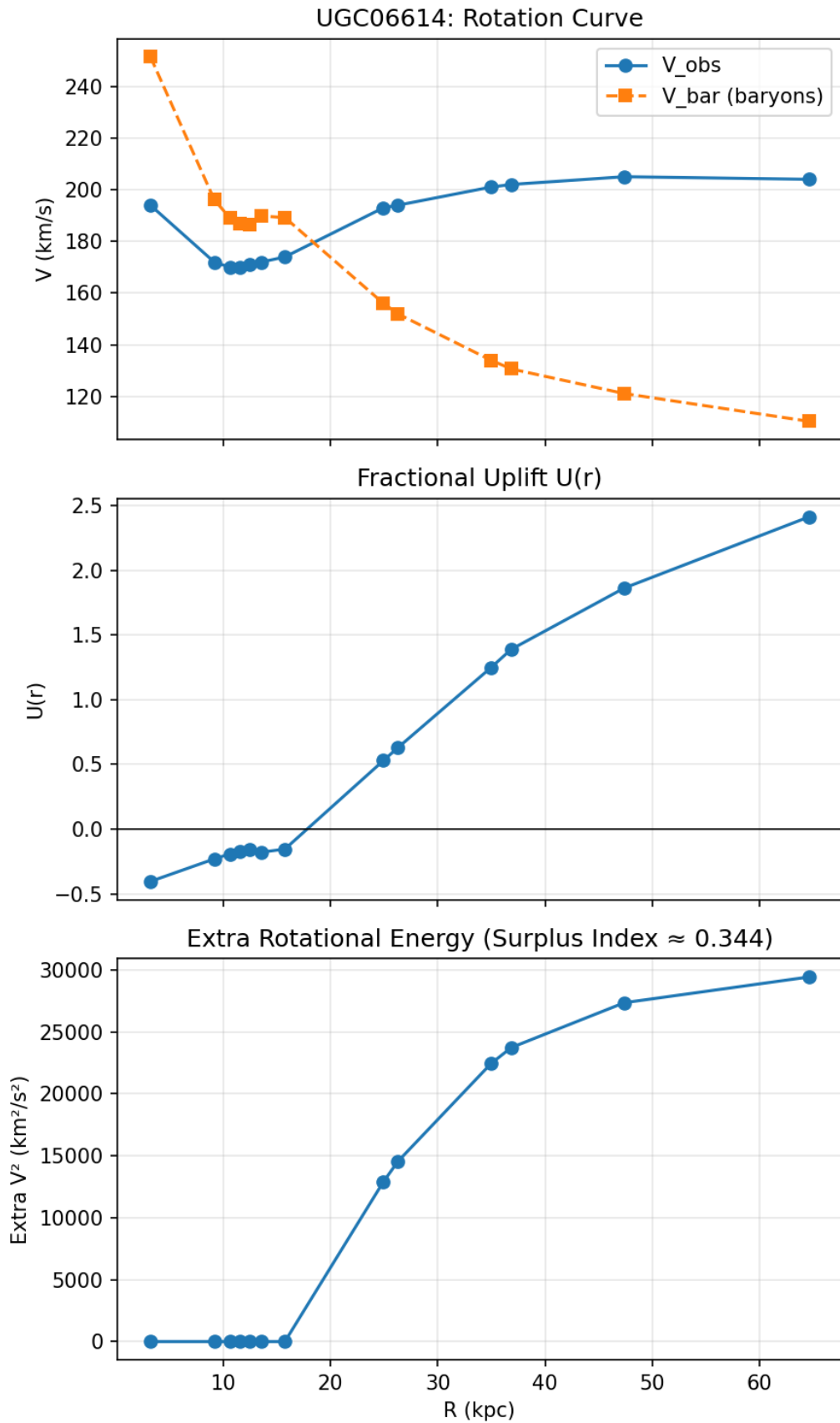


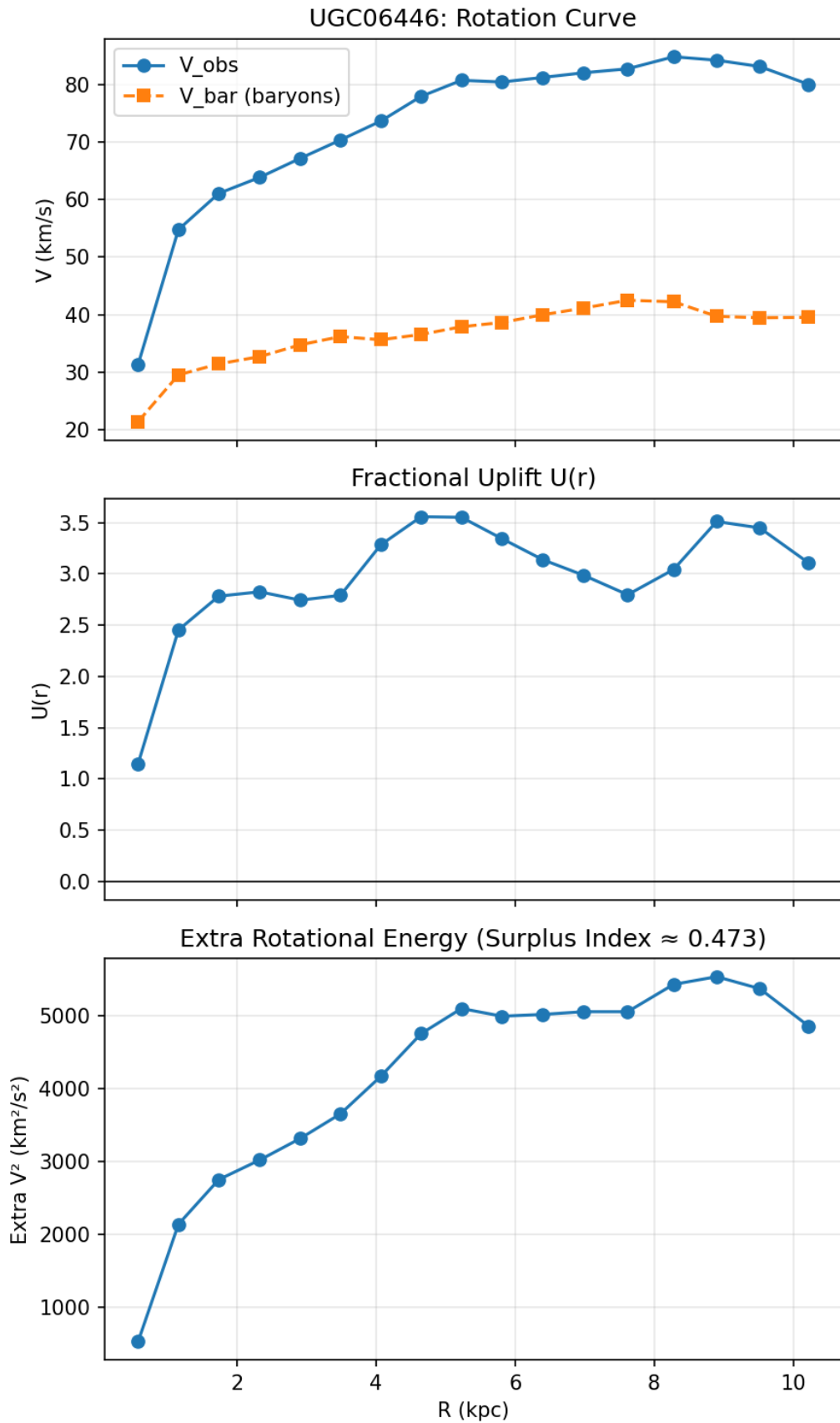


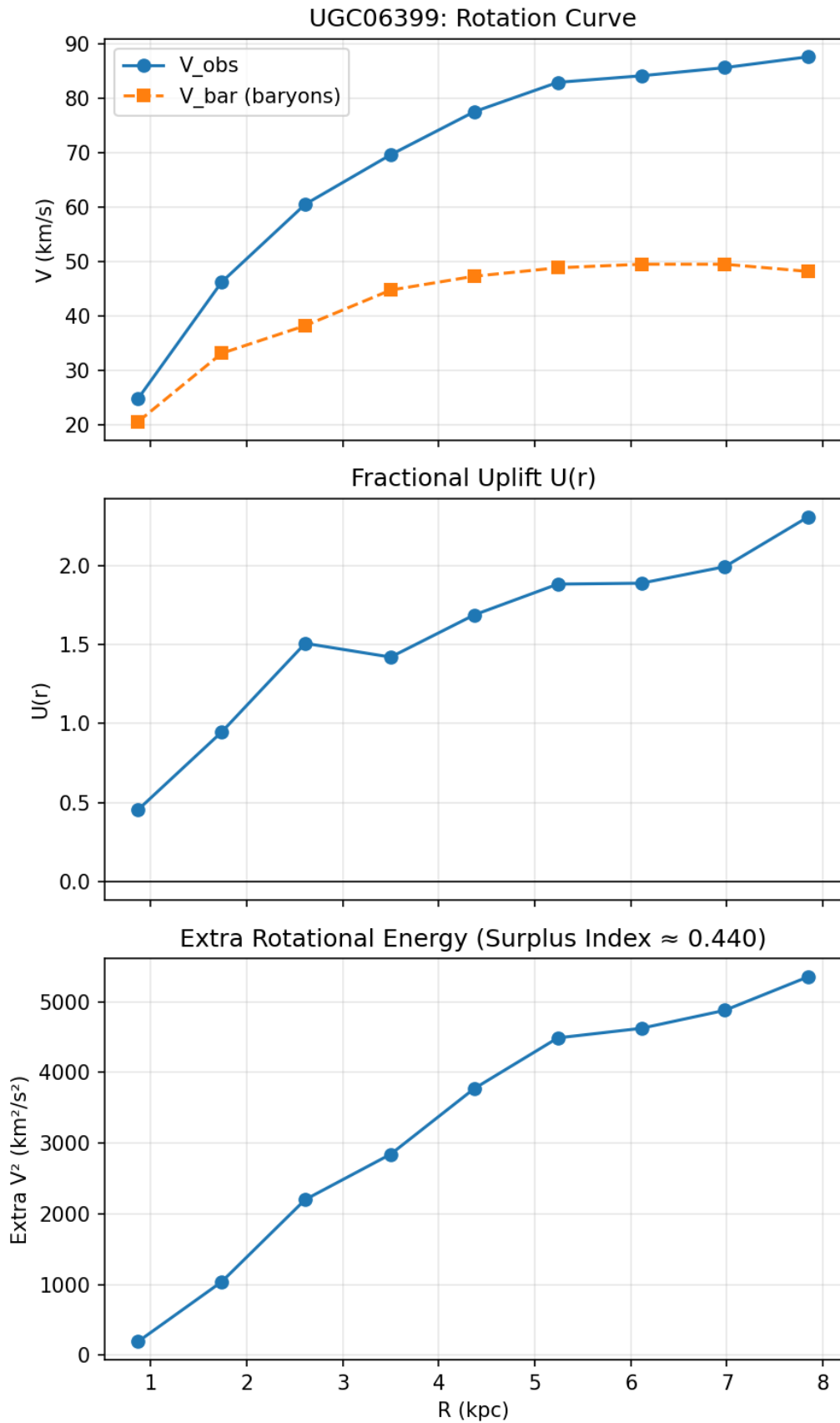


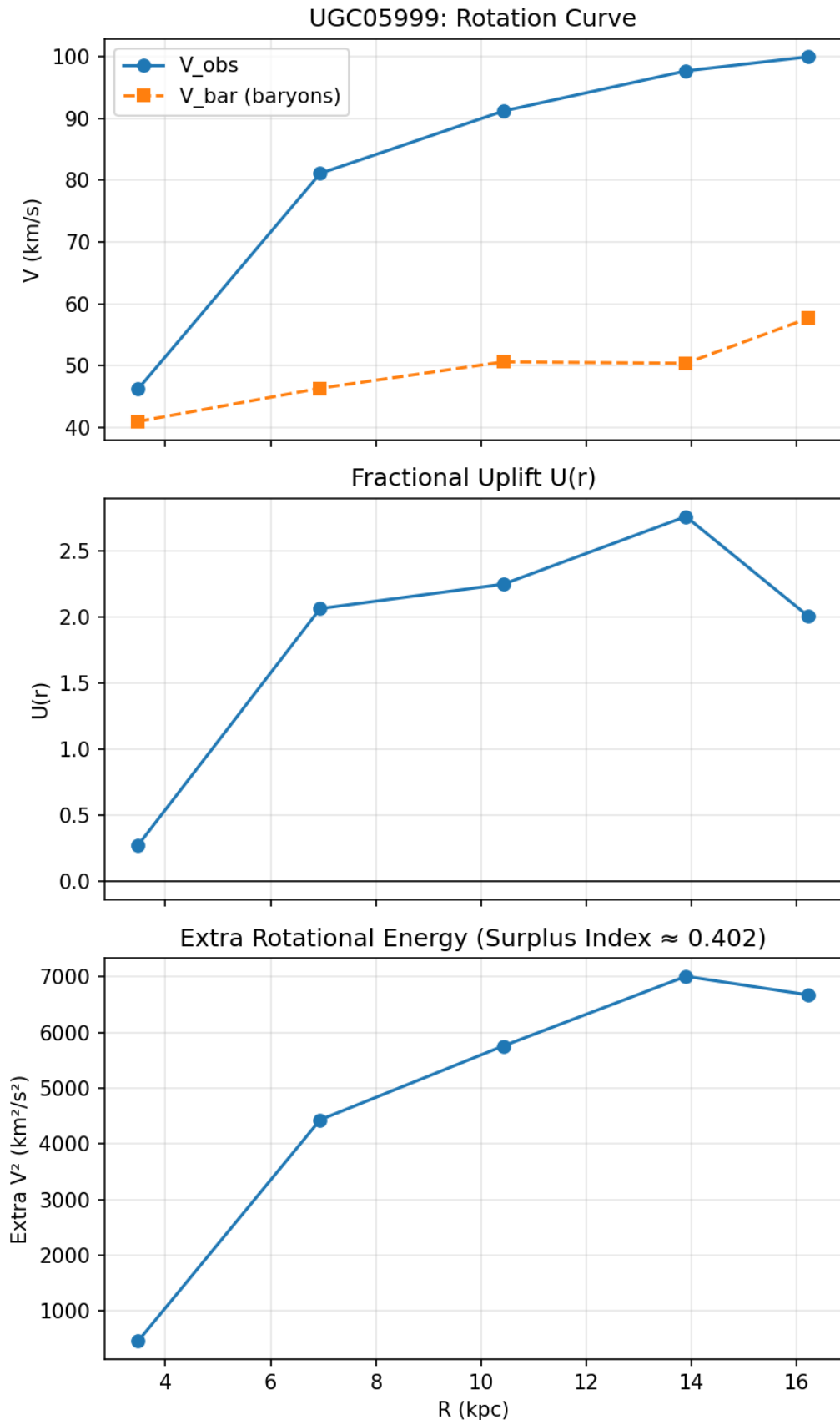


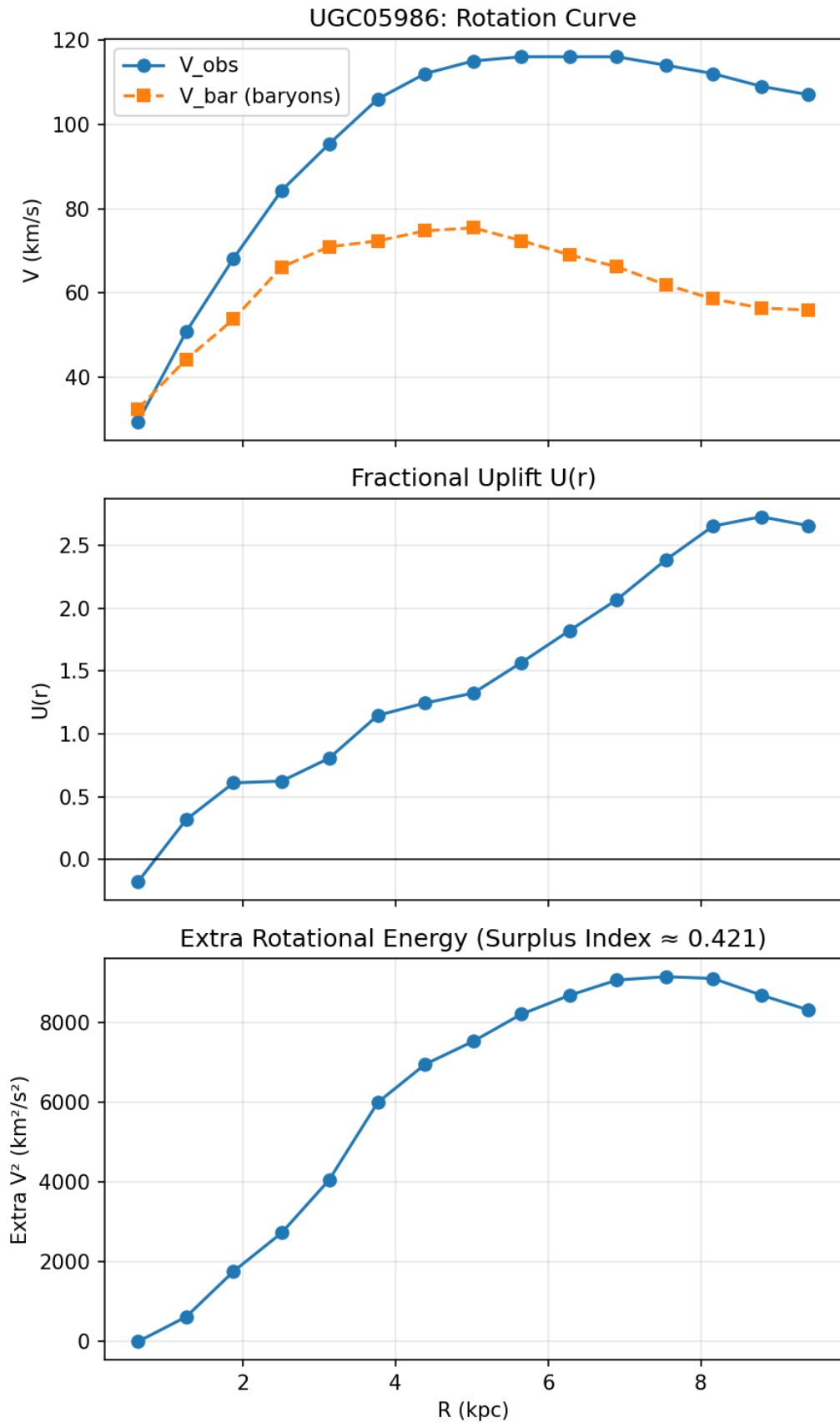


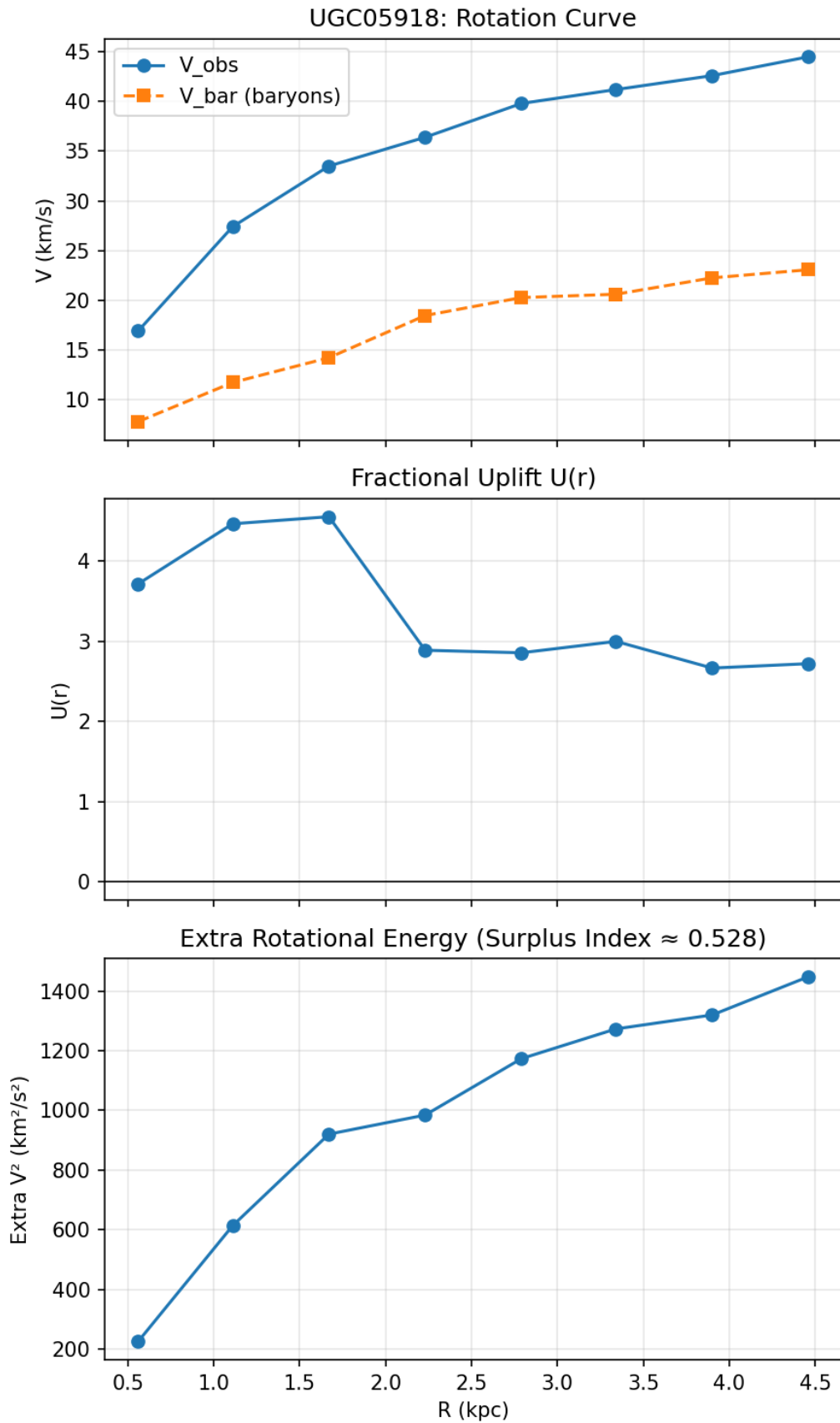


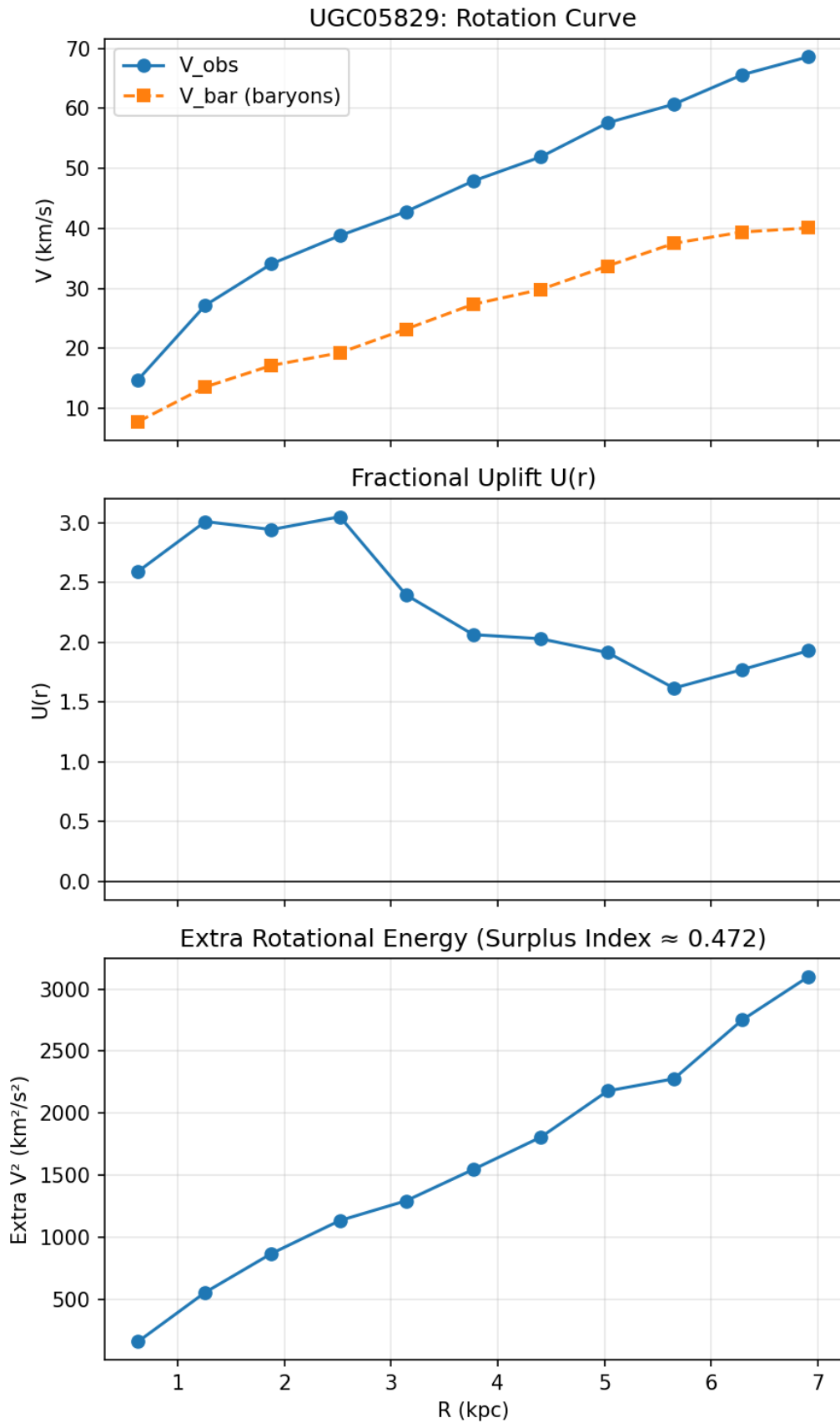


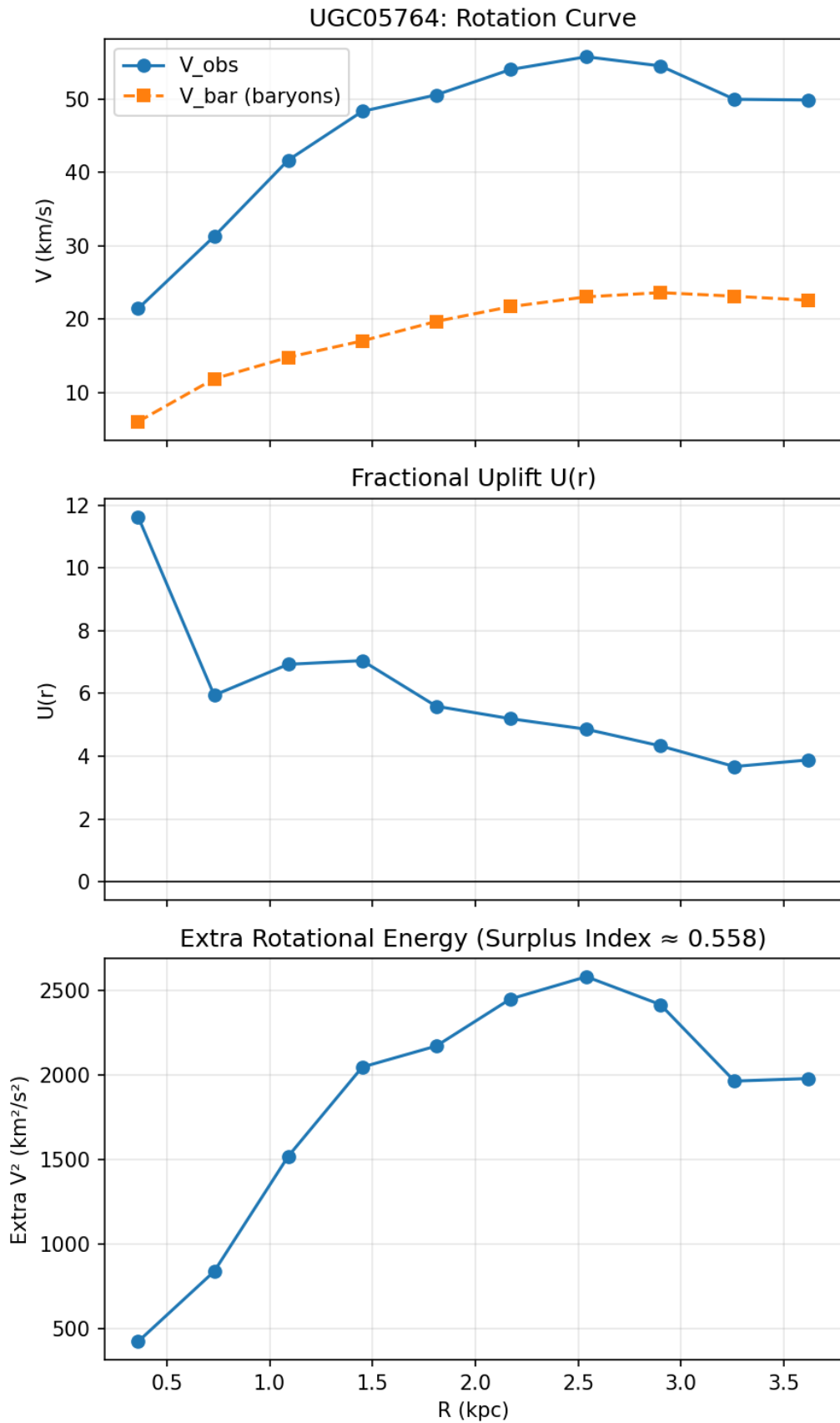


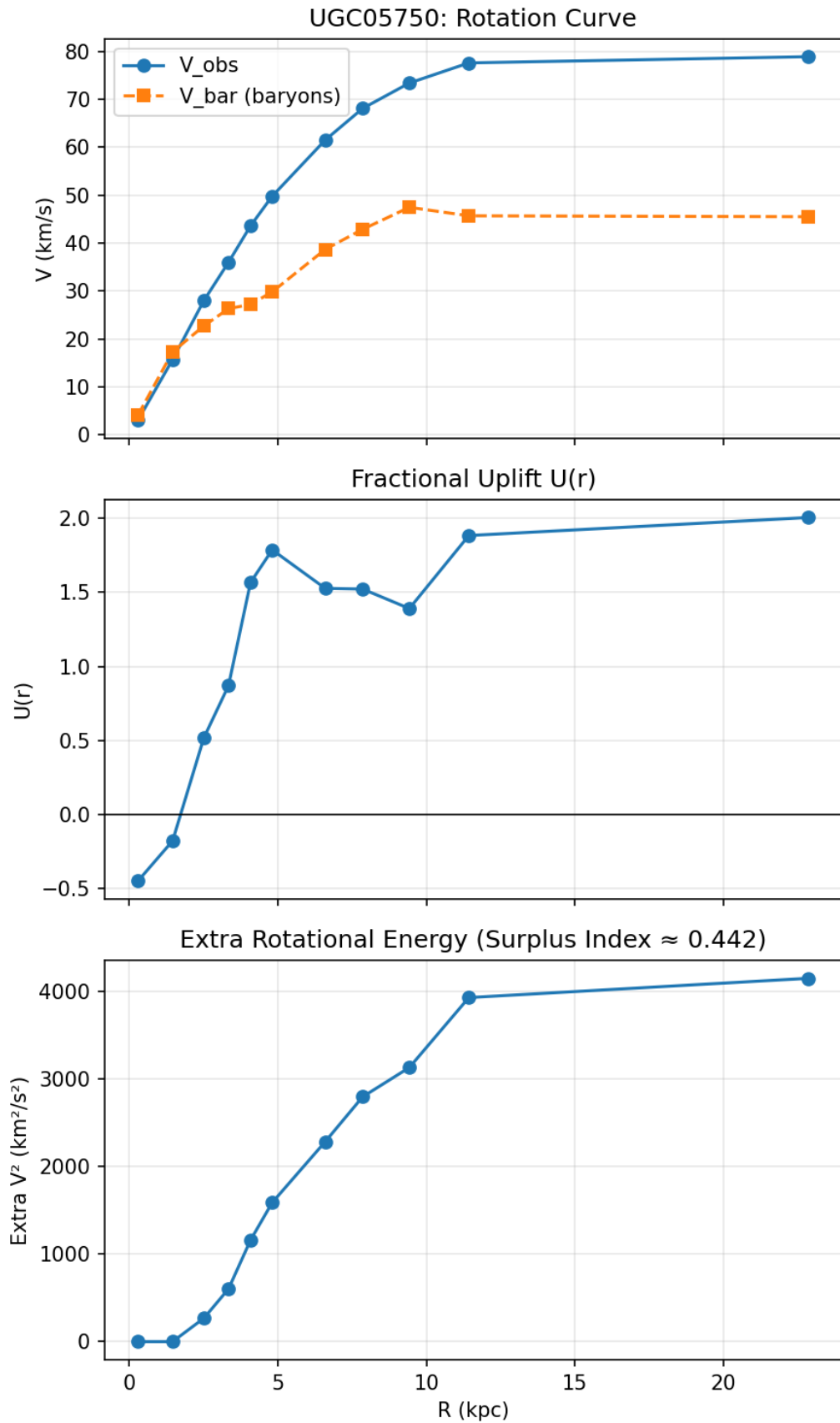


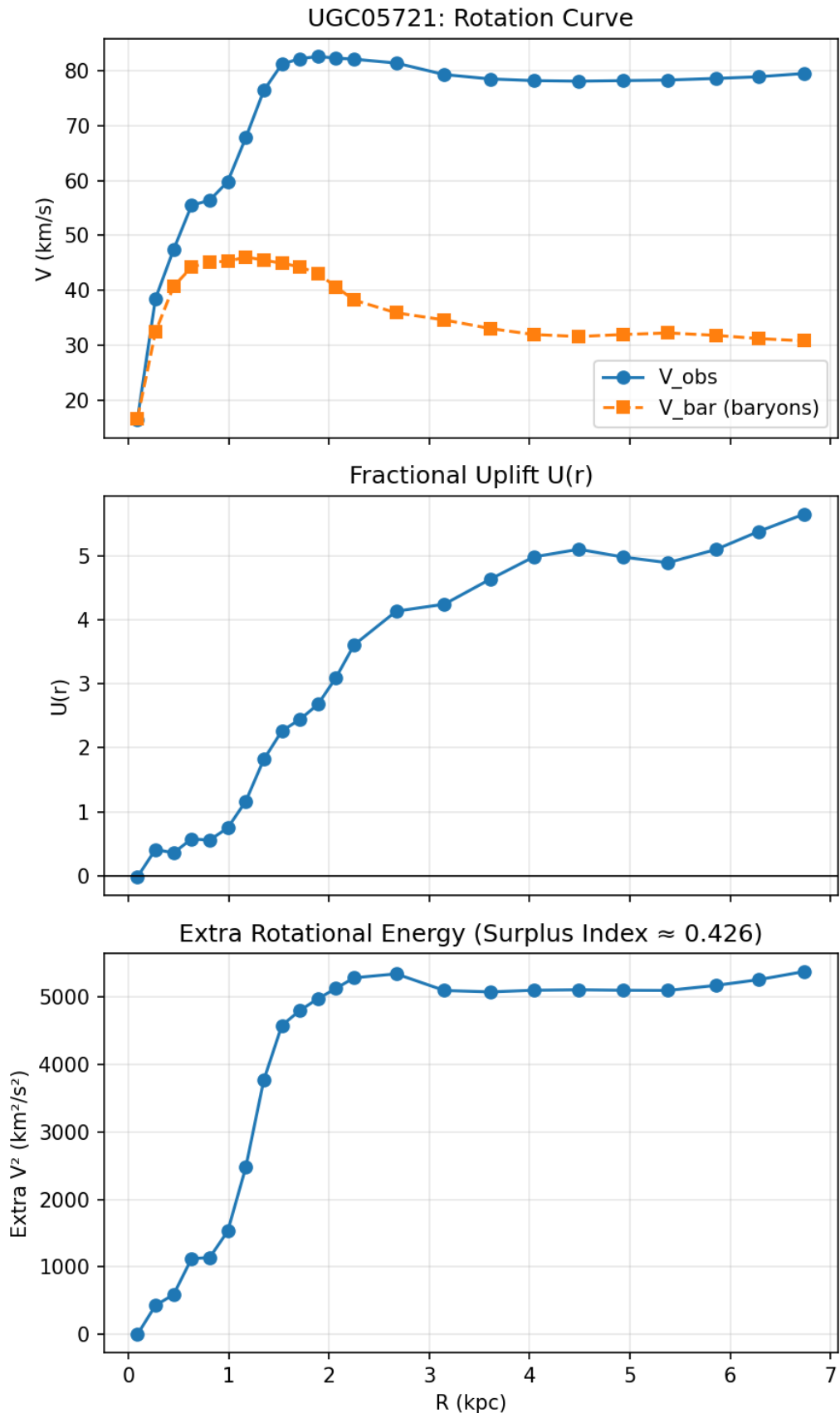


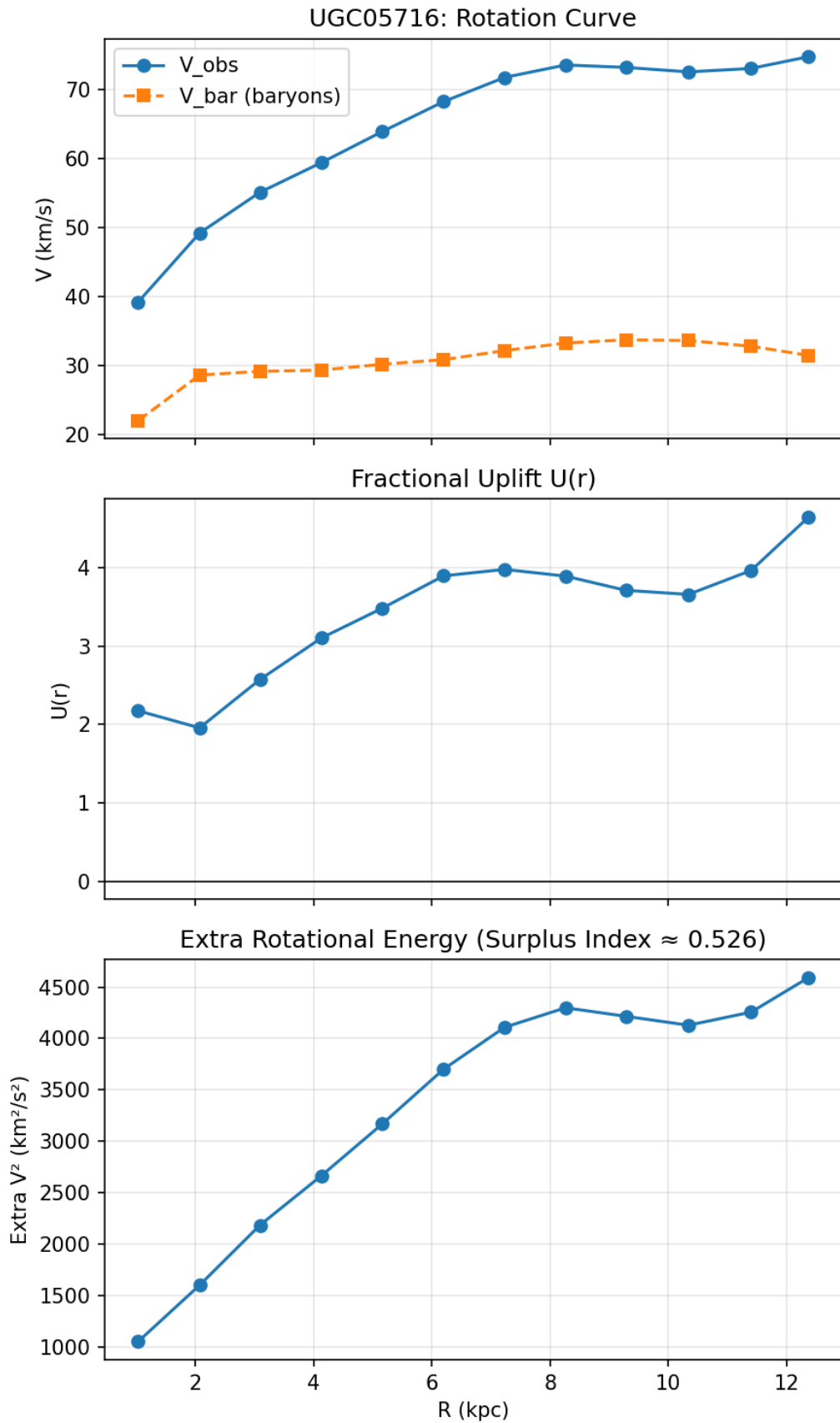


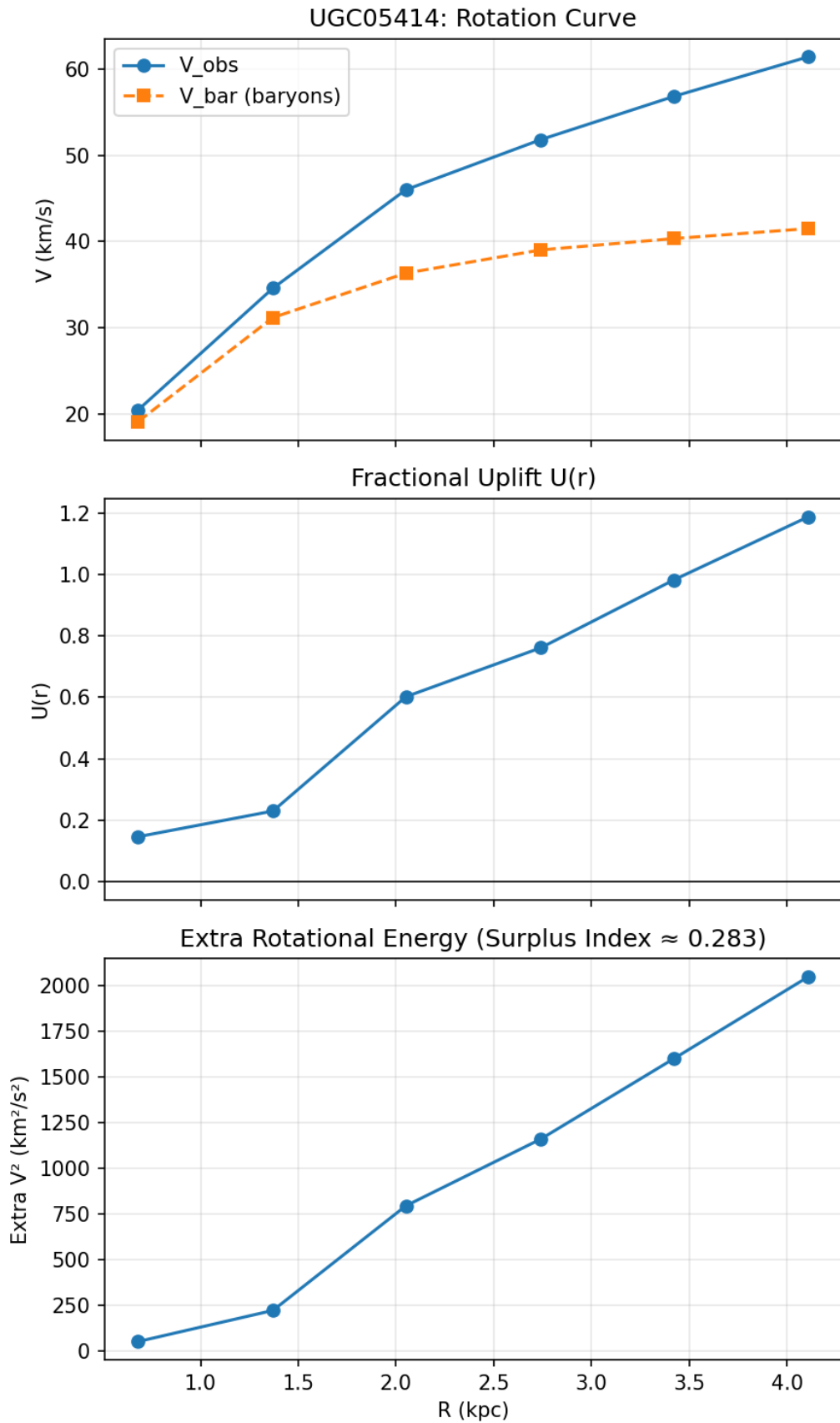




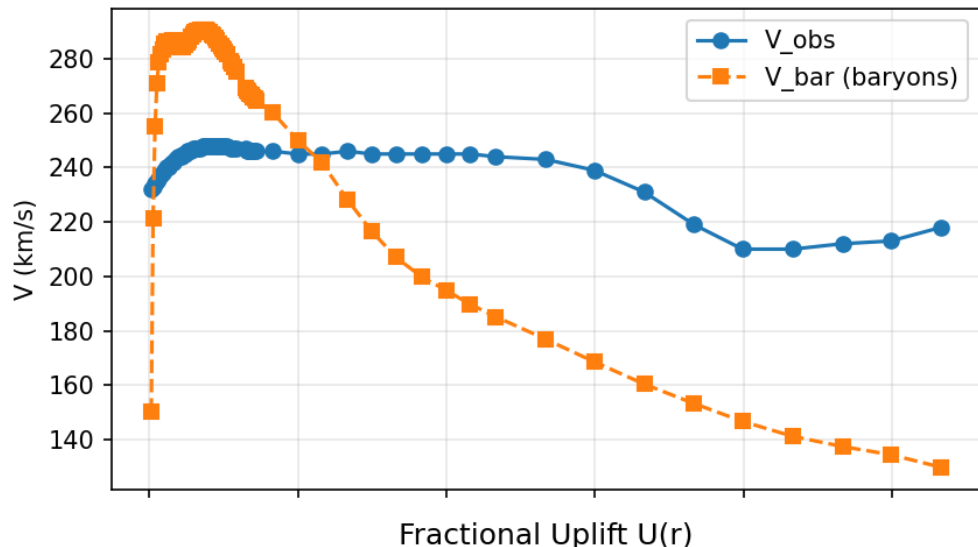
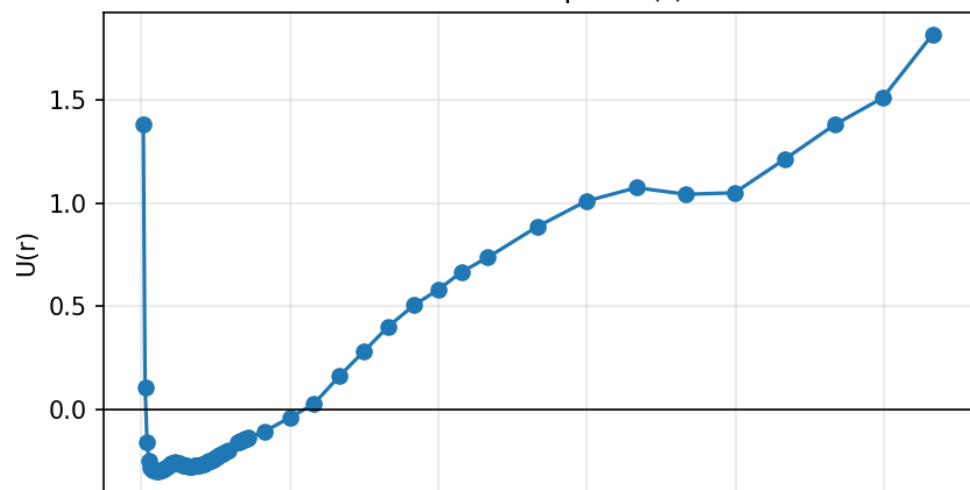
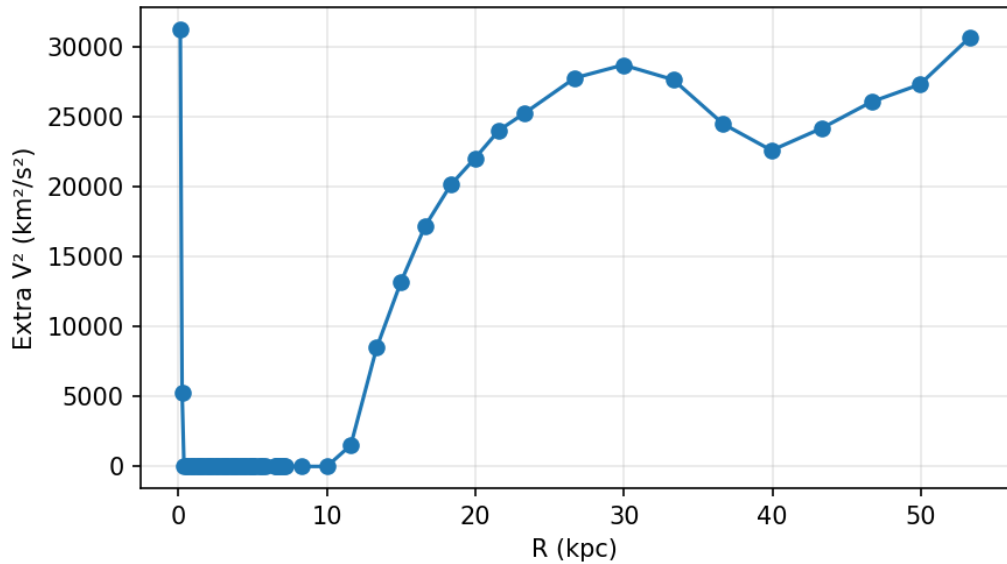


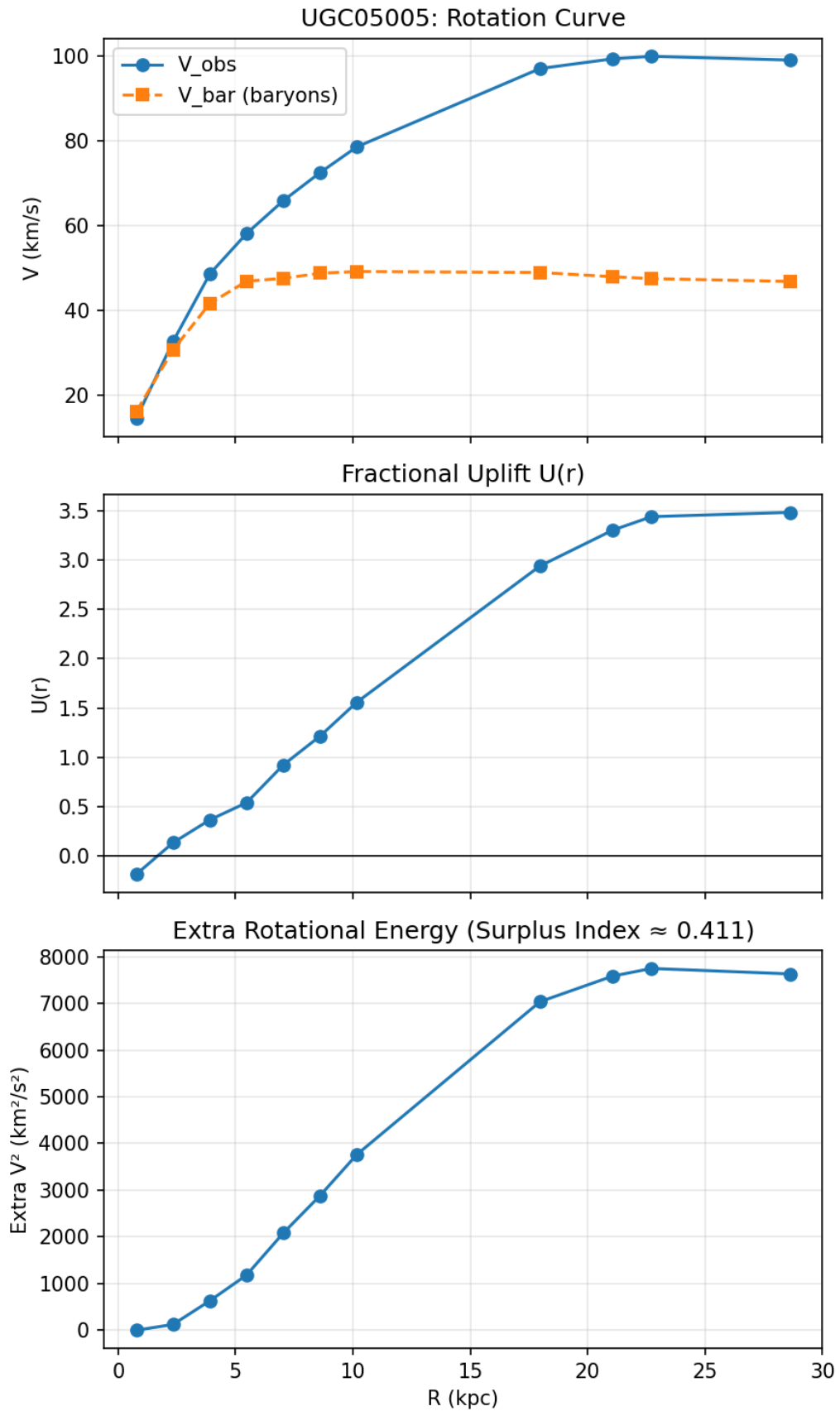




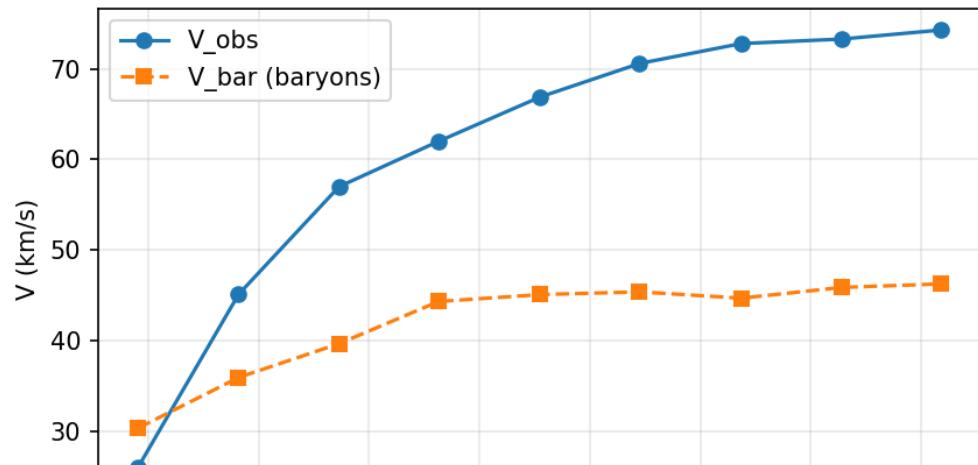
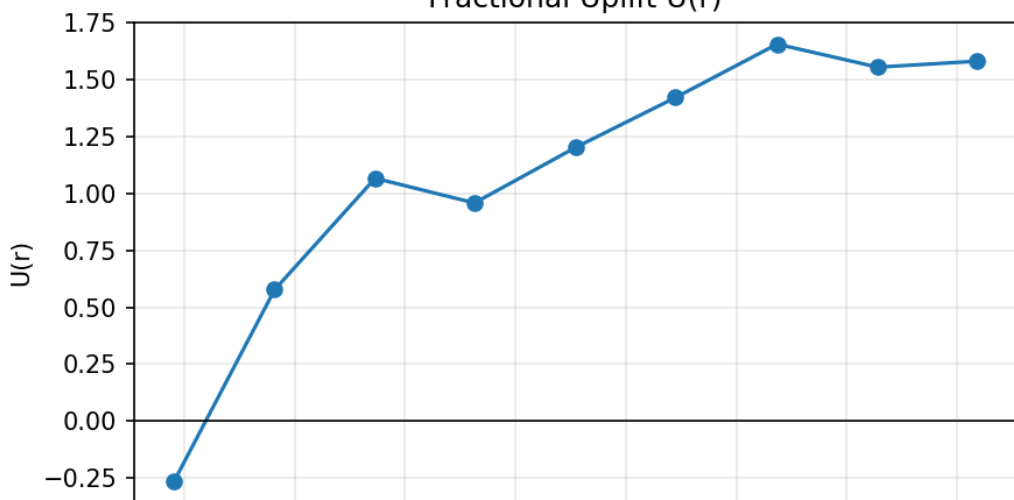
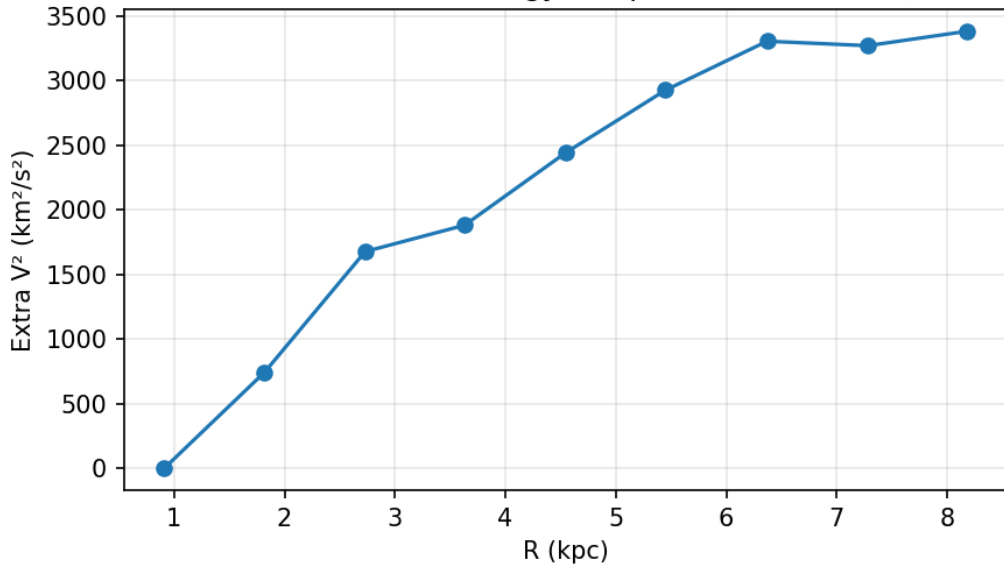


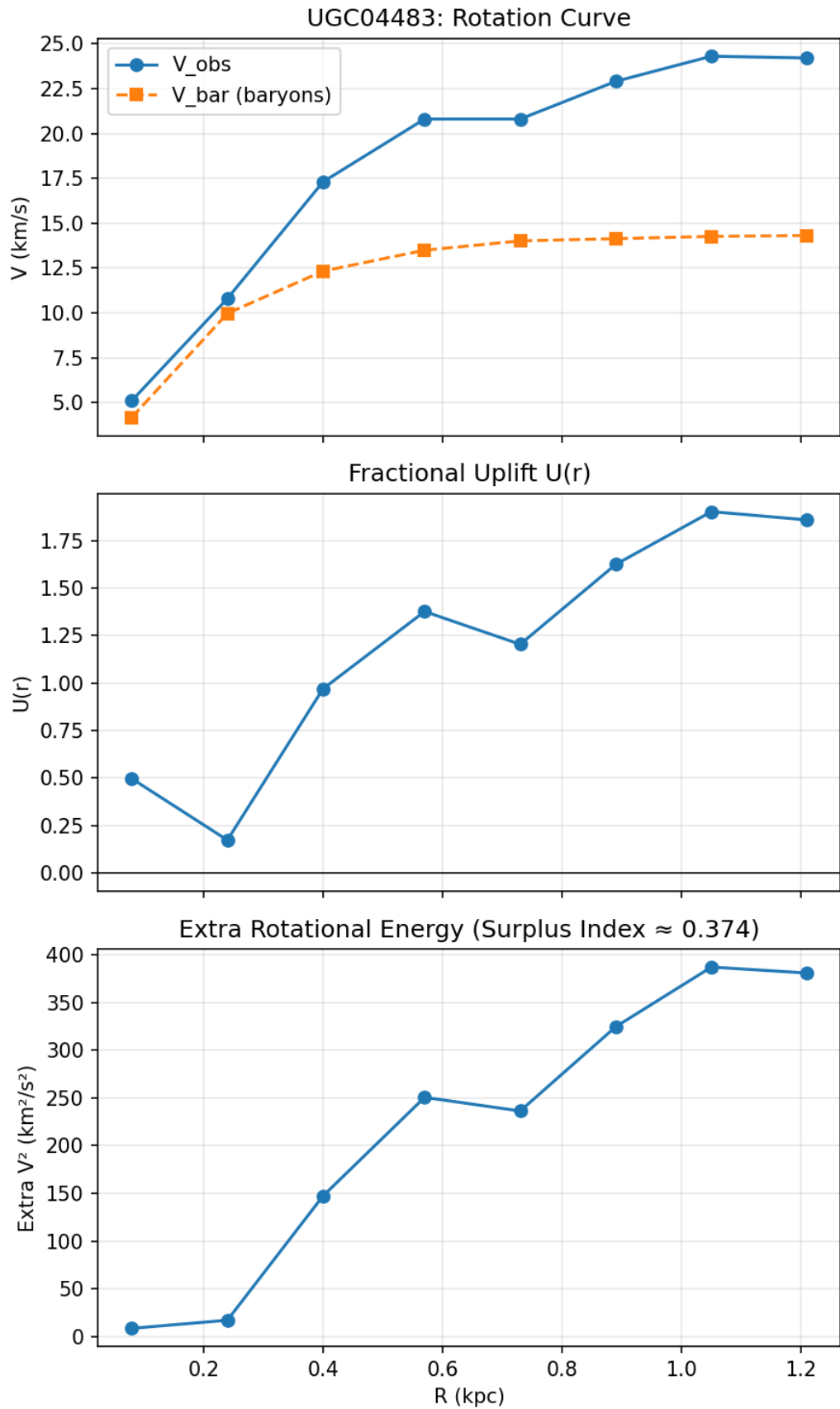
UGC05253: Rotation Curve

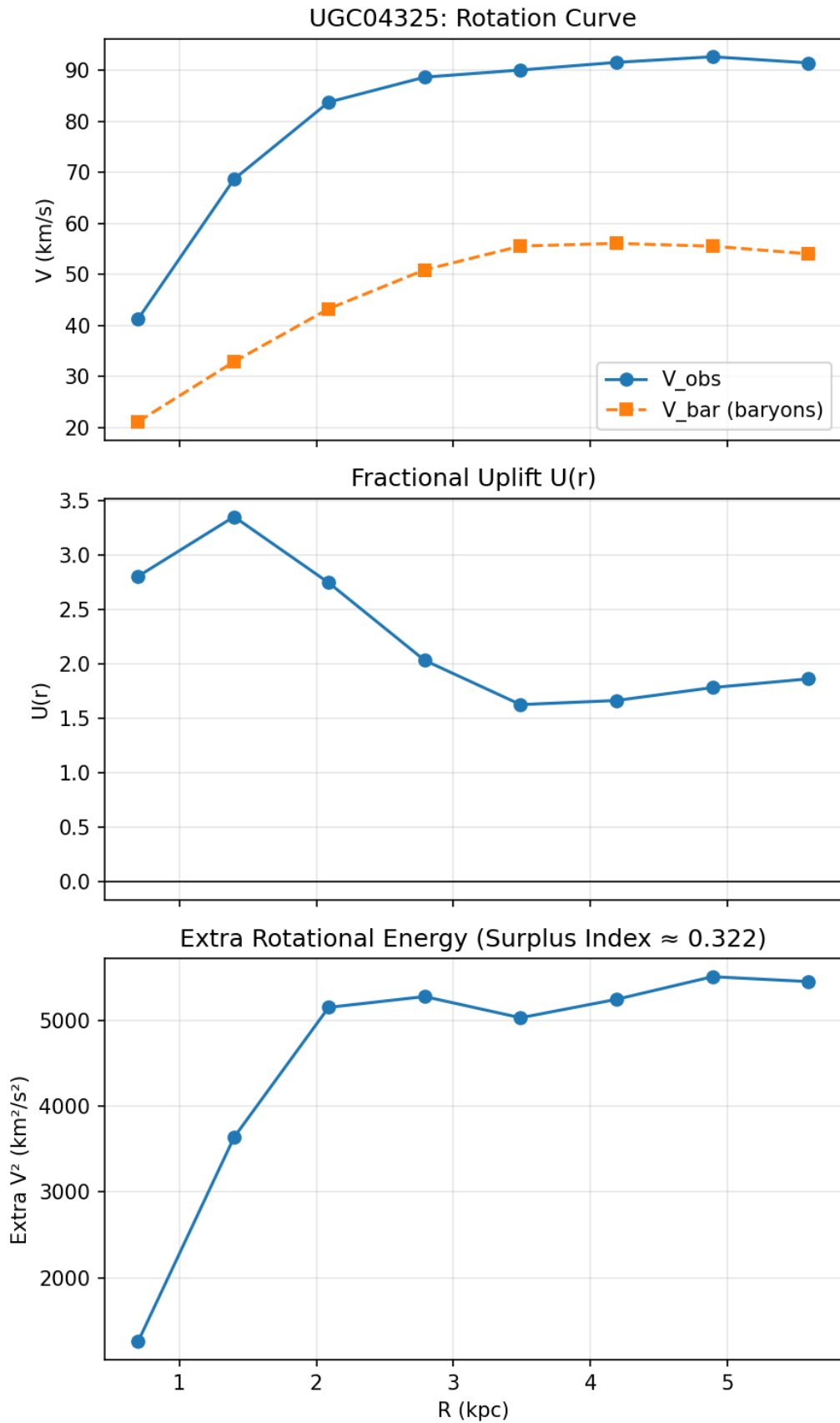
Fractional Uplift $U(r)$ Extra Rotational Energy (Surplus Index ≈ 0.242)

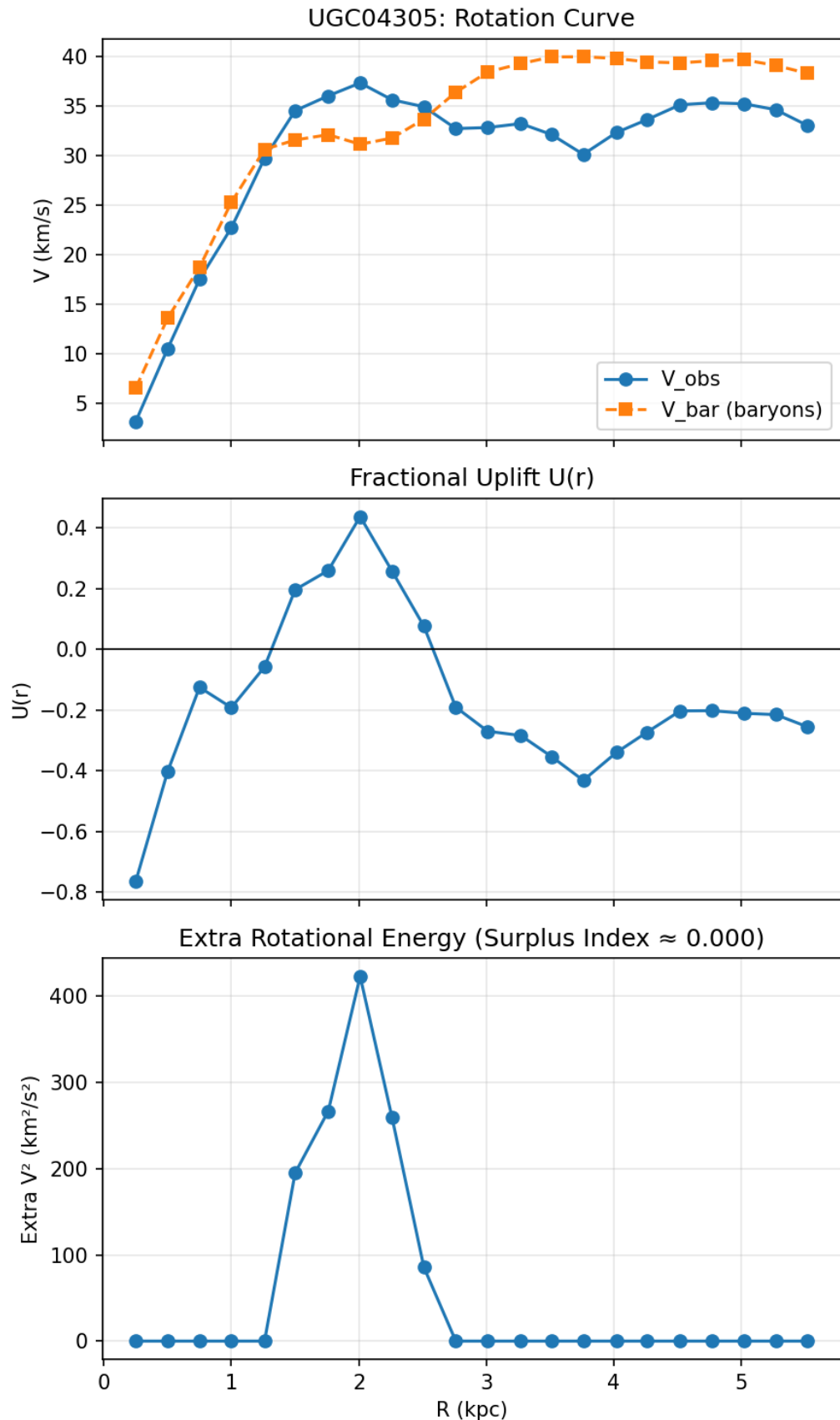


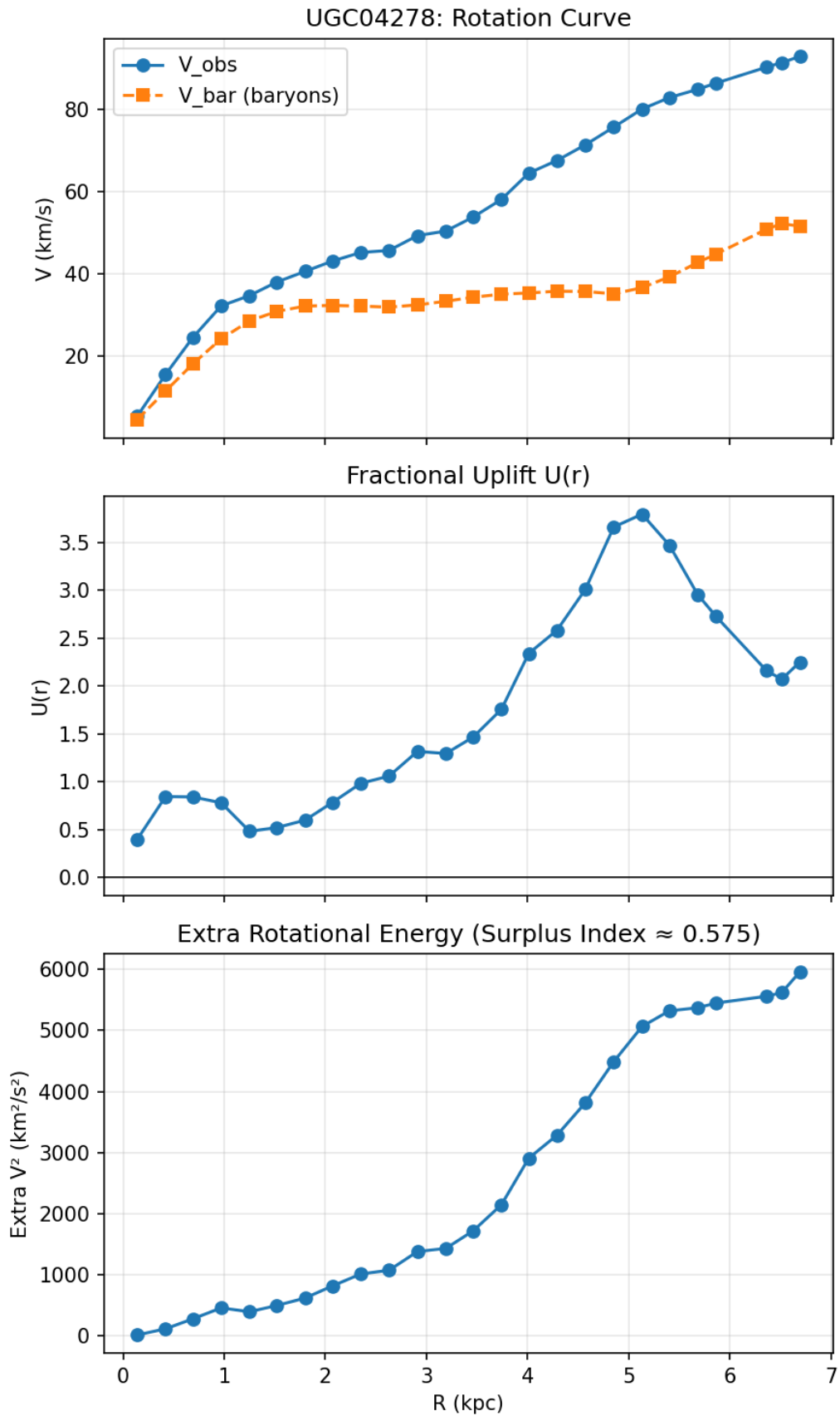
UGC04499: Rotation Curve

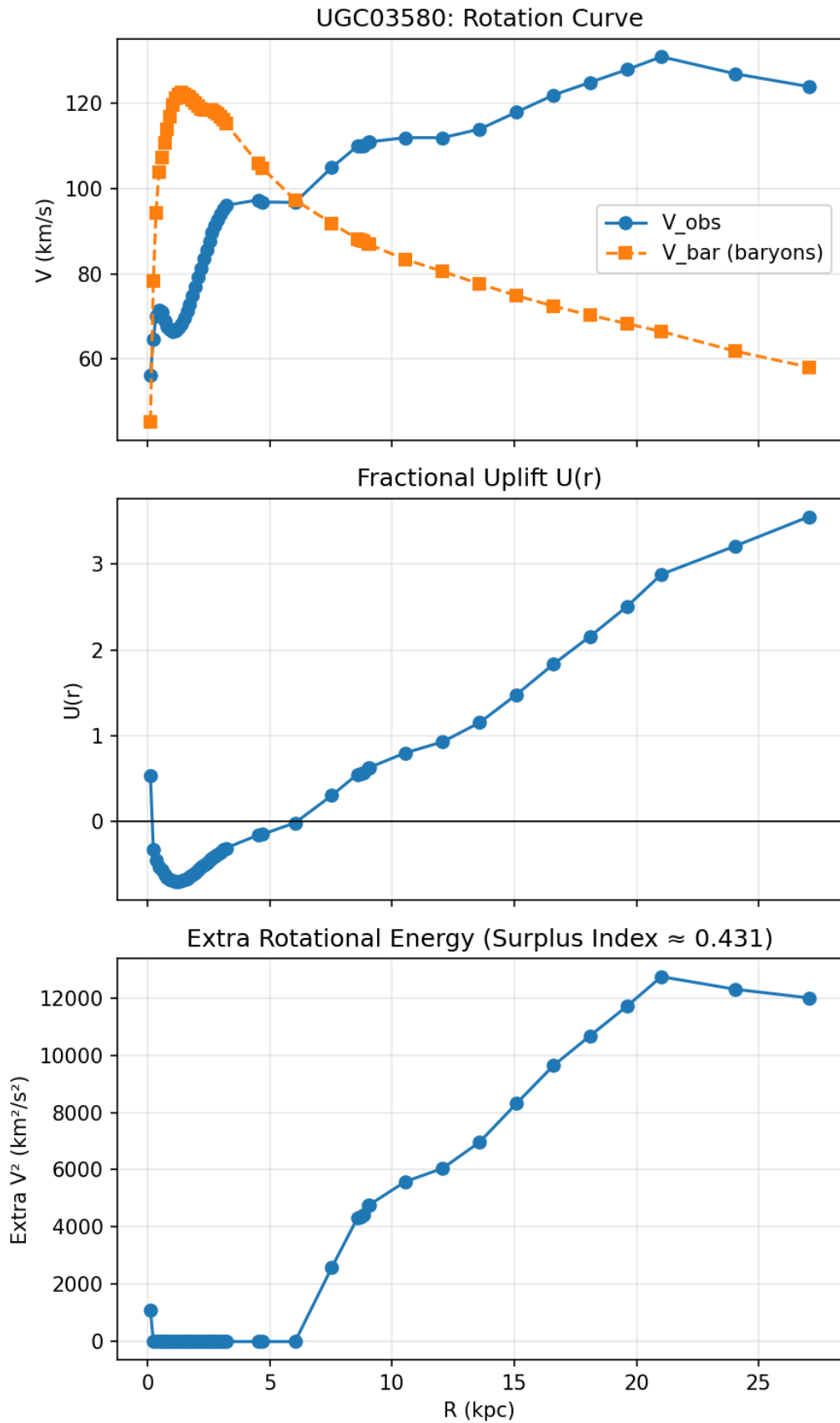
Fractional Uplift $U(r)$ Extra Rotational Energy (Surplus Index ≈ 0.383)

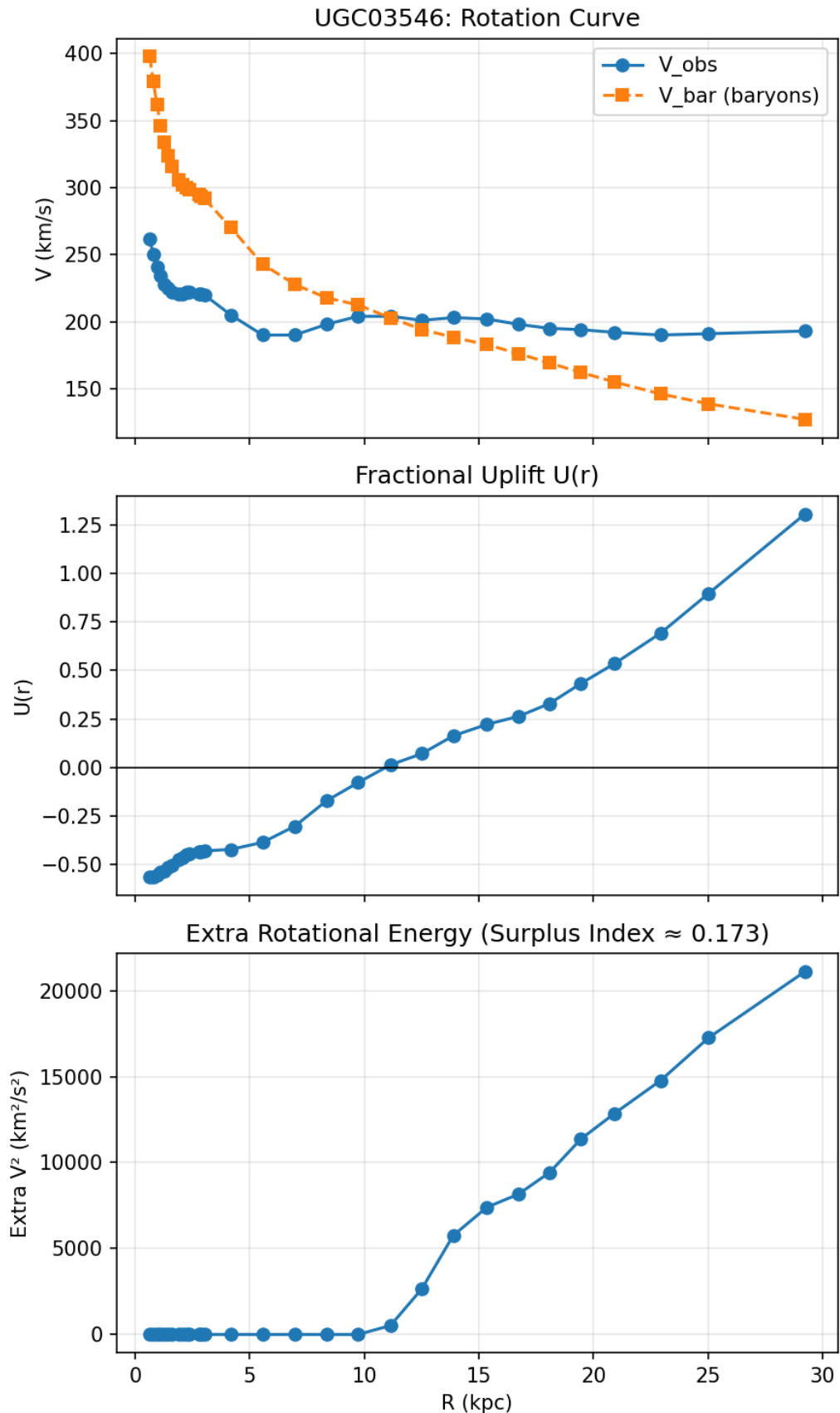


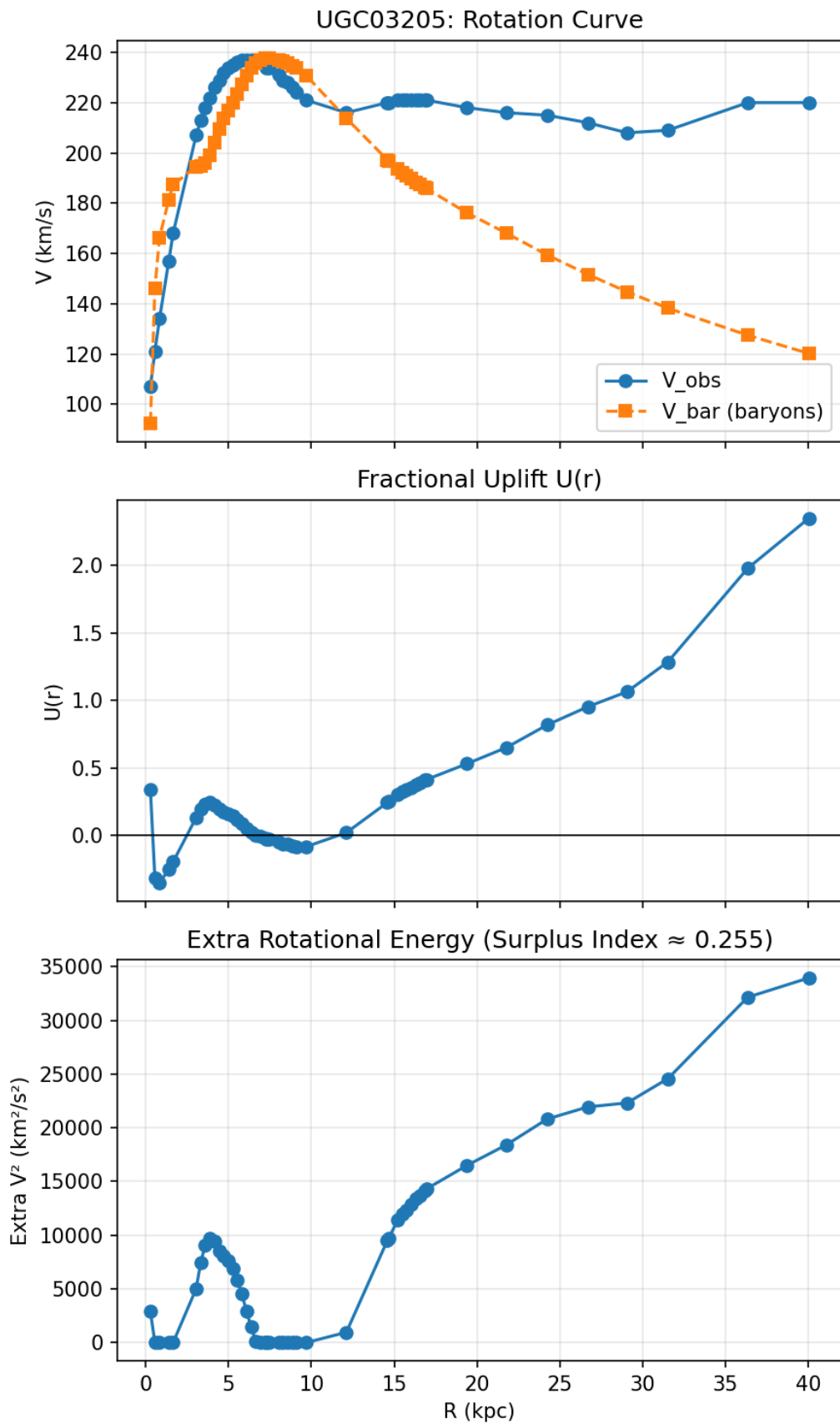


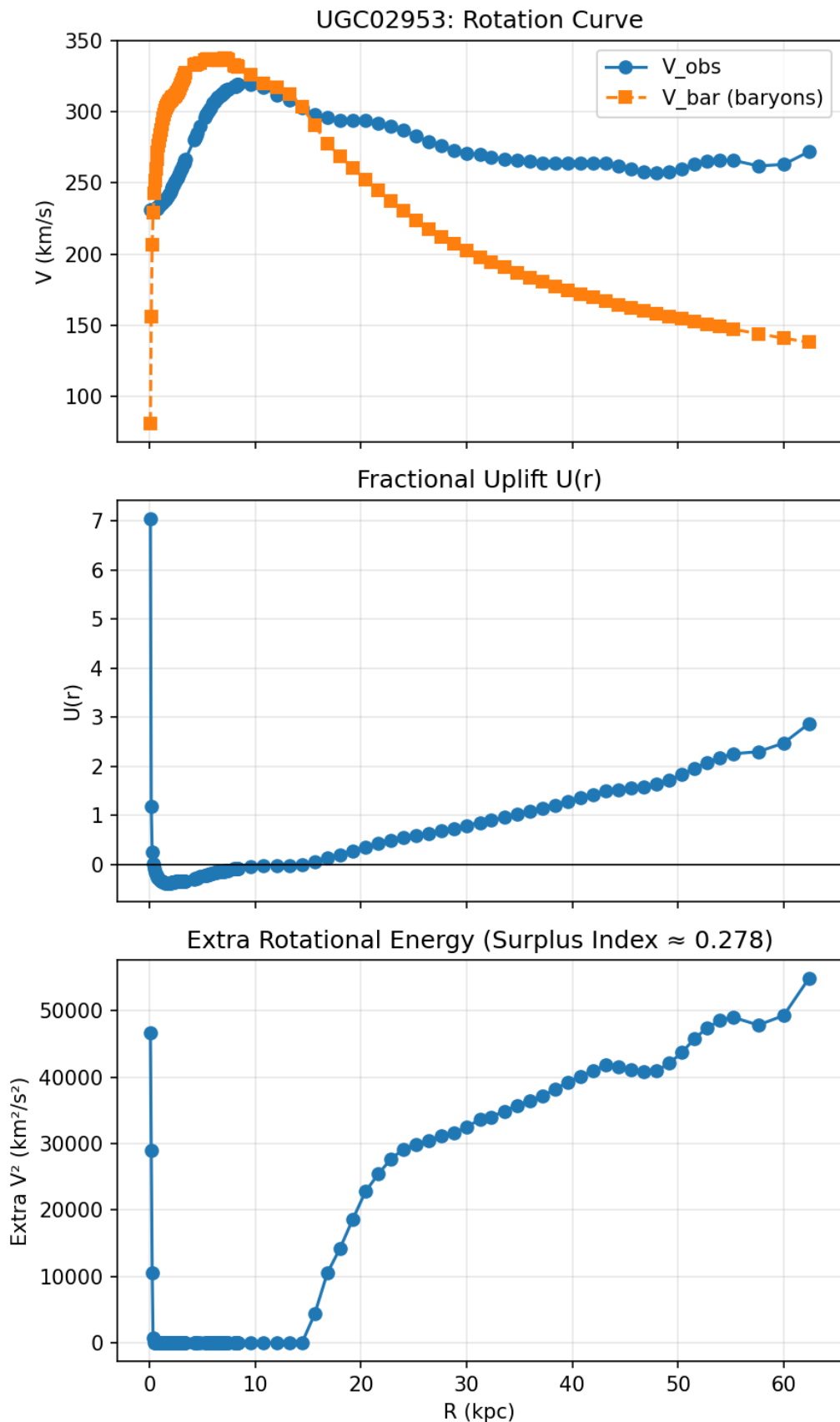


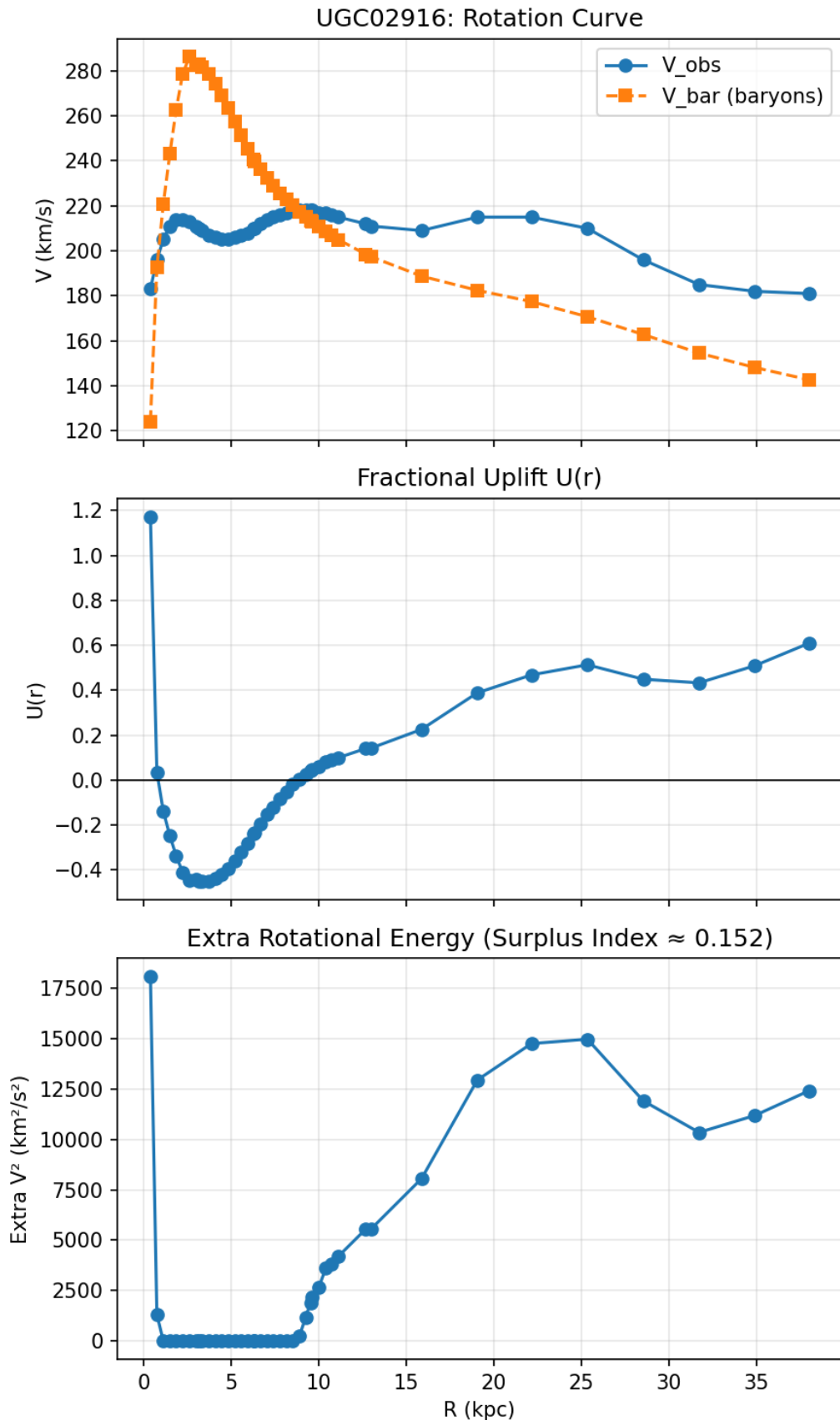


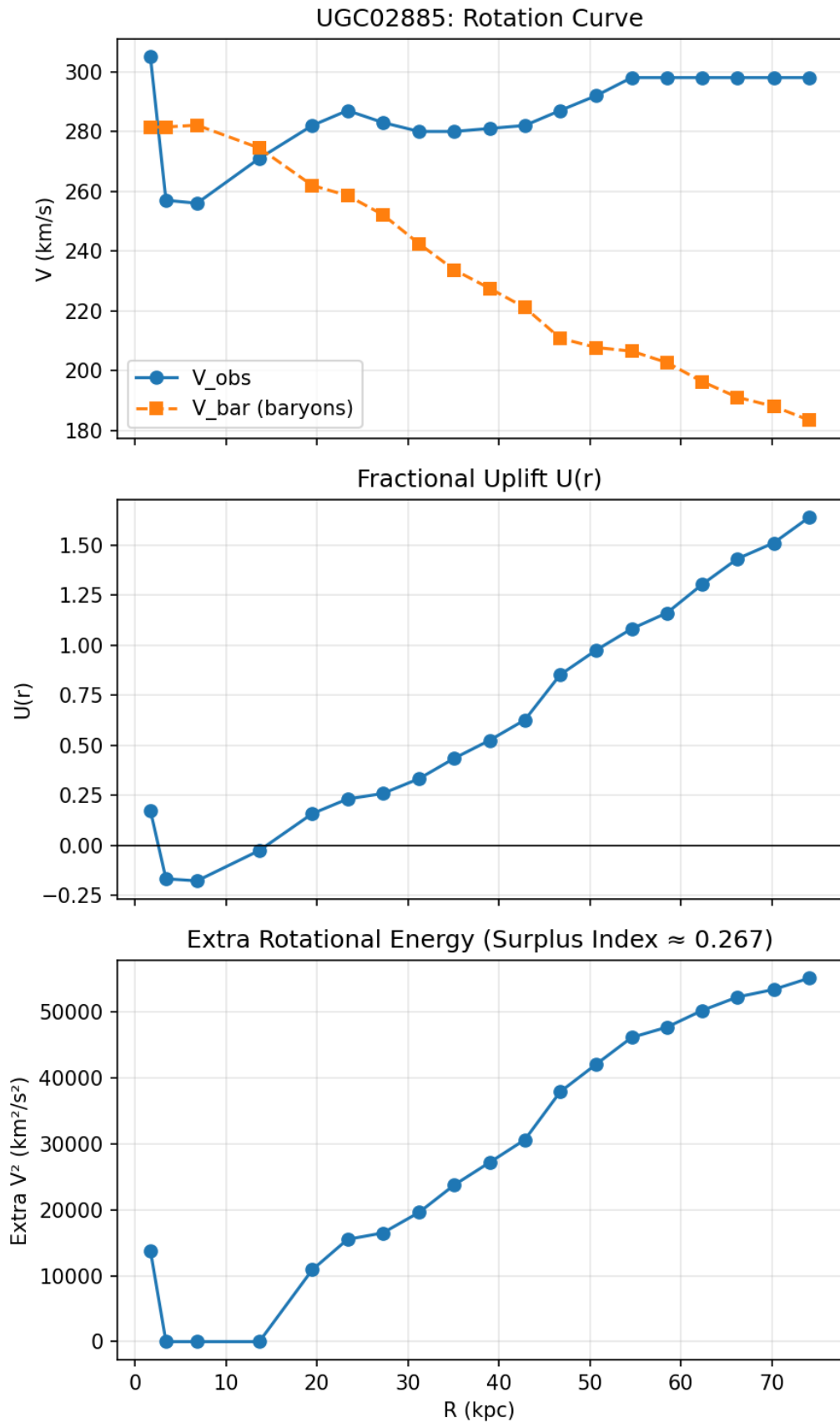


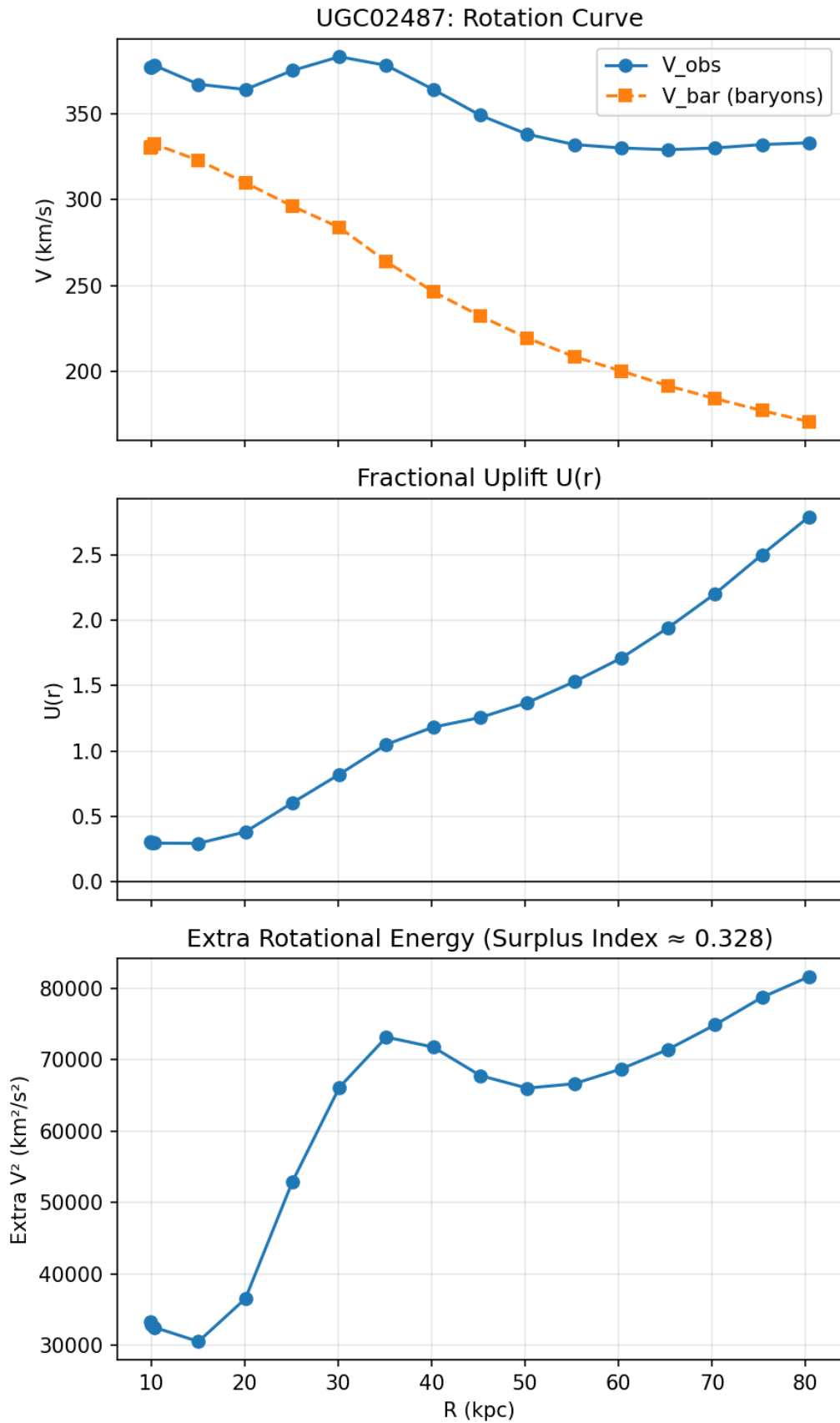


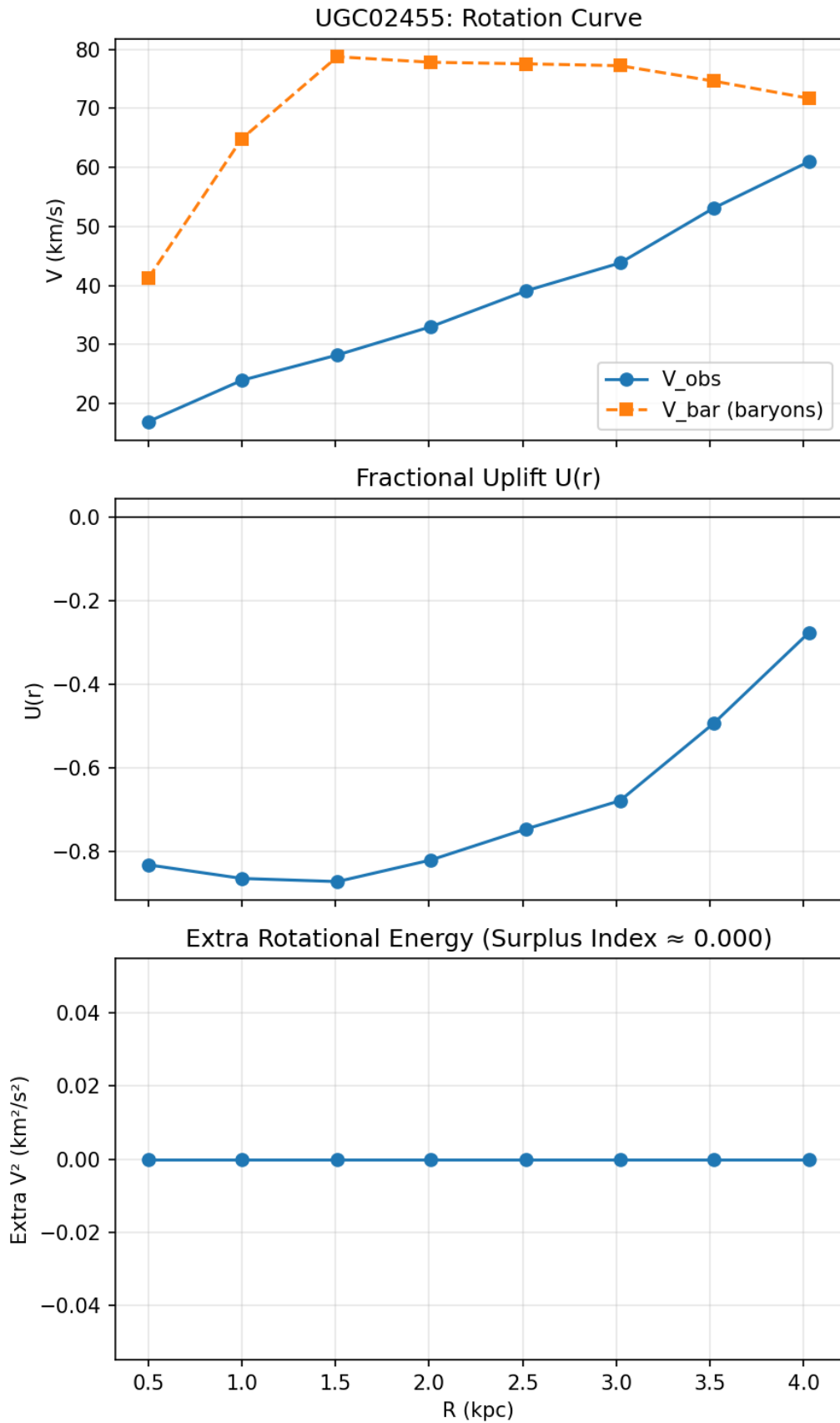


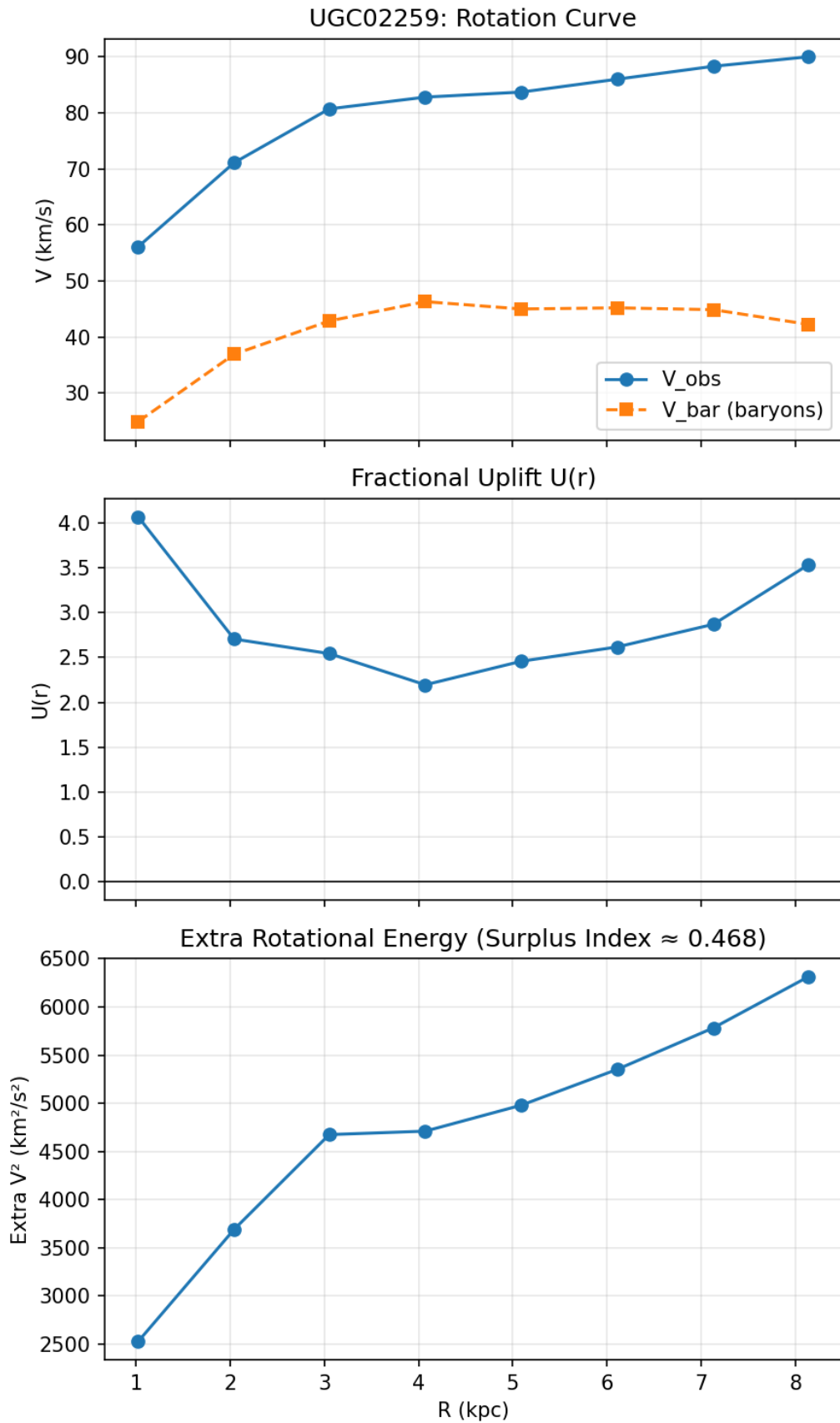


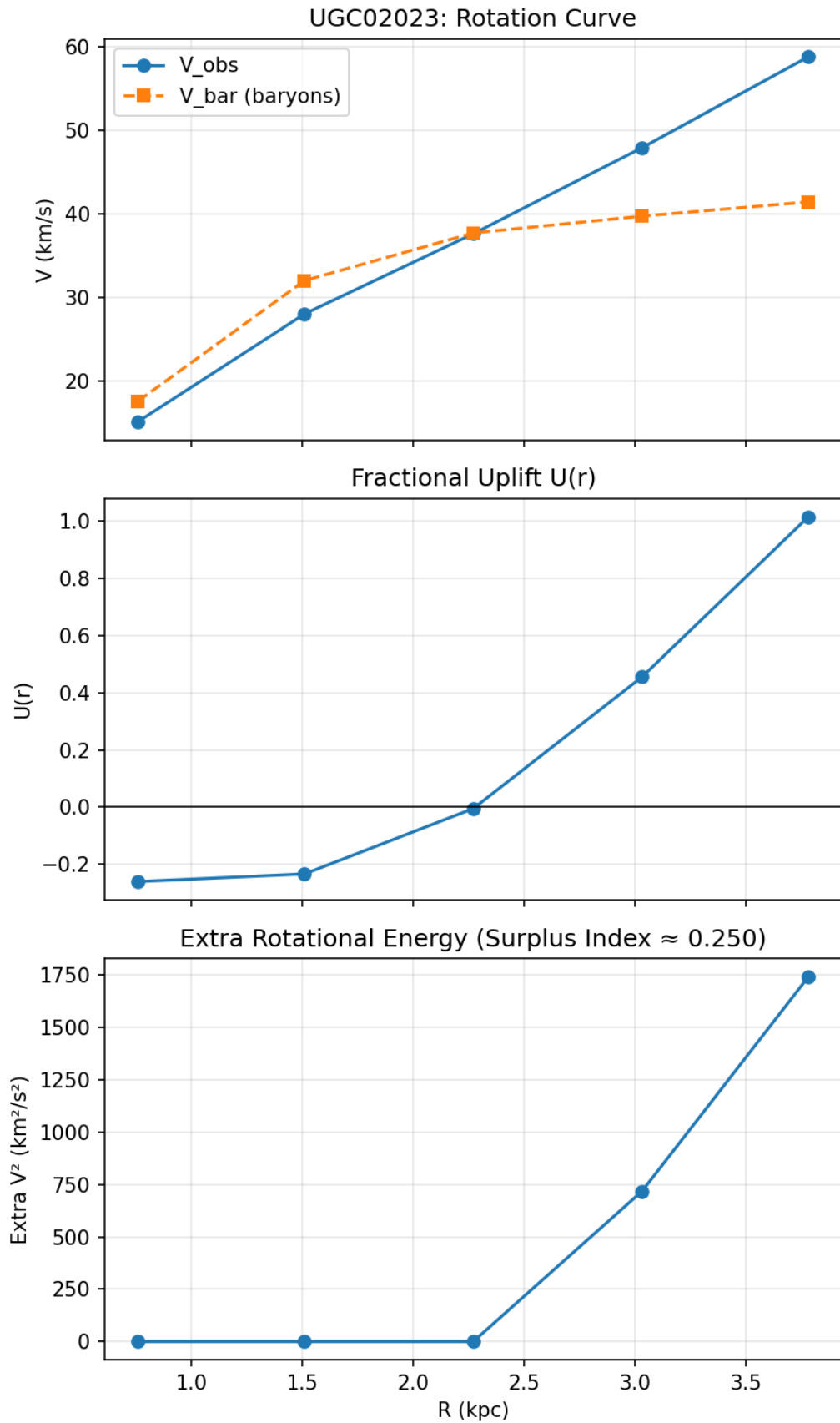


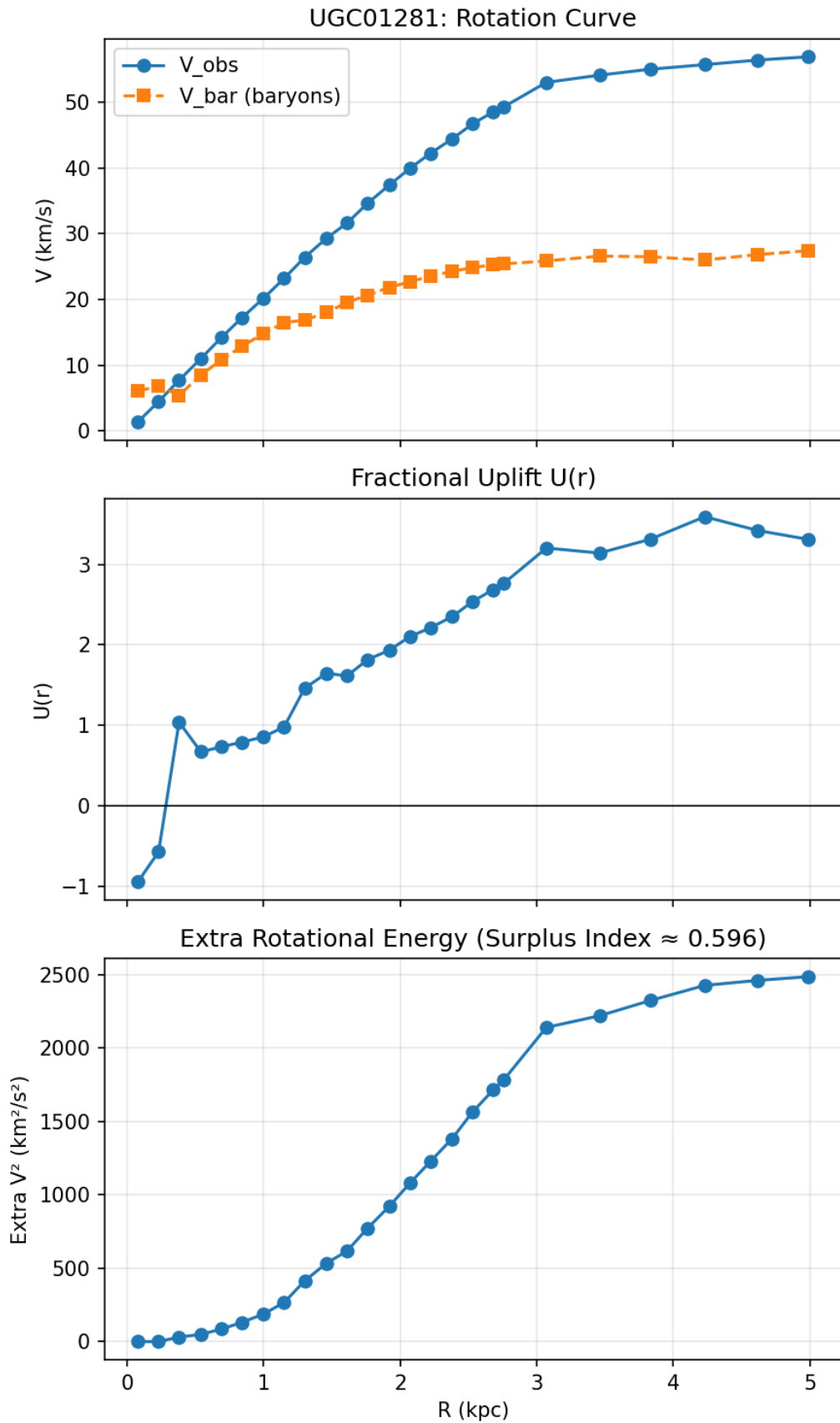


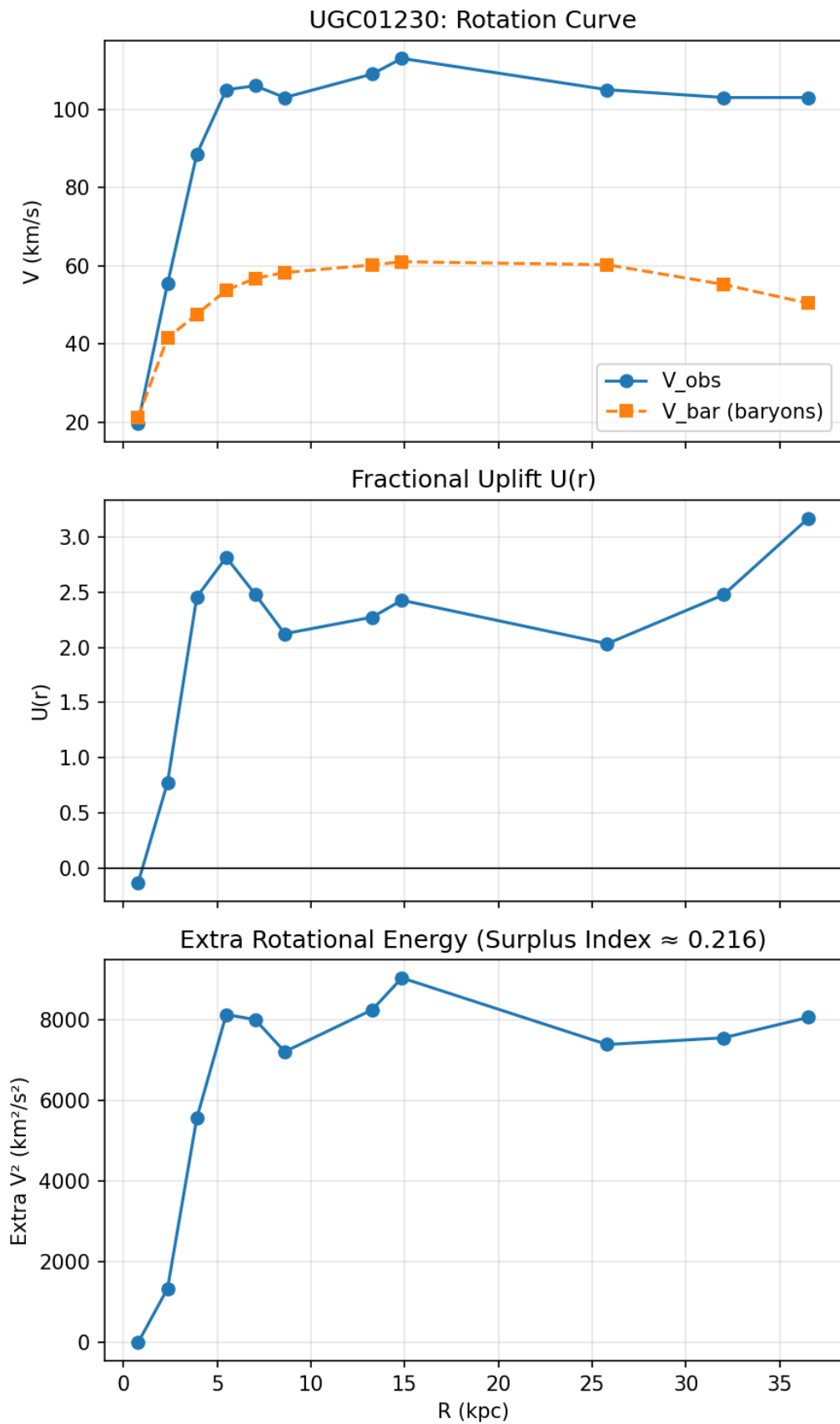


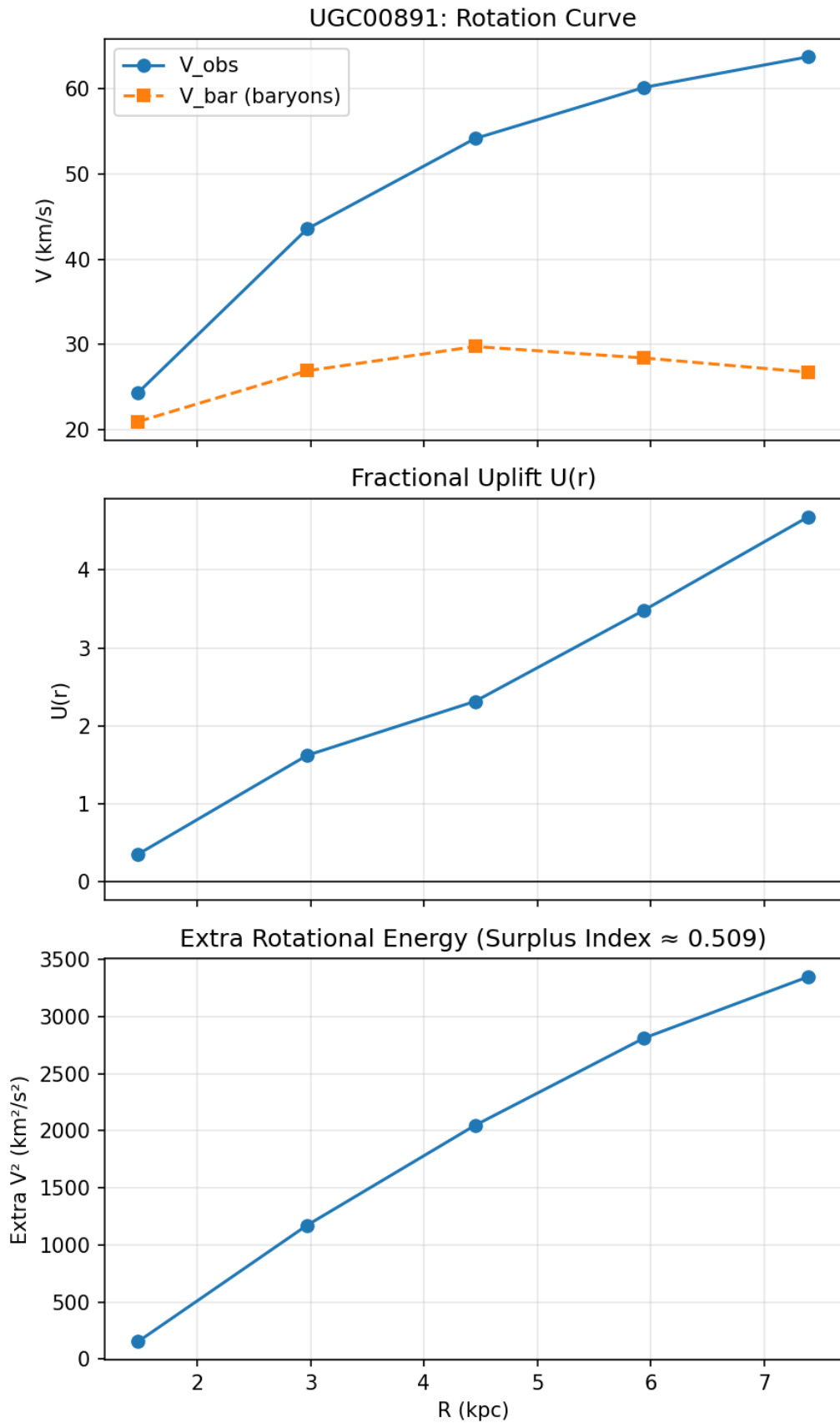


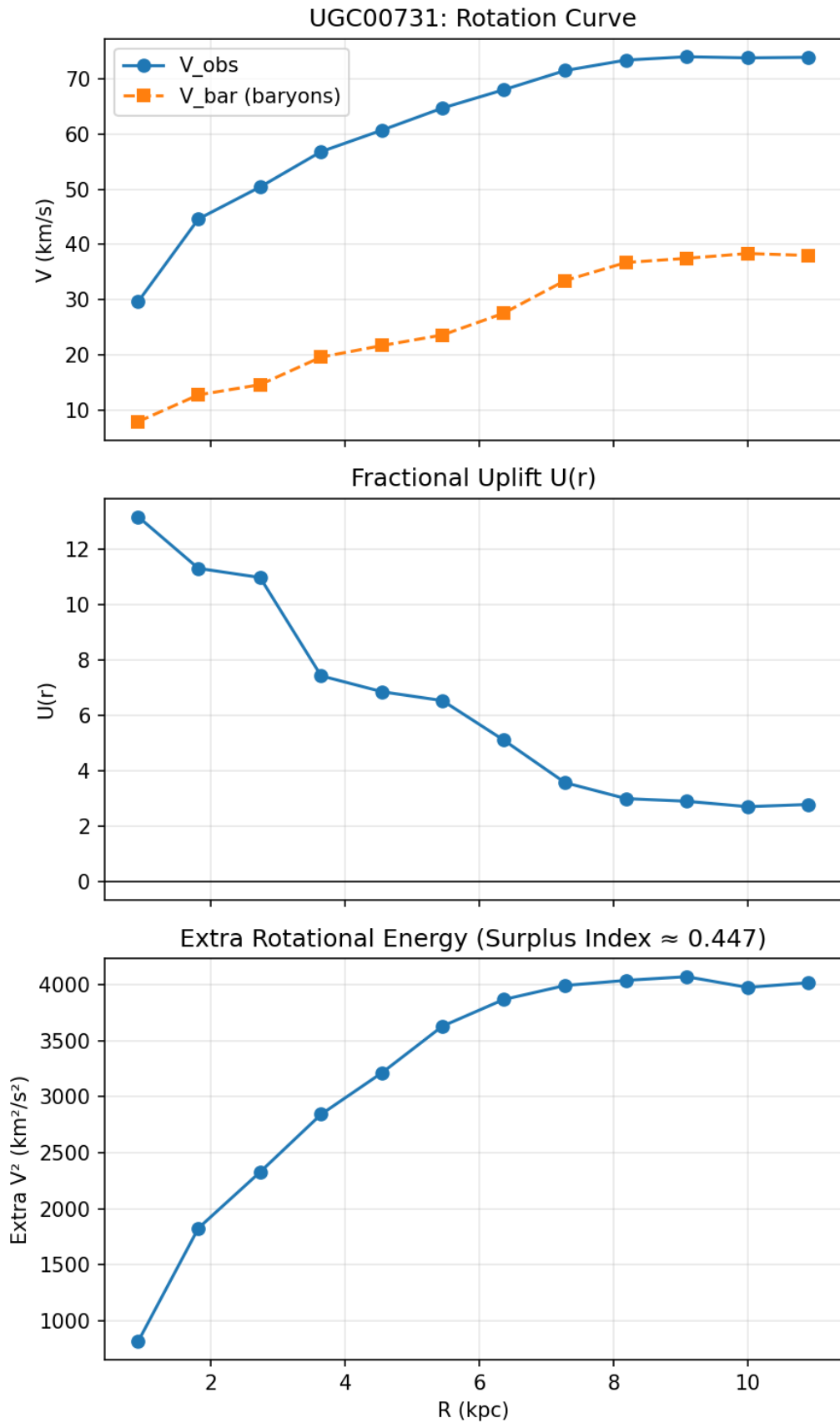


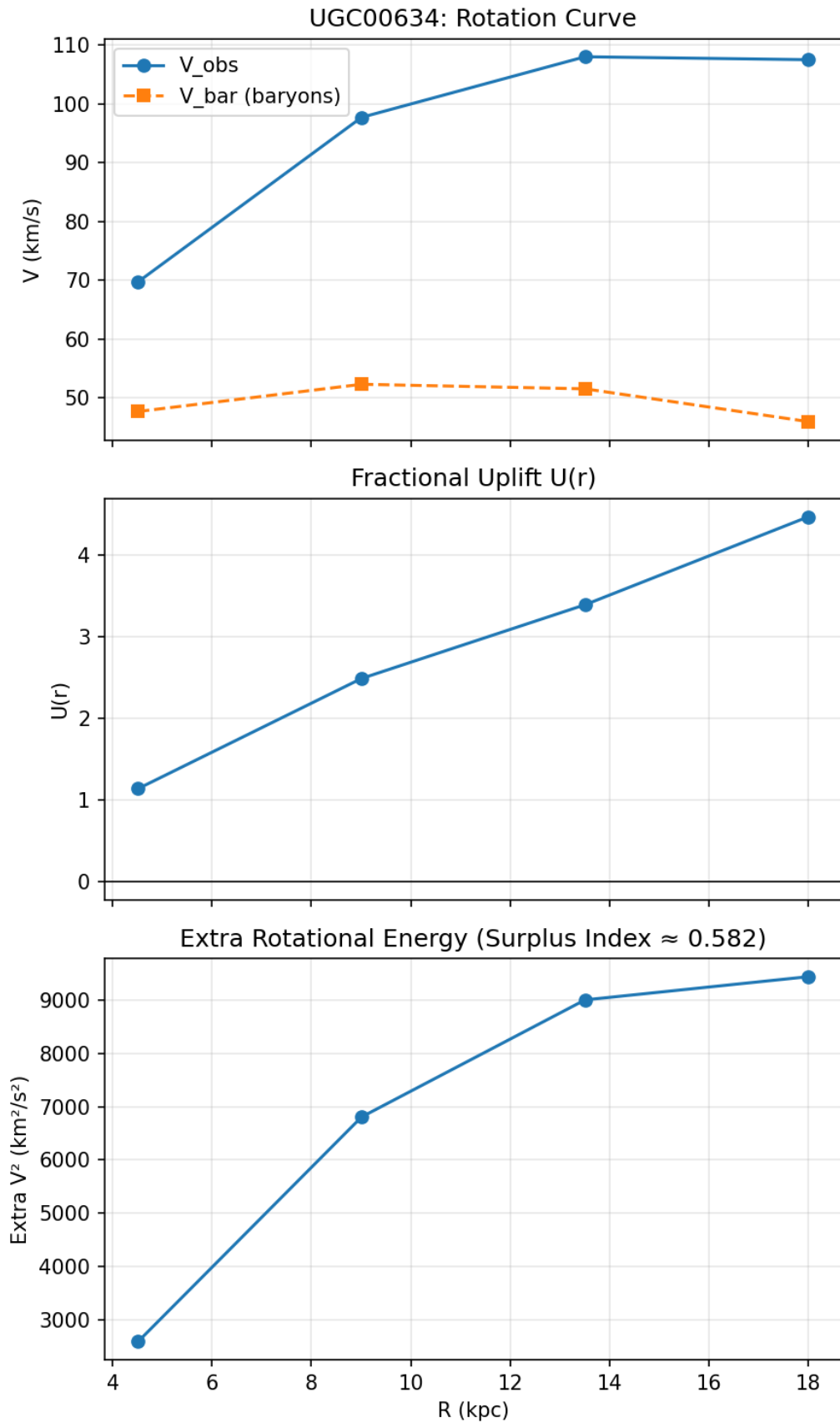


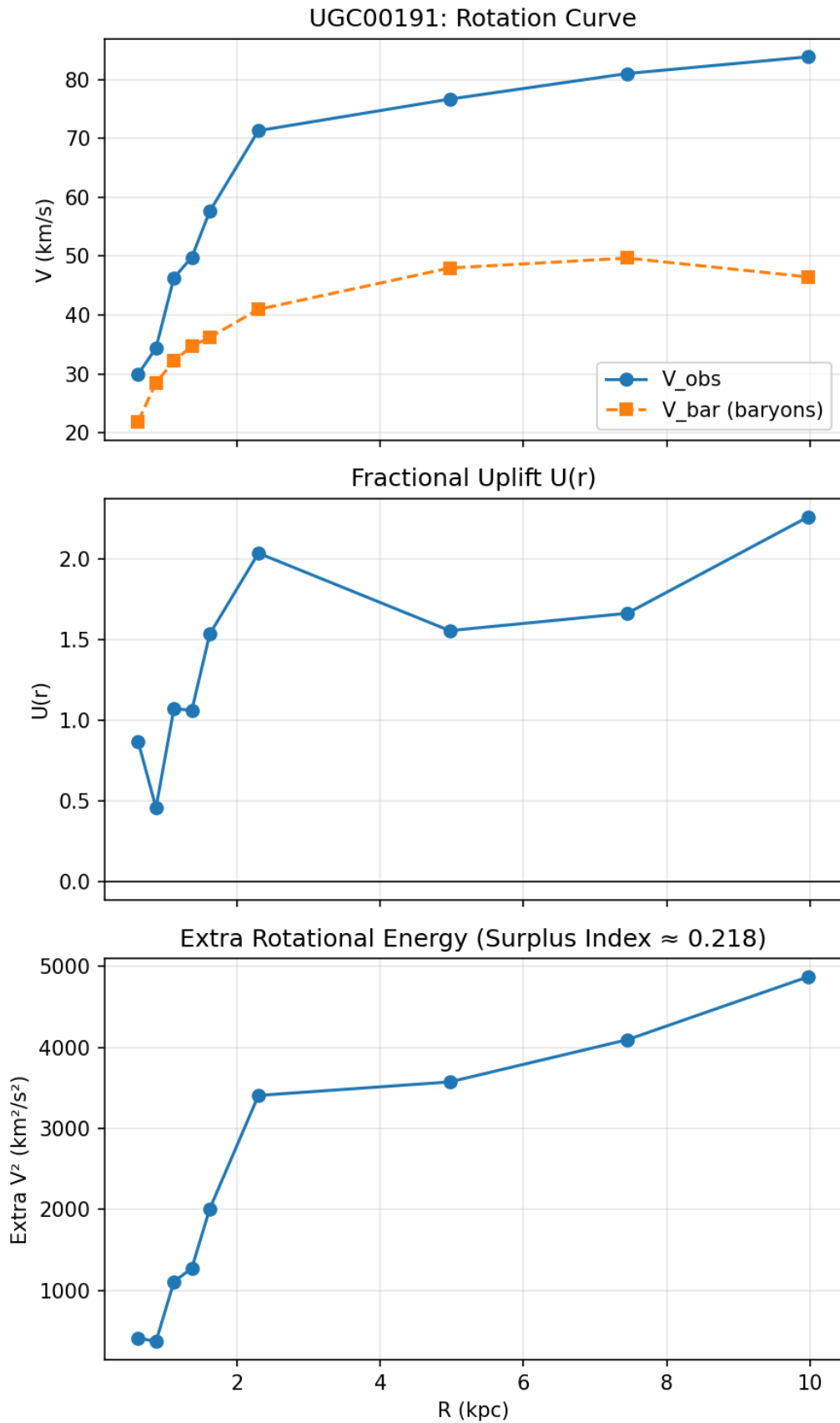


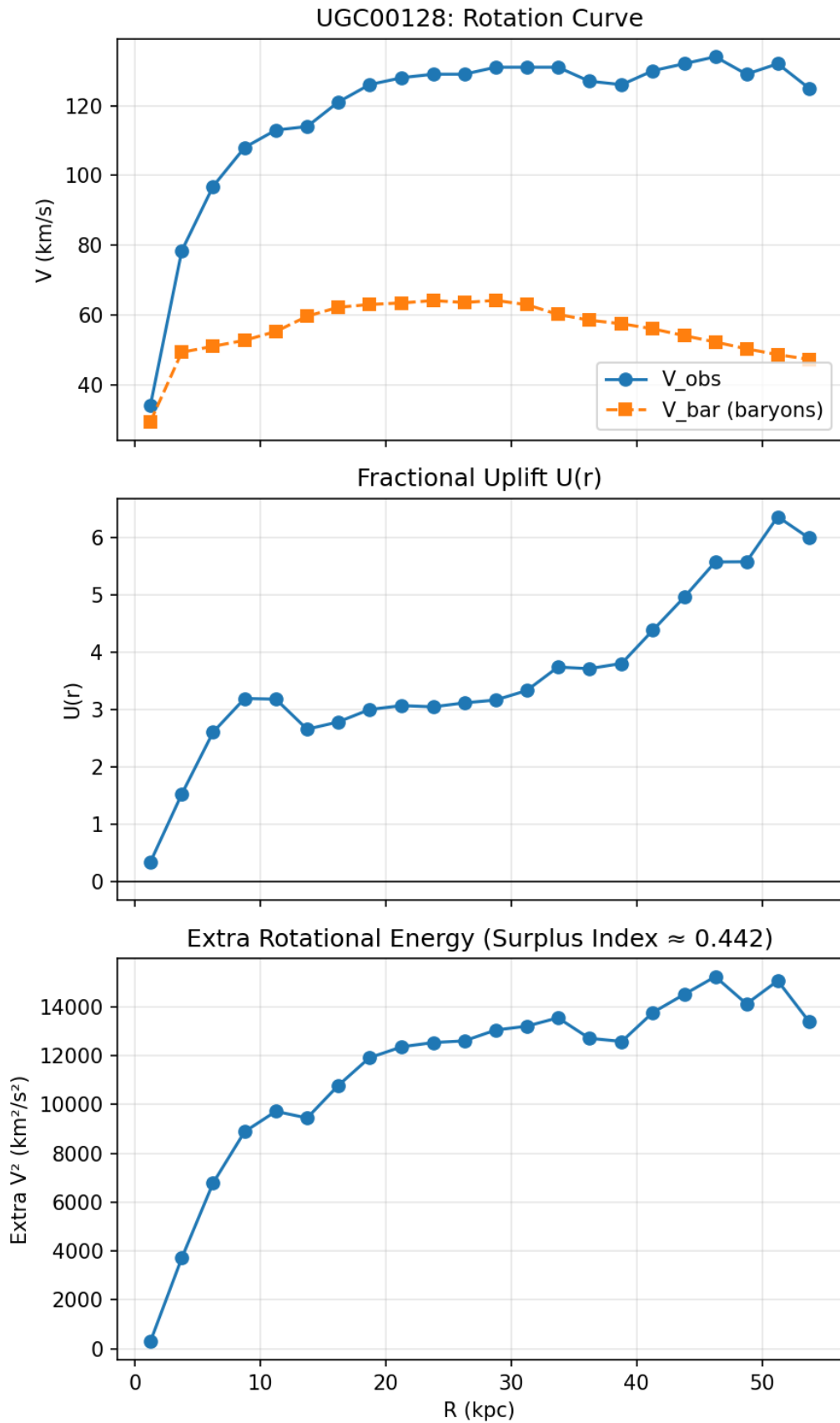


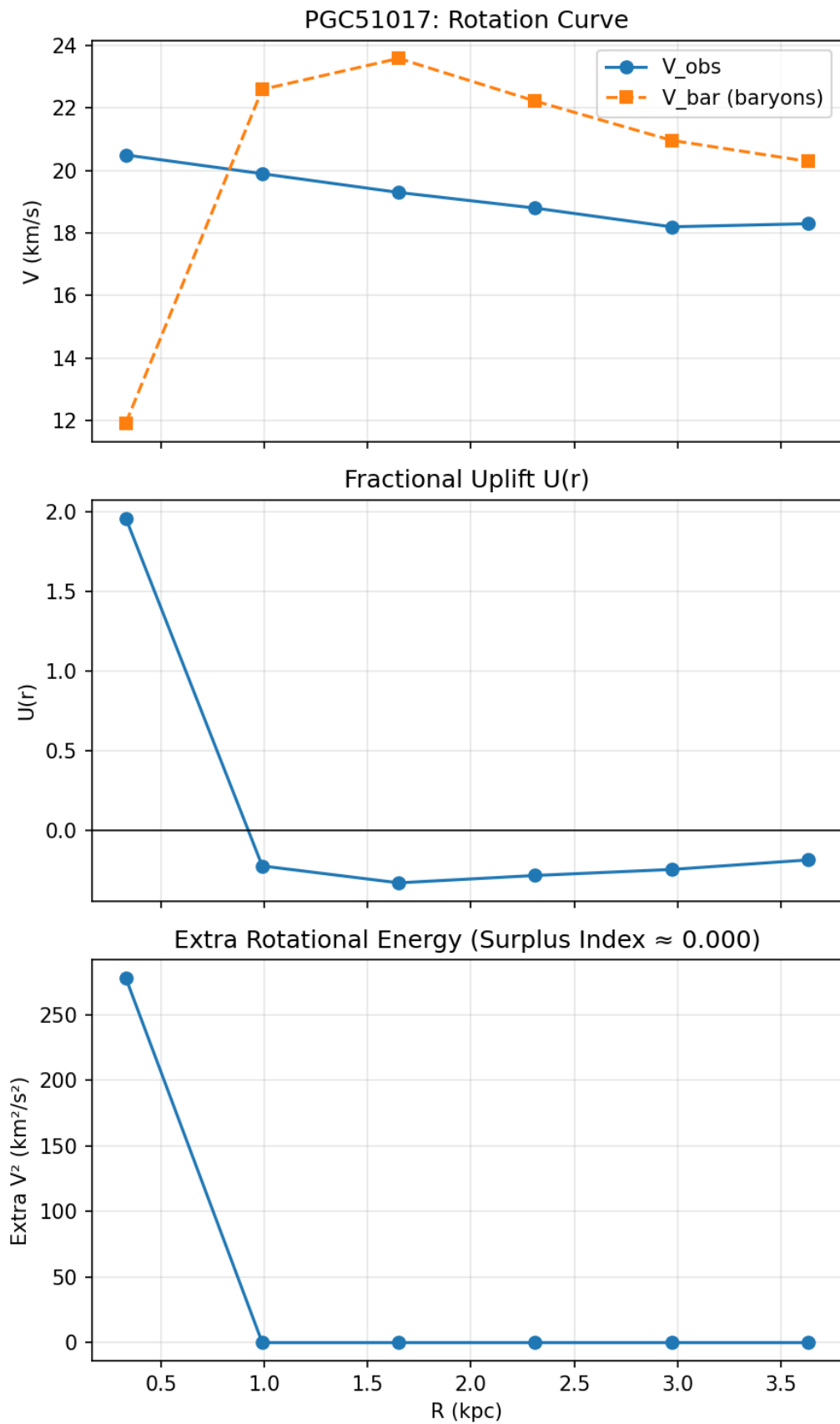


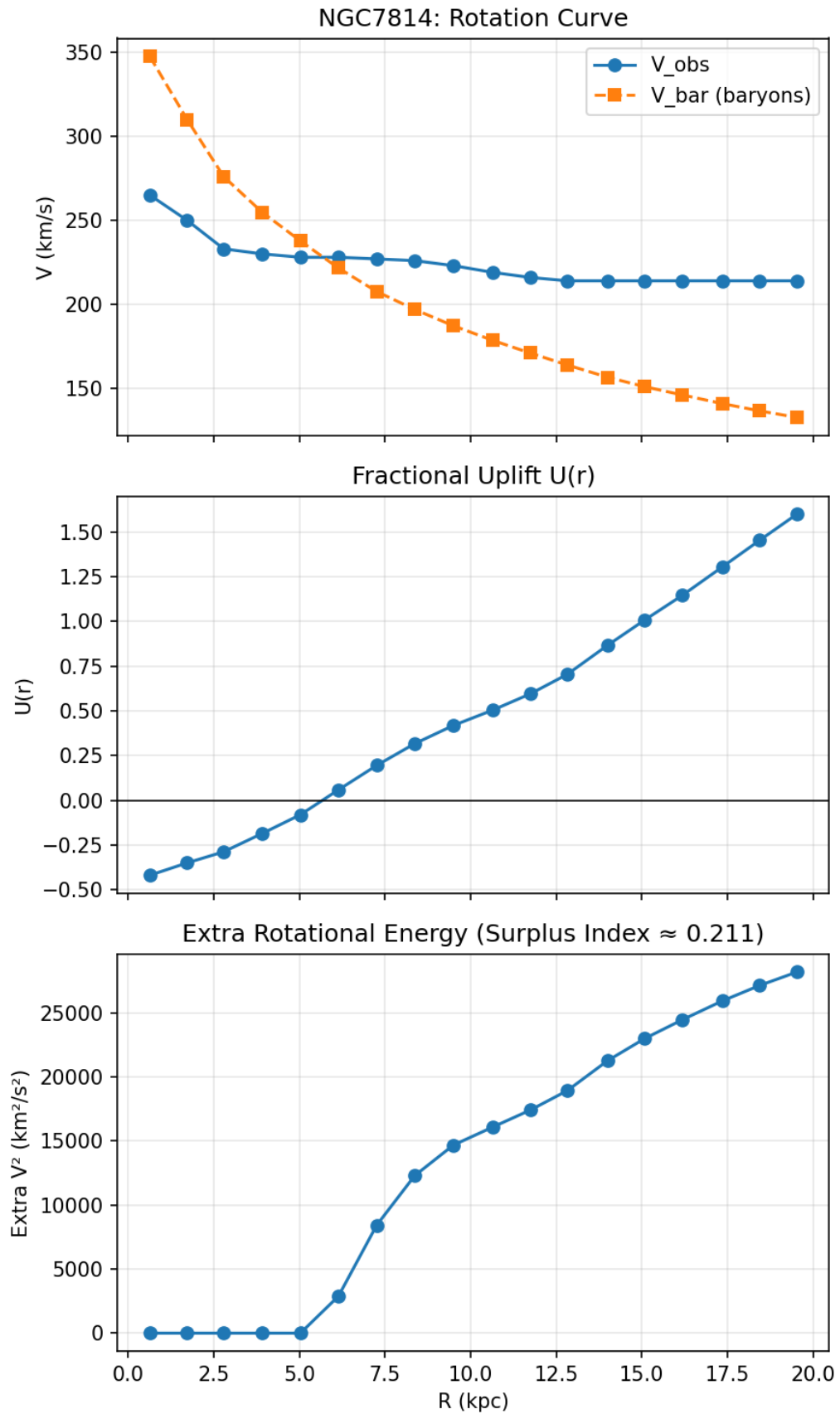


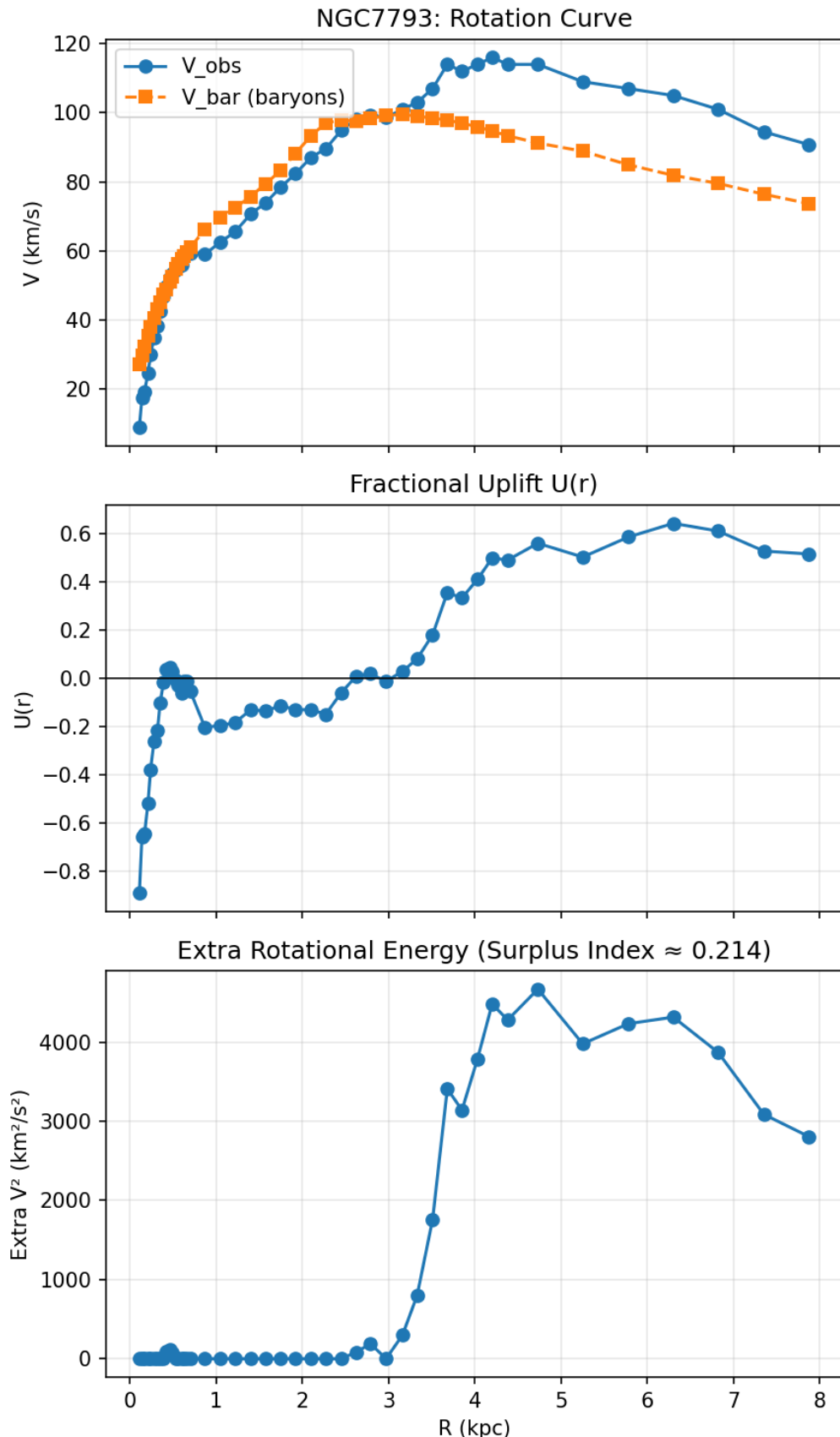


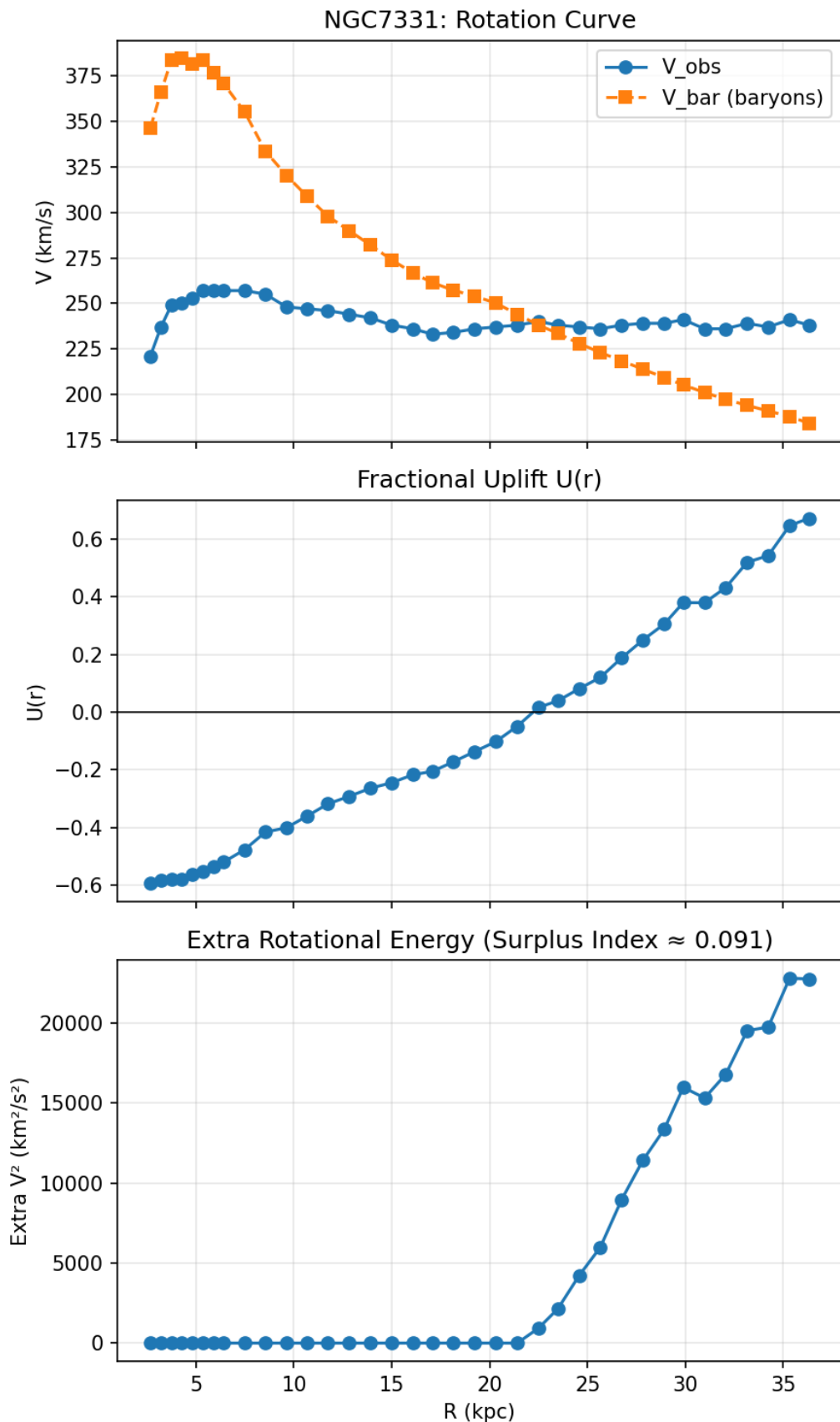


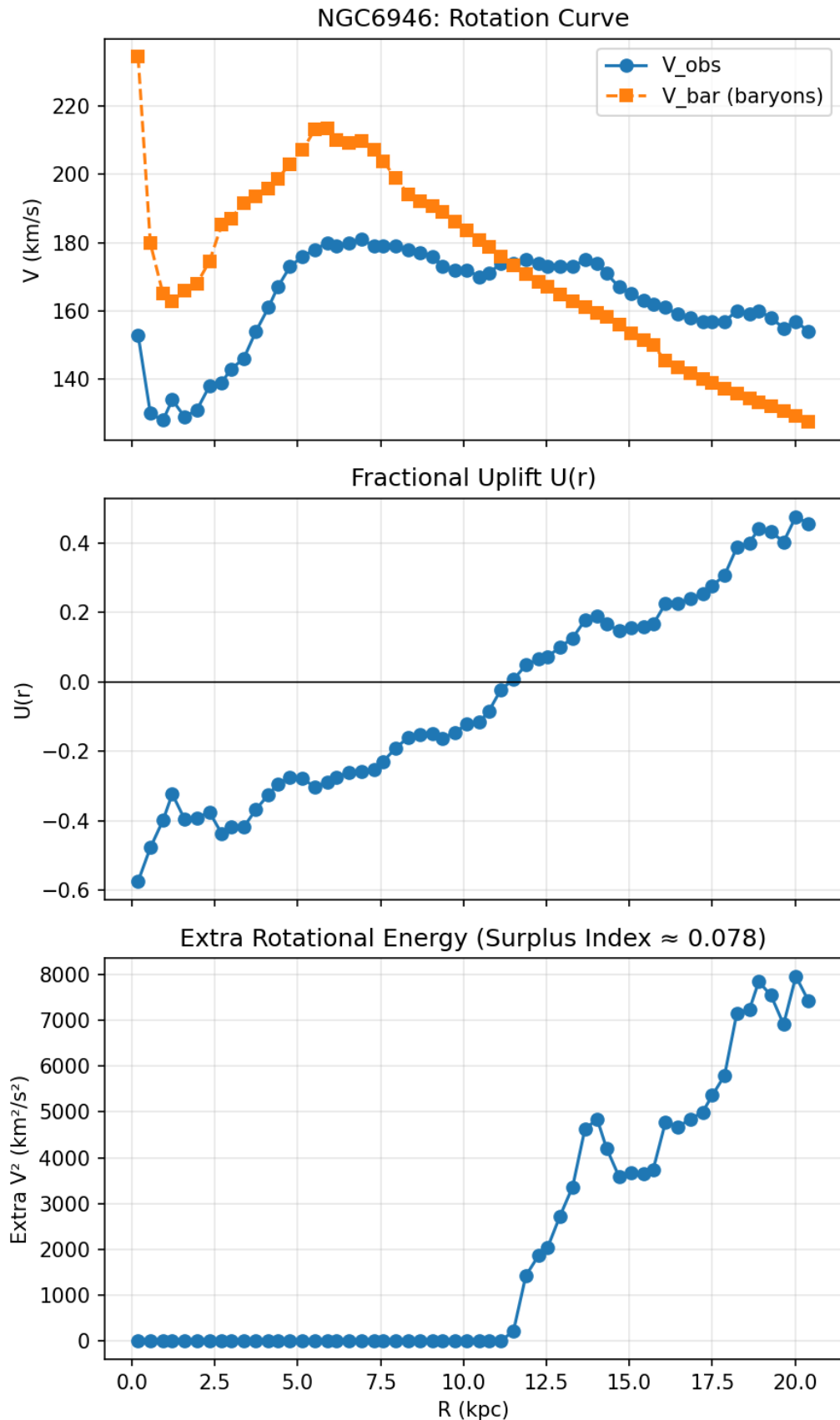


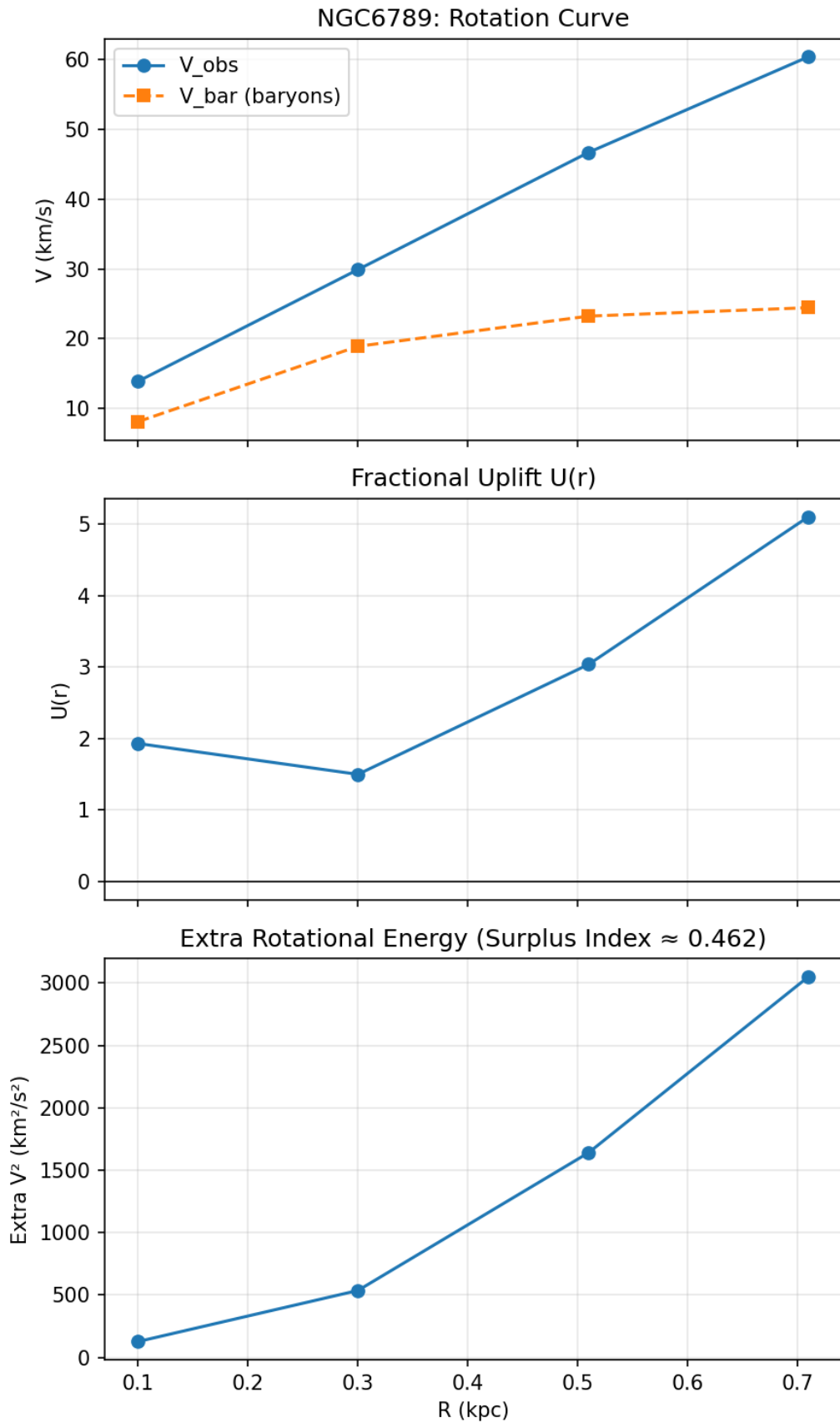


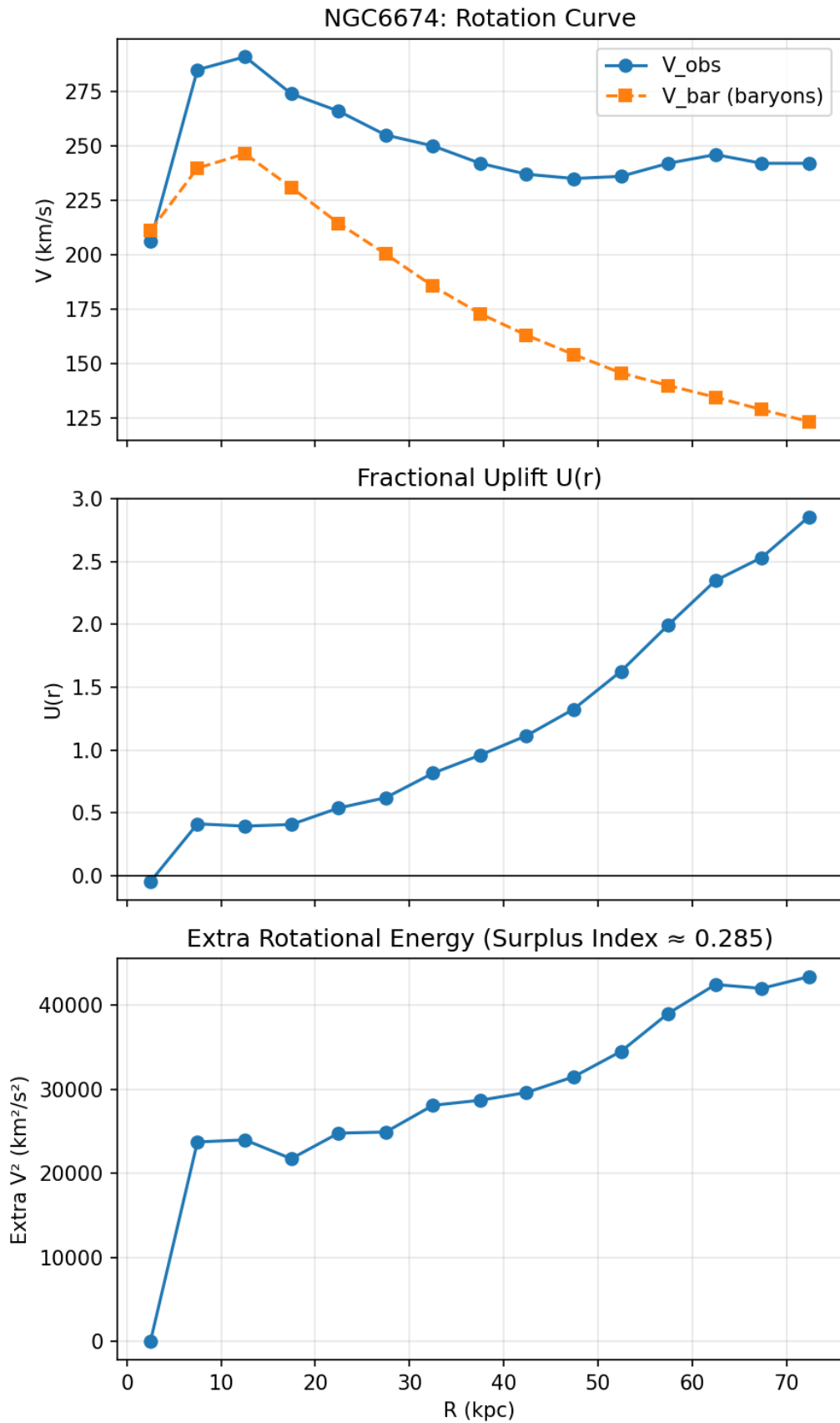


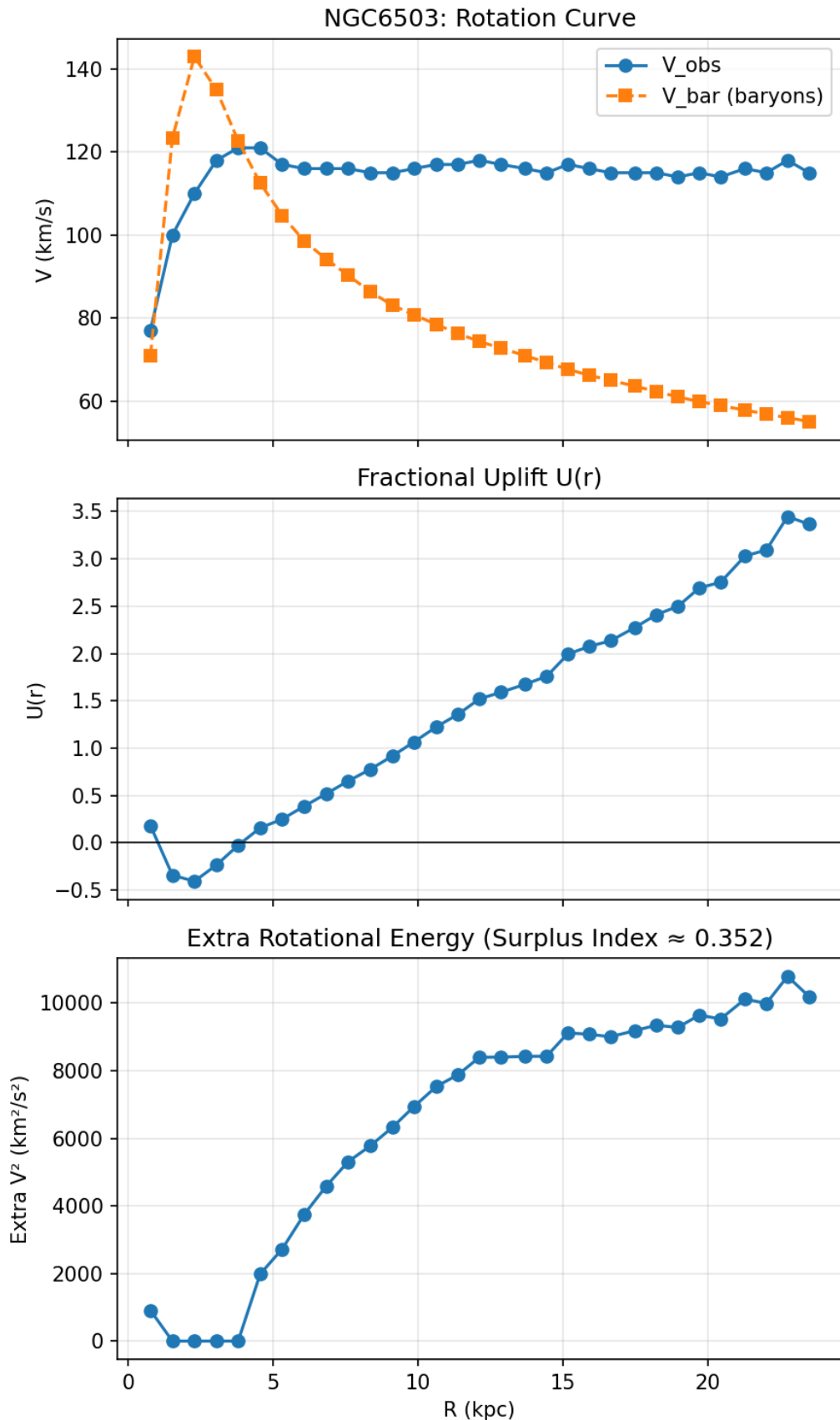


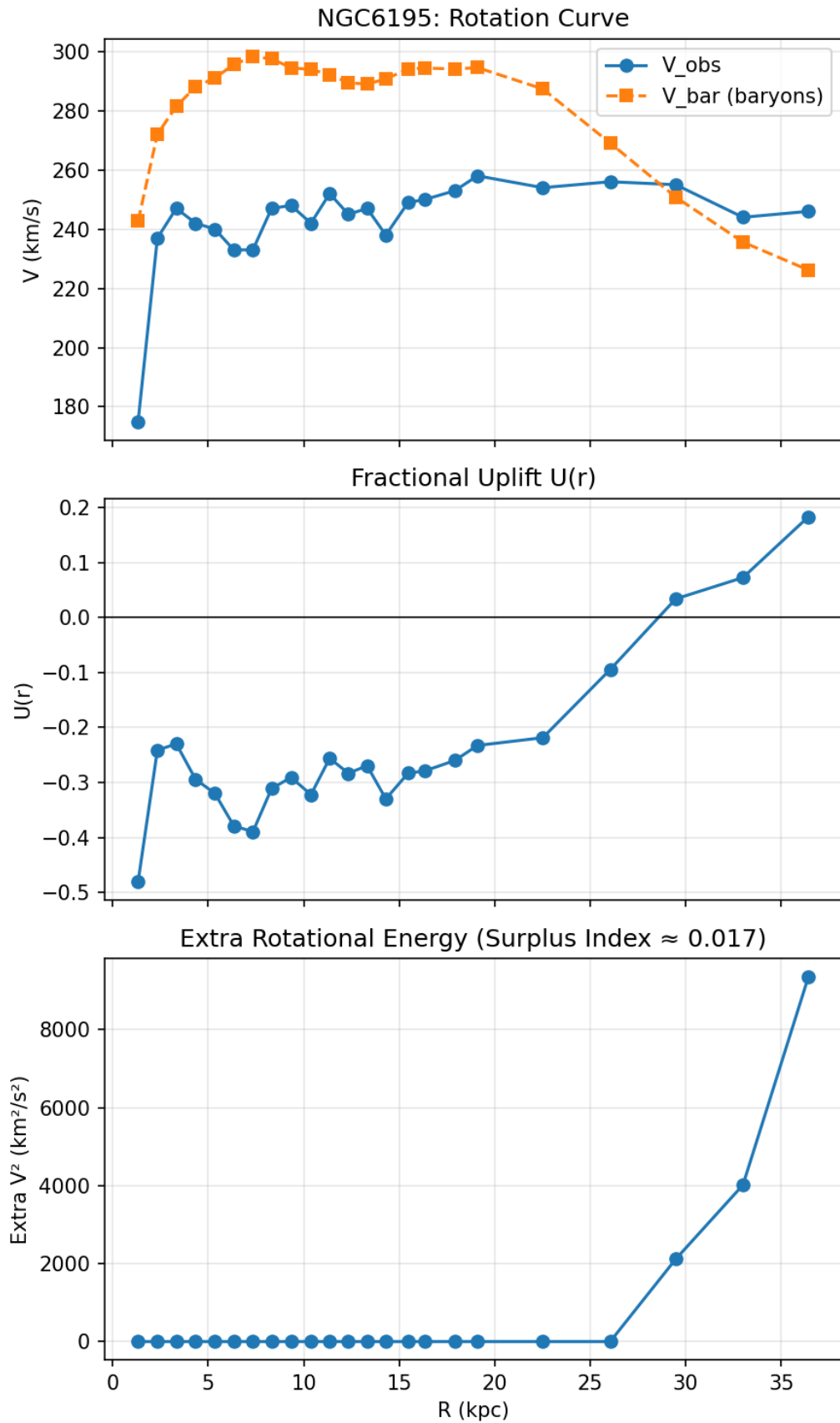


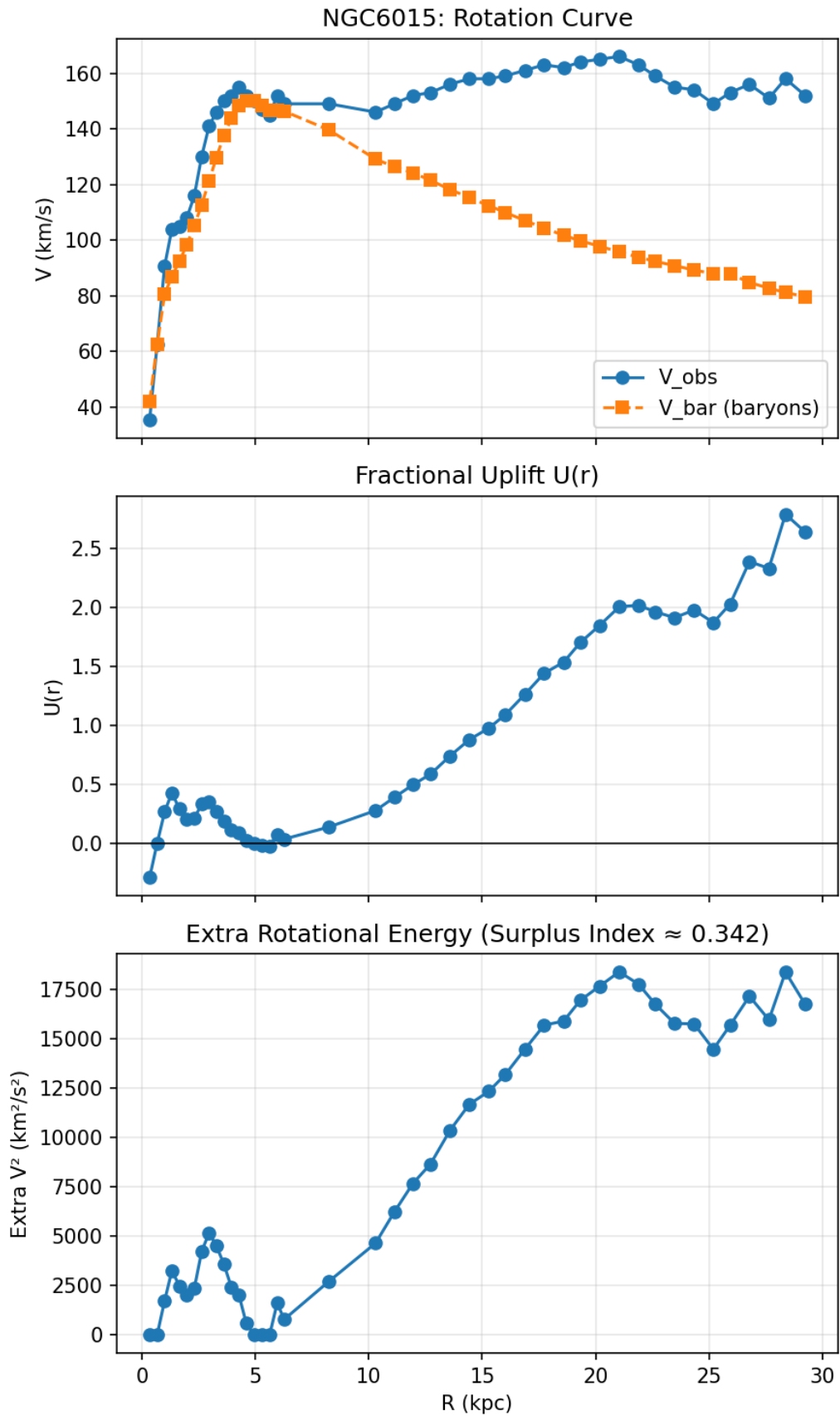


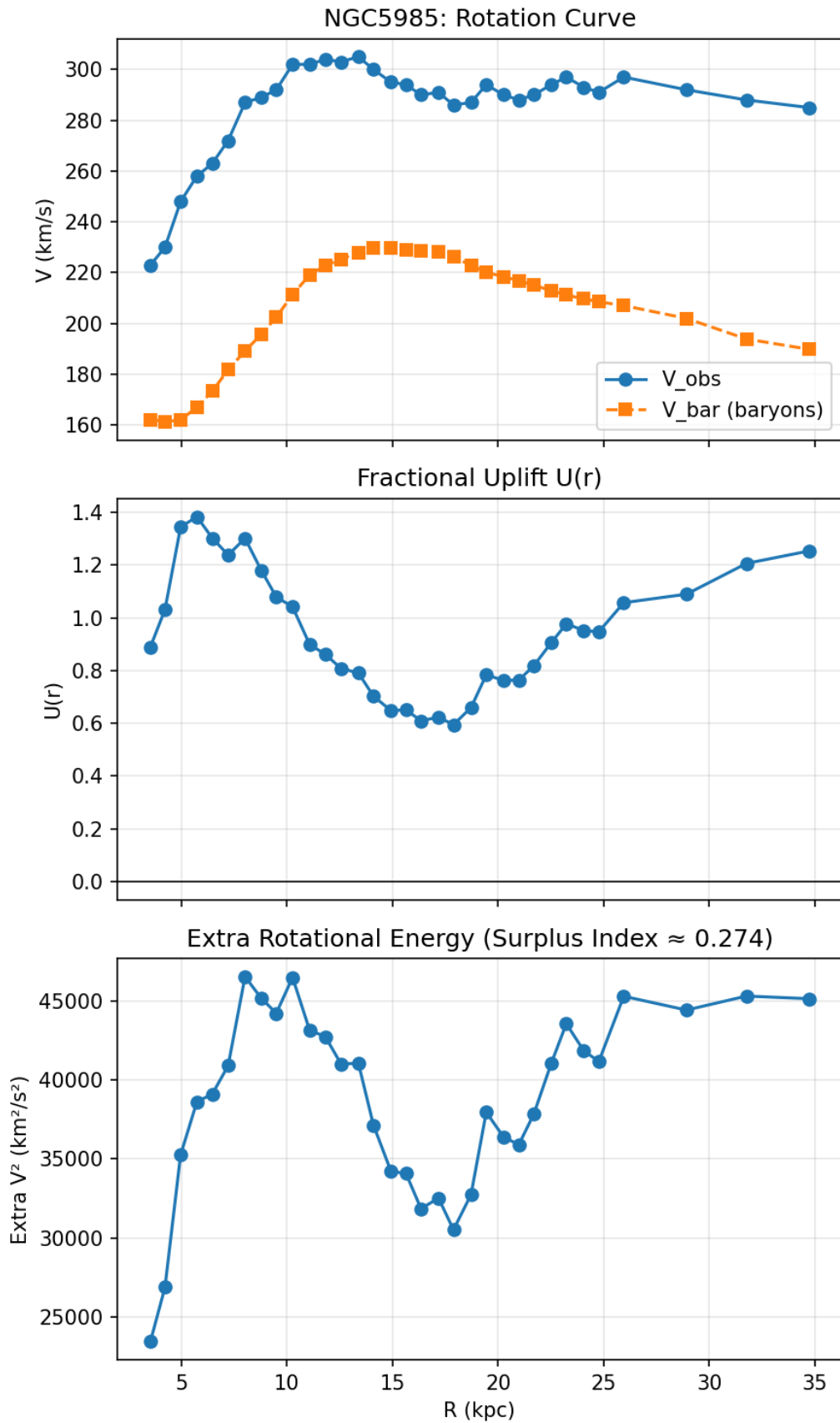


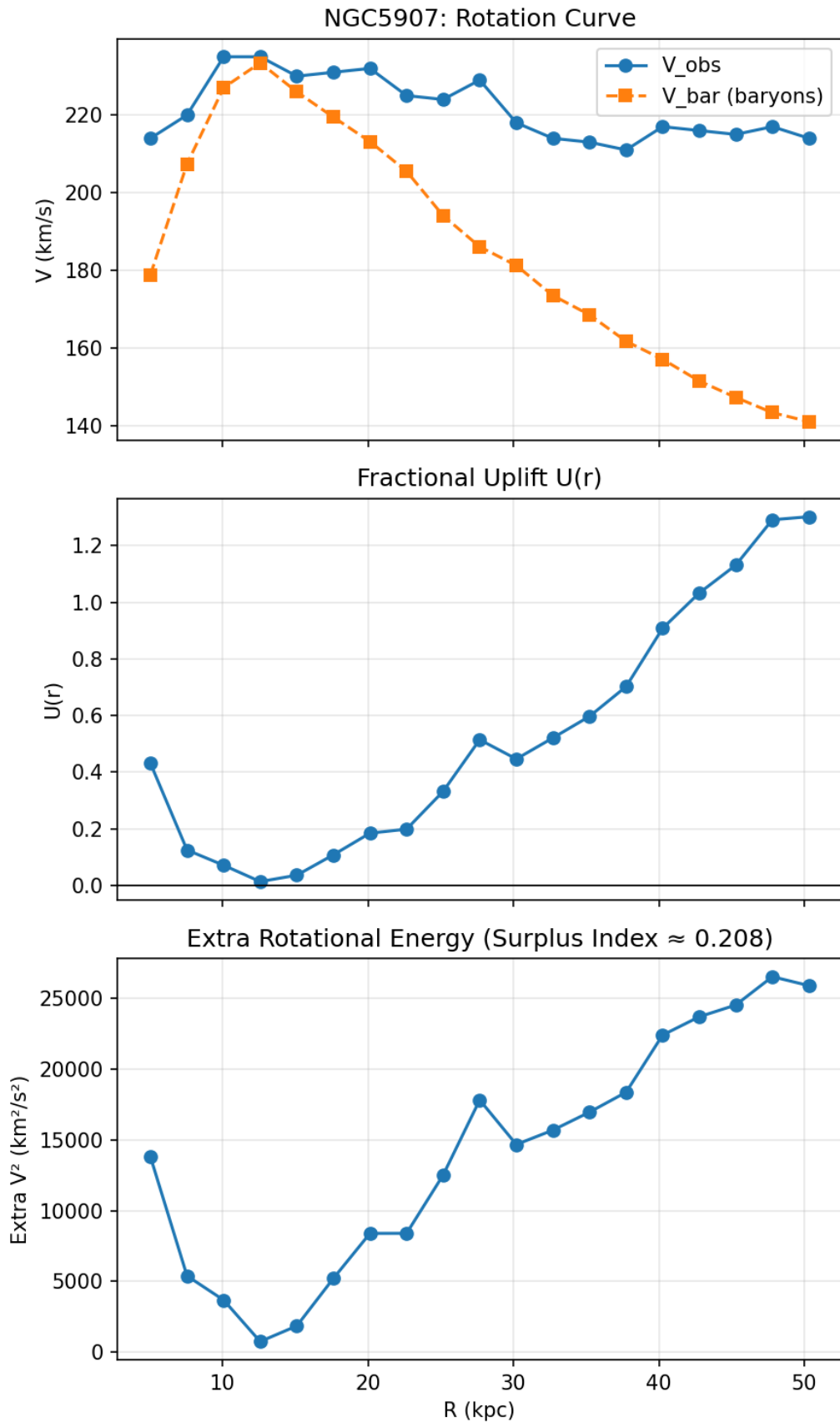


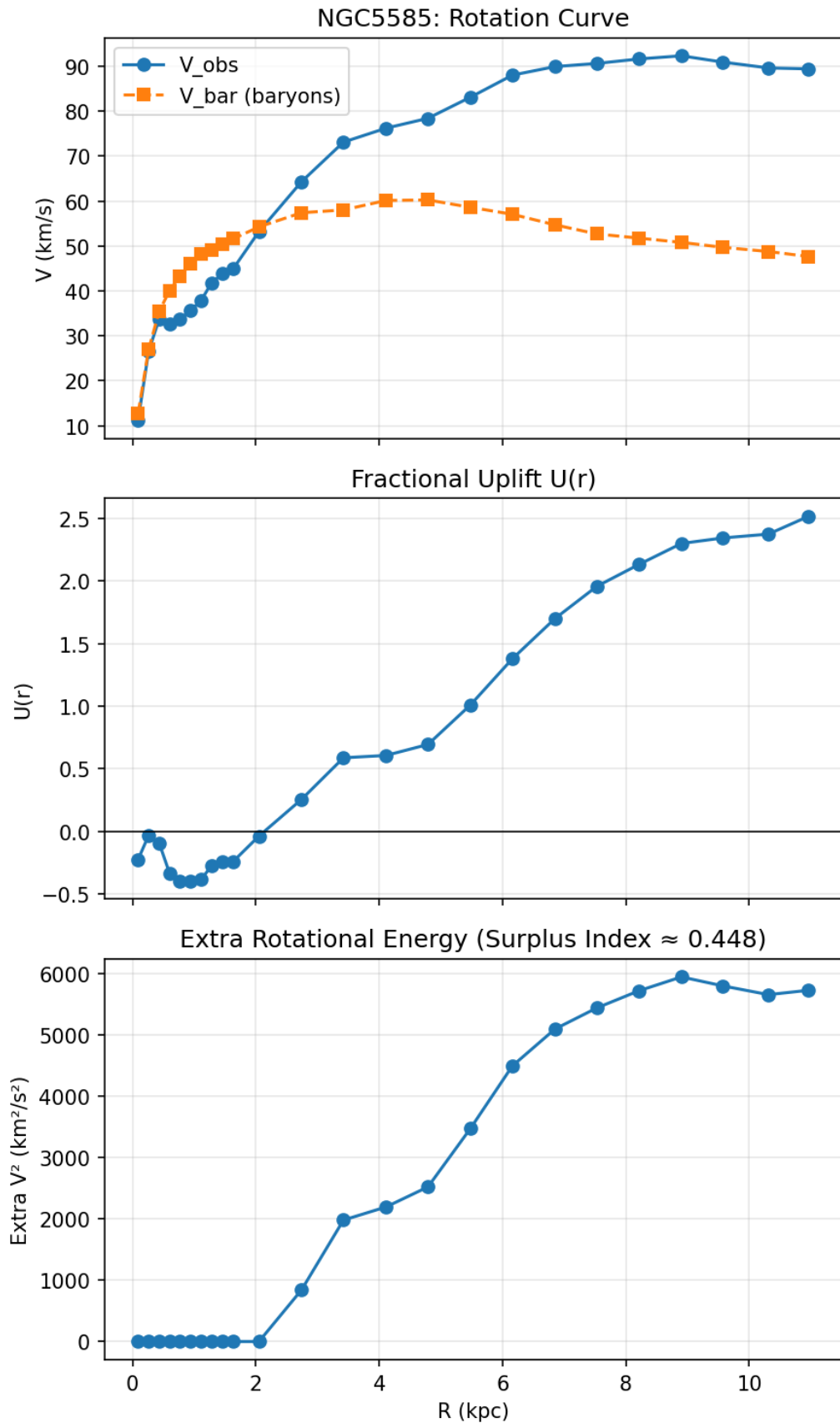


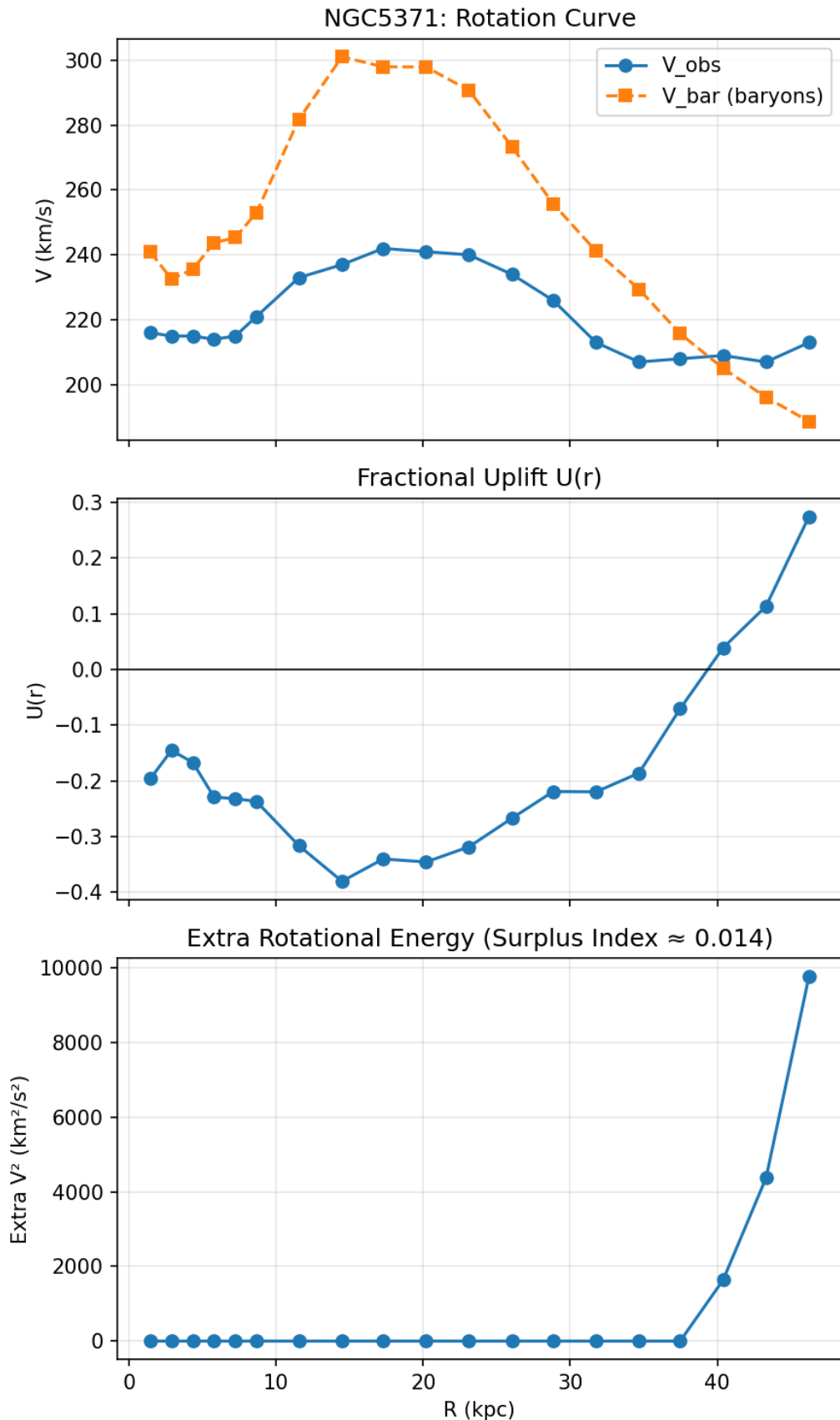


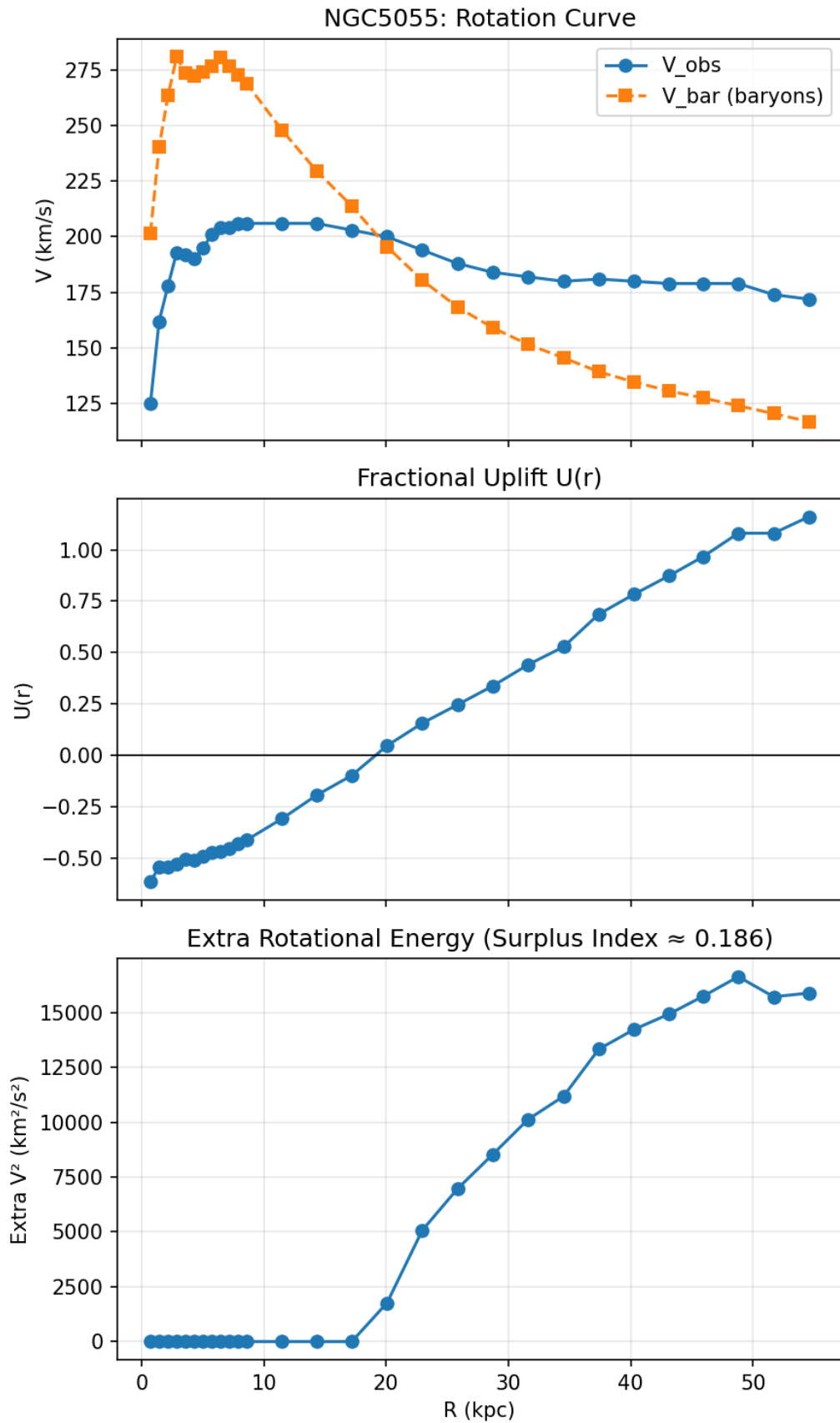


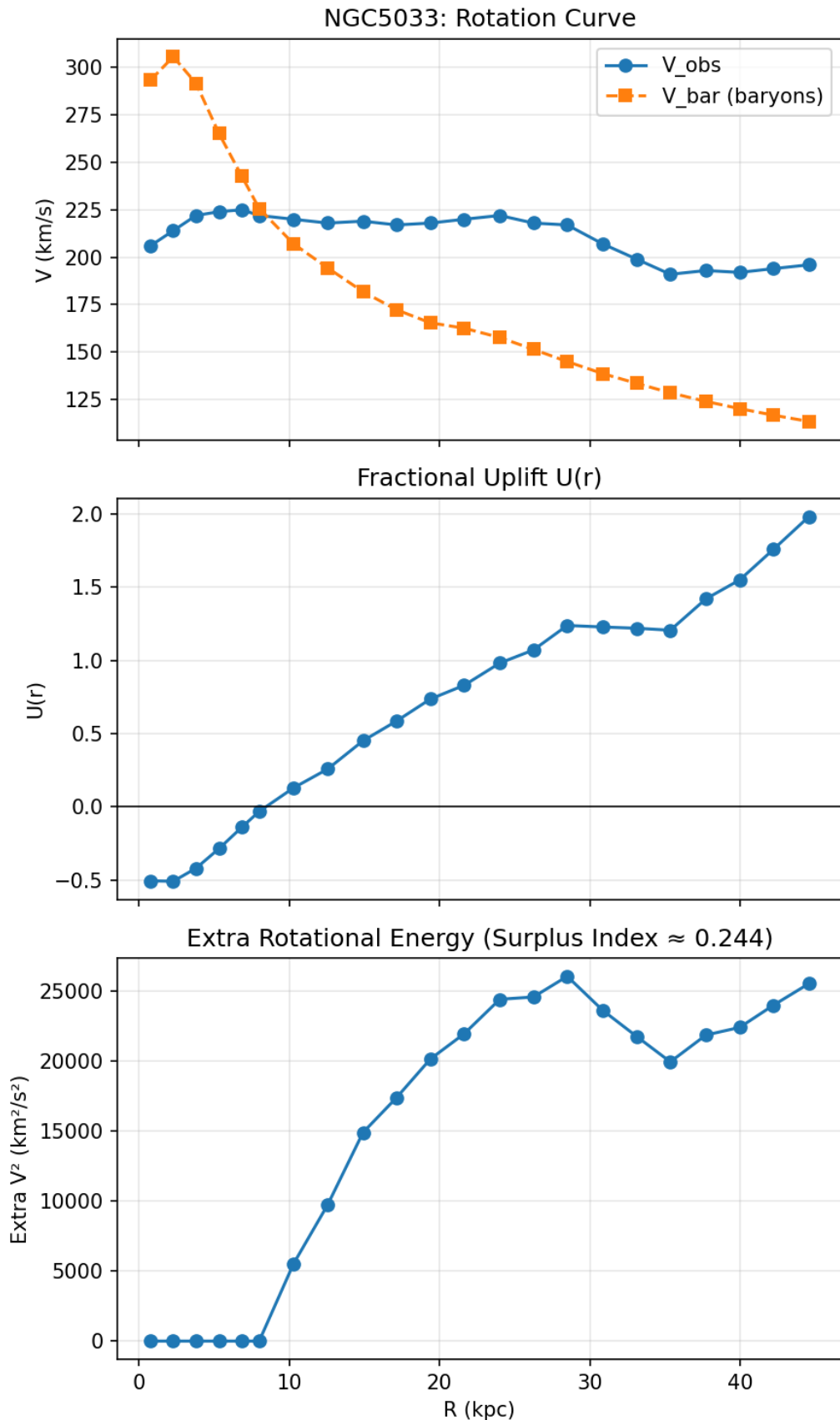


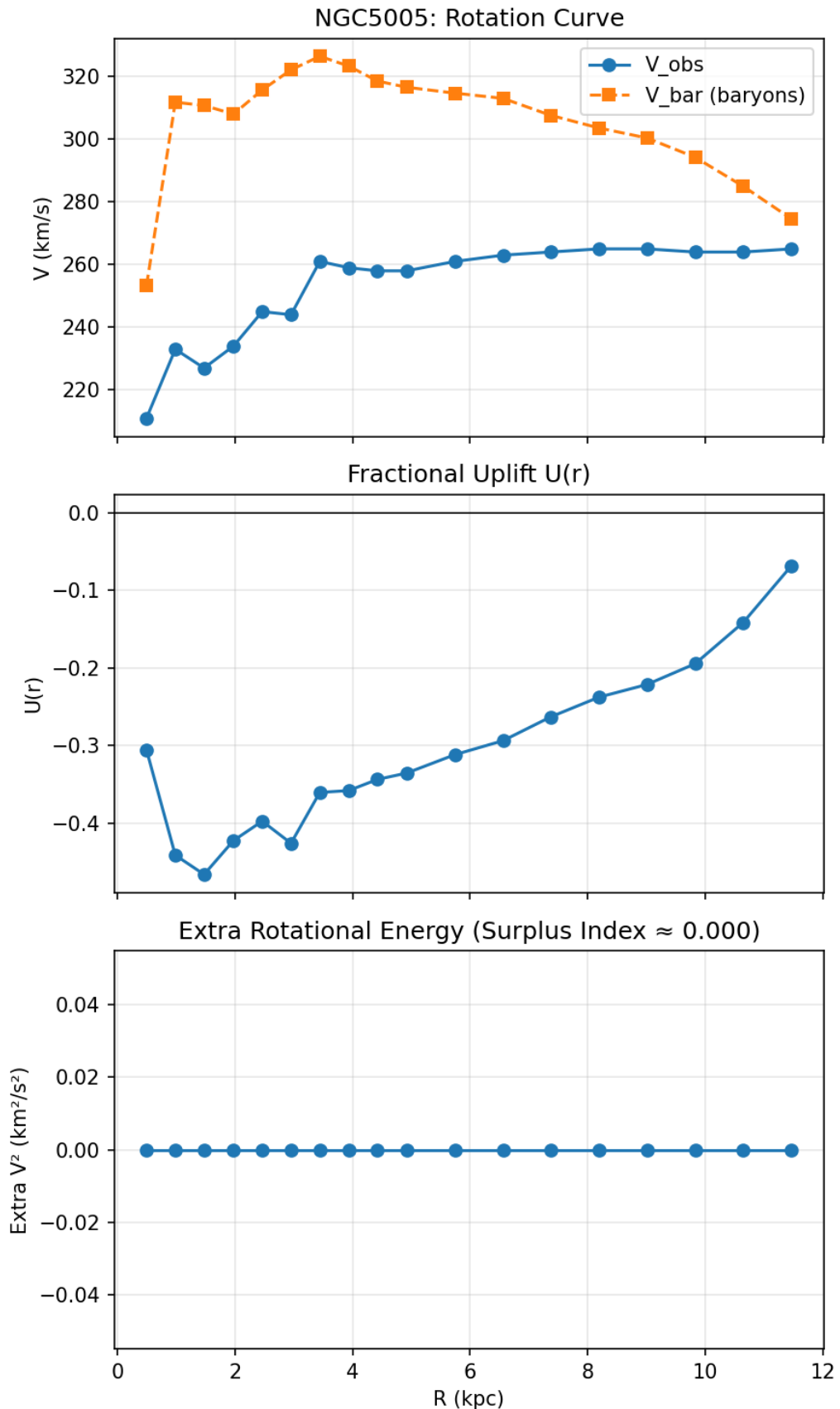


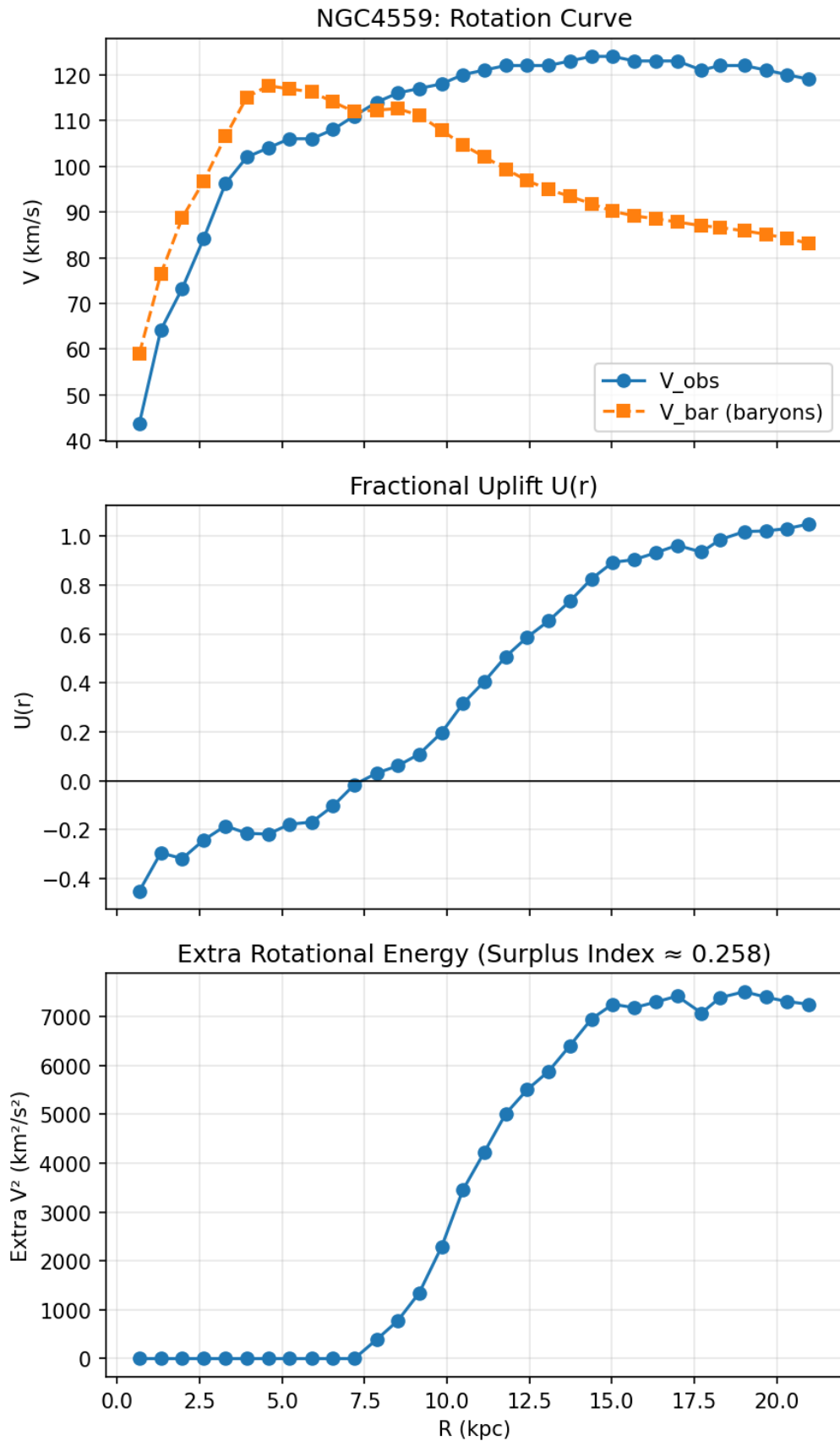


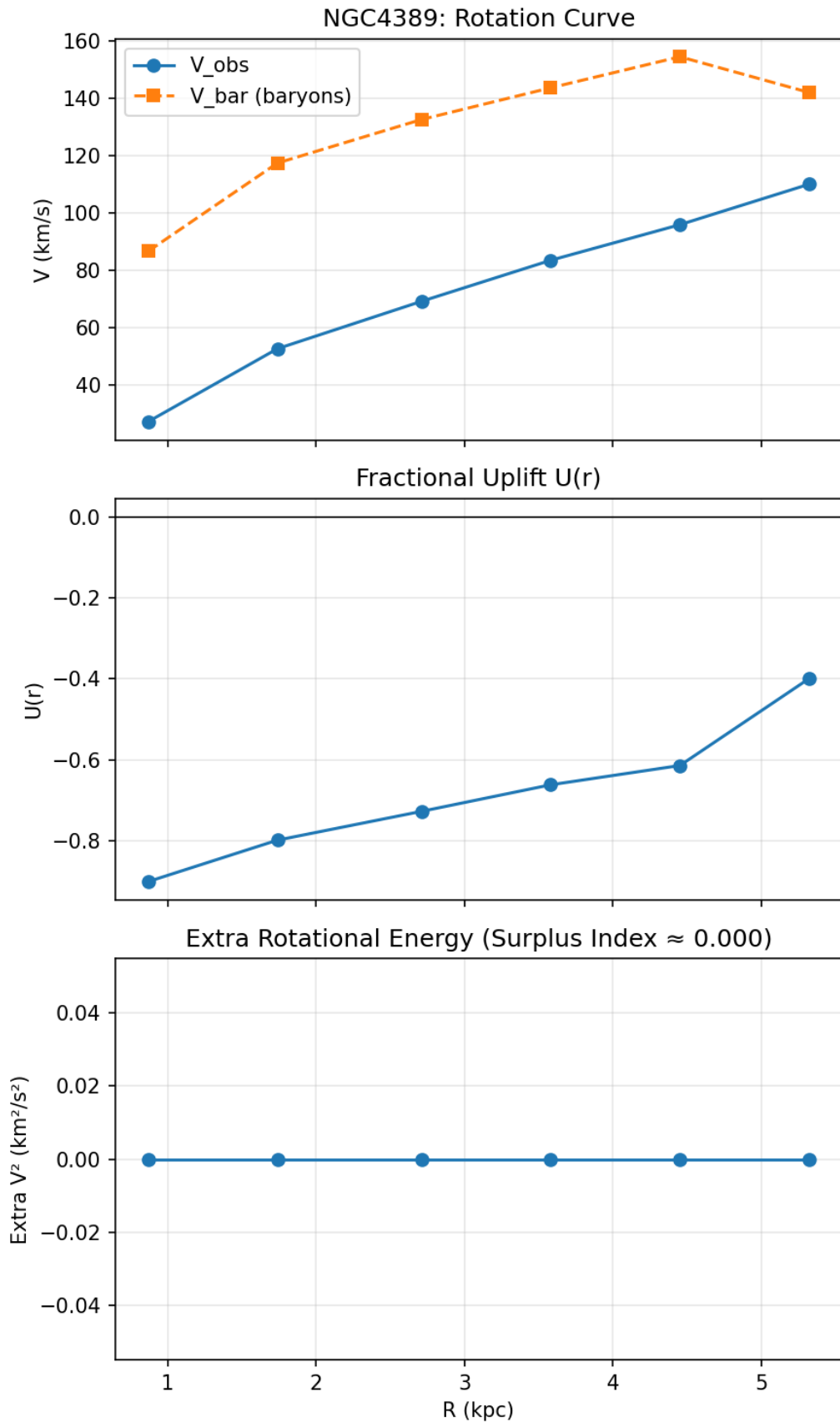


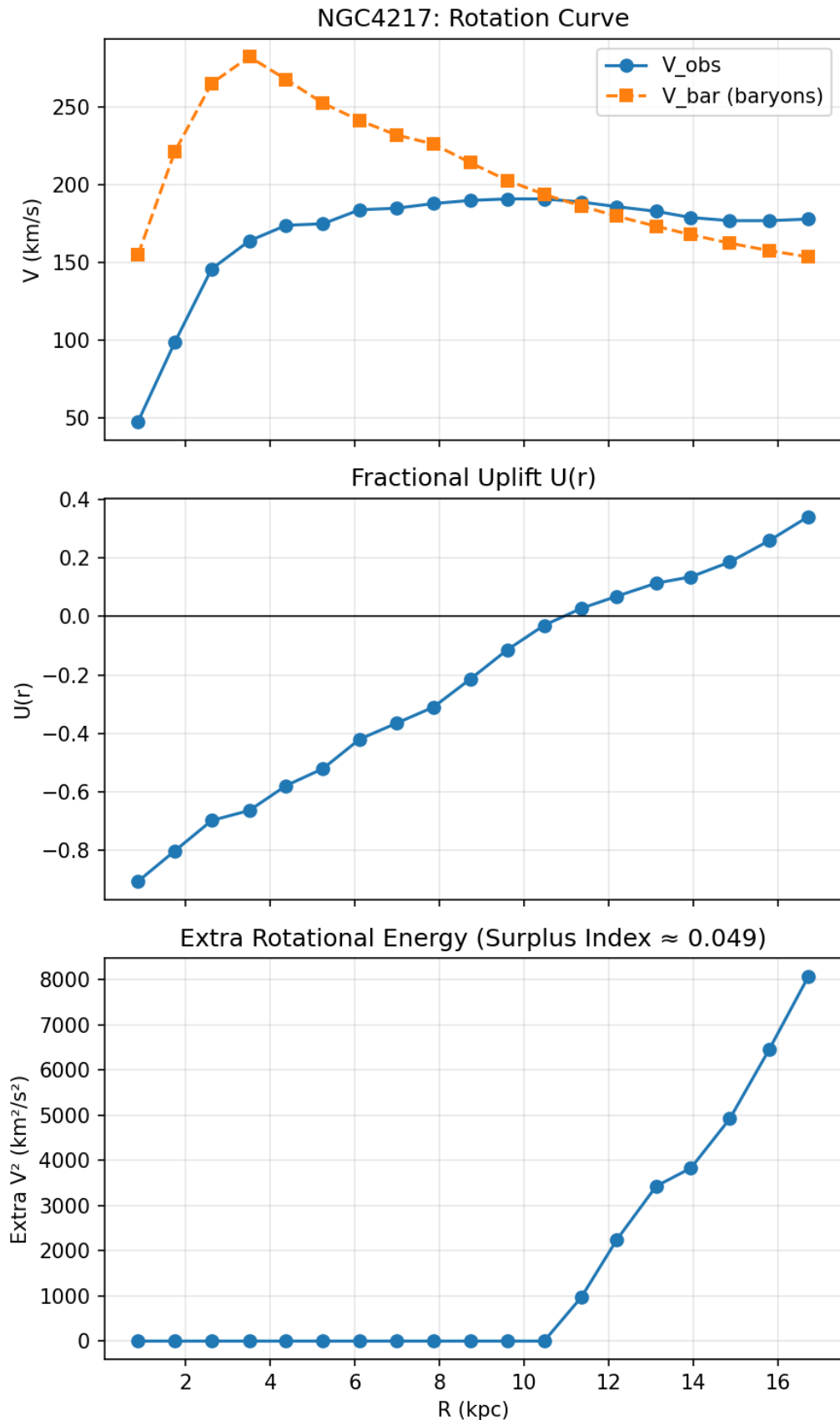


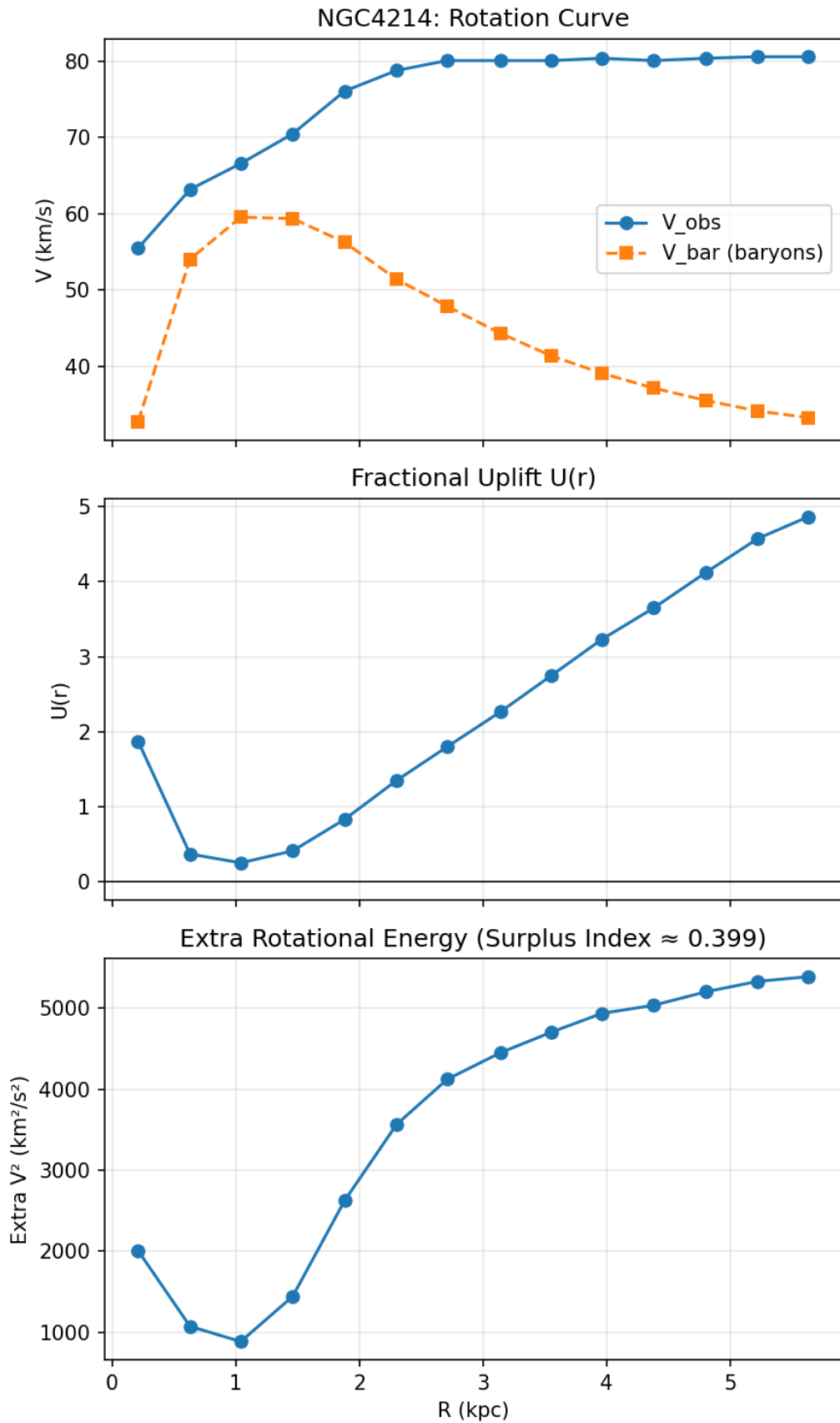


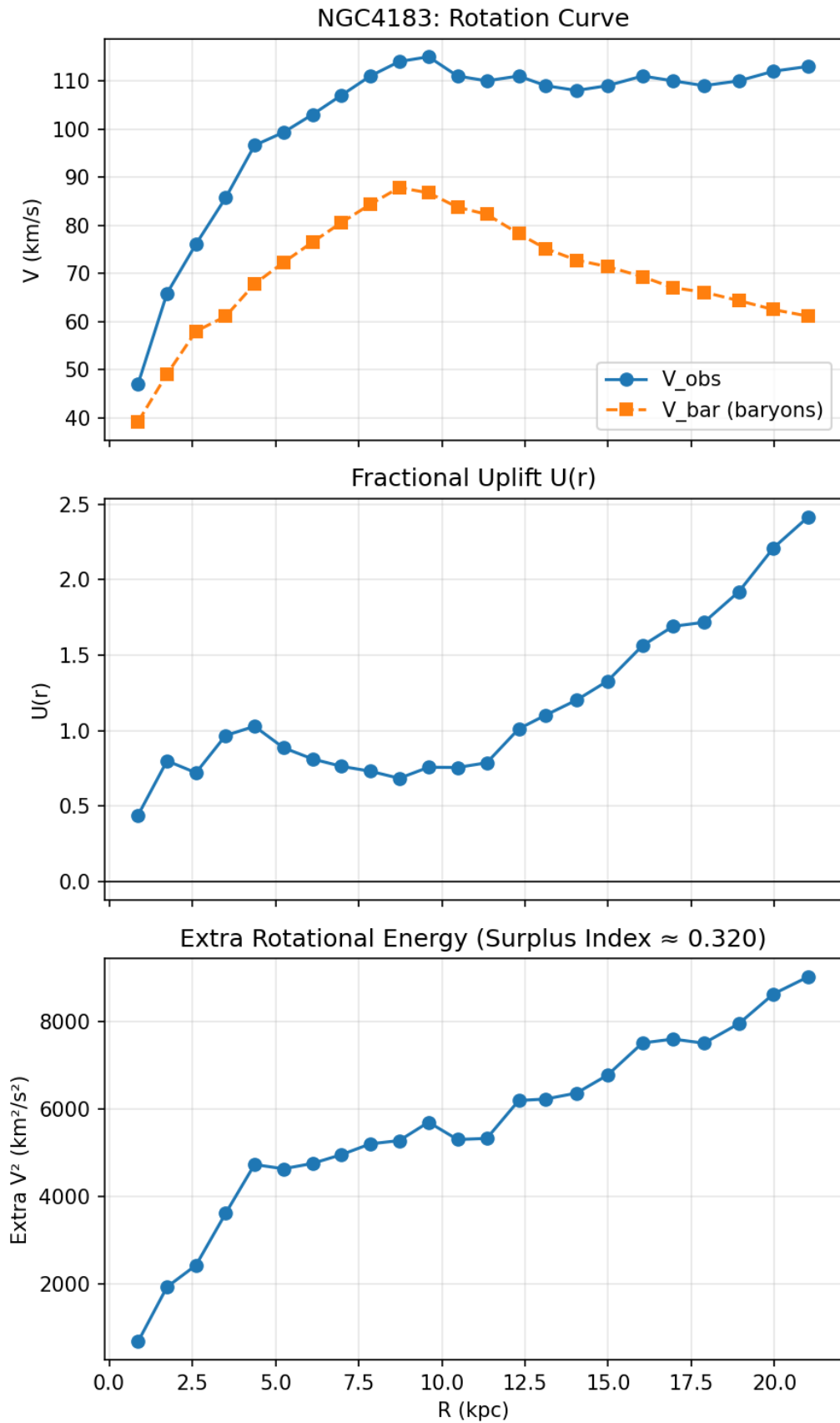


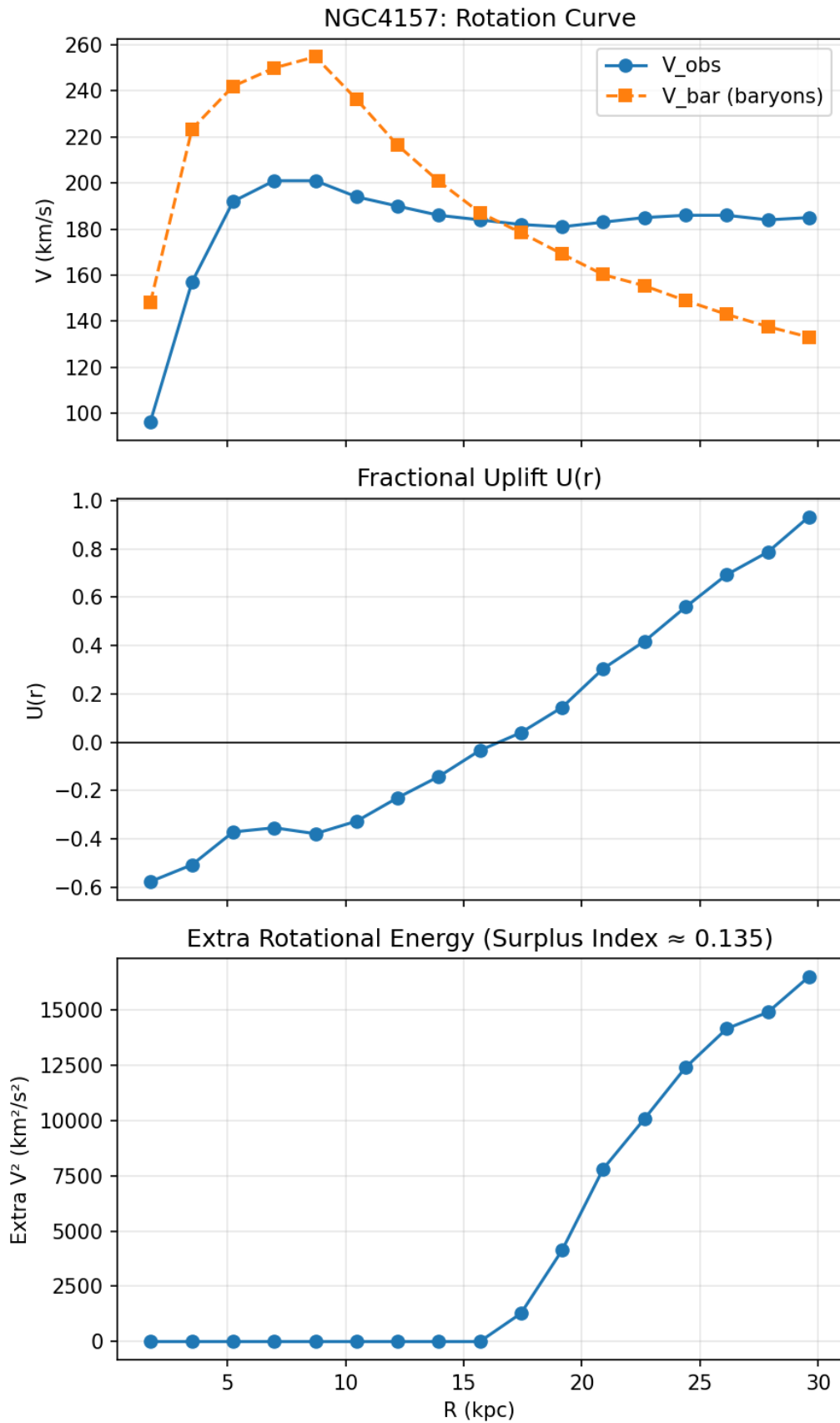




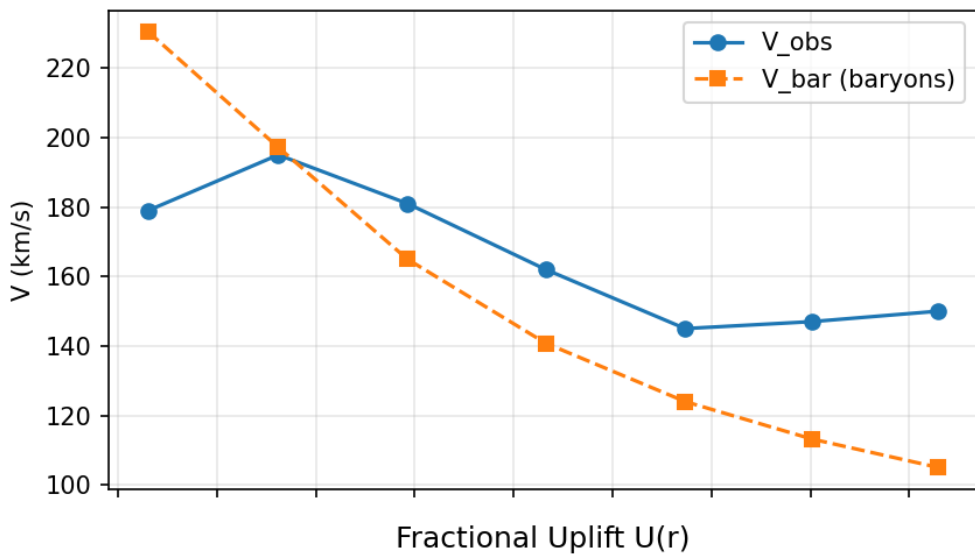
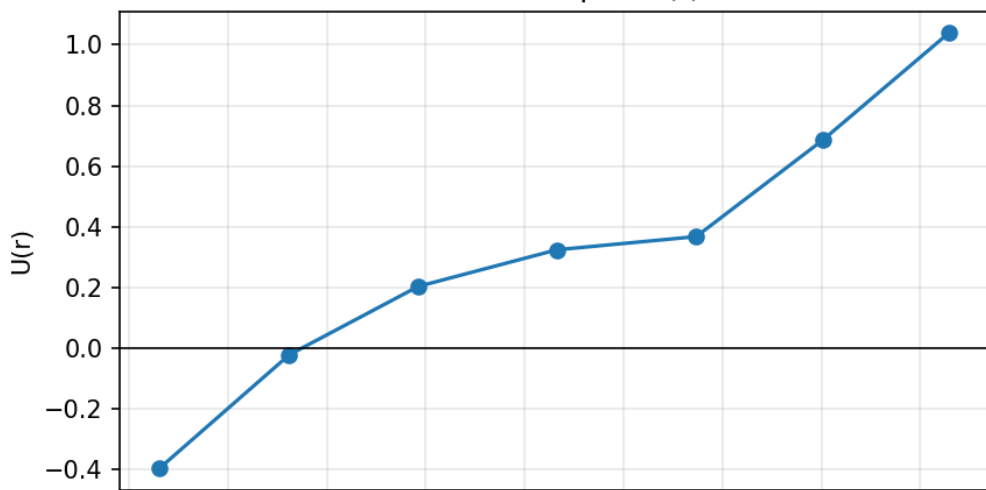
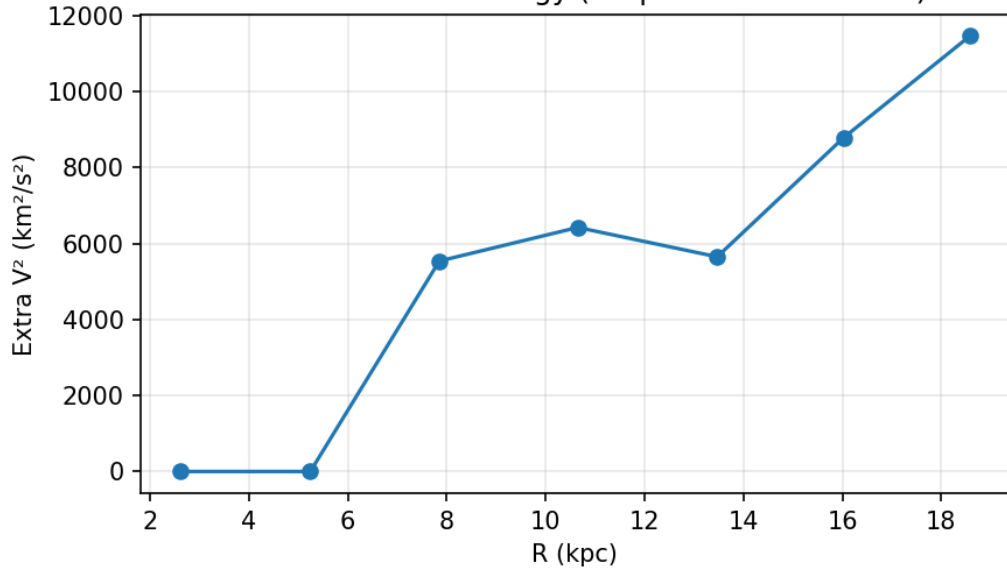


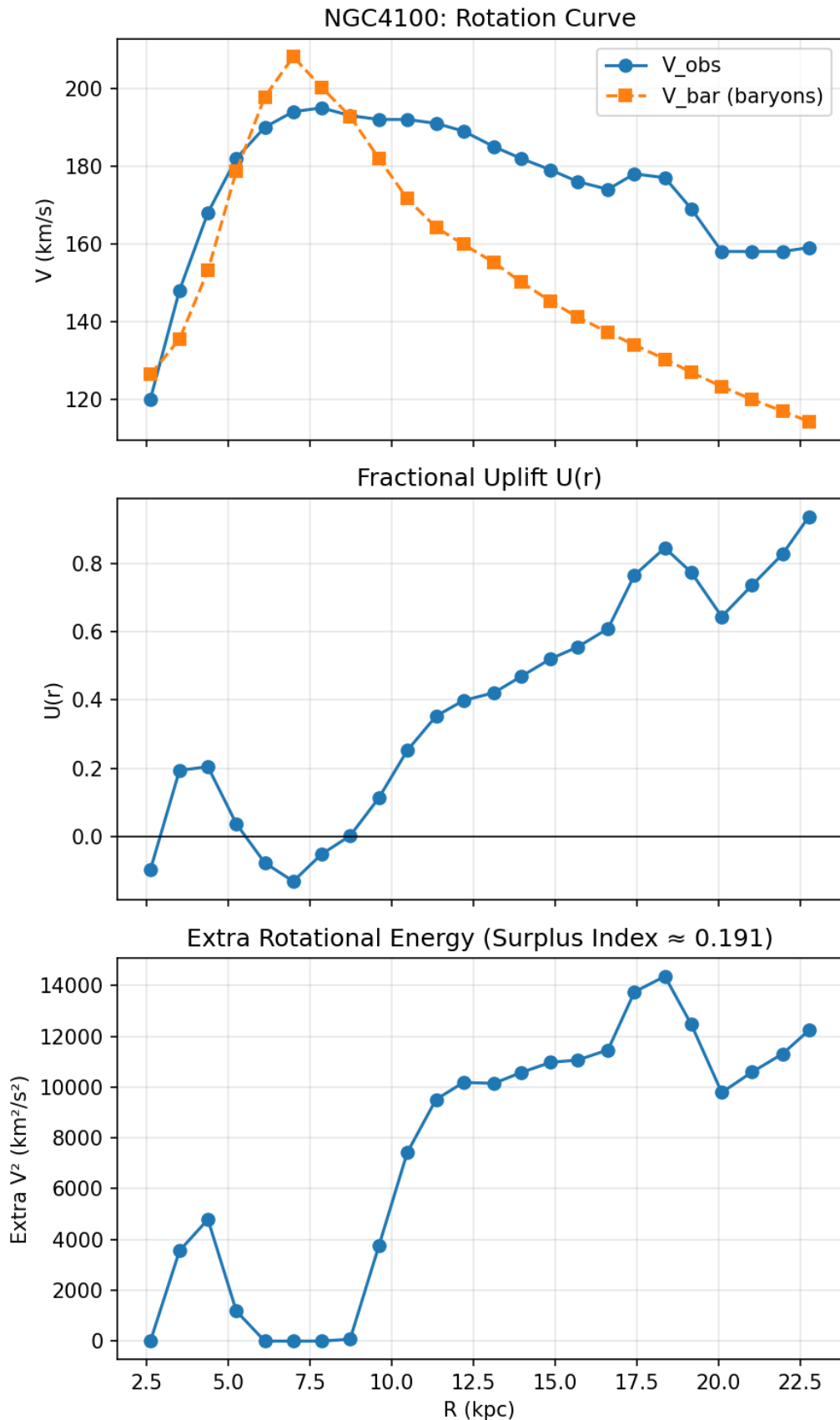


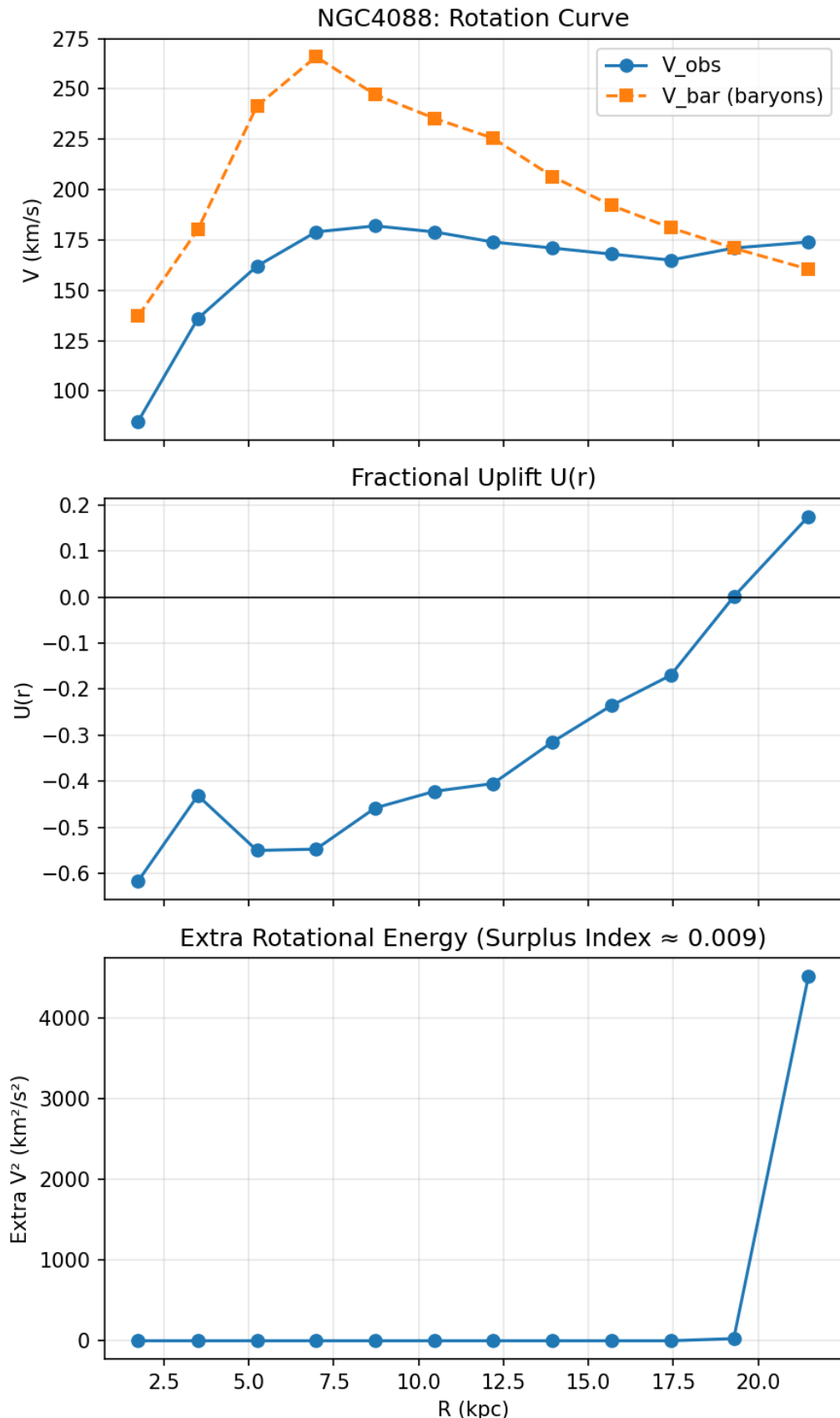


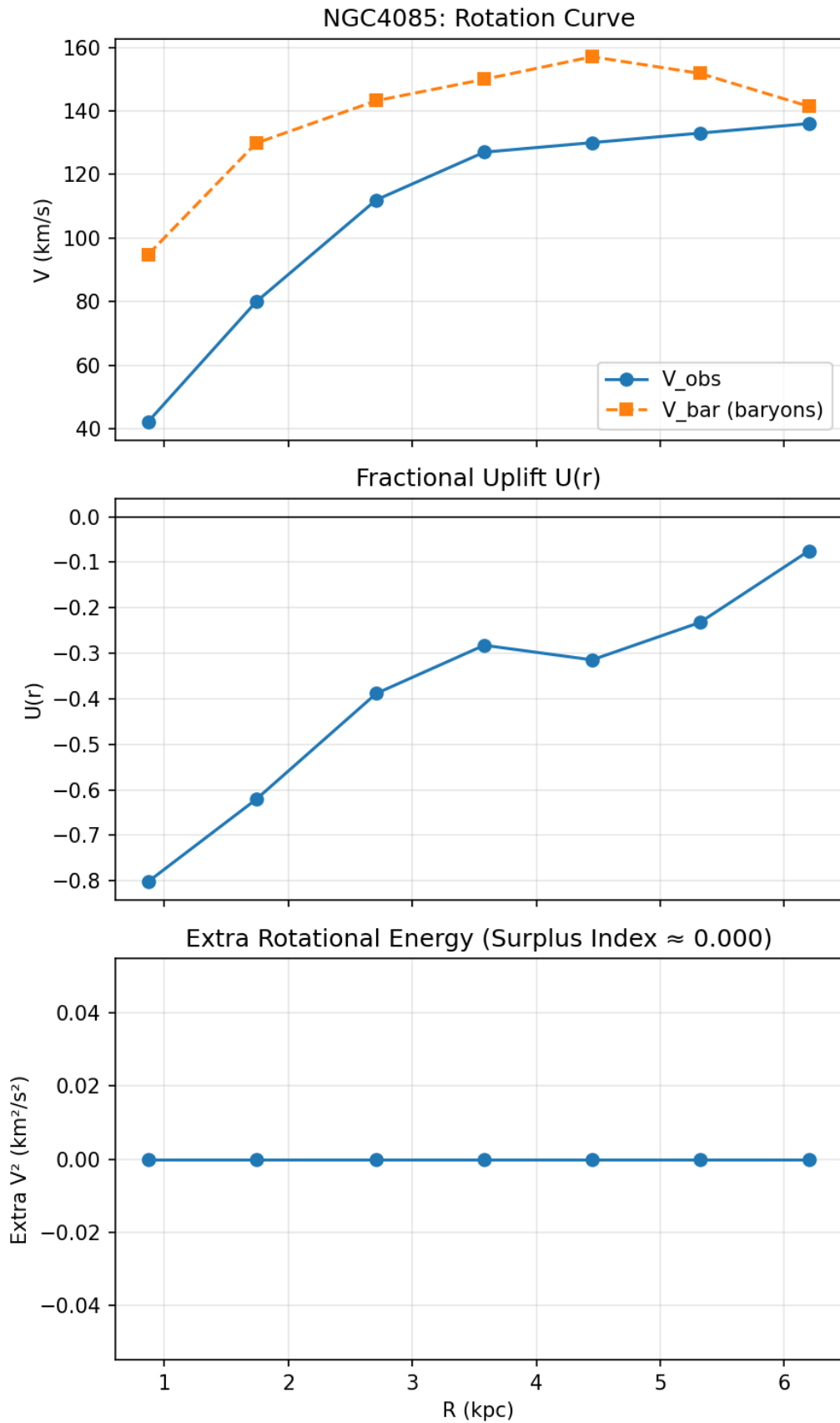


NGC4138: Rotation Curve

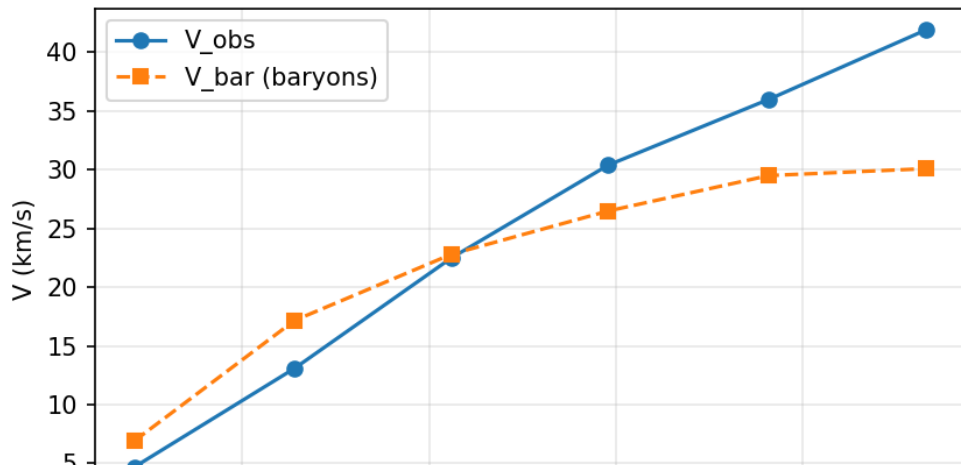
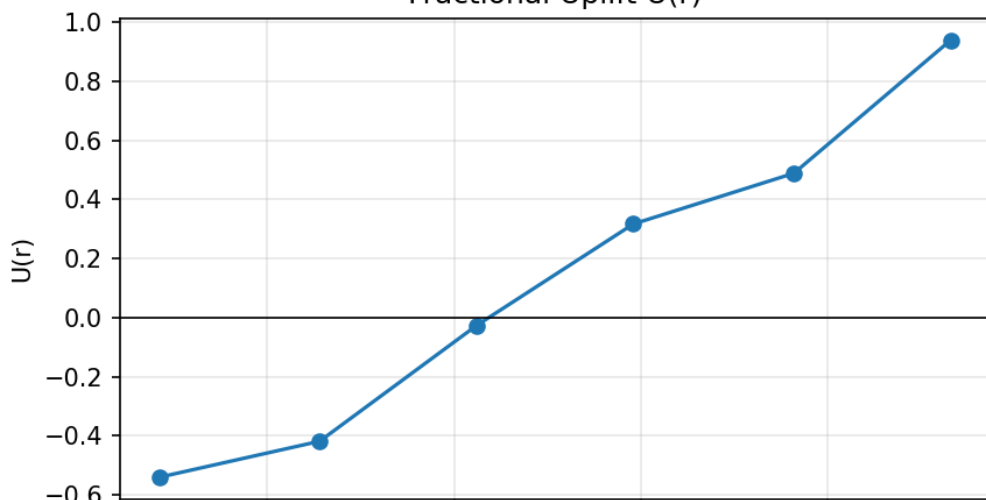
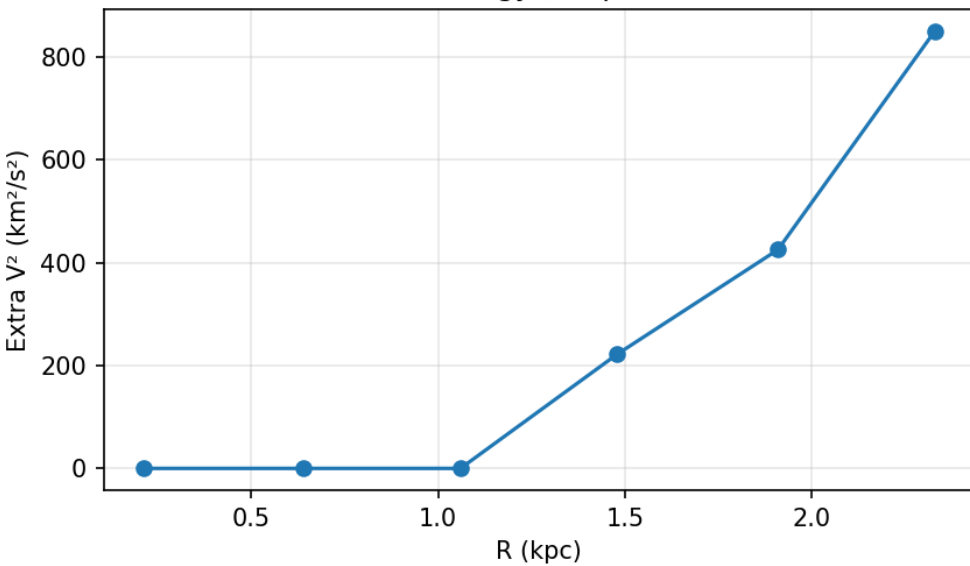
Fractional Uplift $U(r)$ Extra Rotational Energy (Surplus Index ≈ 0.138)

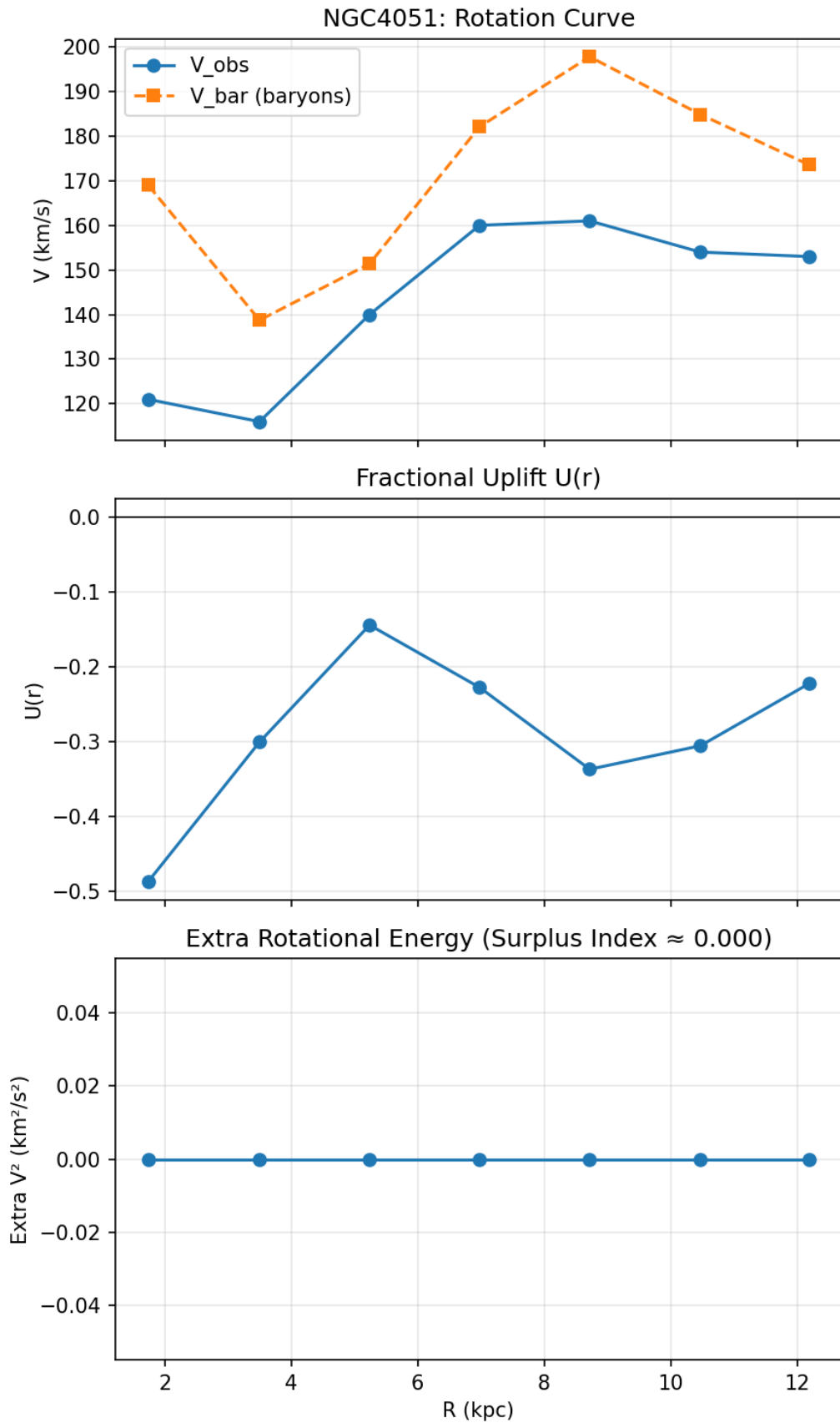


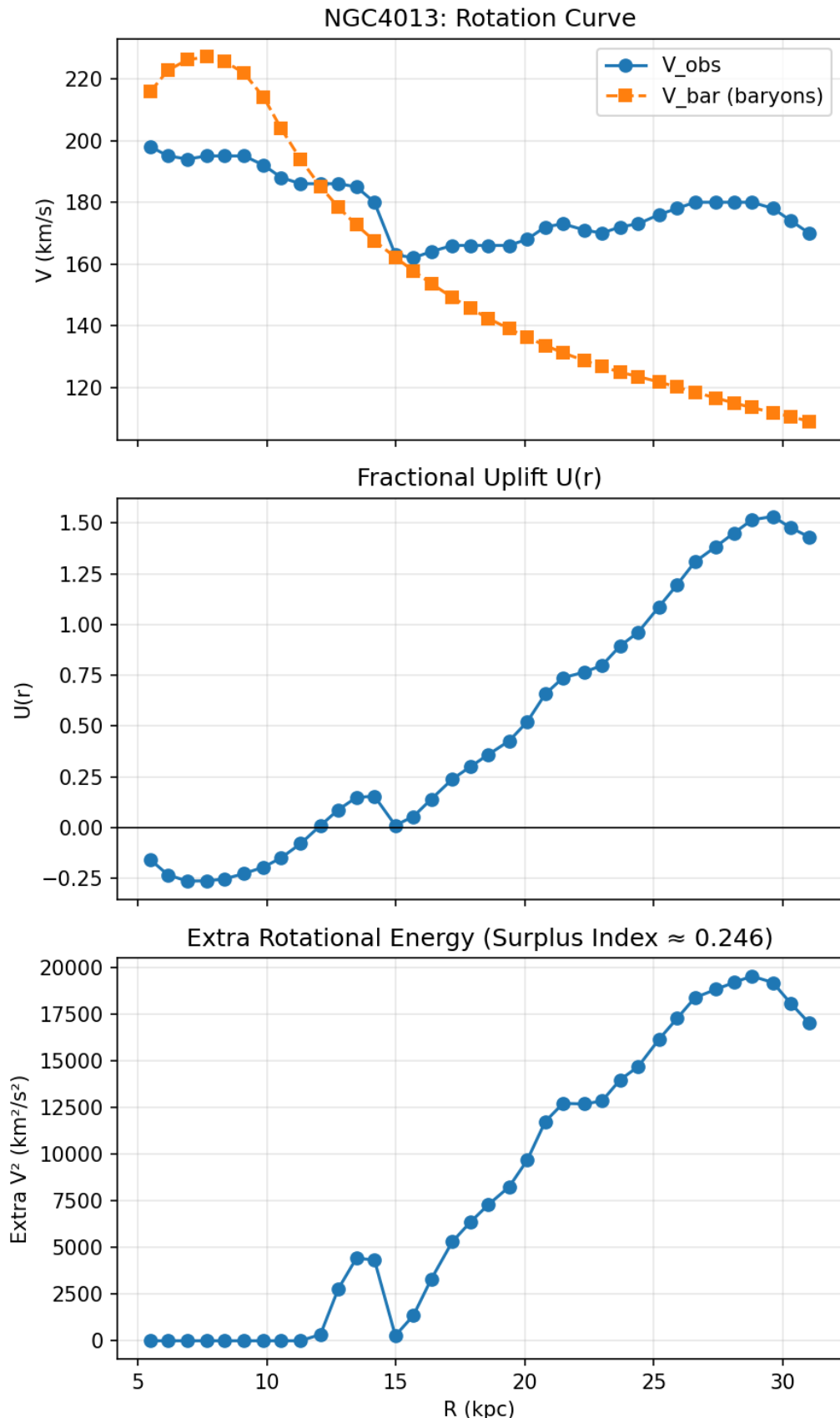


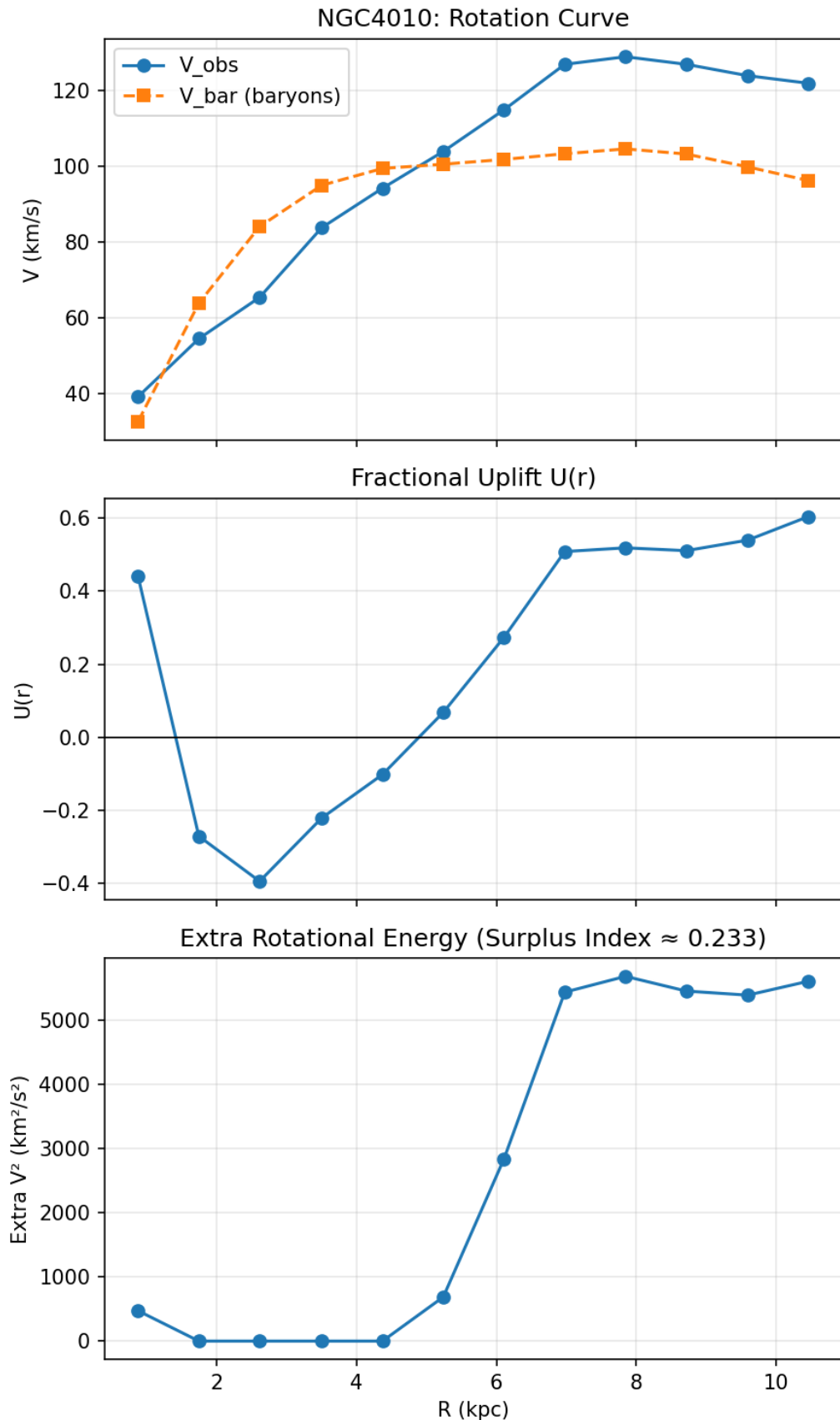


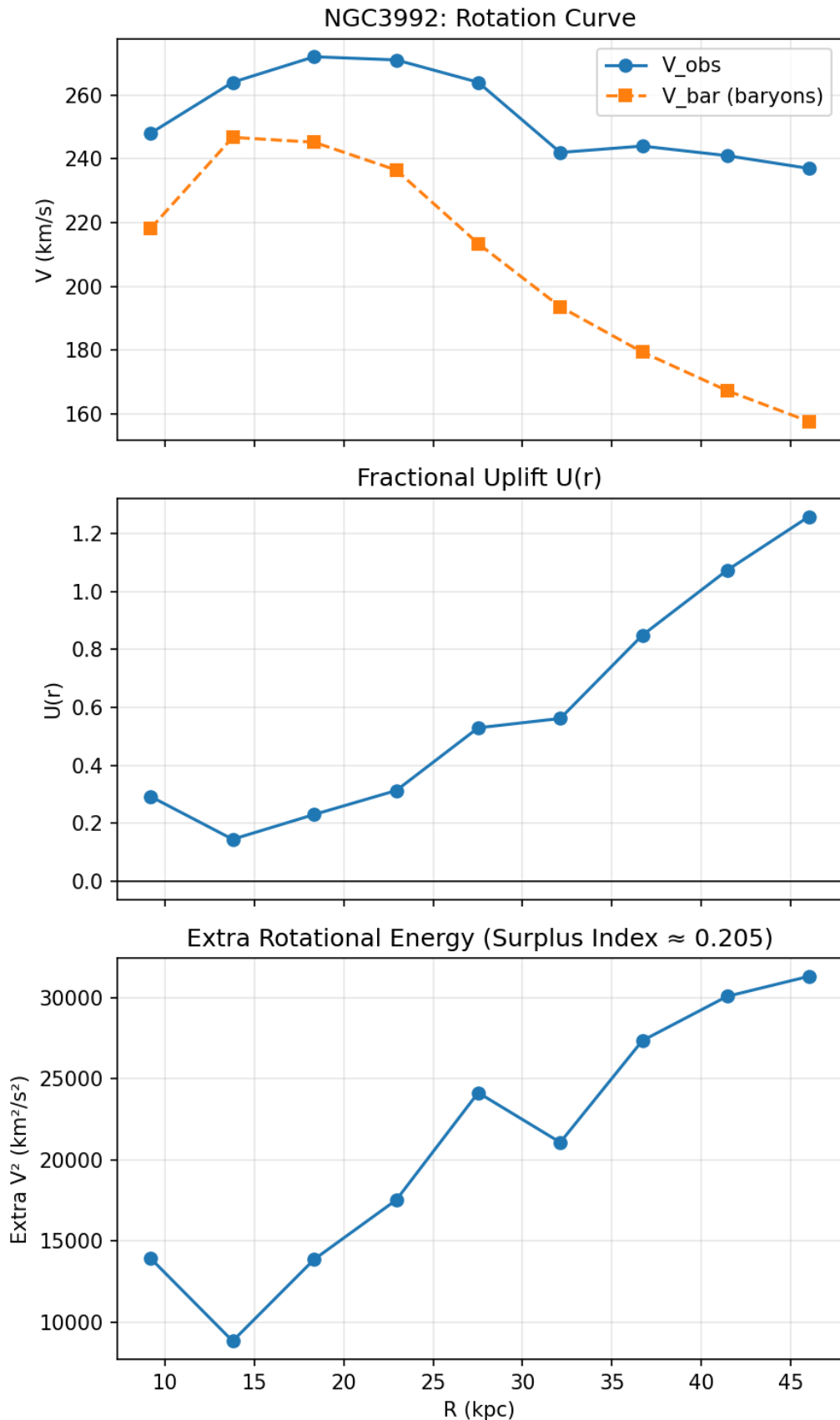
NGC4068: Rotation Curve

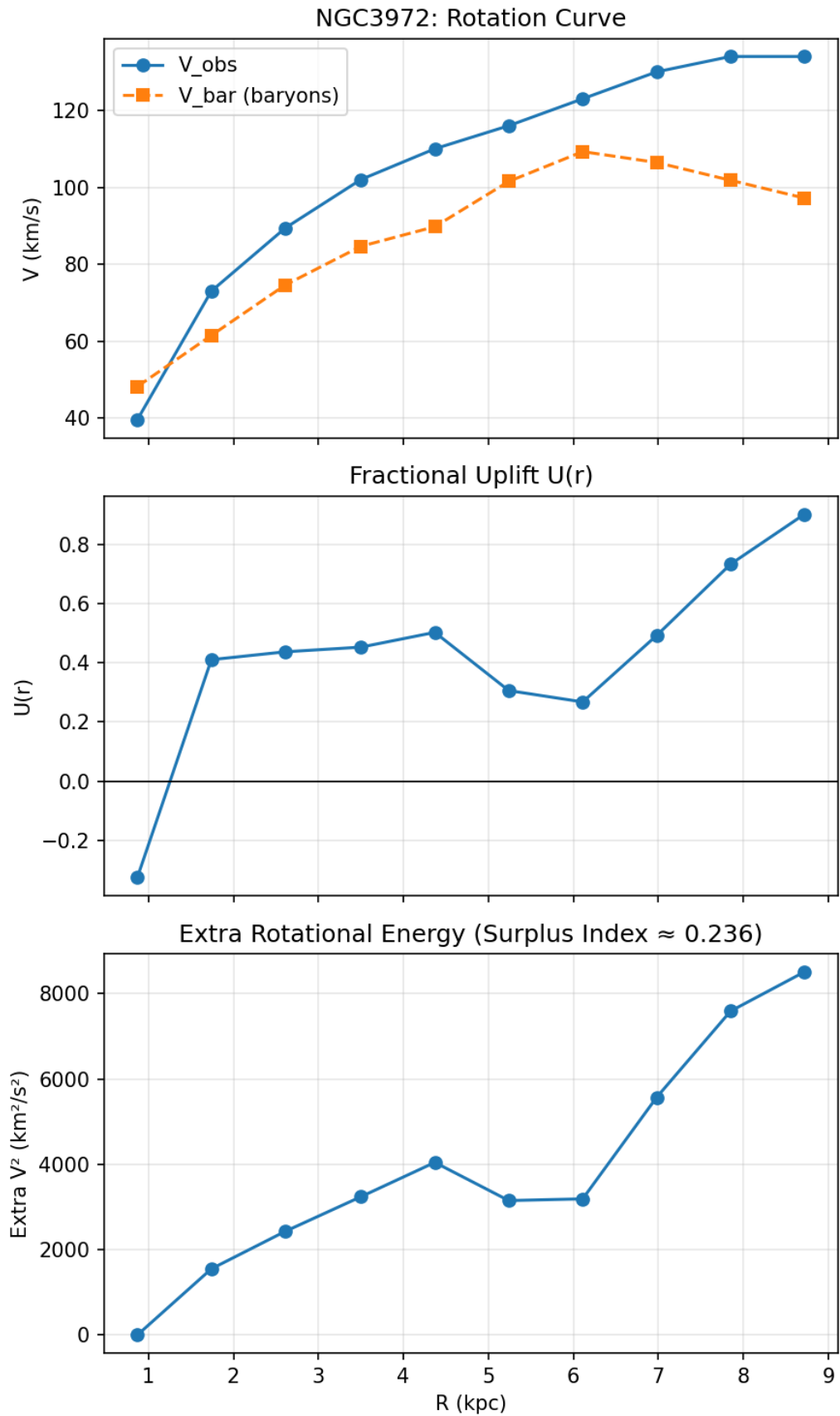
Fractional Uplift $U(r)$ Extra Rotational Energy (Surplus Index ≈ 0.254)

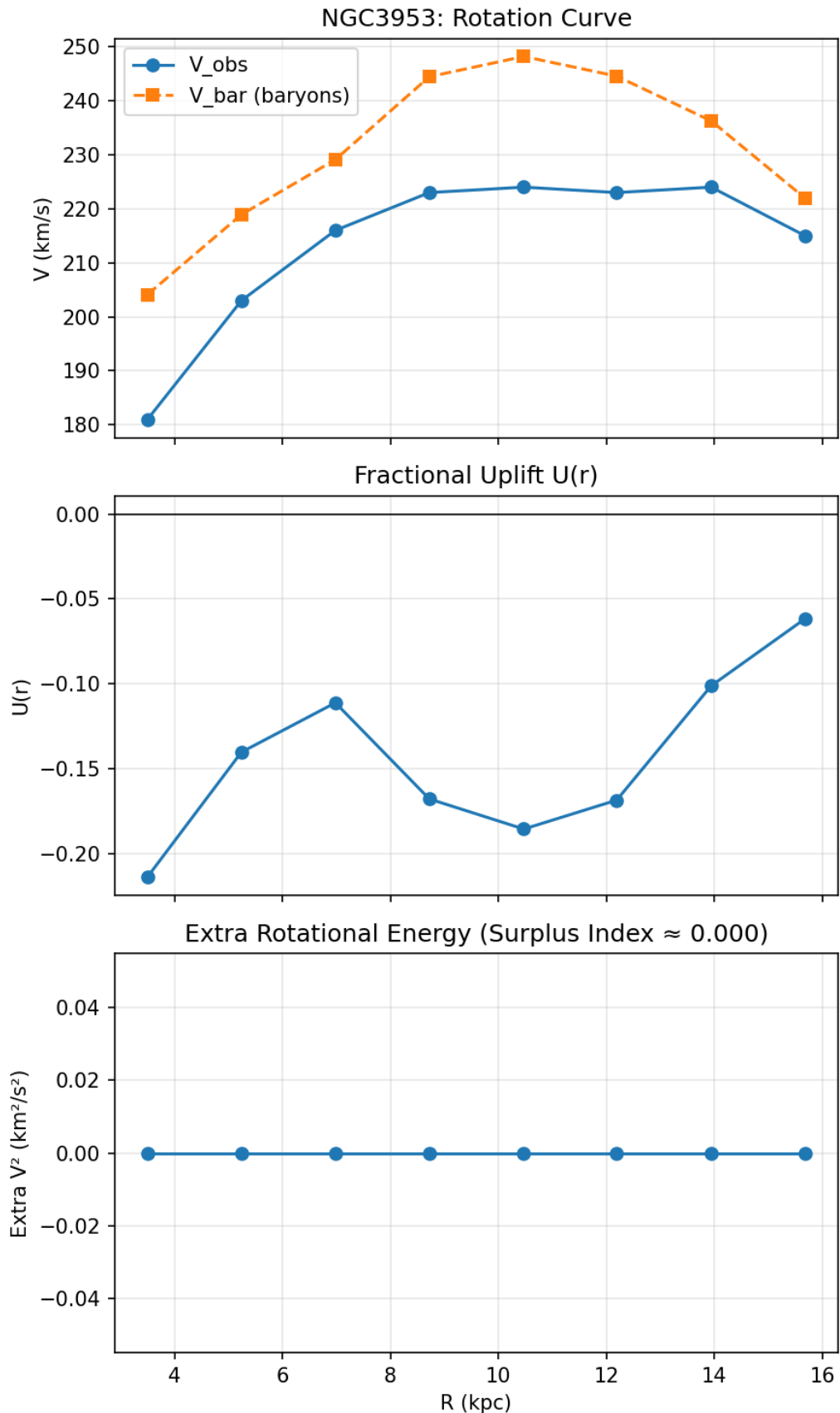


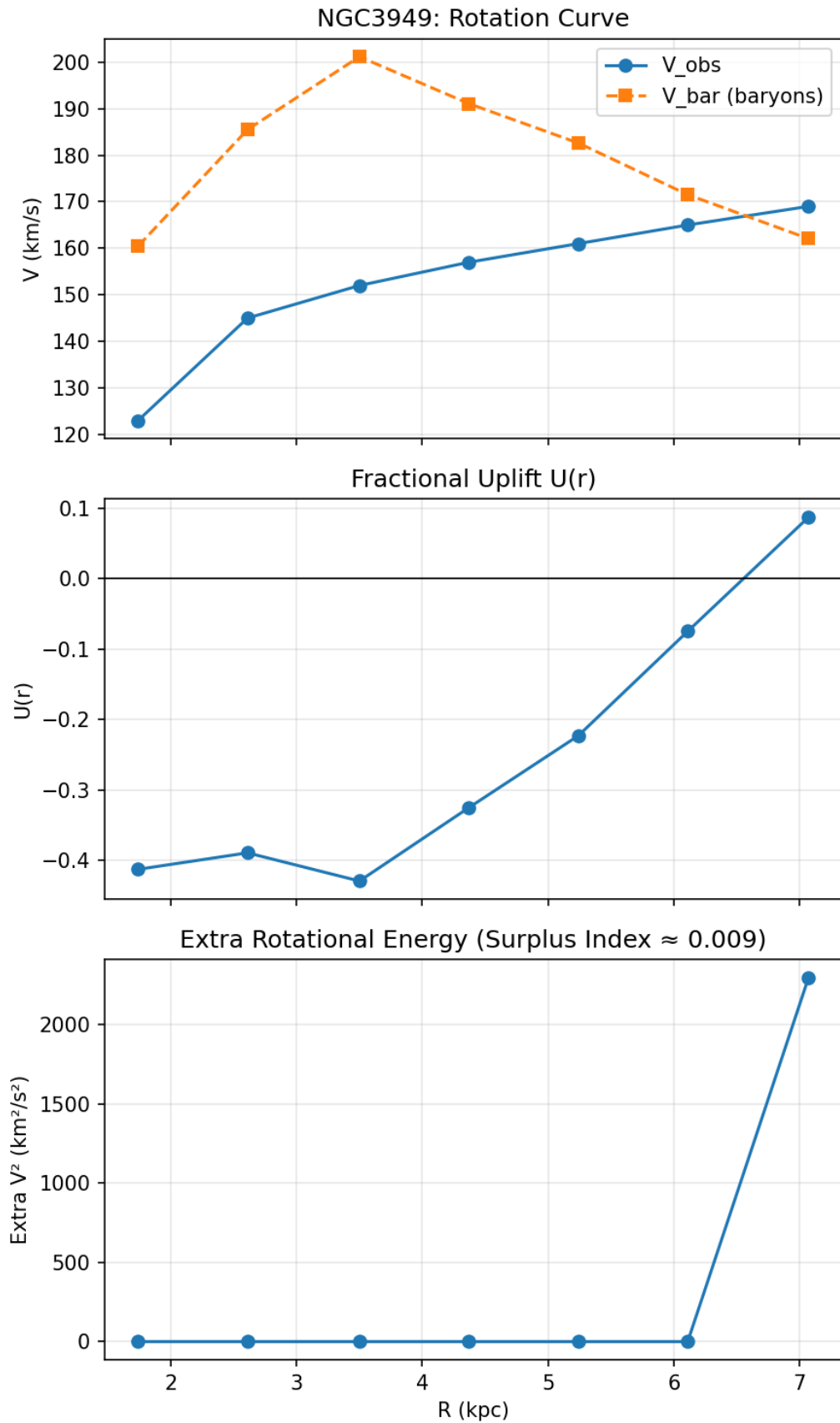


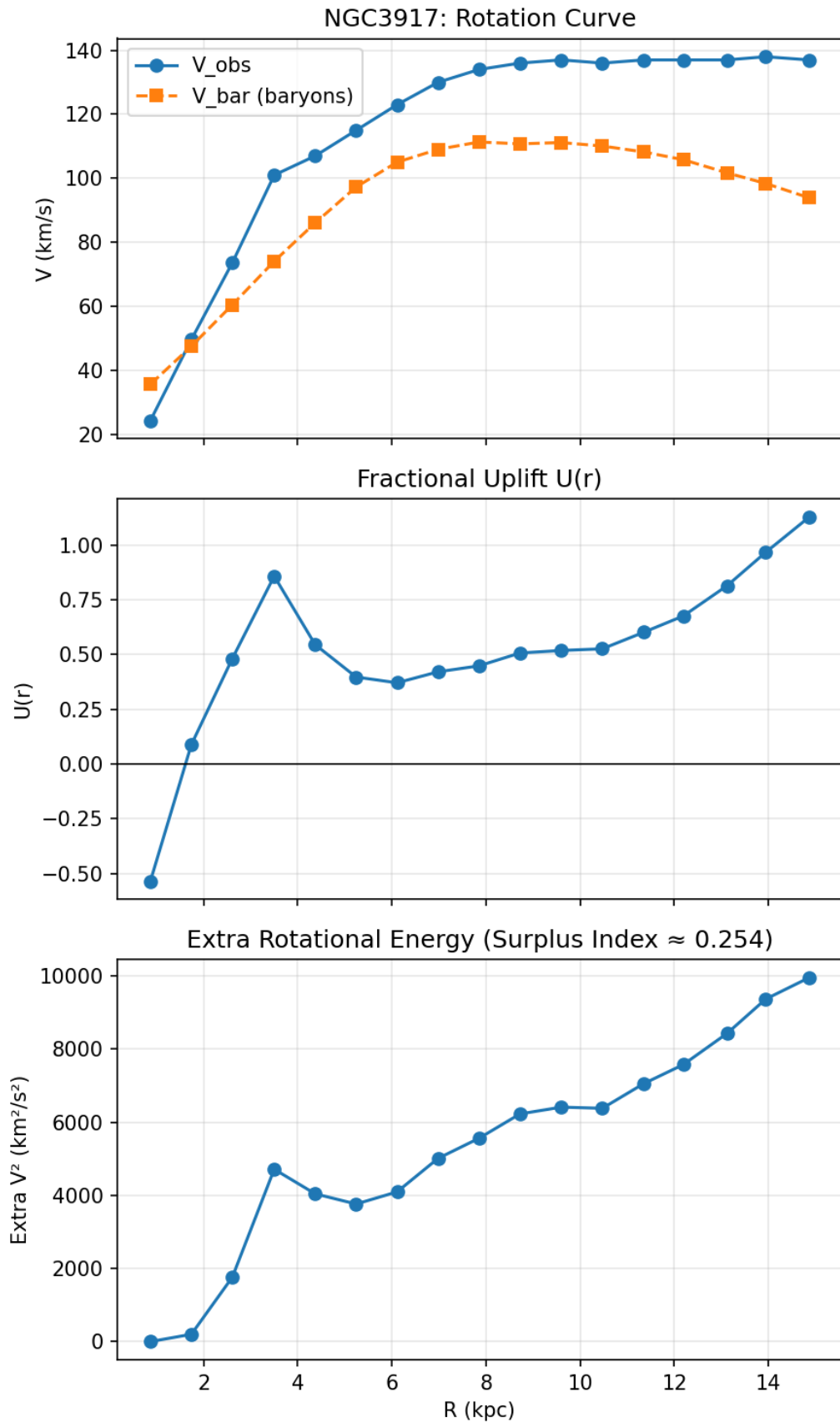


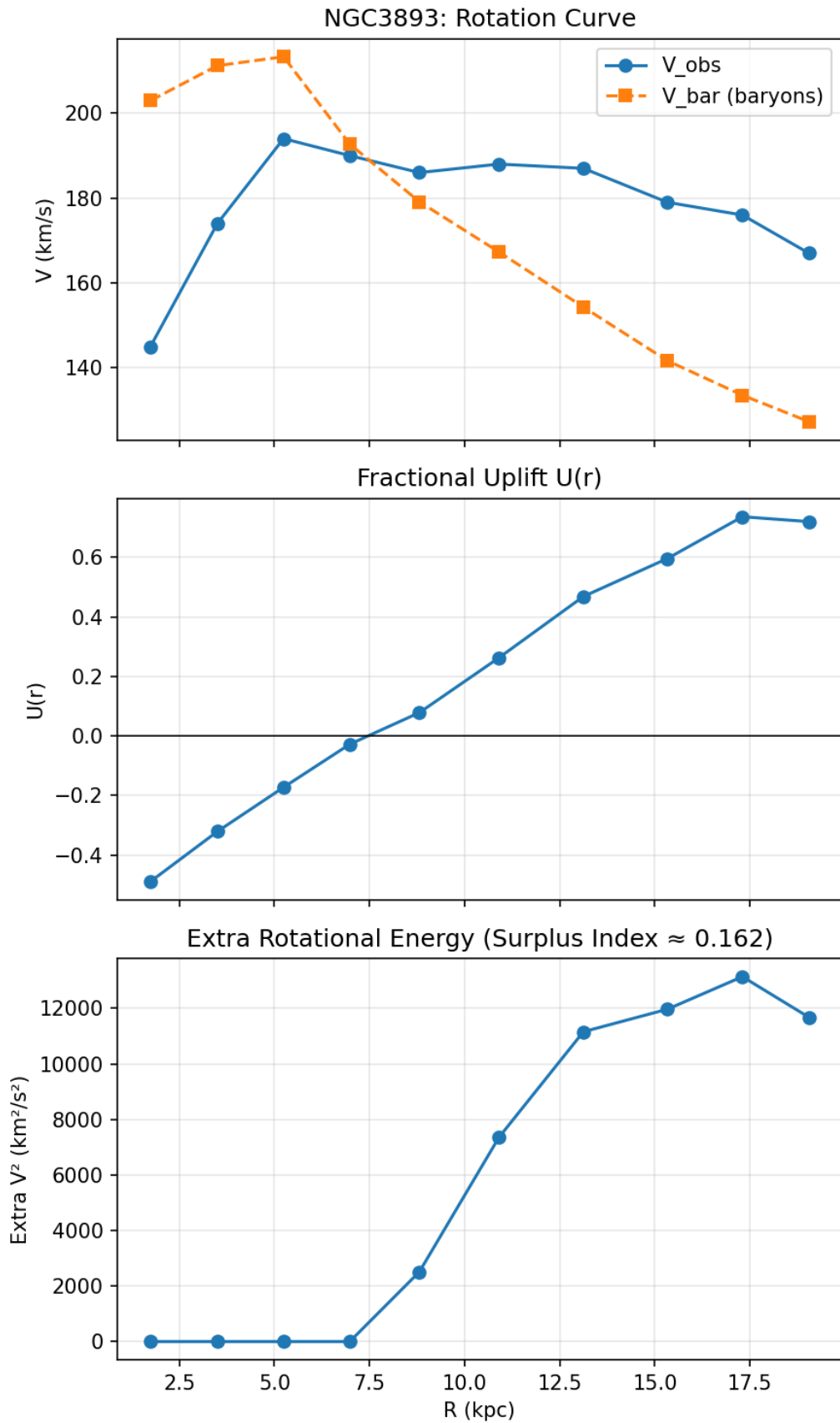


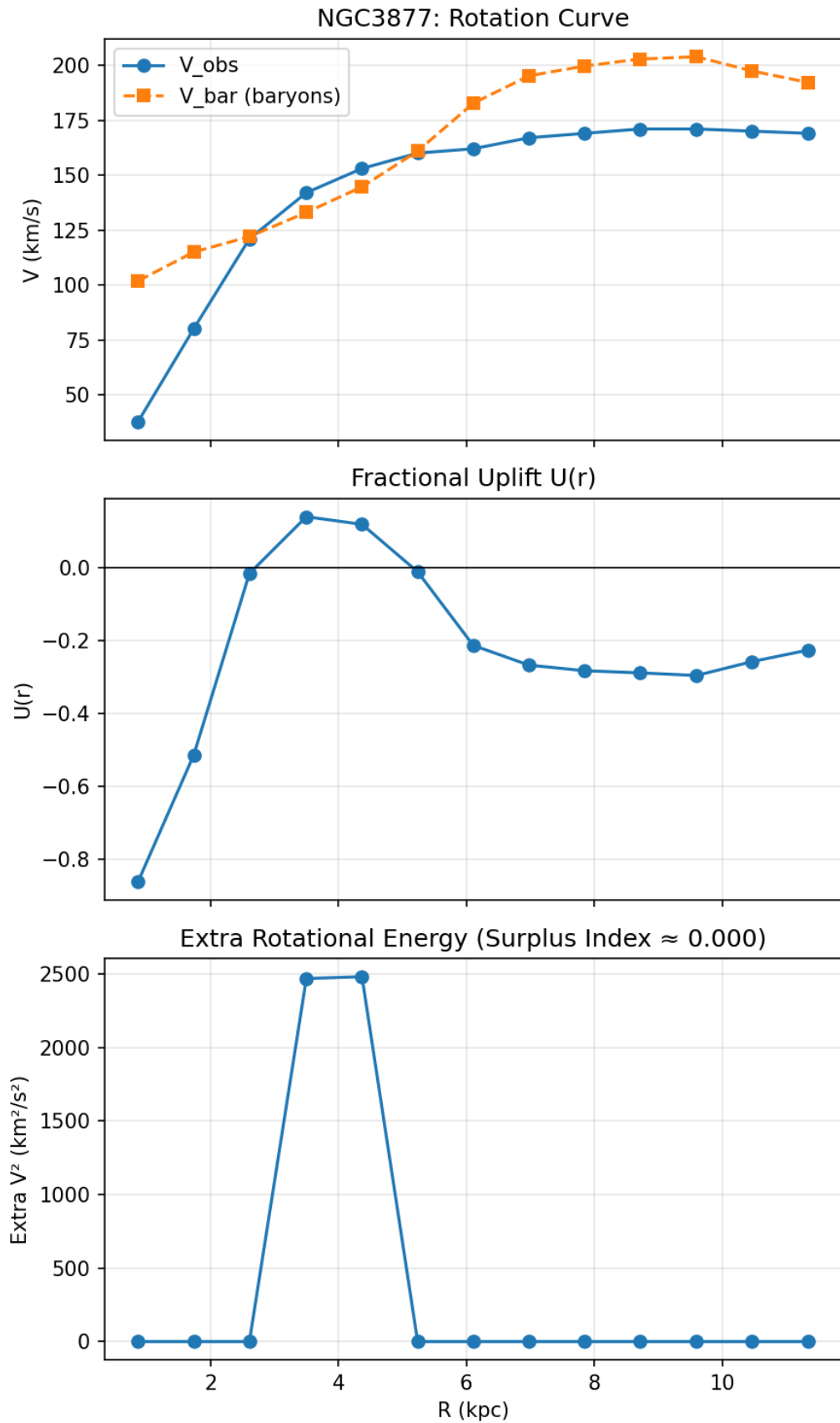


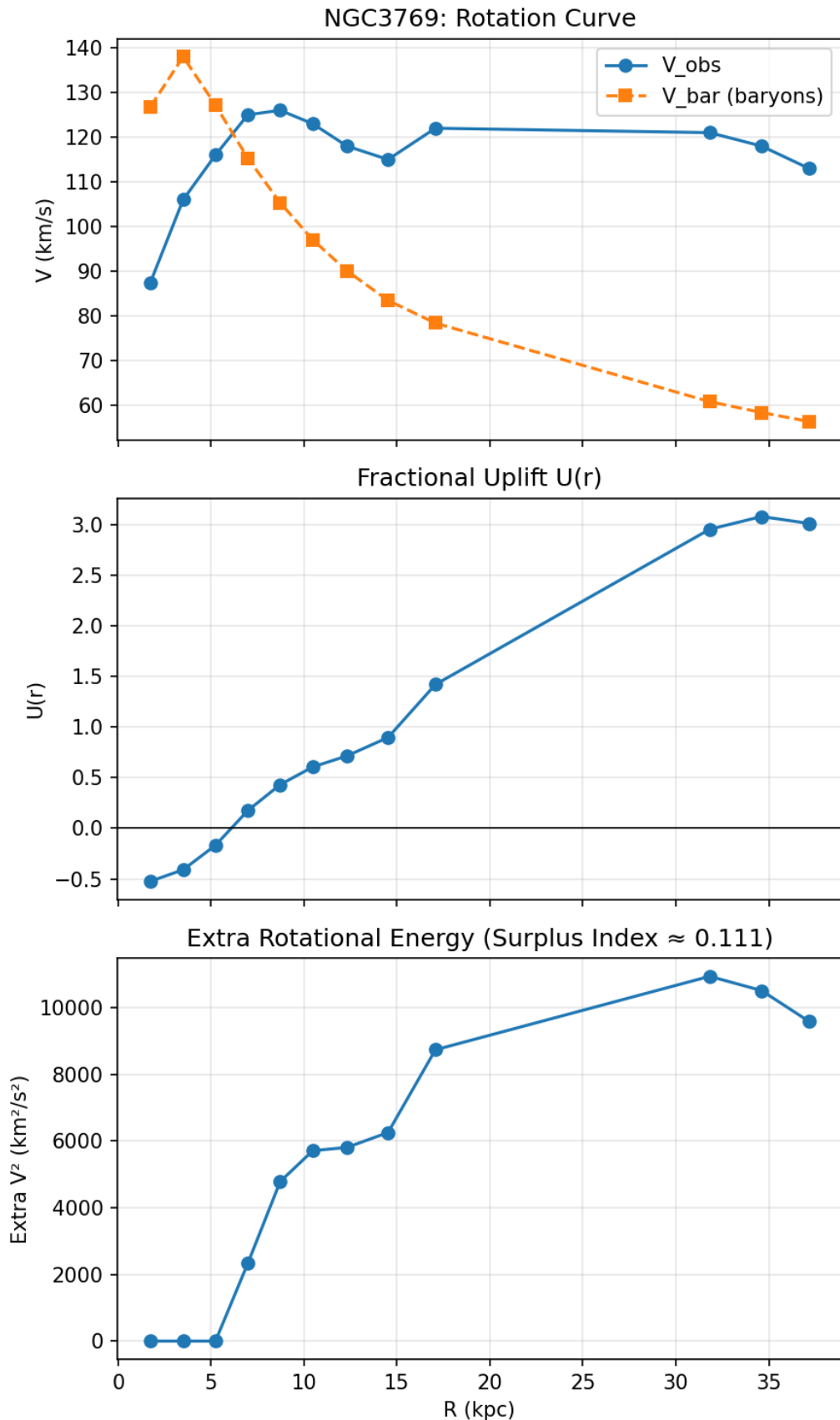


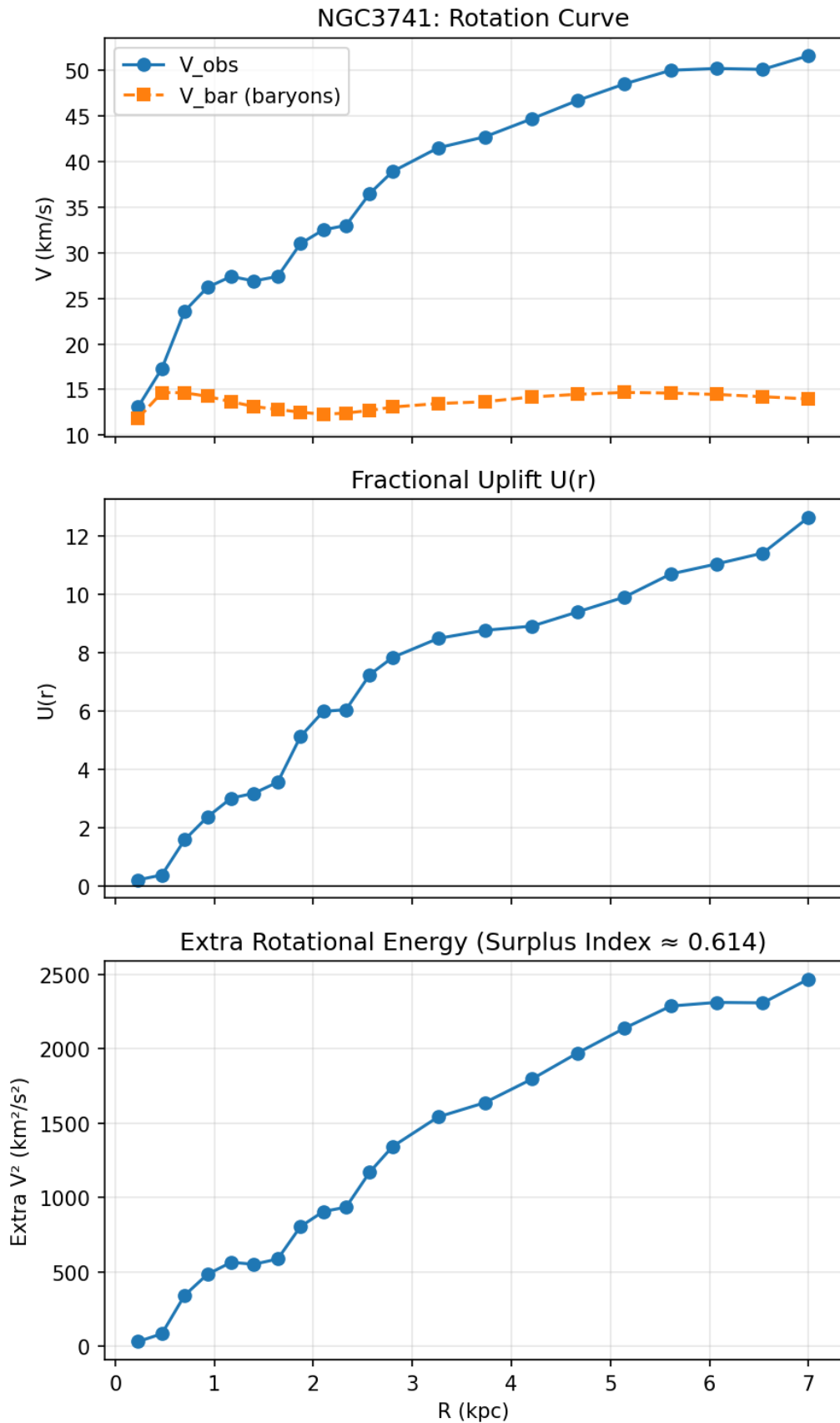


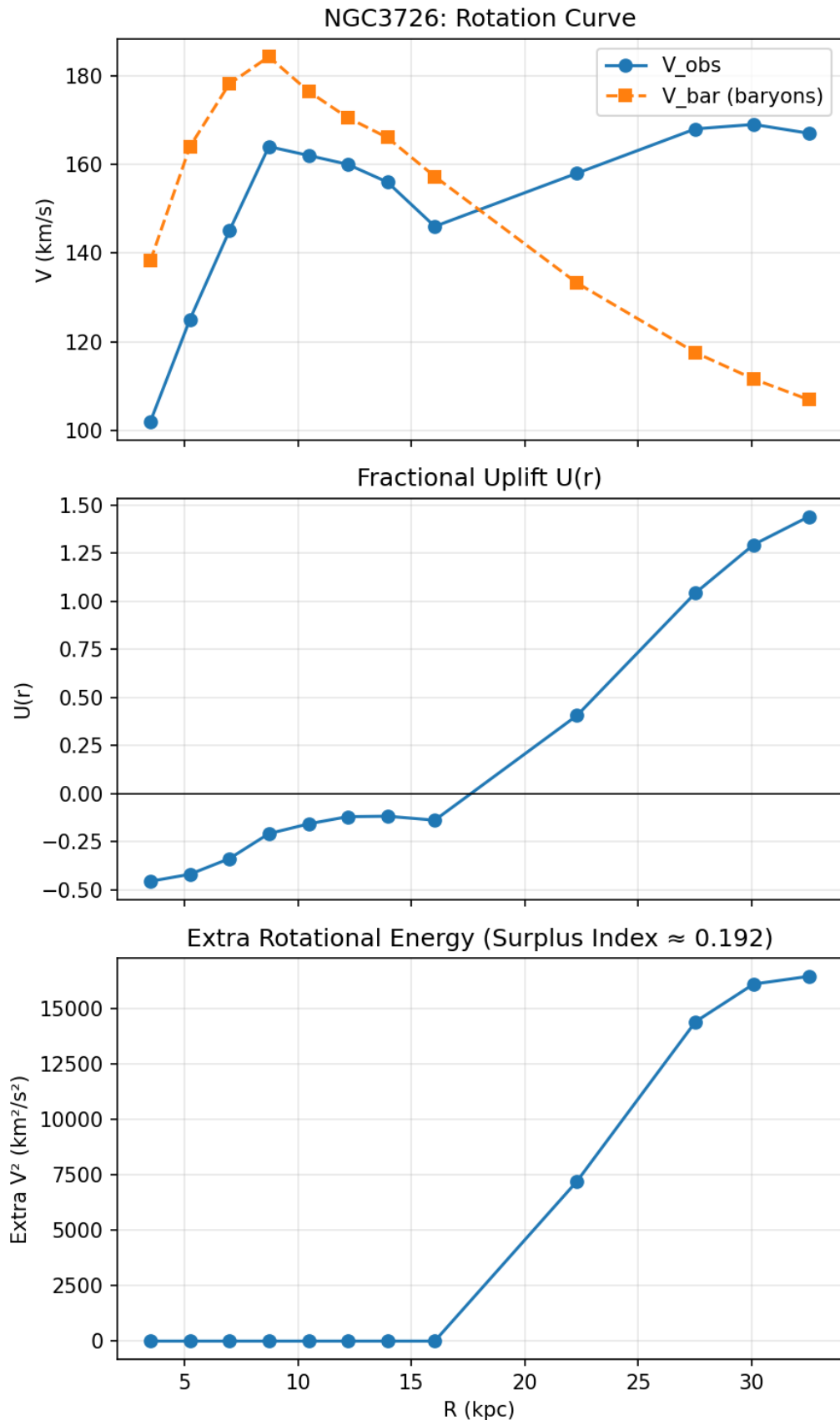


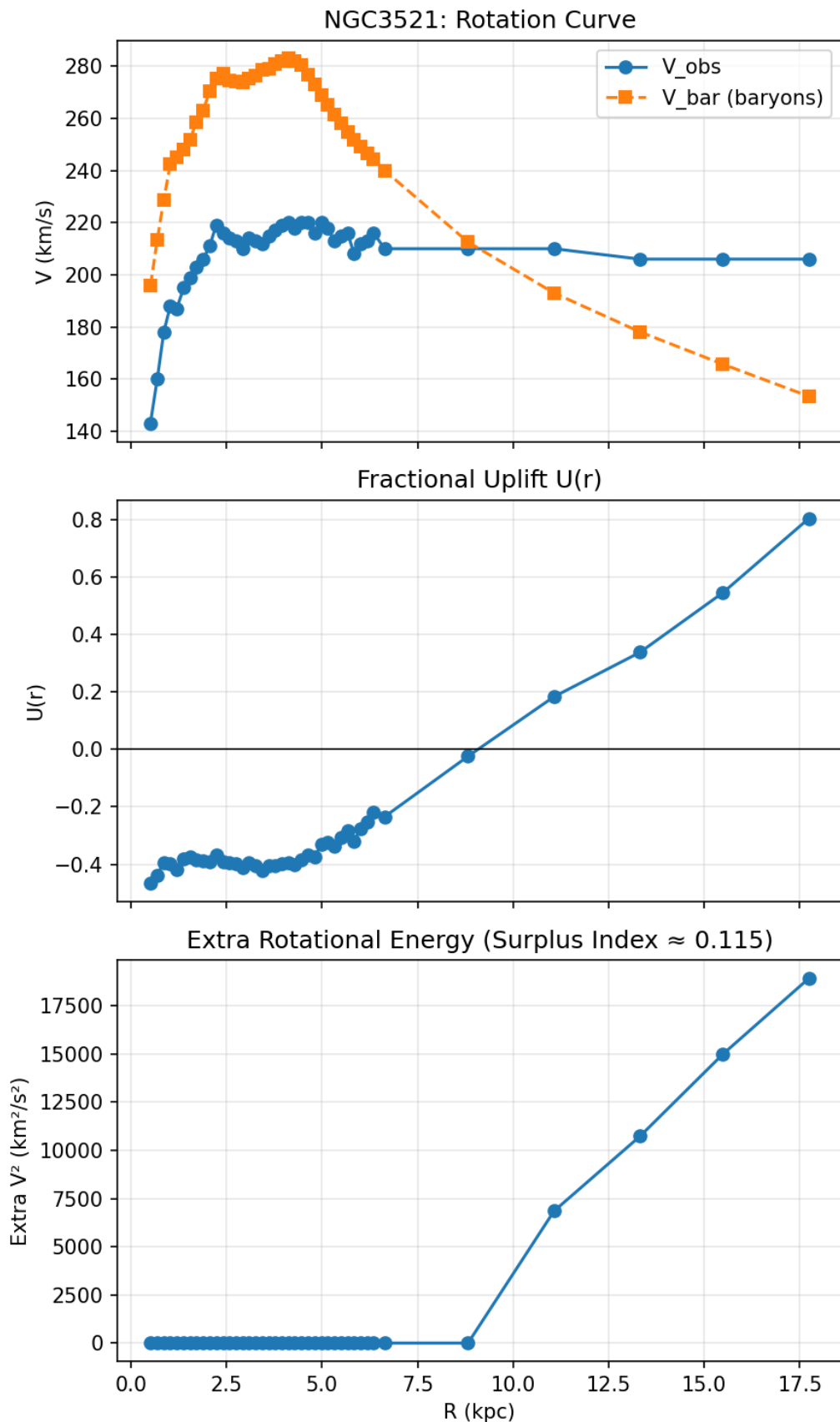


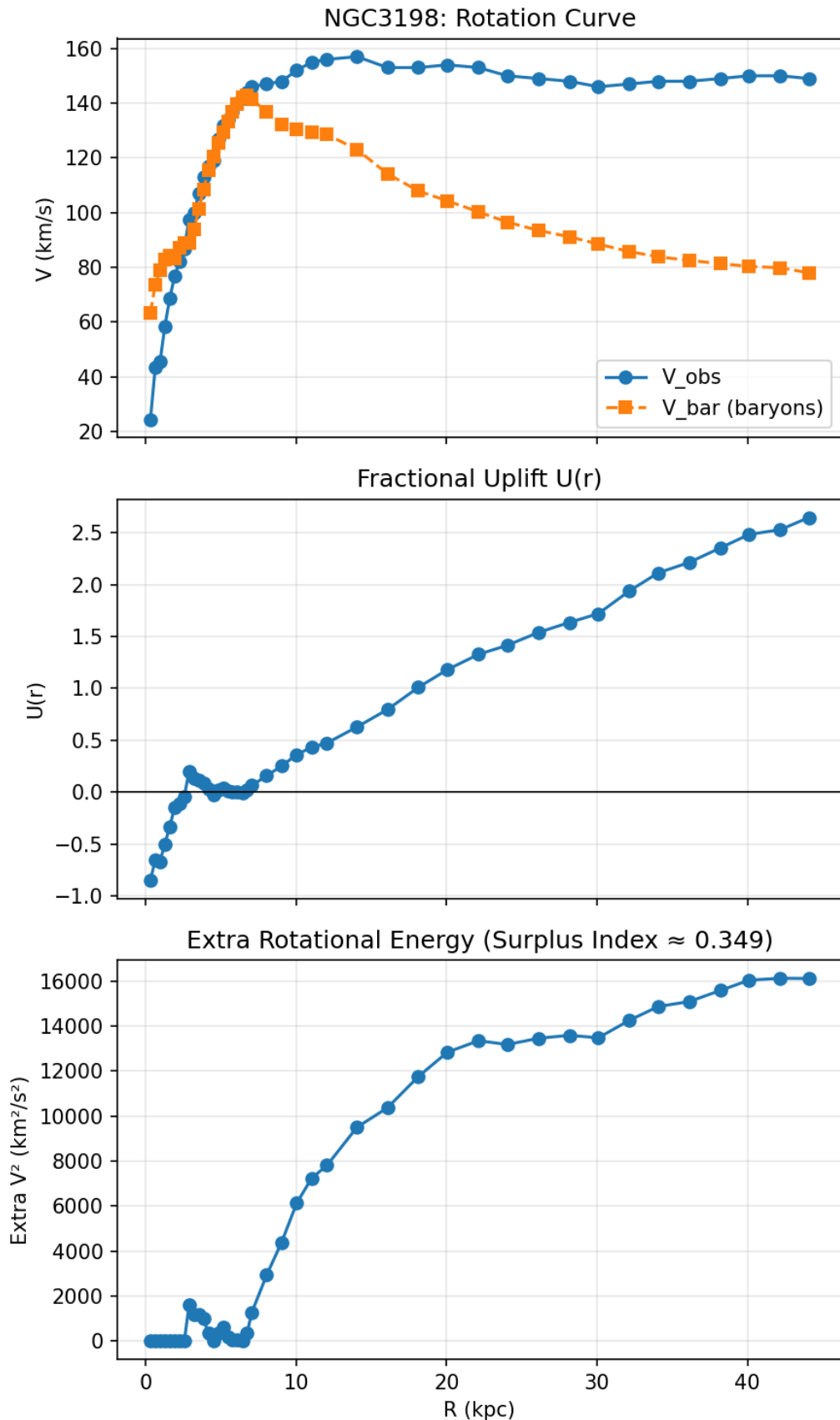


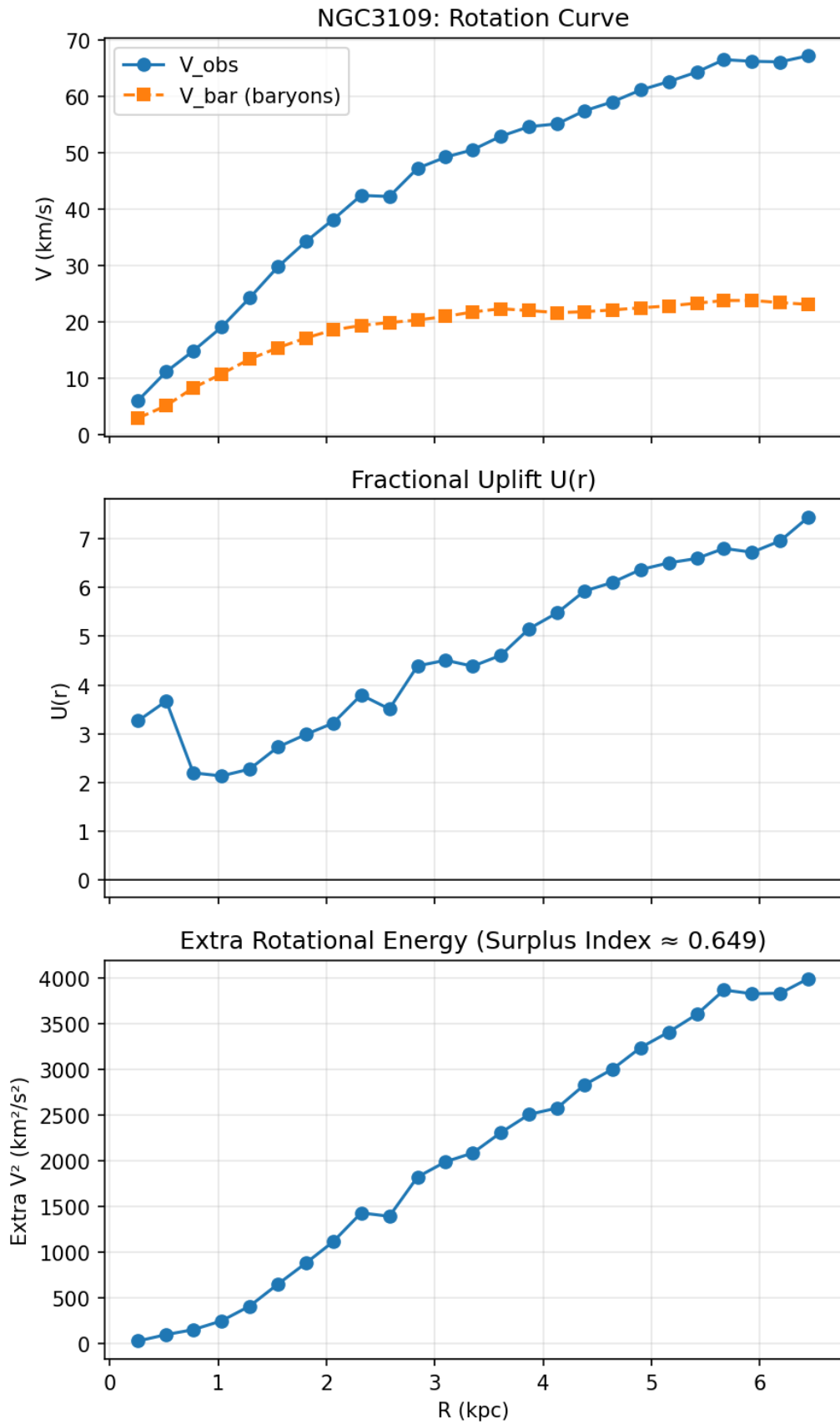


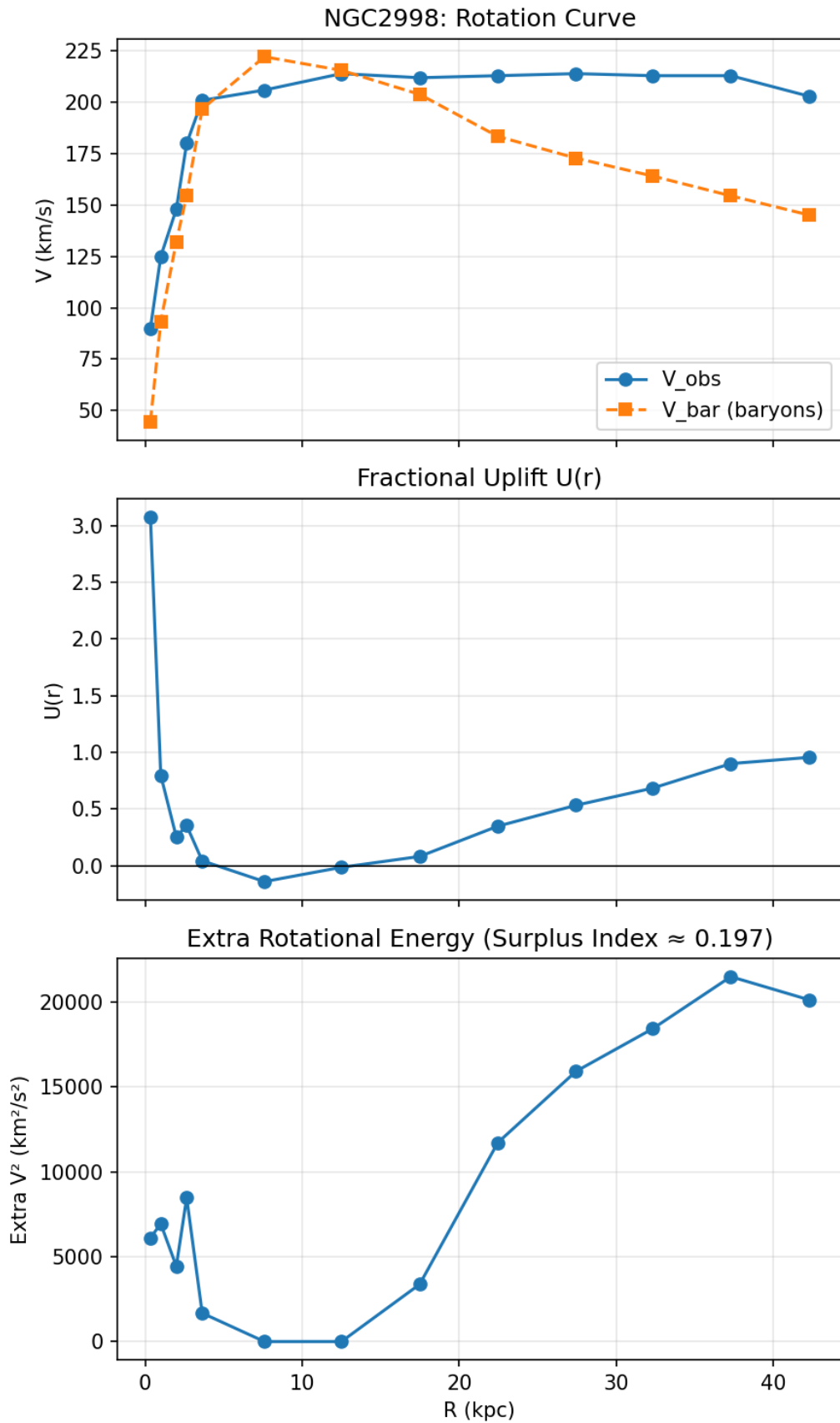


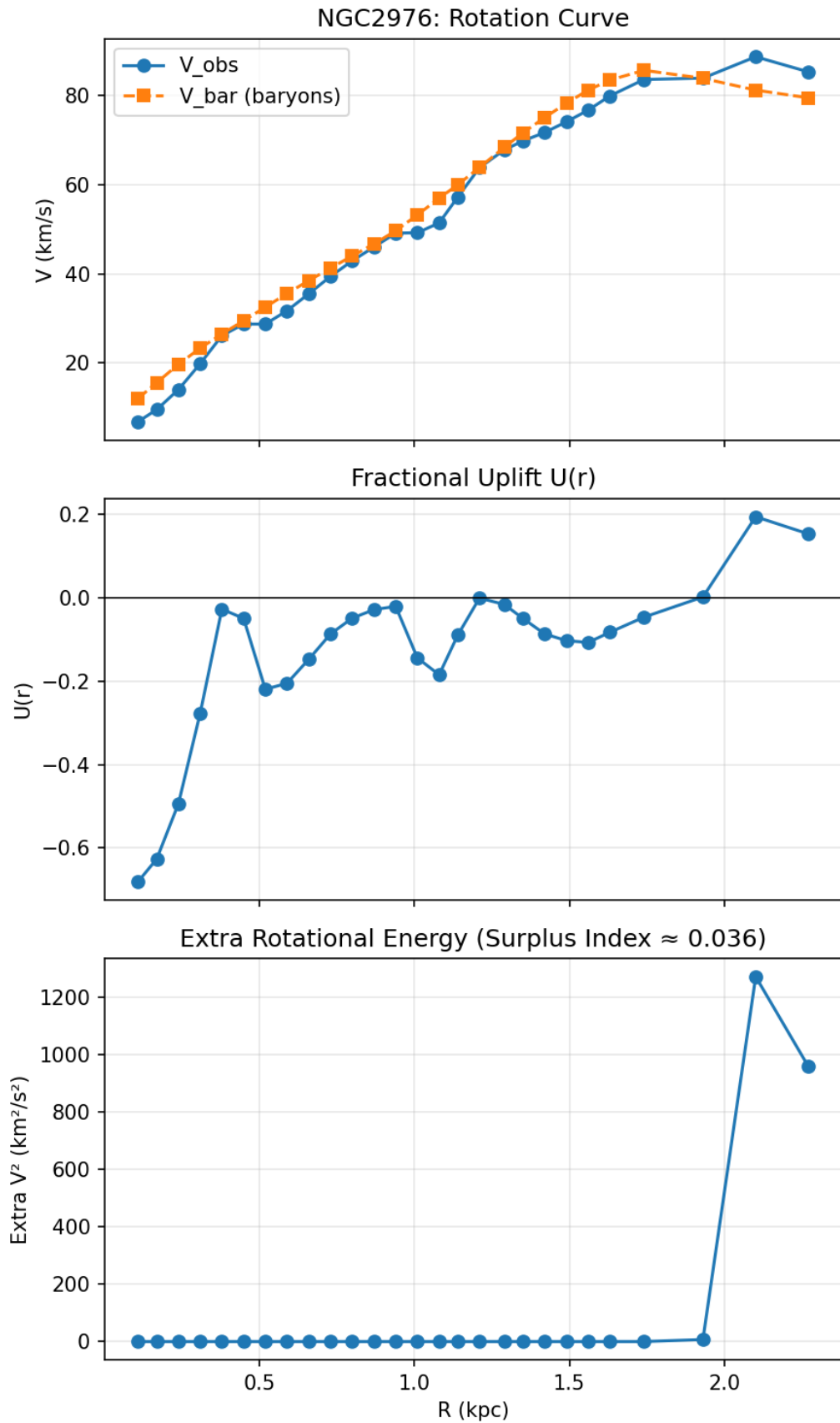


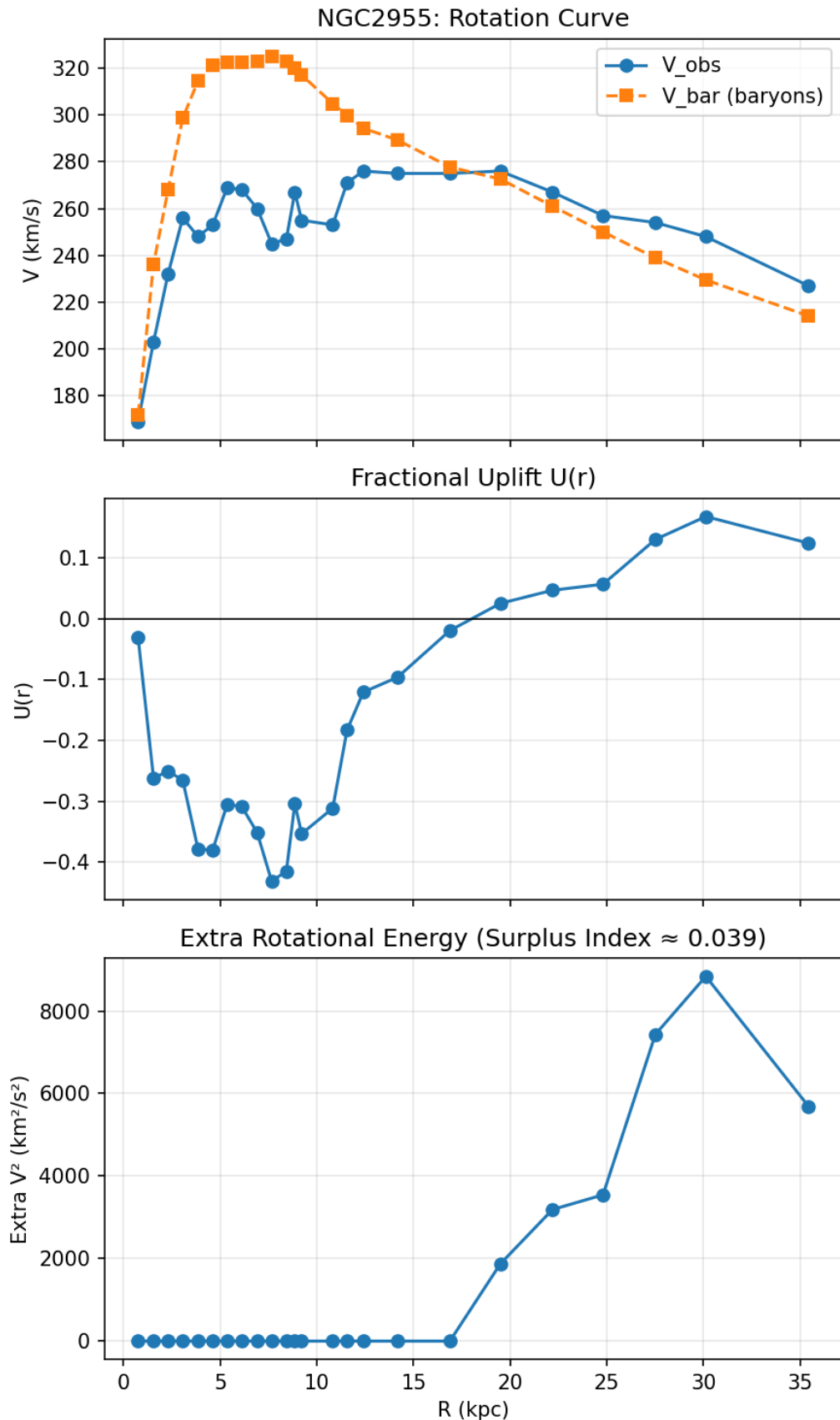


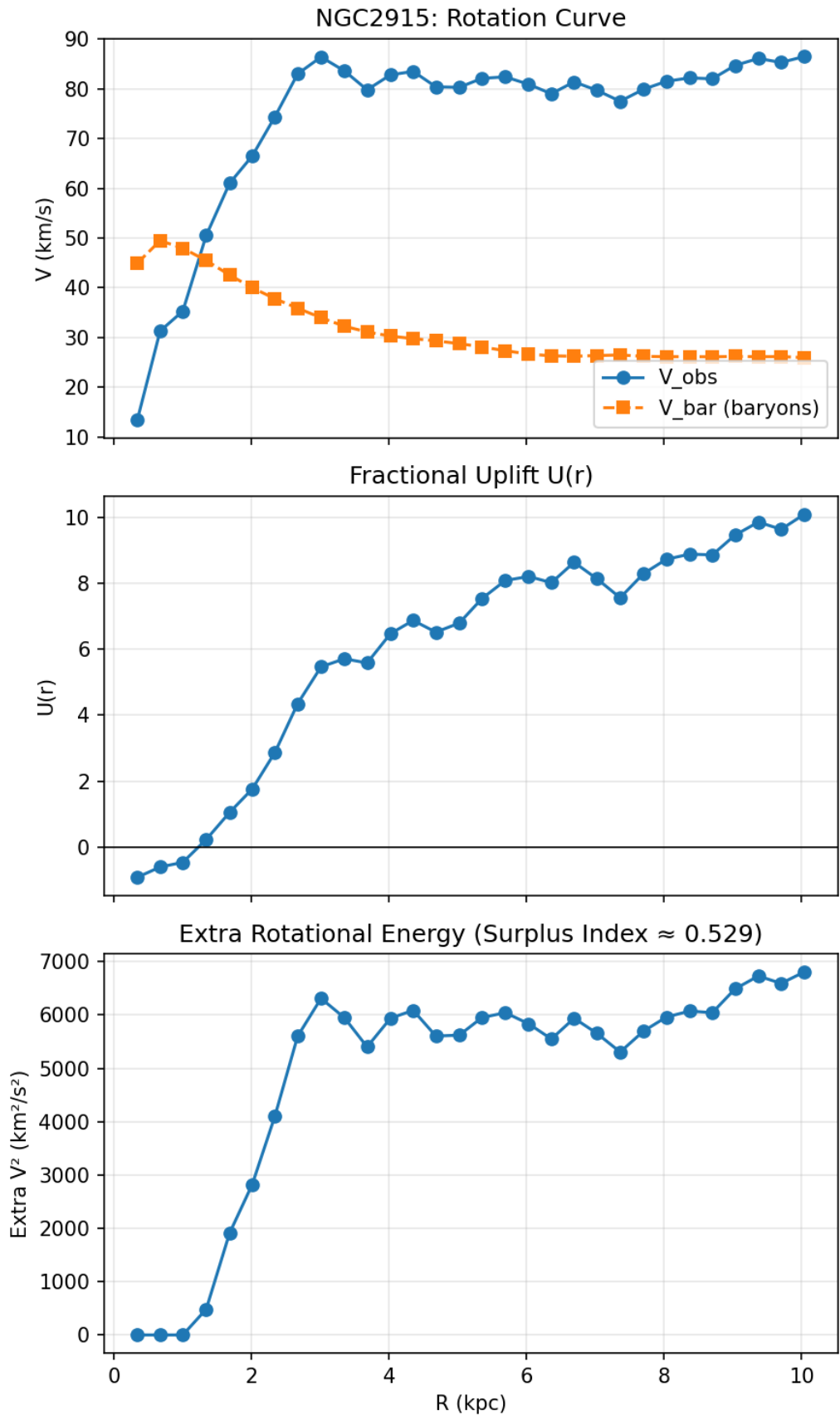


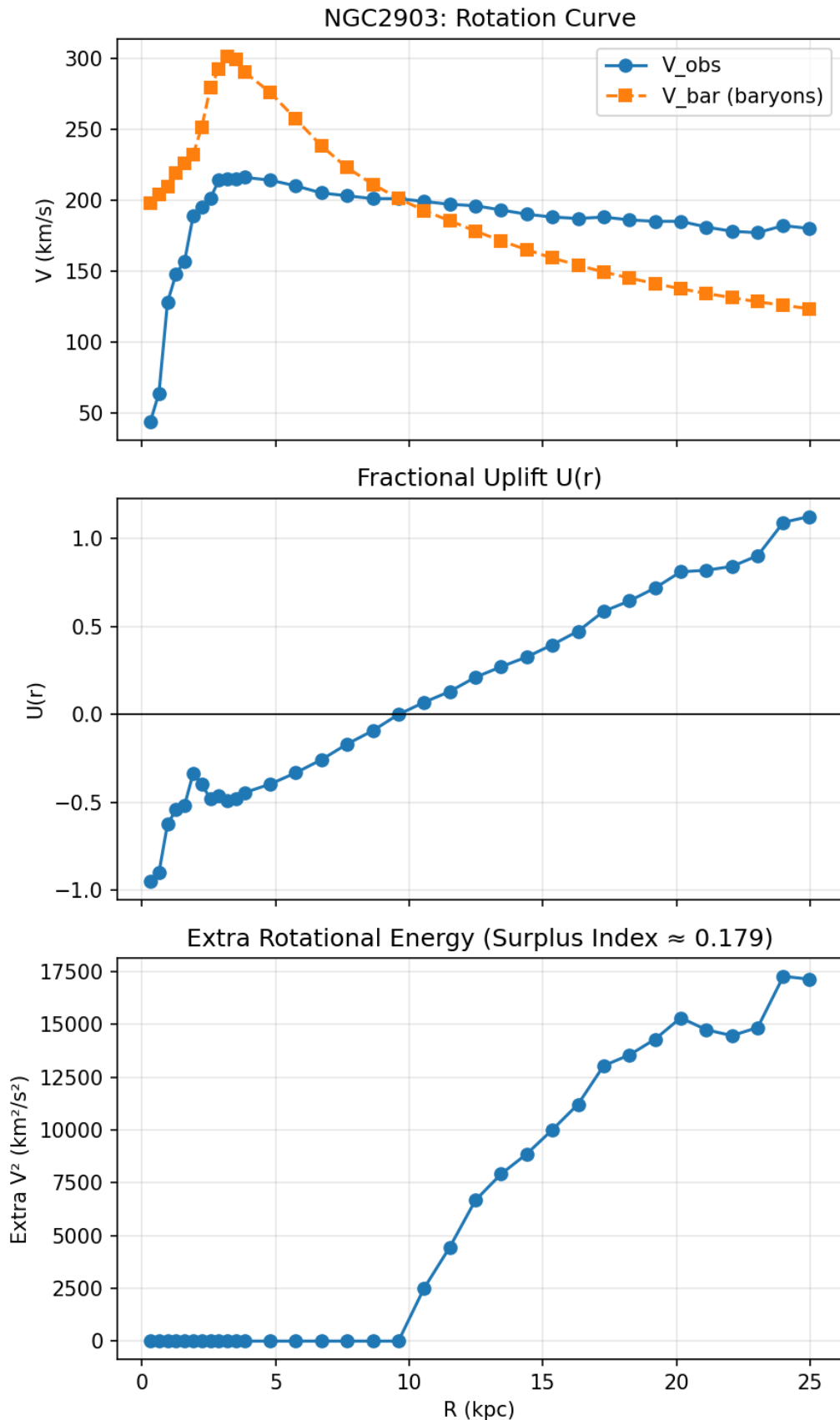


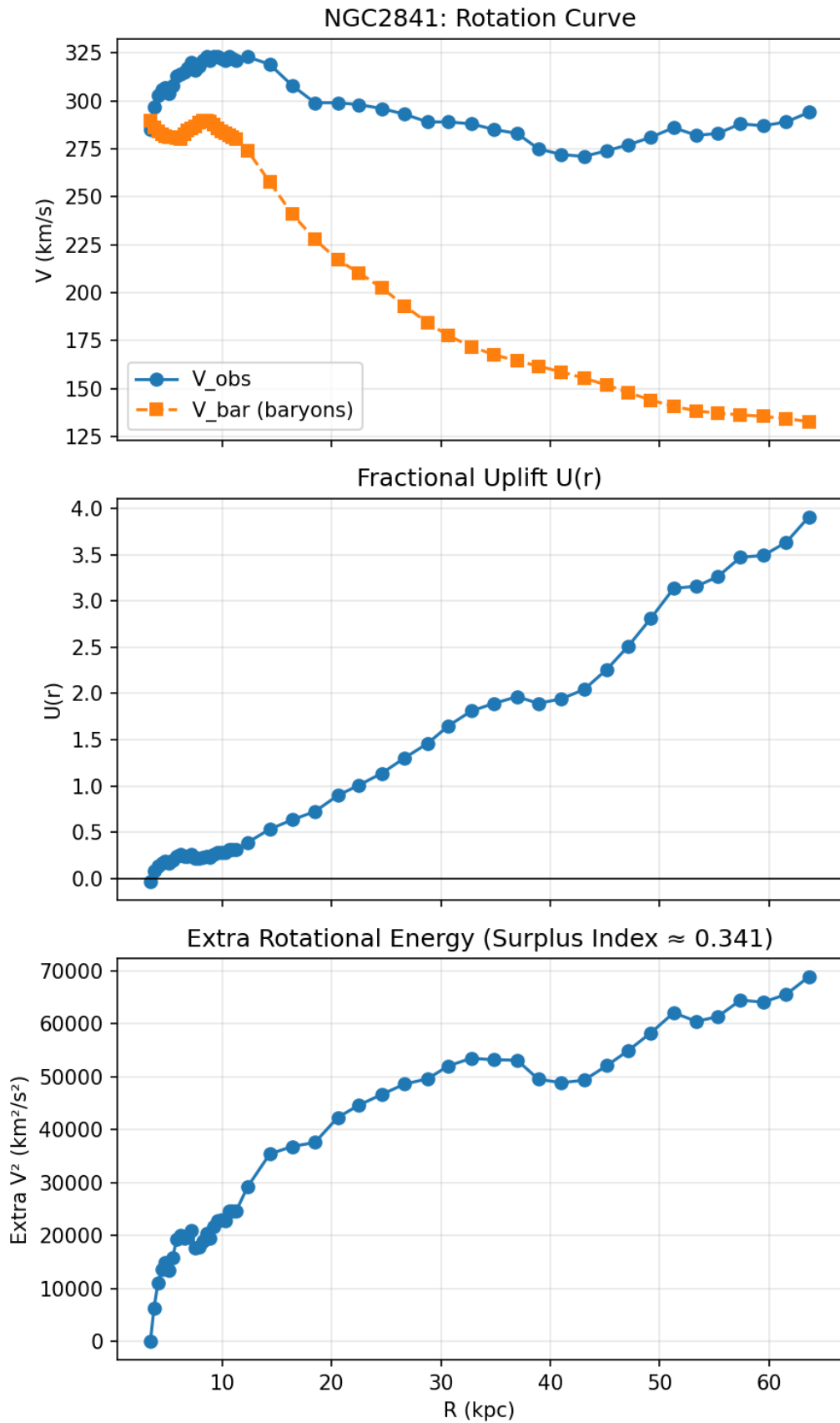


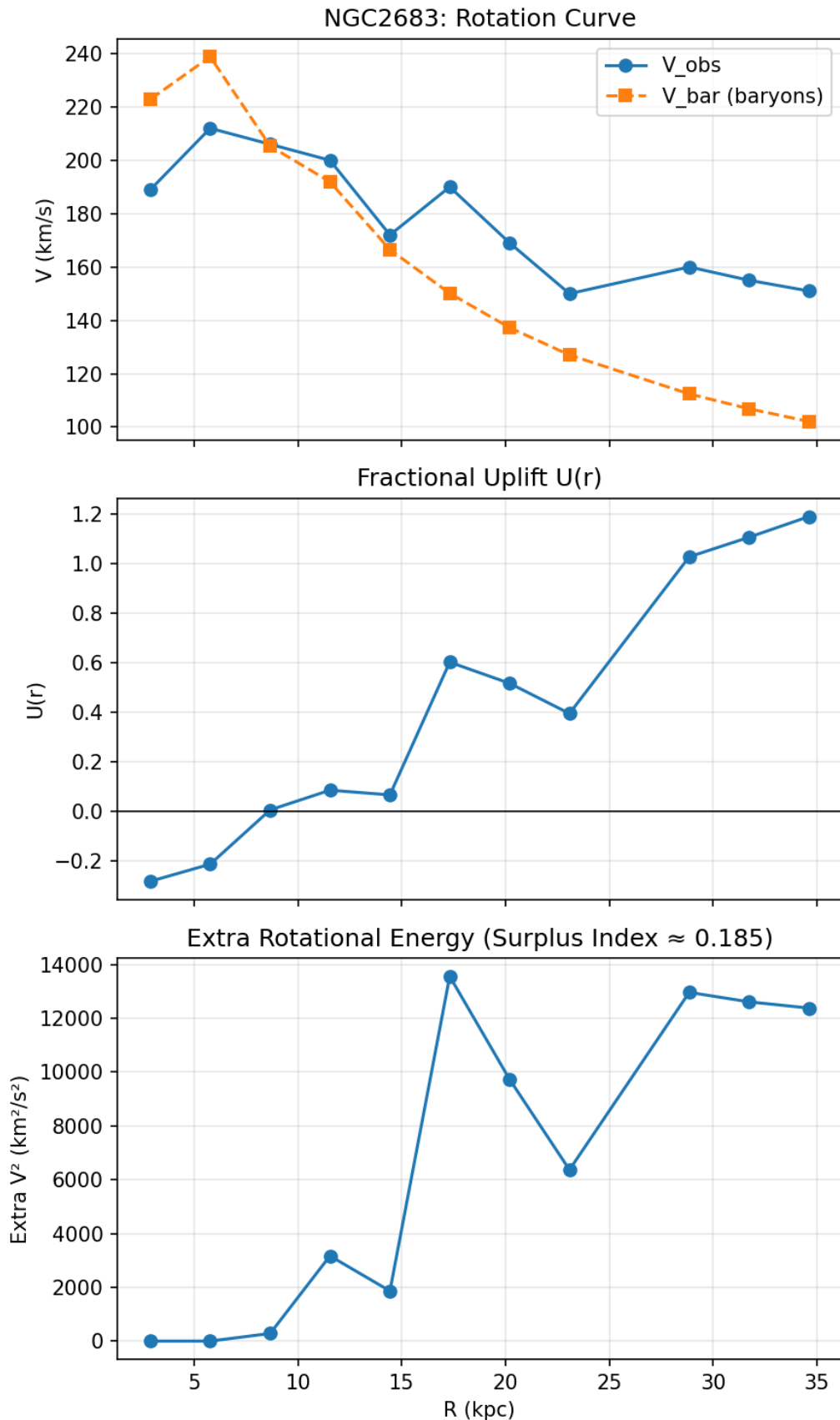


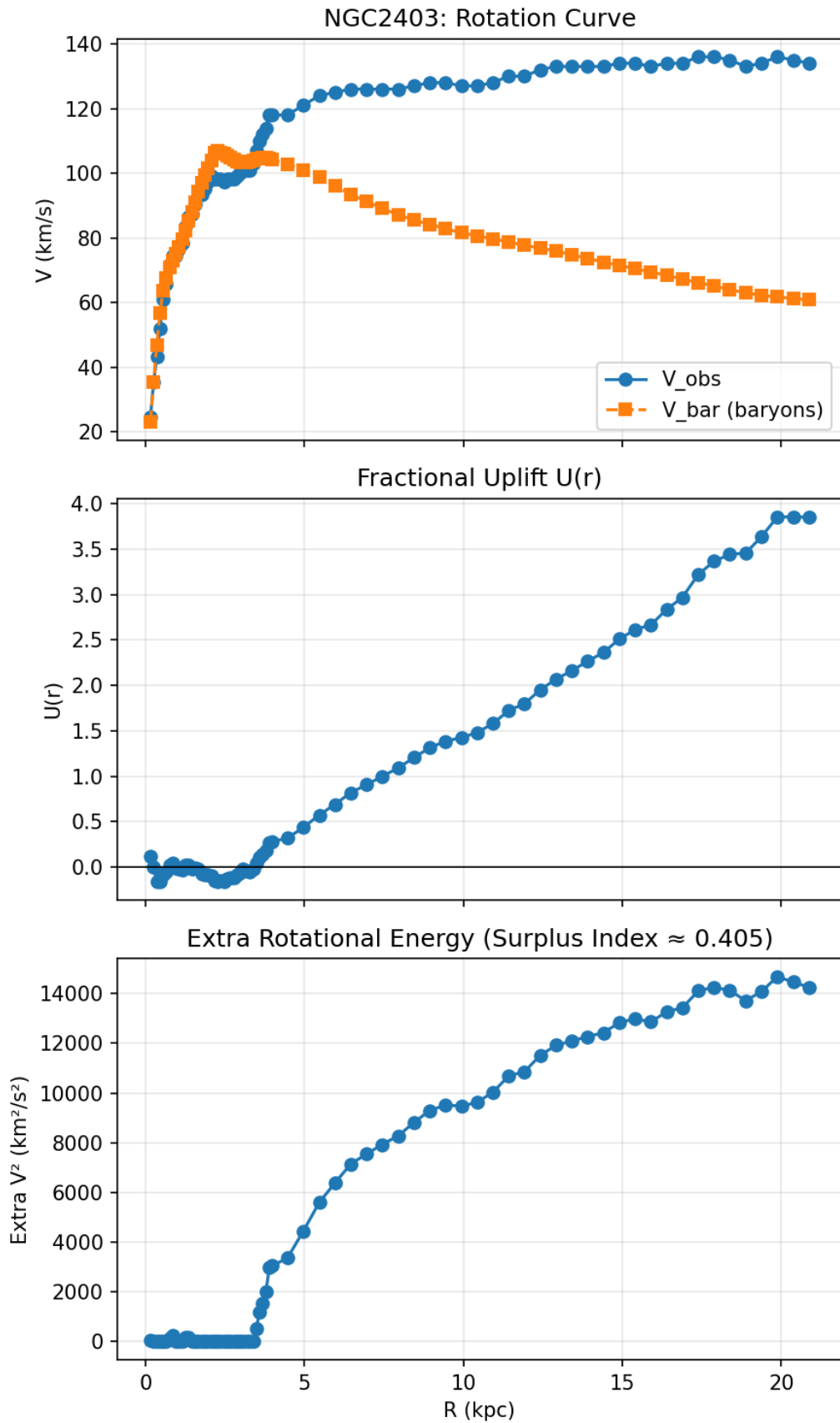


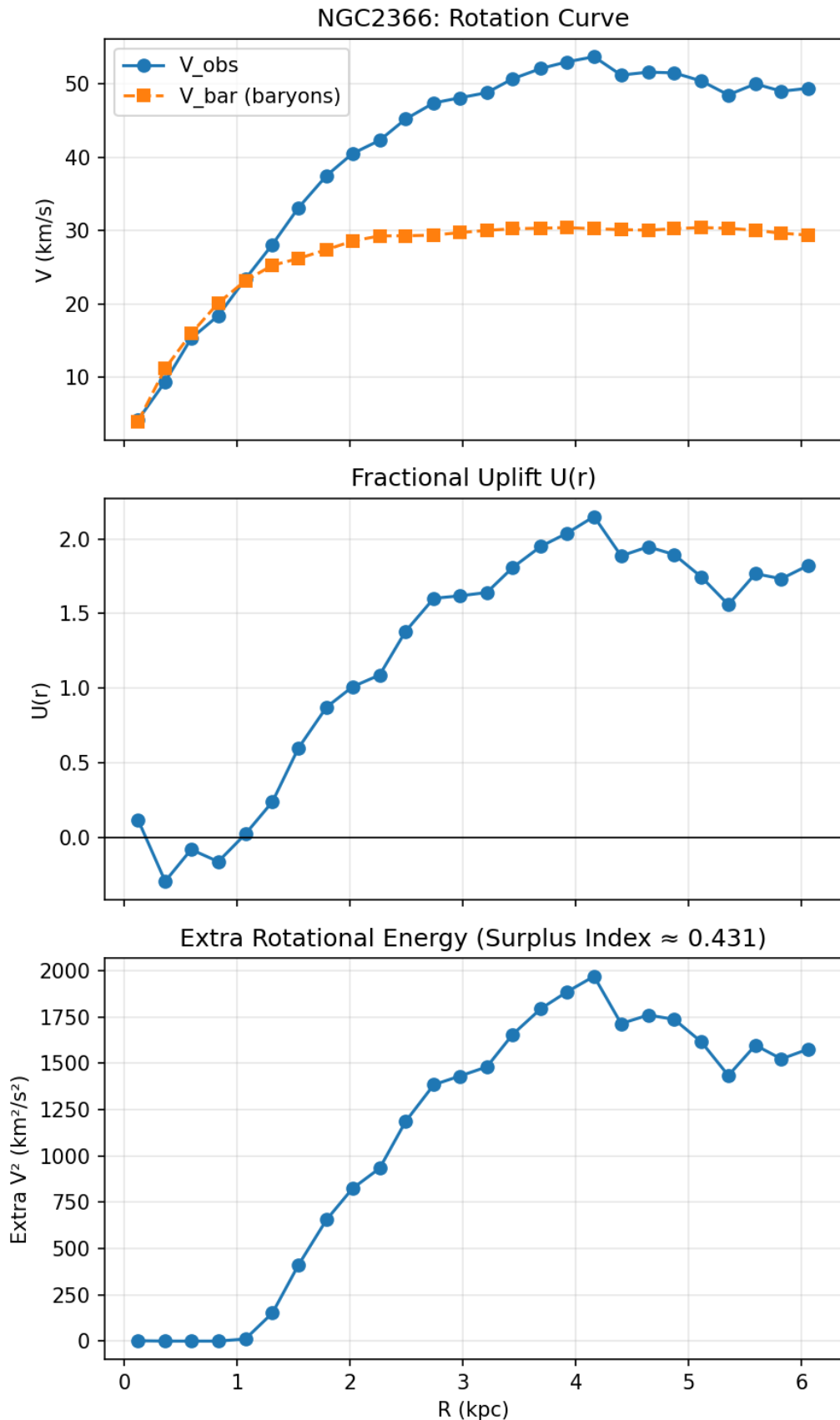


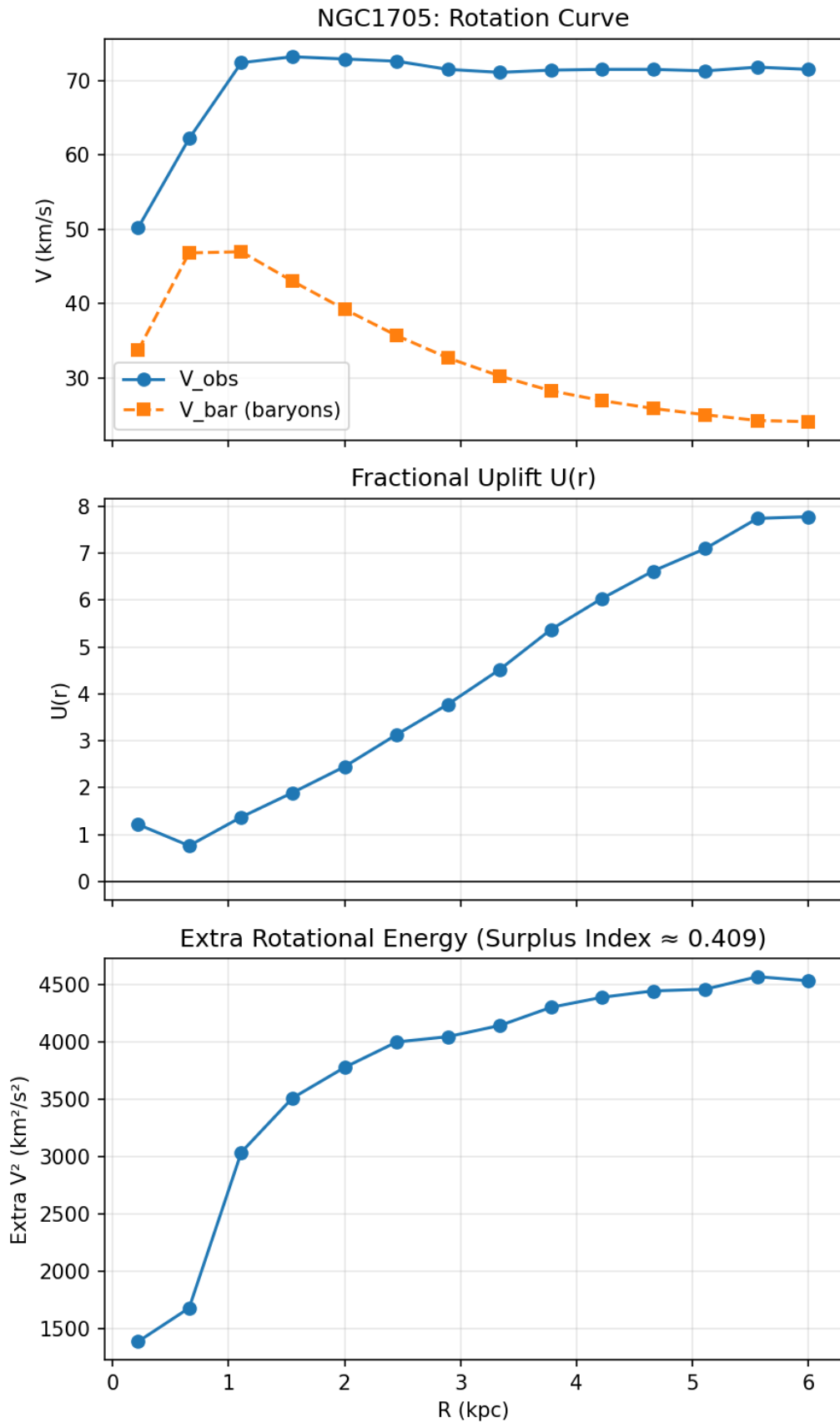


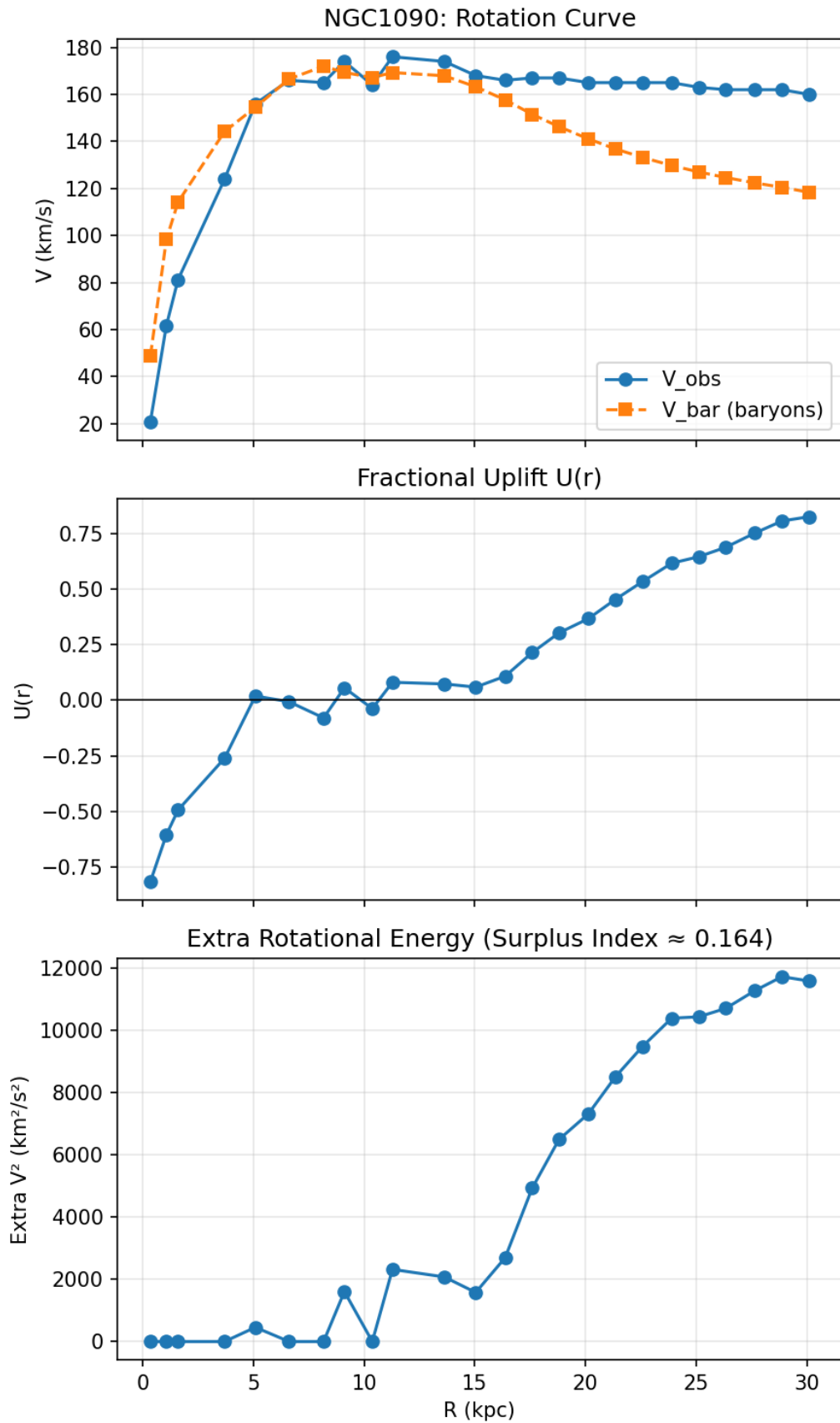


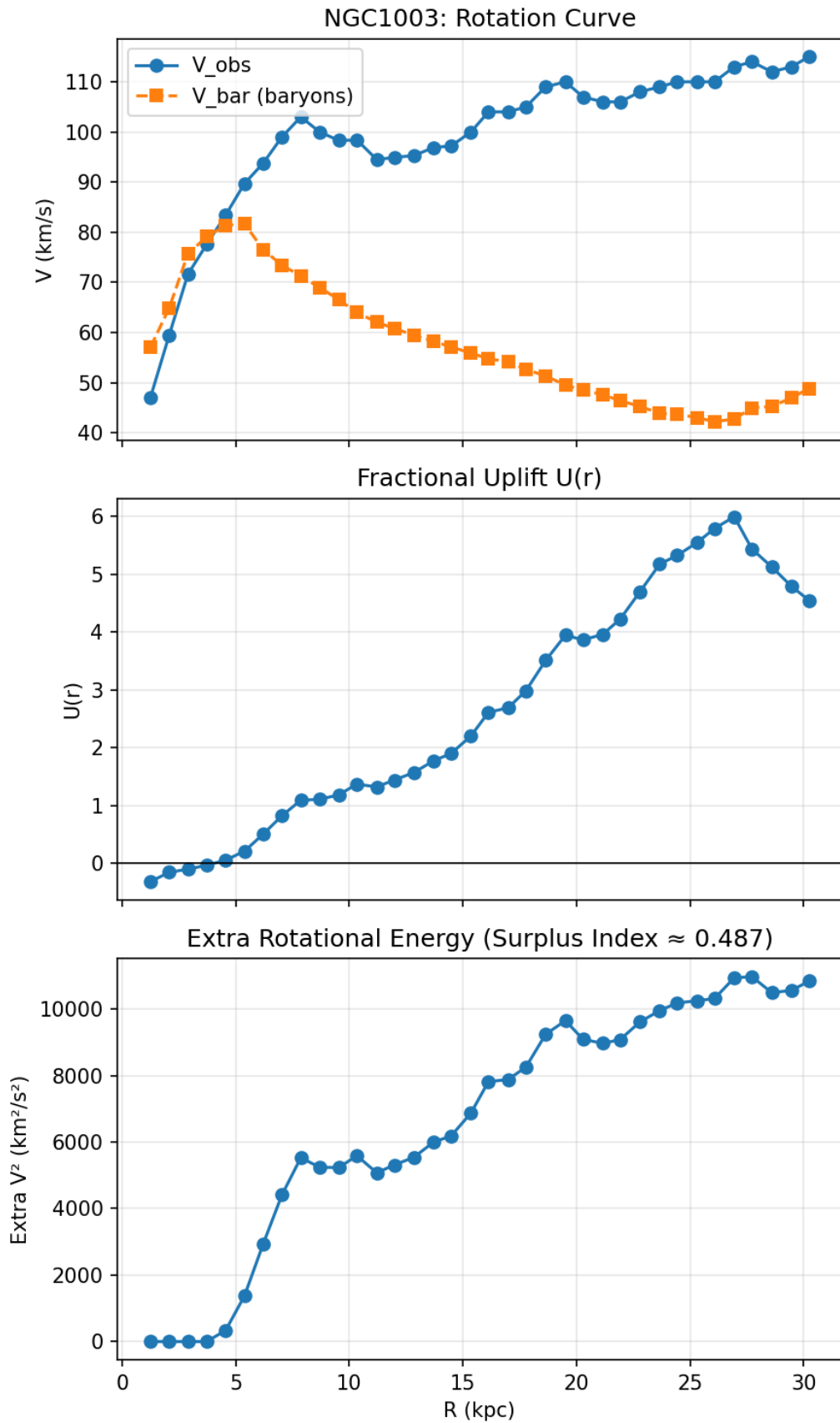


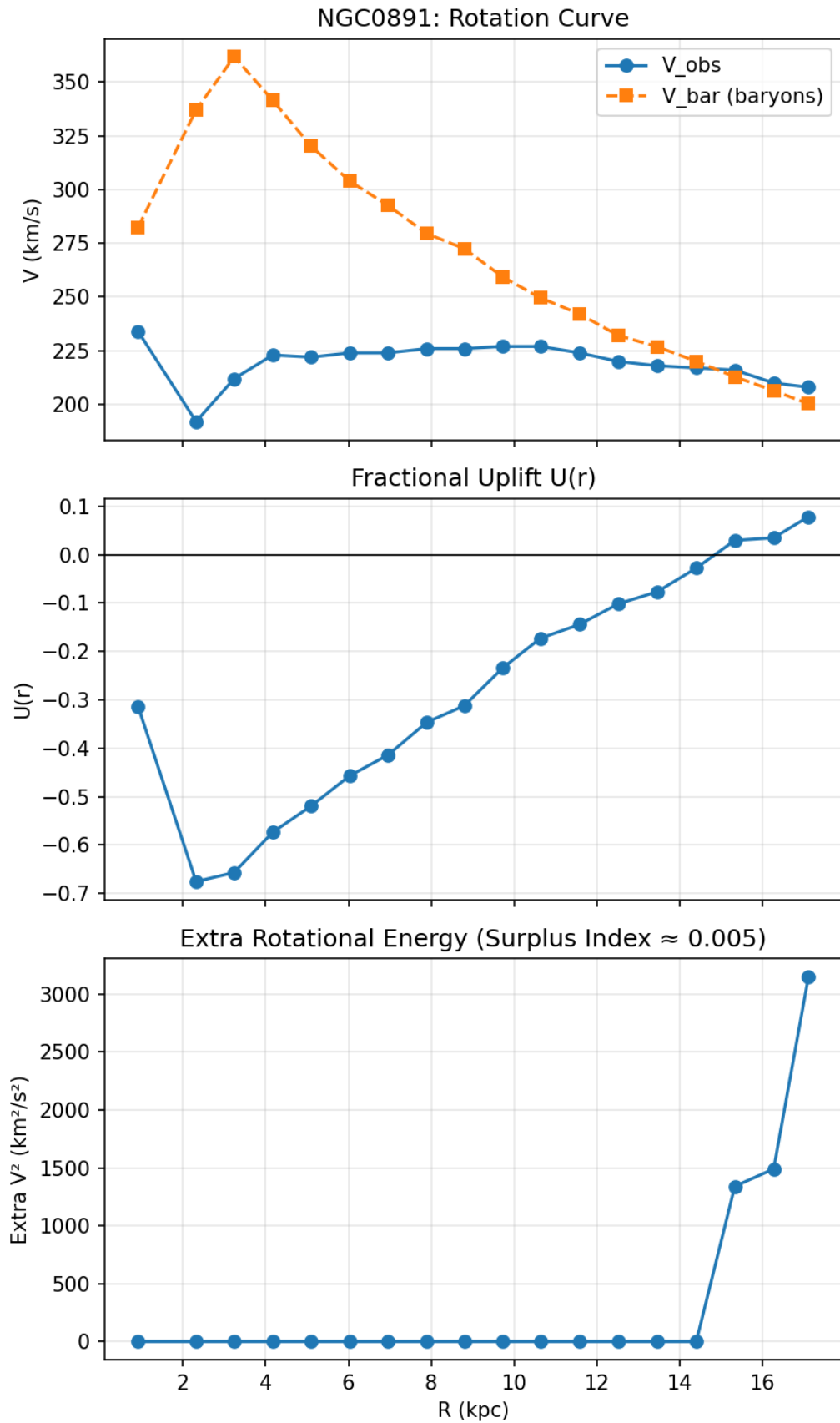


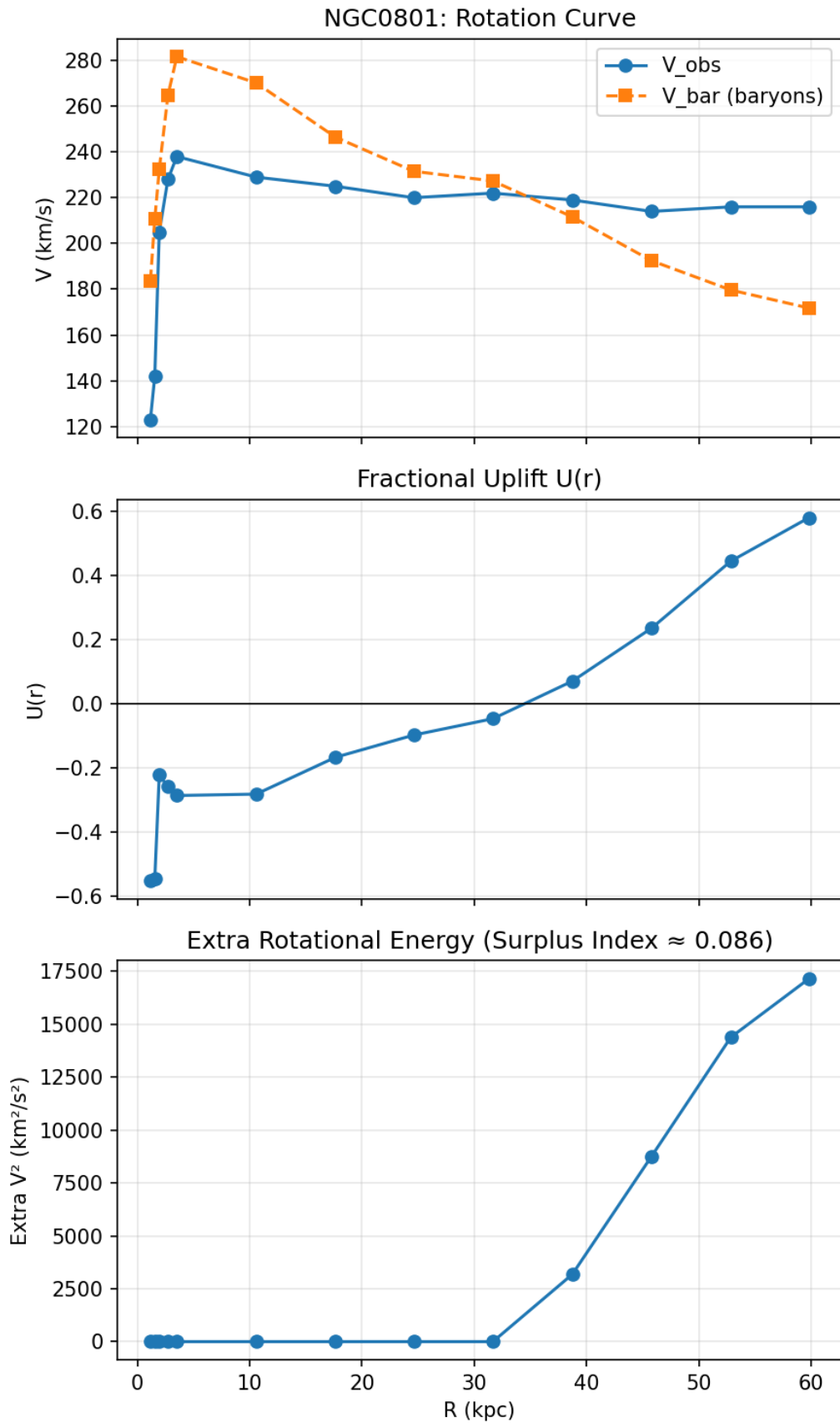


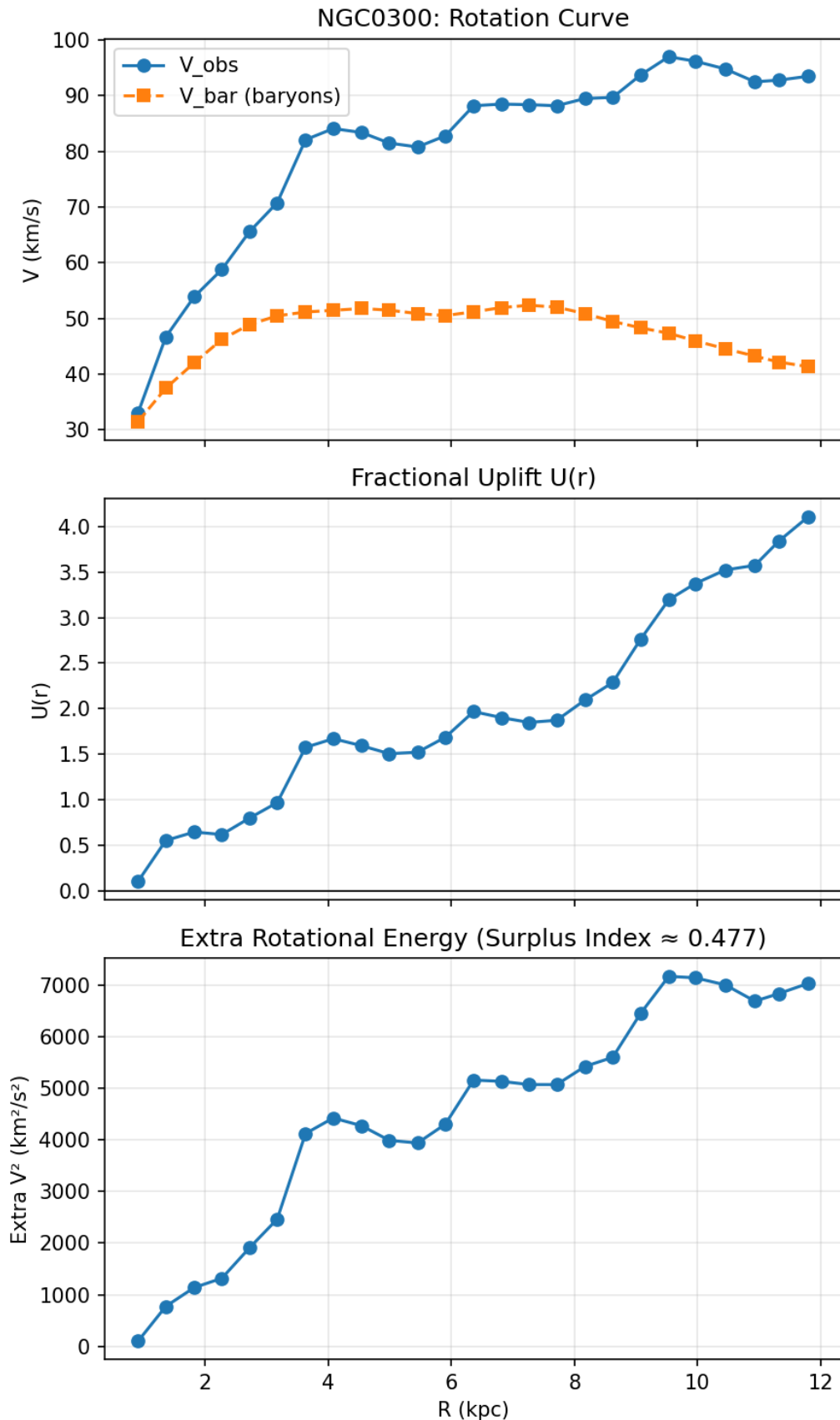


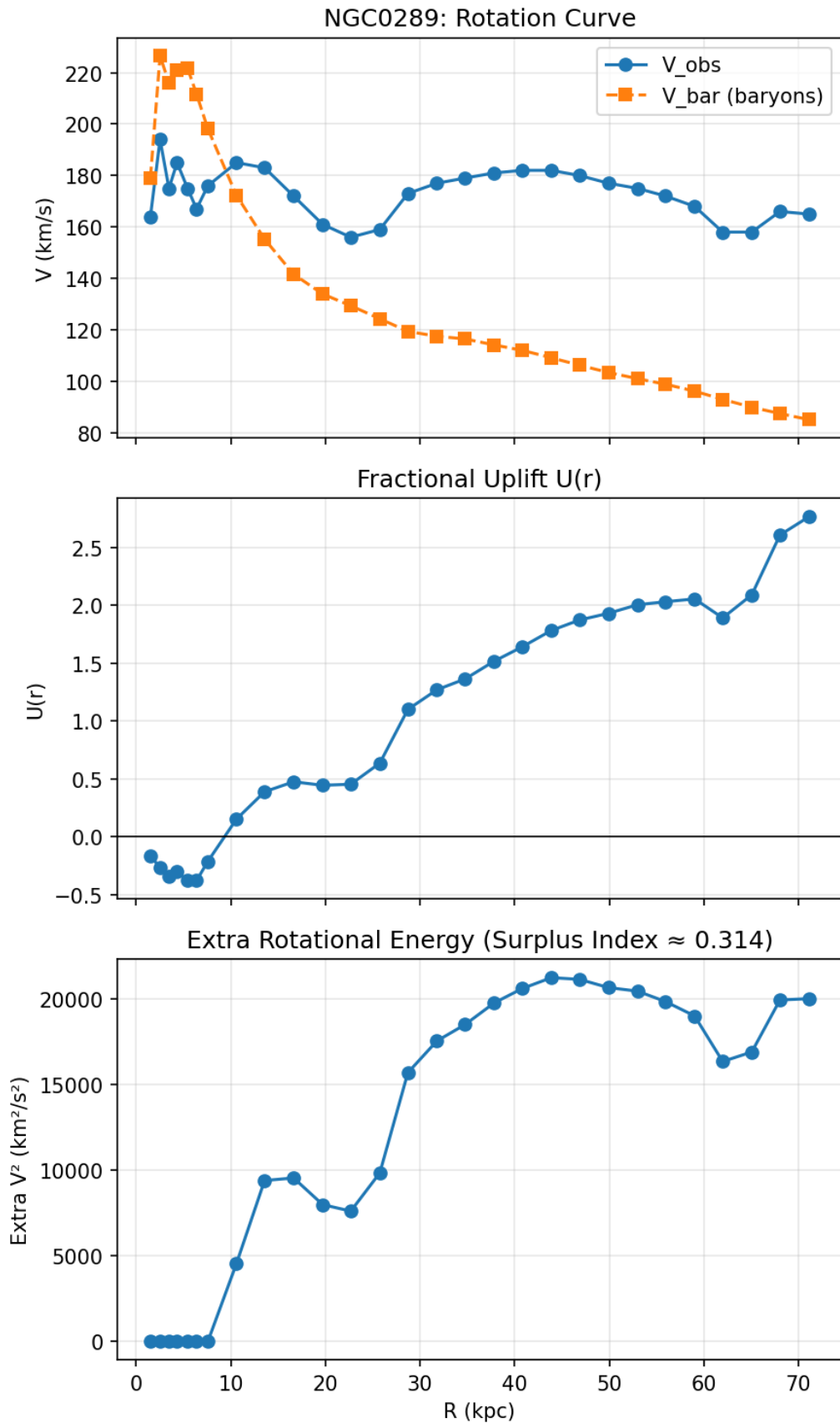


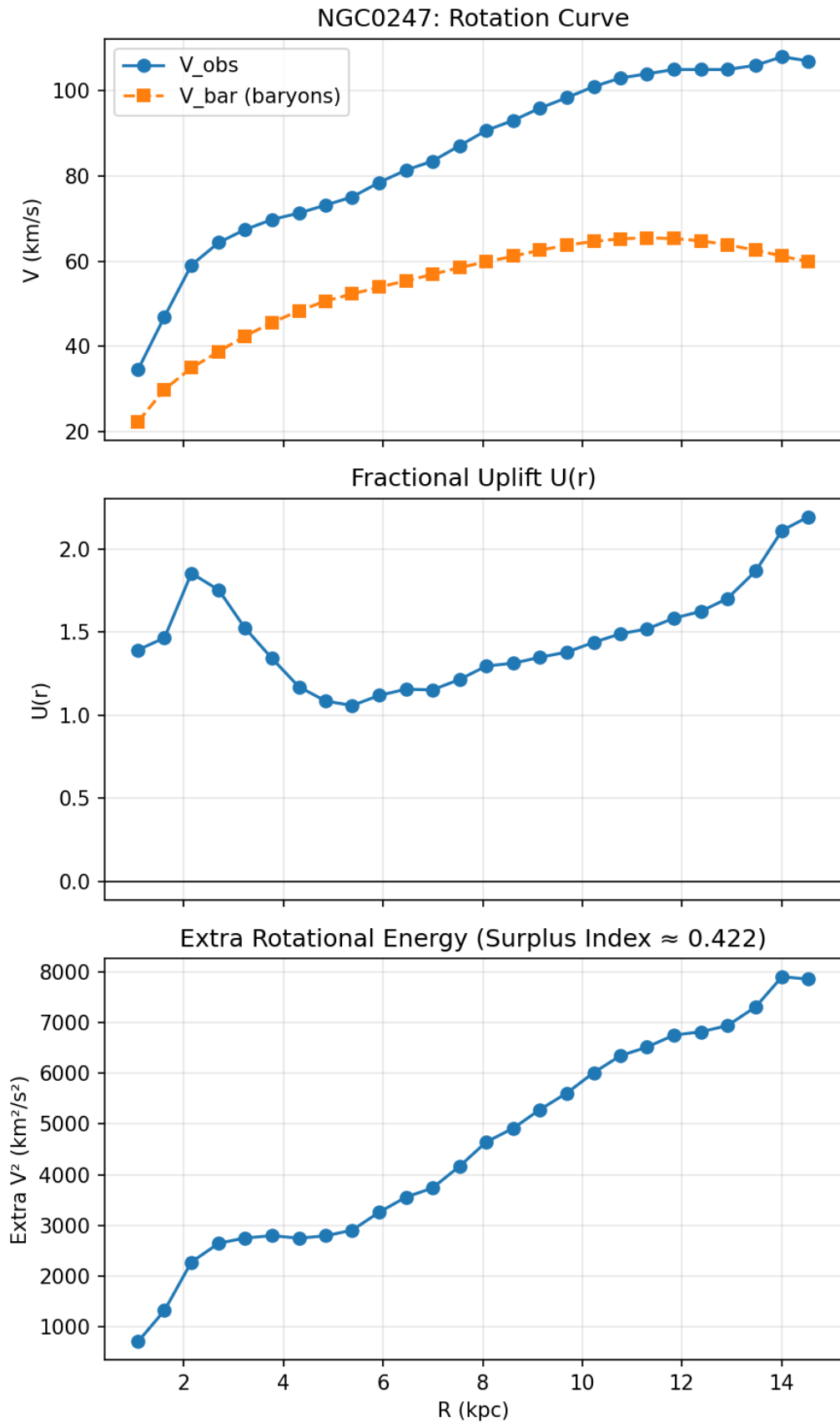


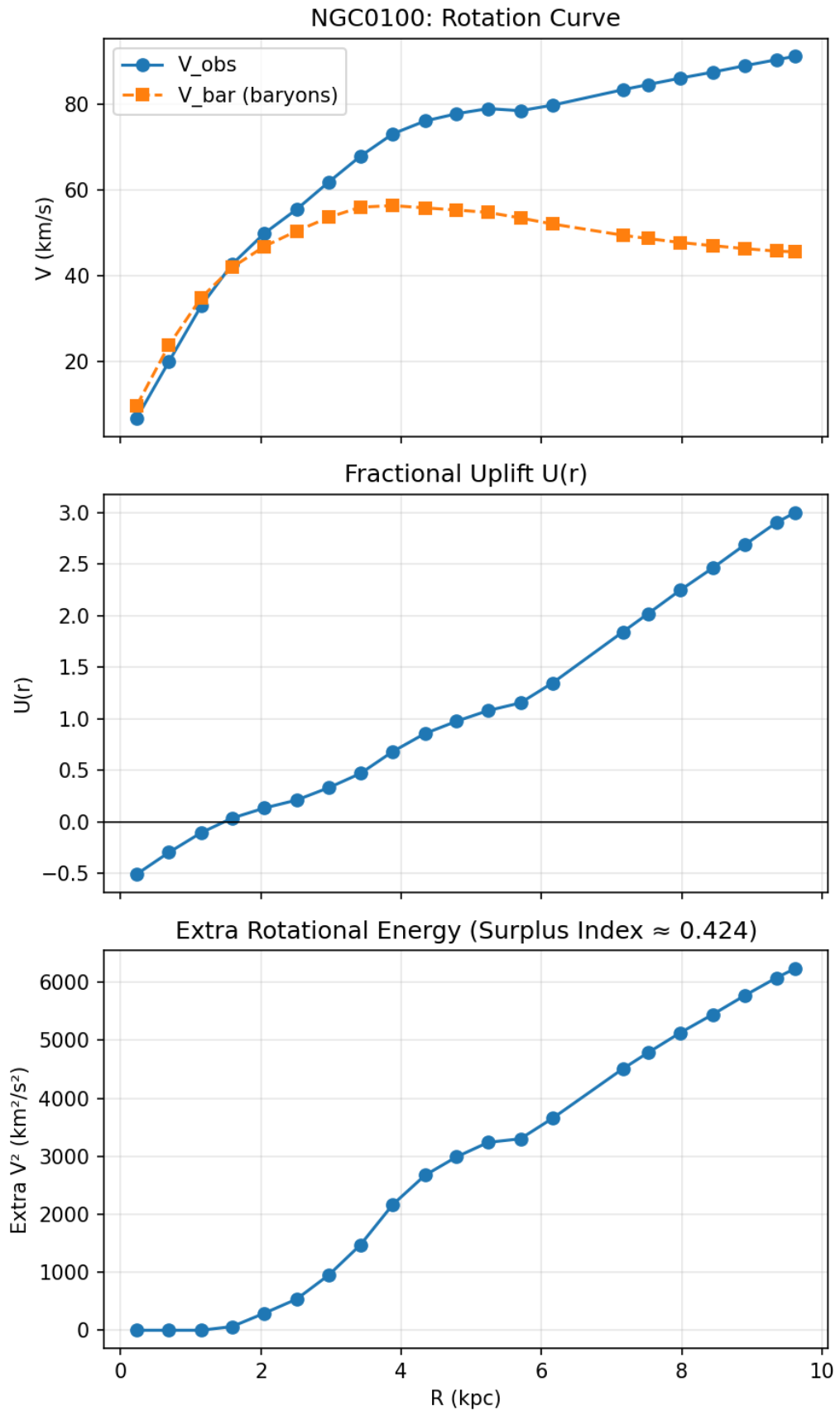


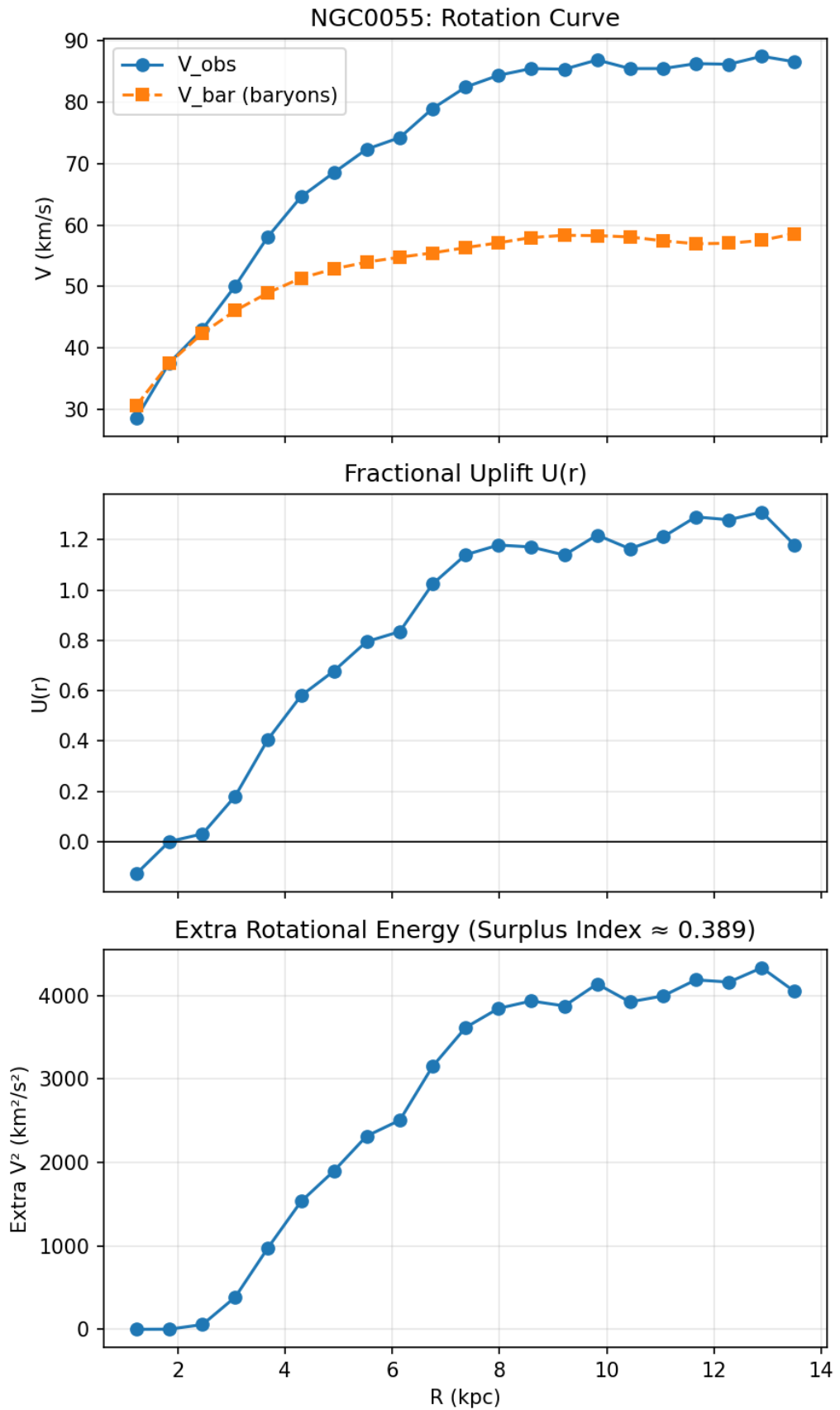


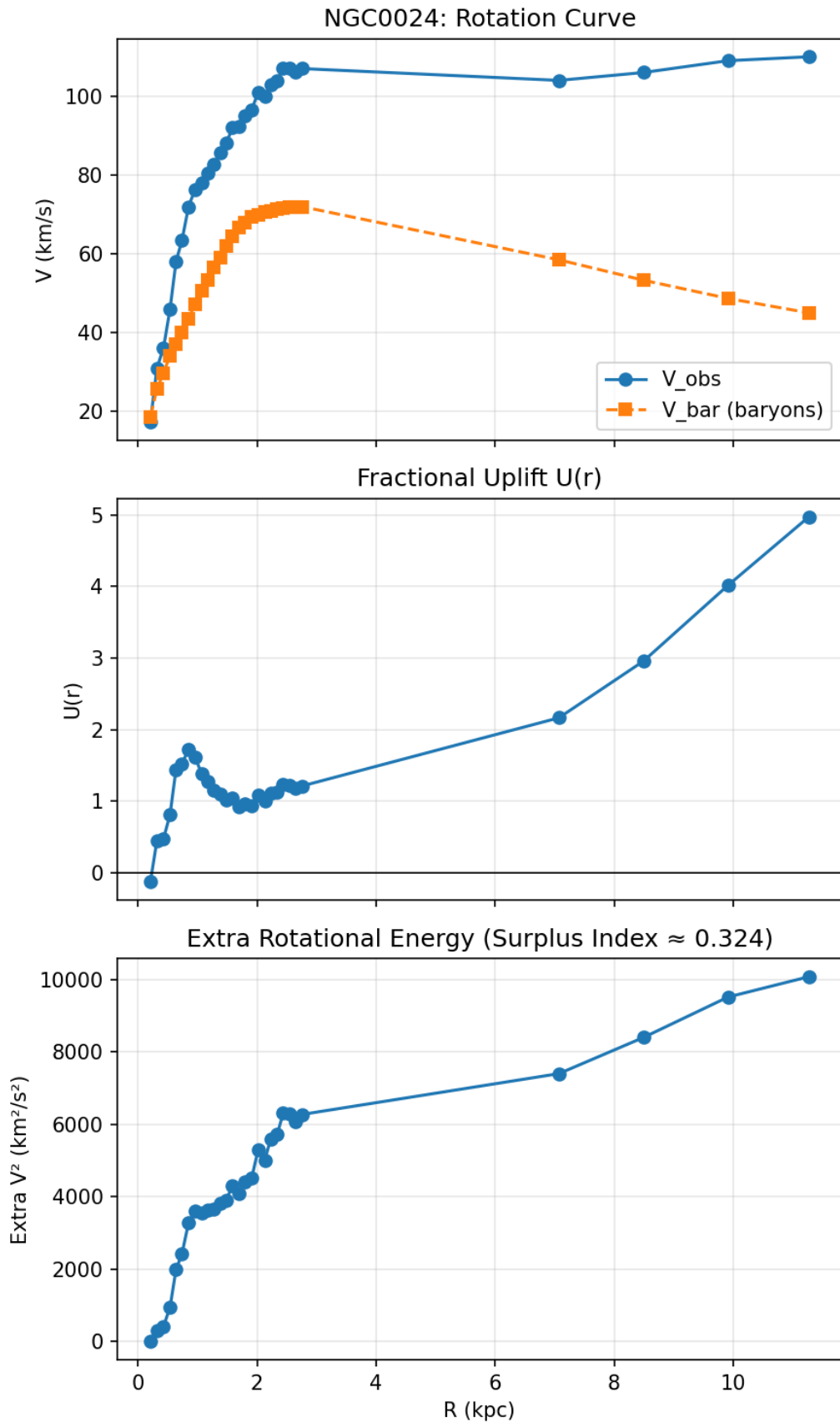


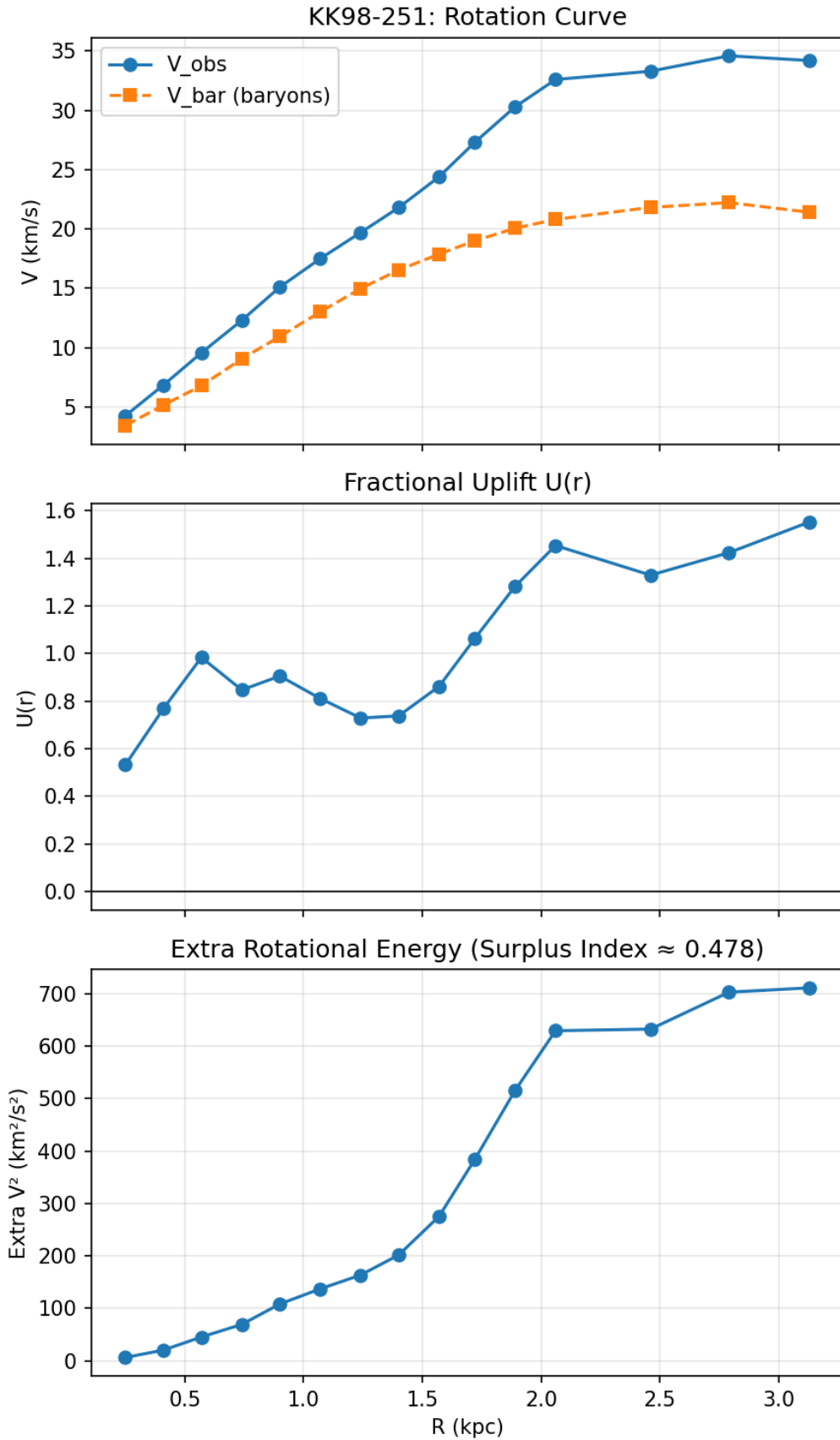


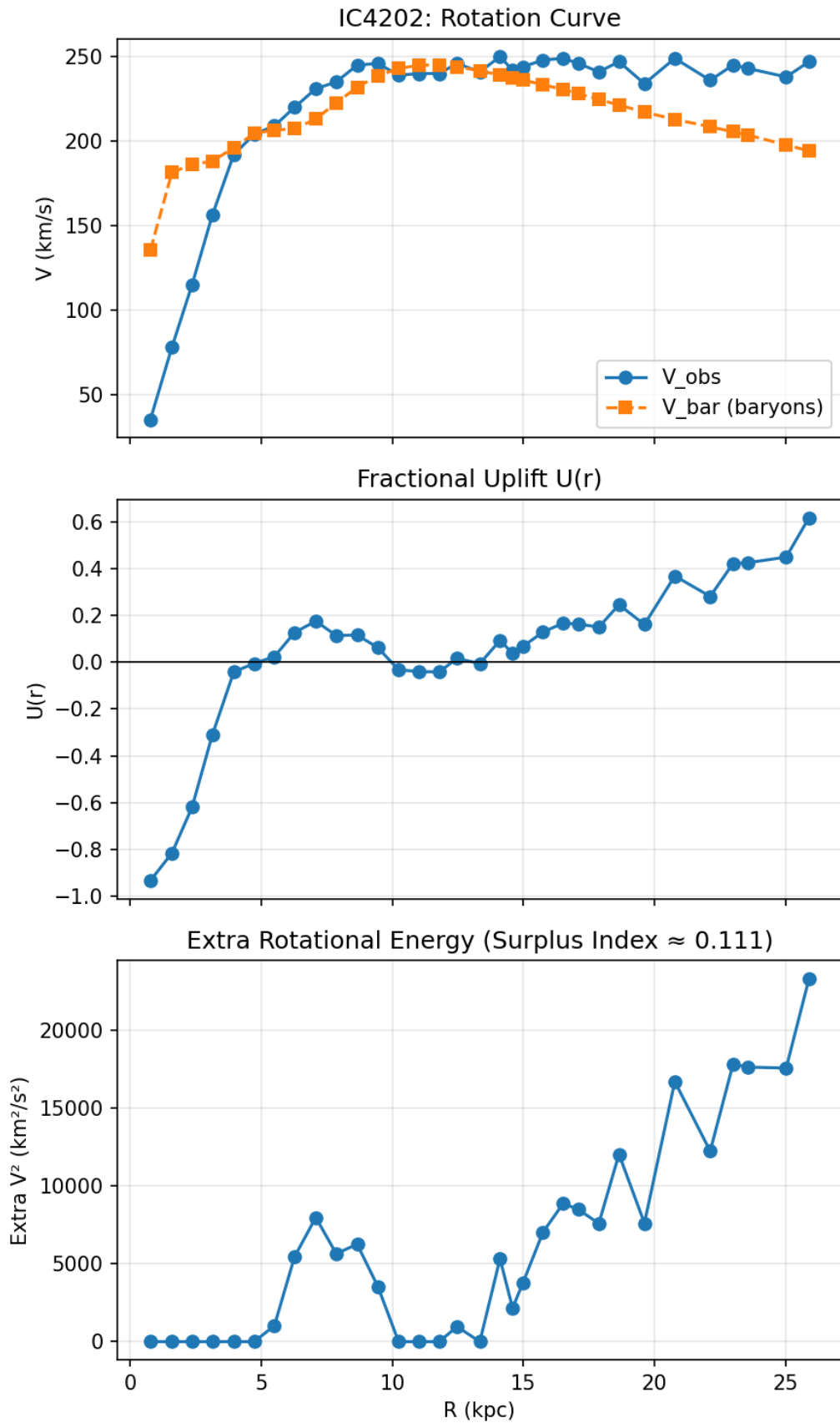


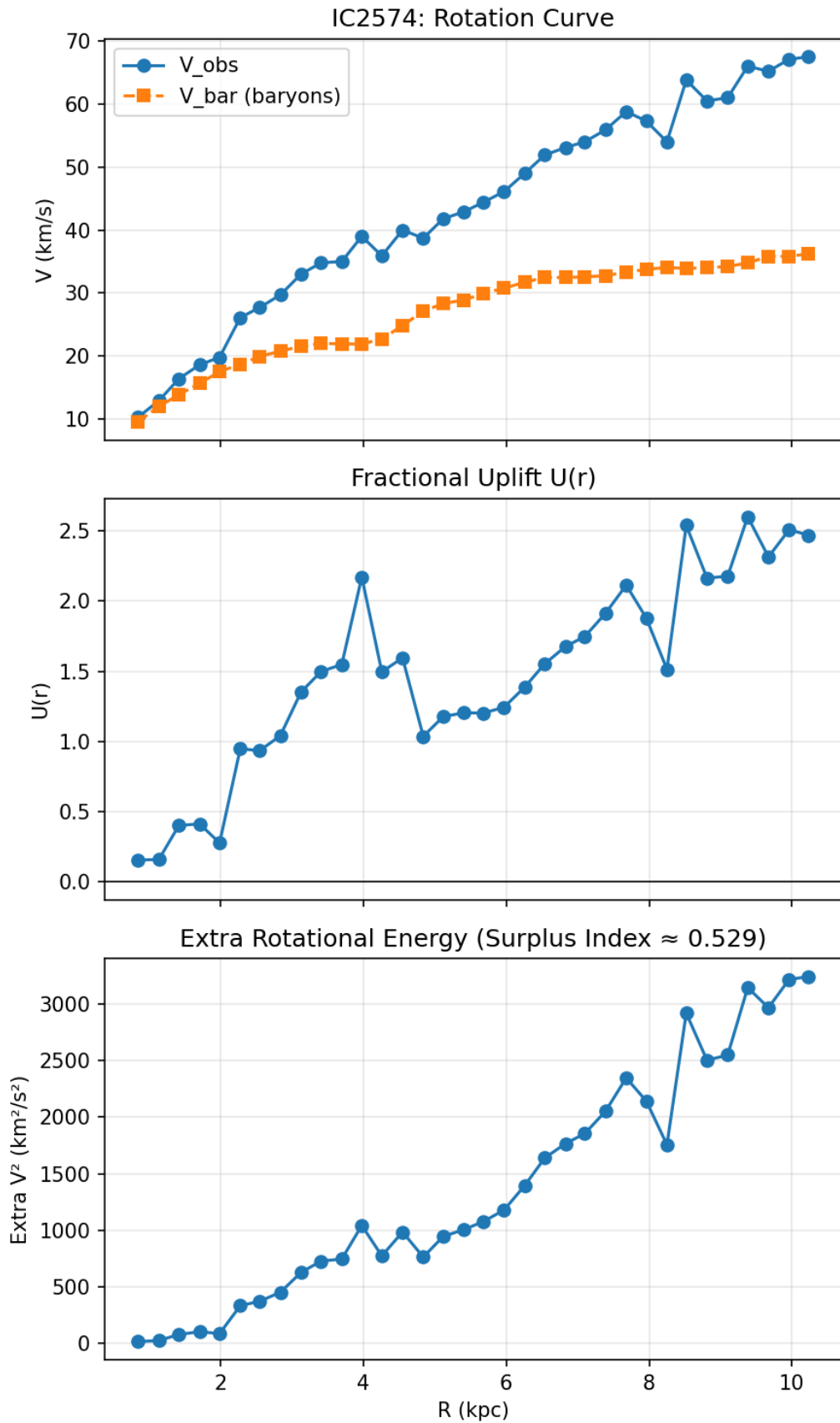




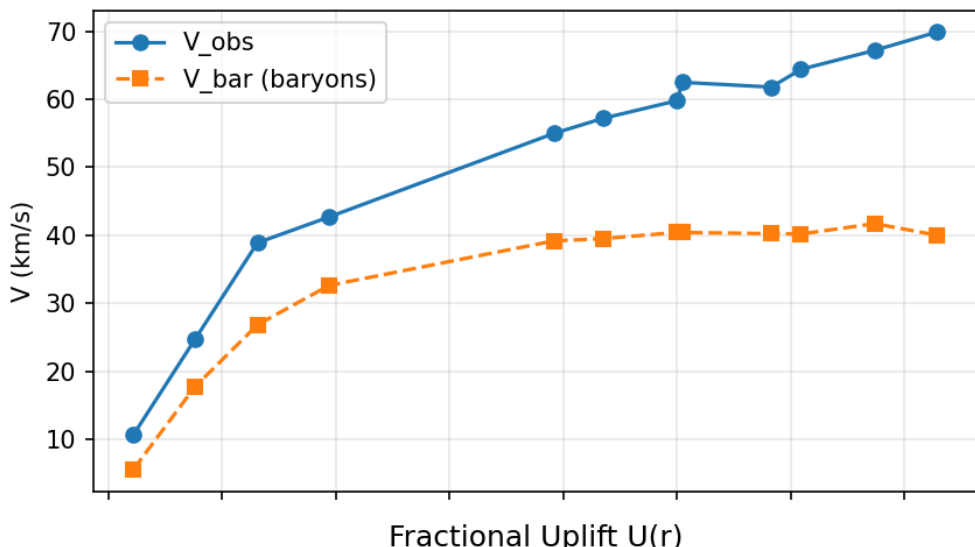
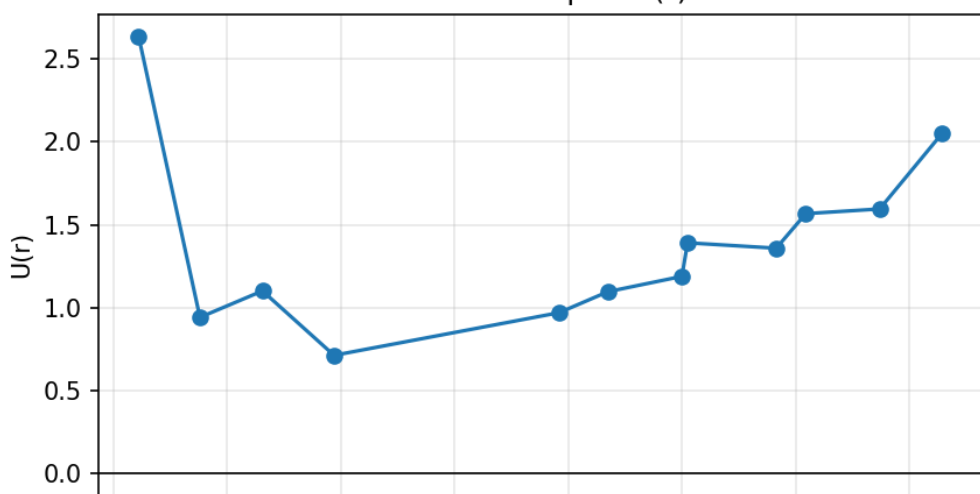
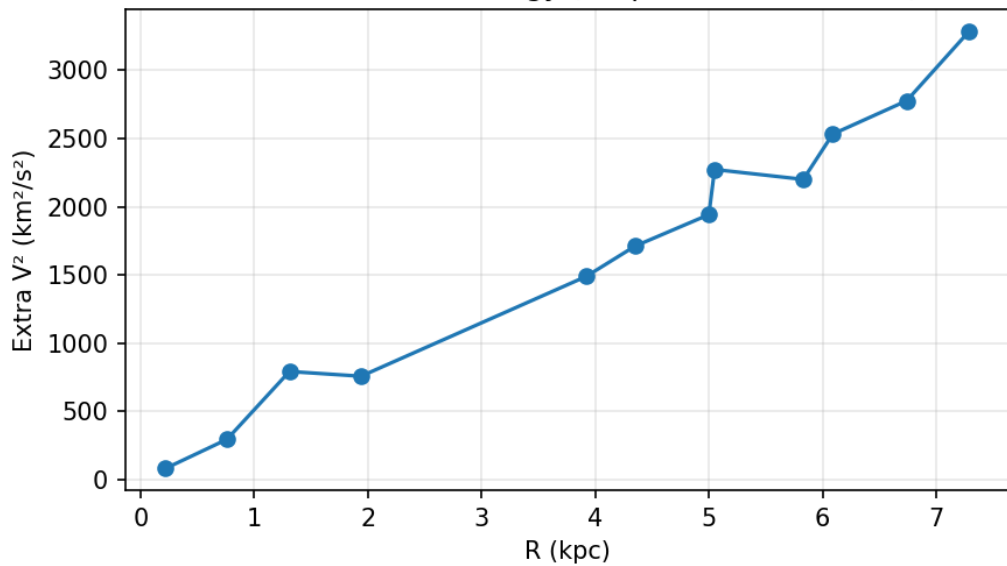


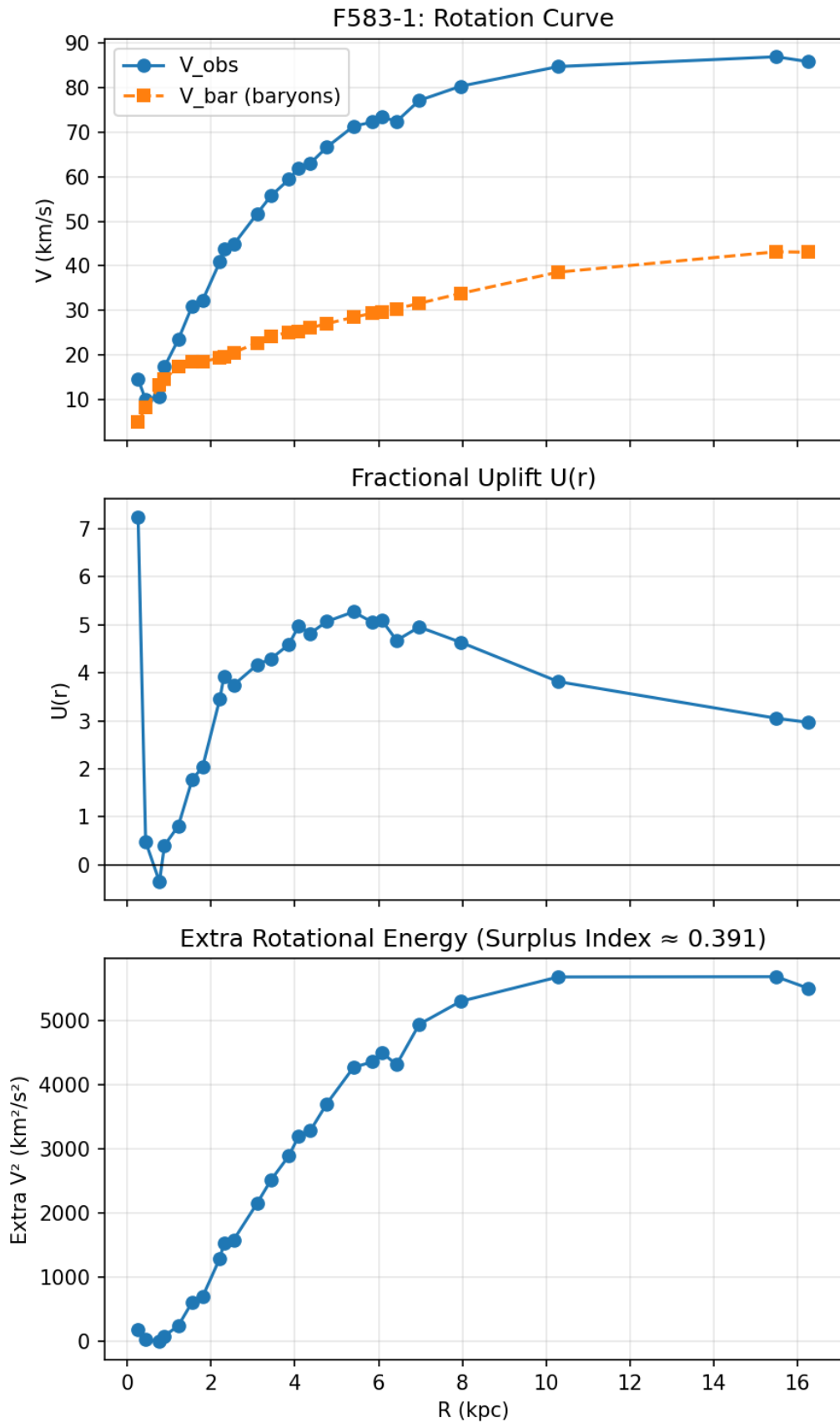


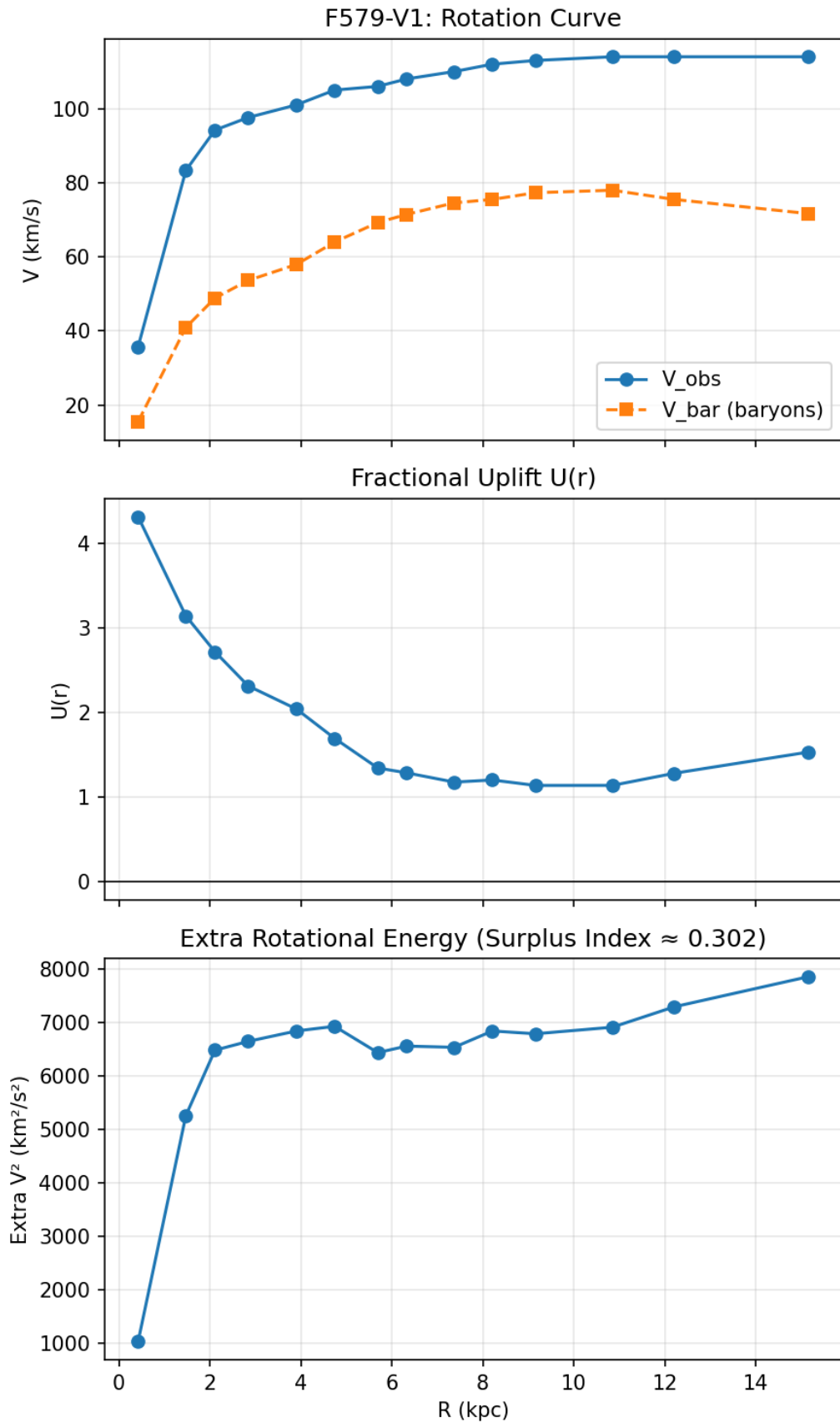




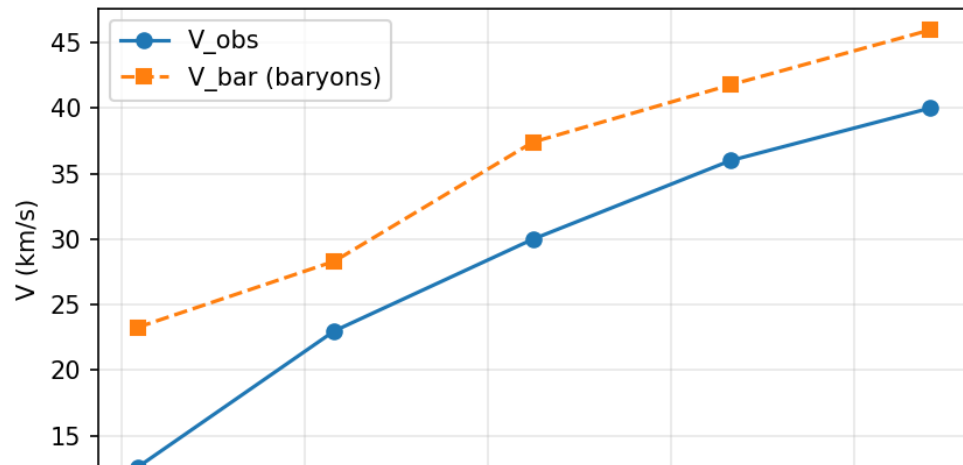
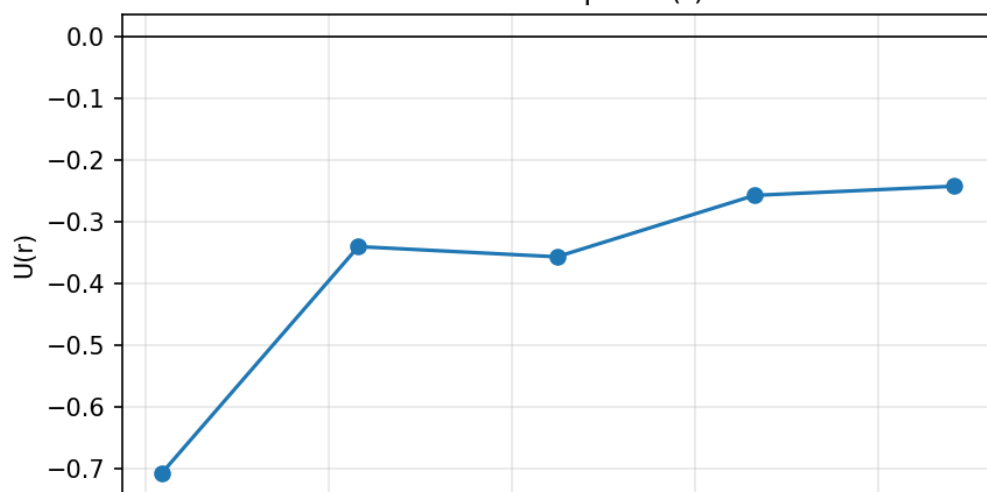
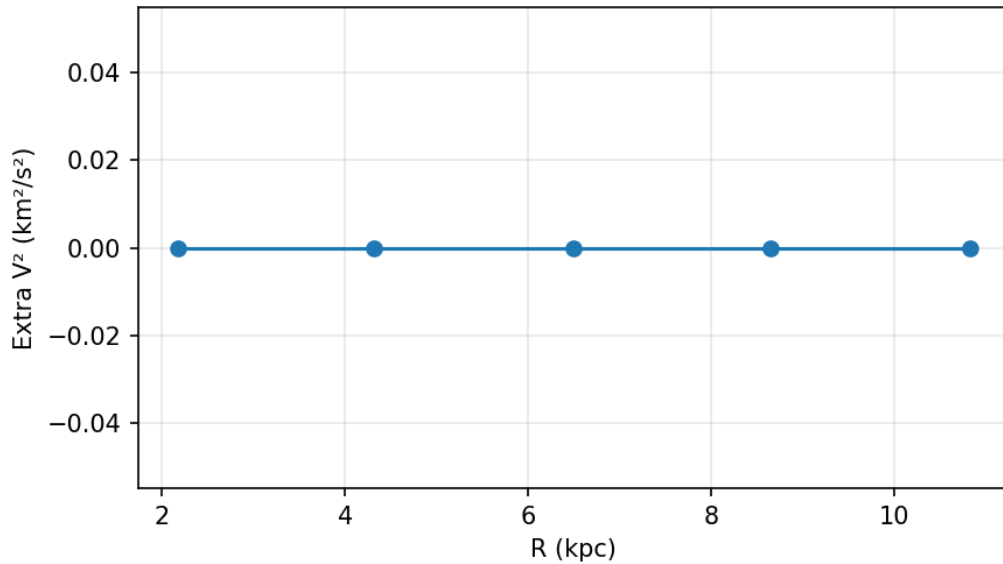
F583-4: Rotation Curve

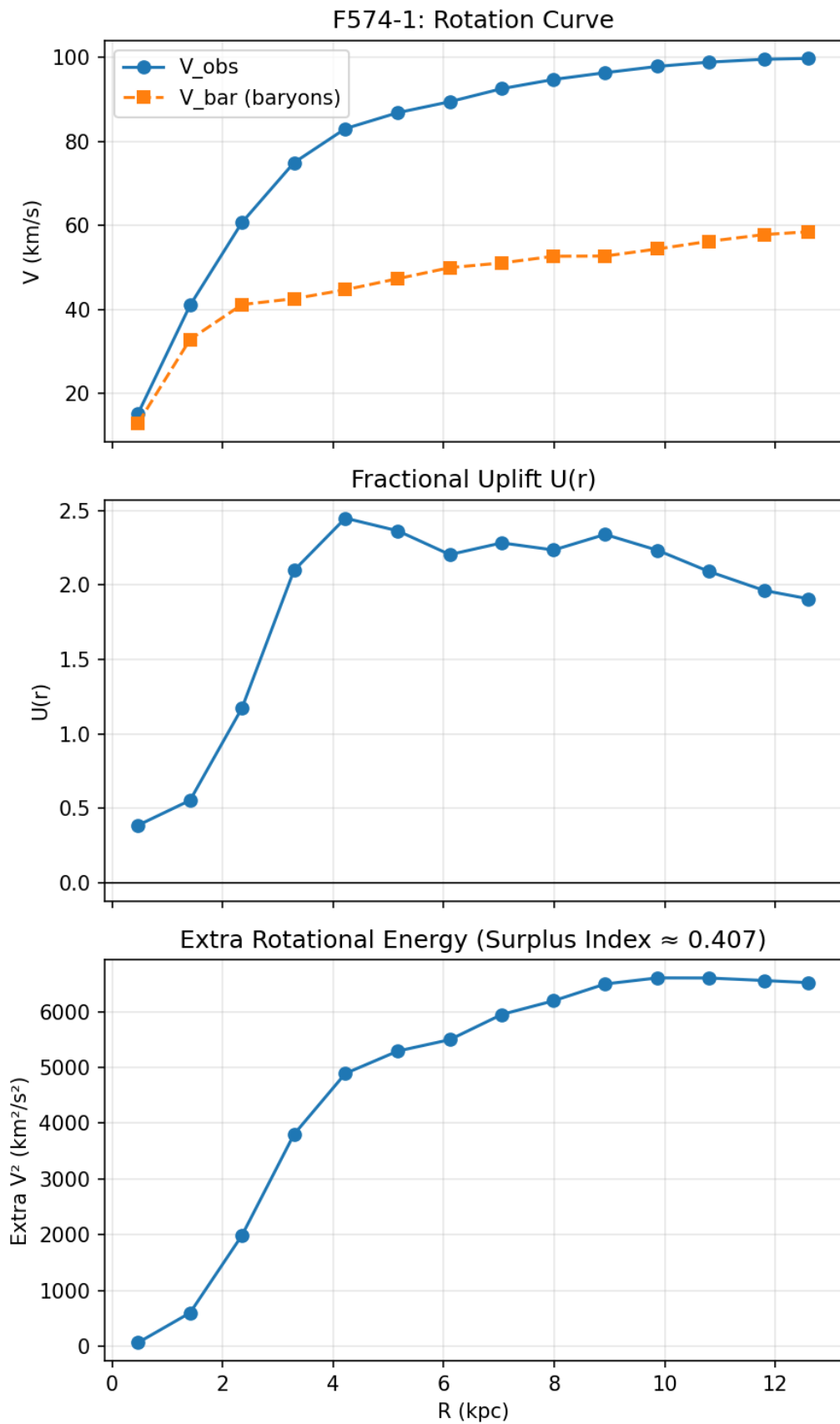
Fractional Uplift $U(r)$ Extra Rotational Energy (Surplus Index ≈ 0.390)

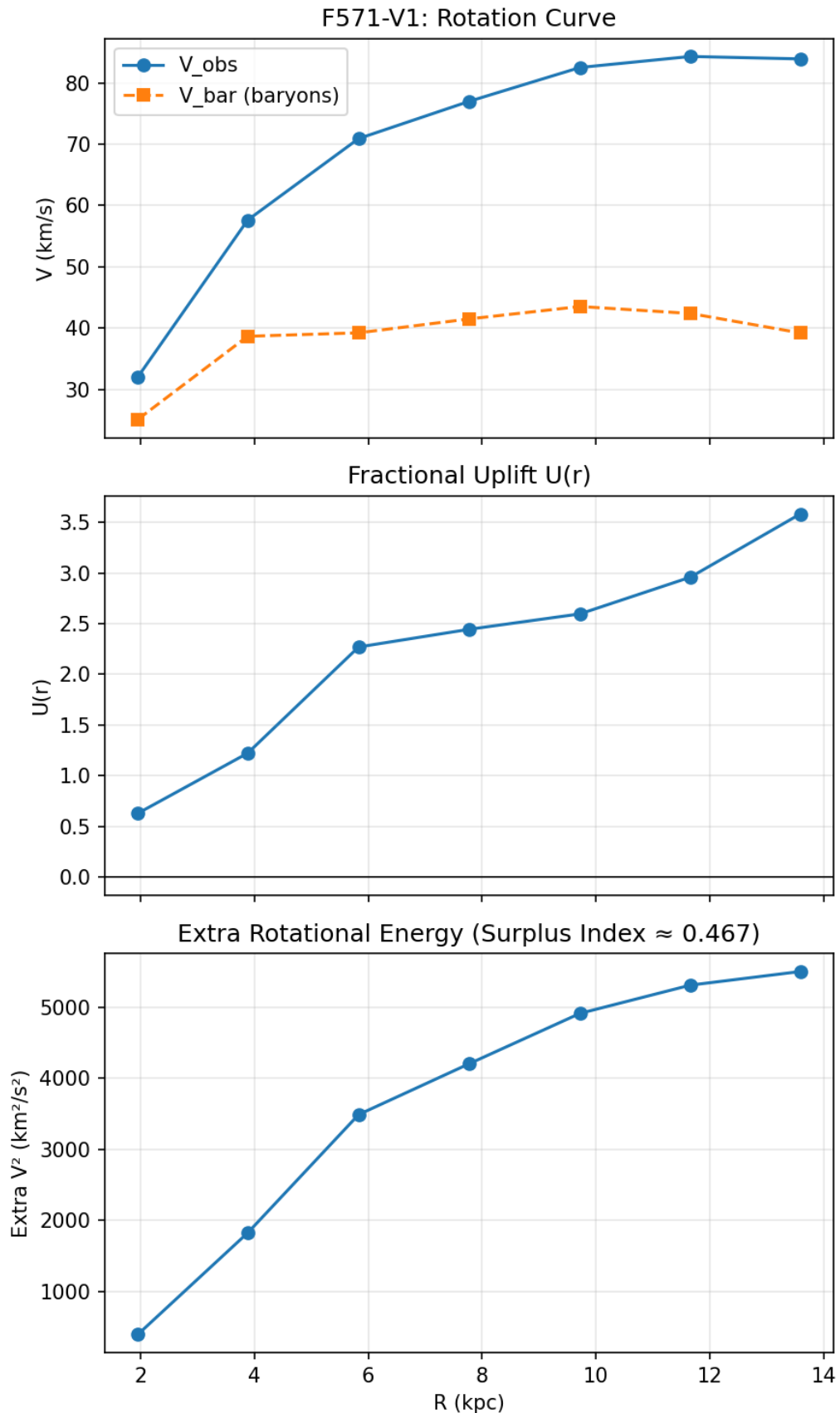




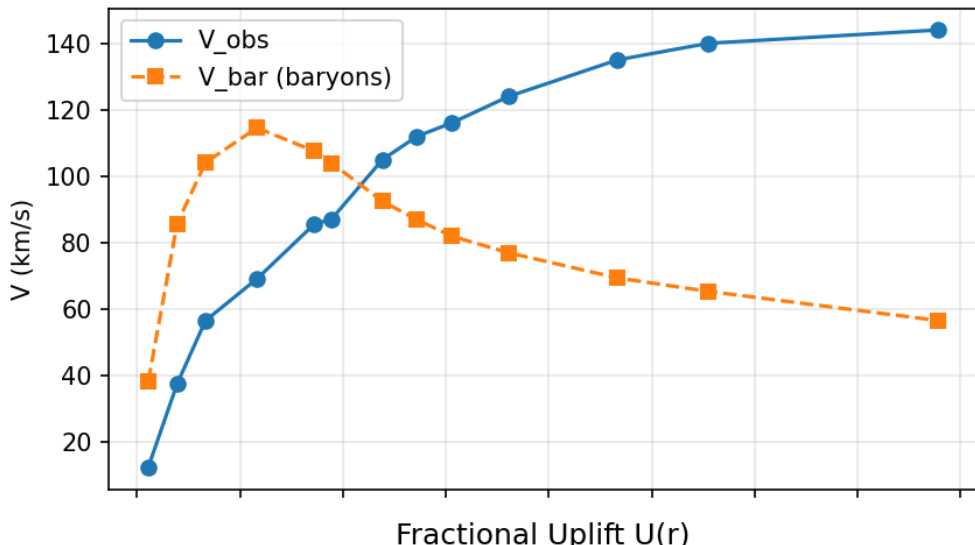
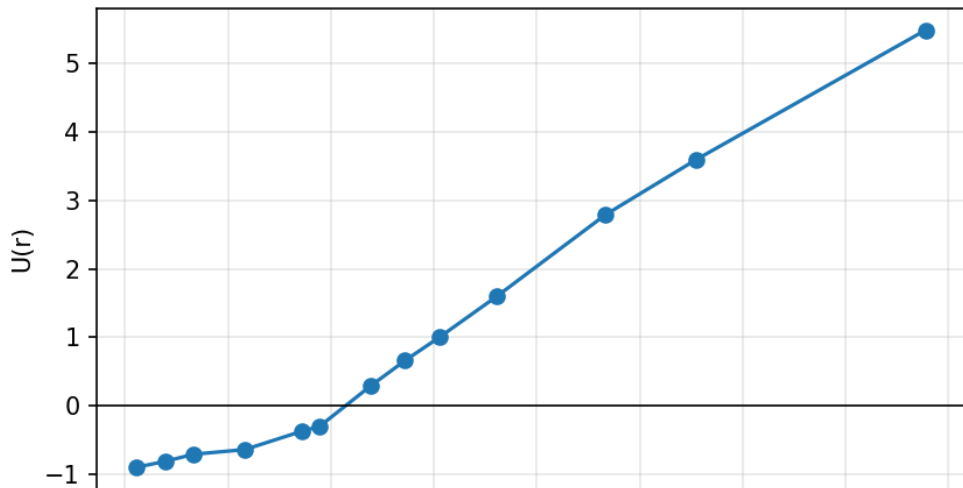
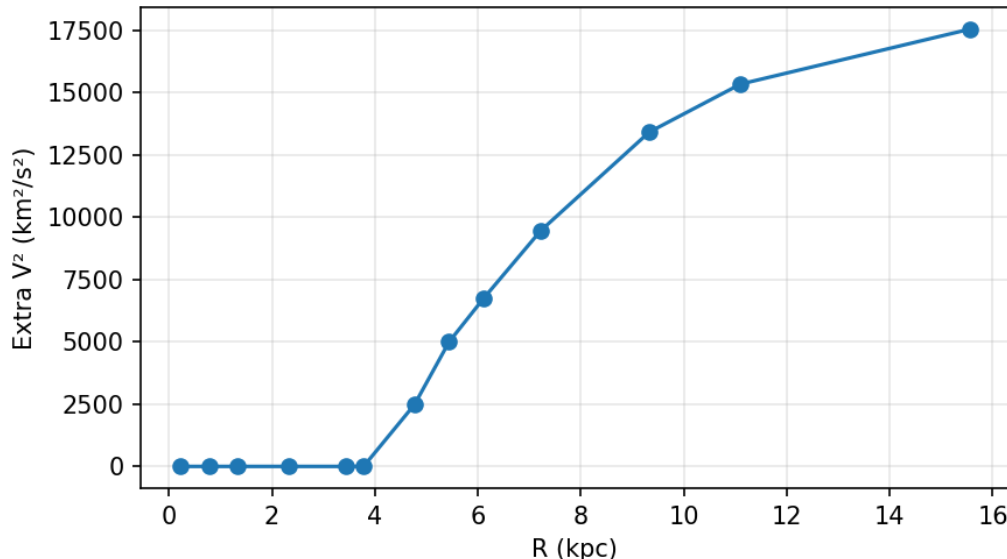
F574-2: Rotation Curve

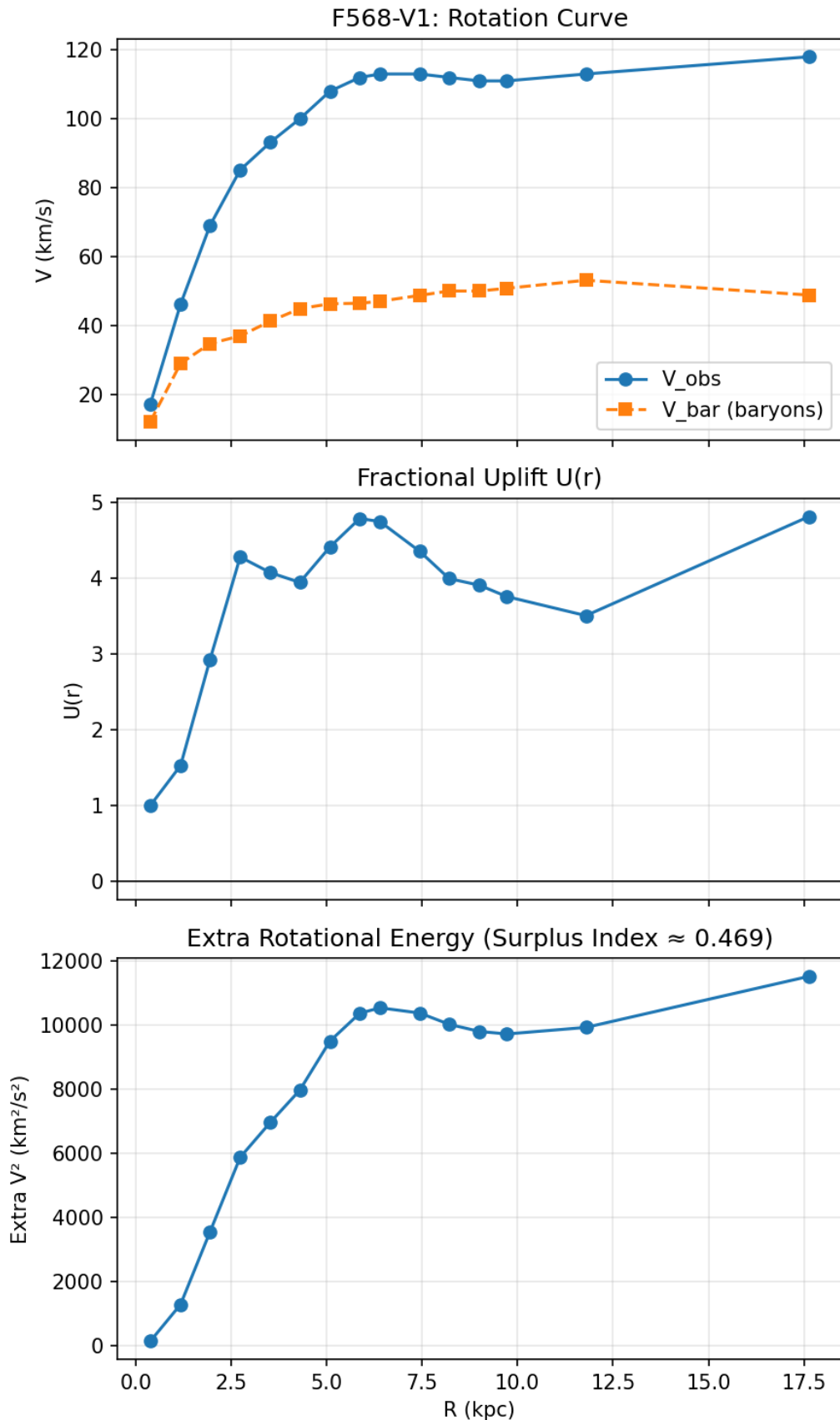
Fractional Uplift $U(r)$ Extra Rotational Energy (Surplus Index ≈ 0.000)

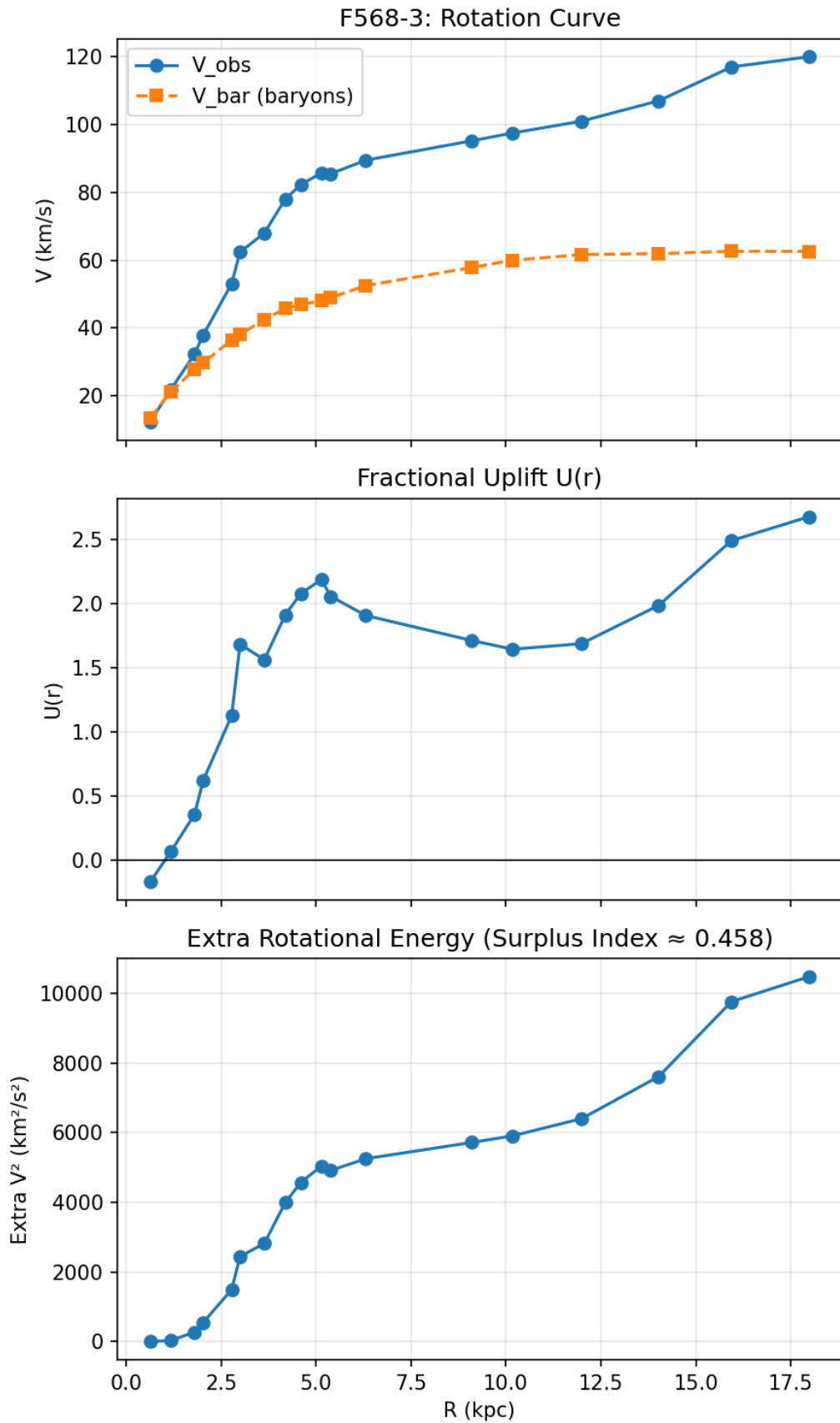


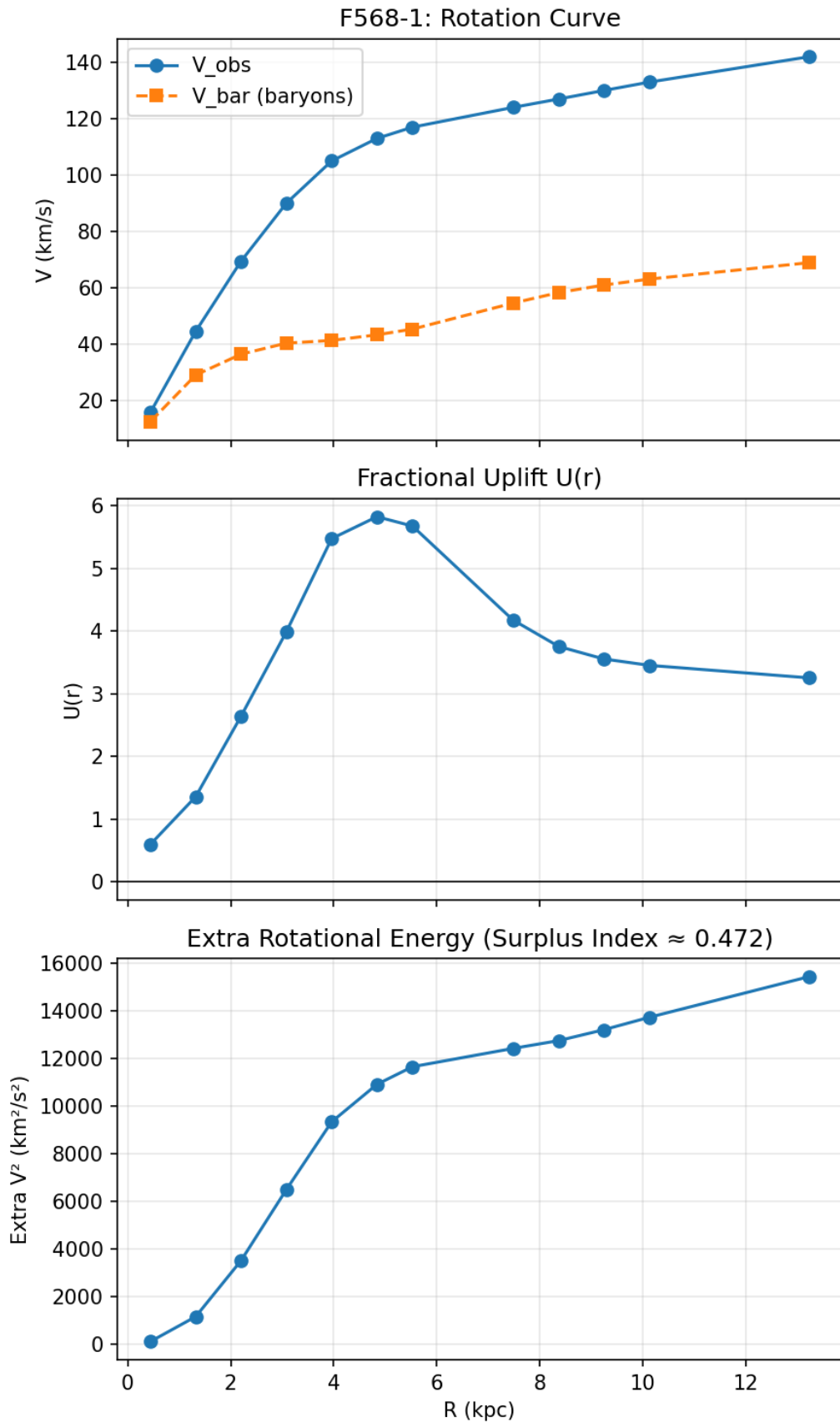


F571-8: Rotation Curve

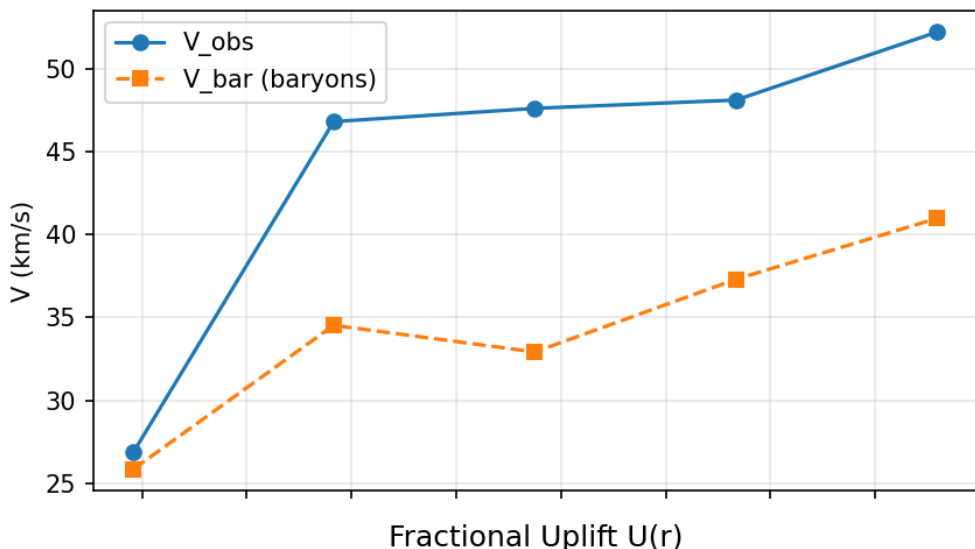
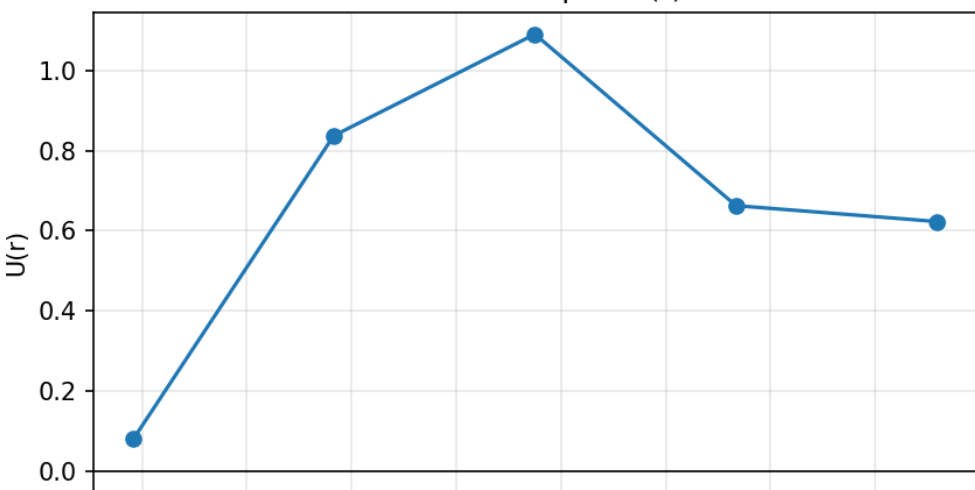
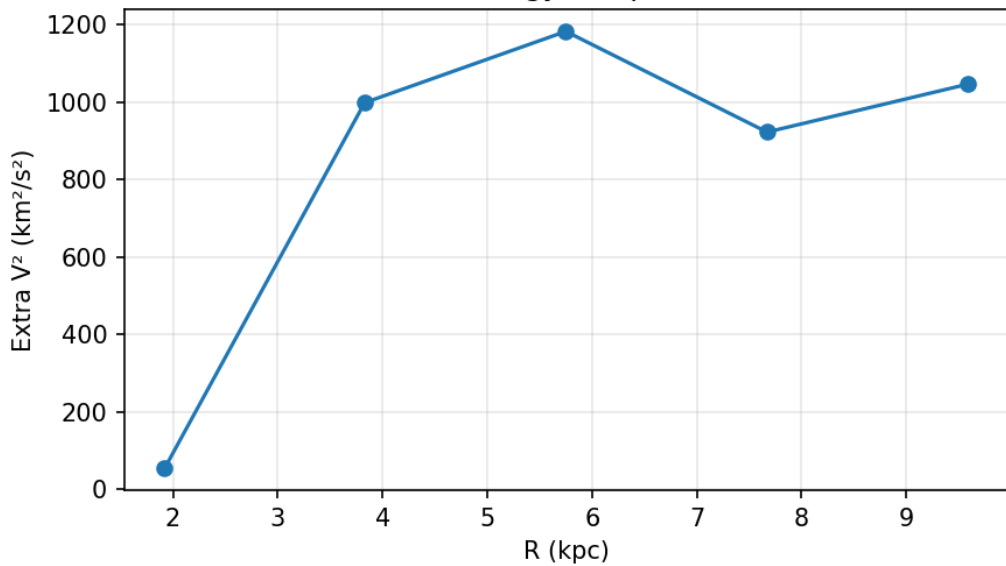
Fractional Uplift $U(r)$ Extra Rotational Energy (Surplus Index ≈ 0.458)



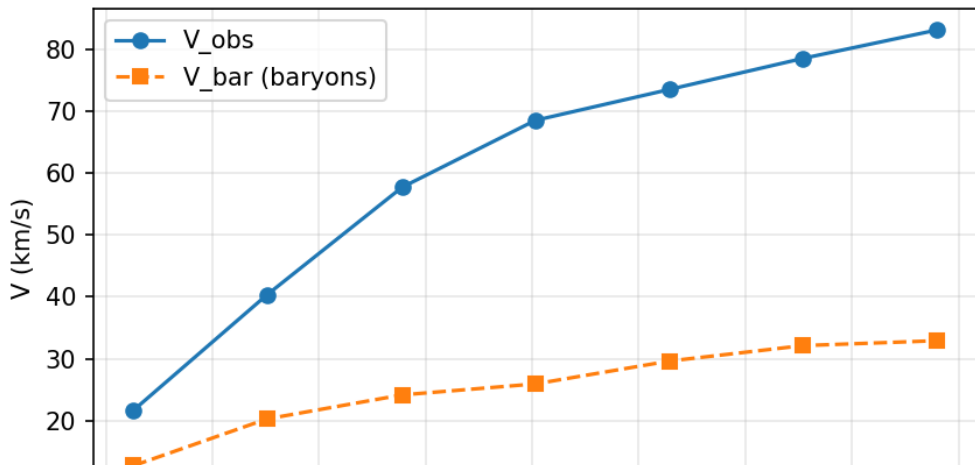
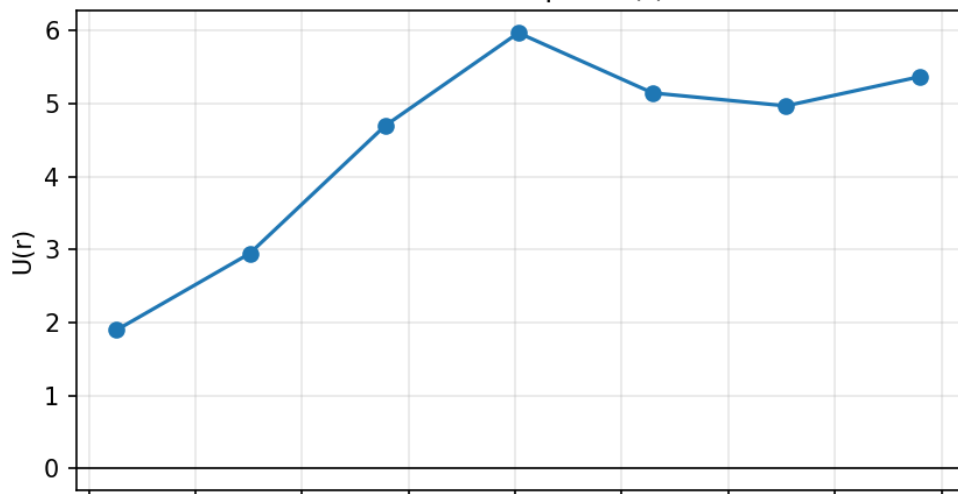
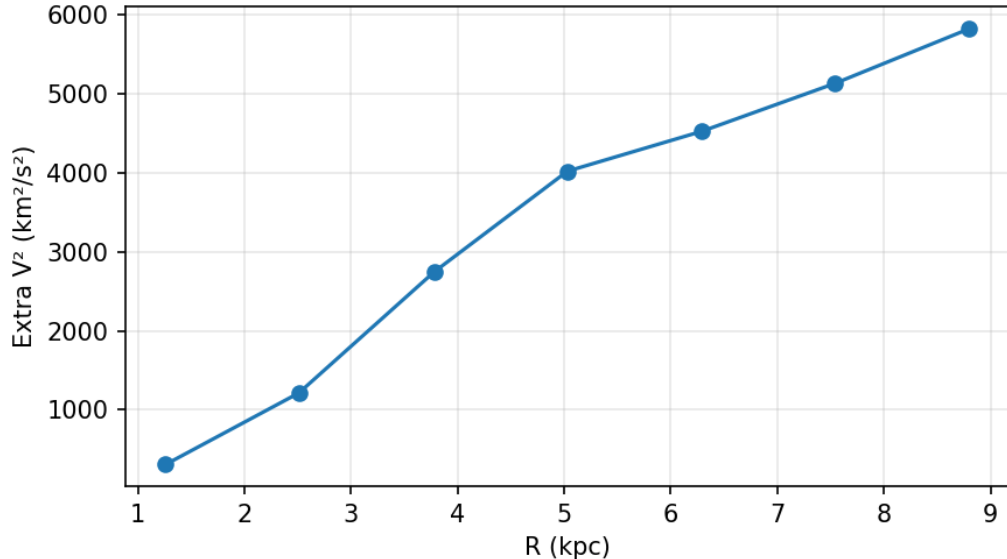


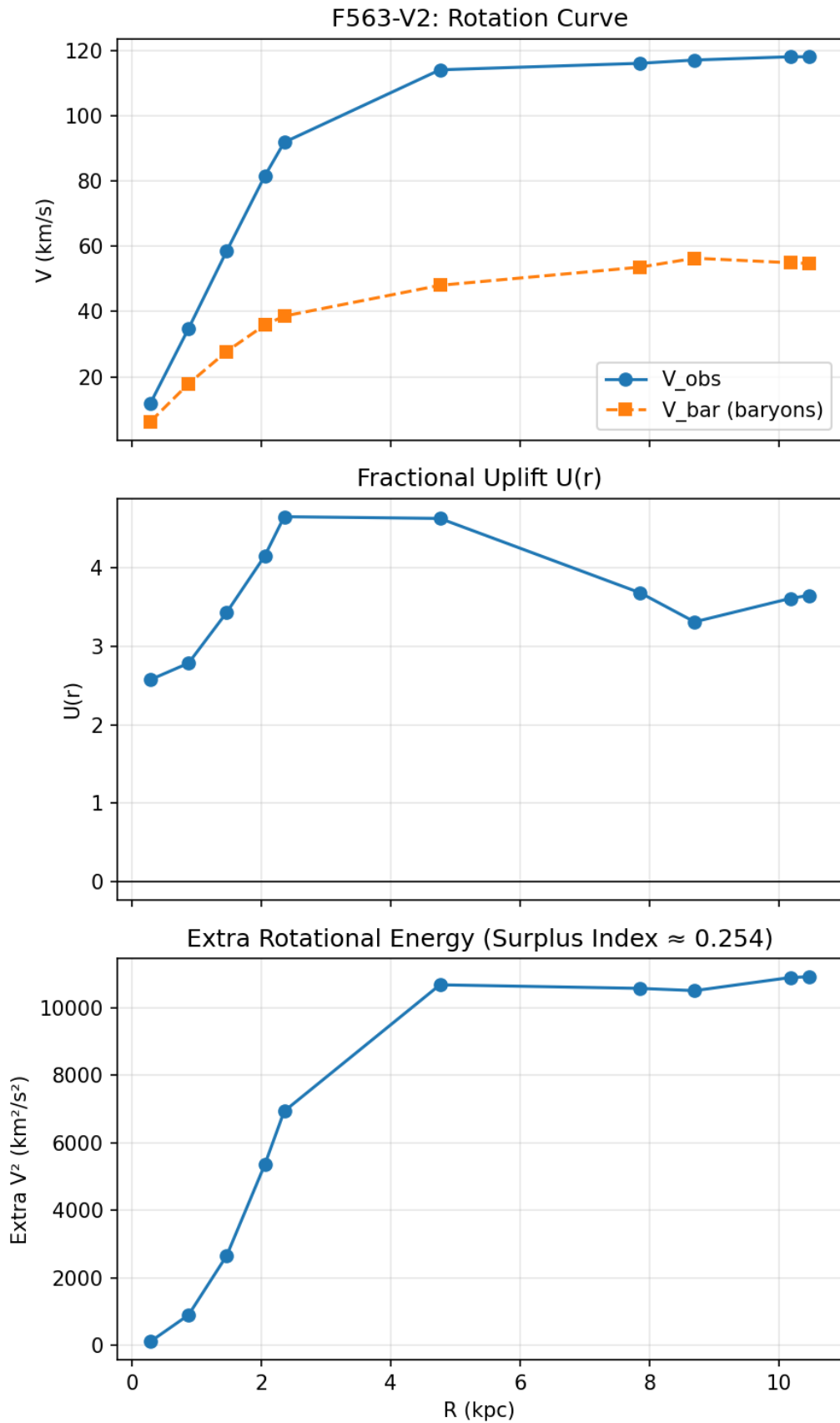


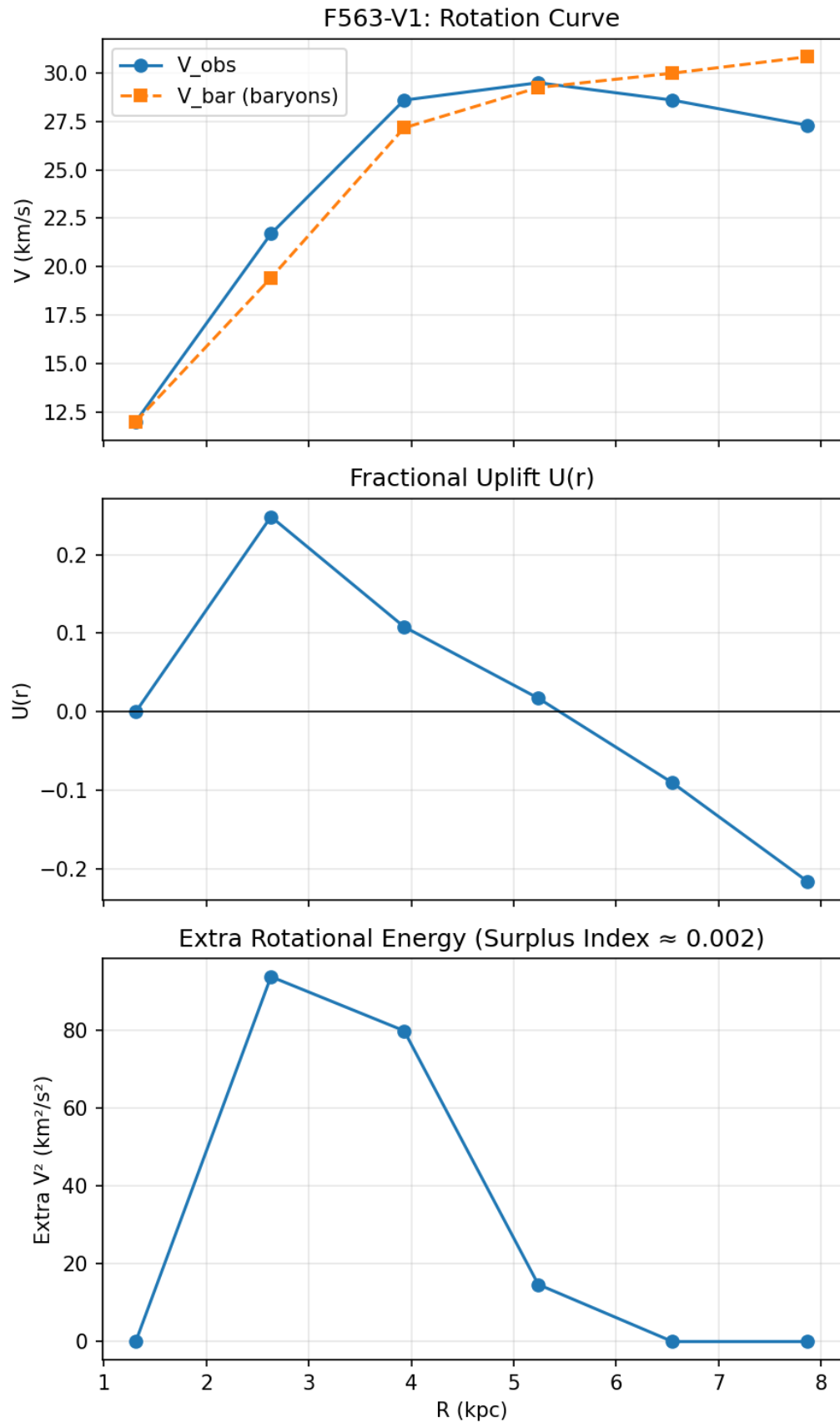
F567-2: Rotation Curve

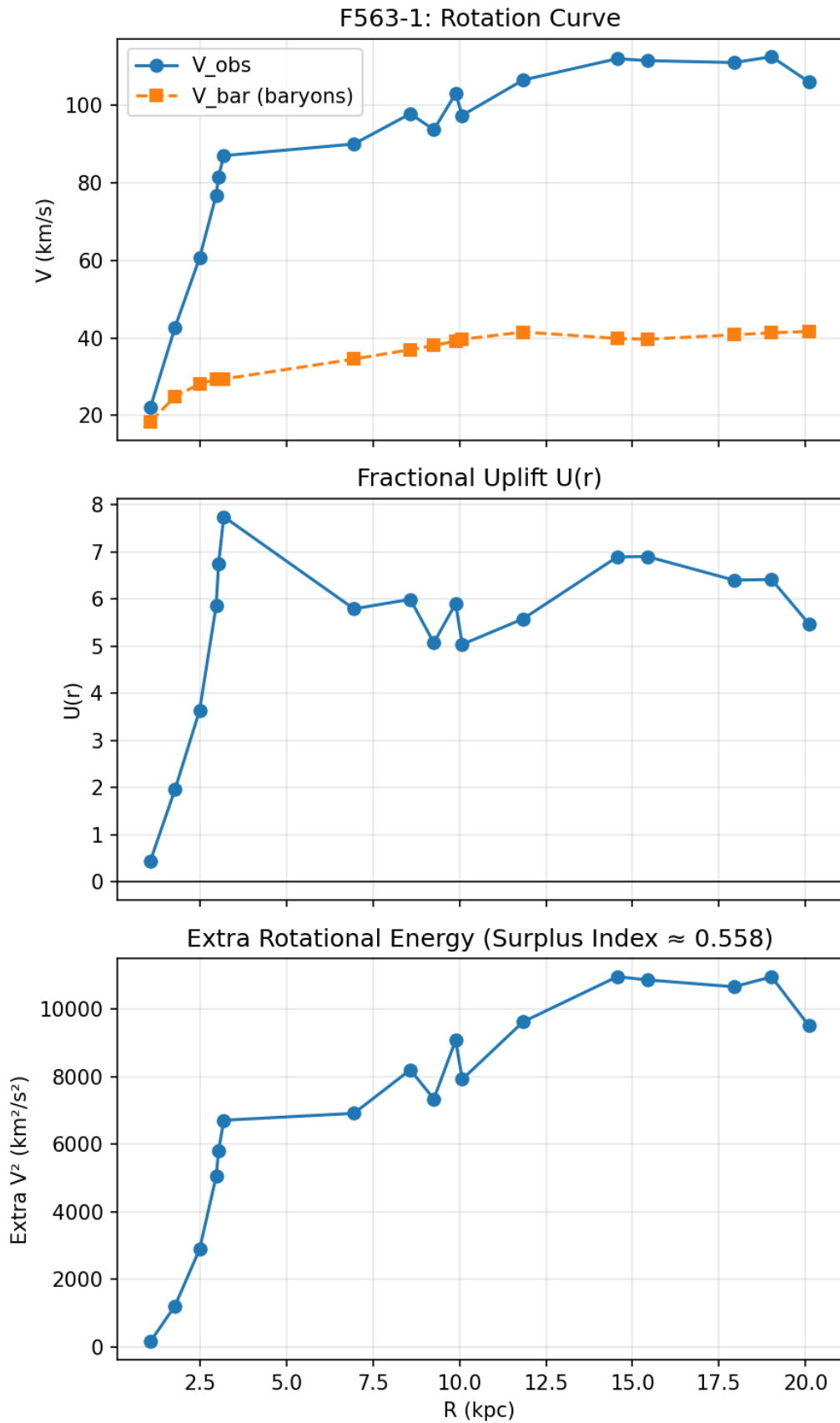
Fractional Uplift $U(r)$ Extra Rotational Energy (Surplus Index ≈ 0.240)

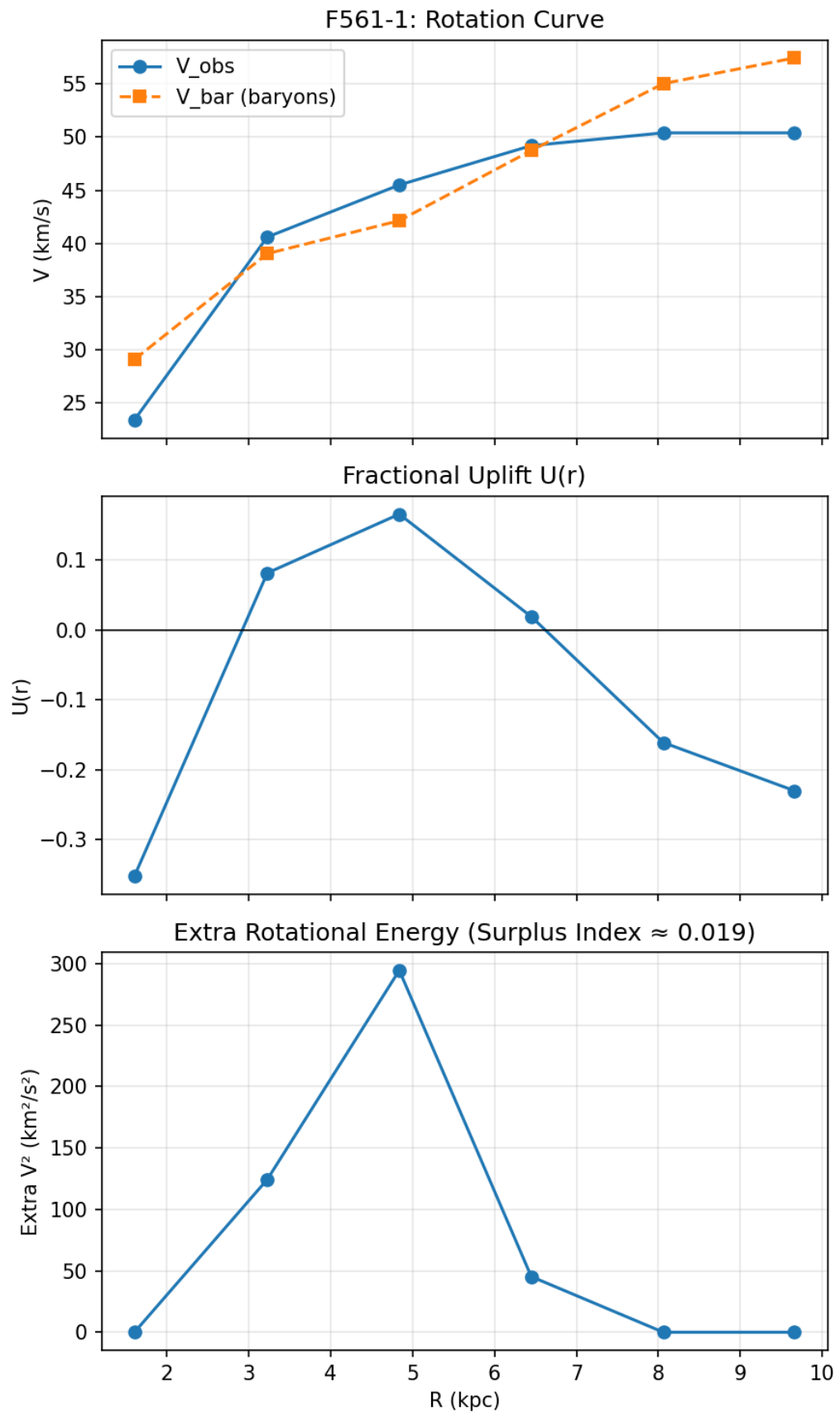
F565-V2: Rotation Curve

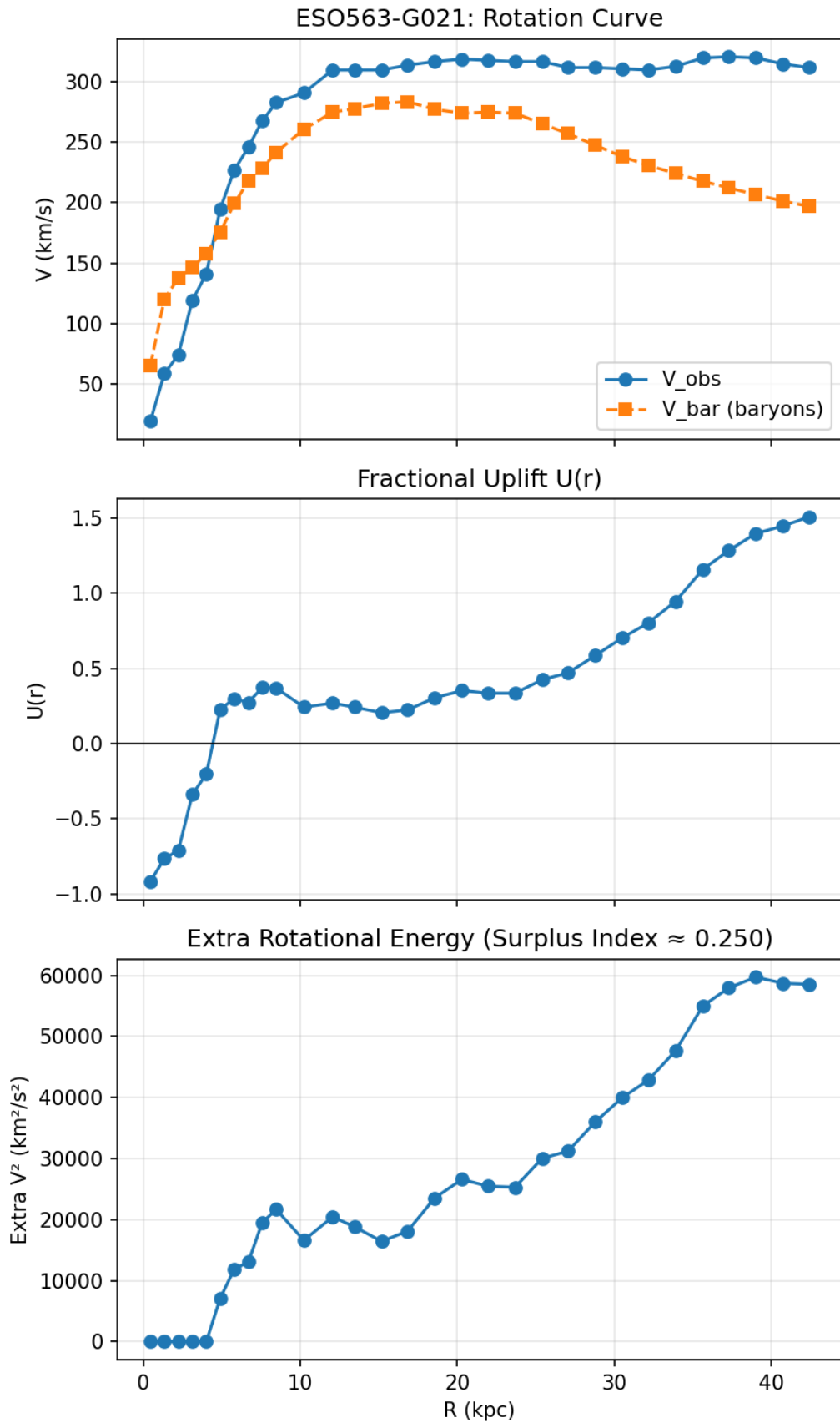
Fractional Uplift $U(r)$ Extra Rotational Energy (Surplus Index ≈ 0.585)

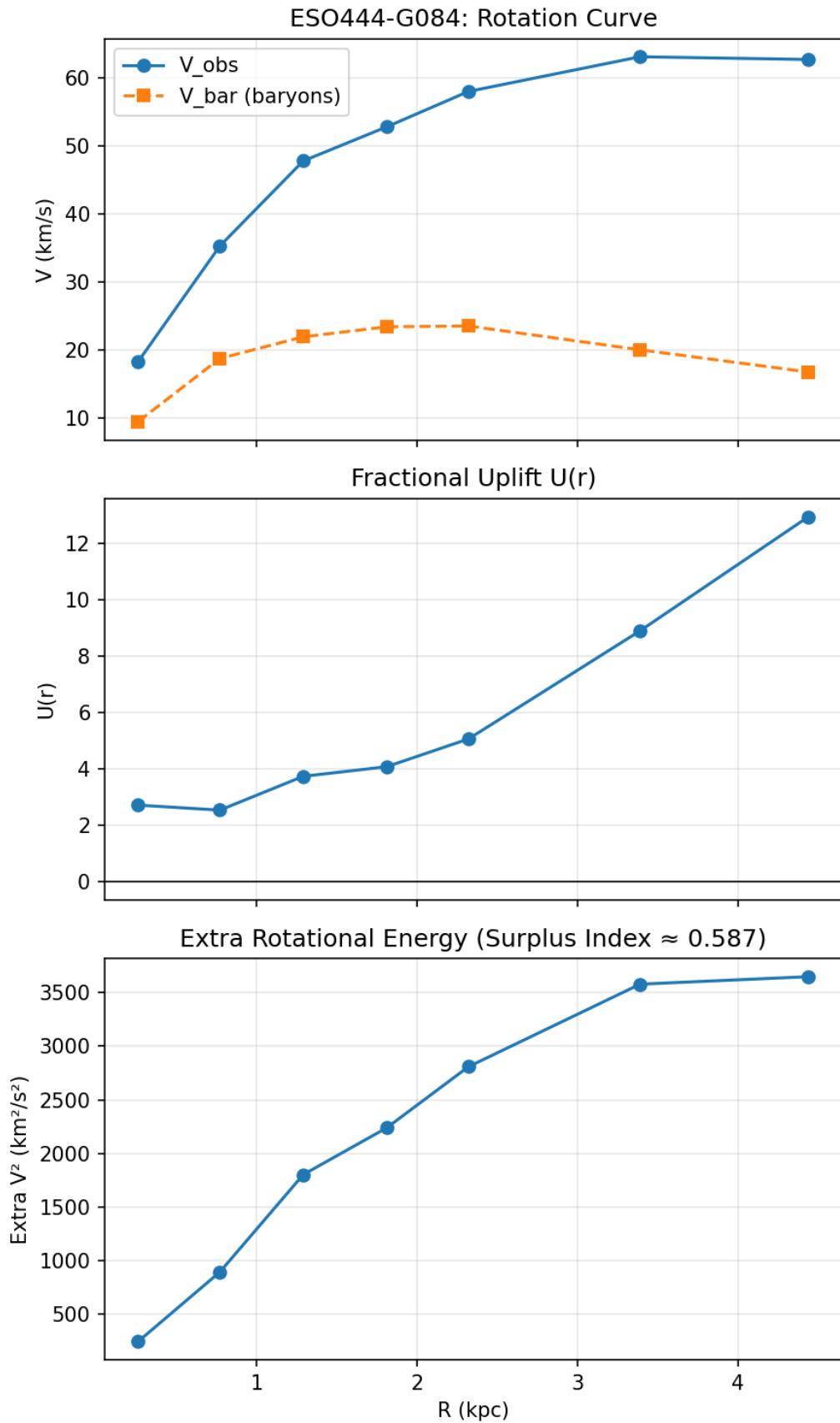


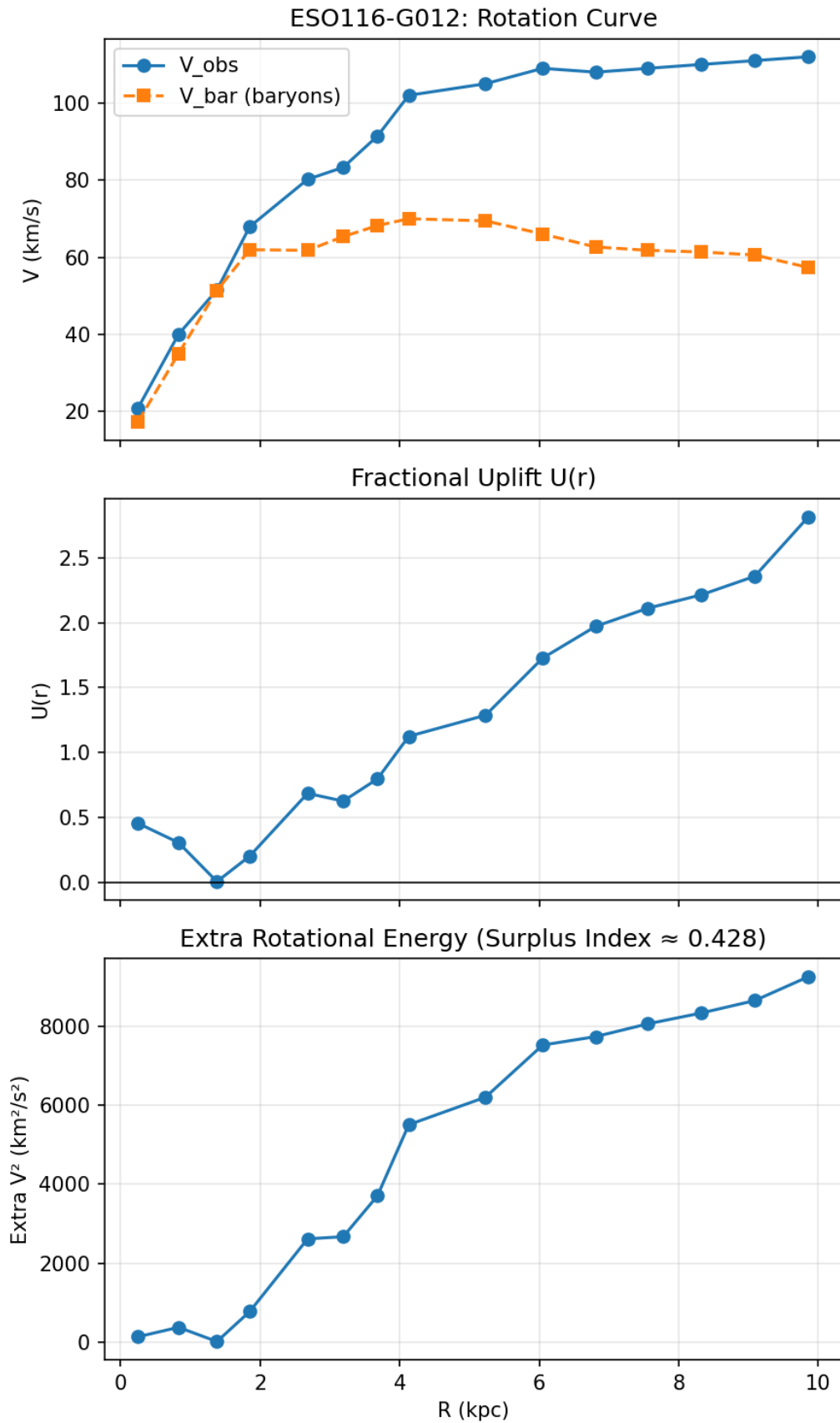


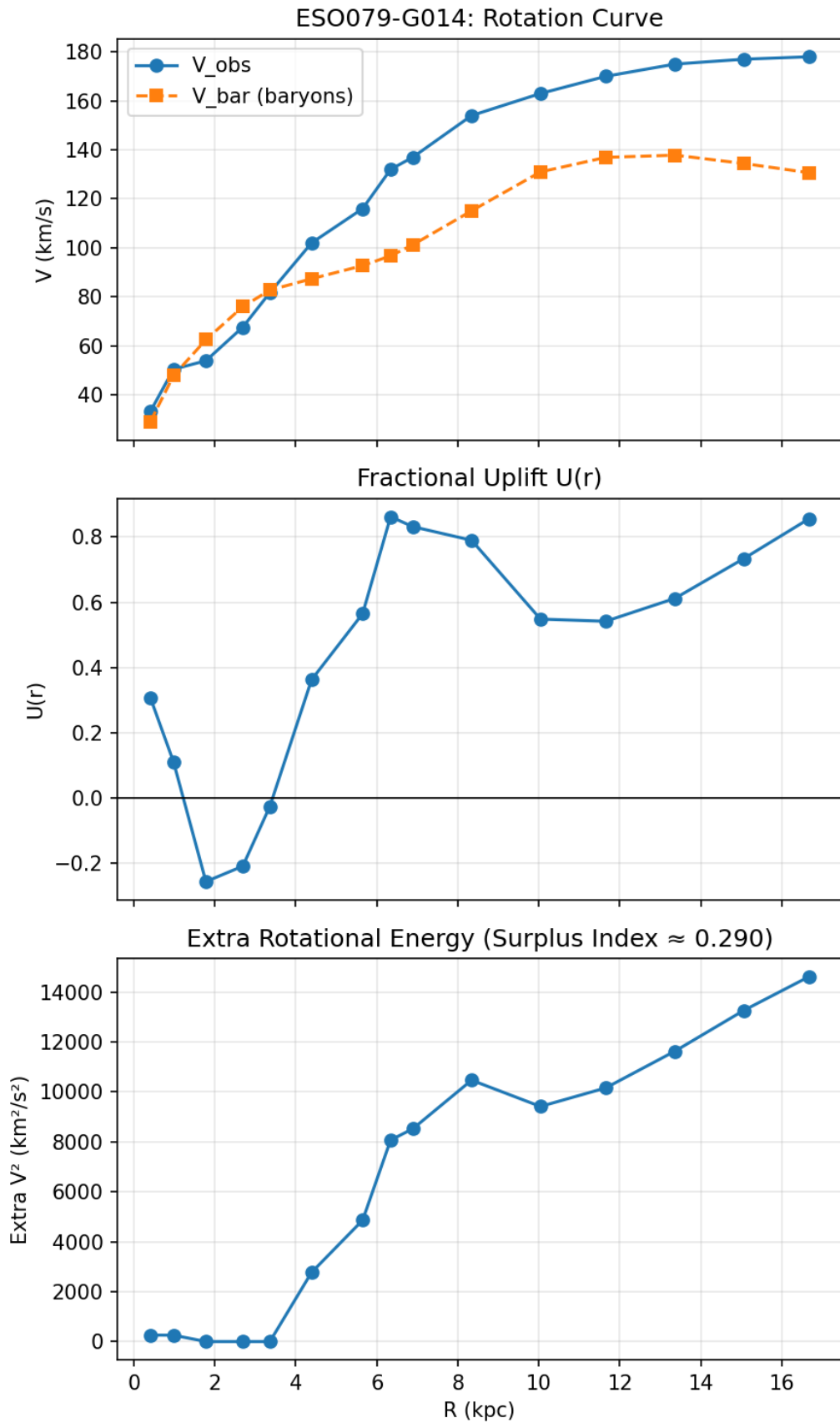


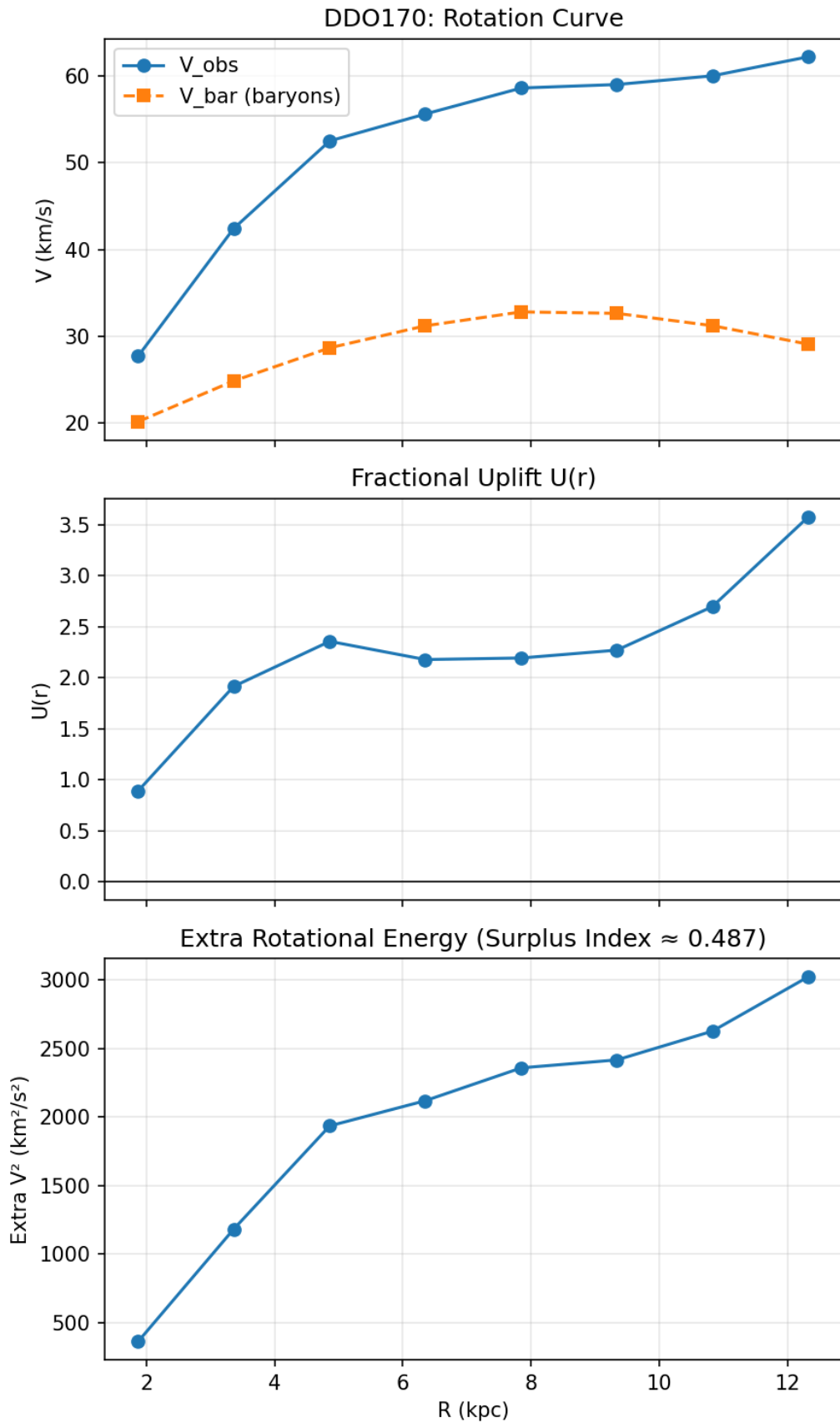


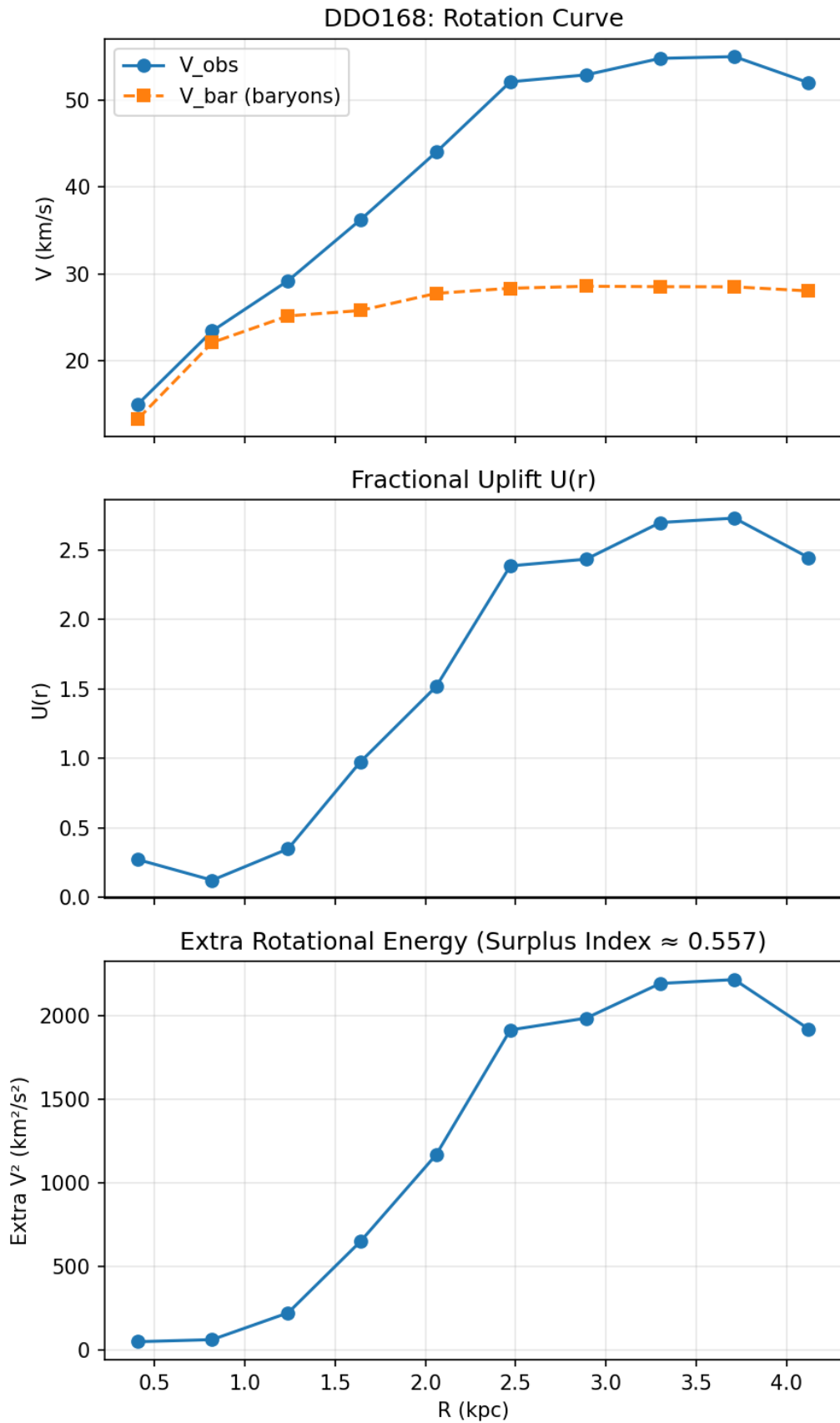


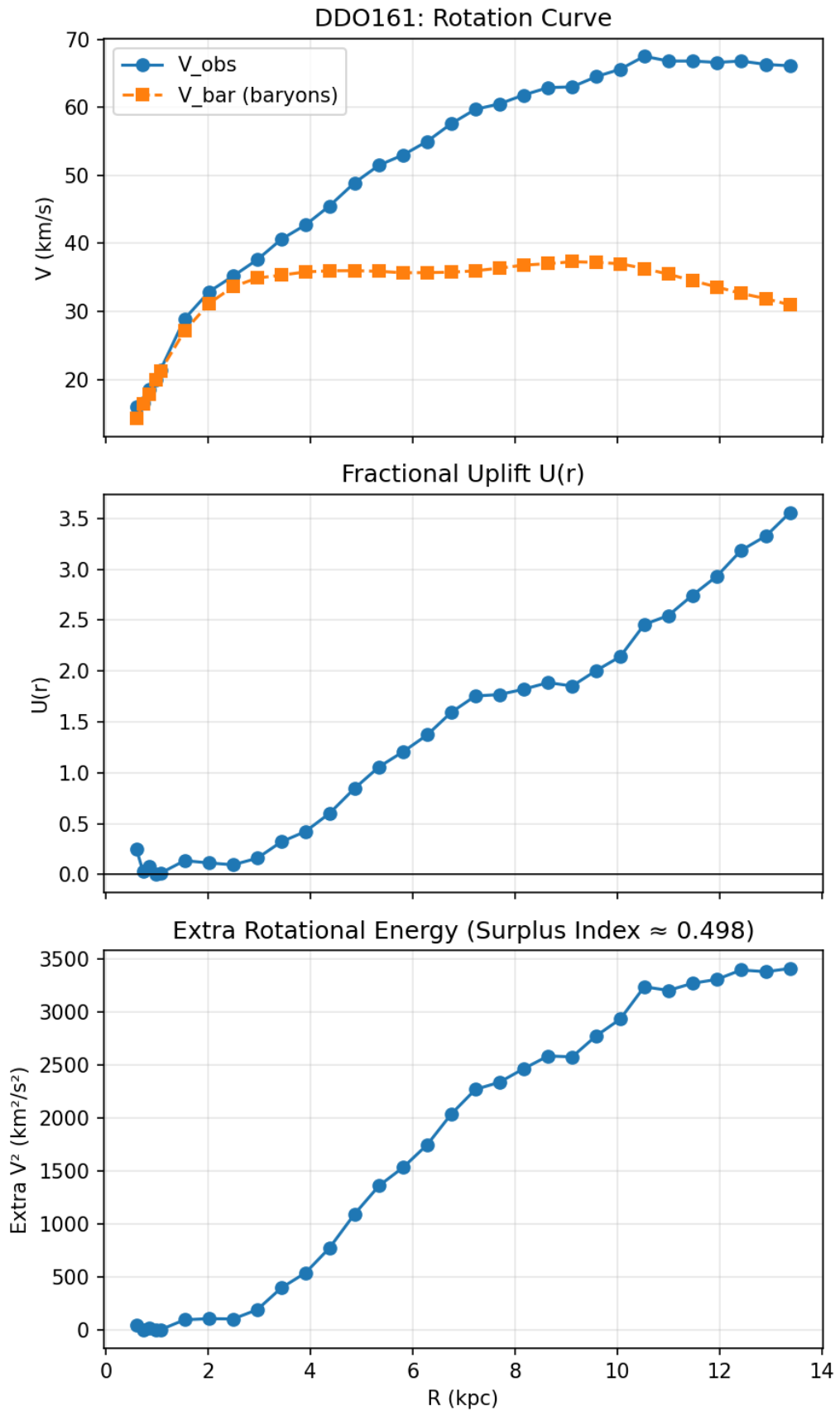


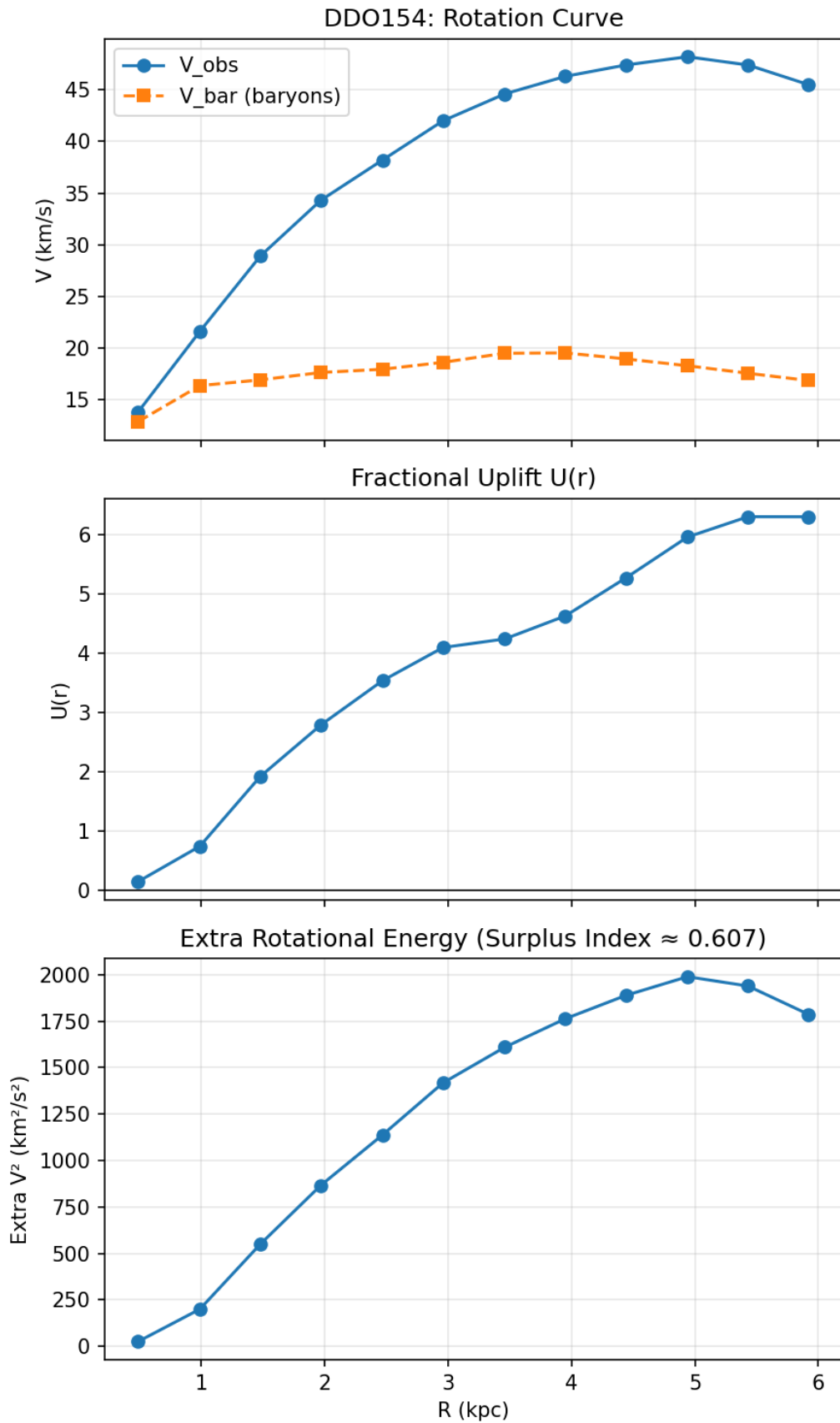


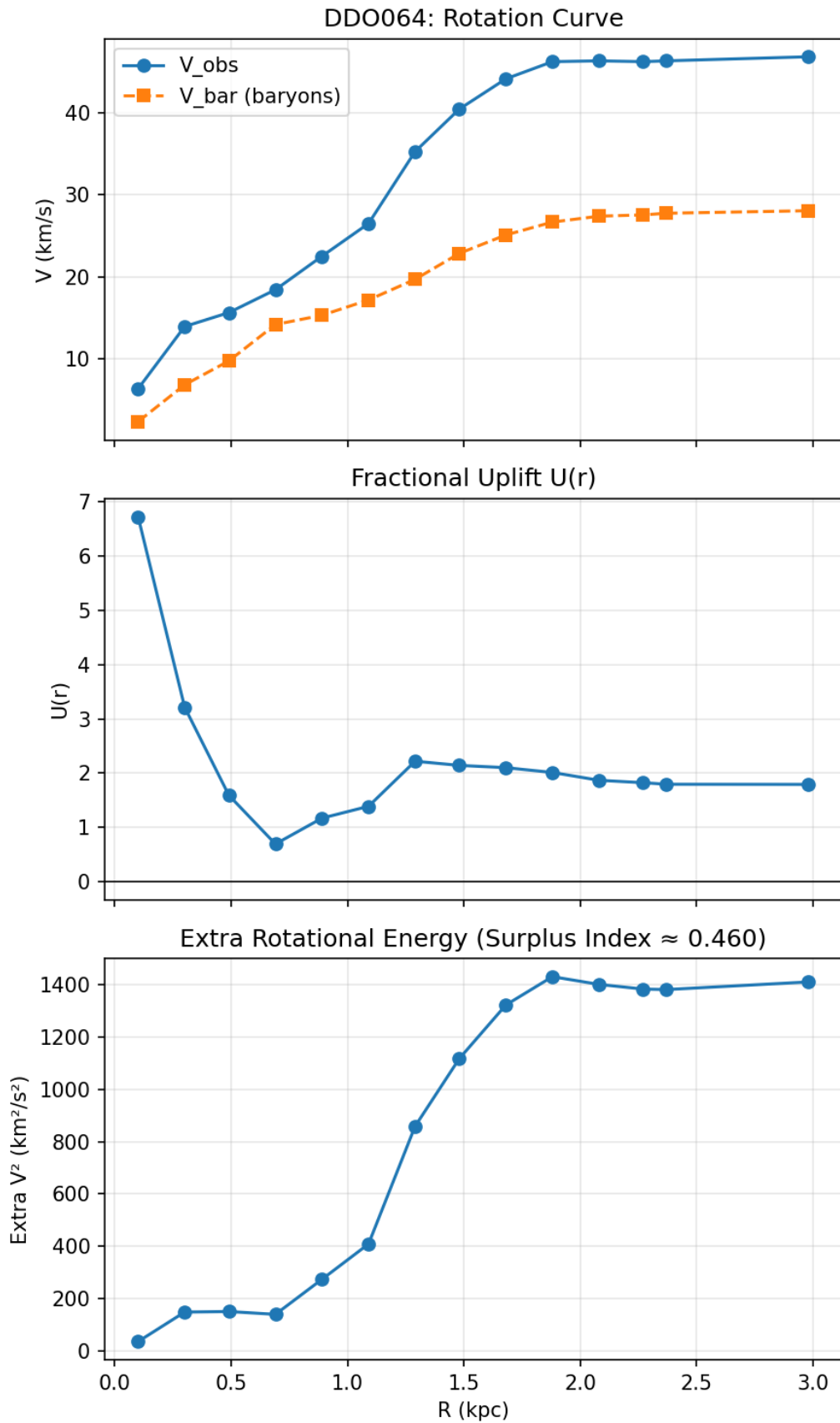


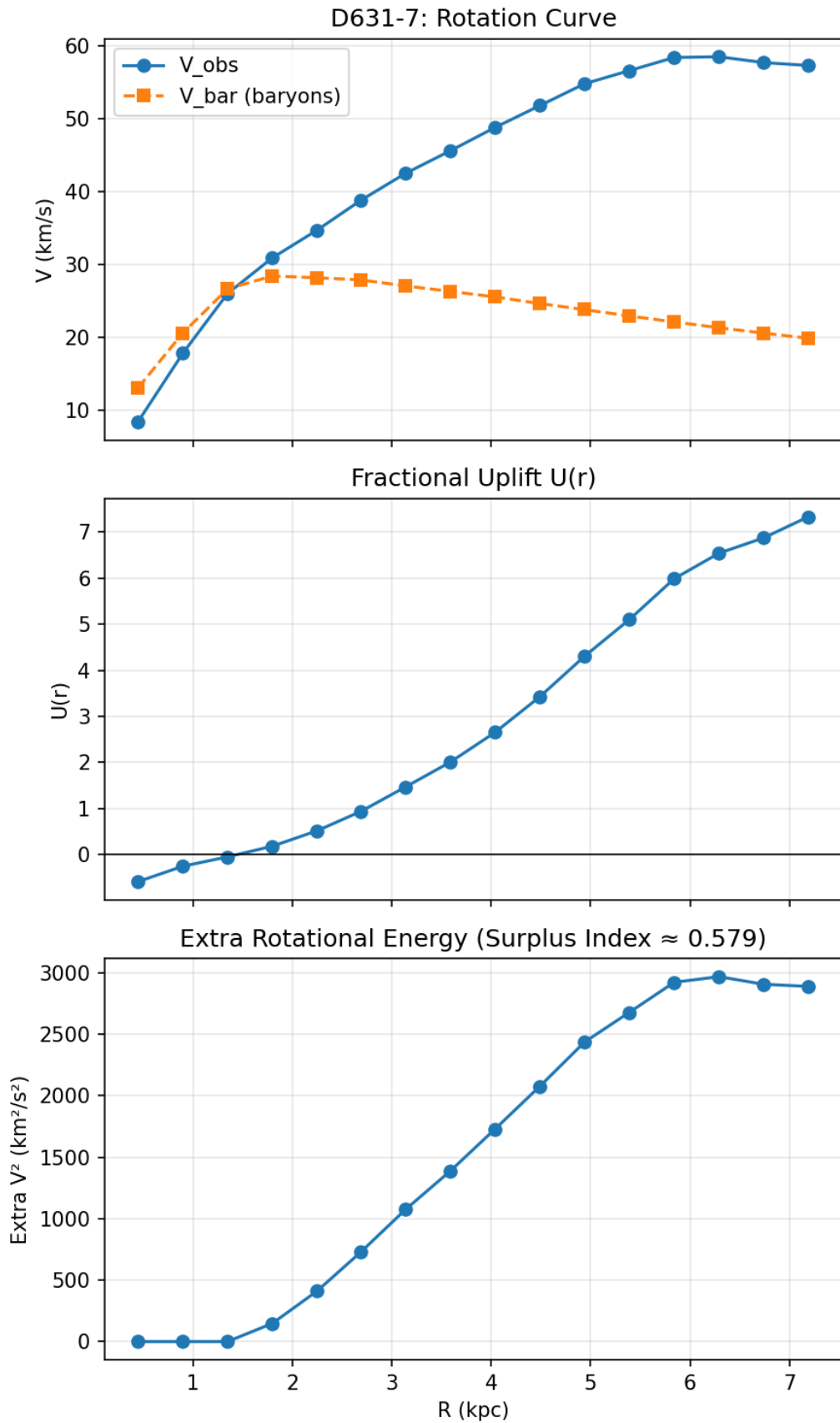


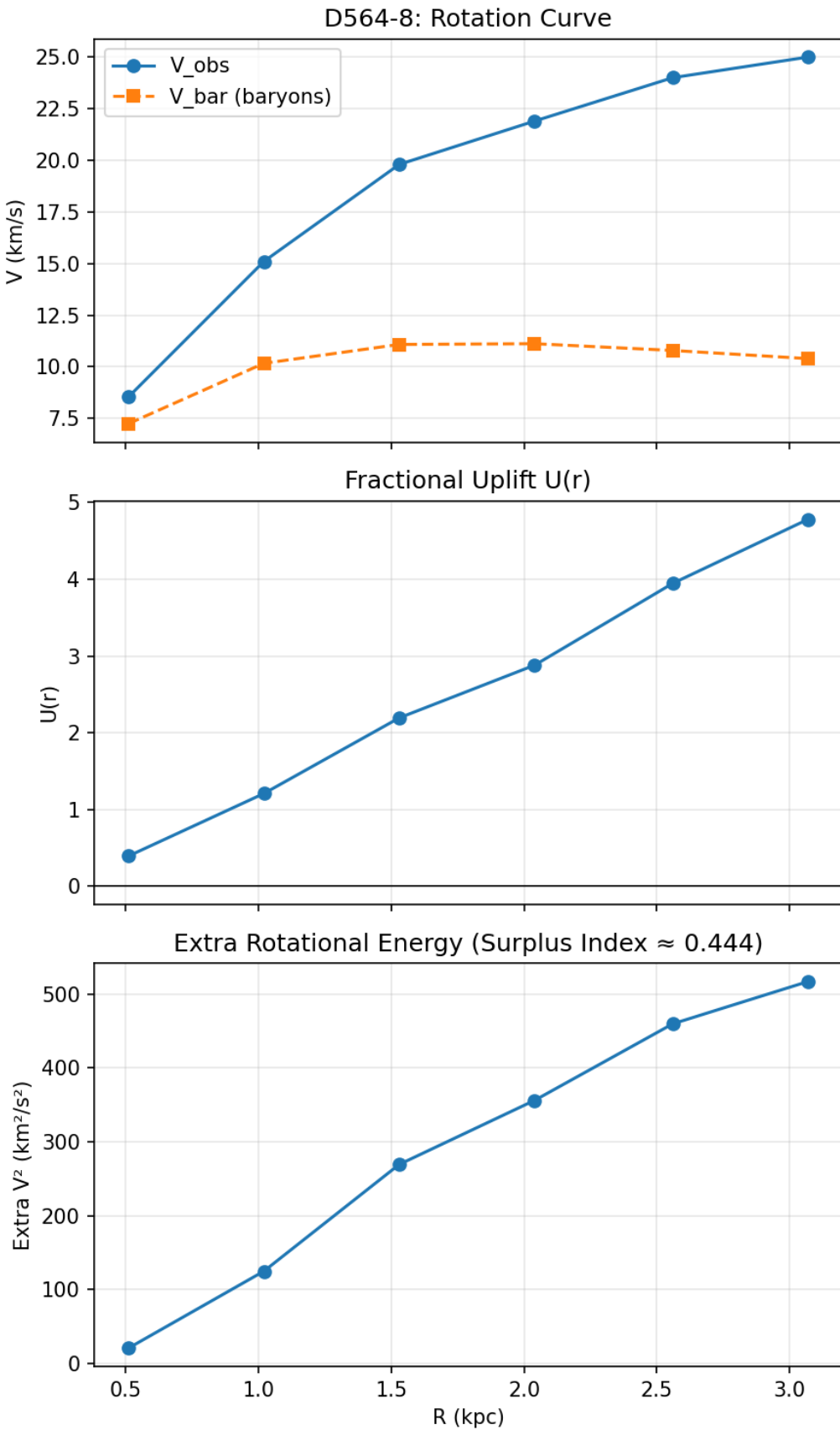




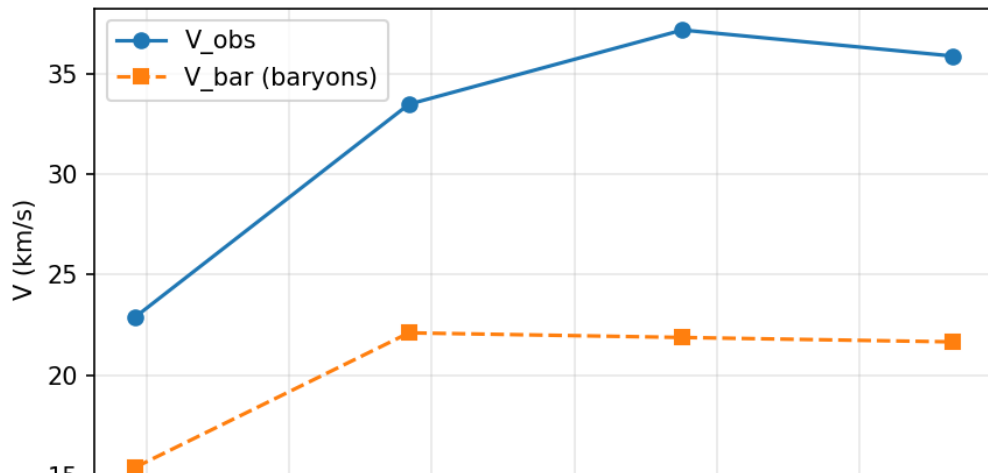
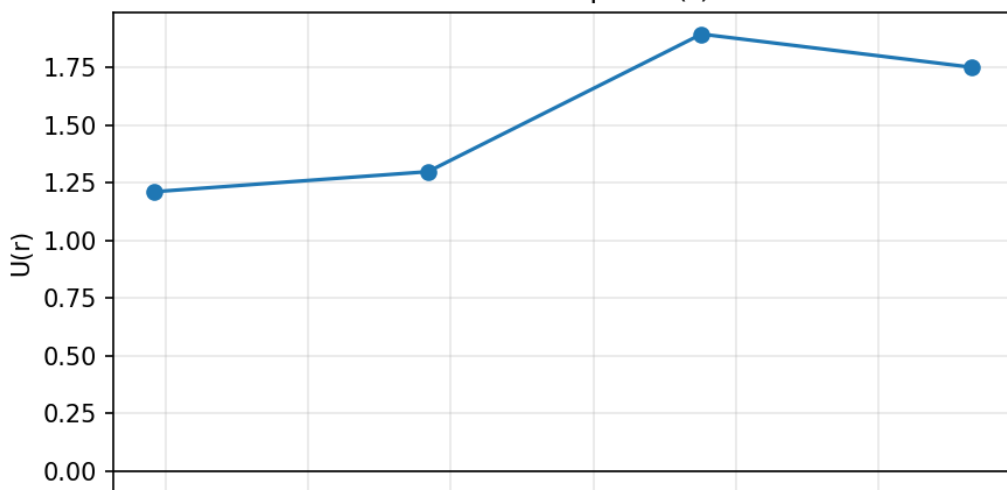
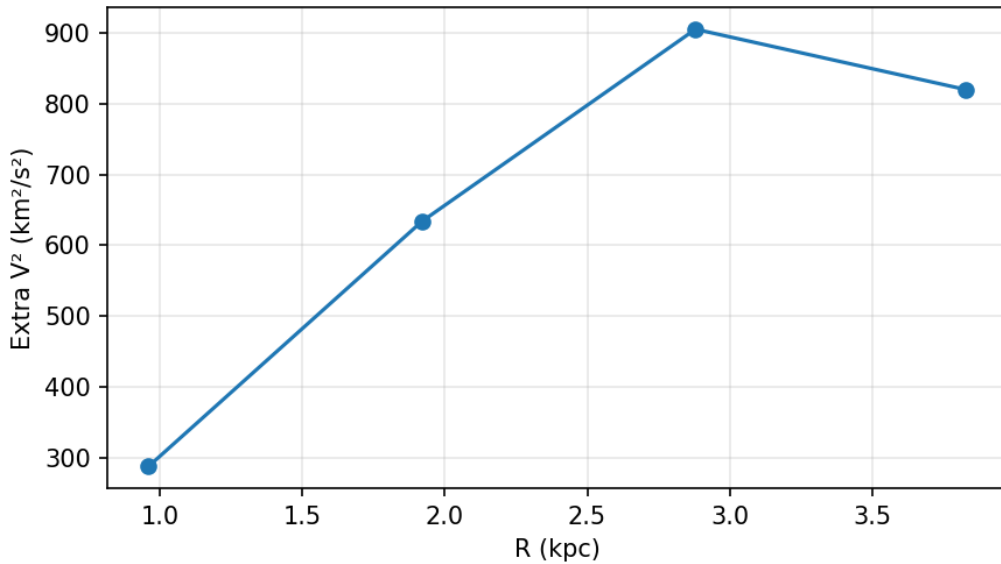


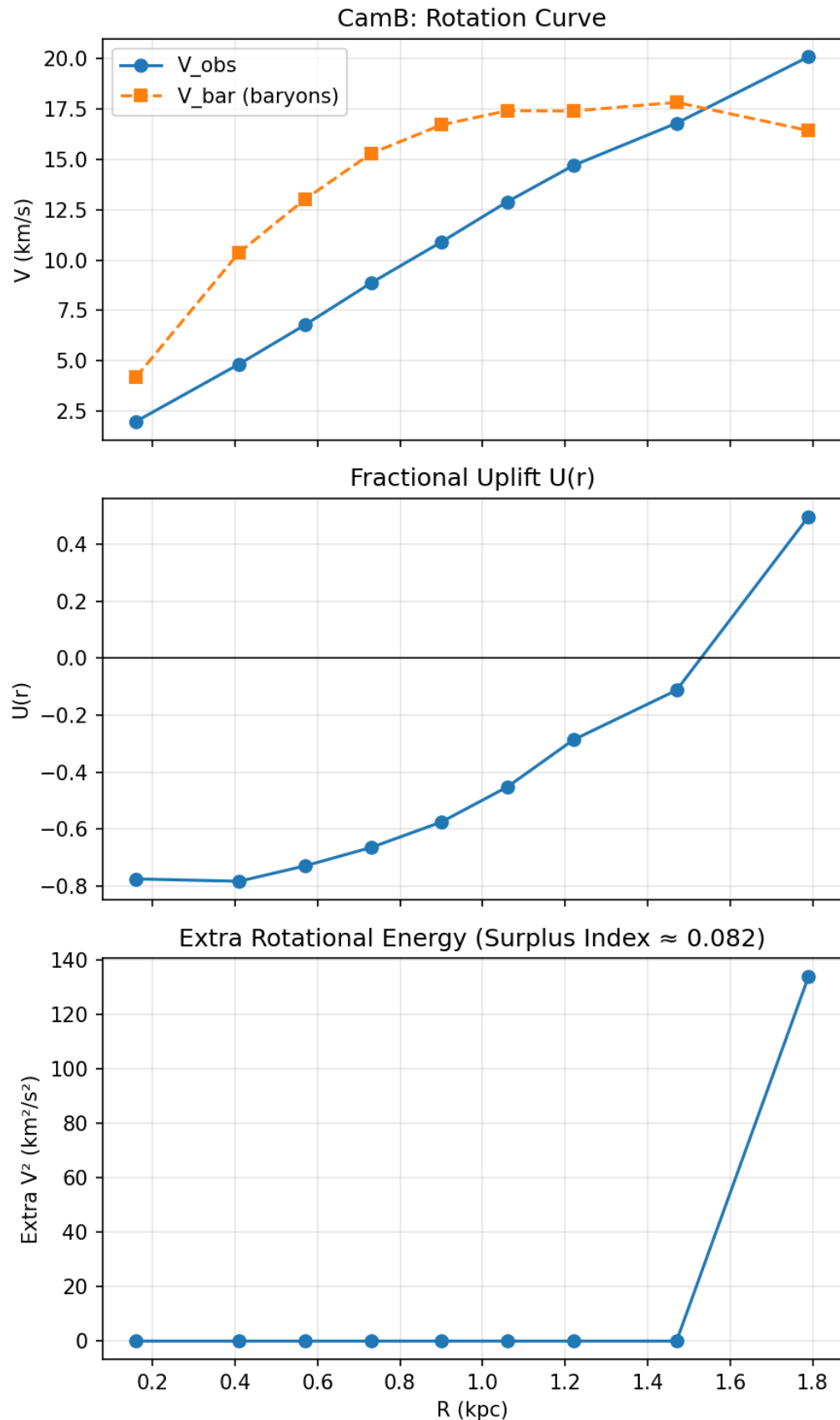






D512-2: Rotation Curve

Fractional Uplift $U(r)$ Extra Rotational Energy (Surplus Index ≈ 0.478)



SUPPLEMENTARY H. Extreme-Case Galaxies in the SPARC Sample

This supplement provides detailed case studies of the galaxies listed in Table 1. Each entry describes the observed morphology and kinematics, the diagnostic values of Surplus Index and Curl Index, and the structural conditions that enforce or suppress non-local torque transport. Together, these narratives furnish the empirical foundation for the transmission framework.

A. HIGH SURPLUS ENERGY INDEX

1. NGC 3109

NGC 3109 is a Magellanic-type dwarf galaxy with an elongated stellar disk and a strongly warped H I disk. Observations show that the warp and distortions are linked to past interactions with the nearby Antlia Dwarf. NGC 3109 is also part of a narrow, filament-like group of dwarf galaxies with a coherent velocity pattern, indicating a highly ordered and non-random dynamical environment.

Detailed H I mapping reveals a pronounced warp in the outer disk that aligns in velocity with gas associated with Antlia, supporting the idea of a past tidal encounter. This long-lived distortion provides a clear physical source of asymmetry in the gas disk, rather than a transient or noisy feature. On the stellar side, evidence for massive evolved stars indicates strong internal feedback, which can further maintain asymmetries in the disk.

Transmission diagnostics place NGC 3109 among the highest-surplus systems, with strong curl and positive uplift across much of the disk. These values indicate sustained angular-momentum and energy transport driven by both tidal distortion and internal feedback. The surplus extends from the inner regions into the warped outer disk, showing that transport is not confined to a narrow radius.

NGC 3109 therefore serves as a high-surplus reference case in which rotational energy is actively redistributed by structural forcing. Its dynamics show that angular-momentum transport is controlled by asymmetry and feedback, rather than by galaxy size or radial extent.

References: Jobin & Carignan, *AJ*, **100**, 648 (1990)[27]; Bellazzini et al., *A&A*, **559**, L11 (2013)[28]; Barnes & de Blok, *AJ*, **122**, 825 (2001) [29]; Menzies et al., *MNRAS*, **483**, 5150 (2019) [30].

2. NGC 3741

NGC 3741 is a dwarf irregular galaxy with one of the most extended H I disks ever observed, reaching far beyond its stellar body. The gas disk is strongly warped but remains broadly symmetric, and detailed analysis of its velocity field shows clear non-circular motions across a wide range of radii. These motions are persistent and systematic, indicating ongoing angular-momentum transport rather than random noise, with torque flux remaining active ($F_L \neq 0$) over most of the disk.

Transmission diagnostics place NGC 3741 in a regime where angular-momentum and energy redistribution are strong and sustained. The high Surplus Index and Curl Index show that rotational energy is being transferred outward through these non-circular motions. The surplus appears where the disk is warped and asymmetric and would vanish if the velocity field were purely circular, satisfying a clear falsifiability condition.

Independent studies of the galaxy's H I bar show that it rotates slowly, consistent with strong dynamical friction from a dominant dark-matter halo. While these measurements do not directly track torque flux, they support the picture of sustained structural asymmetry and ongoing angular-momentum redistribution. With a compact stellar component and an extremely extended, distorted gas disk, NGC 3741 provides a clear example in which large-scale transport is driven by structure rather than radius or stellar mass.

References: Gentile et al., *A&A*, **472**, 925 (2007) [31]; Banerjee et al., *MNRAS*, **434**, 1257 (2013) [32].

3. DDO 154

DDO 154 is a gas-dominated dwarf irregular galaxy with very little stellar mass and one of the most extended H I disks known. Deep H I observations trace the disk to extremely large radii and show clear warps and asymmetries, especially in the outer regions. These features break axisymmetry and produce measurable departures from simple circular rotation.

The transmission diagnostics show a high Surplus Index and a substantial Curl Index, placing DDO 154 in a regime where angular-momentum and energy transport are actively sustained by disk asymmetry. The surplus appears where the H I disk is warped or distorted, indicating that torque-driven transport remains active ($F_L \neq 0$) even at very large radii. Where the disk becomes smoother and more symmetric, the surplus declines, providing a clear falsifiability condition.

Independent studies of the stellar population show that much of the outer H I disk is dynamically quiet, with suppressed star formation, while localized asymmetric regions host ongoing activity. In the transmission picture, these quiet zones correspond to regions with little or no torque flux, while warped regions sustain transport and redistribution. DDO 154 therefore demonstrates, in a clean and isolated system, that extended gas asymmetries alone can drive angular-momentum transport without the need for interactions or massive stellar components.

References: Carignan & Purton, *AJ*, **506**, 125 (1998) [33]; Watts et al., *MNRAS*, **477**, 5554 (2018) [34].

4. UGC01281

UGC 01281 is a low-surface-brightness disk galaxy with a slowly rising rotation curve. Studies of large galaxy samples show that it follows the radial acceleration relation with very small scatter, indicating that its observed dynamics are tightly linked to its baryonic mass distribution rather than requiring fine-tuned modeling.

Independent analysis of UGC 01281 shows that its baryonic mass is unevenly distributed. When this asymmetry is taken into account, models based on dark-matter-only assumptions fail to reproduce the inner velocity profile, consistently overpredicting the observed rotation. This demonstrates that baryons, and especially their asymmetric distribution, play a dominant role in shaping the galaxy's kinematics.

Using transmission diagnostics, UGC 01281 shows a moderate Surplus Index and a high Curl Index, placing it in a regime where angular-momentum transport is active but not fully saturated. In this

regime, surplus energy is sustained by ongoing torque gradients produced by disk asymmetry. When asymmetry is reduced, the surplus diminishes, directly linking the observed dynamics to internal torque-driven transport rather than hidden mass.

Taken together, independent observational analyses and transmission diagnostics point to asymmetry as the controlling factor in UGC 01281. The galaxy therefore provides a clear example where internal structure, rather than unseen matter, governs the redistribution of angular momentum and energy.

References: Li et al., *A&A*, **615**, A3 (2018) [35]; Bar et al., *Phys. Rev. D*, **99**, 103020 (2019) [36].

5. ESO 444 G084

ESO 444 G084 is a compact dwarf irregular galaxy with a clearly asymmetric disk. H I observations show strong lopsidedness and outer distortions that break axisymmetry, placing the galaxy among the many dwarfs known to be morphologically and kinematically asymmetric. This sustained non-axisymmetry provides a natural source of internal torques.

The measured diagnostics show a large Surplus Index and Curl Index, indicating active angular-momentum and energy transport. The surplus appears where the disk is most distorted, demonstrating that transmission is controlled by structural asymmetry rather than galaxy size or radial extent, with $F_L \neq 0$.

More recent MeerKAT observations reveal a warped H I disk beyond the inner region, together with a steeply rising rotation curve and ongoing localized star formation. These features indicate that transport is spatially selective: regions that are symmetric remain dynamically quiet, while warped and lopsided regions sustain angular-momentum flux. ESO 444 G084 therefore provides a clear example of a low-mass dwarf in which internal transport is driven by structural forcing rather than scale.

References: Swaters et al., *A&A*, **390**, 829 (2002) [37]; Namumba et al., *A&A*, **699**, A372 (2025) [38].

B. EXTREME TRANSPORT-SUPPRESSED GALAXIES

This section documents a small set of galaxies frequently cited as extreme cases of dark matter deficiency and explains, for each system, why their observed velocity fields are dynamically consistent with suppressed internal transport. These galaxies are not treated as counterexamples to the transmission framework, but rather as limiting cases in which angular-momentum redistribution is minimal or dynamically irrelevant.

1 NGC 1052-DF2

NGC 1052-DF2 is an ultra-diffuse dwarf galaxy whose stellar and globular-cluster motions can be explained by the mass of its stars alone, with little evidence for dark matter. The galaxy shows no rotating disk, spiral arms, bar, or other long-lived asymmetric structures.

Its stars are supported mainly by random motions rather than rotation, placing the system close to a configuration where angular-momentum transfer is minimal. In this setting, the lack of inferred dark matter is consistent with a geometry in which internal transport is strongly suppressed.

References: van Dokkum et al. (2018), *Nature*, 555, 629[39]; Danieli et al. (2019), *ApJ*, 874, L1[39].

2 NGC 1052-DF4

NGC 1052-DF4 is an ultra-diffuse galaxy with structural and kinematic properties very similar to those of DF2. It shows no clear signs of disk rotation, spiral structure, or other non-axisymmetric features. The motions of its stars and globular clusters are dynamically cold and are well explained by the gravitational potential of the stellar mass alone, with little evidence for dark matter.

Because the galaxy lacks both significant rotation and structural features that could generate internal torques, angular-momentum and energy transport within DF4 is expected to be weak. The system is therefore consistent with a transport-suppressed configuration rather than one undergoing active internal redistribution.

References: van Dokkum et al. (2019), *ApJ*, 880, 91[39]; Shen et al. (2021), *ApJ*, 907, L7[40].

3 FCC 224

FCC 224 is an ultra-diffuse dwarf galaxy in the outer Fornax Cluster. Measurements of stellar and globular-cluster velocities show that its internal motions can be explained by the mass of its stars alone, with little evidence for dark matter within one effective radius. The galaxy contains an extended system of bright globular clusters and has an old, metal-poor, and fully quenched stellar population.

FCC 224 shows no clear signs of disk rotation, spiral arms, bars, or other asymmetric structures that could drive angular-momentum transfer. Its stellar motions are dominated by random velocities, with only very weak rotation. Because there are no strong torque-producing features, the galaxy is consistent with a state in which angular-momentum and energy transport are strongly suppressed, corresponding to the near-zero-flux ($F_L \approx 0$) limit of collisionless dynamics.

References: Buzzo., et.al., A&A, Volume 695, March 2025[41]

4 AGC 114905

AGC 114905 is a gas-rich ultra-diffuse dwarf galaxy whose H I rotation curve can be explained entirely by the mass of its observed baryons, with little or no need for dark matter within the measured disk. The galaxy is rotationally supported but has very low surface density and weak rotational shear. It shows no strong bars, spiral arms, or other asymmetric features.

The H I gas forms a thin, smoothly rotating disk with low velocity dispersion. Because the disk lacks strong non-axisymmetric structures, internal gravitational torques are weak. As a result, angular-momentum and energy transport within the disk are strongly suppressed, and the observed velocity field is consistent with a transport-inefficient, near-steady-state configuration rather than active redistribution.

References: Mancera Piña et al. (2019), *ApJ*, 883, L33[42]; Mancera Piña et al. (2020), *MNRAS*, 495, 3636[43].

5 NGC 1277

NGC 1277 is a compact, massive early-type galaxy whose stellar motions can be explained by the mass of its stars and central black hole alone, without requiring dark matter within several effective radii. Detailed dynamical models show that the galaxy is highly regular and nearly perfectly axisymmetric. It shows no bars, spiral features, warps, or other asymmetries.

Because the system is dynamically smooth and well ordered, there is little need for angular-momentum or energy transport beyond local stellar motions. In this case, the lack of inferred dark matter reflects the fact that large-scale transport is not required, rather than being actively suppressed. NGC 1277 therefore serves as a control example where the absence of dark matter coincides with a naturally transport-inactive dynamical state.

References: Yıldırım et al. (2015), *MNRAS*, 452, 1792[44]; Comerón et al. (2023), *A&A*, 675, A143[45]

Across these extreme systems, the absence of dark matter consistently coincides with morphologies and velocity fields that suppress internal angular-momentum and energy transport. These galaxies therefore define the transport-free boundary of the dynamical continuum explored in the main text, complementing the transport-dominated disk galaxies that populate the SPARC sample.

SUPPLEMENTARY I: Geometry-Controlled Angular-Momentum Transport in a Collisionless N-Body Disk

I.1. Purpose and Scope

This supplement documents the N-body simulations used in Section 10 of the main text to illustrate how **disk geometry controls angular-momentum transport** in collisionless stellar systems. The goal is not to simulate a realistic galaxy or to demonstrate spontaneous structure formation, but to provide a **controlled dynamical experiment** showing that, once coherent non axisymmetric geometry is present, the angular-momentum flux predicted by the Vlasov–Poisson moment equations becomes active and produces outer-disk rotational inheritance. All simulations are performed using the REBOUND N-body integrator with Newtonian gravity. No modification of gravity, no additional mass components, and no non-Hamiltonian dissipation are introduced.

I.2. Continuum Transport Equation

The collisionless evolution of a stellar disk is governed by the Vlasov–Poisson system,

$$\frac{\partial f}{\partial t} + \mathbf{v} \cdot \nabla_x f - \nabla \Phi \cdot \nabla_v f = 0, \quad \nabla^2 \Phi = 4\pi G \rho.$$

Defining the specific angular momentum $l = Rv_\phi$, the surface density of angular momentum is

$$L(R, t) = \int Rv_\phi f d^3v dz.$$

Multiplying the Vlasov equation by Rv_ϕ and integrating over velocity yields the exact transport identity

$$\frac{\partial L}{\partial t} = -\frac{1}{R} \frac{\partial}{\partial R} [RF_L(R, t)],$$

where the angular-momentum flux is

$$F_L(R, t) = \langle Rv_R v_\phi \rangle.$$

This equation contains **no source term**: angular momentum is conserved locally and globally. Any redistribution arises solely from the **divergence of the flux**.

I.3. N-Body Representation

In the N-body realization, the phase-space distribution is approximated by discrete particles,

$$f(\mathbf{x}, \mathbf{v}) \simeq \sum_{i=1}^N m_i \delta(\mathbf{x} - \mathbf{x}_i) \delta(\mathbf{v} - \mathbf{v}_i).$$

Within a radial bin centered at R , the continuum quantities become

$$\begin{aligned} L(R) &\rightarrow \sum_{i \in R} m_i R_i v_{\phi,i}, \\ F_L(R) &\rightarrow \langle Rv_R v_\phi \rangle_R = \frac{1}{M_R} \sum_{i \in R} m_i R_i v_{R,i} v_{\phi,i}. \end{aligned}$$

Thus the particle system directly samples the same transport equation as the continuum theory, with the flux measured from correlated radial and azimuthal velocities.

I.4. Initial Disk Model

The simulations begin with a cold, self-gravitating exponential disk with surface density

$$\Sigma(R) \propto e^{-R/R_d},$$

sampled using $N = 3000$ equal-mass particles. Particle positions are drawn from an exponential radial distribution and uniform azimuth. Initial velocities are assigned to produce circular motion consistent with a smooth baryonic rotation curve.

A Plummer softening length $\epsilon = 0.05$ is used to suppress close two-body encounters and ensure that the evolution remains in the collisionless regime.

I.5. Controlled Geometry: Axisymmetric vs Spiral Disk

To isolate the role of geometry, two simulations are evolved under **identical numerical and gravitational conditions**, differing only in their imposed symmetry:

Case A: Axisymmetric Control

No non axisymmetric forcing is applied. The disk remains close to spherical/axisymmetric throughout the evolution.

Case B: Spiral Geometry

A weak, rotating $m = 2$ tangential acceleration is applied using REBOUND's additional_forces interface. This forcing maintains a long-lived spiral-like pattern but does **not** add mass or net angular momentum to the system. Its role is purely geometric: to sustain coherent non axisymmetric structure and prevent cancellation of velocity correlations.

This setup is intended to mimic the dynamical role of spiral structure, not its origin.

I.6. Measured Quantities and Figure Definitions

At each output time, particles are binned radially and the following diagnostics are computed:

- **Mean rotational velocity**

$$\bar{v}_\phi(R) = \langle v_\phi \rangle_R.$$

- **Angular-momentum flux**

$$F_L(R, t) = \langle R v_R v_\phi \rangle_R.$$

- **Rotational energy proxy**

$$E_{\text{rot}}(R) = \frac{1}{2} R^2 \bar{v}_\phi^2(R).$$

Figures 3–6 in the main text correspond to:

- particle snapshots (orbital geometry),
- surface-density evolution $\Sigma(R, t)$,

- angular-momentum flux $F_L(R, t)$,
- rotational uplift and surplus diagnostics.

I.7. Results

Axisymmetric Case

In the axisymmetric control simulation, particle orbits remain quasi-circular and radially confined. The angular-momentum flux fluctuates around zero at all radii. While finite- N noise produces instantaneous nonzero values, the flux divergence averages out over time, and no secular redistribution of angular momentum or rotational energy is observed. The outer disk remains dynamically cold and rotationally under-supported.

Spiral Geometry Case

In the spiral-geometry simulation, coherent correlations between v_R and v_ϕ persist over extended radial ranges. As a result, a structured angular-momentum flux develops: the inner disk exports angular momentum ($F_L < 0$), while the outer disk inherits it ($F_L > 0$).

Although the surface density at large radii remains low, the outer disk acquires enhanced rotational support because the transported quantity scales with specific angular momentum Rv_ϕ , not mass alone. This produces a clear outer-disk rotational surplus consistent with the behavior shown in Figures 3–6.

I.8. Interpretation

The simulations demonstrate that **angular-momentum transport in collisionless disks is controlled by symmetry rather than conservation laws or numerical resolution**. In perfectly symmetric systems, angular momentum remains trapped despite local fluctuations. Once coherent non axisymmetric geometry is present, correlated radial–azimuthal motion organizes into a sustained flux that redistributes rotational support outward.

Crucially, this redistribution does not create angular momentum. It reflects the activation of the transport channel already present in the Vlasov–Poisson hierarchy.

I.9. Conclusion

This N-body experiment provides a controlled dynamical illustration of the transmission mechanism discussed in the main text. When coherent non axisymmetric geometry is maintained, angular-momentum flux emerges naturally from collisionless dynamics and produces outer-disk rotational inheritance without invoking additional mass components or modified gravity.

The experiment therefore supports the central claim of the paper: **extended rotation curves can arise from geometry-enabled angular-momentum transport within standard Newtonian dynamics**.